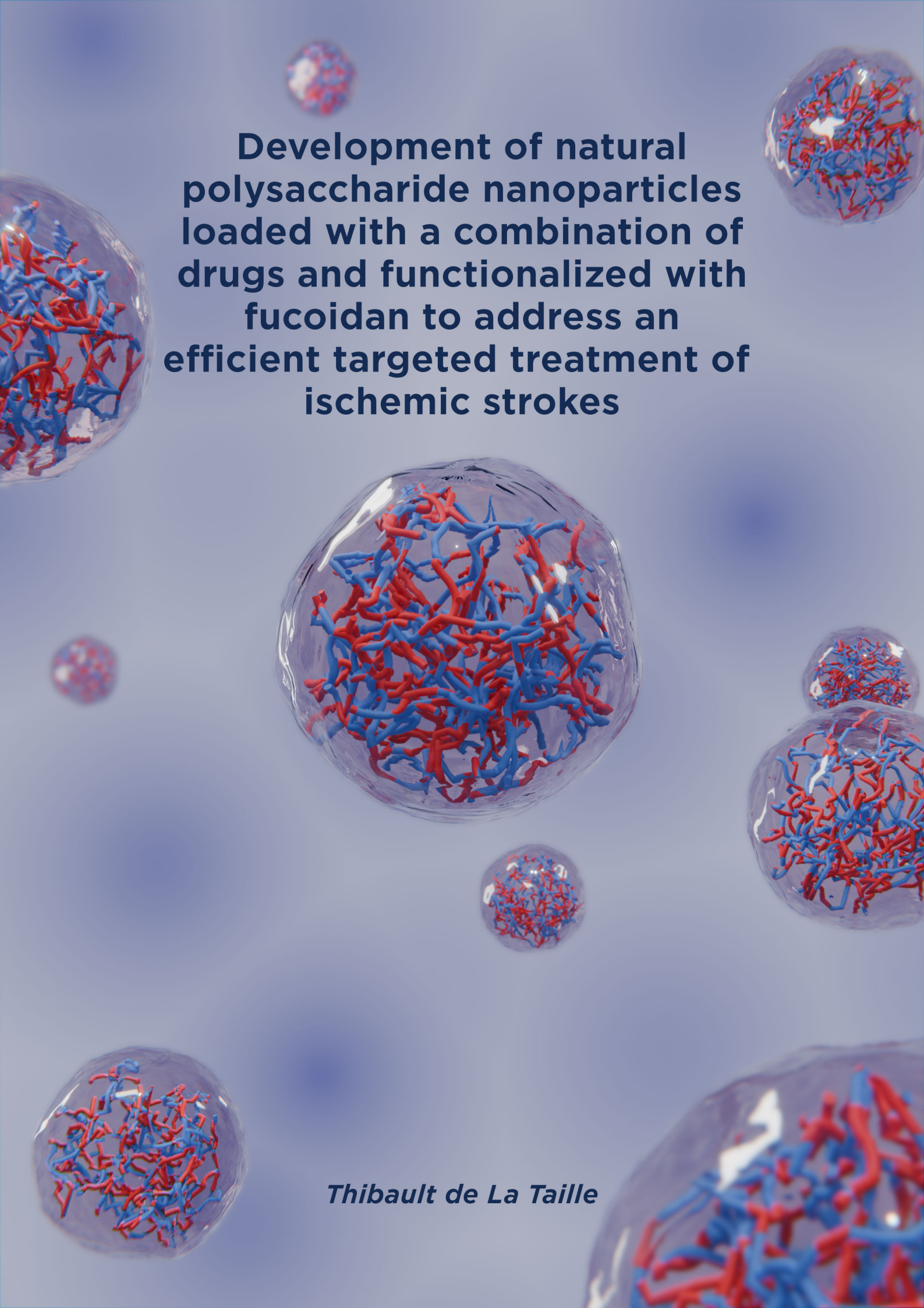
Development of natural polysaccharide nanoparticles loaded with a combination of drugs and functionalized with fucoidan to address an efficient targeted treatment of ischemic strokes



Thibault de La Taille

Cover by Thibault de La Taille

UNIVERSITÉ PARIS XIII – SORBONNE PARIS NORD

École doctorale Sciences, Technologies, Santé Galilée

Développement de nanoparticules de polysaccharides naturels, chargées avec une combinaison d'actifs et fonctionnalisées avec du fucoïdane afin de réaliser un traitement ciblé et efficace des accidents vasculaires cérébraux

---

Development of natural polysaccharide nanoparticles loaded with a combination of drugs and functionalized with fucoidan to address an efficient targeted treatment of ischemic strokes

---

THÈSE DE DOCTORAT
présentée par

Thibault DE LA TAILLE
Laboratoire de Recherche Vasculaire Translationnelle, INSERM UMRS1148
Team 4: Nanotechnologies for vascular imaging and medicine

pour l'obtention du grade de
DOCTEUR EN SCIENCES DE LA VIE ET DE LA SANTE

soutenue le Jeudi 12 Décembre 2024 devant le jury d'examen constitué de :

BOUSQUET Guilhem	*USPN*	Président du Jury
MIGNET Nathalie	*CNRS*	Rapportrice
MATRICARDI Pietro	*"Sapienza" Università di Roma*	Rapporteur
AZIBANI Feriel	*INSERM*	Examinatrice
PAPAGIANNAKI Chrysanthi	*CHU de Rouen*	Examinatrice
CHAUBET Frédéric	*USPN*	Directeur de thèse
CHAUVIERRE Cédric	*INSERM*	Co-Directeur de thèse

Acknowledgements

First, I would like to thank Dr. Nathalie Mignet and Pr. Pietro Matricardi for agreeing to be rapporteurs for this thesis manuscript, and for assessing my work. I also wish to thank Dr. Feriel Azibani, Pr. Guilhem Bousquet and Dr. Chrysanthi Papagiannaki for their role as examinators and their dedication in evaluating my PhD defense.

I express my most sincere gratitude to my two PhD supervisors, Pr. Frédéric Chaubet and Dr. Cédric Chauvierre (Head of Team 4: Nanotechnologies for vascular imaging and medicine). Thank you for having taken the time at the beginning of summer in 2021 to present me with your work and having convinced me to start this PhD, even though this path was not yet clear to me. Throughout this journey, I could always count on you to provide me with kind supervision, to offer support whenever I needed it and to entertain passionate scientific exchanges to discuss the good (and the bad) ideas that I could propose. You knew how to offer me enough independence so that I may grow as a researcher while always having my back and offering guidance when necessary. Thanks to Pr. Frédéric Chaubet's vast scientific expertise as well as knowledge of polysaccharides and nanoparticle synthesis, the development of this project was possible, but his energy and optimistic outlook on research were also key to this project's outcome. I cannot thank Dr. Cédric Chauvierre enough for knowing when to push me, provoke me and challenge me to improve my science and always look forward, but for also knowing when to tell me to step back, rest and change perspectives. This journey was accompanied by good and difficult days, and he taught me how to navigate through both.

My grateful thanks go to Dr. Didier Letourneur, the head of the LVTS laboratory and of the Team 3 "Cardiovascular Bioengineering", who provided me an opportunity to join the LVTS laboratory and Team 3, for sharing his expertise on biomaterials, valuable guidance, critical outlook and constant encouragement.

My gratitude also goes to all the LVTS members who shared their positiveness, their scientific knowledge and who participated in making these three years both exciting for the scientific part, and fun and enjoyable through the human connections that exists there. No scientific work could be possible alone, and you can find at the LVTS all the help you need when necessary. It is therefore my pleasure to thank Dr. Graciela Pavon-Djavid for her counselling

during these three years and her help with some of our experiments, including histochemistry, which would not have been possible without her. Similarly, I especially thank Rachida Aid, without whom this Team could not function as she concentrates all the techniques and methods acquired in this lab, and patiently transmits them to new team members; her experience and participation in all my *in vivo* experiments were fundamental to their completion. I want to thank Dr. Teresa Simon Yarza for sharing scientific discussions and good addresses in the Basque country, Dr. Véronique Arocas for her support establishing *in vivo* protocols and authorization, Dr. Yoann Lalatonne for his support with characterization methods such as TXRF, Dr. Benoit Ho-Tin-Noé for his help with designing adequate thrombosis models, Stéphane Loyau for his guidance when working with human blood samples and thrombosis, and Joaquim Li with Inserm Transfert who helped us for the writing and submission of our patent. My thanks also go to Khadija Bertino and the LTVS secretary, without whom our research would not be possible. I want to acknowledge the guidance and experience of former LVTS members, such as Dr. Paola Aprile, Dr. Alessandra Dellaquila, Dr. Lucie Gernez, Dr. Mélodie Doute, Dr. Zakaria Mougin, Dr. Mathilde Maillard, Albane Carré and Dr. Louise Fournier, a former PhD student of Dr. Cédric Chauvierre working with microbubbles, who guided me through the beginning of my PhD. I warmly thank the current members of our team for their warm support, including Dr. Baptiste Amouroux, Dr. Xiaochen Huang, Dr. Vanessa Morais Lima and others. I especially want to acknowledge the future doctors of LVTS, Eliott Lopez, Ophélie Chapellier, Yang Zhang and all the others with whom we shared hopes, failures and good times throughout this adventure, and notably Pierre Sarfati who started his PhD in our team a year after me on a neighboring project, as we worked together on many specific issues of nanoparticles formulation and characterization.

I also present my gratitude to Chloé Dujardin, a PhD student in our team and a friend for quite some years already, without whom this PhD would not be possible. Thank you for providing me with this opportunity and for our continuing friendship, and I look forward to following your brilliant scientific career.

I thank my parents and my sisters for their unconditional love and encouragement, even if it meant listening to a lecture on how gondola lifts work. My gratitude also goes to my grandparents who welcomed me during the writing of this PhD, and to my family and close friends who supported me all along this journey. Finally, I must express my warmest thanks to my partner, Auriane Monti, for her love, her ever comforting presence and her patience during these years.

« Science is fun. Science is curiosity. We all have natural curiosity. Science is a process of investigating. It's posing questions and coming up with a method. It's delving in. »

Sally Ride

Table of contents

Acknowledgements ***2***
Table of contents ***6***
Abbreviations and Acronyms ***10***
List of Figures ***11***
List of Tables ***12***
General introduction and project description ***14***
Part One. Thrombotic diseases and the nanomedicine opportunity ***18***

I. Thrombotic diseases: a challenge for human health 19
A) Cardiovascular and thrombotic diseases: a global health crisis *19*
B) Thrombosis pathophysiology *22*
B.1) General thrombus formation 22
B.2) Venous thromboembolism 25
B.3) Atherosclerosis and arterial thrombi 26
B.4) Stroke: a special case 28
C) Treatment of thrombotic diseases *33*
C.1) Anticoagulants 33
C.2) Antiplatelets 34
C.3) Fibrinolytic drugs 35
C.4) Mechanical thrombectomy 40
C.5) Limitations of current treatments for thrombotic diseases 41

II. Nanomedicine: another approach for thrombotic diseases 44
A) Nanomedicine relevance *44*
B) Nanoparticle types *49*
B.1) Systematic literature review 50
B.2) Polymeric nanoparticles 52
B.3) Lipid-based nanoparticles 56
B.4) Inorganic nanoparticles 59
B.5) Miscellaneous nanoparticles 62
C) Nanoparticle targeting strategies *64*
C.1) Passive targeting 65
C.2) Single molecular targeting 65
C.3) Multiple molecular targeting 67
C.4) Magnetic targeting 69
D) Applications of nanomedicine for stroke and clinical translation *71*
D.1) Preclinical developments 73
D.2) Clinical advancement 78
D.3) Summary 80

III. Polysaccharide-based hydrogel nanoparticles 81
A) Hydrogels and nanogels *81*
A.1) Hydrogel composition and structures 82
A.2) Nanogels 85

B) Polysaccharide nanoparticles for drug delivery 86
B.1) Chitosan 87
B.2) Cellulose 87
B.3) Starch 87
B.4) Hyaluronan 88
B.5) Alginate 88
B.6) Dextran 89
Part Two. Experimental results 90
I. Nanoparticle design 91
A) Materials and methods 91
A.1) Materials 91
A.2) Nanoparticle synthesis 91
A.3) Physico-chemical characterization 92
A.4) Size optimization 93
A.5) Microemulsion 93
A.6) Fucoidan and phosphate chemical quantification 94
A.7) Statistical analysis 95
B) From an emulsion to nanoparticles synthesis 95
B.1) The choice of polysaccharide hydrogel nanoparticles 95
B.2) Previous works and established protocol 97
B.3) Crosslinking control 99
B.4) Improved emulsification 104
B.5) Optimized formulation and characterization 108
C) Preliminary works and future directions 112
C.1) Towards a translatable formulation 112
C.2) Exploring the microemulsion formulation 116
II. Biological characterization and drug loading 118
A) Materials and methods 118
A.1) Materials 118
A.2) Cell culture and cytotoxicity assay 118
A.3) Hemolysis assay 119
A.4) Blood margination 120
A.5) In flow platelet aggregates targeting assay 120
A.6) Drug loading 120
A.7) Drug encapsulation efficiency and release rates 121
A.8) Fibrin Agar Plate Assay (FAPA) 121
A.9) NET degradation assay 122
A.10) Image analysis and statistical analysis 122
B) Transforming nanoparticles into potential therapeutic agents 123
C) Preliminary works and future directions 133
C.1) Biological assays 133
C.2) Drug loading 134
III. Thrombolysis 137
A) Materials and methods 137
A.1) Materials 137

A.2) *In vitro* static thrombolysis 137
A.3) *In vivo* $FeCl_3$ mesenteric vein thrombosis model 138
A.4) Biodistribution in mice by histological analysis....139
A.5) Image analysis and statistical analysis 139
B) In vitro *thrombolysis assays* *140*
C) In vivo *thrombolysis*....*144*
D) *Preliminary works and future directions*....*154*
D.1) An accurate in vitro AIS thrombolysis model....154
D.2) *In vivo* assays 158
General discussion ***160***
State of thrombotic diseases treatment and nanomedicine 161
The gap between preclinical nanomedicine research and clinical applications for AIS....162
Developing polysaccharide hydrogel nanoparticles to deliver a combo treatment for thrombotic diseases....166
General conclusion and Perspectives ***174***
Personal conclusion ***178***
References....***181***
Abstract....***222***
Résumé ***226***
Annexes ***229***

Table of contents

Abbreviations and Acronyms

rtPA: recombinant tissue plasminogen activator	MPS: mononuclear phagocytic system	STMP: sodium trimetaphosphate
CVD: cardiovascular diseases	LSPR: localized surface plasmon resonance	EDC-NHS: EDC, carbodiimide; NHS, N-hydroxysuccinimide
DALYs: disability-adjusted life years	NIR: near infrared	GRAS: generally recognized as safe
YLLS: years of life lost	US: ultrasound	DMAP: 4-5(Dimethylamino)pyridine
YLDs: years lived with disability	PNP: polymeric nanoparticle	TBA: tetrabutylammonium hydroxide
BMI: body mass index	PLGA: poly(lactic-co-glycolic acid)	PGPR: polyglycerol polyricinoleate
MI: myocardial infarction	EV: extracellular vesicle	GMP: good manufacturing practices
AIS: acute ischemic stroke	MSC: mesenchymal stem cell	TXRF: total reflection X ray fluorescence spectroscopy
DVT: deep vein thrombosis	LNP: lipid nanoparticle	FTIR: Fourier transform infrared spectroscopy
PE: pulmonary embolism	AV: apoptotic vesicle	w/o: water-in-oil emulsion
RBC: red blood cell	IONP: iron oxide nanoparticle	o/w: oil-in-water emulsion
VWF: Von Willebrand Factor	NE: nanoemulsion	TEM: transmission electron microscopy
NET: neutrophil extracellular trap	MB: microbubbles	PDI: polydispersity index
TF: tissue factor	NB: nanobubbles	DLS: dynamic light scattering
VTE: venous thromboembolism	PEG: poly(ethylene glycol)	ELS: electrophoretic light scattering
LDL: low-density lipoproteins	tMCAO: transient middle cerebral artery occlusion	RT: room temperature
ECM: extracellular matrix	PBS: phosphate buffered saline	HLD: hydrophilic lipophilic difference
ROS: reactive oxygen species	OGD/R: oxygen-glucose deprivation-reoxygenation	EACN: effective alkane carbon number
PAD: peripheral artery disease	ER: endoplasmic reticulum	Cc: characteristic curvature
BBB: blood-brain barrier	HAS: human serum albumin	WOR: water-to-oil ratio
DAMP: damage-associated molecular pattern	NSC: neural stem cell	SOR: surfactant-to-oil ratio
MMP: matrix metalloproteinase	PFC: perfluorocarbon	EIP: emulsion inversion point, or PIC: phase inversion composition
HT: hemorrhagic transformation	DDFPe: dodecafluoropentane nanoemulsion	PIT: phase inversion temperature
LVO: large vessel occlusion	HLA: human leukocyte antigen	ME: microemulsion
MT: mechanical thrombectomy	IV: intravenous	S: salinity
DOAC: direct oral anticoagulant	IVT: intravenous thrombolysis	NMR: nuclear magnetic resonance
CAD: coronary heart disease	EVT: endovascular thrombectomy	BCA: bicinchoninic acid assay
ICH: intracranial hemorrhage	pMCAO: permanent middle cerebral occlusion	Dex-NP: dextran polysaccharide nanoparticles obtained through our protocol
tPA: tissue plasminogen activator	dMCAO: distal middle cerebral occlusion	Fuco-NP: Dex-NP containing fucoidan as an additional polysaccharide
PCI: percutaneous coronary intervention	eMCAO: embolic middle cerebral occlusion	HUVEC: human umbilical vein endothelial cell
MVO: medium vessel occlusion	BCCAO/TGI: bilateral common carotid artery occlusion/transient global ischemia	FAPA: fibrin agar plate assay
NP: nanoparticle	Fuco-NP-rtPA: Fuco-NP loaded with rtPA	LC: loading capacity
MRI: magnetic resonance imaging	Fuco-NP-DNase: Fuco-NP loaded with DNase I	EE: encapsulation efficacy
CT: computed tomography	NAC/NACA: N-acetylcysteine/ N-acetylcysteine amide	AB: Alcian blue
PET: positron emission tomography	HES: haematoxylin, eosin, and natural saffron	

List of Figures

Figure 1: Global impact of cardiovascular diseases since 1980. 21
Figure 2: Thrombus composition in various thrombotic diseases..... 22
Figure 3: Schematic representation of the coagulatory system. 23
Figure 4: Differences between arterial and venous thrombus formation. 26
Figure 5: Onset of permanent and salvageable damages in stroke. 30
Figure 6: Schematic representation of an AIS thrombus. 32
Figure 7: A general principle of thrombolysis. 36
Figure 8: Size dependent drainage and hemodynamics of nanoparticles..... 47
Figure 9: Main NP types used for stroke treatment and imaging. 50
Figure 10: Selection process of articles published in the last five years regarding the use of nanoparticles for stroke treatment. 52
Figure 11: The different NP targeting strategies for stroke treatment and diagnosis..... 65
Figure 12: The gap between a rich preclinical research and low clinical translation of nanomedicine for acute ischemic strokes. 71
Figure 13: Classification of NPs by mechanism of action. 72
Figure 14: Repartition of preclinical in vivo models of AIS..... 77
Figure 15: Publication boom for nanoparticles and hydrogels. 81
Figure 16: Various preparation techniques for polymer nanoparticles. 85
Figure 17: Schematic synthesis of polysaccharide nanoparticles. 97
Figure 18: Assessing alternative bases and crosslinker. 101
Figure 19: Modifying synthesis parameters. 103
Figure 20: Ultrasonication assay..... 105
Figure 21: Nano- and microemulsions..... 106
Figure 22: Comparison of classical and optimized formulations. 110
Figure 23: Composition and stability of Fuco-NPs. 111
Figure 24: Counting the nanoparticles' individual components. 114
Figure 25: Cytotoxicity assays. 124
Figure 26: rtPA loading. 125
Figure 27: DNase I loading. 126
Figure 28: Freeze-drying stability of loaded Fuco-NPs. 128
Figure 29: Physiologic activity of Fuco-NP-loaded rtPA and DNase I. 130
Figure 30: Targeting and flow behavior of Fuco-NPs. 132
Figure 31: rtPA and DNase I co-encapsulation..... 135
Figure 32: Static thrombolysis by rtPA on "young clots". 141

Figure 33: Thrombolysis with DNase I and rtPA. 143
Figure 34: $FeCl_3$ mesenteric vein thrombosis murine model. 145
Figure 35: *In vivo* thrombus targeting. 146
Figure 36: Representative in vivo thrombi evolutions over time. 147
Figure 37: *In vivo* thrombus area evolution over various treatments. 149
Figure 38: Biodistribution of Fuco-NPs after thrombosis. 151
Figure 39: CD68 staining and Fuco-NP biodistribution. 153
Figure 40: Representative in vitro microfluidic AIS thrombus formation. 155
Figure 41: Microfluidic AIS thrombolysis assay. 157
Figure 42: Extracellular DNA in the $FeCl_3$ murine model. 159

List of Tables

Table 1: Major thrombolytic agents. 38
Table 2: Synthesis parameters. 99
Table 3: Parameters and values for the HLD equation. 108
Table 4: Physico-chemical characteristics of Dex-NPs and Fuco-NPs. 112

General introduction and project description

Cardiovascular diseases are a major threat to human health, and rank as the first global cause of mortality and disability-adjusted life years. Several underlying causes can explain the continuous rise of these pathologies, including population aging, environmental factors and the deterioration of lifestyles. Among them, thrombotic diseases represent the most lethal ones, including pulmonary embolism, myocardial infarction and acute ischemic stroke. While blood homeostasis is a complex balance involving several molecular and cellular players, these diseases are characterized by the pathological formation of thrombi, or blood clots. The latter are composed of aggregated platelets, a dense fibrin network and many other cell types and molecular elements which contribute to the thrombus stability. Moreover, the dynamic structure and composition can vary between physiological thrombi depending on their localization and etiology. The main consequence of pathological thrombi is the blood flow restriction, which is followed by tissue ischemia with sometimes severe consequences depending on which organ is concerned.

Therefore, prevention and treatment of thrombotic diseases is crucial. The role of environmental and lifestyle factors in developing the latter has been strongly evidenced, and thus primary prevention is paramount for curbing those preventable deaths. While it achieved overall impressive results in the last decades, this has not been sufficient to prevent the continuous increase in cardiovascular diseases deaths, partly because of socioeconomical disparities and failure to communicate this urgency to the public. Consequently, establishing reliable and accessible therapeutic treatment options is necessary. Depending on the pathology subtype and thrombus etiology, three main lines of pharmaceutical treatment were developed: anticoagulants, antiplatelets and thrombolytics. They all suffer nonetheless from a broad range of side effects and limitations. Notably, the latter category is adequately represented by the current gold standard thrombolytic treatment for arterial thrombosis, a recombinant tissue plasminogen activator (rtPA, or alteplase). This enzyme, once injected in the circulation, will activate plasminogen in proximity of thrombi by cleaving it into plasmin, which will degrade the fibrin network and thus participate in the thrombus degradation. However, this drug suffers from a short half-life, strong inhibition and quick clearance from the blood, as well as severe side effects like bleeding, neurotoxicity and hemorrhagic transformation. In addition, it offers a limited recanalization efficacy, resulting in a benefits/risk balance that only offers a short therapeutic window. Besides, the recent development of endovascular therapies with impressive recanalization rates has greatly improved patient's care, but this remains limited in its use due to accessibility and patient

stratification reasons. On the other hand, some research has focused on the management of ischemia damages, with for instance neuroprotection in the case of acute ischemic stroke, quick and efficient recanalization remains the most urgent therapeutic goal. Therefore, there is still a critical need for improved therapeutic options that may achieve thrombolysis and recanalization, with above all requirements for a safer and more targeted treatment with reduced safety issues.

Nanomedicine is a growing biomedical field which explores how ultrasmall materials may be used to improve patients' care through unique properties. One of the main approaches relies on the targeted delivery of one or more agents directly where they are needed. Consequently, our Team and others have investigated the use of polymer-based nano- to microscale materials to deliver rtPA to thrombi as an improved strategy for thrombolysis. The work undergone throughout this PhD was therefore inscribed in this global effort and focused on the formulation of adequate polysaccharide-based hydrogel nanoparticles which could be loaded with multiple therapeutic agents to improve the thrombolytic treatment of thrombotic diseases such as acute ischemic strokes.

This manuscript, recapitulating the work of my PhD, is divided into three main chapters.

First, the "Thrombotic diseases and the nanomedicine opportunity" chapter establishes the context of our work. It begins with the description of thrombotic diseases, their etiology and a presentation of the current knowledge on the thrombus composition and the current therapeutic approaches for thrombolysis. This is followed by the investigation of why nanomedicine is a relevant field to expand potential treatments of thrombotic diseases, including a description of current preclinical nanomedicine approaches for the latter, and for acute ischemic stroke in particular. This part included adaptations from a review published in *Neuroscience* in 2023, with a shared co-first authorship with Pierre Sarfati, Dr. Corinne Portioli and Raffaele Spanò, as well as from a review (*Nano Today*, currently with Editor) that was written in 2024 with Diana Doukhi (neurologist) and focusing on current limitations of nanomedicine to reach clinical translation. Finally, the pertinence of hydrogels and more specifically polysaccharide-based materials as drug delivery systems was discussed.

Thereafter, the "Experimental results" chapter presents the experimental work pursued along this PhD to answer the abovementioned problematic. It is divided into three parts, each describing specific methods and results as well as the relevant perspectives and prospective works. Each part contains elements

that were adapted from an original research article that was submitted in September 2024 to *ACS Nano* (in revision). First, the development of a synthesis protocol for polysaccharide hydrogel nanoparticles was described, with notably the use of microemulsion as a theoretical framework to improve formulation. The resulting original method and nanoparticles were subsequently protected by a patent filed in December 2023 by Inserm Transfert, with Dr. Cédric Chauvierre and I as inventors. Then, the perspectives of broadening this microemulsions concept and expanding this synthesis towards a translatable formulation were discussed. Second, the biological characterization of these nanoparticles, including targeting capacity and the loading of two different drugs, rtPA and DNase I, was presented. This also included the cytotoxicity and stability assessments of our nanoparticles, followed by a discussion expanding among others the drug loading aspects. Subsequently, results of thrombolytic experiments were recapitulated. Starting with *in vitro* experiments, and completed with an *in vivo* thrombosis model, the data procured allowed a discussion on the relevance of thrombosis modeling and potential therapeutic approaches. Noteworthy results included the improvement of thrombolysis by rtPA vectorized in our nanoparticles at 50% and 10% the recommended free drug dose.

Finally, the “General discussion” broadened the scientific discussion with regards to the treatment of thrombotic diseases. Notably, this part evoked the current low clinical translation of a rich preclinical nanomedicine research for stroke treatment was evoked, with perspectives to improve future developments, and these considerations were adapted from the review written in 2024. It also explored the achievements and future perspectives of our nanoparticles as a potential drug delivery system for thrombotic diseases. This work was concluded with a “General conclusion and Perspectives” as well as a short “Personal conclusion”.

Part One. Thrombotic diseases and the nanomedicine opportunity

I. Thrombotic diseases: a challenge for human health

A) Cardiovascular and thrombotic diseases: a global health crisis

Cardiovascular diseases (CVD) are the major causes of deaths around the world, accounting for 18.8 million deaths in 2019 alone, with a continuous increase over the years [1–3]: this represented 33% of all deaths worldwide in 2019. However, in contrary to the global lethality which tends to diminish over time (excluding the effects of the global COVID19 pandemia post 2020), the rate of fatalities linked to CVD remained constant since the 1980s with around 240 deaths per 100’000 people each year as displayed in Figure 1.A. [1]. Notably, the two main killers among CVDs are ischemic heart diseases and strokes, which both account for respectively 105 and 95 deaths per 100’000 people per year, totaling 83% of all CVD-related fatalities. Yet, fatalities are not the only relevant readout when addressing global human health. For instance, disability-adjusted life years (DALYs) is the reference indicator for impact on human health by taking into account non-fatal disease sequelae with their respective weighted disability: it is calculated by summing years of life lost (YLLs) and years lived with disability (YLDs) [2]. In that regard, ischemic heart diseases and strokes also represent the second and fourth leading causes of global DALYs in 2020 with more than 188 and 160 million DALYs each [2], as illustrated in Figure 1.C. This is followed by a substantial economic impact including high annual health-care costs, which can be estimated at $ 422.3 billion in the US [3], while the European Heart Network reported in a total cost of € 210 billion in 2015 in the European Union, noting that 53% of this cost is due to healthcare costs, 26% to productivity losses and 21% to informal care of CVD patients [4]. These figures illustrate the heavy burden that CVDs impose on society, both in economic and healthcare terms. Importantly, the risk of CVDs impacts the whole society: CVD in Europe are responsible of 45% of all deaths in males, and 39% in females, while making up 29% and 33% of all premature deaths (deaths before 70 years) for males and females respectively. In terms of YLLs in Europe again, CVD account for 40% YLLs for females and 35% for males [4]. Even though CVDs have historically been associated to males, it is now clear that CVDs affect females to similar extents. Importantly, CVD epidemiology has revealed a strong impact of environmental, lifestyle and clinical risk factors, with resulting socioeconomical disparities in CVD: premature mortality is less prevalent in high-income countries [4]. Based on these risks factors, the concept of

cardiovascular health, resumed by “Life’s simple 7”, then “Life’s essential 8”, was introduced by the American Heart Association in order to help reduce CVD deaths: these include health behaviors (diet quality, physical activity, smoking, sleep health) and health factors (blood cholesterol, body mass index (BMI), blood pressure, blood glucose). For instance, high-blood pressure, poor diet, abnormal glucose levels, smoking, total cholesterol level and insufficient physical activity could be associated to CVD mortality by 47.5%, 13.2%, 11.6%, 10.7%, 10.1% and 5/9% respectively [5]. The ideal settings for each of these criteria have been independently associated with decreased CVD risk: healthy diet pattern, regular physical activity, no smoking, healthy sleep and normal levels of the different health factors [5,6]. Primary prevention and promotion of an healthy lifestyle could significantly reduce prevalence and mortality of CVDs [7], with notably some studies in the US and in UK suggesting that achievable major risk reduction could yield 50% decreases in ischemic heart diseases annuals deaths [8–10]. Even so, such changes take time and face multiple obstacles, while around 50% of the death rate decrease for ischemic heart diseases between 1980 and 2000 in the US was attributed to treatments [9]. Furthermore, global population ageing and lack of information and surveillance of CVH factors, especially in high-risks patients, hinders the reduction of these risk factors and poses an obstacle to reducing these otherwise preventable CVD deaths: for instance in high-income European countries, people with high CVD risks often had poorly managed diabetes, blood pressure or lipid levels, and half were obese [4,11]. Besides, there are certain CVDs risk factors which are challenging to tackle in a timely manner, and which exceed healthcare considerations. For instance, air pollution and noise account for 75% of the CVD burden that can be attributed to the environment; and while air pollution is responsible by itself of 7.6% of global DALYs, 58% of the related mortality is mediated by CVDs [4]. Inequalities in living conditions can also increase CVD risks as demonstrated by various studies: in Sweden, living a low-deprivation neighborhoods could be linked to an increase coronary heart disease of 90% for females, and 50% for males [4,12]. Nonetheless, social risks factors, such as low family income, education, appurtenance to underrepresented racial groups or single-living status, have been associated in the US to a decreased likelihood of satisfying the CVH criteria, further amplifying social disparities against CVDs [13,5]. Continuing parallel efforts in prevention and improving treatment quality are thus necessary.

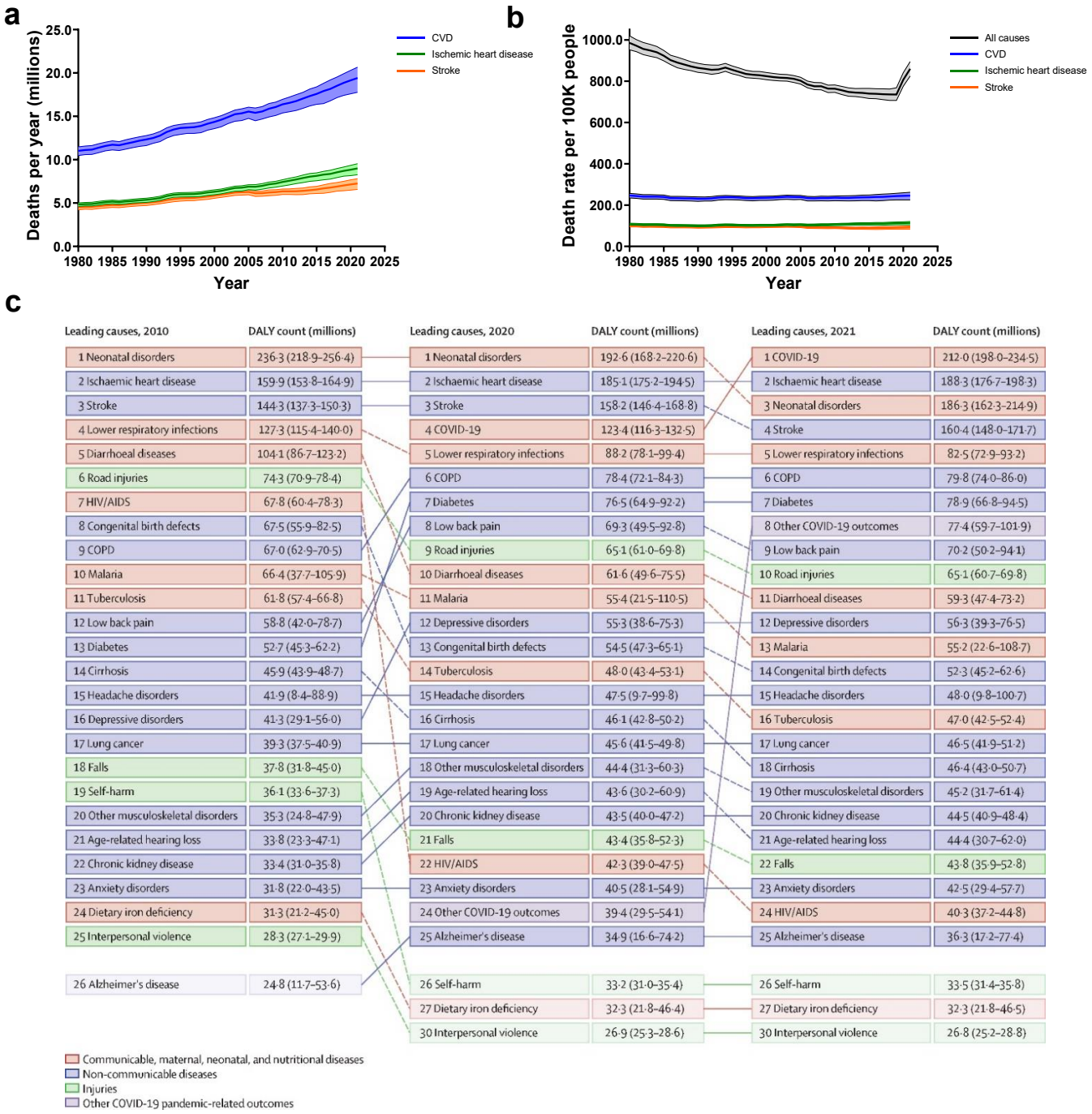


Figure 1: Global impact of cardiovascular diseases since 1980. (a) Total number of deaths per year from 1980 to 2021. (b) Death rate per year from 1980 to 2021. Data extracted from GBD results, 2021 [1]. (c) Top 25 leading causes of global DALYs in 2010, 2020 and 2021. Adapted from Ferrari et al., 2021 [2].

Thrombosis plays a major role in the mechanism of multiple lethal CVDs. Thrombosis is defined as the formation of a blood clot, or thrombus, inside a blood vessel. There are two main types of thrombosis, depending on the thrombus location: arterial, and venous. Arterial thrombosis mostly concerns myocardial infarction (MI, one of the main complication of ischemic heart

diseases [14]) and acute ischemic strokes (AIS), which themselves represent around 87% of all strokes [5]. Venous thrombosis consists of deep vein thrombosis (DVT) or pulmonary embolism (PE). Since 85% of all CVD deaths result from MI and strokes, the etiology and composition of thrombi for these specific cardiovascular pathologies are discussed in the following paragraphs.

B) Thrombosis pathophysiology

Thrombi are composed of various cell types, such as red blood cells (RBCs), platelets, or leukocytes, as well as multiple other components including fibrin, Von Willebrand Factor (VWF), coagulation factors or neutrophil extracellular traps (NETs). However, the structure and exact composition vary between the etiology and location of the clot (see Figure 2), and between individuals [15,16]. Therefore, it is necessary to explore how thrombi differ, and to understand how they are formed. This includes a description of atherosclerosis, the underlying cause of most ischemic heart diseases and many strokes [17,18] and other arterial thrombi, followed by description of venous thrombosis.

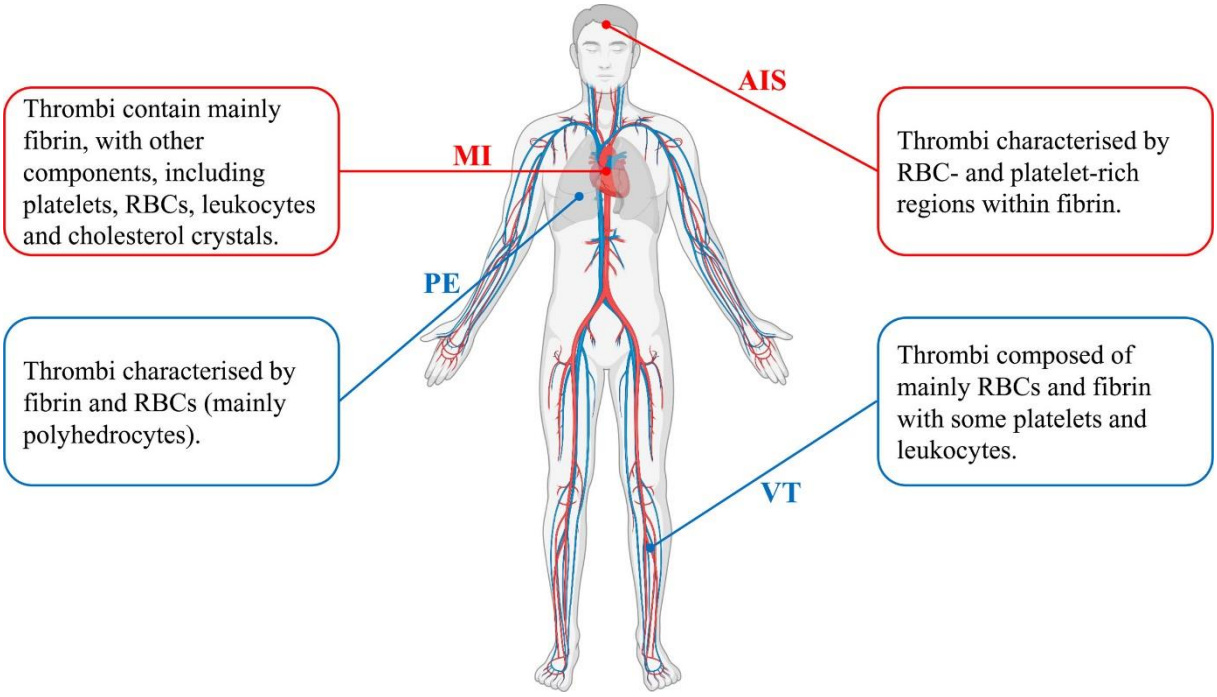


Figure 2: Thrombus composition in various thrombotic diseases. Adapted from Alkarithi et al., 2021 [15].

B.1) General thrombus formation

Thrombi formation involves platelet activation and aggregation, which is mediated by platelet activation and aggregation after exposure of various plaque

components such as fibronectin, collagen, VWF and tissue factor (TF), which is followed by coagulation and the ensuing thrombosis [17–19]. This is followed by blood coagulation, generally described as a cascade of coagulation involves multiple actors through two pathways, the intrinsic (or contact pathway), notably activated without presence of TF such as laboratory glassware exposure, and extrinsic pathways, involved by TF exposure, as shown in Figure 3. The latter is generally considered to be the primary source of coagulation in the case of atherosclerosis-induced thrombosis [20]. This coagulation system ultimately converges after amplification towards the formation of fibrin, ensuing thrombosis and knitting together the resulting thrombus (see Figure 4.A).

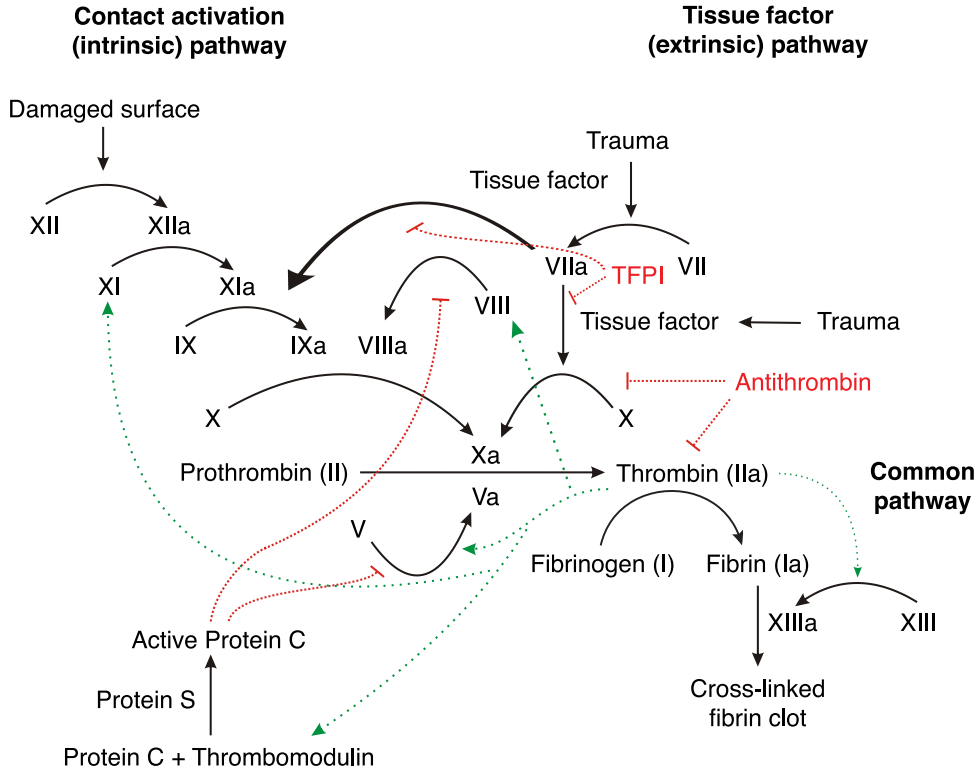


Figure 3: Schematic representation of the coagulatory system. "Coagulation full updated with FVII and TF to FIX arrow" by Joe D is licensed under CC BY-SA 4.0.

Fibrin is formed by the cleavage of fibrinogen, a 340 kDa circulating protein, by thrombin after the initiation of coagulation. Fibrin then polymerizes into protofibrils then branched fibrin fibers that constitute a mesh, and is a major constituent of thrombi [21,15,16,22]. Notably, the fibrin content of thrombi has been linked to changes in overall mechanical clot properties, with for instance increased "stickiness" with higher fibrin content or how thrombus rupture (relevant for mechanical procedures for instance) is dependent of fibrin fibers

break [23,24]. Recent studies have also explored 3D organization of fibrin as constitutive of continuous protective films around clots, associated with protection against infection [15,25].

Platelets play a critical part in the initiation of thrombosis. These are small anucleate cells with a crucial role in coagulation. Aggregation of platelets is initiated by contact of surface receptors (for example GPVI) to collagen and VWF, and pursued through changes of integrins on platelets, mediating their binding of additional platelets. This goes hand in hand with their activation and release of granules, which further exacerbate recruitment, activation and adhesion [15,17,19]. They also play a part with fibrin in the so-called clot contraction, which helps consolidate thrombi [21].

Many other cell types are constitutive of thrombi. RBCs become entrapped in the clots, with varying content between thrombi or between individuals [19,16]. However, their role goes beyond simply filling the space as many studies reported active roles of RBCs in clot evolution and resistance to thrombolysis. Notably, they can contribute to thrombin production [26], they were linked to increased inflammatory phenotypes in a subset of MI patients [27] and, in the case of sickle cell disease, their higher rigidity could be linked to reducing the thrombi permeability [15,28,29]. Leukocytes are also present, with reports of leukocytes present in thrombi [15,16], including also monocytes, which can act as a source of tissue factor and participate in prothrombotic activities [30].

Recently, the role of neutrophils has also been expanded. These cells can also be found in thrombi, and they can release NETs, which are networks of DNAs with multiple bound proteins such as histones or granular proteins. This release happens through a specific form of cell death, NETosis, which has been massively studied for their role against microbes and in the innate immunity [31,32,22], and can promote inflammation [32,33]. Besides, in the context of blood clots, they also play a different role, in particular by promoting thrombosis. NETs serve as scaffolds for platelet aggregation [34], but also might promote the intrinsic coagulation pathway and activate platelet and thrombin generation through exposed histones [34,35]. Overall, they can enter a vicious pathological thrombosis cycle as platelets are also thought to promote NETosis through P-selectin priming of neutrophils [36]. Once formed, NETs can impair thrombolysis as they modify the thrombus mechanical properties and modulation of fibrin properties and lysis [37]. Moreover in 2015, Jiménez-Alcázar *et al.* found that normal degradation of NET by circulating DNase was diminished in patients with acute thrombotic microangiopathies, which exhibited markers of NETs,

suggesting that hindered NETs removal might be involved in such thrombotic diseases [38]. Strikingly, evidence of NETs presence could be found in arterial and veinous thrombi [34], though their role and relevance it not fully characterized in both situations [22,39]. Other molecular components have been evidenced to play a role in thrombus formation and may impede its lysis, such as VWF with notably *in vivo* studies that described how VWF-directed treatment helped degrade model AIS thrombi [22,40].

The presence of a thrombus will disrupt blood flow, potentially even occluding the blood vessel and causing ischemia in the downstream (distal) tissue; in the case of strokes, the distinction between the irreversibly damaged ischemic core and the penumbra, where the tissue is not yet infarcted and which might be salvaged, is also used [41].

B.2) Venous thromboembolism

Deep vein thrombosis (DVT) happens in the veins located deeply in the limbs, generally the legs. Sometimes, part or whole DVT thrombi can break apart and be taken towards the lungs, causing PE, which is therefore a complication of DVT. Together, these two thrombotic pathologies are referred to as venous thromboembolism (VTE), which affects indiscriminately male and female with an annual occurrence of 1 to 2 cases per 1000 people [39]. The apparition of VTE is dependent on three major thrombogenic mechanisms, the Virchow's Triad (see Figure 4): altered blood flow, endothelial dysfunction, and altered intrinsic blood properties (e.g., hypercoagulability, thrombophilia) [42]. There are multiple factors contributing to VTE, which is assumed to be initiated after additive (or synergic) interplay. There are strong risk factors like active cancer, major surgery, prolonged immobility or major trauma, which can be associated with weaker risk factors such as inflammatory disorders, obesity, or infection [39]. The initiation of thrombosis can take multiple days in contrast to fast-forming hemostatic and arterial thrombi [42], and relies on the interaction of coagulation and inflammation, while also implicating immune cells [39]. Altered blood flow was demonstrated to be an important pathogenic mechanism, potentially involving hypoxia and blood stasis, which was also illustrated by the role of valve pockets in VTE [39,42]. Endothelial dysfunction can be subsequent to these altered hemodynamics, which prime the endothelium to shift from antithrombotic surface to prothrombotic, with hypoxia and inflammation playing key roles: adhesiveness of the cell wall increases with P-selectin expression on the cell wall, as well as prothrombotic factors like TF and VWF [39,42]. Blood properties can also be altered with hypercoagulability for various pathological reasons,

including genetic mutations, or thrombophilia [17]. The thrombus genesis remain unclear, but may involve interplay of activated leukocytes and platelets, including NETs released by neutrophils, with the activated endothelium to initiate a procoagulant state [42].

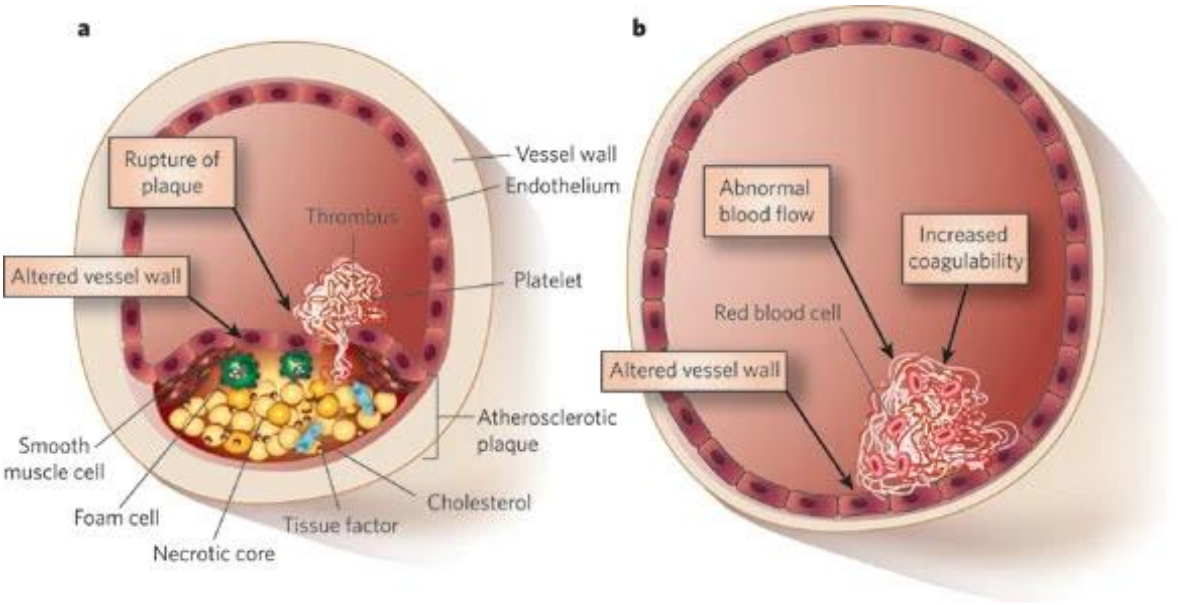


Figure 4: Differences between arterial and venous thrombus formation. (a) In arteries, thrombosis usually follows the erosion or rupture of an atherosclerotic plaque, disrupting the endothelium and exposing prothrombotic factors such as collagen and tissue factor, which promote platelet aggregation, coagulation and finally thrombosis. (b) In veins, thrombosis usually occurs on intact endothelium, but is primed by altered blood flow, abnormal endothelial function and altered blood properties (e.g. hypercoagulability, thrombophilia). Adapted from Mackman, 2008 [15,17].

Sometimes called “red clots” in opposition to platelet-rich “white clots” found in arteries, VTE thrombi are mostly composed of trapped RBCs and fibrin. In these “red clots”, RBCs and fibrin constitute the two major components, with respectively 63% and 35% of the volume fraction [43]. Moreover, the RBCs displayed compressed phenotypes such as polyhedrocytes (around 40% of all RBCs). Notably, very few platelets and leukocytes are usually found in these thrombi [43]. However, retrieval of *ex vivo* thrombi is rarer for VTE than for arterial thrombi since endovascular therapy is less common, which does not help further the understanding of VTE composition and structure [42,15,39], especially given the long maturation and differences in retrieved clots’ age [15].

B.3) Atherosclerosis and arterial thrombi

Atherosclerosis consists of a systemic inflammation with the formation of atherosclerotic lesions, composed of lipids, leukocytes and macrophage

accumulation in the intima of blood vessels. This accumulation of materials causes a thickening of the vessel wall, resulting in vessel stenosis and subsequent downstream ischemic events, and can evolve into plaques or atheromas, with various negative consequences. Despite the importance of this pathology and the attention it received in research, many aspects remain unclear [44].

Atherosclerosis begins with the infiltration of low-density lipoproteins (LDL) in the subendothelial layers in blood vessels. Many risks factors have been described which contribute to this initiation, such as high plasma levels of LDL cholesterol or blood pressure. While the causal effect of LDL on atherosclerosis has been demonstrated [18,44], other lipid abnormalities have been observed in atherosclerotic disease patients, including low high-density lipoproteins and increase of triglyceride-rich lipoprotein [44,45]. Moreover, mounting evidence describes how systemic inflammation participates in atherogenesis [44,46], though mechanisms are still subject to debates. The retention of LDL within the intimal layer is followed by various modifications which further the disease progression. This is followed by the adhesion and migration of blood-borne cells such as lymphocyte and monocytes, which will form foam cells after uptake of lipids, though recent research indicated that some local smooth muscle cells could also give rise to these foam cells [47,48]. This is followed by remodeling of the vasculature structure, with changes in the extracellular matrix (ECM) and cell composition with a decrease in vascular smooth muscle cells content from 90-95% to 50% between initial and late lesions [18]. Over time, these lesions evolve, giving rise to vulnerable plaques, characterized by a lipid-rich necrotic core covered by a fibrous cap [18,44]. Notably, platelet attachment can occur even without plaque rupture through diminishing normal antithrombotic properties of the endothelium, presence of reactive oxygen species (ROS), and local increase of prothrombotic and pro-inflammatory factors [18], and once activated can increase the inflammation and accelerate plaque formation. Interestingly, it was also demonstrated in atherosclerotic murine models that P-selectin, an adhesion molecule found on activated endothelial cells and platelets, played a crucial role in the development of atherosclerotic lesions through both endothelial and platelet involvement [18,49].

Most arterial thrombi, which form in high shear-stress blood vessels, are caused by atherothrombosis as illustrated in Figure 4.A. The rupture of these plaques is responsible for 60-80% of all MI [17,19,15] and are also a major

cause of AIS [15,44,50], as well as peripheral artery disease (PAD). Typically, the thrombosis process follows either plaque erosion or plaque rupture [19,44]. Moreover, this thrombosis formation was noted to be highly dependent on the glycoprotein GPVI-mediated adhesion and aggregation at the beginning of platelet aggregation and activation, which may open clinical perspectives [20]. There are broad variations in the composition and structure of arterial thrombi, specifically between patients [16]. These variations can originate from blood parameters including fibrinogen concentration, pre-existing risk factors like diabetes, infection, or the etiology of thrombi, with recent acknowledgments in the case of that clots of cardioembolic or large artery atherosclerotic origins show differences in composition [51,52,22]. However, they are generally characterized by high amounts of fibrin and platelets [15,17,22,43], but they also contain leukocytes, RBCs, VWF and NETs [15,22]. Besides, specific structures have been observed in arterial thrombi: the presence of a fibrin film was evidenced in some clots from MI patients as evoked above, and an “onion”-like organization of multiple layers was noted [15,43], including surfaces containing more fibrin and platelets, while inner regions contained compressed RBCs, the polyhedrocytes [15]. Moreover, structure and composition have been noted to evolve as clots age, with clot contraction, decrease in platelet content, polyhedrocyte formation, fibrin reorganization and accumulation [15,22].

B.4) Stroke: a special case

Stroke is a special case of CVDs: these cerebrovascular accidents result in brain damage either through ischemia (ischemic strokes or AIS) or hemorrhage (hemorrhagic strokes). AIS represents around 62-87% of all strokes [5,53,54] and the emboli responsible for brain ischemia is most often caused by arterial clots [5,14,15], with the major etiological categories being cardioembolism or large vessel disease [55,56]. The cardioembolism etiological subtype is defined by the Trial of Org 10172 in Acute Stroke Treatment (TOAST) classification as arterial occlusions within the cerebrovascular area with evidence pointing towards an embolus arising in the heart. These emboli usually stem from thrombi generated in the heart for various reasons, and represent 21% of ischemic strokes in a subset of AIS patients in Korea [55]. For instance, atrial fibrillation, the prevalence of which is increasing with population ageing and obesity, can also generate thrombosis which can result in strokes. Other known causes involve coronary heart disease, MI, viral infections, infective endocarditis or hematological disorders [57,50]. On the other hand, the large vessel disease comprises first of large artery atherosclerosis, which is

evidenced by significant (>50%) stenosis or occlusion of a major brain artery or branch cortical artery, presumably due to atherosclerosis. Interestingly, the location of these atherosclerotic lesions can differ among populations: in western populations, the internal carotid artery is most often concerned, possibly through lower shear stress, while intracranial atherosclerosis is mostly seen in Asian patients (30-50% AIS in this population compared to 5-10% in white patients) with repercussions on prognosis and treatment [57,58]. Another source of large vessel disease can be for instance arterial dissection, especially in strokes that occur in young patients without other risk factors [57,50]. Nonetheless, the emboli consists most of the time of an arterial thrombus throughout these various origins [15,50,57]. Besides, transient ischemic attack can happen, which are quick self-resolving ischemic strokes, often with no direct consequences, but they can serve as “warning strokes”, as transient ischemic attack patients have a 1.2% risk of stroke at 2 days, and 7.4% at 90 days [3].

When these strokes happen, the particular setting of the cerebrovascular area can impact pathological development. First, owing to the blood flow disruption and ensuing ischemia, cerebral infarction with eventual irreversible brain lesions evolves quickly as shown in Figure 5, with notable difference between the ischemic core which shows rapid injury, and the penumbra that might eventually be salvaged [50], with various mechanisms involved like ion imbalance, apoptosis, inflammation, or oxidative stress [59]. Furthermore, the integrity of the blood-brain barrier (BBB) can be disrupted once an ischemic or hemorrhagic stroke happens. This specific structure of the brain microvessels is designed to protect the latter against aggression or harmful substances and provides a homeostatic environment where the passage of water, nutrients and other chemicals is strictly monitored. Nonetheless, its disruption was evidenced following ischemic damages and neuroinflammation. This can lead to vasogenic brain edema, influx of toxic substances, and increase neuroinflammation through the release of damage-associated molecular patterns (DAMPs, such as heme, fibrinogen, or heat shock proteins) and ROS, prompting apoptosis, microglia activation toward inflammation [60,61]. Matrix metalloproteinases (MMPs) are also involved in the BBB disruption, and are associated with poor neurological scores and increased infarct areas [60]. The fluid influx also results in increased intracranial pressure, which can worsen the ischemia [61]. This pathological BBB opening can be seen clinically in the following 48-72 h post stroke but is not limited to the subacute phase: there is some evidence of long-lasting (up to 3 months) persisting BBB dysfunction in clinical studies. Moreover, the deleterious effects of BBB disruption extend beyond those pathological

phenotypes, as it was also shown to interfere with treatments, for instance by mediating the hemorrhagic transformation (HT) when thrombolytics or endovascular therapy was used, and association of imagery-mediated measurement of BBB disruption with HT risk was demonstrated [61,62]. However, the specific blood vessel distribution in the brain means that collateral flow can occur, where the penumbra is still partially irrigated by neighboring non-occluded arteries, with important repercussions on extending the time window during which a patient reperfusion might reverse the damages, with for instance the circle of Willis, a brain circulatory anastomosis which can help establish collateral flow [57].

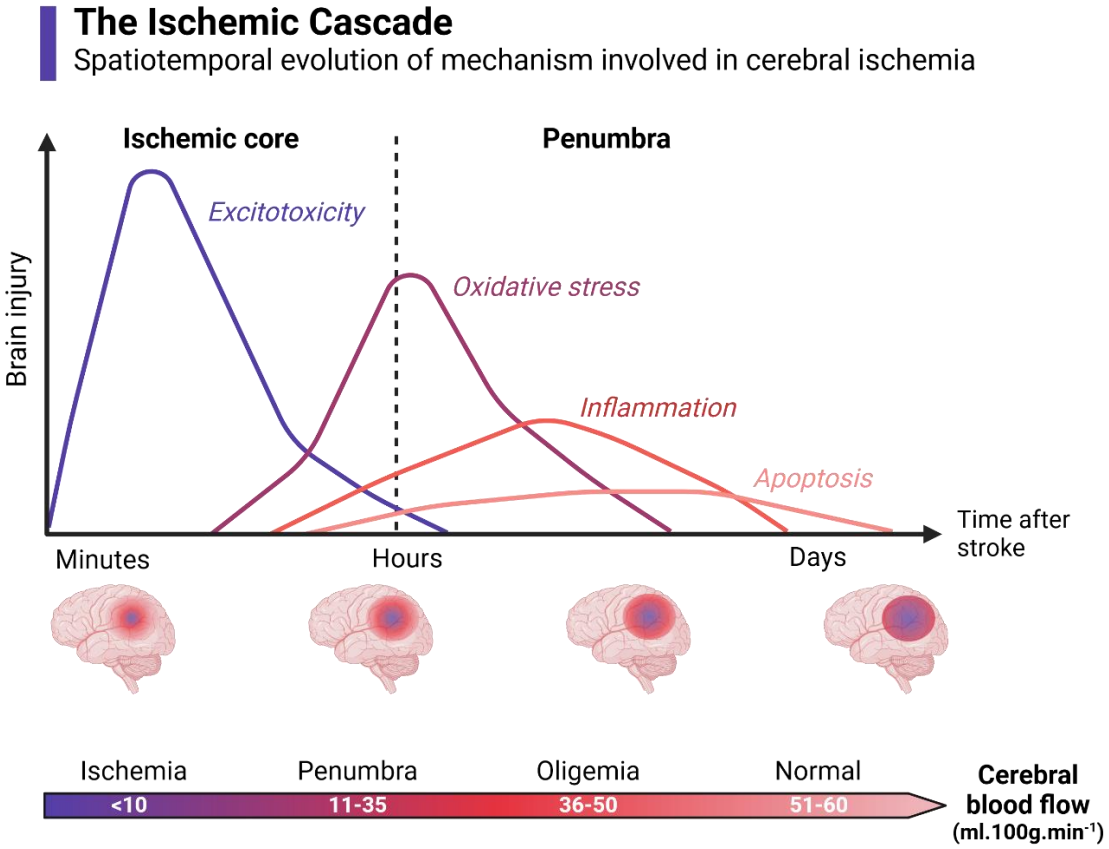


Figure 5: Onset of permanent and salvageable damages in stroke. Cerebral infarction is flow- and time-dependent in ischemic strokes, with different underlying mechanisms that each yield different brain injuries over separate time periods. The y-axis is an arbitrary estimation of the damage based on literature. Adapted from Cloé Moëlo (created with BioRender.com) [59].

Besides, there has been accumulating evidence that AIS thrombi exhibit specific characteristics. While they display arterial thrombi composition and general characteristics, several studies have indicated that thrombi retrieved

from thrombectomy contained at least two distinct domains, one rich in RBCs which were packed together in a fibrin network, with entrapped leukocytes and a relative low complexity, while other areas exhibited higher platelets count, with complex scaffold incorporating fibrin, VWF and DNA. [63–65,15]. Some authors notably attributed this separation to local hemodynamics and clot contraction, which might explain the redistribution of platelets to the exterior and pack the RBCs into polyhedrocytes [65]. Accordingly, Di Meglio *et al.* described in 2019 that AIS thrombi retrieved from large vessel occlusion (LVO) patients shared a core-shell structure, where the shell was composed of a platelet-rich area containing dense compacted materials. Not only is this compaction described as potentially altering clot porosity, but its content was also linked to thrombolysis resistance: altered fibrin morphology and its chemical modifications, and presence of VWF, extracellular DNA and fibrinolysis inhibitors [64]. The structure of such AIS thrombi, with indications of how this can impair its degradation, is illustrated in Figure 6. For instance, VWF was also found in AIS clots, with drugs targeting VWF providing enhanced thrombolysis on otherwise treatment-resistant clots [22,65]. Besides, the presence of neutrophils has been exposed in these shell regions, and have been recognized as major actors in the thrombus fate [66,67,34,68–71,22]. Their extensive abundance in thrombi retrieved from AIS patients, along the NETs that they can release, has been confirmed by various groups based on *ex vivo* thrombi retrieved from patients since 2017, with observations arising that they could be pivotal in the AIS thrombi formation, and be associated with worse clinical outcomes [70,66,69,67]. Furthermore, it was noted by Peña-Martínez *et al*. in 2019 that *in vivo* thrombosis in a murine photothrombotic model was averted under NET-preventing treatment, and that DNase I, which can lyse NETs, succeeded in recanalizing stroke thrombi from this model (which exhibited no fibrin). They also noted that thrombolysis of *ex vivo* platelet-rich clots from AIS patients could be achieved with DNase I [72]. Similar studies demonstrated that DNase I could indeed participate in enhancing thrombolysis when *ex vivo* thrombi from AIS patients were treated with a combo of DNase I and the golden standard thrombolytic treatment [66,67]. These results tend to indicate a significant role of NETs in AIS thrombi by notably affecting how they respond to treatment [22]. Moreover, recent *in vivo* investigations by Wang *et al.* in 2021 highlighted the apparition of NETs in a murine AIS model after golden standard treatment, and could correlate this NET apparition with BBB disruption, while also reversing this BBB degradation with DNase I or inhibition of NET production [73], while clinical results correlated NET formation throughout the brains of AIS stroke patients

with worse outcomes [71]. Overall, these results converge towards a critical role of NETs in the formation and treatment response of AIS thrombi.

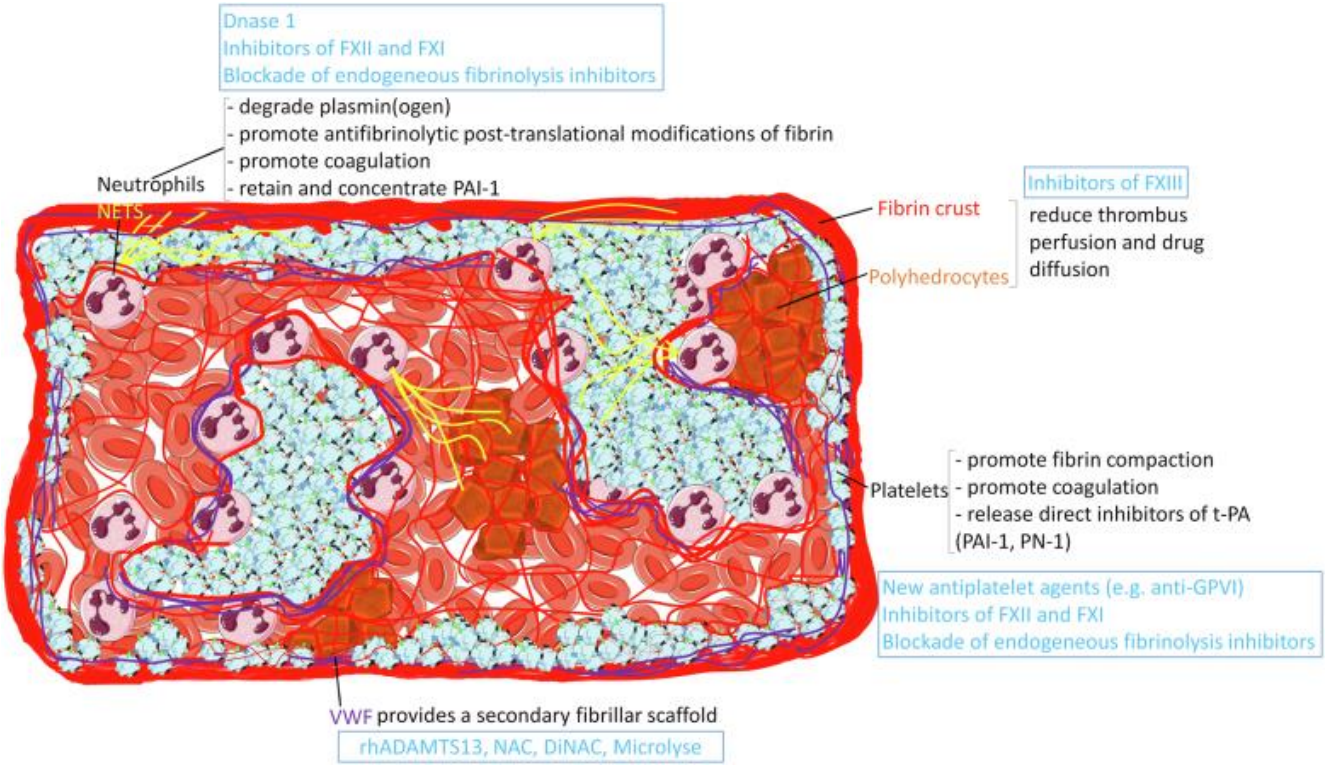


Figure 6: Schematic representation of an AIS thrombus. The RBC core, with compressed polyhedrocytes, is intertwined with a fibrin mesh (red), with incorporation of neutrophils (purple cells) with releases NETs (yellow). These are also found at the frontier and inside the outer shell, which mostly comprises aggregated platelets (pale blue) and fibrin, with VWF (purple) providing a secondary scaffold. Indications of thrombolysis resistance are reported in black, with potential therapeutic targets indicated in blue. Adapted from Ho-Tin-Noé et al., 2023 [22]

Nevertheless, there is no unique AIS thrombus, and variations have been demonstrated between patients, including relative ratios between the different clot components [16,22]. AIS thrombus structure, just as described before in the general case of arterial thrombi, evolves with time [15,22], and their etiology might also have an impact on their final composition and structure, as cardioembolic thrombi appear to contain more leukocytes, NET and DNA than others, though the exact mechanism nor the therapeutical implications are not fully determined yet [22,52,66,74]. Besides, the damages caused by AIS go beyond mere hypoxia, and while the mechanism of ischemia-induced cascade of nefarious consequences is generally well understood, the eventual reperfusion that is sought after can induce a different set of ischemia-reperfusion related damages, which might involve ROS, inflammation, neutrophil

accumulation, distal capillary collapse, and eventual apoptosis, as shown in Figure 5 [57]. Similarly, a gene-profiling study in transient or permanent ischemia stroke models in rats hinted at very different pathways (the former related to inflammation and apoptosis, while the latter involved among others neurotransmitters, ion channels and growth factors, with different neuronal deaths pathways) [75,76], which indicates that management of neuroprotection may differ between patients with or without reperfusion.

C) Treatment of thrombotic diseases

There are three main lines of pharmaceutic drugs that are used in treatment and prevention of thrombotic diseases: antiplatelets, anticoagulants, and fibrinolytic agents. In recent years, mechanical thrombectomy (MT) has become another promising alternative. Depending on the pathology and its etiology, either one or combination of some of these therapeutic approaches can be used. Their specificities, mechanism of action, and examples are recapitulated below. Notably, while anticoagulant and antiplatelet drugs mostly play a role in prevention as antithrombotic agents, fibrinolytics and MT are specifically used to treat an already formed thrombi as recanalization rate was strongly correlated to improved patient prognosis [77].

C.1) Anticoagulants

Anticoagulant drugs target the coagulation pathway in order to prevent this molecular cascade from forming fibrin. Since VTE is primarily dependent on fibrin formation during its pathogenesis, anticoagulants are the central line of prevention and treatment for VTE and PE. Nonetheless, patients with atrial fibrillation can also be proposed these drugs to prevent strokes as the involved thrombi formation is also fibrin dependent [78].

There are four main classes of FDA-approved anticoagulants. The heparins, including unfractionated heparin or low molecular weight heparin, are natural highly sulfated glycosaminoglycans which potentiate the antithrombin III action. A related synthetic compound is the fondaparinux, with similar action as low molecular weight heparin. These drugs are based on antithrombin III-mediated inhibition of coagulation factor FXa for low molecular weight heparin and fondaparinux, and both FXa and thrombin inhibition for unfractionated heparins [78,79]. The vitamin K antagonists, such as warfarin, are used to prevent vitamin K-dependent production of multiple coagulation factors, including FII, FVII, VIX or FX. The two final categories are direct thrombin inhibitors such as bivalirudin or dabigatran, and direct FXa inhibitors like

apixaban, edoxaban or rivaroxaban. Furthermore, some require parenteral administration like heparins or bivalirudin, while others can be orally ingested like vitamin K antagonists. Moreover, the development of oral direct inhibitors of thrombin or FXa, named direct oral anticoagulants (DOACs), which present more predictable pharmacokinetics, have improved the care for VTE [78,79]. They can be used as thromboprophylaxis, but also for treatment of VTE, though they also come with limitations. For instance, unreliable pharmacokinetics hinder the use of unfractionated heparin or vitamin K antagonists, which also exhibit inter-patients variability. However, DOACs are not recommended when patients present renal or hepatic failures. Moreover, by targeting the coagulation pathways, all these treatments are associated with increased hemorrhages [78,79], prompting research into safer anticoagulants.

C.2) Antiplatelets

On the other hand, antiplatelet drugs are primarily used for arterial thrombi. Their main purpose is to prevent platelet aggregation and activation, thus preventing the formation or growth of a thrombus. Notably, they have also been shown to be effective for secondary prevention for ischemic strokes in patients that presented non-cardioembolic transient ischemic attack or AIS, even though the exact agents are still debated [78].

The main categories of antiplatelets currently in use are aspirin (a cyclooxygenase inhibitor, thus inhibiting platelet activation); $P2Y_{12}$ antagonists (e.g., clopidogrel, prasugrel or ticagrelor) to prevent propagation of activation and aggregation between platelets; αIIbβ3 integrin antagonists (abciximab) which aim to prevent platelet aggregation by blocking this activated integrin; and a protease-activated receptor 1 antagonist (vorapaxar), which blocks thrombin-dependent platelet activation [78]. Similar to anticoagulants, some can be parenterally or orally administered. They can be used for secondary prevention following transient ischemic attack, PAD or coronary heart disease (CAD) as single antiplatelet treatment, or in the event of acute thrombosis with for instance the parenteral αIIbβ3 integrin antagonists. Moreover, dual antiplatelet therapy is now also in patients with acute coronary syndrome, with both aspirin and a $P2Y_{12}$ antagonist. Mechanistically, all these drugs rely on inhibiting platelet activation and aggregation, thus also hindering hemostasis. Therefore, bleeding remains the major side effects of all antiplatelets, with often limited ways to reverse antiplatelets effects. This bleeding complication can be high, with a 1% risk of major bleeding per year with aspirin and the $P2Y_{12}$ inhibitors, and often outweigh the benefits in several situations: for instance, combination of

antiplatelets drugs can substantially increase the bleeding risk with little to no benefits [78]. Moreover, the inter-patient variability greatly hinders clinicians when choosing the agent and the appropriate dosage, due to heterogeneity in platelet reactivity [78]. Interestingly, genotype-based approaches have shown promising results, but overall safer and more controllable antiplatelet agents are necessary. For instance, anti-GPVI antibodies have been developed as a safe and promising antiplatelet therapy in the recent years [80].

Furthermore, combination therapies of antiplatelet and anticoagulants were assessed to overcome their individual limitations, and in order to address the broader thrombosis mechanism for arterial thrombi, with notably overwhelming benefits demonstrated by the combination of aspirin with rivaroxaban, a direct FXa inhibitor, in prevention of death, MI or stroke when compared to each alone in patients with stable cardiovascular diseases [81].

C.3) Fibrinolytic drugs

Nonetheless, anticoagulants and antiplatelets are mostly used in prophylaxis, including secondary prevention, or accompanying other procedures. Therefore, fibrinolytic drugs can be used to directly degrade the fibrin network and thus achieving thrombolysis. While these mostly concern arterial thrombi, they can be used for PE patients with high risk of dying, and in some restricted DVT cases, be infused through catheter for local delivery [39,79].There are several fibrinolytic agents that have been discovered or engineered, but all of them eventually aim at activating plasminogen, a circulating enzyme, by cleaving it into plasmin, as illustrated in Figure 7, thus regrouping them in the plasminogen activator denomination [82]. Besides the direct activation by serine proteases (cleaving plasminogen), like the golden standard alteplase, a recombinant tissue plasminogen activator (rtPA), some exhibit indirect action like streptokinase and staphylokinase, as described below. Major thrombolytics are recapitulated in Table 1, with notably only the two most discussed rtPA 3rd generation, tenecteplase and reteplase.

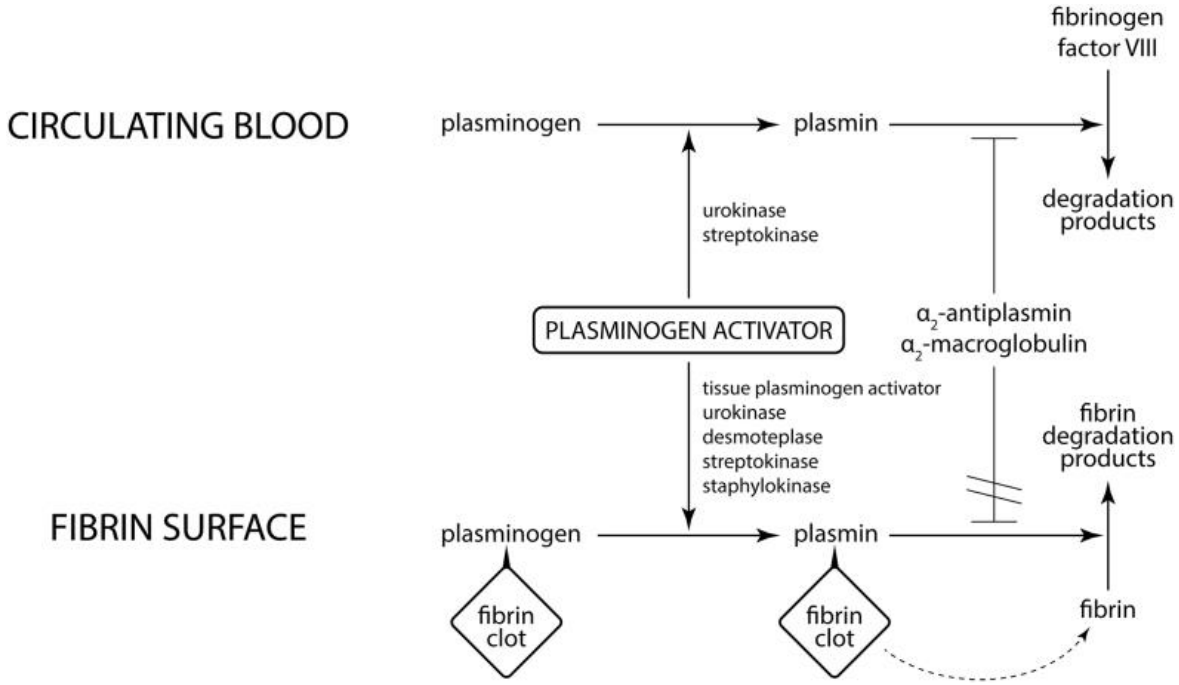


Figure 7: A general principle of thrombolysis. Plasminogen activators can either activate circulating or fibrin-bound plasminogen. The latter is cleaved into plasmin, which will degrade fibrin in bound conditions, or fibrinogen and FVIII in circulation. Circulating plasmin can be inhibited by α2-antiplasmin and α2-macroglobulin, but this inhibition is prevented when the plasmin is fibrin-bound. Adapted from Mican et al., 2019 [82].

The first generation of fibrinolytics were composed of streptokinase and urokinase. They are characterized by their lack of fibrin affinity, and high fibrinolytic power. Streptokinase is an exocellular enzyme produced by bacteria, the β-hemolytic *Streptococci.* It acts as indirect plasminogen activator by first binding free plasminogen or plasmin, and the resulting equimolar complex can cleave another plasminogen into active plasmin. Due to a lack of fibrin affinity or clot targeting, its systemic action degrades fibrin and depletes circulating fibrinogen and plasmin (which is rapidly inactivated in the circulation by α2-antiplasmin and α2-macroglobulin), which results in extensive bleeding complications. Moreover, the bacterial origin of streptokinase is responsible for its high antigenicity, meaning that neutralizing antibodies are produced which lower its efficacy under repeated administration; its immunogenicity can also elicit febrile and allergic responses [82,83]. Urokinase is a physiologic thrombolytic which can be purified from human urine or recombinantly produced. Urokinase is a direct plasminogen activator, and actually stems from the cleavage of a single-chain urokinase, or prourokinase, into a two-chain form. This urokinase is inhibited by plasminogen inhibitors in the circulation and does not need fibrin binding to cleave plasminogen, thus resulting in systemic

plasminogen activation, similar to streptokinase, with ensuing bleeding complications [82,84]. While these two first generation thrombolytics come with severe complications such as bleeding, they are routinely used in developing countries due to low production costs compared to the golden standard rtPA, and in certain indications like DVT, PE, or MI.

A significant improvement in thrombolysis was achieved with the second generation of fibrinolytics: rtPA (alteplase). This fibrinolytic originates like urokinase from a physiologic enzyme, the tissue plasminogen activator (tPA), under a recombinant form. tPA has multiple biological roles, including fibrinolysis which is sought here, and various brain activities such as modulating neuronal migration, cerebral blood flow, BBB properties or vascular tone (vasoconstriction or vasodilatation) [82,84]. Similar to urokinase, this enzyme exists in single-chain or two-chain protein. tPA is a direct plasminogen activator, but its activity is however mostly restricted to fibrin-bound plasmin; it also has a high affinity for fibrin, with high selectivity for fibrin over fibrinogen. Thus, its fibrinolytic action is mostly limited to fibrin in the direct vicinity of clots, with obvious safety advantages over the previous fibrinolytics by limiting the bleeding complications. It is inhibited by circulating inhibitors like PAI-1 and PAI-2. The recombinant form, rtPA, has been approved by the FDA for the management of MI and PE in 1987 and 1990 respectively, followed by approval for AIS in 1996, becoming the main line of treatment for ischemic strokes in developed countries [84,85]. Yet, rtPA suffers from major limitations like a short half-life (4.5 min), high inhibition in the circulation through various inhibitors such as PAI-1, quick blood clearance by the liver, and severe side effects: intracranial hemorrhage (ICH), further characterized as hemorrhagic transformations (HT, where the ICH is subsequent to an ischemia), bleeding despite the rtPA fibrin affinity, and neurotoxicity [82,85]. This has limited its use in MI due to lack of improvement over Streptokinase or surgical interventions, and restricted its PE use to patients with high risk of dying [79,85]. In AIS where it serves as golden standard, recanalization is nonetheless low, with only around 20% patients who show a recanalization [86]. This, combined to the low rate of rtPA use in AIS patients even in developed countries (less than 10% of AIS patients received rtPA in the US in 2018) [87], illustrate the need for alternative or improved treatments.

Thrombolytic agent	Source	Mode of action	Fibrin specifi-city	Half-life (min)	Inhibition risk	Safety issues	Indication
First generation							
Streptokinase	β-hemolytic *strepto-coccus*	Indirect	(-)	10	Low	Immunogenic Bleeding	MI, AT, PAD, DVT, PE
Urokinase	Human urine & kidney	Direct	(-)	8	High	Bleeding	DVT, PE, AIS
Second generation							
rtPA (alteplase)	Recombinant human	Direct	(++)	4.5	High	Bleeding HT Neurotoxic	MI, AIS, PE, PAD
Third generation							
Staphylokinase	Lysogenic *Staphylo-coccus aureus*	Indirect	(++)	6	Low	(Low) immunogenic	***AIS***
Desmoteplase	Vampire bat saliva	Direct	(+++)	138	Low	Low	***AIS***
Prourokinase	Recombinant human	Direct	(+)	9-12	High	Lower than urokinase	***MI, AIS***
Reteplase	Recombinant human	Direct	(+)	14-18	Medium	Bleeding HT Neurotoxic	MI, PAD
Tenecteplase	Recombinant human	Direct	(+++)	11-20	Medium	HT Neurotoxic Less bleeding than rtPA	MI, ***AIS***

Table 1: Major thrombolytic agents. The different thrombolytics are arranged by successive generations, with indications about their action, risks and biological properties. General indications are given in the last column and emphasized in **bold italics** *when currently under evaluation (not commonly approved yet).*

Third generation thrombolytics are either composed of variants of rtPA, or new thrombolytics from different sources, with the purpose of achieving safer thrombolysis. Staphylokinase is a prokaryotic plasminogen activator, like streptokinase, but secreted by the lysogenic *Staphylococcus aureus*. Similarly, it acts as an indirect plasminogen activator by binding plasminogen or plasmin. However, despite its lack of fibrin affinity, only the plasmin-involving complex is active, thus limiting the subsequent plasmin generation next to thrombi: any

circulating plasmin or plasmin-staphylokinase complex is rapidly inhibited by α2-antiplasmin, but not when plasmin is fibrin bound, which protects it from inhibition. This is further enhanced by preferential binding of staphylokinase to fibrin-bound plasmin compared to the circulating one [82,88]. Even though its bacterial origin initially elicited immunogenicity which would prevent repeated administration, later recombinant versions were associated with reduced immunogenicity, improved half-life and higher efficiency [82]. While not commonly used yet, it is registered in Russia as an AIS treatment following a non-inferiority clinical trial published in 2021, which compared it to alteplase [88,89]. Desmoteplase is a thrombolytic of eukaryotic origin, as it was discovered in 1974 in the saliva of vampire bats [84]. Thus, it benefited from a reduced immunogenicity compared to other non-human thrombolytics. Exhibiting an extremely high fibrin specificity, it displays the highest stimulation by fibrin among known thrombolytics, which virtually prevents side effects like bleeding and fibrinogen depletion [82]. Recent and ongoing clinicals trials tried to assess its eventual use for AIS notably [82,84]. Prourokinase is a rediscovered thrombolytic. Even though urokinase has already been used in patients, its single-chain precursor has been ignored for some time. In this form the enzyme displays lower activity and a specificity towards fibrin-bound plasminogen. Reciprocally, plasmin activates prourokinase by turning it into the non-specific urokinase, but with significantly increased fibrinolytic power. This first fibrin-bound specificity, and the plasmin-dependent increase in activity grant prourokinase a good specificity towards fibrin in clots, thus diminishing side effects such as systemic bleeding [82,85]. Furthermore, studies have suggested that, while both tPA and urokinase were needed in endogenous fibrinolysis, urokinase may be the dominant and necessary activator endogenously, with tPA responsible mostly for initiation of fibrinolysis [85]. However, initially high therapeutic concentrations of prourokinase were sufficient in past clinical trials to activate circulating plasminogen with subsequent bleeding complications, thus slowing its further developments [85]. Nonetheless, new ongoing trials in MI and AIS demonstrate promising results including safety and efficacy [85,88,90,91]. On the other hand, improved recombinant versions of rtPA were explored. Several iterations exist such as reteplase, tenecteplase, duteplase, monteplase, lanoteplase, pamiteplase, amediplase, etc., but here are mentioned the two already approved by the FDA. Reteplase exhibits mutations that grant a longer half-life and resistance to inhibition by reducing binding to clearance receptors and PAI-1, and a reduced fibrin affinity that may improve its thrombolytic activity [83,92]. Moreover, these mutations and reduced number of

disulfide bridges have allowed its expression in prokaryotic production systems [82,92]. Tenecteplase contains mutations which result in increased half-life, decreased inhibition by PAI-1, decreased recognition by clearance receptors and increased fibrin activity in contrary to reteplase. These modifications led to decreased risks of non-cerebral bleeding compared to rtPA, and simpler administration: while rtPA is administered as a bolus followed by 60 min infusion, tenecteplase is administered through a simple bolus injection [82–84,88].

C.4) Mechanical thrombectomy

Several surgical interventions for mechanical thrombectomy (MT) have been developed over the years to overcome limitations of antithrombotic and thrombolytic drugs, depending on the pathology.

For DVT, various non-pharmacological methods were developed to help prevent emboli or manage complications, including compression stockings, sequential compression devices, or inferior vena cava filters which can prevent PE transformation in patients with acute DVT, but have mostly displayed suboptimal results compared to anticoagulant therapies, with notably the latter being mostly restricted to patients with acute PE who cannot receive anticoagulant therapy [39,79]. While less commonly performed, percutaneous mechanical thrombectomy can be performed to remove or degrade the thrombi on site, but scarce decisive clinical evidence has not clarified how much and in which patients this procedure can be beneficial [39,79,93] .

For MI, percutaneous coronary intervention (PCI) is a nonsurgical, invasive procedure used to restore blood flow to ischemic tissue. PCI is the primary intervention recommended by the American Heart Association for patients with acute coronary syndrome including MI, replaced by fibrinolytics administration when PCI is not available under 120 min (followed by ulterior PCI if possible) [94,95]. Coronary artery bypass graft can be performed under certain conditions and if PCI is not available, though the latter is preferred [94,95]. PCI consists of various methods to restore blood flow. The main techniques are balloon angioplasty where a balloon is introduced inside the coronary artery, then inflated to open the stenosed blood vessel; or stent implantation, where a stent can be introduced with or without prior balloon inflation to maintain the artery opened [96].

Regarding AIS, five pivotal studies in 2015 established the safety and efficacy of MT with thrombolytic administration for patients which presented large vessel occlusion (LVO) within 6 hours of onset [97–101]. This became the

standard of care for AIS patients with LVO or medium vessel occlusion (MVO), with further extension over the years to patients within 16 h to 24 h of onset depending on brain imaging [102]. Despite impressive recanalization rates, which have been estimated to reach up to 90% [103], this procedure suffers from some limitations. The current European recommendations indicate that if possible the MT procedure should be undertaken in comprehensive stroke centers [104], but the setup of these infrastructures does not allow yet to include all eligible patients. In France, there are 42 stroke centers (interventional neuroradiology center, NIR in French) which are competent for MT, with circa 50 neurovascular unit (UNV in French) to help diagnose and triage patients [105]. Nonetheless, recommendations from the French “Haute Autorité de la Santé” include reinforcing current NIR centers while implementing intermediate UNV with MT capacity (without fulfilling all the comprehensive care offered in NIR) in order to accommodate for increased MT requirements [106]. Similarly, based on AIS patients from 2015 to 2023 in the US, 5% of American AIS patients underwent MT, which represented 27% of all LVO+MVO patients which could potentially receive MT [107]. This indicates that there is a potential to increase MT numbers to fulfill current needs, however it also means that, under current recommendations, no more than circa 30% of AIS patients would be eligible for MT. Thus, despite impressive recanalization results, thrombolytic therapies are still necessary and continuing research to improve AIS patients care is needed.

C.5) Limitations of current treatments for thrombotic diseases

Despite pharmacological and interventional therapeutic options, thrombotic diseases still pose a heavy burden on human health and require continuing improvements to prevent and improve patient care. Notably, there are important socioeconomical disparities which have not yet been addressed in the current range of therapeutic procedures.

Regarding thrombolytic options, current fibrinolytics have not lived up to expectations, with the severe side effects of first generation thrombolytics limiting their use [83]. Their replacement with rtPA allowed for a broader use of thrombolytic therapy which greatly improved patient care, yet the risk/benefit ratio still remains an issue as rtPA associated bleeding, HT and neurotoxicity pose a significant risk in exposed patients. Several studies have participated in broadening rtPA use while accounting for these challenges, with in the AIS examples, extension of rtPA therapeutic window from 3 h to 4.5 h after 2008 [108] and in patients with unknown stroke onset or within the 4.5 – 9 h window under brain imaging criteria [109]; further recent studies also indicated that rtPA

use in patients over 80 years of age, despite polypharmacy risk, may benefit from rtPA administration; or patients with stroke mimics (e.g., epileptic seizures, conversion disorder, complicated migraines), exhibited good rtPA tolerance which might reduce withholding of rtPA when AIS cause is suspected [110–112]. However, its use in DVT and MI is now restricted to acute PE with high risk of death and secondary treatment when PCI is not available respectively [39,79,83,95], and for AIS where it remains the mainline treatment, administration is limited to around 10% of patients in developed countries [87] and ensuing recanalization rates remain low (around 20-40% improved recanalization rate depending on sources [77,86,113]). While rtPA mutants such as tenecteplase and reteplase address some of its limitations, they haven't offered yet breakthroughs in thrombolytic therapy. Other fibrinolytics such as staphylokinase or desmoteplase display promising properties which might improve over rtPA but are still ongoing testing to verify whether they would offer a better care for patients. Similarly, prourokinase offers an interesting complimentary thrombolysis with rtPA. It exhibits increased safety over urokinase and evidence of its role in physiological fibrinolysis may indicate a way to change how fibrinolysis is performed [85].

Nonetheless, these thrombolytics are still limited to fibrin degradation, which may be insufficient for complete thrombus destruction as evoked above. Indeed, thrombi composition includes more than a simple fibrin network, and multiple evidence have indicated that this may explain failures of fibrinolytics when trying to destroy thrombi. In the case of AIS thrombi, the role of NETs in providing rtPA resistance against thrombolysis has been well characterized thanks to *ex vivo* experiments on thrombi acquired from AIS patients through MT [22,66,67]. Several studies have demonstrated that DNase I may play a potent adjuvant role to improve rtPA-mediated thrombolysis of AIS thrombi [22,67,69,114]. Moreover, NET participation in thrombi has also been investigated in other arterial thrombi with correlation to patients' prognosis [38,69] and their presence is VTE thrombi was suggested based on preliminary studies, though the rarer use of MT has prevented the extensive characterization made possible for MI and AIS clots [34]. Other thrombi components may prove useful targets, like VWF: results in murine models have evidenced a rtPA-independent thrombolytic effect of VWF-targeting drugs [22,40]. Another key aspect of thrombolysis is the heterogeneity of thrombi, not only between pathologies as previously evidenced, but also between patients [16,22,34,69] and may differ based on the etiology of the clot formation, as

indicated by differences between thrombi of cardioembolic or large artery atherosclerotic origins in AIS [51,52,22].

Finally, another key aspect of global human health is equal access to treatment and sociological equality. Despite tremendous advancements in managing thrombotic diseases with notably the rtPA-mediated thrombolysis, which is the standard of care for AIS and useful in other indications, and the rise of MT in MI and AIS with impressive recanalization results, these treatments are not widely available yet, with socioeconomic disparities even though less privileged populations have an increased risk of CVD [2,4,13]. On one hand, access to MT procedures is mitigated by the presence of comprehensive intervention centers, with adequately trained medical personnel and may face multiple structural barriers barring people from certain socioeconomic status or race/ethnicity to access these procedures [87,115]. This is also true for thrombolytic treatment [87], which are also plagued by high prices which limit its access in less developed countries where less expensive, first generation thrombolytics are preferred when they can be prescribed [83,116,117]. This cost and limited availability may be due to the eukaryotic recombinant natures of these new thrombolytics which are harder to produce, even though efforts in that direction were made: reteplase for instance can be produced in prokaryotic systems, but must be properly refolded after production for instance [82,92]. Therefore, to improve thrombotic diseases' treatment while mitigating the limitations of highly demanding MT procedures and the costs of new thrombolytics, new approaches must be explored. In that regard, management of ischemic tissue damages through neuroprotection, inflammation mitigation or promoting tissue repair is among the possible improvements of thrombotic disease therapy. Nevertheless, proper delivery and targeting of new and old therapeutic agents with efficient side effects decrease are key developments that are needed.

II. Nanomedicine: another approach for thrombotic diseases

With adaptations from:

- **ANNEX 3**: **de La Taille T**, Sarfati P, Portioli C, Spanò R, Lalatonne Y, Decuzzi P, et al. REVIEW: “ISCHEMIC STROKE: from fibrinolysis to functional recovery” Nanomedicine: emerging approaches to treat ischemic stroke. *Neuroscience*. 2024 Jul 9;550:102–13.
- **ANNEX 5**: **de La Taille T**, Doukhi D, Mazighi M, Chauvierre C. Ischemic Strokes: Exploring the Challenges of Translating Nanomedicine into Clinical Practice. *Nano Today*, With Editor (2024)

One approach that could change the landscape of thrombotic diseases treatment is nanomedicine. Behind this designation, a plethora of different materials, shapes and structures at the nanometric scale exist, with each their specific characteristics, properties and applications. The following exploration of nanoparticles (NP) is focused on the management of AIS for simplification, though many key takeaways are easily translated to other thrombotic diseases.

A) Nanomedicine relevance

The application of nanomedicine for stroke treatment has been investigated for several years since the introduction of liposomes by Imaizumi *et al.* in 1990 to reduce cerebral infarction in a rat model of ischemic strokes [118]. The central principle is similar to most nanomedicine approaches. In the early 19th century, the German Nobel prize Paul Ehrlich created the concept of a “magic bullet” specifically directed against pathogens in the organism, like bullets fired from a gun that hit a specific target [119,120]. His initial works on chemical dyes paved the way for modern medicine, and his groundbreaking introduction of the receptor theory inspired the ensuing immunological research. Beyond these achievements, this concept was extended to various pharmacological approaches in order to improve the way therapeutic agents are delivered in the organism: drugs that are designed to go straight for a specific cell or tissue and exert their specific action only on the intended targets. Nanotechnology itself can be traced back to the physicist Richard Feynman who first evoked machines at the molecular level, with the term “nanotechnology” being coined in 1974 [121]. Subsequently, nanomedicine emerged in 1964 with the discovery of liposomes, spanning decades of continuing development and discovery of NPs, converging to the first FDA-approved nanomedicine in 1995

for a liposomal formulation of the antitumoral drug doxorubicin (Doxil®) [122], with currently an extremely rich preclinical research involving several types of NPs, and multiple clinical applications [123].

Initially, the main goal was to bring an active drug with poor availability and adverse toxicity profile to a specific target by encapsulating it into a controlled vector - the nanoparticle. In this context, the encapsulation and targeted delivery of thrombolytic agents would benefit from: i) protection from the physiological environment, thus increasing the agent's half-life; ii) limitation of systemic adverse effects; iii) improvement in therapeutic efficacy by increasing its accumulation at the thrombus site [124]. The use of nanoplatforms is not limited to drug delivery however, as diagnostic tools can also be designed, with for instance direct contrast agents (e.g., iron oxide NPs for magnetic resonance imaging (MRI), or to transport imaging compounds such as radioactive markers. Thanks to their targeting capacity, they can accumulate at the cerebral blood clot and enhance the imaging signal of the stroke that can be obtained with MRI, computed tomography (CT), positron emission tomography (PET) or doppler ultrasonography [125].

Nonetheless, these objectives could also be achieved with other drug delivery methods, such as microparticles (in the micrometer scale range) or molecular composites such as antibody-drug conjugates. Even so, the nanometric size benefits from specific advantages and properties that emerge at this scale. The size reduction is associated with an increase in the surface/volume ratio, which can play a critical role in functionalization and target recognition by increasing the number of exposed moieties relative to the particle mass, volume and internalized content, and can improve surface exchanges which may be useful for drug release [126]. Furthermore, in a biological context, the size plays an important role in circulation and biological behavior, notably for drainage, excretion or sequestration as shown in Figure 8.a [127,128]. Below a threshold of around 10 nm, NPs are more likely to be excreted through renal clearance by passing the glomerular filtration barrier, which is 8-9 nm wide [129,130], even though some soft NPs of a slightly higher size can also be excreted [129]. Therefore, a size cutoff above 10-20 nm is generally accepted as enough to limit renal excretion of NPs [130,131]; furthermore, there are reports that hepatic clearance is increased for particles between 10-20 nm due to the liver physiological role in clearing virus and other small objects [132]. On the other hand, large particles (above the micron) are more likely to aggregate and block capillaries, while also being more susceptible to momentum from a

hydrodynamic point of view, which increases wall collisions and thus interactions with the mononuclear phagocytic system (MPS), resulting in rapid clearance [130]. It was also shown that MPS capture was linked to the surface curvature, with high curvature particles (i.e., small NPs) are less likely to be internalized by macrophages than bigger ones [133]. Thus, particles between 20 and 1000 nm are generally desirable to avoid rapid clearance and/or embolization. Furthermore, in some cases a 100 nm threshold should be considered, as multiple studies have found that particles below 100 nm are more likely to avoid sequestration in endothelial fenestra and sinusoids, facilitating their extravasation and endothelial internalization [130,134]: this is necessary for particles that are intended to exit the circulation and enter various tissues, including tumors. However, when particles are intended to remain in the circulation, for example to target a thrombus, this means that particles above 100 nm should be designed. Besides, excretion and extravasation are not the only phenomena that are mediated by size in the circulation. Hemodynamics also dictate where in the blood flow the particles are located. It is known that RBCs tend to preferentially travel in the center of blood vessels, in the low-shear zone, while leukocytes and platelets are pushed near the channel walls [135]. Therefore, other circulating objects, when smaller than RBCs, are also pushed to the sides of the vessels, displaying a “margination” behavior [136–139]. Typically, objects with diameter below a few microns are pushed aside, but this effect decreases as particle size is reduced, with objects below 200-250 nm showing plasma-like homogeneous flow behavior across the blood vessel [137,139]. Thus, depending on whether one aims at near-wall circulation, or rather homogeneous distribution profile through blood vessels, larger or smaller particles could be designed. For instance, the BBB crossing capacity of NP has been largely documented in the case of brain tumors as well as for the treatment of various neurological disorders, including Krabbe, Alzheimer’s or Parkinson′s diseases [140,141], and this property can be essential for treating the insulted tissue postischemia by using the increased BBB permeability to deliver therapeutic agents only in the ischemic area [142]. Such size-related behaviors are recapitulated in Figure 8.b. Despite this strong size dependence, in-blood behavior is also dependent on other factors, such as size, protein corona formation, hydrophilicity/hydrophobicity, surface charge and shape [130,134,137,143].

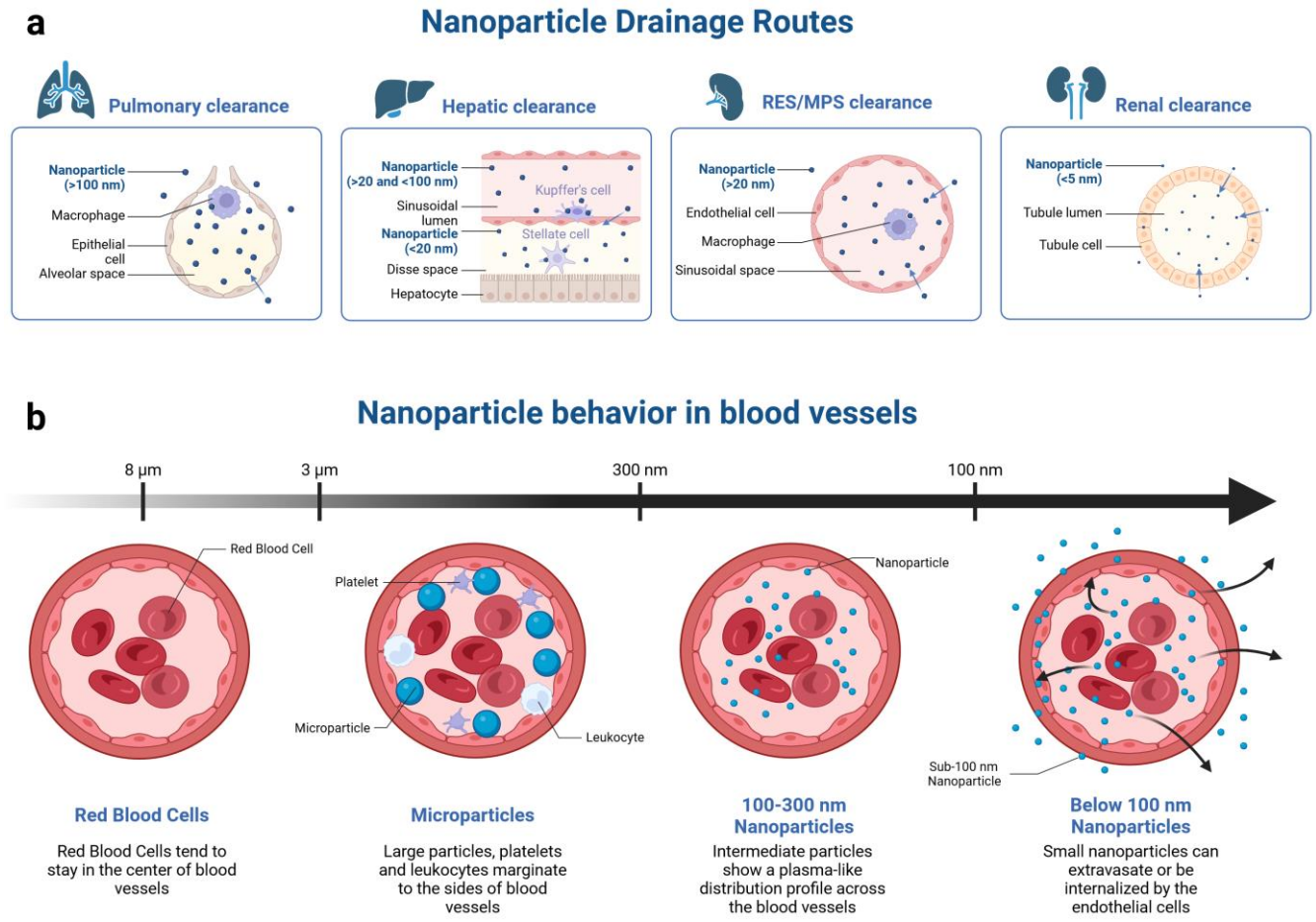


Figure 8: Size dependent drainage and hemodynamics of nanoparticles. (a) *Drainage, excretion and sequestration of circulating particles in different organs depend on their size. Adapted from Zhao et al., 2019 [127]. (b) Distribution profiles of circulating particles in blood flow as a function of their size. Created with BioRender.com.*

Other properties are nanoscale specific. For instance, microbubbles have been extensively used as ultrasound contrast agents [144], but when such gas-filled objects reach the nanoscale – nanobubbles – they exhibit a nonlinear ultrasound response which can be specifically used to improve imaging contrast, for instance in vascular, extravascular, or tumor imaging [144–146]. Besides, inorganic NPs also exhibit size-specific emergence of physical properties. For instance, quantum dots present strong luminescence with tunable absorption and emission wavelengths, notably through size control. They can therefore be useful for imaging, as shown with the near-infrared emitting quantum dots for thrombus imaging from Imamura's group [147]. At the nanoscale, some NPs show great thermal conversion properties due to their naturally high thermal conductivity combined to increased surface/volume ratio, which has allowed the development of a photothermal approach [148]. Moreover, plasmonic NPs such

as gold materials can absorb light at different wavelengths depending on their size through localized surface plasmon resonance (LSPR): while the classical surface plasmon resonance, which characteristic of certain metallic surfaces' interaction with electromagnetic fields, is mostly dependent on the metal itself and the state of the surface (density, thickness, molecular absorption), at nano scales the LSPR characteristic maximum optical absorption peak (often chosen between the visible to infrared region) is also dependent on the nanoparticle size, shape and structure [149,150]. This has been used notably in a proof-of-concept photothermal thrombolytic system based on gold NPs in 2016 [151]. In addition, ferro/ferrimagnetic NPs undergo a superparamagnetism phenomenon: when they are small enough, each NP is made of only one magnetic domain. Thus, in the absence of an external magnetic field, the magnetic moments of all NPs are differently oriented, as dictated by Néel relaxation, leading to zero magnetization. In the presence of an external magnetic field, instead, superparamagnetic NPs exhibit a stronger magnetization than paramagnetic ones [152]. Additionally, through their Néel and Brownian relaxation processes, under stimulation of an alternating magnetic field, superparamagnetic NPs can also be used to produce heat in order to help the dissolution of the clot [153,154].

Thanks to these numerous advantages, nanomedicine can offer a novel approach to the treatment of thrombotic diseases such as AIS. On one hand, the delivery of thrombolytic agents directly to the thrombus could circumvent their severe side effects and increase local concentration, thus circumventing inhibition and improving efficacy. Moreover, addressing therapies to the ischemic brain across the blood-brain barrier (BBB) can be achieved by specific vectorization with NPs and help reduce the lasting damages of ischemia. Finally, NPs can also be used as contrast agents with different imaging modalities to specifically locate and assess the thrombus formation and ischemic lesion, and can even be used in a theranostic manner to couple imaging with controlled IVT [155]. Specifically, this is made possible by NPs' high versatility as carriers, capable of delivering various drugs to a wide range of tissues. Their ability to either remain in the vascular compartment or cross the BBB depending on their size and shape provides great flexibility and a tailored approach to tackle the different phases of ischemic stroke. For example, during the hyperacute phase of stroke (first 6 hours), when the BBB becomes leaky in the ischemic area, thrombolysis and neuroprotection will be the main therapeutic objectives. NPs enable the targeting of the blood clot for thrombolytics delivery or to reach the ischemic tissue through the more permeable BBB to limit neuronal damage with neuroprotectants. NPs could also be used as contrast agents with different

imaging modalities to specifically locate and assess the thrombus formation and ischemic lesion. In the subacute and chronic phases (>48 hours after stroke onset), neoangiogenesis and neurogenesis could be the main targeted processes. Thus, growth factors or miRNAs would be delivered to the infarcted region, notably via targeting agents on the NPs surface that promote the passage of BBB, which is less permeable than in the early stage of ischemic stroke [156]. Therefore, nanomedicine could improve patients from thrombotic diseases, and stroke specifically, in various ways.

Most importantly, nanomedicine has evolved past the preclinical stage, with several projects yielding between 500 and 600 clinical trials by 2023 [157,158], with at least 147 completed. This was followed by the market approval of more than 100 nanodrugs, validating the nanomedicine approach with an impressive success rate of 16-20%: for comparison, clinical trials for all drugs across all applications between 2000 and 2015 have an average success rate of 13.8%, with trials for cardiovascular applications reaching a total 25.5% approval [159]. In comparison, for small targeted molecules - another young and booming technological field for medical application with a first FDA approval in 2001 for imatinib - only 89 drugs received market approval even though thousands of clinical trials are currently listed [160]: thus, nanomedicine can claim good clinical translatability for a relatively young technological approach, which could hopefully result in new advances in thrombotic diseases treatment.

B) Nanoparticle types

NPs can be classified into many different types, based on their base material and structure. The main categories of NPs which may be used for thrombotic disease management are described below. Notably, a systematic review of recent preclinical research for AIS is used to illustrate the current nanomedicine status in thrombotic diseases. The classification used here is recapitulated in Figure 9, with polymeric NPs, lipid-based NPs, inorganic NPs and other, less common nanoparticle formulations.

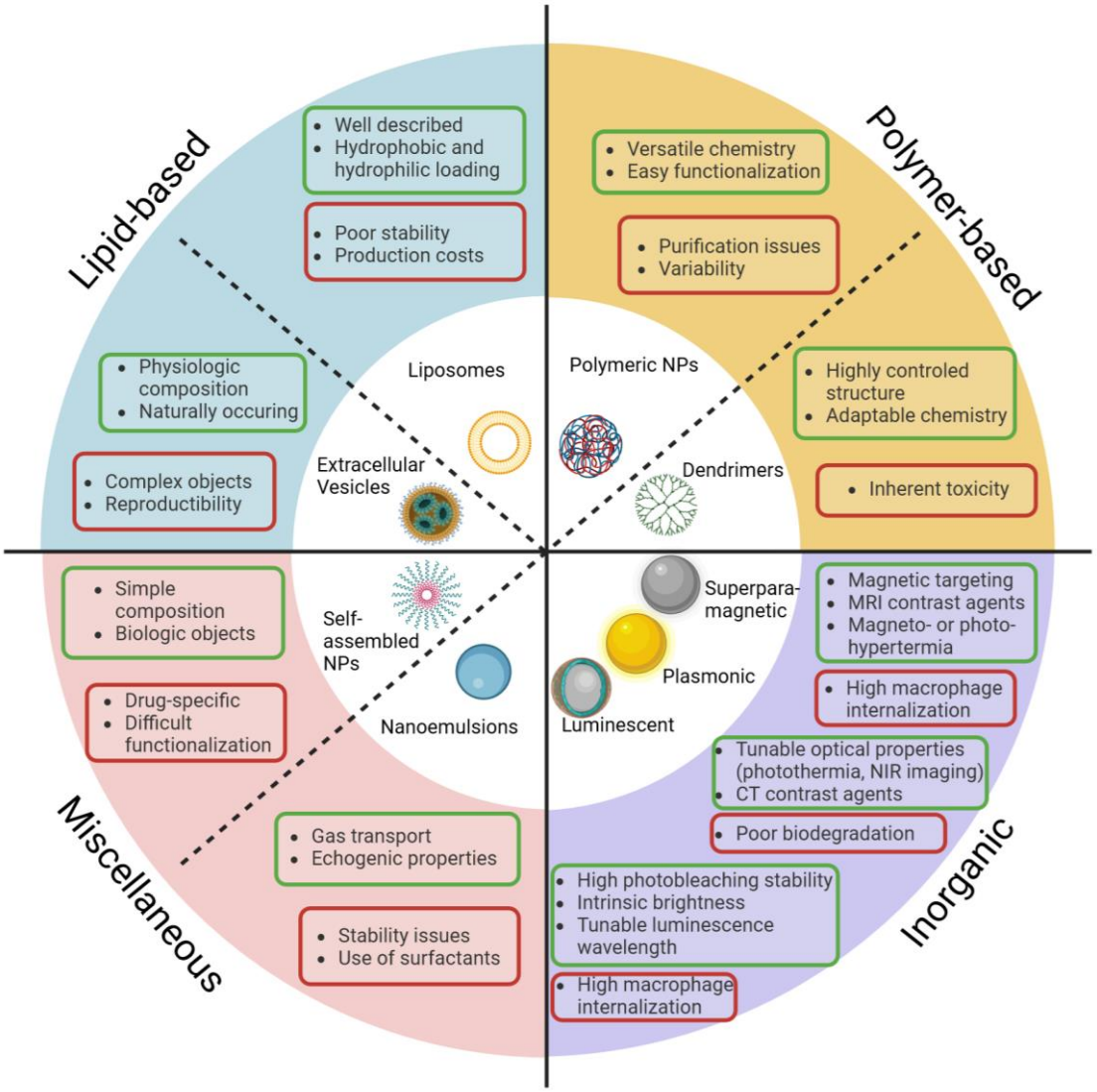


Figure 9: Main NP types used for stroke treatment and imaging. Their associated advantages (green frame)/drawbacks (red frame) are indicated. CT: computer tomography; NIR: near infrared. Respective examples of superparamagnetic, plasmonic and luminescent NPs are iron oxide NPs, gold NPs and quantum dots. Created with BioRender.com.

B.1) Systematic literature review

To better capture the state of current nanomedicine development for thrombotic diseases, a systematic analysis of preclinical research involving NPs for management of AIS was performed. For that purpose, all articles referenced on PubMed in the last five years (2019-May 2024) with the following keywords were extracted: [“stroke”] AND either [“nanoparticle”], [“nano”], [“liposome”], or [“lipo” AND “nano”]. The research yielded 856 articles. 440 of which were not retained for various reasons: 4 of them were duplicates, 1 presented clinical results,4 were inaccessible (1 article in Japanese, 3 where articles were behind

paywalls with no answer from the corresponding authors despite at least 3 contact attempts), 9 evoked fundamental properties of NPs and thus no applicable, 4 articles where no description of the NP used was present, 2 which presented toxic NPs (thus NPs that cannot be used; one was composed of OX26-PEG-coated gold NPs, the other of chitosan-dextran sulfate nanocomplexes), and 8 were rejected for ethical concerns (2 were retracted, 1 was labeled as “expression of concern” by the publishing journal, 1 was identified in a mass fraud investigation, 4 were displaying questionable results with no adequate response by the corresponding authors as identified on PubPeer by various researchers). 408 articles were further excluded as they were outside the scope of this systematic review, including use of extracellular vesicles as biomarkers, labeling of cells by NPs before injection, treatment of atherosclerosis, etc. Of the selected 416 articles, 169 were reviews and thus excluded. The remaining 247 articles were analyzed for their use of NPs in addressing AIS (including 10 which are related to hemorrhagic stroke, but with methods which could also be relevant for ischemic stroke treatment), as well as their relevance towards clinical translation. Notably, their use of *in vivo* models and results regarding scalability (storage, stability, etc.) was assessed. The repartition of these articles by NP type and applications are recapitulated in Figure 10. It is worth mentioning that 15% of the articles report nanoplatforms for imaging of the ischemic area through various modes (MRI, ultrasound (US), near-infrared (NIR) luminescence, etc.), and a third of these imaging NPs were capable theranostic approaches, with for instance the H_2O_2-triggered polymeric nanoparticle (PNP) developed in 2023 by Wang *et al.*, which had antithrombotic capacities *in vivo* coupled with imaging of the clot region through photoacoustic tomography [161].

The systematic analysis of the preclinical nanomedicine research for AIS in the last five years revealed a broad variety of NP types and provenance, as displayed in Figure 10. Among them, PNPs account for the most studied material (34%), with poly(lactic-co-glycolic acid) (PLGA) the most represented polymer used (31% of PNPs) due to its self-assembling properties. As for lipid-based materials (30% of articles), half of them is composed of the well-described liposomes, but also include lipid NPs or nanovesicles such as extracellular vesicles (EV). Finally, inorganics and other types of NPs (nanoemulsions [162], nano-microbubbles [163,164], etc.) represent together the last third. This diversity illustrates how researchers can use specific qualities of certain NPs to aim towards various ways of dealing with ischemic strokes (innate properties, tunable chemistry, etc.). However, 15% of these NPs incorporate cellular

elements (such as membrane-derived coatings [142] for the most part, or EVs [165]), with specific challenges related to sourcing, biological characterization and safety. Nonetheless, some authors have already addressed these, such as Son *et al.*, which described in 2024 EVs sourced from 3D cultured mesenchymal stem cells (MSC) for ischemic tissue regeneration with large-scale production in mind and evaluated batch-to-batch variability [166].

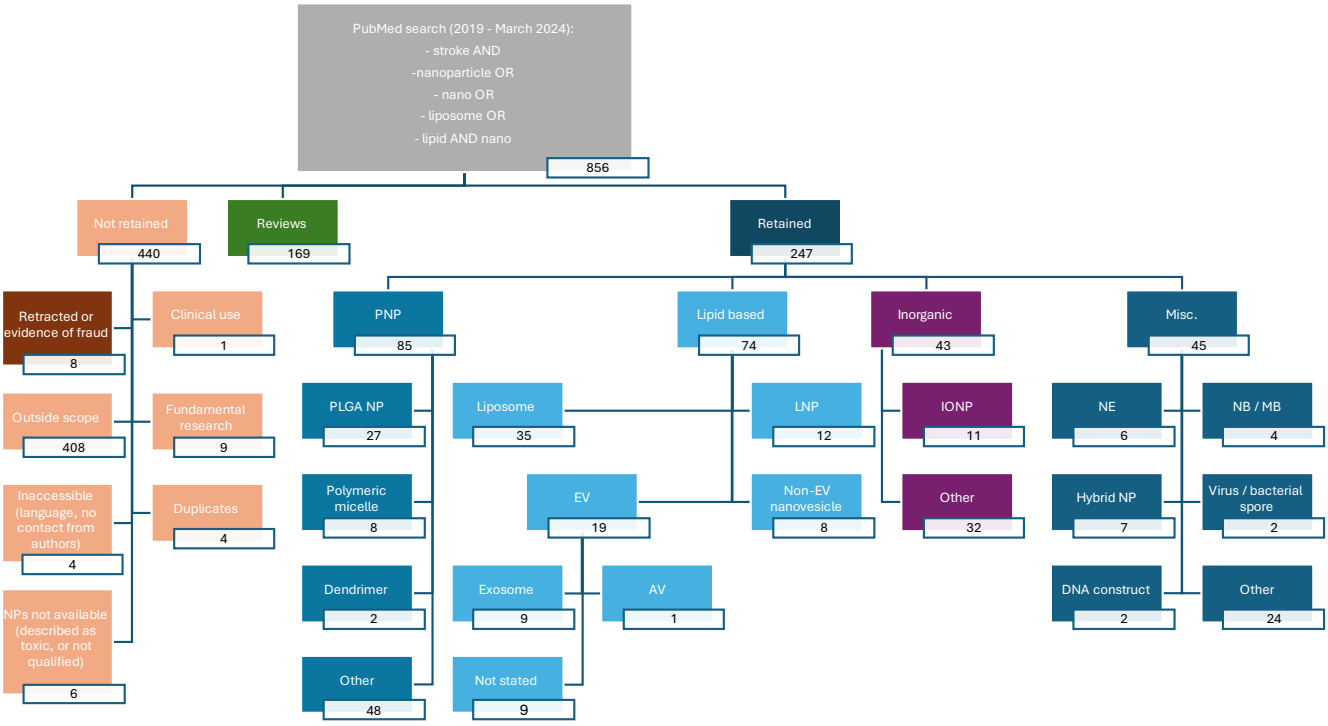


Figure 10: Selection process of articles published in the last five years regarding the use of nanoparticles for stroke treatment. Full selection including causes of rejection, and classification by NP type. LNP: lipid nanoparticle. EV: extracellular vesicle. AV: apoptotic vesicle. IONP: iron oxide nanoparticle. NE: nanoemulsion. NB/MB: nanobubble / microbubble.

B.2) Polymeric nanoparticles

Polymeric NPs (PNPs) are versatile drug delivery systems made of particulate dispersions of polymers and have a size range between 10 and 1,000 nm. Their size, shape and mechanical properties can be precisely designed, thanks to several easy fabrication techniques, and a wide list of natural or synthetic biocompatible and biodegradable monomers/polymers that can be used as bricks for their synthesis. PNP surface can be tailored with the insertion of targeting moieties to increase the particle selectivity to the therapeutic target. For these reasons, PNPs are investigated for different biomedical applications, including stroke treatment. Interestingly, based on the systematic literature

review, the most used PNPs were based of PLGA (Figure 10.a), a well-characterized synthetic polymer, even though many different polymeric materials exist [123].

Our group developed in 2018 fucoidan-labeled PNPs carrying rtPA adsorbed on the surface. PNPs were made of polysaccharide-poly(isobutylcyanoacrylate) by a redox radical emulsion polymerization. With this method, the polysaccharides were distributed on the surface of the PNPs to allow rtPA adsorption. The addition of dextran modified with amino groups increased the stability of the drug. This technology showed, both *in vitro* and *in vivo*, increased affinity to blood clots and enhanced thrombolytic efficacy [167]. Later, our Team developed and tested other PNPs named fucoidan-functionalized dextran submicroparticles (Fuco-SPs), to explore the use of polysaccharides as a biocompatible and biodegradable material. These PNPs were obtained by green chemistry starting from FDA-approved materials. They were successfully loaded with rtPA, with high encapsulation efficiency of about 65% and 80% for control-NPs and Fuco-NPs, respectively. *In vivo*, Fuco-SPs loaded with rtPA could improve the angiographic scores in murine stroke models: Fuco-SPs loaded with rtPA showed a 67% total recanalization rate versus only 33% for free rtPA treated mice at the recommended rtPA dose in this model [168].

PNPs shape can be finely tailored, to enable specific hemo-dynamic performance after systemic administration. For example, Moore *et al*. designed discoidal polymeric nanoconstructs (DPNs) that have a diameter of 1,000 nm and a height of 400 nm, and are composed with a mixture of (PLGA) and poly(ethylene glycol) (PEG). DPNs were successfully tested *in vitro* and *in vivo* for vascular delivery of imaging and therapeutic molecules against tumors [141]. Colasuonno *et al*. tested rtPA-loaded DPNs as a thrombolytic agent, demonstrating a clot lytic activity similar to the free drug in static experimental conditions, while it was increased in microfluidic experiments with dynamic conditions. *In vivo* experiments on the mouse mesenteric vein thrombosis model confirmed the clot lytic efficacy, where rtPA-DPN outperformed free rtPA for occlusion resolution [169]. Another approach based on hemo-dynamic performance was proposed by Korin *et al*. in 2012. Shear-activated nanotherapeutics (SA-NTs) produced by spray-drying concentrated solutions of small PLGA NPs (~180 nm) to form microaggregates (~3.8 μm). These microaggregates are stable in aqueous solution due to the PLGA NPs' hydrophobicity and remain intact under physiological blood flow conditions.

Interestingly, they break when exposed to high shear stress, similarly to what occurs in proximity to an occluded vessel, enabling the release of tPA near the occlusion. *In vitro*, in presence of a simulated clot, SA-NTs showed increased thrombolytic activity in comparison to free tPA. *In vivo*, SA-NTs induced progressive thrombolysis, increased efficacy, and animal survival in two different preclinical animal models [170]. A combined approach mixing targeting, thrombolytics and ultrasound sensitivity was proposed by Marsh *et al*. in 2007. They tested a fibrin-specific liquid perfluorocarbon (perfluoro-octylbromide) NP loaded with the thrombolytic agent streptokinase. Perfluoro-octylbromide is a biocompatible molecule with echogenic properties. The authors confirmed the efficacy of this technology as an acoustic contrast agent, useful for clot imaging and volumetric analysis. Furthermore, the clot lysis was increased in comparison to free streptokinase thanks to the NPs' targeting ability and could be monitored through ultrasound visualization [171]; they expanded this approach by substituting streptokinase by urokinase and performed *in vivo* thrombolytic and targeting assays in dogs [172]. Similarly, Kawata *et al*. combined basic gelatin and zinc ions to carry and control the activity of rtPA Monteplase (Cleactor®). In this complex, rtPA activity is reduced to 45%, but it can be fully restored after ultrasound exposure. This approach allowed the rtPA protection from serum proteins inactivation, and the control of off-site effects of the treatment (i.e., hemorrhagic transformation). rtPA-loaded gelatin-zinc particles have an intrinsic targeting ability due to the affinity between gelatin and VWF, as highlighted by *in vitro* and *in vivo* experiments in the mouse arterial thrombosis model. Animal experiments confirmed the efficacy of the treatment, and the survival rate dramatically increased in comparison to free-rtPA treatment in the swine acute myocardial infarction model [173].

Multifunctional polymers with specific features, such as microenvironment responsiveness, were adopted for PNP crafting. An example is given by the technology proposed by Wu *et al*. in 2022: PNP made with a modified version of PEG, having in the structure a ROS degradable poly(2,2′-thiodiethylene 3,3′-thiodipropionate (PTT) polymer with an antioxidant activity, and a thrombin-cleavable peptide (NH_2-norleucine-TPRSFL-C-SH). This tailored polymer is cleaved in the presence of thrombin, with a resulting particle rearrangement and shrinkage, to improve brain penetration. The synthesized particles made with a modified co-polymer (PTT NP) showed in biodistribution experiments the efficient localization into the ischemic area 24h after stroke induction and treatment. PTT NPs showed positive effect in the transient middle cerebral artery occlusion (TMCAO) mouse model, with a reduction of the infarct area

from about 60% (phosphate buffered saline, or PBS, group) to 30% (PTT NPs). To further increase the brain penetration, the surface of the PTT NPs was decorated with AMD3100 for its specific affinity with a chemokine receptor, CXCR4, specifically expressed in the ischemic tissue. The conjugation with AMD3100 enabled a significant enhancement in NP localization into the ischemic area, as confirmed by whole-animal fluorescence analysis. Lastly, AMD3100-conjugated shrinkable PTT NPs (ASPTT) were loaded with glyburide, an anti-edema drug. ASPTT-glyburide showed a controlled release of the drug, which happens only in presence of thrombin and ROS. *In vivo*, in the TMCAO model, ASPTT-glyburide outperformed the control conditions (ASPTT NPs without glyburide or free glyburide) in terms of reduced infarcted area, neurological scoring, survival and BBB leakage [174]. Similarly, Cheng *et al*. tested a pH-sensitive theranostic rapamycin (RAPA)-loaded NP system (RAPA/Gd^{3+}@NPs), able to selectively release the payload (drug and contrast agent) in the ischemic tissue. RAPA/Gd^{3+}@NPs were synthetized by self-assembly of the pH-sensitive amphiphilic block copolymer (mPEG-b-P(DPA-co-HEMA)-Ce6) in aqueous solution with RAPA and Gd^{3+}, obtaining spherical particles with a mean diameter of 20−30 nm. The biodistribution in the TMCAO rat model showed high accumulation of RAPA/Gd^{3+}@NPs inside the ischemic area 6h-post administration, as displayed by MR T1-imaging and ex-vivo NIR fluorescence imaging. Also, neurological and behavioral tests showed an amelioration of ~50% of the scores after treatment with RAPA/Gd^{3+}@NPs, in comparison to the saline control group. Similar benefits were found when evaluating the lesion size and BBB integrity, with a significant edema reduction in the ischemic hemisphere. Finally, these technologies showed a good safety profile, with no obvious damage detected by histological analysis of the main organs [175].

A subtype of highly ordered multibranched polymeric NPs, called dendrimers has also been investigated for drug deployment in stroke, as it is possible to precisely tune their size distribution, architecture, and functionalization. For example, Lee *et al*. described early-generation polyamidoamine dendrimers (PG2HR), which have been tested as gene carriers in TMCAO stroke animal models and injected together with heme oxygenase-1 (HO-1) plasmid. The complex pHO1/PG2HR reduced apoptosis and infarct sizes (from 40% to 30% total infarct brain area) in ischemic brains, suggesting a potential use as gene therapy of inflammatory diseases including ischemic stroke, also due to the high gene delivery efficiency and low cytotoxicity [176]. Nonetheless, a general consensus emerged on the toxicity of certain

dendrimers with for instance hemolysis and cell death. In 2023, Li *et al*. described PLGA-modified PAPAM dendrimers in order to mitigate their toxicity. They loaded these NPs with a circular RNA, CircOGDH, in order to improve neurological damage in the ischemic penumbra. They observed no toxicity in a murine ischemia/reperfusion model, and improved neuron survival and neurologic function, demonstrating a safe use of these dendrimers for neuroprotection post AIS [177].

Even though PNPs have a great potential as nanomedicines due to their versatility, highly controlled chemistry, tunable architecture, and the broad range of drugs and targeting moieties they can be equipped with, several limitations remain to be overcome. PNPs synthesis often requires the use of catalyzers, organic solvents, photo-polymerizers, which are all potentially toxic reagents for cells and tissues. Therefore, extensive purification steps are needed to limit the presence of impurities. Several biocompatible and biodegradable polymers face reproducibility and scale-up issues with batch-to-batch variations. Finally, to ensure suitability for biomedical application, it is crucial to outline a standardized array of characterization techniques in order to guarantee a complete quantitative analysis.

B.3) Lipid-based nanoparticles

Lipids have been used since the very beginning of nanomedicine, with liposomes first being discovered in 1964 and resulting in the first ever approved nanodrug, Doxil [122,123]. Later developments have offered various other forms, including lipid nanoparticles (LNP) or extracellular vesicles (EVs) [178]. Many different approaches for AIS treatment have been proposed, with liposomes being the most often described (half of lipid-based particles, based on the systematic literature review). Since the obtention and use of EVs differs significantly from other lipid-based particles, they were treated separately in the following paragraph “Part One. II. B.5) Miscellaneous nanoparticles”.

Liposomes are nano- or micrometric sized particles, composed of a phospholipid bilayer which encloses a hydrophilic core. Therefore, they can be loaded with both hydrophobic and/or hydrophilic molecules. Thus, they can offer protection from the circulation, stabilization, and increased circulation half-life to the loaded compounds, but they can also benefit from passive or active targeting, with surface modifications through various targeting moieties[178]. For stroke applications, thrombolytic drugs or contrast agents were principally incorporated in the hydrophilic region. This idea was applied successfully in the

work of Heeremans *et al.* in 1995, where rt-PA (Actilyse®) loaded liposomes showed a significantly higher thrombolytic efficacy than free rt-PA. However, the incomplete and suboptimal encapsulation efficiency led to a fast removal of more than 50% of the circulating drug [179]. To further increase the systemic circulation of thrombolytic agents, Kim *et al*. tested polyethylene glycol (PEG)-ylated liposomes to conceal the particles from the innate body defense. Both *in vitro* and *in vivo* rtPA release rates were slower and more sustained in the presence of the PEG, with a significant improvement (up to 20-times) of the drug's half-life. Furthermore, rtPA entrapment efficiency was constant over 45 days of storage at 4°C [180]. Echogenic liposomes, carrying gas in the core, are ultrasound-responsive, and were tested as contrast and thrombolytic agents, alone or in combination with tPA. The selective and controlled release of the liposome content was driven by ultrasonic pulses that trigger cavitation and the destruction of gas bubbles, thus further affecting clot integrity and tissue permeability. These advantages were confirmed in several studies, where rtPA-loaded echogenic liposomes showed an increased thrombolytic activity in presence of ultrasound, compared to the free drug [181]. Nonetheless, several studies highlighted that the rtPA encapsulation efficiency was limited with this technology, in addition to the limited targeting properties. Overall, further optimization steps are needed before reaching a clinically valuable product [123]. By using different lipids and their relative ratios, the liposome composition can be tailored, for instance, with the addition of surface targeting moieties or stimulus responsive molecules to increase selectivity. Furthermore, the possibility to load multiple and different types of drugs allows one to combine the thrombolytic function with neuroprotection. An example is given by the design developed by Quan and colleagues who encapsulated tPA and aspirin (anti-inflammatory drug) in liposomes associated to cryo-shocked platelets (CsPLTs). In this novel approach, the binding of CsPLTs with liposomes was mediated by an "host-guest" interaction between adamantane, a reactive oxygen species (ROS)-responsive molecule on the liposomes, and cucurbit[7]uril on the platelet membrane. This technology showed high affinity with clots as demonstrated *in vitro* and *in vivo* in a murine model of mesenteric artery thrombosis. *In vivo*, in a photothrombotic stroke mouse model, a significant improvement of neurological scoring, volume of stroke damage, and BBB leakage was documented. This technology showed a safe profile with no negative effects as assessed by histological analyses, coagulation molecular indicators, liver and kidney functions [182]. In 2023, Sun *et al*. proposed a smart liposomal nanocarrier, aiming to tackle neutrophil extracellular traps (NET)

formation (NETosis): this phenomenon, which occurs in several pathological conditions including stroke, is regulated by the neutrophils and is responsible for the immune system overactivation in the brain. Their liposomal system (C-Lipo/CA) was intercalated with ROS-responsive polymers (for ROS scavenging and drug release) and coated with CREKA peptide sequences (for fibrin binding). C-Lipo/CA were loaded with Cl-amidine, a peptidylarginine deiminase 4 (PAD4) enzyme inhibitor, to block the NETosis process. *In vitro*, C-Lipo/CA showed efficient binding to microthrombi. *In vivo* experiments displayed a good safety profile, with no impairments in organ architecture and biochemical indicators. In addition, biodistribution tests displayed high retention of the particles in the ischemic brain area. In the tMCAO animal model, C-Lipo/CA showed positive effects on animal behavior, a lesion size reduction from 46.7% (saline group) to 12.1%, and BBB leakage, resulting from the suppression of NETosis and the cyclic guanosine monophosphate-adenosine monophosphate synthase-stimulator of interferon genes (cGAS-STING) pathway, both overactivated in ischemic area [183]. Interestingly, empty liposomes with a specific lipid composition, but without any encapsulated drug, could also be effective. A brief report published in 2022 explained that empty nanoliposomes (<100 nm size) made of phosphatidylcholine, cholesterol and monosialogangliosides, have a positive effect against stroke. The authors showed an antioxidant protective response *in vitro* on human neuroblastoma (SH-SY5Y) and human microvascular endothelial cells exposed to oxygen-glucose deprivation-reoxygenation (OGD/R). These nanoliposomes also improved neurological scoring, reduced infarct, and edema size in tMCAO mice model [184]. Interestingly, Al-Ahmady *et al*. found two temporal windows to maximize liposomes localization into the brain after stroke: during the hyperacute phase (0.5 h post-stroke), and the sub-acute/chronic phase (48h post-stroke), which may refine how these potential therapies are administered [185]. Overall, drug encapsulation into liposomes increases efficacy, stability, and therapeutic index of the thrombolytic treatment, reducing at the same time toxic and off-site effects. Adverse effects can be further reduced by adding stimulus-responsive molecules to the liposome composition, thus releasing the drug only at the thrombus site. Nevertheless, their use can be limited due to complex synthesis including scale-up difficulties, high production costs, poor stability and short half-life after administration or during storage [178,186].

Lipid nanoparticles (LNP) were developed to address some of the liposomes' shortcomings. The two main types are the solid lipid nanoparticles and nanostructured lipid carriers. In contrast to liposomes with their hydrophilic

core and lipid shell, they are composed only of solid lipids for SLNs, and of a mixture of solid and liquid lipids for NLCs. They benefit from higher drug loading capacity, easier production without using organic solvents, and have a better controlled release of their cargoes [178]. Notably, The COVID mRNA vaccines are composed of LNPs, thus showcasing how useful these NPs can be [187]. Several similar approaches used LNPs to deliver mRNA in order to treat AIS. For instance, Ganbold *et al*. described in 2022 LNPs containing novel peptidomimetics, named DoGo, to allow the delivery of siRNA within LNPs. They used a siRNA against TLR4 to knockdown TLR4 expression in oligodendrocytes in order to favor their polarization towards anti-inflammation. After demonstrating the gene delivery capacity of these siRNA loaded DoGo containing LNP (siTLR4/DoGo310) *in vitro* with oxygen-glucose-deprived murine microglia, they administered these LNPs in a transient ischemia murine model, the tMCAO, and reported accumulation of the siRNA in the peri-infarct zone, accompanied by a significant TLR4 knockdown with a 50% reduction in mRNA and protein levels, and improved neurological scores after 72 h [188].

Nonetheless, such lipid-based delivery platforms still face production and logistic limitations, as exemplified by the challenges of COVID mRNA vaccines, including storage at subzero temperatures [187], and they rely on complex mixtures of various lipids which may impede development, fine-tuning and functionalization – for instance to grant targeting capacities - of these NPs [178].

B.4) Inorganic nanoparticles

Inorganic NPs have been investigated for their intrinsic material features, such as catalytic, magnetic, thermal or optical properties, which sustained their application as a diagnostic and therapeutic tool, notably for stroke application: they can be of various composition, ranging from semiconductors, metals, metal oxides, to lanthanide-doped NPs [123], with iron oxide nanoparticles (IONPs) being the most used (representing 25% of the published preclinical research on nanomedicine for strokes).

For instance, Mn_3O_4 nanoenzymes stabilized by human serum albumin (HSA), named HSA-Mn_3O_4, have been studied as an antioxidative treatment to address ischemic stroke reperfusion injury. Mn_3O_4 NPs can release manganese ions in circulation, which promotes the activity of superoxide dismutase 2 in the body. The positive *in vitro* results against oxygen-glucose deprivation, endoplasmic reticulum (ER) damage and cell apoptosis were further confirmed in animal investigations. The presence of the HSA on the surface enabled

prolonged circulation time (~72h), preserving the ROS scavenging ability from off-site activation. *In vivo*, HAS-Mn_3O_4 showed a strong neuroprotective effect, with reduction in stroke volume and improvement in behavioral score. In addition, the highest dose of HSA-Mn_3O_4 (0.4 mg/kg) reversed the ER stress pathways activation to normal level, counteracting the activation of pro-apoptotic signals [189]. Magnetic NPs such as iron oxide NPs (IONPs) - composed of magnetite (Fe_3O_4), maghemite (γ-Fe_2O_3) or mixed ferrites (MFe_2O_4 where M=Co, Mn, Ni or Zn) - have been proposed and tested for several different applications. IONPs are non-toxic, biodegradable, can modulate cell differentiation and eventually become a source for *in vivo* iron supplements, useful as anemia treatment [190]. A clear example is the approach proposed by Voros *et al*., that aimed to increase thrombolytic activity of rtPA (Alteplase®). They tested clusters of iron oxide nanocubes, coated and stabilized by rtPA (rtPA-NCs), to have a combined pharmacological and thermal therapy of blood clots. Thermal therapy is a strategy already approved by the FDA against cancer, to increase the efficacy of chemotherapy. For stroke, this strategy involves heating local areas through magnetic hyperthermia, in order to improve rtPA clot lysis. *In vitro*, rtPA-NCs showed higher dissolution rates compared to free rtPA, in absence of heating (around 100 times). The exposure to thermal treatment increased even more the efficacy of the rtPA-NCs (10 times) compared to unexposed NPs. *In vivo* experiments on the mouse mesenteric thrombosis model confirmed rtPA-NCs efficacy, leading to a complete clot dissolution in less than 3 min, while the same concentration of free-rtPA was ineffective even after 60 min. Noteworthy, rtPA-NCs displayed high values of transverse relaxivity, suggesting the possible application of these particles for MRI imaging and magnetic targeting of the clot [191]. Indeed, magnetic NPs have been exploited as contrast agent for MRI since 1993 [152,192]. Notably, nanoscale superparamagnetic IONPs (SPIO), with a 20-50 nm core size, are capable of increasing contrast for T2 weighted MRI. Further investigations on IONP magnetic properties revealed that by reducing the NP size, the longitudinal T1 relaxation effect was enhanced. For this reason, ultrasmall superparamagnetic iron oxide NPs and extremely small-sized iron oxide NPs characterized by a core size below 4 nm and a paramagnetic behavior, were suggested as T1 contrast agents for MRI [193]. This is mainly due to the high surface-to-volume ratio of the NPs and the predominance of a magnetically disordered spin-canted shell [194].

ANPs were also applied as agents or carriers of neuroprotective drugs. For instance, Cerium oxide (CeO_2) NPs have intrinsic antioxidant and

neuroprotective effects, in addition to BBB crossing capacity, and were therefore already proposed as drug delivery systems for neurological disorders [195]. For instance, Li *et al*. investigated CeO_2 NPs loaded with dl-3-n-butylphthalide (NBP-CeO_2 NPs). NBP acts on the ischemic area microcirculation promoting angiogenesis, neurogenesis, and neuroplasticity, reducing inflammation and apoptosis, with overall neuroprotective effects. NBP-CeO_2 NPs reduced ROS levels in brain microvascular endothelial cells and hippocampal neurons after OGD/R. In the TMCAO mouse model, NBP-CeO_2 NPs preserved BBB integrity and reduced lesion volume in comparison to control conditions (damaged area of 39.8% in the saline treated group, reduced to 10.6% in the NBP-CeO_2 NPs group). Neuroinflammation was also reduced in the NBP-CeO_2 group, in comparison to the saline condition. Interestingly, empty CeO_2 NPs also showed positive effects on BBB leakage, lesion size reduction and neuroinflammation, supporting the development of this nanotechnology for new stroke therapies [196].

Inorganic NPs also enable theranostic approaches, as shown by Kim *et al*., with glycol-chitosan coated gold NPs, conjugated to fibrin-targeting peptides (fib-GC-AuNP). Gold NPs especially show desirable optical properties due to the surface plasmon resonance effect, enabling photothermal treatment. The particles from Kim's group hold targeting features and the capacity to visualize cerebrovascular thrombi by CT-based imaging. Thus, fib-GCAuNP allowed quantification of cerebral thrombi over the tPA treatment to directly evaluate its thrombolytic effect. Remarkably, fib-GC-AuNP acted as CT contrast agent and enabled the image analysis on recurrent thrombosis by CT for up to 3 weeks, with a single administration and without neurobehavioral or systemic toxicity [197].

Even though possible toxicity issues related to inorganic NPs have been highlighted and debated [198,199], the literature still does not offer a definitive conclusion on this matter [200,201]. Their biodegradation depends mostly on NP material and coating, and for instance, clear degradation issues have been shown with certain inorganic nanomaterials such as gold [202]. Other inorganic technologies showed good biocompatibility and reduced risk of toxic effects [197,203–205]. Overall, further pre-clinical and clinical investigations focusing more on safety and toxicological aspects will be needed to elucidate the potential risks for human health.

B.5) Miscellaneous nanoparticles

Nonetheless, a fifth of the published preclinical research involves NPs that fall outside these main categories. These include among others extracellular vesicles (EVs), nano/microbubbles, nanoemulsions, self-assembled materials or drug aggregates/nanocrystals.

Extracellular vesicles, or EVs, are small cell-derived vesicles delimited by a lipid bilayer membrane. They can range from 20 nm to 10 µm, and contain a wide variety of molecules including DNA, proteins, lipids or metabolites, but they lack the capacity to replicate [206]. They can serve as biomarkers for various physiological states, including pathologies, and can have broad-reaching effects in neighboring cells and distant tissues. Multiple subtypes of EVs have been discovered, depending on their biogenesis mechanism and sometimes role in physiological conditions: the three main recognized EV categories are exosomes, with are secreted through exocytosis of intracellular vesicles, microvesicles which are directly formed by membrane budding, and apoptotic vesicles formed during apoptosis. Interestingly, their content varies based on several factors, such as generating cell type and pathological state, and can be made to transport pharmaceutical compounds; they were found to have several roles in the body such as modulating cell contents, cell-cell communication, inflammation, tissue repair, or cancer metastasis [207]. They have thus been explored in order to influence the evolution of ischemic tissue post AIS, representing 8% of published preclinical nanomedicine research in the last five years. For instance, Zhu *et al*. described in 2021 exosomes that were derived from human neural stem cells (NSC) and loaded with brain-derived neurotrophic factor (BDNF), a neurotrophic factor which acts on cell differentiation, growth and neurogenesis. They characterized the exposomes obtained from NSCs with or without BDNF loading (BDNF-hNSC-Exo and hNSC-Exo respectively) and found no significant differences in their size and composition. I*n vitro*, they were both found to reduce NSC apoptosis in an oxidative damage assay, with DDNF-hNSC-Exos being more efficient at protecting cells against apoptosis. These results were followed *in vivo* neuroprotection experiments with a transient ischemia model in rats. Both formulations were again found to have protective effects, reducing the infarct size from 38% (PBS control) to 22% (hNSC-Exo) and 20% (BDNF-hNSC-Exo). Furthermore, they observed a reduced inflammation and increased neurogenesis in the peri-infarct zone, with increased effects for the BDNF-hNSC-Exos [208]. However, such EV approaches face multiple hurdles: as they are obtained from live cell secretions, their purification is complex endeavor with high batch-to-batch variability, a

critical need for constant extensive characterization, and this origin also limits production scale-up.

Microbubbles (MBs) are microscale core-shell particles, with the particularity of having a gas core. They have been widely used as ultrasound contrast agents due to their cavitation properties [144]. The shell composition can vary from proteins (e.g., albumin), lipid mixture or polymers, and the gas is most often composed of perfluorocarbons (PFCs) or sulfur hexafluoride to increase MBs stability compared to air, nitrogen or dioxygen. In addition to their use as contrast agents, various therapeutic approaches were explored such as gas delivery where dioxygen can be delivered to counter ischemia or with nitric oxide as cell signaling modulation, or directly through ultrasound therapy. Focal ultrasound therapies have been described as tools to disrupt cell membranes, endothelial layers and even the BBB, with potential for therapeutic agents' delivery into cells and tissues, and MBs were found to improve this method through their cavitation capacity, either stable or inertial with MB bursting. Nonetheless, they face some limitations such as stability or micrometric size (which limits their presence in the circulation and their half-lives), which led to the exploration of nanoscale MB-inspired objects such as nanobubbles (NBs) which are MBs of nanometric dimensions, nanodroplets which are stabilized nanometric liquid PFC emulsions, the phase transition of which can be triggered to form NBs/MBs, or *in-situ* generation of NBs/MBs by NPs through physical or chemical catalysis [144]. As such, they may benefit from ultrasound properties of MBs with the advantages of NPs such as extended circulation, extravasation and molecular targeting properties. For example, Ye *et al*. proposed in 2023 nanosized PFC oxygen carriers (NanoBs) composed of liquid PFCs which could vaporize in conditions close to the physio- and pathophysiological temperatures in ischemic brains. They demonstrated *in vitro* that these 300-400 nm NanoBs could release oxygen in a temperature-dependent manner, and an *in vivo* assay in a transient murine ischemia model demonstrated that these oxygen-delivering NanoBs significantly reduced the infarct area compared to saline, dioxygen alone or non-oxygen-loaded NanoBs [163]. Interestingly, some liquid PFC nanoemulsions which do not use their gaseous properties (vaporization, ultrasound contrast) have also been explored. For example, dodecafluoropentane nanoemulsion (DDFPe) is a neuroprotectant perfluorocarbon that was initially proposed as ultrasound contrast agent, with additional investigations that highlighted the *in vivo* potential as oxygen and carbon dioxide transport. Preclinical studies in the rabbit embolic stroke model demonstrated >80% reduction in acute infarction, with repeated administration

of DDFPe over a 24-hour period showing positive improvement in vital signs and cerebral tissue, as highlighted by histological analysis. Different MRI markers of infarct improved in the early hours following vascular occlusion, and even included a clinical trial for AIS in 2019 [209–211].

Many other less common NPs have been described as potential tools for AIS management. Such examples include other biological vectors like viral particles to deliver miRNAs into the ischemic tissues [212], or bacterial spores to deliver drugs like urokinase to the thrombus [213]. Some authors also proposed solid NPs composed of drug aggregates [214] or self-assembled non-polymeric NPs, with for instance the self-assembling antioxidant betulinic acid NPs (A-BAM NPs) that were formulated by Zhang *et al*. in 2022 with modifications to ensure dissociation in an acidic environment and brain targeting capacity through the AMD3100 incorporation. Intravenous administration showed an increased survival of mice in a transient ischemia model, reduced infarct volume by 57%, and improved neurological scores. Furthermore, the neuroprotective peptide NA1, already in clinical trial (phase III) for its neuroprotective activity against NMDA receptor-mediated toxicity, was bound on the surface of A-BAM NPs. The additional conjugation of NA1 further increased the mice survival and reduced the infarct volume by 69.8% [215]. Another less known NP type was described by Zhou *et al*. in 2022, who synthesized tetrahedral framework nucleic acids (tFNAs), self-assembled by four specific DNA molecules. They investigated the role of these tFNAs in modulating the TLR2-MyD88NF-κB signaling pathway *in vitro* and *in vivo*, and demonstrated neuroprotection in a rat transient ischemic model with notably a reduction of infarct volume from 33.9% to 2.7% [216]. While some of these approaches are very promising, they are also very dependent on the nature of the compound used, and their less common use is associated with less characterization and general knowledge of their behavior, therefore making them more complicated to generalize and translate into clinical applications.

C) Nanoparticle targeting strategies

While the structure and composition of NPs can vary considerably, most recent nanoplatforms include some sort of targeting. Indeed, this is critical to ensure that the payload, or desired effect, can be delivered to the thrombus or the ischemic tissue. Limiting the drug delivery only to the thrombus can limit systemic side effects, while ensuring a local high concentration of active agents. Here are described various targeting strategies, from the single molecular targeting to multiple molecular targeting methods, as well as magnetic and

passive targeting (Figure 11). Notably, we focused on quantification of targeting capacities rather than therapeutic efficacy to illustrate the potential of the various methods described hereafter.

C.1) Passive targeting

In most stroke patients, there is a loss of the BBB integrity due to damaged tight junctions, which results in enhanced BBB permeability [217]. This pathological state can be used to increase the BBB crossing of circulating NPs in the ischemic region compared to the healthy one. This is the case in Yuan *et al.* study, where they showed a 33% higher accumulation of oligosaccharide NPs in the ischemic brain than in the healthy tissue in a tMCAO mouse model, only through passive targeting [218] (Figure 11). This strategy is particularly interesting to deliver neuroprotective agents. In addition to this enhanced permeability, the BBB presents a higher rate of transcytosis in stroke conditions which can additionally enhance the passive targeting of ischemia [219]. Although these strategies are less effective than active targeting, they don't require any specific coating, thus limiting the complexity of the nanosystem injected to the patient and making their production and approval easier.

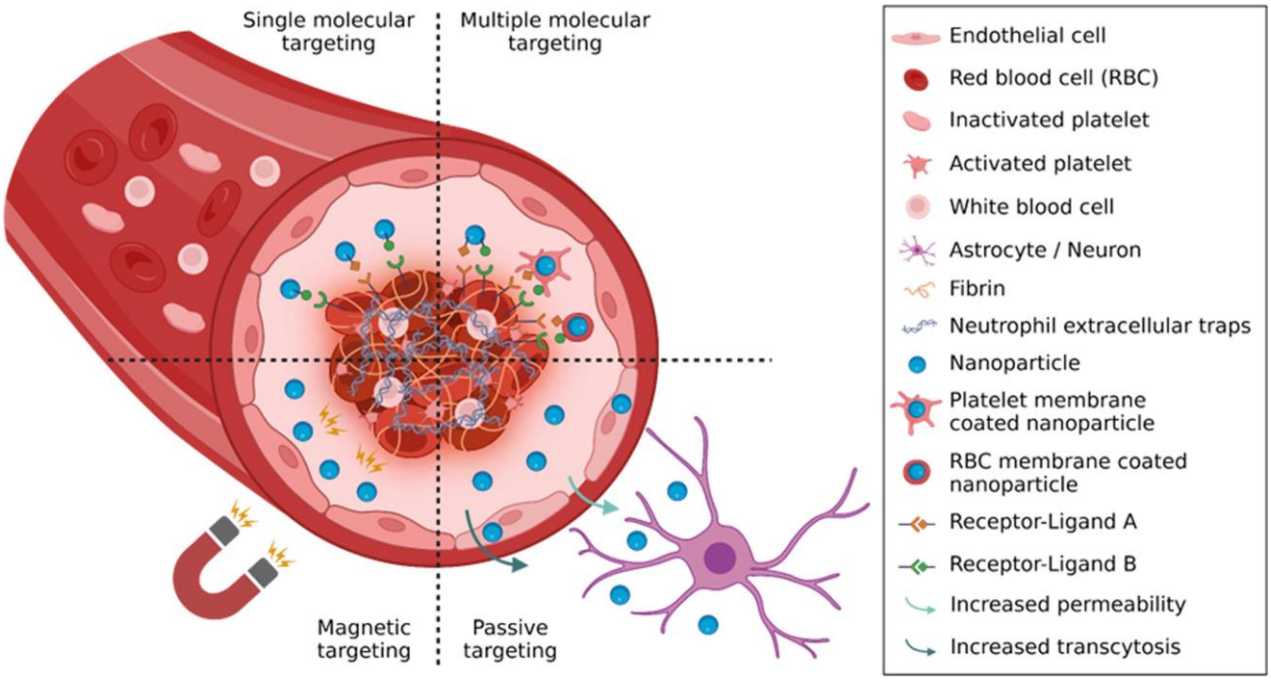


Figure 11: The different NP targeting strategies for stroke treatment and diagnosis. Created by Pierre Sarfati (with BioRender.com) [155].

C.2) Single molecular targeting

Nonetheless, multiple biomarkers have been identified to recognize either the blood clot, or the ischemic region. Regarding the former, some NPs aim to

target activated platelets. The peptide cRGD is among the well-known binding motifs used for NPs, as it was characterized for stroke application, to bind the GPIIb/IIIa receptor, which is expressed on platelets, and play a critical role during their activation and aggregation through fibrinogen and VWF binding [220]. For instance, Liao *et al*. described in 2019 a trimethyl chitosan NP, loaded with lumbrokinase (LK) and functionalized with cRGD. This system showed improved thrombolysis *in vitro* and *in vivo* on rat thrombosis models, compared to free drug (around 60% reduction in clot weight for targeted NPs vs. no difference for untargeted NPs) [220]. More complex designs were also described, such as the Janus-rod micromotors from Cao *et al*., in 2021, in which the cRGD targeting allowed the US-responsive objects to accumulate at the thrombus (3.4-fold improved accumulation at the thrombus vs. no cRGD), where enhanced penetration and thrombolysis (74%) was achieved [221]. Other biomarkers exist for activated platelets, such as the P-selectin, a transmembrane molecule expressed on activated platelets and endothelium, which mediates leukocyte adhesion through the Sialyl Lewis x (SLe x) motif on PSLG-1 ligand. A natural polysaccharide, fucoidan, was found to mimic this motif with high affinity and specificity [222], and can be used as targeting moiety: for instance, the technology developed in 2021 by Zenych *et al*. used it as a targeting agent. Here, fucoidan was crosslinked to PNPs, and the resulting Fuco-NPs could effectively target P-selectin and aggregated platelets *in vitro*, with a significant increase in aggregated platelets' targeting in a microfluidic setup compared to untargeted NPs [168]. Interestingly, some authors took into account the time-wise development of thrombi in their targeting, such as Pan *et al*. who described in 2017 micelles which could be loaded with LK and functionalized with Annexin V. Annexin V have high affinity for phosphatidylserine, a lipid presented on the exterior membrane of apoptotic cells, as well as on platelets during their activation. This allowed a significant accumulation of targeted micelles to the clots (compared to non-targeted) and significantly enhanced thrombolysis in $FeCl_3$ murine thrombosis model, when compared to free LK or non-targeted micelles [223].

Other groups chose to target components of the thrombus, such as the fibrin molecule. For instance, Marsh *et al*. described in 2011 streptokinase-loaded perfluorocarbon NPs decorated with *ad hoc* antibodies against fibrin (10^{-10} M affinity, with no reactivity toward fibrinogen). These NPs retained good streptokinase-mediated *in vitro* thrombolysis (20-30% increase in clot dissolution when compared to empty NPs). Moreover, in the canine thrombosis model, an accumulation of targeted NPs into clots was observed when

compared to the non-targeted NPs. However, they lack evidence of enhanced thrombolysis *in vivo* [172]. Recent literature focused on small peptides to target fibrin, notably CREKA [224], or engineered peptides [225]. For example, Seo *et al*. leveraged peptides, selected through phage display, that could only recognize fibrin-fibronectin complexes (and not fibrin alone), to allow the specific targeting of thrombi. This was incorporated in a transferrin-based nanocage to deliver C-terminal encoded microplasmin (and produced thanks to a single transgene expression). This system was validated *in vitro* for their clot binding properties. In the murine arterial thrombus or deep vein thrombosis models, they showed a 50% reduction of thrombosis, in comparison to non-targeted, non-loaded nanocages, or targeted microplasmin without the nanocage construct [225]. Nevertheless, some approaches aim not at dissolving the clot, but rather alleviating the damage of ischemia, therefore requiring targeting to the ischemic tissue. While the leakiness of the BBB can be exploited to deliver certain drugs with NPs [218], some authors increased the specificity of drug delivery to the damaged tissue by adding targeting moieties to ischemic regions [226], such as Zhang *et al*. who described in 2022 antioxidant NPs targeting CXCR4, a biomarker of ischemic cells in the brain, thanks to a small antagonist molecule, AMD3100. The resulting NPs were shown to significantly accumulate in the ischemic region with high reduction (50%) of the infarct region and significant neurological recovery compared to non-targeted NPs in mice stroke models [215]. Therefore, there is no single gold standard biomarker for thrombus targeting. Instead, multiple biomarkers have been identified. Appropriate targeting strategies should be carefully chosen by identifying the target area: the clot itself, the ischemic tissue, or a single cell type for example.

C.3) Multiple molecular targeting

All the targeting strategies mentioned above involve only one targeting agent and one biomarker. Yet, recent papers proposed alternative strategies, including grafting more than one targeting moiety at the NP surface to increase either their specificity or their accumulation at the thrombus site (Figure 11). Sun *et al*. designed liposomes coated with either platelet-binding peptides (PBP), fibrin-binding peptides (FBP) or a combination of them (PBP + FBP), to compare their thrombus targeting efficacy [227]. With a mouse carotid artery thrombus model, they showed that with a lower total peptide concentration, combination targeting allowed a greater accumulation to the clot than targeting with PBP or FBP only, which can be explained by the possible multiple interaction with receptors or clot components. This approach may also enhance the targeting

specificity to acute ischemic stroke thrombi which are made up of a dense outer shell containing mainly fibrin, VWF, and aggregated platelets [64]. In addition, their results proved that targeting can be impaired when ligand density is too high, and they suggested a role of the steric hindrance between the targeting agent and its target. Rather than targeting different components of the thrombus, several articles proposed to target only platelets with two different peptides grafted, RGD (GPIIb/IIIa binding) and EWVDV (P-selectin binding). In two different articles for respectively thrombus treatment and thrombus imaging, the combination of these peptides increased the accumulation of NPs at the thrombus site, compared to RGD or EWVDV decoration only [228,229]. Indeed, Pawlowski *et al*. demonstrated in a microfluidic dynamic flow experiment that the peptide combination enhanced the targeting to platelet-rich thrombus, doubling the retention onto platelets, compared to either one [228]. Grafting several molecules can also be a strategy to sequentially reach different targets in ischemic stroke [230,231]. For instance, by decorating liposomal nanocarriers with T7 peptide and stroke homing peptide (SHp), Zhao *et al*. aimed to cross the BBB, and then target ischemic neurons to deliver ZL006, a novel promising neuroprotective agent [230]. Their coating combination enabled nanocarriers to accumulate 1.5 times more in the ischemic brain than with T7 alone and reduced the infarction volume by approximately 30% compared to coating with T7 or SHp alone in a tMCAO model on rats. All things considered, grafting several targeting molecules can be performed to improve thrombus homing, to selectively select certain thrombi, or reach sequentially different targets.

Another simple solution for NP targeting without having to settle for one or more biomarkers was described: by leveraging the cellular membrane of critically chosen cells, some researchers addressed both the circulation stabilization (stealth) of their NPs and homing to the clot or the ischemic area. Based on the process behind platelet aggregation and clot formation, the platelet membrane coating of NPs was assessed [231–233]. For instance, Xu *et al*. described polymeric NPs coated with murine platelet membrane to deliver rtPA (PcNP) and compared them to erythrocyte-membrane coated control NPs (RcNP). They showed clear thrombus targeting of PcNPs vs. RcNPs in multiple murine thrombotic disease models, e.g., evidenced in a pulmonary embolism model with a significant fluorescence accumulation to the lungs compared to RcNPs. Moreover, they evidenced that while rtPA alone had a similar thrombolysis rate to their rtPA-loaded PcNP in mesenteric artery thrombosis mice models during thrombus formation, only the targeted NPs could elicit thrombolysis once the clot was fully formed. Finally, they demonstrated a clear

enhancement of neurological and survival outcomes of PcNP-PA in comparison to free rtPA in transient stroke murine models [232]. Notably, other cellular coatings could be used to reach different targets. For instance, Ma *et al*. described in 2019 polymeric NPs coated with neural stem cell (NSC) membrane to deliver an antiedema drug through the BBB membrane at the stroke site. However, they further strengthened the design by using CXCR4-overexpressing NSCs membranes and showed that it relied on the interaction between CXCR4 and SDF-1 (enriched in the ischemic microenvironment) to further enhance drug delivery and improve neurological recovery in a mouse stroke model compared to classic NSC membrane-coated NPs [142]. Comparable approaches relied for example on cellular membrane from highly brain-metastatic tumor 4T1 cells (from a breast tumor cell line) to target the brain ischemic tissue and noted a significant neurological improvement, in comparison to nonmembrane-coated NPs in murine models. These coated NPs accumulated three times more in the brain ischemic region than untargeted NPs [234]. Macrophage membrane coating has also been used to increase targeting and disguise from immune system cells. For instance, macrophage membrane coated manganese dioxide NPs targeted endothelial cell adhesion molecules, thus allowing ROS scavenging, neuroprotection, and macrophage-type polarization [235].

Even so, some key aspects must be considered when resorting to cellular targeting: as discussed by Xu *et al*., provenance of the cell membrane can play a major role in their tolerability by the host body, and human leukocyte antigen (HLA) matching could be an issue for scaling-up these therapies [232]. On the other hand, using platelet membrane to deliver NPs with platelet-affecting drugs can prove ineffective, as demonstrated by Yi *et al*. in 2020, who had to use erythrocyte membrane functionalized with CREKA peptide (for fibrin targeting) instead of platelet membrane since they aimed at delivering tirofiban, a GPIIb/IIIa antagonist which prevents platelets aggregation in thrombi and thus impaired the targeting of platelet membrane coated NPs [224].

C.4) Magnetic targeting

Over the past two decades, magnetic NPs have been increasingly used for biomedical applications (Figure 11). This can be explained by their numerous interesting properties, including their magnetic manipulability. Indeed, by applying an external magnetic field near the brain ischemic region, the circulating magnetic NPs can accumulate there. Ma *et al*. tested the effects of rtPA linked through carbodiimide-mediated amide bound to polyacrylic acid-coated magnetite (PAA–MNP) NPs. Positive results were obtained *in vitro* and

in vivo, in a rat embolic model of iliac artery occlusion. The PAA–MNP–rtPA under magnetic guidance along the artery restored the iliac blood flow, while control groups and free rtPA showed no improvement on hemodynamics [203]. Hu *et al*. designed rtPA-coated iron oxide microrods (rtPA-MRs) to target the cerebral thrombus and dissolve it through combined fibrinolysis and mechanical stimulation by an external rotating magnetic field [204]. With a distal MCAO stroke mouse model, the authors found that the microrods could efficiently target the brain clot by placing a magnet near the distal middle cerebral artery area. Further, the blood flow was restored in 25 minutes with rtPA-MRs at 0.13 mg/kg rtPA accompanied by rotating magnetic field, compared to the 85 minutes needed with free rtPA at 10 mg/kg. Thus, their nanosystem could perform a more efficient thrombolysis with approximately 100 times fewer rtPA. In addition to fibrinolytic agents, magnetic guidance can be used to deliver neuroprotectants to the stroke region and thus limit the cerebral infarction. In their work, Kim *et al*. tested MSC-derived nanovesicles encapsulating IONPs [236]. In tMCAO rat models, they obtained a 5.1-fold higher accumulation of their NPs at the ischemic lesion by magnetic stimulation in comparison to unstimulated ones. Furthermore, IONPs enabled a significant reduction of the infarcted volume through the angiogenic, anti-apoptotic and anti-inflammation properties of the MSC nanovesicles. Nonetheless, the clinical translatability of this approach needs further improvements: in this study, the helmet which enabled the magnetic guidance was kept 3 days on mice. Consequently, it is essential to refine and enhance this technique before considering its application in human use. To further increase the targeting efficacy to stroke lesions, Li's group loaded IONPs and L-arginine (for stimulation of NO generation) in platelet-membrane-based nanovesicles. Their results on a photothrombotic stroke murine model demonstrated that the magnetic guidance of NPs could increase the targeting compared to platelet membrane alone and allowed a faster blood flow recovery through NO-mediated vasodilation [237].

Despite the efficacy of magnetic targeting, one should be aware of the remaining challenges for the transfer to humans: for example, the type of magnet to use and how to implement its use with the human body. Optimized magnets and mathematical models are necessary to predict the movement of magnetic NPs in biological fluids, in addition to the regulatory approvals that will be required [238].

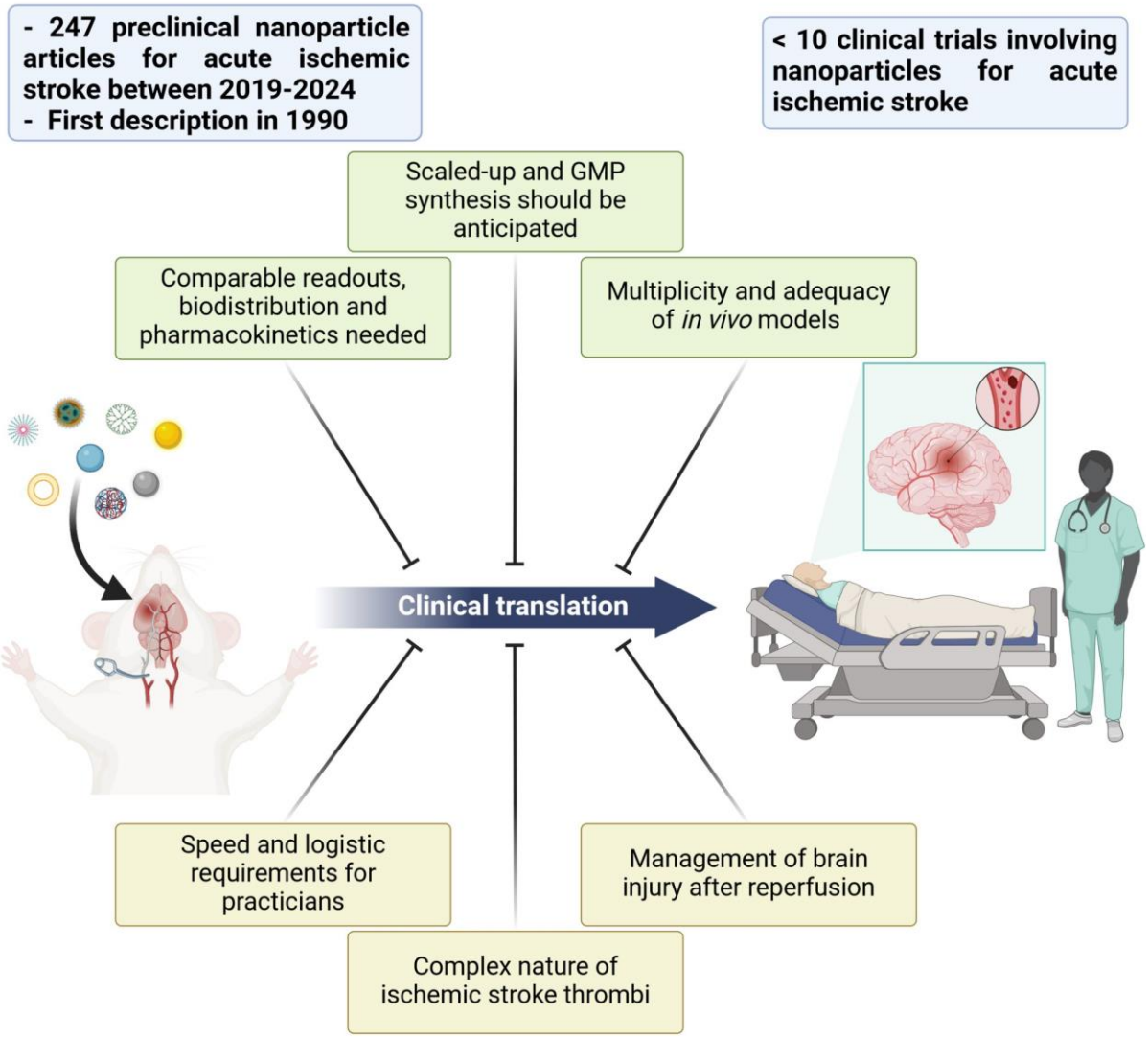


Figure 12: The gap between a rich preclinical research and low clinical translation of nanomedicine for acute ischemic strokes. The blunt-headed arrows represent hindrance to the development of clinical applications. Created with BioRender.com.

D) Applications of nanomedicine for stroke and clinical translation

Not only is nanomedicine rich in different potential materials, structures and objects, with very different ways of targeting the stroke area, but it can also be applied in very different ways to improve AIS management. On one hand, the delivery of thrombolytic agents directly to the thrombus could circumvent their severe side effects. Moreover, addressing therapies to the ischemic brain across the blood-brain barrier (BBB) can be achieved by specific vectorization with NPs and help reduce the lasting damages of ischemia. Finally, NPs can also be used

as contrast agents with different imaging modalities to specifically locate and assess the thrombus formation and ischemic lesion and can even be used in a theranostic manner to couple imaging with controlled IVT. However, while there is a rich literature of preclinical nanomedicine research for AIS, clinical translation is scarce. Therefore, the various ways nanomedicine has been used are described below in the preclinical and clinical setting, with a focus on characteristics that may play a role in clinical translation and recapitulated in Figure 12, diving more specifically in the articles published in the last five years for quantitative assessments.

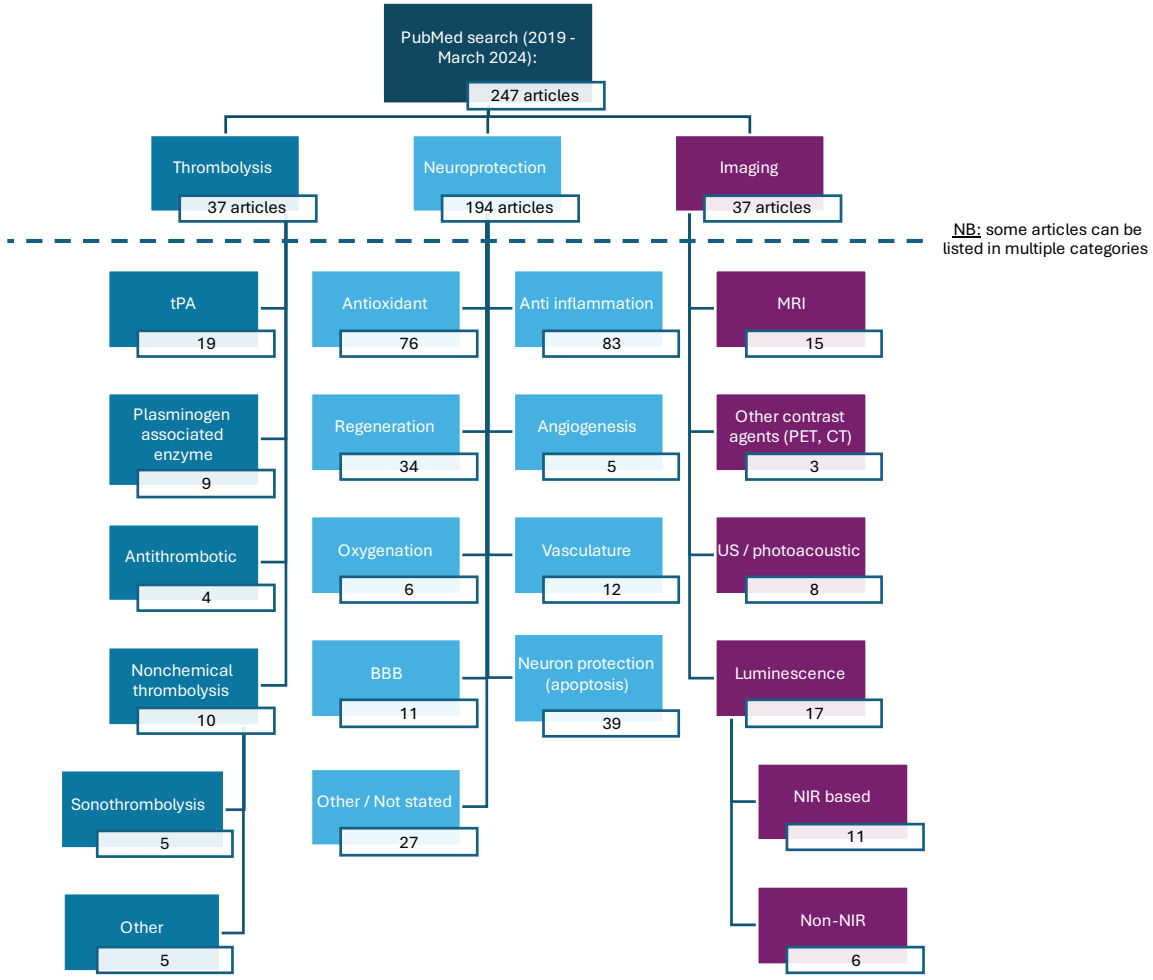


Figure 13: Classification of NPs by mechanism of action. This graph is based on the retained preclinical research on nanomedicine for AIS over the last five years. Since some articles combine multiple approaches, the different mechanisms of action listed below the dotted line exceed the total count of articles retained in this analysis. PET: positron emission tomography. CT: computed tomography. NIR: near-infrared imaging.

D.1) Preclinical developments

Neuroprotection and thrombolysis are the two pathways explored for improvement of patient care through nanomedicine. The various preclinical approaches used in the last five years were categorized as illustrated in Figure 13, with some researchers combining multiple functions in their proposed NPs: 7 articles out of 247 designed NPs with both thrombolysis and neuroprotection capacity, and 14 articles complemented one or both these therapeutic approaches with imaging in a theranostic manner.

194 articles mention neuroprotection to treat AIS patients, representing 78% of all preclinical research over the last five years. In order to achieve it, researchers seek to mitigate the ischemia-induced damages in the brain by various means, including first and foremost anti-inflammation and antioxidant (42% and 39% respectively of articles). For example, Li *et al*. presented in 2021 a manganese oxide NP coated with macrophage cell membrane to target the ischemic site [235]. These NPs could exert antioxidant activity due to the manganese oxide itself, but also incorporated fingolimod, a drug that could reprogram macrophages from M1 to M2 phenotype to alleviate inflammation. Interestingly, in this article the authors addressed translatability of their NPs, by checking their stability in fetal bovine serum supplemented medium, their pharmacokinetic properties in the blood as well as biodistribution and organ toxicity. In some instances, the authors resort to innate capacities of the NPs to exert a therapeutic effect, with for instance Tian *et al*. who described in 2021 extracellular vesicles (EVs) isolated from a human neural progenitor cell line and modified them to display RGD peptide as a targeting moiety. They studied how these modified EVs reduced inflammation in a murine ischemia-reperfusion model, but they also investigated organ toxicity, blood parameters, and biodistribution of these IV administered EVs [239]. This can also be performed with inorganic materials that mimic antioxidant enzymes and can scavenge ROS, like the polymer-coated cerium oxide NPs (CMPs) described by Goujon *et* al. in 2021, who characterized *in vitro* the antioxidant properties of their CMPs and further demonstrated that they were safe to use with *in vivo* biodistribution and organ toxicity [240]. Multiple other biological processes are explored since ischemic damage is a complex process with multiple cellular actors with different mechanisms involved [59] (Figure 5). For example, Peinado *et al.* presented hyaloruronate PNPs which were loaded with neuroglobin in order to specifically improve neuron protection and improve tissue regeneration. Thy demonstrated that, even though there was no reduction in infarct volume or oxidative stress with these NPs in a permanent ischemia model, neurological scores and survival

improved, with proteomic evidence of cell reprogramming towards survival and regeneration. They also investigated the long-term storage stability at 6°C of their NPs, as well as freeze-drying to improve storage and transport [241]. Besides the brain tissue itself, some authors focused on vascular properties, including mitigating BBB opening. As such, Yang *et al*. proposed in 2021 a hydroxyethyl starch-based PNP which could deliver in a pH-controlled manner smoothened agonist (SAG). They demonstrated a 50% reduction in the infarct zone area 14 days post stroke in a transient murine ischemia model, as well as improved BBB integrity and angiogenesis. Furthermore, they measured the stability of their NPs in PBS and PBS with serum over two days, as well as biodistribution and blood parameters post *in vivo* administration [242].However, such in-depth studies are not necessarily the nor. For instance, only 30% of neuroprotection articles display biodistribution results, and 29% have organ toxicity analysis.

On the other hand, 37 articles described approaches for IVT, representing 15% of the preclinical research in the last five years. Most approaches (66%) relied on vectorizing tPA or an enzyme with similar activity (e.g., urokinase, streptokinase, or directly plasmin). As an example of NP-mediated tPA delivery, Xu *et al*. described in 2020 self-assembled PLGA PNPs coated with platelet membrane for shielding and targeting of the thrombus. These NPs were loaded with tPA and demonstrated promising results in two *in vivo* models, while showing no organ toxicity nor changes in blood coagulation parameters, and this study also assessed pharmacokinetics and biodistribution [232]. Another example was provided by Yu *et al*. in 2022 who chose to deliver urokinase but engineered its loading on polyphenol-based NPs to impart a thrombin-dependent release in order to prevent urokinase-associated systemic bleedings. They demonstrated *in vitro* the retained activity of urokinase as well as the thrombin-mediated release, but also its attenuation in absence of thrombin. They also measured stability in various media as well as the biodistribution and pharmacokinetics *in vivo* of their NPs, even though these *in vivo* results were obtained with bovine serum albumin loaded as a model drug [243]. Nonetheless, some resort to nonchemical thrombolysis, such as magnetic hyperthermia [154], photodynamic/ photothermal therapies [244,245], or notably sonothrombolysis, where ultrasound waves are used to induce mechanical forces to disrupt the clot thanks to echogenic NPs [246,247]. One such nonchemical approach was presented by Zhang *et al.* in 2023, with molecular self-assembled NPs, based on two molecules: DiR, a photosensitizer, and BNN6, a photothermally activatable NO donor, which together could under NIR irradiation induce

mechanical (with NO-induced propulsion) and photothermal thrombolytic effects. Notably, stability, both in biological fluids and long-term, was assessed, as well as organ toxicity, pharmacokinetics and biodistribution [244]. Another work by Guan *et al*. in 2020 explored the use of ultrasound (US) enhanced urokinase delivery by RGD-targeted microbubbles and showed that US cavitation of urokinase-loaded targeted microbubbles significantly restored blood flow in a femoral artery thrombosis model in rabbit compared to urokinase alone, US alone, or targeted microbubbles with urokinase without US [248]. Yet only 50% of the articles mentioning any form of thrombolysis presented biodistribution results, and only 40% of them described toxicity assessments in organs. Overall, on average 90% of both thrombolysis and neuroprotection-oriented papers present *in vivo* results, but less than 40% display certain key aspects of technology translation such as biodistribution and organ toxicity data.

Nonetheless, some preclinical research has also focused on nanotechnology to improve imaging methods. First, some authors designed NPs that can improve contrast in the current imaging protocols by targeting specific markers, such as Tang *et al*. who described in 2021 IONP that were coated with neutrophil vesicles' membrane in order to grant a targeting capacity to activated endothelium, and demonstrated in a transient ischemia murine model how they could provide enhanced MRI contrast of the damaged endothelial layer, which may be useful for modulating neuroprotective treatments for patients [249]. NPs can also offer alternative imaging modalities, as shown by Yao *et al.* in 2023 with liposome incorporating a PH-responsive NIR probe in order to deliver it in the ischemic zone, where these new organic and stable dyes could differentiate different ischemic states based on local pH and NIR fluorescence imaging [250]. Others used the vectorization capacity of NPs to propose multimodal imaging, like Debatisse *et al.* who presented in 2020 how their AgulX® NPs, capable of enhancing MRI and PET contrast, can be used in a model of AIS treated by mechanical thrombectomy in macaques, and notably explored how this could be used to assess BBB damage [251]. Furthermore, this platform capacity can be used to co-deliver an imaging contrast agent and a therapeutic agent, thus allowing a theranostic approach. For instance, Hoogendijk *et al*. described perfluorocarbon (PFC) and ^{19}F loaded PLGA PNPs, and after presenting an innovative synthesis protocol, they explored the multimodal imaging capacity through MRI and US, as well as oxygen delivery potential [252], and Wang *et al*. designed self-assembled PNP based on amphiphilic phenylboronated fucoidan/maltodextrin that could scavenge ROS first to offer antithrombotic activity, but also trigger a release and activation of an

H2O2-sensitive fluorophore. They demonstrated with a murine model of carotid thrombosis that these NPs could not only be used for photoacoustic imaging of thrombi, but also reduce thrombosis [161]. However, for imaging NPs as well, biodistribution data are not always presented (43% of articles), and only 51% explored *in vivo* toxicity.

Besides, the wide array of *in vivo* models used can make comparison challenging. For instance, 14 different ischemic stroke models can be identified, with 159 temporary occlusions and 64 permanent ones. A visual representation is provided in Figure 14. Among the permanent occlusion models, 54 involve some sort of clot formation or introduction, making these models relevant for thrombolysis evaluation: the most common are the photothrombotic stroke model (with Rose Bengal injection) [233] or the $FeCl_3$ (applied to various blood vessels, from the middle cerebral artery [253] to the carotid arteries [161]); notably, newly developed models include thrombin injection to the middle cerebral artery [168]. Regarding these clot models, their variety can make comparison of efficacy results challenging, and even more so since AIS clot composition has been shown to be peculiar [19,22], with notably a core-shell structure and neutrophil-derived NETs (neutrophil extracellular traps) [22]. Thus, there is no clear consensus appearing over the last five years regarding thrombosis models for nanoparticle therapeutic development, especially since the model choice can depend on the physiopathological path targeted by treatment. On the other hand, the most common model used for tackling stroke-related ischemic damage or microcirculation damage is the transient middle cerebral artery occlusion (tMCAO), accounting for 65% of all *in vivo* ischemic stroke models. Relying on the temporary occlusion of a blood vessel with a filament retracted after some varying time [205,254,255], this model is well-described and very useful for the investigation of ischemia-induced brain damages and appropriate candidate drugs. Even so, its regular implementation (artery choice, time of occlusion for instance) still leaves a clear room for improvement [75]. Most notably, the relevance of an ischemia/reperfusion model is debatable as most patients (around 90% of patients admitted with LVO stroke in the US between 2014 and 2015) never presented a recanalization, and that permanent occlusion damages differ from those of ischemia/reperfusion, yet, as discussed below, EVT could significantly change this rate [256]. Therefore, there remains a broad range of *in vivo* models with no obvious best-in-class model, while the most used, tMCAO, remains relevant for investigation on microcirculation and ischemia-reperfusion damages, but its overuse does not correlate to the current low proportion of recanalized patients [256]. Overall, the

variety of *in vivo* models prevents comparison between efficacy results, especially given that ensuing pathological behavior can differ: for instance, transient ischemia-reperfusion damages are very different from total ischemia (permanent occlusion) [256].

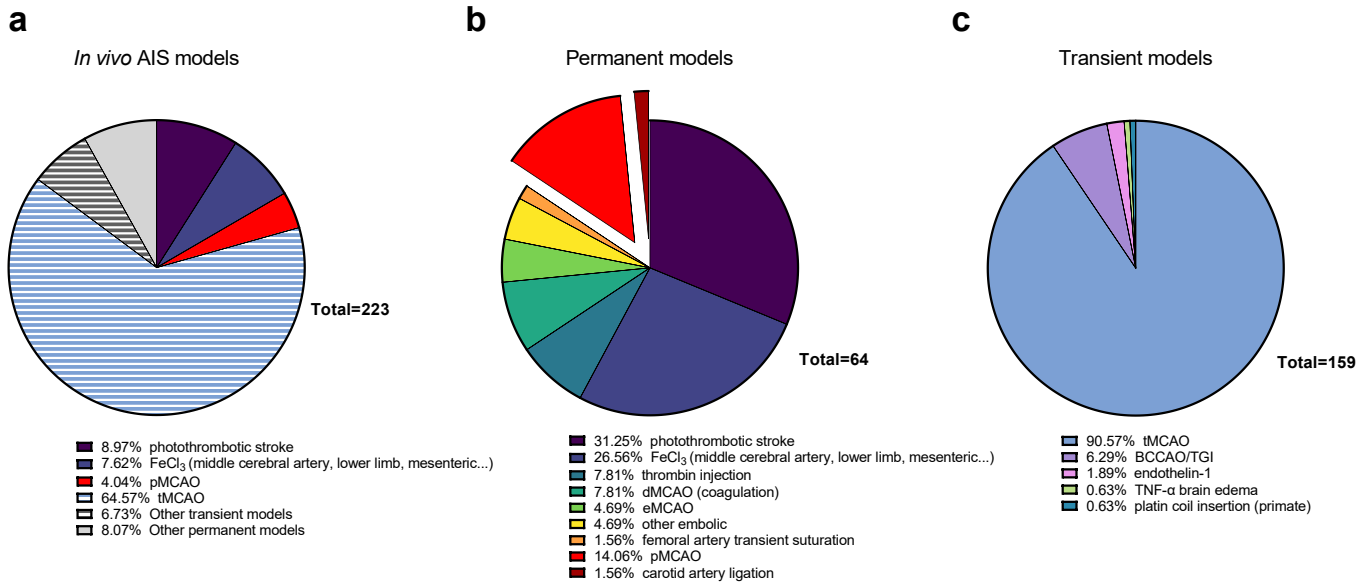


Figure 14: Repartition of preclinical in vivo models of AIS. (a) Repartition between permanent models (full slices) and transient models (hacked slices). (b) Repartition of the various permanent models, all composed of clots except the pMCAO and carotid artery ligation. (c) Repartition of the various transient models. pMCAO: permanent middle cerebral occlusion. dMCAO: distal middle cerebral occlusion. eMCAO: embolic middle cerebral occlusion. BCCAO/TGI: bilateral common carotid artery occlusion/transient global ischemia.

Moreover, for technology evaluation, storage stability as well as stability in bodily fluids are key criteria that should be investigated. Among the 247 articles analyzed, only 21% mention any form of such stability investigation. Overall, the suspension media vary widely, from ultrapure water [257], saline or phosphate-buffered saline [244], to cell culture medium [258] or serum [216]. Though it may not be easy to measure the stability of NPs in complex bodily fluids, this is a critical parameter to consider as stability in storage “clean” media such as saline or water does not necessarily equate to colloidal stability in blood. Furthermore, long-term stability assessment is necessary to make sure that the described NPs can be successfully stored and used by clinicians. Here again, no clear measurement window is defined as some authors investigate stability only for a few days [163] while others report months-long stability [259]. Obviously, differences arise based on the material considered (as extracellular vesicles for instance might not be stable in storage as inorganic NPs) but should

be discussed with regards to potential applications. Interestingly, 29 articles have disclosed freeze-drying as a means to store their NPs for long-term storage [260], or other forms of drying [261,262] or precipitation [263]. Not only must the storage be questioned, but delivery methods can also be critical: while most authors rely on IV injections, 8 articles mention an oral or nasal delivery which could be favored as fast and easy delivery methods [264]; whereas 14 describe administration methods (stereotaxic, cisternal or intracarotid injections) that might be less suitable to clinical use.

D.2) Clinical advancement

Therefore, the current preclinical nanomedicine research on AIS treatment is rich, diverse and promising, though clinical translation remains rare, possibly due to the aspects investigated above.

As previously mentioned, IV nanoemulsions have been described as potential neuroprotectants, including dodecafluoropentane emulsion (DDFPe) which has demonstrated neuroprotective effects in animal models of AIS by improving oxygen transport in the ischemic zones [209]. Preclinical studies have also shown the safety of this strategy [265]. Based on this, Culp *et al*. conducted a phase Ib/II randomized, placebo-controlled, double-blind, dose-escalation trial in 24 AIS patients to further establish the safety of DDFPe (NuvOx Pharma, LLC) [211]. Patients were randomly assigned to receive either DDFPe or a placebo every 90 minutes, starting within 12 hours of symptom onset. The study results indicate that there were no significant differences in adverse events between the treatment and placebo groups. Additionally, the high-dose DDFPe group exhibited better outcomes on the modified Rankin scale at 1 and 3 months. Two additional clinical trials are currently underway. One is a phase 2 study on DDFPe (NuvOx LLC) for LVO stroke is ongoing (ClinicalTrials.gov ID: NCT05389748), while the other is a phase 2 study using another perfluorocarbon, ABL-101 (Aurum Biosciences) (ClinicalTrials.gov ID: NCT03463551).

Few clinical trials have shown particular interest in sonothrombolysis with mixed results. The initial trials focused on ultrasound use - without the injection of NPs - in conjunction with standard treatment, to produce cavitation and fluid motion into the thrombus. The CLOTBUST trial involved 126 patients presenting with AIS consecutive to middle cerebral artery occlusion treated with IV tPA. They were randomly assigned to receive either adjunctive continuous high-frequency (2 MHz) transcranial Doppler ultrasound or a placebo. The study

found that the ultrasound group had a significantly higher incidence of complete recanalization or early or dramatic clinical recovery at 2 hours, with a non-significant trend towards an increased rate of stroke recovery compared to the placebo [266]. Smaller trials and meta-analyses [267,268] have confirmed better early recanalization without improvement in outcome at 3 months. However, the CLOTBUST-ER trial, a large, phase 3, multicenter, double-blind, randomized controlled trial, enrolling 676 AIS patients receiving IV alteplase with or without ultrasound, was stopped early due to futility [269]. The primary outcome was functional autonomy assessed by modified Rankin scale at 90 days, and there was no increased risk of symptomatic intracerebral hemorrhage compared with tPA alone [266–269]. On the contrary, exposure to tPA plus low-frequency ultrasound (300 Hz) showed an increased rate of cerebral hemorrhage in a trial including 26 patients [270]. Nonetheless, microbubbles were postulated to reduce the energy required for cavitation by acting as cavitation nuclei. Their administration in conjunction with ultrasound demonstrated a significant improvement in two-hour recanalization in a study of 111 AIS patients consecutive to middle cerebral artery occlusion treated with IV tPA [271]. The NOR-SASS study investigated contrast-enhanced sonothrombolysis with Sonovue® in an unselected AIS population, with or without occlusion, receiving tPA, but showed no significant clinical effect [272]. Another technique for targeting thrombus involves using magnetic NPs under external magnetic force irradiation. The Pulse NanoMED System (Euphrates Vascular) is currently undergoing testing (ClinicalTrials.gov ID: NCT06052969 and NCT03098732). It combines an external rotating magnet with IV administered iron-oxide NPs to enhance flow near the occlusion, facilitating the delivery of tPA to the clot.

Finally, NPs could be interesting for diagnosing AIS. Saleh *et al*. used IV ultrasmall IONPs in conjunction with multimodal stroke imaging to track macrophage recruitment into ischemic brain lesions, which reflects the inflammatory component of stroke damage [273]. The authors observed different patterns of macrophage infiltration during the early stages of AIS. This suggests that anti-inflammatory treatment could be tailored to the stroke profile. Iv *et al.* planned to use IONPs to measure inflammation in patients with brain tumors or other conditions of the central nervous system, including ischemic stroke, to help with diagnostic and potential treatments. However, the trial was stopped after only 10 patients over 120 were enrolled, all of whom had glioma (ClinicalTrials.gov ID: NCT02452216). The challenge of diagnosing AIS before brain imaging has triggered many research studies, but finding a biomarker has been unsuccessful so far.

D.3) Summary

Overall, there is no shortage of promising preclinical nanomedicine projects for the AIS diagnosis and treatment. Many different approaches are being explored to better answer the current limitations of AIS management, and in general thrombotic diseases. Some focused in improving how thrombolysis is performed, either by targeted delivery of the main thrombolytic agents such as rtPA [168,232,233], while other investigate the crosstalk between NPs properties and certain agents in order to achieve thrombolysis: this includes granting specific targeting to fibrinolytic agent which were deprived of the latter, like urokinase [213,243,274]; mastering the release of these agents by external stimuli such as ultrasound or light [154,248,275]; or co-delivering multiple agents together to improve thrombolysis [233,276,277]. On the other hand, many researchers explored how NPs could be used to improve neuroprotection, either through modulating inflammation or oxidative stress [235,239,240], by promoting regeneration [208,241,278] including macrophage polarization [277,279], or by improving the vascular regeneration and BBB function [258,280–282]. Furthermore, some authors used NPs to improve imaging modalities, for instance by offering alternative imaging methods [250,283], combining treatment and imaging [161,252] or proposing multimodal imaging [229,251,284]. Yet, the broad array of NPs displayed in recent research articles varies widely in terms of maturity, feasibility and cannot most of the time be easily compared. This can be explained by the disparity in measurable readouts, *in vivo* models and often absence of certain key aspects towards future translation, such as storage viability or biodistribution data. Additionally, the methods used to obtain these data - such as fluorescence, radiotracing, or mass spectrometry - may not always be directly comparable. Conversely, only a few projects have reached the clinical stage, despite research on NPs to treat AIS ongoing for more than three decades [118]. Current trials are underway to study the potential of NPs in the AIS setting, to facilitate a more accurate and rapid diagnosis and to improve the efficacy of standard drug delivery and to enhance reperfusion and improve functional outcome.

III. Polysaccharide-based hydrogel nanoparticles

In our project, we used polysaccharide-based hydrogels, synthesized in a manner that allowed us to obtain nanogels. It is therefore necessary to explore the definition, current applications and synthesis of such materials.

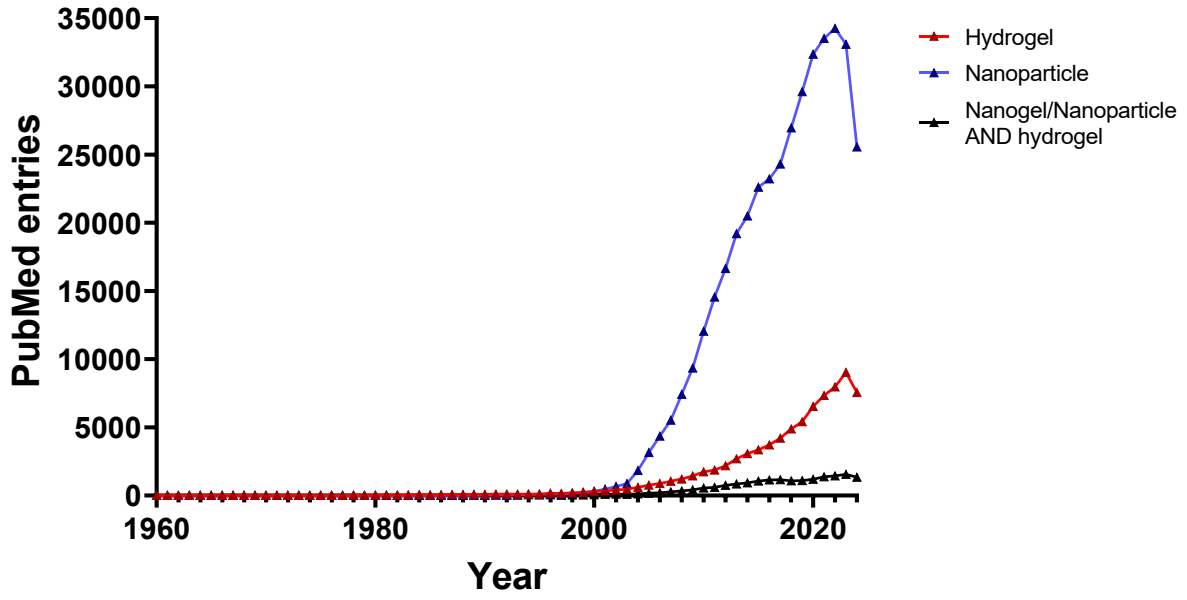


Figure 15: Publication boom for nanoparticles and hydrogels. PubMed entries between 1960 and August 2024 were retrieved with the respective queries ["hydrogel"], ["nanoparticle"], ["nanogel" OR ("nanoparticle") AND "hydrogel")] to assess publications in the biomedical field.

A) Hydrogels and nanogels

Hydrogels are polymeric materials organized in a three-dimensional network, which can absorb large amounts of water and are capable of swelling based on water exposure, and depending on several parameters such as pH or ionic strength. This high water content, porosity, and the resulting viscoelastic properties can be compared to living tissues [285]. Notably, the extracellular matrix (ECM), a dynamic network of proteoglycans and proteins which serves as scaffold for cells, providing anchoring sites and modulating access to soluble molecules such as metabolites or growth factors, can be structurally compared to hydrogels, which have themselves been explored as platforms to better understand ECM, but also to mimic it for cell culture scaffolds and tissue engineering [285]. The first hydrogel-based biomaterials were described in 1960 by Wichterle and Lim, with a synthetic poly-2-hydroxyethyl methacrylate (PHEMA) hydrogel for optical applications [286], and their development increased over the years with a step increase starting in 2000 for biomedical

research as measured with PubMed entries, as shown in Figure 15. Multiple applications have been described over the years, from external applications (eyes, open wounds) to implantable, injectable or sprayable materials that can be used in virtually any living tissue. Moreover, from a biomaterial perspective, several compositions, synthesis and properties have been explored. One interesting approach was the use of aqueous dispersions of nanoscale hydrogel objects, or nanogels.

A.1) Hydrogel composition and structures

Hydrogels are composed of polymer chains, which can be synthetic or from natural origin. They can also be classified based on their crosslinking method and structure.

Synthetic polymers are prepared from controlled polymerization of monomers. Many different monomers have been explored, benefiting from advances in polymer chemistry from various industries, with among others polyvinyl alcohol (PVA), polyethylene glycol (PEG), polyethylene oxide (PEO), poly-2-hydroxyethyl methacrylate (PHEMA), poly-N-isopropyl acrylamide (PNIPAM), polyacrylic acid (PAA), and polyacrylamide (PAAM) [287,288]. They benefit from good stability, tunable mechanical strength with a broad range of rigidity, reliable production with consistent and high yields, but also many various controlled properties such as porosity, density, or conductivity [289]. Some synthetic hydrogels directly stem from industrial procedures, including polyesters, polyethers, or polyurethanes. Among them, polyethylene glycol (PEG) is a well-known hydrophilic polymer that has been widely used for its good biocompatibility and versatile chemistry. Interestingly, this led to its extensive use as a coating to extend circulation, stealth and stability of NPs [290], and notably 8% of all nanomedicine preclinical research for AIS mention PEG as a part of their nanoparticle synthesis, and only 30% of the latter were actual polymeric NPs. For instance, it could be used in a hydrogel to deliver cells and growth factors to palliate ischemia-reperfusion injury in rats, by modifying it to present adherence moieties (RGD peptide), and a protease-degradable crosslinking [291], or formulated into a synthetic copolymer of PEG and poly-ε-caprolactone (PCL) with collagen incorporation so as to deliver pluripotent stem cells in a temperature-dependent manner [292]. Other synthetic hydrogels stem from natural molecules artificially polymerized such as lactic acid or glycolic acid, which gave birth to their respective polymers, PLA and PGA, as well as the copolymer PLGA. The latter is extensively used thanks to its biocompatibility, lack of toxic degradation products and well-known chemistry and properties,

representing for instance 31% of the polymeric NPs described in the last five years for nanomedicine application in AIS (Figure 10). However, most synthetic polymers are not inherently biocompatible or biodegradable, with often low biological activity, lacking natural moieties such as adhesion patterns or recognition moieties [287–289]; they may also face toxicity issues, most notably through degradation products, and their synthesis are not always compatible with green chemistry principles (e.g., organic solvents, waste) [293].

Natural hydrogels are promising alternatives since they have inherent low toxicity, biocompatibility, bioactivity and, depending on the material, biodegradability. Furthermore, they are usually easy to access through various natural sources [289,294]. Examples of materials that can be used include collagen, fibrin or gelatin. For example, Eyrich *et al*. described how fibrin hydrogels could be engineered to support chondrocyte proliferation and subsequent ECM production, which may be applicable for tissue engineering or *in vitro* culture [295] Collagen is the most abundant fibrous protein in human, while notably playing roles in ECM structure and biological properties. As such, it was used among others by Tamaddon *et al.* in 2017 to explore how the different collagen types, when formulated as hydrogels to form scaffolds for mesenchymal stem cells, and promote their chondrogenic differentiation without growth factors addition [296]. Moreover, one class of natural polymers has been specifically investigated: polysaccharides are natural carbohydrates formed by the condensation of monosaccharides, giving way to multiple and complexes molecular structures with often multiple functional groups for modification, and sometimes innate biological functions [297–299]. Some examples include cellulose and chitosan, associated in an injectable hydrogel to act as a scaffold for cartilage tissue engineering, releasing insulin and supporting differentiation of mesenchymal stem cells [300], and an implantable hydrogel composed of dextran and pullulan, which could support self-assembly of hepatocytes and improve survival after implantation into murine models of liver failure [301]. Even so, these natural hydrogels often lack mechanical strength and can be less tunable than synthetic ones and can suffer from stability issues. In certain cases, they may pose immunogenic risks depending on the individual and which material was used [287,288]. Consequently, some hydrogels are formulated by mixing certain natural and synthetic polymers to benefit from the advantages of both. For instance, Berkovitch and Seliktar explored in 2017 how PEG backbones combined with various ECM proteins could support neuronal growth, migration and morphogenesis [302].

Besides their synthetic or natural origin, hydrogels can also be separated between physical or chemical crosslinking. Physical crosslinking involves transient conjugation of polymer molecules through several possible mechanisms, like crystallization, ionic interactions or hydrophobic forces [287,288,303]. These hydrogels are usually more fragile than chemically crosslinked ones, and more sensitive to external stimuli, with weaker mechanical properties. These approaches can sometimes also be described as self-assembly since the formation of NPs/nanogels happen in given conditions without chemical modifications [303]. For example, Aamir *et al*. described in 2021 polyionic NPs based on the electrostatic interaction between arginine and a plasmin-heparin complex. The resulting 370-470 nm NPs could be used to improve plasmin delivery in an *in vivo* photothrombotic murine model while avoiding systemic side effects [304]. On the other hand, chemically crosslinked hydrogels rely on covalent bonds between polymeric molecules, either through direct polymerization, with for instance miniemulsion polymerization, which can be used to obtain for instance 150-200 nm 1,2-polybutadiene NPs as described by Monteil *et al*. in 2005 [305–307], or by crosslinking preformed polymer chains with different molecules such as formaldehyde, genipin, glutaraldehyde, various enzymes or trough phosphate diesters bonds [308] with for example sodium trimetaphosphate (STMP) or phosphorus oxychloride ($POCl_3$) [287,288,303]. Through chemical crosslinking, hydrogels usually benefit from good thermal, mechanical and chemical stability. Examples of small molecule crosslinking can be found with the infamous EDC-NHS (carbodiimide, EDC; N-hydroxysuccinimide, NHS) reaction for amine coupling, as described by Kuijpers *et al*. in 2000 with hydrogels formed by crosslinking gelatin by EDC-NHS in order to serve as lysozyme delivery materials [309], and similarly NPs formed by EDC-NHS crosslinked gelatin were described in 2010 as potential drug delivery systems [310]. However, small crosslinkers are often faced with toxicity and biocompatibility issues, with for instance the commonly studied glutaraldehyde [288,303,311].

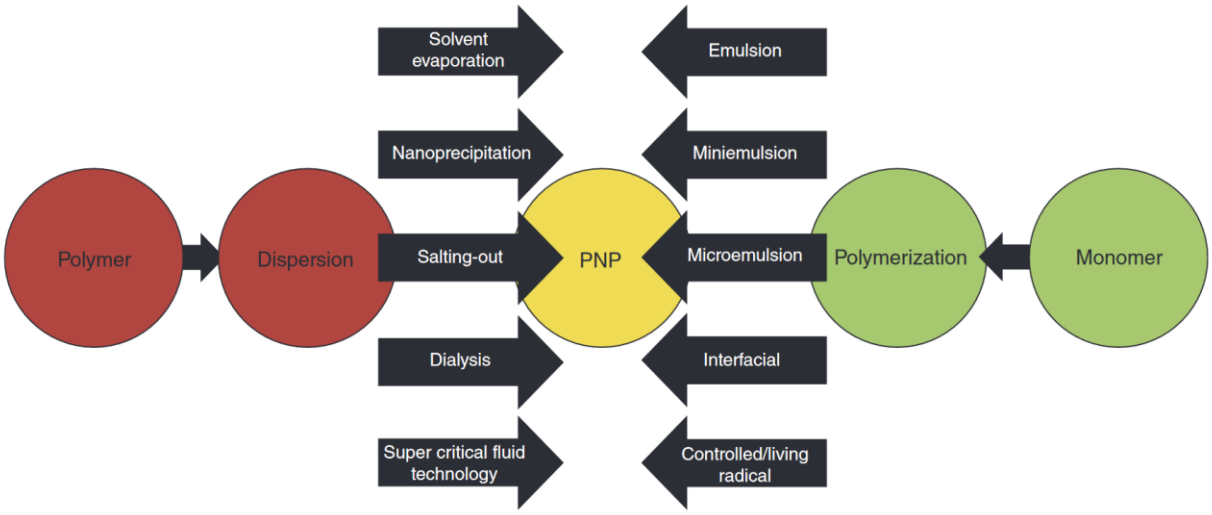


Figure 16: Various preparation techniques for polymer nanoparticles. Adapted from Rao et al., 2011 [312].

A.2) Nanogels

Nanogels have been explored as drug delivery systems that benefit from the rise of both nanomedicine and hydrogels (Figure 15). They are defined as aqueous of hydrogel particles, with nanometric (10-1000 nm) dimensions [298], and have been explored for three decades [313,314], with notably the work of Sunamoto's group in 1993, who described physical crosslinking of cholesterol-modified polysaccharides to form aggregates with average diameter of 25 nm [315] Nonetheless, this field represents only a small fraction of nanoparticle research (less than 5% in 2023, Figure 15), as researchers combine advantages of hydrogels with nanomedicine to improve drug delivery, but also their challenges. They benefit from the flexibility, hydrophilicity, biocompatibility, and high water content of hydrogels, which may facilitate the loading of various agents through electrostatic, Van der Waals or hydrophobic interactions in addition to other chemical conjugation methods [313]. Many different synthesis methods exist, either by assembling pre-formed polymers, or by starting from monomers and controlling the hydrogel formation [316,317], with some of them recapitulated in Figure 16. Regarding the latter, it is most often performed by procuring a confined environment where the polymerization reaction occurs, therefore limiting the spatial extension of the polymer. This can be performed using emulsion, where two immiscible liquids are mixed, which generally results in the formation of droplets made of one of these two, dispersed in the other. Emulsion polymerization involves separate surfactant micelles and monomer droplets, while miniemulsion requires the formation of monomer-containing,

kinetically stabilized droplet with surfactants (while microemulsion involves a thermodynamically stable emulsion). Controlled/living radical synthesis benefits from specific polymerization kinetics, allowing for homogeneous growth of polymer chains, possibly in an emulsion setting. Interfacial polymer synthesis differs by having the polymer form at the interface of two immiscible liquids by two reactive agents, one in each phase and not necessarily in emulsion. Yet in all these techniques, the polymerization reaction remains the critical one and most complex to control, which may limit its widespread use. Size control is also not always easily attained [312,316,318].Regarding the dispersing techniques, pre-formed polymer chain are associated into NPs by various methods, usually involving hydrophobicity of the polymer present and/or displacement of an organic solvent (nanoprecipitation, solvent evaporation, salting-out, dialysis); this use of organic solvent however can be costly and rarely environment-friendly, which led to the use of super critical fluids to replace organic solvents, though this is not yet achievable for many polymer due to lack of solvability [312,317]. Additional methods can involve the use of physical or chemical crosslinking as evoked above, sometimes in controlled nanoscale reactors such as patterned scaffolds or emulsions [299].

B) Polysaccharide nanoparticles for drug delivery

As evoked above, polysaccharides are good candidates for hydrogel formulation, and have been used to synthesize NPs thanks to their adequate innate biological properties like biocompatibility, low immunogenicity, biological activity, and their natural sourcing is usually associated with high availability and low costs [297–299]. They are in general non-toxic, and many are classified as GRAS (Generally Recognized as Safe) [298]. They can be composed of various monosaccharide units (e.g., glucose, sucrose, fucose) and most often differ based on their structure (linear, branched, subunit arrangements, molecular weight, etc.), water solubility and ionic charge [299]. Most interestingly, they can be easily functionalized as they present numerous functional groups such as carboxyl and hydroxyl groups. Hereafter are presented some commonly used polysaccharides for nanoparticle preparation, though many others have been investigated (e.g., scleroglucan, guar gum, gellan, carrageenan) [297–299,319]. Moreover, different polysaccharides are often associated together in one nanosystem to broaden their potential, with notably interpenetrating polymeric networks that were described as offering improved hydrogel properties (mechanical, biological, etc.) [298].

B.1) Chitosan

Chitosan is obtained from partial deacetylation of chitin, which makes up the exoskeleton of various crustaceans. While chitin is hydrophobic, chitosan is water soluble in acidic conditions, which allows easier manipulation for nanoparticle synthesis [299]. Moreover, it is the second most abundant polysaccharide in nature [320]. Notably, this was used by Tóth *et al*. in 2018 and 2020 to synthesize pH-sensitive chitosan NPs, loaded with nimodipine for neuroprotection by inhibiting spreading depolarization of neurons. They demonstrated that acidic conditions could trigger the release of nimodipine, and used that in a permanent ischemia rat model to demonstrate release in the acidic brain tissue and subsequent neurological improvement [320,321]. Chitosan acidity-dependent solubility and positive charge density are key characteristics of this polysaccharide, though cationic charges may increase both cell uptake and toxicity [298,299].

B.2) Cellulose

Cellulose is the most abundant natural polysaccharide, as a major component of plants. It can be extracted from numerous different organisms, ranging from wood, other plants (e.g., cotton, soybean, wheat straw), algae, or bacteria [299,322], and the broad range of resulting structures, crystallinity, as well as the availability of this material, has been long explored for nanomaterials [322], either alone, modified or in combination with other polysaccharides. For example, Vashist *et al.* described chitosan, hydroxyethyl cellulose and “Linseed oil” based polyol NPs, synthesized through an emulsion polymerization, which displayed autofluorescent and BBB crossing properties [323]. Its broad availability, variety based on sourcing and described modifications make it a promising candidate for nanomaterials [299,322], but its relatively difficult dissolution and extraction complicate its large-scale use [293].

B.3) Starch

Starch is another common plant-originating source of carbohydrates, extracted among others from corn and potato, and chemically composed of amylose and amylopectin polysaccharides. Many various starch-based NPs have been described, owing to its availability, limited water solubility and thermoplastic behavior, though if is often necessary to modify it prior nanoparticle synthesis since its native form usually yield poor mechanical properties and processability [293,299]. For example, hydroxyethyl starch was used to form NPs by Yang *et al*. in 2021, which could be decorated with an

activated endothelium targeting moiety (covalent bonding of PHSRN) and smoothened agonist (SAG) pH-dependent adsorption. These NPs could exert a targeted neuroprotective action through angiogenesis in a transient murine ischemia model [242].

B.4) Hyaluronan

Hyaluronic acid, or hyaluronan, is a water-soluble, negatively charged polysaccharide found in human ECM, and therefore exerts many different biological activities such as adhesion, proliferation and wound healing [293,299]. It has been therefore exploited in the cosmetic and wound healing industry and can be formulated into hydrogels that benefit from its innate properties, notably in order to deliver therapeutics across natural barriers [297]; for example, in ocular applications, cholestrerol-hyaluronan nanogels were designed to improve drug delivery thanks to its bioadhesive properties, as demonstrated by Zoratto *et al.* in 2021 [324]. For AIS application, Peinado's group described NPs made from sodium hyaluronate, chitosan and glycerol tripalmitin, which were optimized for BBB crossing, and demonstrated how these could be used to deliver neuroglobulin in rat transient ischemia models and improve tissue regeneration [325,241]. Nonetheless, its bioactivity might be a double-edged sword since complications through inflammation, cell recruitment and adhesion, and the resulting degradation with free radical release have been described for hyaluronan hydrogels [326], thus requiring a fine tuning of its activity *in vivo*.

B.5) Alginate

Alginate is an anionic polysaccharide extracted from algae and bacteria which has been extensively used in hydrogel formulation. Most notably, the interaction of alginate with Ca^{2+} cations leads to hydrogel formation, providing a simple synthesis method [299]. However, this also results in a relative instability in presence of other salts leading to its dissolution[293], prompting alternative synthesis process through coacervation or chemical crosslinking [293]. For example, Motawni *et al*. presented in 2008 chitosan-alginate NPs obtained through coacervation, with mucoadhesive properties for ocular drug delivery [327], and Cardia *et al*. explored the use of chitosan-alginate polyelectrolyte complexes chemically crosslinked into NPs for brain delivery of progesterone [328].

B.6) Dextran

Dextran is a water-soluble branched exopolysaccharide produced by bacteria, with good stability and that can be easily functionalized through high density of hydroxyl groups [299,319]. First clinical use was described in Sweden in 1944 [329], followed by numerous biomedical applications including blood plasma expander, molecule carrier [319,330], or heparin substitute under sulfated form [331–333], and even non-medical application in the food, photography and cometic industries [330]. Interestingly, despite its bacterial origin, dextran has a relatively low antigenicity depending on the production source, and initial concerns of its immunogenicity and antigenicity were linked to chemical structure and higher molecular weight, now lowered using specific dextrans [334–336,329]. They are produced in large quantities due to their commercial use [329,337], and even though they are relatively stable against degradation in the human body, low molecular weight (M_w < 40-60 kDa) are rapidly excreted through renal clearance while higher molecular weight can stay longer in the circulation before sequestration in liver or spleen for hydrolysis [319,329,330]. Many different forms of dextran, from low to high molecular weight, with various chemical modifications, were investigated as biomaterial [319,330]. For example, hydrogels for tissue repair based on crosslinked dextran with another polysaccharide, pullulan, have been described for several application including liver repair, bone regeneration and vascularized tissue modeling [301,338,339]. Dextran-based nanogels have also been described, for instance Xu *et al*. in 2019. They described acetal-modified dextran (m-dextran) PNP prepared by solvent evaporation and coated with platelet membrane for thrombus targeting, incorporating a neuroprotectant for ischemic tissue repair and decorated with thrombin-cleavable rtPA bound to a cell penetrating peptide. As such, the NP could target the thrombus, where rtPA would be delivered by thrombin cleavage, simultaneously allowing BBB crossing of the modified NP where the neuroprotectant was delivered. The authors observed a decrease in ischemic area with a transient ischemia rat model, though this model did not fully recapitulated the sequenced delivery of their NPs as no thrombus was present [231]. Therefore, dextran is a promising polysaccharide for biomaterial use due to its availability, biocompatibility and stability, with easily tunable characteristics through various chemical modifications [319,329,330,340].

Part Two. Experimental results

I. Nanoparticle design

In this chapter, the synthesis of targeted polysaccharide hydrogel NPs is presented. The rationale behind this specific subtype of nanoparticle is discussed, followed by a description of the development and optimization of the synthesis protocol. Finally, future developments regarding the synthesis itself are discussed, while evoking perspectives for future development of these NPs.

Some of the results presented in “Experimental results. I, II. and III. ” are adapted from **ANNEX 6**: de La Taille T, Sarfati P, Aid R, Fournier L, Pavon-Djavid G, Chaubet F, Chauvierre C. Microemulsion-inspired polysaccharide nanoparticles for an advanced targeted thrombolytic treatment. *ACS Nano*, with Editor (2024) and have been protected by a patent (**ANNEX 4**: “Crosslinked polysaccharide nanoparticles”. EP23307118. 2023 December 1; Inventors: Thibault de La Taille and Cédric Chauvierre. Assignee: INSERM Tranfert).

A) Materials and methods

A.1) Materials

Dextran 40 kDa was purchased from Pharmacosmos (Holbæk, Denmark, #5510 0040 1007); FITC-Dextran 40 kDa and TRITC-Dextran 40 kDa were purchased from TDB Consultancy (Uppsala, Sweden, #FD40 and #TD40). Fucoidan (#14093, MMW: Mn = 18 kDa/Mw = 104 kDa) was a gift from Algues & Mer (Ouessant, France, #MMWFSA14093). Vegetable sunflower oil (Lesieur - Huile Coeur de Tournesol, Lesieur S.A.S, Asnieres-sur-Seine, France) was purchased from a local supermarket (Monoprix, Paris, France). Polyglycerol polyricinoleate (PGPR) was kindly supplied by Palsgaard (Lyon, France, # PGPR 4150). Tween 80 (#P1754), Trisodium trimetaphosphate (STMP, #T5508), Sodium Dodecyl Sulfate (SDS, #L3771), Sucrose (#S7903), Phosphorus (V) oxychloride (#201170-250G), Tetrabutylammonium hydroxide (TBA, #86866-25g), 4-5(Dimethylamino)pyridine (DMAP, #29224) were purchased from Sigma Aldrich (Saint-Quentin-Fallavier, France). PBS 1X and 10X (#14040133 and #14080055) were purchased from Thermo Fisher Scientific (Massachusetts, United States).

A.2) Nanoparticle synthesis

Polysaccharide nanoparticles (NPs) were obtained through a water-in-oil (w/o) microemulsion, with chemical crosslinking in the aqueous phase. A polysaccharide solution (300 g/L dextran, 6 M NaCl) was prepared; for

fluorescent NPs, a 5:95 mass mixture of TRITC-Dextran 40 or FITC-Dextran 40 with Dextran 40 was used. For targeting NPs, fucoidan was substituted to dextran at a 10 wt.% ratio. 15 mL organic phase composed of sunflower oil and 6 wt.% surfactant (60:40 PGPR and Tween 80) was cooled at -20°C for 30 min. Meanwhile, 1200 mg of the polysaccharide solution is mixed with 60 µL of 10 M NaOH for 10 min. 240 µL of 30 wt.% STMP solution was added before quick mixing for 1 min. 600 µL of this aqueous mix are then added dropwise to the organic phase under dispersion with a high-speed homogenizer (UltraTurrax Polytron PT 3100, dispersing aggregate PT-DA 07/2 EC-B101, Kinematica, Luzern, Switzerland) for 2 min 30 s at 30'000 rpm on ice. The resulting emulsion was incubated at 50°C for 20 min before successive purification by ultracentrifugation (50 000 g, 30 min): the pellets were resuspended first with SDS 0.04 wt.% four times, then with ultrapure water three times. The resulting NPs were stored at 4°C in ultrapure water. Further concentrating of NPs could be performed with ultracentrifugation devices with size cutoff of 300 000 Da (Vivaspin, Dutscher, Issy-les-Moulineaux, France). Stable freeze-dried NPs were obtained with the LyoVac GT2 freeze dryer (SRK Systemtechnik, Riedstadt, Allemagne) after -80°C freezing for 1 h in a 1 wt.% sucrose solution. Submicroparticles for comparison were synthesized as per Zenych *et al*., 2021 [168], which was defined as the "classical" protocol. For the synthesis with ultrasonication, the high-speed homogenizer was replaced by an ultrasonication device (Sonicator Branson SLPE 40 kHz, with a 1/4" Microtip P/N 109-122-1064) in Pulse Mode (70% Amplitude, 3 s on / 10 s off).

A.3) Physico-chemical characterization

The NPs characterization included particle morphology, hydrodynamic size and zeta potential distributions, mass concentration, elemental composition and stability in different solutions for varying periods of time. Hydrodynamic size (diameter, determined from an autocorrelation coefficient with the Stokes-Einstein equation), polydispersity (PDI) and Zeta potential (ζ-potential, with Henry's equation and Smoluchowski model) were measured by Dynamic Light Scattering (DLS) and Electrophoretic Light Scattering (ELS), respectively (Zetasizer Nano ZS, Malvern Instruments, Orsay, France). Samples were diluted in distilled water, 0.9 wt.% NaCl or PBS 1X for size, and in 1 mM KCl for ζ-potential determination. All runs were performed at 25°C in triplicate. Particle morphology was visualized by Transmission Electron Microscopy (TEM) (Philips FEI Tecnai 12, Amsterdam, Netherlands), negatively stained with 1 wt.% uranyl acetate for 5 min. Mass concentration was determined by freeze-drying.

Elemental composition was assessed by total reflection X-ray fluorescence spectroscopy (TXRF) technique to quantify the phosphorus and sulfur content (S2 PICOFOX Bruker, Massachusetts, United States). Fourier transform infrared spectroscopy (FTIR) spectra were obtained after drying and inclusion in KBr pellets (Thermo Nicolet AVATAR 370 FTIR spectrometer, Thermo Electron Corporation, Waltham, MA). The stability of Fuco-NPs and compared submicroparticles in various solvents (ultrapure water, 0.9 wt.% NaCl, PBS 1X) was evaluated 6 h after solvent exchange, or after various timepoints after storage at 4°C or at 37°C.

A.4) Size optimization

Gelation assays were performed on aqueous phase containing dextran 40, a base (NaOH, TBA or DMAP) and a crosslinker (STMP or $POCl_3$): the time before a gel is visibly formed was measured either at room temperature (RT) or at 50°C. To measure the droplet size in the water-in-oil emulsion during the synthesis protocol, the classical protocol was followed but with or without STMP addition. Using a 1 mL syringe and a microfluidic soft tubing with an inner diameter of 0.432 mm (#TUBING-TYGON-B1IC-B1OC-ROLL, Cellix Ltd, Dublin, Ireland), 750 uL samples were taken every 30 s and analyzed by DLS. Viscoelastic properties (shear storage modulus G' and shear loss modulus G") were measured with an Elastosens Bio™ (Rheolution Inc., France). 2 mL of the synthesis aqueous phase were prepared for each sample at 4°C, then after STMP addition and homogenization, the samples were transferred to Elastosens holders and incubated in the Elastosens. The temperature ramp was manually controlled from 10°C to 25°C to mimic the emulsification process, then increased to 50°C to mimic 50°C oven incubation for 20 min. Nanoemulsions screenings were performed by mixing water or the synthesis aqueous phase with a surfactant-oil continuous phase. The latter was prepared beforehand (1 h agitation) by mixing surfactants (surfactant-to-oil ratio between 5% and 30%) with the oil in a 5 mL beaker und kept under constant magnetic agitation (200 rpm to 1'500 rpm explored). The water phase was added dropwise (water-to-oil ratio between 2.5% and 25%), then the mixing was kept for 3 to 15 min).

A.5) Microemulsion

Hydrophilic Lipophilic Difference (HLD) screenings were performed by mixing surfactants together for a total of 90 mg in centrifuge tubes, then adding oil phase (750 µL sunflower oil) with agitation for 1 h. The water phase is then added (750 µL ultrapure water, saline solutions, or aqueous phase from the NP

synthesis) slowly. A gentle agitation by three up-and-down inversion is performed then the tubes are left to incubate at RT for more than 1 h, before they are observed and photographed. Surfactant gradients were used to determine unknown parameters (EACN: Effective Alkane Carbon Number, or EACN, for the oils; Characteristic Curvature, or Cc, for the surfactants) as described by Abbott [341]: two known surfactants (Tween 80 and Span 80) to determine sunflower oil EACN, then Tween 80 with PGPR in sunflower oil were used to determine PGPR Cc. HLD was found to be independent of salinity for PGPR. Constants used: k = 0.16, F(S) = 0.13*S, and α was ignored by working at 25°C (RT). Known values were: $Cc_{Tween80}$ = -3.7, Cc_{Span80} = 3.1. Determined values were: Cc_{PGPR} = 4, $EACN_{sunflower\ oil}$ = 16.

A.6) Fucoidan and phosphate chemical quantification

The fucoidan content of NPs was determined by a semi-quantitative solid-phase colorimetric assay for sulfate titration [342]. Briefly, 12.5 µg of Fuco-NPs in suspension at a concentration of around 1 mg/mL were added by 5 µL drops on a piece of Whatman Chromatography paper grade 1 with drying between each drop addition. The paper was first soaked into a methanol/acetone (6:4) solution for 3 min and then into a methanol/acetone/water (6:4:15) solution with 50 mM HCl and 0.1 wt.% methylene blue for 10 min. Finally, the paper was extensively washed with acetic acid/methanol/acetone/water (5:6:4:85) until no coloration was detected in the washing solution. The paper was then transferred to the Eppendorf, containing 0.5 mL methanol with 2 wt.% SDS, and incubated for 15 min at 50°C. 0.2 mL of the extracted dye was placed in a 96-well plate, and its concentration was determined by reading absorbance at 663 nm with a Varioskan LUX multiplate reader (Thermo Fisher Scientific, Massachusetts, United States). Standard curves were obtained from fucoidan in solution with known concentrations. The phosphate content of NPs was determined by a colorimetric assay. Briefly, two solution A (2.5 g/L ammonium metavanadate NH_4VO_3, 13 wt.% HNO_3) and B (5 g/L ammonium heptamolybdate $(NH_4)_6Mo_7O_{24}$) are prepared. 1 mL of around 1 g/L NPs are incubated with 1 mL HNO_3 10 wt.% for 3 h at 105°C, then 0.4 mL HNO_3 65 wt.%, 2 mL solution A, 2 mL solution B and 3.6 mL water are added. After 15 min incubation at room temperature (RT), concentration was determined by reading absorbance at 405 nm. Standard curves were obtained from H_3PO_4 solutions with known concentrations.

A.7) Statistical analysis

Quantitative data were analyzed with the software GraphPad PRISM 9.5.0., with a significance level α taken at 0.05 in the different statistical tests used. Whenever applicable, presented replicates consist of biological replicates, or, when appropriate, different NP batches. Unless explicitly mentioned, results are presented as mean ± standard deviation. Depending on the design of the experiments, data significance was evaluated with unpaired t-test (two groups, assumed equal variance), unpaired t-test with Welch's correction (two groups, variance not equal), paired t-test (two groups of paired values, with assumed equal variance), one-way ANOVA (one factor explored, with more than two groups, variances assumed equal) with Tukey's multiple comparison test, one-way Welch's ANOVA (one factor explored, with more than two groups, variances not equal) with Dunnett's T3 multiple comparison test, repeated measures one-way ANOVA (one factor explored, with more than two groups of repeated measures compared to the initial group, variances assumed equal) with Dunnett's multiple comparison test, two-way ANOVA (two factors explored). Unless explicitly specified in the legend, unpaired t-tests and one-way ANOVA with Tukey's test are performed. Every p-value below α threshold was represented as follows: * $p < 0.05$; ** $p < 0.01$; *** $p < 0.001$, **** $p < 0.0001$ (ns was indicated for "not significant" if no significant differences are present in the data presented).

B) From an emulsion to nanoparticles synthesis

B.1) The choice of polysaccharide hydrogel nanoparticles

The aim of this project was to develop NPs which could vectorize two or more drugs in order to exert improved thrombolytic effect in the circulation in a safe manner. As presented in "Part One. II. Nanomedicine: another approach for thrombotic diseases", NPs are a promising technique to improve delivery of therapeutic agents to thrombi, protecting them from the circulation and delivering them where needed. However, multiple different NPs may be used for that purpose. The main objectives for this project were: the design of biocompatible objects, displaying no toxicity; obtention of stable NPs, either in storage or in various suspensions; a simple and robust synthesis, respectful of green chemistry incentives; incorporation of a moiety for targeting the thrombi; capacity of loading several agents for improved thrombolysis. Polymeric NPs are versatile tools, with good tunability and they can be easily functionalized, but their synthesis sometimes lacks robustness and may involve toxic solvents and

products. On the other hand, hydrogels and nanohydrogels are especially interesting with impressive loading properties for hydrophilic drugs due to their high water content and are most often biocompatible. Furthermore, polysaccharides are a good material candidate for polymeric NPs, including nanogels, as they are biocompatible, and often biodegradable, nontoxic, and imbued with innate biological activity. Moreover, they are easily available through various natural sources. Finally, several modifications and crosslinking methods are possible since polysaccharides usually contain many functional groups. Dextran is an appropriate choice, since it is readily available due to many commercial uses, and it has a history in biomedical applications thanks to its stability, nontoxicity, and high functionalization potential. Therefore, a dextran nanohydrogel as basic formulation was chosen.

Furthermore, another polysaccharide could be used for targeting, thus fitting adequately in the synthesis. Fucoidan is a sulfated polysaccharide composed of fucose monosaccharides, derived from brown seaweeds and echinoderms [343], and has a similar structure to heparin, a common anticoagulant [343,344]. Due to the high content of sulfonic acidic groups, it is generally negatively charged [343]. Similar to many polysaccharides, fucoidan exhibits various biological activities depending on its molecular weight: studies have investigated its mucoadhesive [343], anticoagulant [343], antithrombotic [344,345] and anti-inflammatory [344,345] properties among others; notably, interaction with platelet receptors was found to either provoke platelet aggregation for high-molecular weight fucoidan, or inhibited its aggregation and subsequent thrombosis for low and medium molecular weight fucoidan [343,345]. Yet it is another biological property that is of interest in this project. P-selectin is a transmembrane glycoprotein, expressed on activated platelets and endothelium, which mediates leukocyte adhesion through the PSGL-1 ligand. This interaction notably implicates the Sialyl Lewis x (SLe x) tetrasaccharide motif on PSLG-1 ligand, which can also be found in other cell-cell interactions. Our Team demonstrated in 2009 that fucoidan exhibited a strong affinity towards P-selectin, with a remarkable K_D of 1.2 nM, while also showing that fucoidan could inhibit P-selectin binding to PSGL-1 and Sialyl Lewis X with respective IC_{50} of 5 nM and 20 nM [222]. They further explored how this could be used for targeting platelets in the activated state, thus potentially granting it a thrombus targeting capacity. This was indeed investigated by several studies from our laboratory, who explored fucoidan as a targeting moiety for thrombi or activated endothelium [164,167,168,346–353], while other groups have also used fucoidan as a targeting moiety for thrombotic diseases [161,354,343]. Moreover,

a fucoidan good manufacturing practices (GMP) formulation was validated and it was subsequently used in a Phase I clinical trial in 2019 [349,350].

Besides, determining an adequate size range for the NPs is critical. As described in “Part One. II. A) Nanomedicine relevance”, and illustrated in Figure 8, NPs should be above 100 nm to avoid renal filtration, extravasation and endothelial internalization, but in order to be homogeneously distributed in the blood flow, their diameter should be below 200-300 nm. Indeed, this would warrant that NPs may encounter the thrombus and not flow around it through hemodynamics.

Therefore, the proposed nanoparticle design in our project consisted of a polysaccharide hydrogel nanoparticle composed of dextran and fucoidan, as illustrated in Figure 17: the synthesis relied on chemical crosslinking of polysaccharides in water droplets of a water-in-oil (w/o) emulsion. In this one-pot protocol, the w/o droplets serve as nanoreactors, inside of which the polysaccharides are crosslinked into hydrogels. The isolation of the latter and resuspension in water finally yields nano-, submicro- or microparticles.

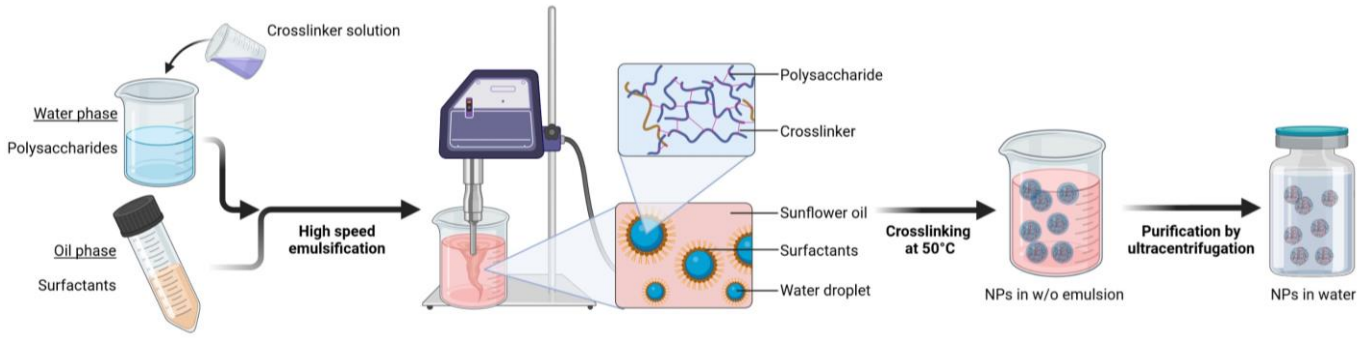


Figure 17: Schematic synthesis of polysaccharide nanoparticles. A water phase containing the polysaccharides, is mixed with the crosslinker, then added dropwise in the oil phase constituted of vegetable oil and surfactants. The emulsification is performed with a high-speed homogenizer (UltraTurrax) followed by transfer in a 50°C oven for crosslinking. The resulting nanoparticles are purified and isolated by multiple rounds of ultracentrifugation.

B.2) Previous works and established protocol

An initial protocol was proposed by Bonnard *et al*. in 2014 for the synthesis of polysaccharide microparticles, with a 2.5 µm diameter [346,347], which was further improved by Forero Ramirez *et al*. and Zenych *et al*. in 2020 and 2021 to produce polysaccharide submicronic particles with a size varying between 800 and 1500 nm [168,352]. Both protocols relied on the chemical crosslinking of polysaccharides coupled with a water-in-oil emulsion where

water droplets serve as individual reactors to limit particle size, and thus shared the following features: an aqueous phase containing polysaccharides, salts, NaOH, and a crosslinker, is mixed with a vegetable oil and surfactants; the preparation is then emulsified with a high-speed homogenizer (UltraTurrax) before crosslinking at 50°C. The crosslinker is sodium trimetaphosphate (STMP), which can crosslink polysaccharides at hydroxyl groups with phosphate ester bonds [355,356,308]. Its crosslinking mechanism has been investigated by Lack *et al*. in 2007 by spectroscopy, who notably described the role of a basic pH in the activation of STMP as well as polysaccharides [357]. There are however key differences between protocols owing to the successive improvements, which are compared in Table 2.

Protocol	**Bonnard *et al.*, 2014**	**Forero Ramirez *et al*., 2020**	**Zenych *et al.*, 2021**	**de La Taille *et al*., 2024**
Polysaccharides	75% Dextran 500 25% Pullulan 200	100% Dextran 70	100% Dextran 40	100% Dextran 40
Polysaccharides concentration	1.7x10² mg/mL	1.6x10² mg/mL	1.6x10² mg/mL	1.6x10² mg/mL
NaCl	-	3.1 M	3.1 M	3.2 M
NaOH	0.92 M	0.85 M	0.85 M	0.44 M
Crosslinker (STMP)	2.8x10^{1} mg/mL	5.1x10^{1} mg/mL	5.1x10^{1} mg/mL	5.1x10^{1} mg/mL
WOR (v/v)	1.1 / 98.9	2.0 / 98.0	3.8 / 96.2	3.8 / 96.2
Oil	Colza oil	Sunflower oil	Sunflower oil	Sunflower oil
Surfactants	75% Span 80 25% Tween 80	100% PGPR	100% PGPR	60% PGPR 40% Tween 80
SOR (w/v)	1.5%	6%	6%	6%
Ultraturrax dispersion	28’000 rpm 2 min	30’000 rpm 4 min	30’000 rpm 4 min	30’000 rpm 2.5 min
Filtration	5 µm filter or 3’000G centrifugation	3’000G centrifugation	3’000G centrifugation & 1.2 µm filter	-
Final size in water	2500 nm	790-850 nm	850 nm	315 nm

Table 2: Synthesis parameters. The protocols of Bonnard, Forero Ramirez and Zenych are compared with the one developed in this project (de La Taille). The concentrations given correspond to the situation right before mixing the two phases. Values that were changed between protocols (from left to right) are indicated in greyed cells. WOR: water-to-oil ratio. SOR: surfactant-to-oil ratio. The final size corresponds to the Z-average hydrodynamic diameter measured by Dynamic Light Scattering (DLS).

The major differences consisted in making the protocol “greener” and reducing the final size of the particles. Forero Ramirez and Zenych’s works therefore involved the use of a highly lipophilic emulsifier, polyglycerol polyricinoleate (PGPR), which is considered GRAS and is used in the food industry, notably for chocolate molding [358–360]. Its use as a surfactant for emulsions as also been described, including the role of salinity [361–364] Furthermore, Forero Ramirez’s work was instrumental in reducing the particle size, by investigating various synthesis parameters such as salinity, relative polysaccharide and crosslinker ratio or aqueous phase viscosity. According to our criteria defined above, the first goal of our project was to further reduce the particle size, keeping the protocol as robust as possible. All the size optimization assays were initially performed with dextran 40 exclusively as a polysaccharide, and fucoidan was incorporated later to produce functionalized particles containing both polysaccharides.

B.3) Crosslinking control

Starting from these protocols with notably Zenych *et al*. protocol defined as the reference “classical” protocol, different methods were assessed to reduce the nanoparticle size. Initially, the goal was to delay as much as possible the crosslinking reaction: since all reagents are present in the aqueous phase prior emulsification, the crosslinking reaction may occur during all the synthesis. To avoid early gelation, the emulsification is therefore performed on ice with cold reagents (oil phase kept for 20-30 min at -20°C, other reagents at 4°C) and the crosslinking is favored after the emulsion with an incubation at 50°C for 20 min. Even so, early gelation may prevent correct emulsification, increasing the viscosity of the aqueous phase, and thus affecting its dispersion in small w/o droplets.

Indeed, it was observed that the w/o droplet size (400-450 nm) in the emulsion was smaller than the final particles (850 nm) obtained with the classical protocol, as shown in Figure 19.a (with polydispersity index, PDI, below 0.2). Therefore, we first attempted to modify the crosslinking in order to slow it.

Notably, STMP crosslinking is dependent on basic activation of hydroxyl groups in the polysaccharides, which explains the use of NaOH as a reagent. Therefore, we assessed whether an oil-soluble base could be used to induce hydrogel gelation. Tetrabutylammonium hydroxide (TBA) and 4-5(Dimethylamino)-pyridine (DMAP) are two bases commonly used in nonpolar or organic solvents as well as in water. Therefore, the gelation of the aqueous phase with NaOH, TBA or DMAP as base at different concentrations was assessed without emulsification (Figure 18.b). Accordingly, TBA could achieve gelation under 20 min at 50°C at 200 mM but could not be correctly solubilized at concentrations above 300 mM, while DMAP was insufficient to activate gelation. Synthesis attempts where NaOH was replaced by the addition of 200 mM TBA to the formed emulsion were unsuccessful due to solubilization issues in the oil phase. Similarly, other phosphate crosslinkers could be used, notably $POCl_3$, which is soluble in a broader range of solvents than STMP. While it was possible to form gels with this crosslinker, notably by increasing the dextran molecular weight (see Figure 18.c), when adding the $POCl_3$ in formed emulsions with various dextran mixtures, no particles were obtained, likely due to crosslinking or solubility issues. Therefore, STMP and NaOH were kept as the crosslinker and base. Interestingly, based on Figure 18.b, gelation was possible with NaOH even at lower concentration than the one previously in use.

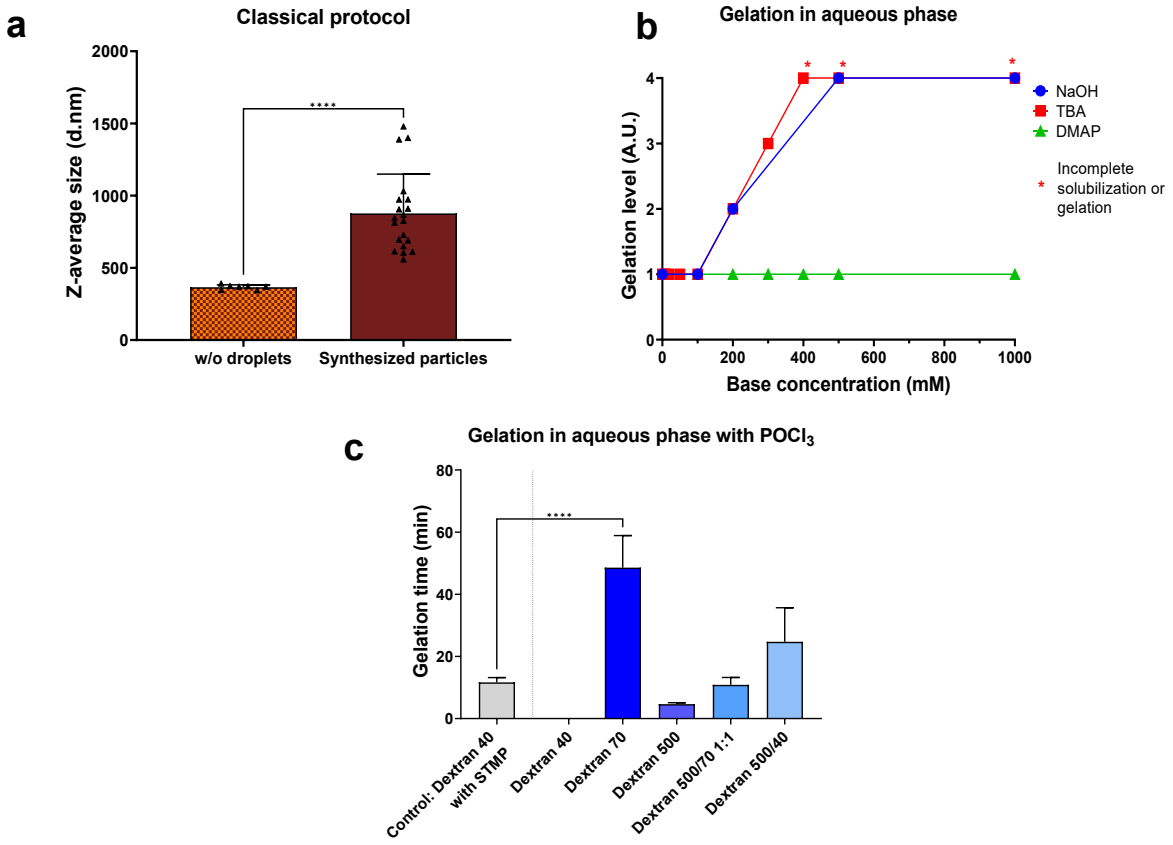


Figure 18: Assessing alternative bases and crosslinker. (a) The Z-average size of aqueous phase droplets in the oil emulsion is compared to the final particle size with the classical protocol. An unpaired t-test was used (n≥7). (b) Gelation assay of the aqueous phase with different bases. The gelation levels were defined as: 1- no gelation; 2- gelation under 20 min at 50°C; 3- gelation under 10 min at 50°C; 4- gelation under 20 min at RT. (c) The gelation time at 50°C using POCL3 with various dextrans were compared. A one-way ANOVA was performed, with Dunnett's multiple comparison test to compare dextran 40 with STMP with other formulations (n=3).

Moreover, the size of water droplets in the emulsion was measured over time by taking samples at 30 s intervals during the emulsification, as illustrated in Figure 19.a. It appeared that the droplet size was reduced during the first 120 s then remained stable (PDI indexes after 30 s were below 0.2). Thus, repeating the protocol but with emulsification time reduced from 4 min to 2.5 min was assessed. Another possible explanation for the size disparity between the emulsion and the nanogels may lie in the preparation of the aqueous phase. In order to delay the crosslinking reaction, the aqueous phase is prepared on ice with mixing for 20 s at low speed (200 rpm). However, the aqueous phase is a viscous solution due to the high dextran concentration [352], with a measured viscosity at 25°C of 85.6±2.1 mPa.s, which is comparable to the sunflower oil

used in the synthesis (57.7±0.1 mPa.s and 76.9±0.1 mPa.s with PGPR addition). This may impede how the different reagents are mixed, and therefore the mixing of STMP within the aqueous phase was increased from 20 s, 200 rpm to 60 s, 400 rpm. Since the base addition is necessary to activate the polysaccharide reaction, but that lower concentration than the one classically used (~0.9 M) could still achieve gelation (Figure 18.b), a reduction in NaOH by half was assessed to further delay crosslinking. As shown in Figure 19.b, each modification (reducing NaOH concentration, increasing STMP mixing or reducing the emulsification time) was enough to reduce particle size to around 600 nm, while the combination of these three (hereafter designated “intermediate” protocol) achieved particles of 525±30 nm compared to the classical protocol (850±153 nm). Moreover, the actual gelation process was investigated by viscoelastic measurements with an Elastosens, allowing continuous storage (G’) and shear stress (G”) moduli to be measured during hydrogel crosslinking: no emulsification was performed, but the temperature ramp (including emulsion heating by the homogenizer in the first 150 s or 240 s, based on in-process temperature measurements) and delay before 50°C incubation were simulated. At similar NaOH concentrations, the intermediate protocol could start the gelation earlier than the classical one due to an earlier temperature increase, but the final storage modulus was the same; while decreasing the NaOH in both situations resulted in delayed gelation, but increased final storage modulus at the incubation stop (1350 s and 1440 s). These results are recapitulated in Figure 19.d-e. Interestingly, after some time all formulations showed a decreased shear storage modulus, which may be due to NaOH-mediated hydrolysis at 50°C. Overall, this validated that the intermediate protocol with reduced NaOH concentration yielded similar hydrogels (with a slight increase in shear storage modulus) as the classical one, but with size reduction.

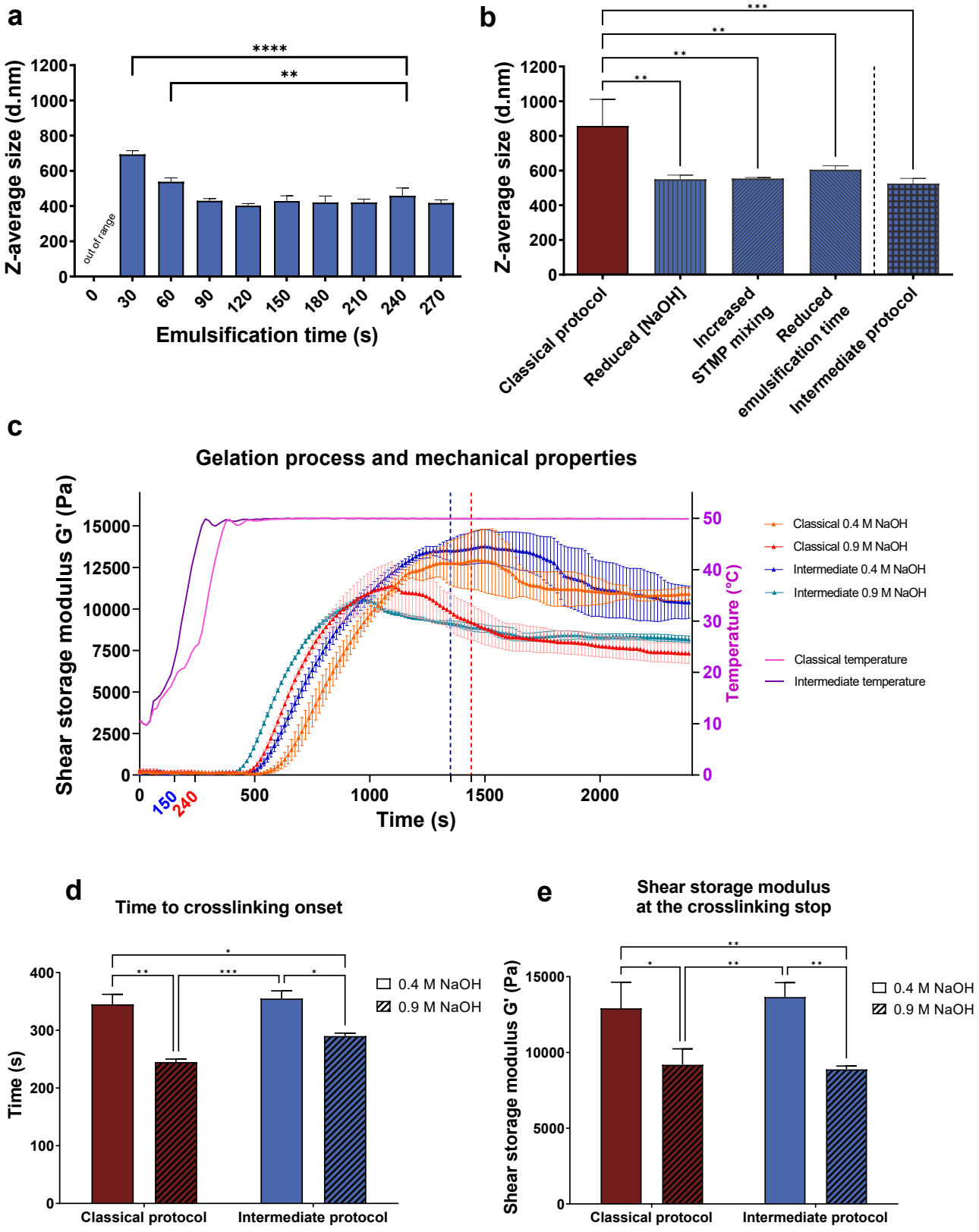


Figure 19: Modifying synthesis parameters. (a) Z-average size of aqueous phase droplets in the oil emulsion using the classical protocol. A one-way ANOVA was performed, with Dunnett's multiple comparison test to compare each timepoint to 240 s, corresponding to the synthesis protocol (n=3). (b) Z-

average size comparison between the classical protocol, halving the [NaOH], increasing the STMP mixing pre-emulsion, or reducing emulsification to 2.5 min. The intermediate protocol consisted of all three improvements combined. A one-way ANOVA was performed, with Tukey's multiple comparison test (n=3). (c) Storage modulus (left axis) by Elastosens during hydrogel gelation with the classical and intermediate formulations, either with 0.9 M or 0.4 M NaOH. The imposed temperature ramp is indicated on the right axis. The 150 s and 240 s timepoints indicate when the temperature is ramped up to 50°C, and the dotted lines indicate when the incubation is stopped in the synthesis process (red: classical, blue: updated) (n=3). (d) Time between 50°C incubation start and crosslinking onset, measured as the moment when dG'/dt exceeded the limit-of-detection (LOD) threshold of 4.5 Pa/s; and (e) Final shear storage modulus when the crosslinking stops (respectively 1350 s and 1440 s) for intermediate and classical protocols. Two-ways ANOVA with Tukey's multiple comparison tests were performed (n=3).

B.4) Improved emulsification

Another method to reduce the final hydrogel size is to improve the emulsification process, to obtain nanoscale smaller and stabler w/o droplets, or nanoemulsions.

Several protocol changes were investigated, including surfactant ratio, WOR, mixing, surfactant change or using a different oil (for instance M812, with a different viscosity and solubilization of TBA, DMAP or $POCl_3$). Notably, the use of ultrasonication as an alternative high-energy dispersion method was investigated [363,365]. In general, ultrasonication is performed after a pre-emulsification step with a homogenizer (UltraTurrax), therefore we compared ultrasound-only and homogenizer-ultrasound emulsifications. As illustrated in Figure 20.a, all formulations which included ultrasonication steps produced unsatisfactory particles due to their high PDI (above 0.2), and notably for the 4 min ultrasonication only, only one batch produced micrometric particles, with high dispersity. Nonetheless, ultrasonication coupled with pre-emulsification was expected to produce smaller droplets, therefore we investigated the size of droplets without STMP addition (and thus no gelation). As shown in Figure 20.b, there was indeed a size reduction in the droplet size for the two conditions combining pre-emulsification and ultrasonication. Therefore, the issue was not in the emulsion. Temperature measurements during the emulsification revealed that while the classical protocol with high-speed homogenizer reached temperatures of 20-25°C after 4 min, temperatures as high as 40°C could be reached with ultrasonication. Thus, the temperature increase might be responsible for early gelation and the resulting impaired particle synthesis. Other

methods for high-energy emulsification, such as high-pressure homogenization or microfluidization, could be explored but were not available to us [366].

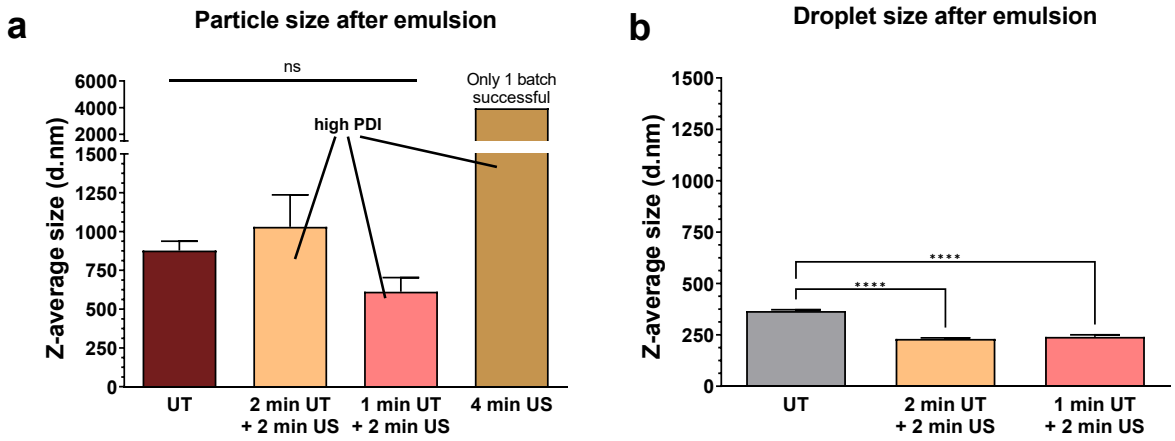


Figure 20: Ultrasonication assay. (a) Z-average size comparison between the particles obtained with the classical protocol with homogenizer (UT), US alone (two batches failed and were not measured) or combination of homogenizer then US (UT + US). The intermediate protocol consisted of all three improvements combined. PDI above 0.2 is considered high. A one-way ANOVA was performed except from the 4 min US, with Tukey's multiple comparison test (n=3 with US and n=21 for UT only). (b) Z-average size of aqueous phase droplets in the oil emulsion using the classical protocol. A one-way ANOVA was performed, with Tukey's multiple comparison test (n=7 for UT, n=3 for both US conditions).

Another approach that was considered was low-energy emulsification to form nanoemulsions [366,367]. The methods rely on the inversion from macroemulsion to nanoemulsion by surface curvature inversion, with a low interfacial tension at the inversion point, where a water-in-oil (w/o) transforms into an oil-in-water (o/w) emulsion or *vice-versa* in presence of surfactants. The two common methods are emulsion inversion point (EIP, or PIC: phase inversion composition, which are mostly similar definitions), where changes in the certain physical parameters at a constant temperature, mostly the composition by dilution with the oil or water, is used to trigger this phase inversion; or phase inversion temperature (PIT), where a sudden temperature change from a given balance of hydrophilic and lipophilic properties allows the obtention of kinetically stable nanoemulsions. The latter can be more complex to implement as it depends on temperature sensitive surfactant such as those with poly(oxyethylene) chains, and requirements for sudden temperature change [366,367]. We therefore explored spontaneous emulsification by EIP as described by Akram *et al*. in 2021 to prepare w/o nanoemulsions [368], relying on slow water addition to the oil phase (spontaneous nanoemulsions through

swollen micelles). Various modifications were explored to achieve EIP, including changing the surfactants (lecithin, Span 80, Tween 80, PGPR), the oil (colza oil, olive oil, M812, sunflower oil), the WOR and surfactant-to-oil ratio (SOR). Initial development involved only pure water as the aqueous phase for simpler exploration, with the aim of later progressive switching to the reactive aqueous phase (including the dextran and salts), and nanoemulsions of circa 150 nm with PDI below 0.2 were obtained with slow water addition to the oil phase in the following conditions: WOR = 10%, oil = sunflower oil, surfactant = PGPR, SOR = 9%, with magnetic agitation for 10 min at 700 rpm at RT. Yet when switching to the reactive aqueous phase, the nanoemulsions could not form, as illustrated in Figure 21.a, resulting in macroemulsions with poor polydispersity. This may be explained by the changes in viscosity, which may impose a kinetic barrier to emulsification by low-energy (turbulent) methods [369].

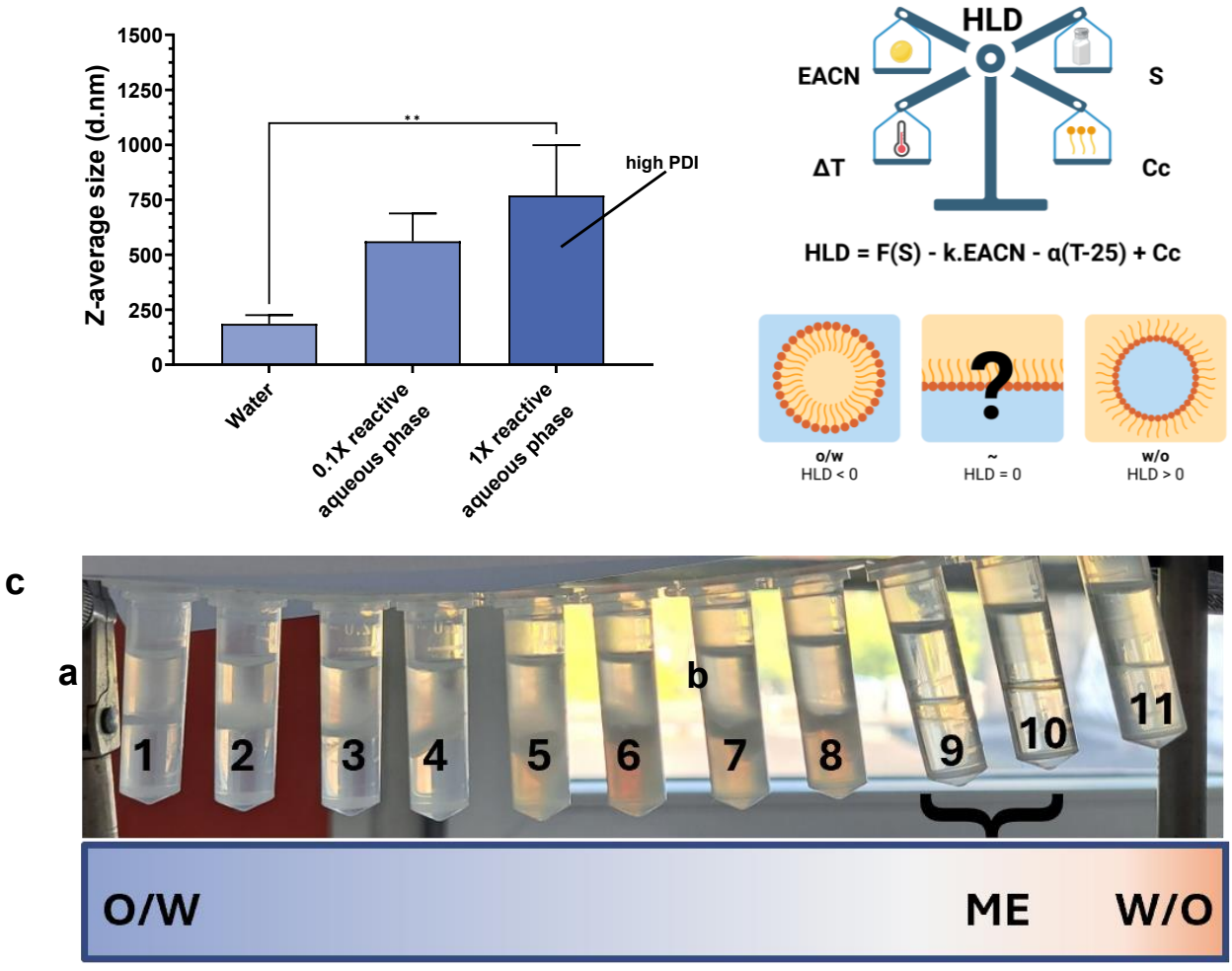


Figure 21: Nano- and microemulsions. (a) Z-average size of aqueous phase droplets generated by EIP. A one-way ANOVA was performed, with Tukey's multiple comparison test (n=3). (b) Illustration of the Hydrophilic Lipophilic Difference (HLD) model. Top, the HLD equation is represented. Bottom,

representative emulsion behavior depending on HLD values. S: salinity; EACN: "oiliness" of the oil; Cc: characteristic surfactant value; k and α fixed constants. (c) Representative HLD microemulsion scan based on sunflower oil, water, and a mix of surfactants displaying a microemulsion (ME) in tubes 9 and 10. The surfactant mix was designed to have the Cc (and thus HLD) increasing from left to right.

The nanoemulsion approach could therefore not yield improved emulsion for the synthesis. This opened however the way for the microemulsion framework, which is defined as a thermodynamically stable emulsion (despite a misleading name, it only refers to its stability and not a size, in contrary to macro- or nanoemulsions) [341,366], which is theoretically predicted under strict surfactant conditions (SOR, critical micelle concentration, etc.) and form due to the interfacial tension approaching zero [370]. Pragmatically, microemulsions can be used to form stable, small droplets, or more complex motifs such as bicontinuous, cylindrical or lamellar emulsions [366,367,371], and have been used to formulate stable nanoemulsions for drug delivery and other applications [372–375]. Microemulsion formulation ca be performed with the Hydrophilic Lipophilic Difference (HLD) theory, which is based on the following equation, as described by Abbott in 2017 [341]:

$$(1) \quad HLD = F(S) - k.EACN – \alpha.(T-25) + Cc$$

Where HLD is an arbitrary physical quantity, F(S) represents a function of the salinity S in the aqueous phase, EACN is the Effective Alkane Carbon Number determining the "oiliness" of oils, T is the temperature in Celsius, Cc the characteristic value of the surfactant, and k and α fixed constants depending on the surfactants. Hence, the key to emulsion formulation becomes a balancing game between all four variables in order to achieve different outcomes, as illustrated in Figure 21.b. When the HLD value is close to 0, the mixture obtained presents a balance between hydrophilic and lipophilic components with extremely low interfacial tension, resulting in Type III Winsor emulsions, or microemulsions (which could be spherical, but not necessarily due to low interfacial tension). When HLD < 0, we obtain Winsor Type I oil-in-water (o/w) emulsions, and with HLD > 0, we obtain Winsor Type II water-in-oil (w/o) emulsions. In practice, these values can be determined from tables or determined experimentally, as shown in Figure 21.c, where a gradient in Cc values with two surfactants was prepared, thus obtaining a range of tubes displaying o/w emulsions, microemulsions and w/o emulsions. To form stable w/o emulsions, a strictly positive HLD value close to 0 was therefore chosen. Through screenings (with the known surfactants Tween 80 and Span 80) as

displayed in Figure 21.c, the EACN of sunflower oil and the Cc of PGPR were determined. For ethoxylates like Tween 80, F(S) = 0.13*S; but no dependence on salinity was found for PGPR. By working at RT throughout the experiments, α could be ignored. The final parameters are recapitulated in Table 3.

Surfactants	**Span 80**	**Tween 80**	**PGPR**
Cc	3.1	-3.7	**4.0**
Molecular weight (g/mol)	428	1310	521

Sunflower oil EACN	**16**

Salinity (g/100 mL)	18.8

HLD parameters		
F(S)	**0.13*S*x**	With x the Tween 80 molar fraction
k	0.16	Based on Abbott, 2017
α	**-**	Ignored by working at RT

Table 3: Parameters and values for the HLD equation. The values and parameters in bold were measured experimentally. Constants were determined from the HLD description by Abbott, 2017 [341].

Based on these experimental values, we aimed for a formulation with HLD = 0.80, obtained by mixing PGPR with Tween 80 in 60/40 relative fractions to achieve an overall Cc of 2.4.

B.5) Optimized formulation and characterization

Thus, the optimized formulation, used hereafter, was improved by delaying crosslinking (“intermediate” protocol) while improving the emulsion through the microemulsion framework, with the effective parameters recapitulated in Table 2. Notably, the filtration and neutralization steps were also removed, as they were found to be unnecessary in this optimized protocol. This synthesis was used to produce full dextran NPs, named Dex-NPs, and 5 wt.% fucoidan-incorporating dextran NPs, named Fuco-NPs, which may target P-selectin. The Z-average hydrodynamic diameter was respectively 313.7 ± 14.4 nm and 316.5 ± 15.3 nm, with low dispersity (polydispersity index, or PDI, considered as monodisperse below 0.2) as measured by Dynamic Light Scattering (DLS), without significant differences between both formulations

(Figure 22.a-b). When comparing the former classical formulation to the microemulsion-based optimized formulation, the synthesis yielded batches in a robust manner with narrow Z-average size distribution which retained the same dispersity throughout batches (Figure 22.c-d), with an overall size reduction from around 850 nm to 315 nm. Moreover, in contrary to previous protocols, no filtration was necessary to obtain particles at the desired size.

Size distribution and sphericity were also confirmed by TEM, notably illustrating that filtration was not needed (Figure 22.e). Furthermore, a major challenge with NPs remains their stability in various colloidal suspensions, with stabilizing agents often used. As shown in Figure 22.f, with the “classical” submicronic particles, size increase through aggregation and sedimentation is seen when resuspended in saline without addition of the surfactant Tween 20; in contrast, with the optimized protocol, the Fuco-NPs do not show any significant differences in size in ultrapure water, saline, or saline with a stabilizer.

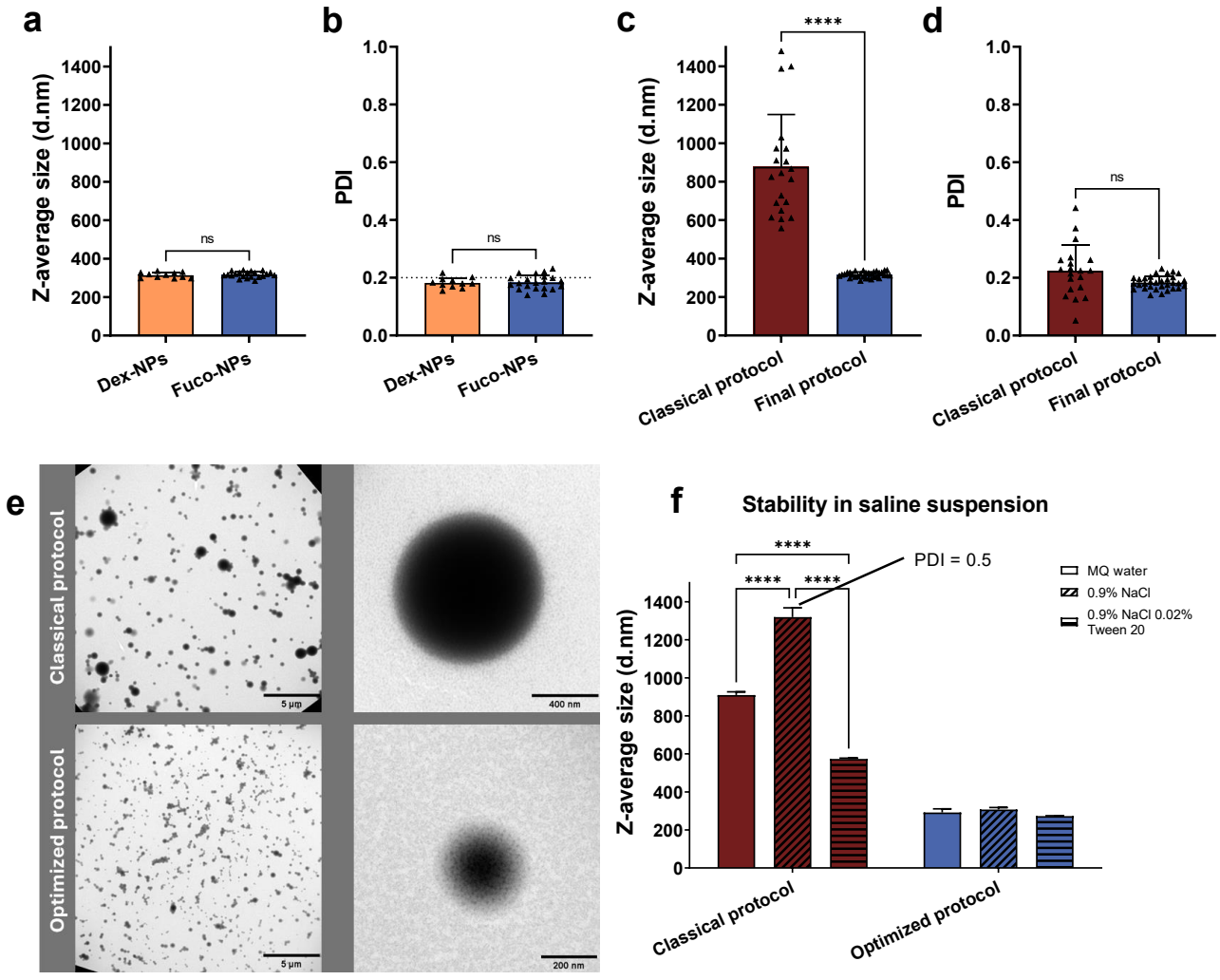


Figure 22: Comparison of classical and optimized formulations. (a) Z-average size and (b) dispersity comparison of the optimized formulation for Dex-NPs and Fuco-NPs. Unpaired t-tests were performed (Dex-NP: n=11; Fuco-NP: n=21). (c) Z-average size and (d) dispersity comparison of the optimized formulation with the classical protocol, including formulations with or without fucoidan. Unpaired t-tests were performed (classical: n=21; optimized: n=32). (e) Representative TEM images for classical particles (top row) and optimized Fuco-NPs (bottom row). The left column was acquired at 1'900X magnification, while images on the right were obtained at higher magnification (top: 30'000X, bottom: 49'000X). (f) Size comparison of fucoidan containing particles between classical particles and Fuco-NPs in water, saline or saline with 0.02% Tween 20 as surfactant. When not indicated, PDI was below 0.2. A two-way ANOVA was performed, with Tukey's multiple comparison test to compare only the suspension medium effects (n=3).

FTIR spectra were obtained to verify the composition of Dex-NPs and Fuco-NPs (Figure 23.b). Since fucoidan was indistinguishable from dextran (and thus from the physical mix of fucoidan with dextran), these only validated the polysaccharide composition of both formulations. The surface charge of NPs was measured as it often plays a key role in colloidal stability. This was performed by Electrophoretic Light Scattering (ELS) with a fixed ionic force of the media to ensure comparability of our measurements. Across a broad pH range, the Zeta potential measured by ELS was below -20 mV for Dex-NPs and below -25 mV for Fuco-NPs (Figure 23.a), with specifically the Zeta potential at neutral pH of -25.9±1.2 mV for Dex-NPs and -32.2±1.8 mV for Fuco-NPs. Based on a two-way ANOVA, both pH and fucoidan incorporation were significantly responsible for the changes in Zeta potential (pH: 14% of total variation; fucoidan: 60% of total variation), and therefore the Zeta potential of Fuco-NPs significantly differed from Dex-NPs. Since Dex-NPs are composed of dextran, a neutral polysaccharide, the low Zeta potential of Dex-NPs clearly indicated the incorporation of negatively charged components: the phosphate diester crosslinking bonds. This incorporation of negatives charges through crosslinking has already been described for other polysaccharide hydrogels [376]. As for Fuco-NPs, the decreased Zeta potential compared to Dex-NPs could be attributed to fucoidan incorporation, a negatively charged polysaccharide. Such negative surface charges are generally considered low enough to impart electrostatic colloidal stability [377]. Indeed, this was verified by the long storage stability of Fuco-NPs in water evaluated by size measurements over a year at 4°C (Figure 23.c). Besides, freeze-drying of Fuco-NPs in 1% sucrose was possible without loss in size or dispersity as verified in Figure 23.d-e. This long-

term stability in cold storage above 0°C and freeze-drying capacity are especially interesting for logistic and pharmaceutical purposes [187].

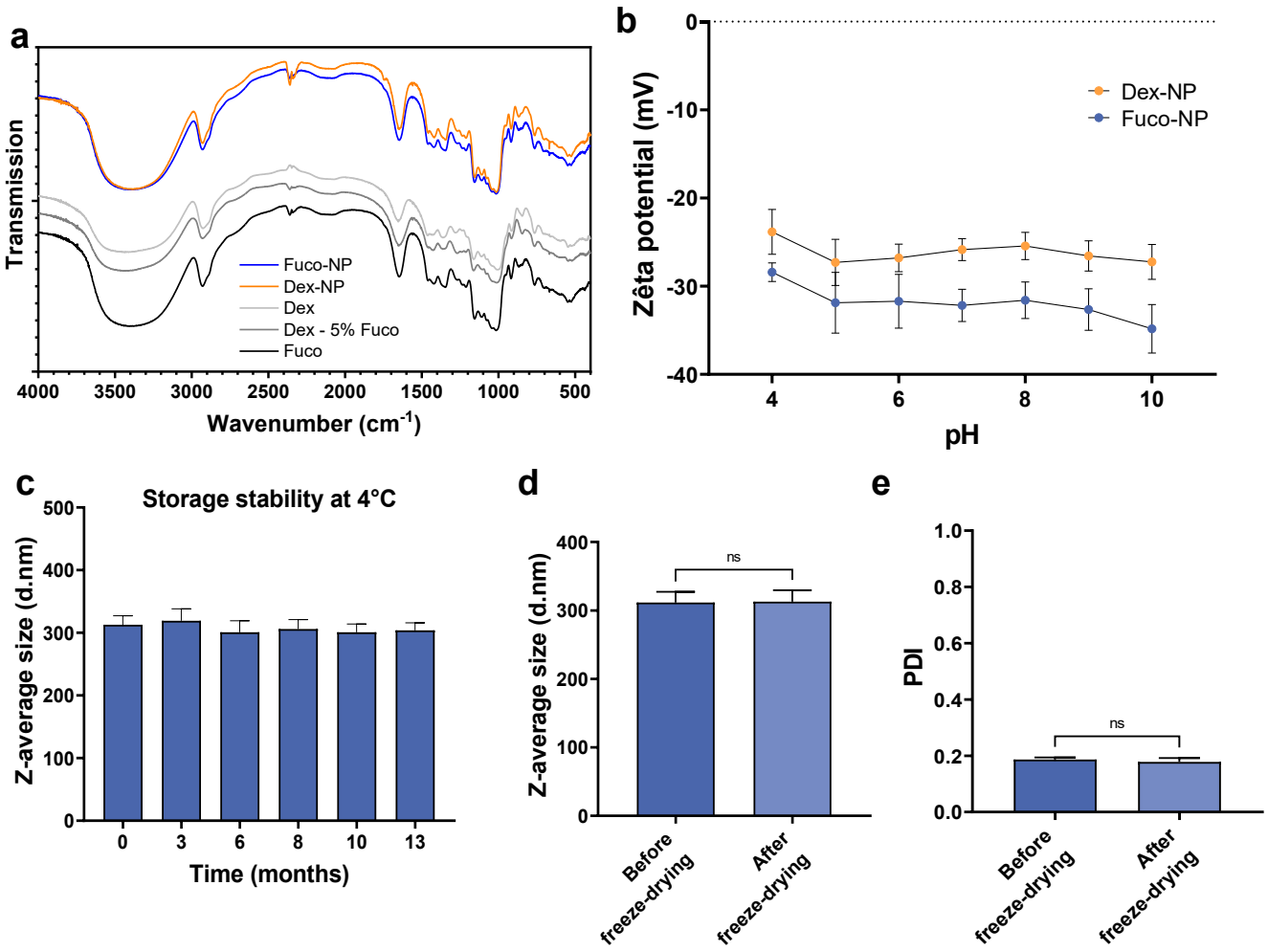


Figure 23: Composition and stability of Fuco-NPs. (a) FTIR spectra of Dex-NPs and Fuco-NPs compared to dextran (Dex), fucoidan (Fuco) and a physical mix of fucoidan 5 wt.% and dextran (Dex – 5% Fuco) corresponding to the relative mass distribution of both polysaccharides in Fuco-NPs. (b) Zeta potential of Dex-NPs and Fuco-NPs measured at various pH by Electrophoretic Light Scattering (ELS) (n=3). (c) Z-average evolution measured by DLS over storage time at 4°C. A one-way ANOVA with Dunnett's multiple comparison test to compare every column to t=0 was performed (n≥3). (d) Size and (e) dispersity of Fuco-NPs were measured by DLS before freeze-drying in 1 wt.% sucrose at -80°C and after resuspension. Paired t-test were performed (n=3).

The final characteristics of the Dex-NPs and Fuco-NPs are recapitulated in Table 4. Notably, the phosphorus and sulfur content were measured by total reflection X-ray fluorescence spectroscopy (TXRF), which respectively validated the incorporation of phosphorus through the phosphate diester crosslinking bonds, and incorporation of sulfate-containing fucoidan in Fuco-NPs; these

measurements were confirmed by chemical titrations of sulfate and phosphate. Overall, the synthesis directly yielded NPs in the desired size range, with an increased synthesis robustness (Figure 22.c-d) and without the need for filtration. These NPs also exhibited good stability and were fully characterized, including chemical composition. Among others, the long-term storage stability at 4°C was observed, as well as freeze-drying capacity.

	Z-average size (d.nm)	PDI	Concentration post synthesis (g/L)	Zeta potential at pH=7 (mV)	Fucoidan content (wt.%)	Phosphorus content (wt.%)
Dex-NPs	313.7 ± 14.4	0.18 ± 0.02	1.4 ± 1.0	- 25.9 ± 1.2	-	1.0 ± 0.3
Fuco-NPs	316.5 ± 15.3	0.18 ± 0.03	1.8 ± 0.8	- 32.2 ± 1.8	4.4 ± 2.0	1.3 ± 0.4

Table 4: Physico-chemical characteristics of Dex-NPs and Fuco-NPs. The concentration was measured by freeze-drying. The fucoidan and phosphate content presented were obtained by TXRF.

C) Preliminary works and future directions

While we demonstrated the potential of these NPs and characterized them, there remains some room for further improvement, notably to achieve a scalable, pharmaceutical industry-compatible formulation. Moreover, the microemulsion framework may be pushed further to improve different nanoparticle synthesis.

C.1) Towards a translatable formulation

As evoked in “Part One. II. Nanomedicine: another approach for thrombotic diseases”, NPs are a promising approach for drug delivery, including in the context of thrombotic diseases. However, we described several aspects that limit the current translation of preclinical NPs development into the clinical setting. Yet our proposed nanoparticle formulation may answer some of these limitations, while still necessitating further development in other aspects.

Regarding the NP composition, a broad variety of materials have been described as illustrated in Figure 9 and Figure 10. The lipid-based particles may suffer from production costs, scalability and reproducibility of the synthesized objects, with also storage and stability conundrums, as exemplified by lipid nanoparticles-based COVID19 mRNA vaccines with stringent subzero storage requirements, which have been linked to distribution and accessibility issues, which may particularly affect less developed areas [187]. Inorganic NPs provide multiple innate properties which may enhance their applicability, with for instance imaging-related properties as contrast agents, which can be coupled

with therapeutic approaches for theranostics, which may facilitate medical personnel's management of thrombotic diseases [192]. These innate properties may also be used directly to provide treatment: some inorganic materials have been described to possess antioxidant capacities, which have been used for neuroprotection or thrombosis management [196,240]; similarly, magnetic properties were used for targeting and increased thrombolysis [153,191,236,237,282], while photothermal thrombolysis has been explored as a non-pharmaceutical approach [151,245,378]. However, there are some concerns about inorganic particles toxicity [198,199] as well as their clearance and degradation [199,202]. Therefore, polymeric particles, including hydrogel-based ones, propose a practical alternative thanks to their versatility, general biocompatibility and good functionalization potential. However, polymer synthesis may involve toxic organic solvents or crosslinkers, which could produce toxic degradation products, even though natural polymers can be used to alleviate this; they can nonetheless face sourcing issues. Moreover, such synthesis methods are often plagued by reproducibility issues and batch-to-batch variability. Other less common approaches could also prove useful, yet their scarcer description may limit the scientific knowledge about their *in vivo* behavior.

On the other hand, irrespective of the chosen synthesis method or nanoparticle types, the basic materials used may be problematic for nanoparticle approval. Notably, NPs are usually classified as combination products by the FDA and other regulatory bodies as combination products, which may result in complex approval procedures especially when multiple components are being used. To help quantifying this issue, the literature corpus used in "Part One. II. B.1) Systematic literature review" was analyzed by counting the different components used in each proposed particles: while this quantification is partly subjective as individual components may not be defined similarly by everyone, the following criteria were used: each component counted individually is composed of a separate chemical entity than the others; in the case of complex material that have been well-characterized as a whole such as classic liposome-forming lipids, they can be counted as one material; each drug is counted as a separate entity; materials that originate from biological or cellular origin are counted as one (e.g., cell membranes used for coating). As an example, the PLGA polymeric NPs, coated with platelet membrane and loaded with rtPA developed by Xu *et al*. were counted as containing 3 distinct components [232]. Based on this count (shown in Figure 24), the median count of individual components was 3, while the mean was 3.2. Therefore, it can be

considered that the 38% preclinical research articles with 4 or more components are “more complex” objects compared to the other candidates. While this is not a defining advantage *per se*, limiting the complexity of proposed nanomedicines may help accelerate the approval for further clinical research, as well as facilitating comprehension and characterization of their behavior (including clearance and degradation).

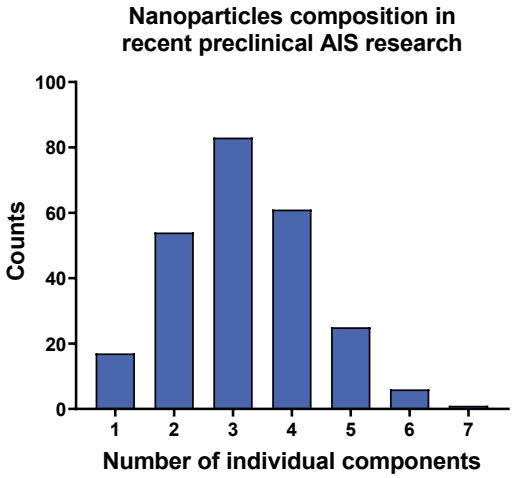


Figure 24: Counting the nanoparticles’ individual components. The 5 years systematic literature analysis described before was used to count individual components in each formulation described in nanomedicine preclinical research for AIS.

The proposed polysaccharide hydrogel nanoparticle from our project answers some key aspects. The resulting object is simple, as it is composed of crosslinked polysaccharide hydrogels, which may load the drugs by adsorption. Most importantly, the constitutive materials were chosen with safety and simplicity in mind. Dextran is a known, biocompatible polysaccharide which has been extensively described in biomedical applications, with simple and easily available sourcing (notably due to its important commercial use) [319,330]. Fucoidan is a polysaccharide, the formulation of which has been shown to be GMP-compatible and which has already been used in clinical trials and described as safe [343,350]. The phosphate diester crosslinking is a safe approach for hydrogel formation as the resulting bonds are simple and present already in the human molecular biology, while the reagent used, STMP, is rapidly hydrolyzed in water, thus limiting risks post synthesis, and hydrogels crosslinked with this molecule have been described and studied *in vivo* [301,357].

In addition, the synthesis itself comes with advantages. As a one-pot process with emulsification and crosslinking happening without intermediate steps, the synthesis itself is performed in less than an hour. This facilitates its

eventual industrial translation. Moreover, it satisfies several green chemistry considerations such as the simplicity and small number of steps, the use of nontoxic, simple reagents such as vegetable oil, GRAS surfactants which can be found in the food industry, as well as the naturally sourced polysaccharides, and lack of synthesis byproducts.

Besides, this optimized synthesis, due to the microemulsion-inspired approach and better controlled crosslinking, yielded NPs with significantly improved robustness and stability. As shown in Figure 22, the batch-to-batch variability was significantly reduced without even requiring a filtration step, and the NPs retained their size and colloidal stability even in various suspensions, including saline suspension without the need for a stabilizing surfactant [379]. These improvements have been the object of a patent deposition in December 2023 by INSERM Transfert under the name “Polysaccharide nanoparticles for a targeted combo treatment of ischemic strokes” (patent number EP23307118.2 filed on December 1st, 2023; **ANNEX 4**). While other 100% polysaccharide NPs have been described, notably with dextran [168,380–385], they usually involve chemical modification of the latter; the proposed protocol offers a simple synthesis with an easy-to-transfer process, displaying good robustness and stability. Importantly, storage at 4°C was possible for more than a year, and the validated freeze-drying capacity is a key logistical consideration: only 21% of the preclinical research articles on nanomedicine for AIS evoked stability measurements for their NPs, and 13% mentioned any form of dry storage (freeze-drying, vacuum drying or precipitation).

Nonetheless, there are some developments to be pursued before the formulation can be validated for industrial production. While robustness was confirmed, the process is currently used to produce small batches of products which are not sufficient to envision clinical use yet. Therefore, scaling up must be assessed. Furthermore, production in a GMP compliant manner is more stringent than the current protocol, meaning that adaptations must be prepared. For instance, some work was performed to optimize the purification and isolation steps, which is currently performed with ultracentrifugation: notably, some unnecessary steps were removed, and ethanol precipitation was assayed. While the synthesis was performed partly with FDA-approved and pharmaceutical grade reagents, this should be extended to all intrants. Overall, some translational aspects were taken into account for this synthesis, but it remains yet a laboratory protocol that should be optimized for scaled-up and clinically compatible production.

C.2) Exploring the microemulsion formulation

A key finding to improve the formulation of the polysaccharide hydrogels was the microemulsion framework. Based on the thermodynamic stability of certain emulsions, mediated through ultralow interfacial tension with extensive surfactant use, this approach may have been overlooked as a way to improve emulsions. Interestingly, its use in various scientific fields and industrial domains was limited to certain applications. For example, since microemulsion happen at very low interfacial tension (HLD=0), this also corresponds to the condition where oil and water mix the most easily, implying the highest solubilization of either one in the other, increasing capillary number or faster separation time [341]. This has been extensively used for instance by the oil industry through extended oil recovery, where a fine-tuned HLD greatly improves oil recovery (e.g., oil extraction) or contaminant removal [341,386,387]. Besides, the extension of this framework to nanomaterial synthesis has been proposed, as it could improve nanoemulsion formulation or provide nanoreactors for key reactions [387,371]. For example, while scarcely researched compared to other polymerization methods discussed earlier, microemulsion polymerization relies on a microemulsion formation to control monomer polymerization [312]. Yet, PIC and PIT can be considered as applications of HLD microemulsions, as they involve sudden inversion of interfacial tension by composition or temperature: the design of PIT or PIC-based polymerization could therefore be made much easier and with broader surfactants trough the microemulsion framework [341].

The concept of microemulsion has often been obscured partly because of its inappropriate name, often spewing confusion with the scale-based macro- and nanoemulsions [388]. Moreover, finding the microemulsion domain is usually described as a complicated endeavor involving complex ternary phase diagram explorations [389,390,372]. This could be solved through the HLD model which provides a theoretical framework for microemulsion design (HLD=0). However, even with this equation, the practical emulsion exploration is not straightforward, as kinetic considerations often intersect the thermodynamic behavior. For example, viscosity can play a significant role in droplet (or lack of) formation [369], and the formation of kinetically stable emulsion may be hard to distinguish from microemulsions, impeding the various methods necessary for HLD parameters' determination [341,388]. In the development of our microemulsion-based synthesis, this was the case as PGPR resulted in frequent metastable emulsion, and the high viscosity of the water and oil phases also disturbed the HLD screening experiments.

In practice for biomedical application, using the microemulsion model may help design stable nanoemulsions to serve as drug carriers, or to improve the synthesis of NPs. Microemulsion-involving approaches for NPs are scarce, and this may be due to the distance between the biological chemical or physical background of nanomedicine scientists and the microemulsion concept, as it was most commonly associated to research for oil recovery, cosmetics, and emulsion formulations that did not necessarily encompass medical applications [341]. Nonetheless, at least 8 articles out of 247 in preclinical nanomedicine research for AIS explicitly mention emulsion as part of their process, while many others may benefit from enhanced emulsion control, most notably for polymerization and polymeric NPs.

In our protocol, this could effectively reduce by half the size of the resulting NPs, thus validating that a microemulsion-based conceptual approach to formulation may be beneficial in controlling the size of certain NPs. While we did not investigate other HLD values for nanoparticle formulation since the resulting formulation produced particles of an adequate size and stability for our purposes, it may be interesting to change the HLD to values closer to 0 and hereby reducing interfacial tension during the synthesis, which may further decrease the nanoemulsion droplet size, and consequently for the NPs. Besides, bringing the HLD in a controlled manner closer to 0 may have increased the emulsion stability, helping to make it less dependent on experimental setup (homogenizer speed, reaction volume, etc.). This might be crucial for scale-up, as high-energy dispersion methods, such as the high-speed homogenizer used here, usually produce emulsions that are very dependent on external experimental parameters (speed, container volume, etc.). On the contrary, low-energy methods including spontaneous emulsification or PIT/PIC, are more dependent on internal parameters, identical to the ones controlling microemulsion (composition, temperature, etc.) [366,367]. Interestingly, the increased robustness of our protocol may indicate that part of the emulsification process was controlled by internal parameters, since similar external parameter variations could be expected for one experimenter across the classical and optimized protocols. This remains nonetheless to be experimentally verified. Overall, this case study of using microemulsion for the synthesis of NPs with biomedical application may open new avenues for nanomedicine formulation.

II. Biological characterization and drug loading

Once the Dex-NPs and Fuco-NPs had been fully characterized, their biological behavior was investigated, including flow behavior and targeting, toxicity, and drug loading.

A) Materials and methods

A.1) Materials

Fetal bovine serum (FBS) was purchased from Pan-Biotech (Aidenbach, Germany, #P30-3306). HUVEC cells line (ATCC, Manassas, Virginie, #ATCC-CRL-1730) was used at fewer than 40 passages. Sucrose (#S7903), fibrinogen type I from human plasma (#F3879), thrombin from human plasma (#T7009), plasminogen from human plasma (#528175), Phorbol 12-myristate 13-acetate (PMA, #P8139-5MG), were purchased from Sigma Aldrich (Saint-Quentin-Fallavier, France). DMEM, low glucose, pyruvate (#31885049), Antibiotic Antimycotic solution (#15240062), PBS 1X and 10X (#14040133 and #14080055), Rhodamine phalloidin (#R415), low melting point agarose (#R0801), DIOC6 (D273), DAPI (#62247), SytoxGreen (#S7020) were purchased from Thermo Fisher Scientific (Massachusetts, United States). Horm® collagen type I was purchased from Takeda Pharmaceutical (Tokyo, Japan). rtPA (alteplase) was purchased from Boehringer Ingelheim (Ingelheim am Rhein, Germany, # Actilyse®). DNase I (dornase alfa) was purchased from Roche – Genentech (San Francisco, United States, #Pulmozyme® 2500 U/2,5 mL). The PefaFluor® kit (#CG8433) for rtPA titration was purchased from Interchim (Montluçon, France). The DNase I detection kit (#JE-PP-410L) was purchased from Euromedex (Souffelweyersheim, France). Polymorphprep (#1114683) was purchased from Proteogenix (Schiltigheim, France). Anti-$H3_{cit}$ (#ab5103), anti-MPO (#ab90810), were purchased from Abcam (Amsterdam, Netherlands). Human whole blood was acquired from EFS (Bichat Hospital, Paris, France), the French blood donation institute, under a research convention, in PPACK, sodium citrate or EDTA collection tubes.

A.2) Cell culture and cytotoxicity assay

To evaluate the cytotoxicity of the NPs, a resazurin Fluorometric Cell Viability Assay (#TOX-8 kit) was used on confluent Human Umbilical Vein Endothelial Cells (HUVECs). The cells were cultured in low glucose DMEM supplemented with 10% v/v FBS and 1 % v/v antibiotic-antimycotic; the cells were kept in an incubator at 37°C in a humidified atmosphere of 5% CO_2. Cells

were seeded into 96-well plates with 30 000 cells per well. Following 24 h of incubation, the medium was changed to Fuco-NPs resuspended in culture medium in a range of 100 mg/L to 1 g/L, and the cells were cultured for another 24 h. Cells cultured with equivalent PBS 1X medium dilution were set as control. Negative controls were culture medium only, and positive controls were 1 % (v/v) Triton X-100 in culture medium for 15 min. Then the medium was replaced with 100 µL 10% (v/v) Resazurin solution in culture medium, and the plates were covered in foil and incubated for another 2 h. The Resazurin absorbance signals were monitored at 570 nm and 590 nm wavelengths with a Varioskan LUX multiplate reader (Thermo Fisher Scientific, Massachusetts, United States). The corrected absorbance values were blank corrected: $A' = A_{570nm} - A_{590nm}$, and the relative cell viability was expressed as $(A' - A'_{neg}) / (A'_{pos} - A'_{neg}) \times 100\%$, with the negative and positive control absorbances respectively averaged in the control wells as detailed above. To examine possible cell morphology changes after co-incubation with Fuco-NPs, HUVECs cells were seeded in 8-wells Lab-Tek II Chamber Slide (Thermo Fischer Scientific, Massachusetts, United States) with 10 000 cells per well. The medium was changed 24 h to Fuco-NPs resuspended in culture medium in a range of 100 mg/L to 1 g/L, and the cells were cultured for another 24 h. Cells cultured with equivalent PBS 1X medium dilution were set as control. Next, cells were fixed with 4% (v/v) paraformaldehyde for 30 min at 4°C. After rinsing with PBS, cells were permeabilized with Triton X-100 0.1 wt.% in PBS for 5 min at RT then washed twice with PBS before incubation for 60 min at RT with 1% (v/v) Phalloidin-Rhodamine in PBS. After two PBS washes, the slides are mounted with a Mounting Medium with DAPI. Visualization was performed with a confocal microscope (Zeiss LSM 780, Iena, Germany).

A.3) Hemolysis assay

To evaluate hemolysis, human whole blood was collected in EDTA tubes, then centrifugated at 500 G for 5 min. After plasma removal, add an equivalent volume of saline. Repeat centrifugation and saline addition. After a third centrifugation, add PBS instead of saline, then dilute the erythrocyte suspension to 1/50 in PBS. After visual verification (turbidity, sedimentation), mix 1 volume of samples to 19 volumes of diluted erythrocytes in V-bottom 96-well plates. For negative and positive controls, PBS and 20 % (v/v) Triton X-100 are respectively used. After 60 min incubation at 37°C with slow agitation, the plate is centrifuged for 5 min at 500 G, then the supernatants are collected, and the absorbance is read at 541 nm.

A.4) Blood margination

An *in vitro* blood flow assay was performed to evaluate the margination of NPs within blood flow. Micro-channels of Vena8 Fluoro+ chambers (width: 0.04 cm, height: 0.01 cm, and length: 2.8 cm; Cellix Ltd, Dublin, Ireland) were rinsed with NaCl 0.9 wt.% before use. Human whole blood was collected in sodium citrate tubes and labeled with 5 µM DIOC6, then NPs were added to a concentration of 1 mg/mL. The blood was then perfused at venous shear stress (here, 7 µL/min) for 2 min and fluorescence images were acquired with a microscope (Axio Observer, Carl Zeiss Microscopy, Oberkochen, Germany). Fluorescence was measured across 5 cross-sections per channel and averaged over 2 min for each sample.

A.5) In flow platelet aggregates targeting assay

An *in vitro* flow adhesion assay was performed to evaluate the targeting of NPs to activated platelets. Micro-channels of Vena8 Fluoro+ chambers (width: 0.04 cm, height: 0.01 cm, and length: 2.8 cm; Cellix Ltd, Dublin, Ireland) were coated overnight with fibrillar type I collagen (50 µg/ml) at 4°C and rinsed with NaCl 0.9 wt.% before use. Human whole blood, collected in the PPACK tubes and labeled with 5 µM DIOC6, was perfused at arterial shear stress (here, 60 µL/min) for 5 min to induce platelet activation and aggregation. Platelet aggregation through contact with collagen was visualized in real-time with a microscope (Axio Observer, Carl Zeiss Microscopy, Oberkochen, Germany). After rinsing with NaCl 0.9 wt.%, fluorescent Dex-NPs or Fuco-NPs (unloaded or loaded with rtPA) resuspended in 0.9 wt.% NaCl at 1 mg/mL, were injected into the channels for 5 min. Their accumulation onto activated aggregates was monitored in real time. Channels were then washed for 5 min with NaCl 0.9 wt.%. Finally, quantification of bound NPs to aggregated platelets were performed with ImageJ by measuring total fluorescence intensity and colocalization with the Pearson's coefficient (with a PSF size of 6x6 pixels) on mosaic images composed of 10 aligned microscope images (corresponding to a whole channel). Care was taken to always include all different conditions on each chamber with the same blood, and replicates were performed across different blood samples as platelet aggregation differed between individuals.

A.6) Drug loading

rtPA was loaded onto the NPs by adsorption. Typically, 50 µL of NPs (5 mg/mL) were mixed with 25 µL rtPA (1 mg/mL) and 25 µL ultrapure water then incubated for 15 min. Free unabsorbed rtPA was removed by ultracentrifugation

(15 min, 15 000 g). The rtPA loaded NPs were resuspended in ultrapure water, and rtPA encapsulation was determined as described below by bicinchoninic acid assay (BCA) and PefaFluor® tPA assays. DNase I was loaded onto the NPs by adsorption in acidic conditions. Typically, 25 µL of NPs (10 mg/mL) were mixed with 50 µL DNase I (1 mg/mL), 5 µL of HCl ($2x10^{-2}$ M), 20 µL $CaCl_2$ (650 µM) in water then incubated for 60 min. Free unabsorbed DNase I was removed by ultracentrifugation (15 min, 15 000 g). The DNase I loaded NPs were resuspended in 130 µM $CaCl_2$ and DNase I encapsulation was determined as described below by BCA and a fluorescent substrate DNAse detection kit assays.

A.7) Drug encapsulation efficiency and release rates

The amount of drug (rtPA or DNase I) loaded on the NPs was measured using the Pierce BCA protein assay kit (Life Technologies SAS, Courtaboeuf, France). Briefly, 200 µL of working reagent was added to 25 µL of each sample in 96 wells multiplate. The absorbance at 562 nm was read with a Varioskan LUX multiplate reader (Thermo Fisher Scientific, Massachusetts, United States) after 30 min incubation at 37°C. The concentration of the drug was extrapolated by a calibration curve prepared with different concentrations of rtPA or DNase I respectively. The encapsulation efficacy (EE) was calculated as EE (%) = 100% x $[Drug]_{loaded}/[Drug]_{initial}$ and the loading capacity (LC) was calculated as LC (%) = 100% x $[Drug]_{loaded}/[NP]$. The release of each drug was investigated by diluting drug-loaded NPs (2.5 mg/mL NPs, loaded with respectively 167.5 µg/mL rtPA or 450 µg/mL DNase I) in PBS 1X in order to achieve equivalent respective drug concentrations of 1 mg/kg rtPA and 5 mg/kg DNase I in human. This corresponds to a dilution by a factor 13X for rtPA (diluting from 167.5 µg/mL to 12.8 µg/mL rtPA) and by a factor 7X for DNase I (diluting from 450 µg/mL to 64 µg/mL DNase I). During incubation at 37°C, supernatant samples are taken at regular intervals with respectively ultracentrifugation and ultrafiltration, then concentrations in supernatants are measured with respectively PefaFluor® and DNase detection kits.

A.8) Fibrin Agar Plate Assay (FAPA)

To assess the fibrinolytic activity of rtPA-loaded Fuco-NPs, a fibrinolysis experiment was performed. 5 mL of TBS Buffer (0.1 M Tris, 0.8 wt.% NaCl, 0.02 wt.% KCl, pH = 7.4) with 3 wt.% low melting agarose were heated above 65°C, while 5 mL of TBS buffer with 25 mg fibrinogen and 1 U plasminogen was slowly heated to 37°C. Once the agarose solution reached 65°C, it was cooled to 37°C,

and 2 U of thrombin were added. Next, the two solutions were slowly mixed, then poured into a 9 cm Petri dish and incubated at 37°C for 2 h (gels can be kept a few days at 4°C). On the solidified agarose gel, round wells were formed using a 3 mm punch as sample reservoirs. 5 µL of each sample (diluted 1:10) was dropped into the wells and incubated at 37°C in a humid environment. Pictures were taken every hour by a commercial smartphone (64 MP F1.8 OIS camera) for 8 h. The degree of fibrin lysis was quantified with ImageJ by comparing the rate of expansion for fibrinolysis rings between samples and free rtPA standards as per the method described in Wang *et al.*, 2012 [391].

A.9) NET degradation assay

To assess the NETolytic activity of DNase I-loaded NPs, a semi-quantitative assay was performed. Human whole blood was collected in EDTA tubes. Following the supplier's protocol for Polymorphprep, neutrophils were isolated and resuspended in 0.05 wt.% BSA in DMEM. Purity and cell count were determined with a hematology analyzer (ABX Pentra 60, Horiba, Vénissieux, France). Neutrophils were seeded at 1.0 x 10^5 cells/cm^2 on 8-wells Lab-Tek II Chamber Slide (Thermo Fischer Scientific, Massachusetts, United States) and incubated at a humidified atmosphere of 5% CO_2 for 60 min. PMA was then added to a final concentration of 50 nM, and the neutrophils were left to incubate for 4 h. Medium was then changed to incubate the formed NETs with DNase I-loaded Fuco-NPs resuspended in 0.05 wt.% BSA-DMEM to a concentration equivalent to 0.5 mg/mL or 0.1 mg/mL DNase I. After a 60 min incubation, the samples were fixed with 4% (v/v) paraformaldehyde for 30 min at RT. After rinsing three times with PBS, the samples were blocked with 1% BSA in 0.1% (v/v) Tween 20 PBS (PBS-T) for 30 min at RT, then washed with PBS three times. Then, the samples were incubated with 100 nM SytoxGreen and 1 µg/mL DAPI in 1 wt.% BSA PBS-T for 10 min at RT, then washed with PBS twice before slide mounting and imaging with a microscope (Axio Observer, Carl Zeiss Microscopy, Oberkochen, Germany).

A.10) Image analysis and statistical analysis

Images were analyzed with ImageJ (Fiji), and the macros that were used are made available in **ANNEX 14**. When images are shown, the same contrast values are applied to each channel displayed. Quantitative data were analyzed with the statistical analysis software GraphPad PRISM 9.5.0., with a significance level α taken at 0.05. All presented data consisted of n=3 or more replicates per condition (when not shown on the graphs, replicate number is indicated in the

legend). Whenever applicable, presented replicates consist of biological replicates, or, when appropriate, different NP batches. Unless explicitly mentioned, results are presented as mean ± standard deviation. Depending on the design of the experiments, data significance was evaluated with unpaired t-test (two groups, assumed equal variance), unpaired t-test with Welch's correction (two groups, variance not equal), paired t-test (two groups of paired values, with assumed equal variance), one-way ANOVA (one factor explored, with more than two groups, variances assumed equal) with Tukey's multiple comparison test, one-way Welch's ANOVA (one factor explored, with more than two groups, variances not equal) with Dunnett's T3 multiple comparison test, repeated measures one-way ANOVA (one factor explored, with more than two groups of repeated measures compared to the initial group, variances assumed equal) with Dunnett's multiple comparison test, two-way ANOVA (two factors explored) with Tukey's (comparison of all conditions) or Šidák's (comparison between factors) multiple comparison test. Unless explicitly specified in the legend, unpaired t-tests and ANOVA with Tukey's test are performed. Every p-value below α threshold was represented as follows: * $p < 0.05$; ** $p < 0.01$; *** $p < 0.001$, **** $p < 0.0001$ (ns was indicated for "not significant" if no significant differences are present in the data presented).

B) Transforming nanoparticles into potential therapeutic agents

Once the NPs were obtained at the desired size, with adequate stability and good protocol robustness, we aimed at describing their potential for thrombolysis by investigating their absence of toxicity, drug loading potential, targeting capacity and flow behavior.

First, the biocompatibility of the targeting Fuco-NPs (which are designed to be intravenously injected) was assessed. As they are meant to act within the circulation, cytotoxicity was evaluated by measuring the metabolic activity by resazurin reduction after 24 h incubation of HUVEC endothelial cells in contact with the Fuco-NPs, as shown in Figure 25.a, where all concentrations assayed displayed a viability above the 70% threshold (decided as per ISO 10993-5 [392]), with notably the highest assayed concentration, 1000 µg/mL Fuco-NPs, associated with a 92.8±5.7% viability. PBS was used as a control to compare effects of the different medium dilutions. Moreover, HUVEC cell morphology was verified after incubation of 100, 400, 800 (not shown) and 1000 µg/mL Fuco-NPs for 24h (Figure 25.b): the cells retained the cobblestone aspect and preservation of the actin cytoskeleton when comparing PBS exposure to Fuco-NPs. Finally,

since the Fuco-NPs are meant to be circulating, the absence of hemolytic properties was also verified.

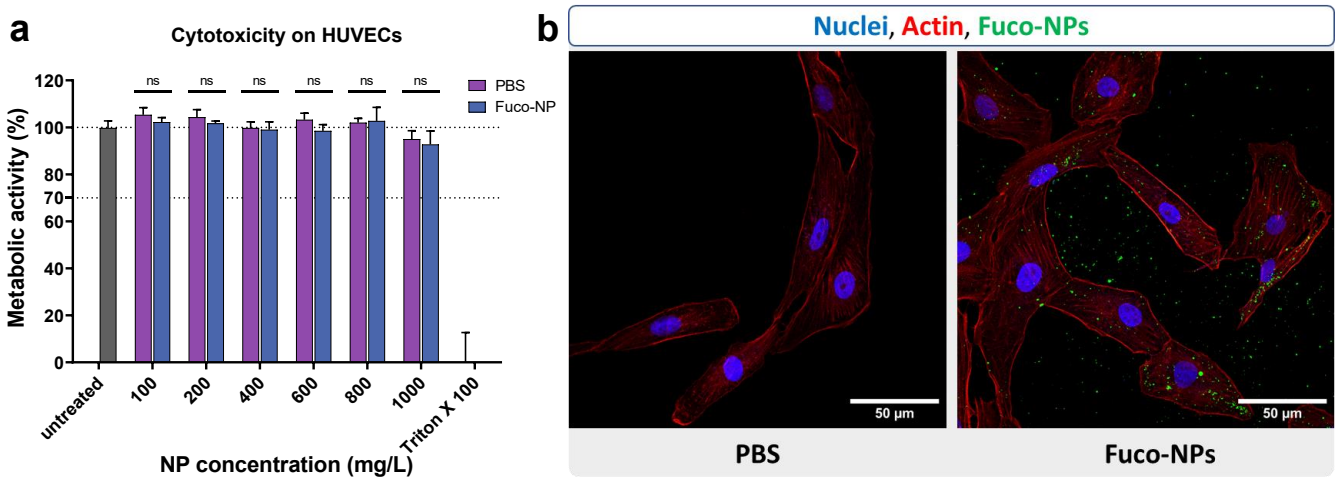


Figure 25: Cytotoxicity assays. (a) Cytotoxicity test performed by measuring HUVECs viability through the metabolic activity by resazurin after 24 h incubation with Fuco-NPs or PBS (similar medium dilution as a control). 1% Triton X-100 for 15 min served as a positive control. A two-way ANOVA with Šidák's multiple comparison test was performed to compare only the differences between PBS and Fuco-NP (n=4). (b) HUVEC morphology after 24 h incubation with 1 mg/mL FITC-labeled Fuco-NPs visualized with the nuclei (DAPI) and actin (Rhodamine phalloidin) (scale bar = 50 µm).

Then, the loading of the main fibrinolytic drug, rtPA, was investigated. The loading capacity (LC (%) = [drug loaded]/[NP]) was measured by BCA (total protein quantification) across various rtPA and Fuco-NP concentrations, as displayed in Figure 26Figure 26.a. For a fixed 2.5 mg/mL Fuco-NP concentration, co-incubation with 0.25 mg/mL rtPA yielded the highest LC. This loading condition was kept in all further experiments, and the resulting loaded NPs designed as Fuco-NP-rtPA, with a LC of 6.7±0.6% (Figure 26.b). Interestingly, it was observed that, in similar loading conditions, rtPA loading was significantly increased in Fuco-NPs, due to a previously undescribed affinity of rtPA to fucoidan [164], compared to Dex-NPs (Figure 26.b). Moreover, the release of rtPA was investigated in PBS at 37°C, at a dilution corresponding to the injection of a 1 mg/kg rtPA dose in mice (10 times lower than the effective dose usually used [393]) or equivalent to 0.9 mg/kg dose of rtPA in humans, the current clinical recommendation for AIS treatment [394]. As shown in Figure 26.c, a release curve illustrative of a burst release in the first 15 min and reaching a complete release after 60 min was obtained, in PBS at 37°C and at a concentration equivalent to a 0.9 mg/kg administration in human, or 1 mg/kg in mice (one of the concentrations assayed in the later *in vivo* experiments).

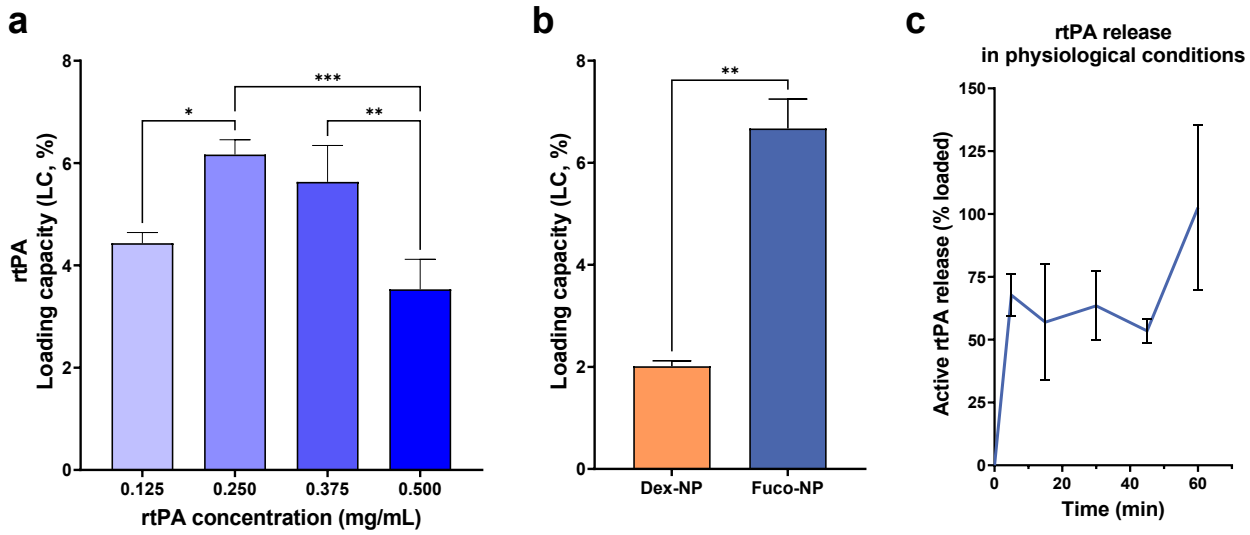


Figure 26: rtPA loading. (a) rtPA loading capacity in Fuco-NPs 2.5 mg/mL for various rtPA concentrations, measured by BCA. A one-way ANOVA with Tukey's multiple comparison test was performed. (n=3). (b) Comparison of rtPA loading capacity in Dex-NPs and Fuco-NPs by BCA ([rtPA]=0.25 mg/mL, [NP]=2.5 mg/mL). An unpaired t-test was performed. (n=3). (c) rtPA release in PBS at 37°C with a dilution equivalent to 1 mg/kg in mice or 0.9 mg/kg in human measured by PefaFluor® (n=3).

However, in the same loading conditions, barely any DNase I was loaded in Fuco-NPs. The isoelectric point of rtPA is around 7.5, while the isoelectric point of Pulmozyme® (the DNase I used) is reported at 4.6, meaning that at neutral pH, rtPA is either neutral or slightly positively charged, while DNase I is negatively charged, which could prevent loading onto Fuco-NPs by electrostatic repulsion. As the latter remained negative across a broad pH range (Figure 23.b), loading at different pH values was tested (Figure 27.a), demonstrating a successful adsorption of DNase I at pH = 3. Based on this acidic condition, various DNase I and Fuco-NP conditions were tested, with notably the incubation of 0.5 mg/mL DNase I with 2.5 mg/mL Fuco-NP yielding the highest LC (Figure 27.b). This condition was used in all following experiments and labeled Fuco-NP-DNase: the LC of DNase I was 16.9±0.4%. This LC remained similar for both Dex-NP-DNase and Fuco-NP-DNase (Figure 27.c), with a similar release profile as rtPA (Figure 27.d) at a dilution equivalent to the one used in later *in vivo* experiments in PBS at 37°C.

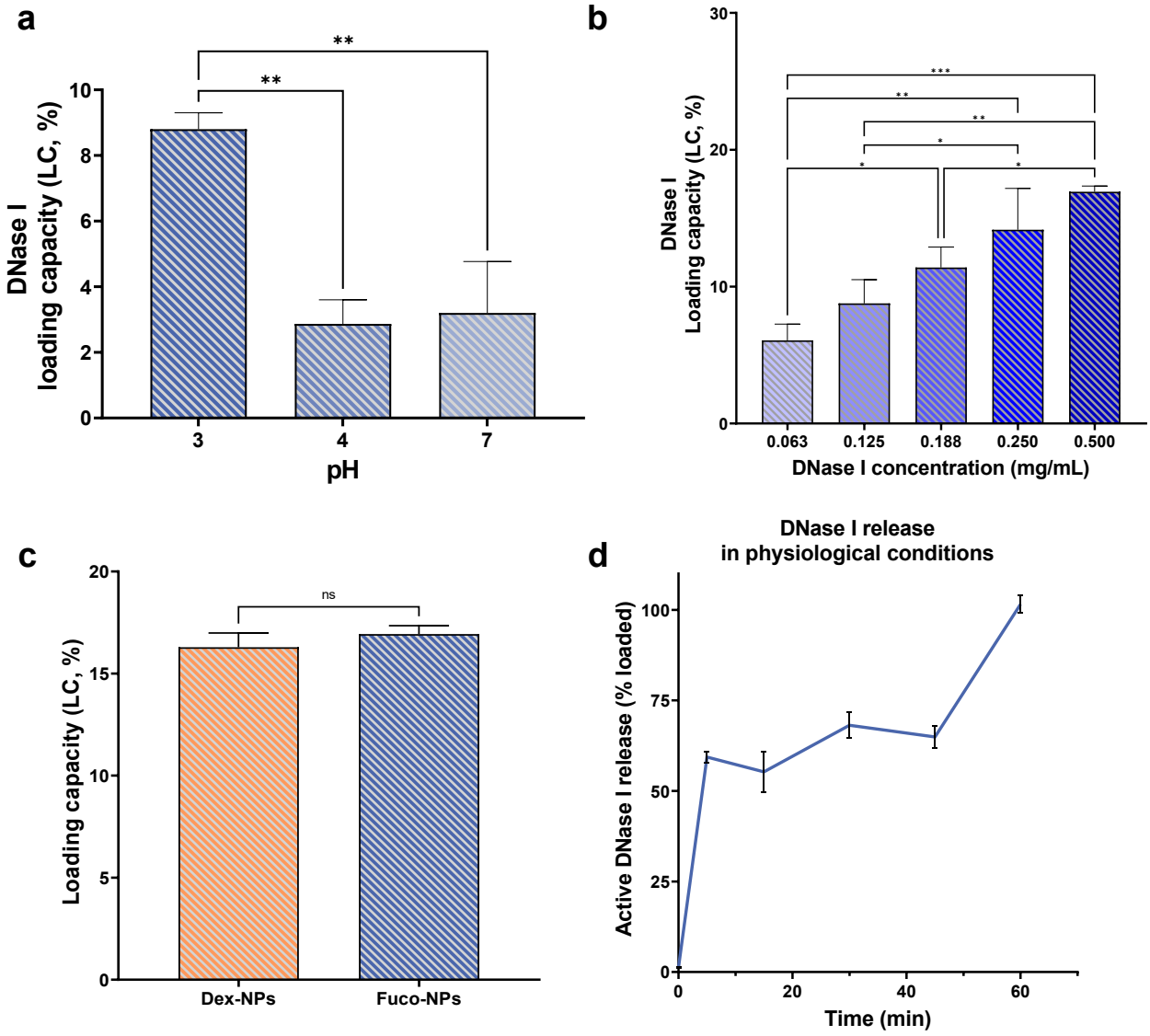


Figure 27: DNase I loading. (a) Loading capacity of DNase I in Fuco-NPs depending on pH variation measured by BCA. A one-way ANOVA with Tukey's multiple comparison test was performed (n=3). (b) DNase I loading capacity in Fuco-NPs 2.5 mg/mL for various DNase I concentrations, measured by BCA. A one-way ANOVA with Tukey's multiple comparison test was performed. (n=3). (c) Comparison of DNase I loading capacity in Dex-NPs and Fuco-NPs by BCA ([DNase I]=0.5 mg/mL, [NP]=2.5 mg/mL). An unpaired t-test was performed. (n=3). (d) DNase I release in PBS at 37°C with a dilution equivalent to 5 mg/kg in mice measured by DNase I kit (n=3).

Therefore, both drugs could be loaded in Fuco-NPs, and it was verified that the NPs suspensions retained their size and dispersity. Since the latter could be stably freeze-dried, we therefore assessed whether drug incorporation would affect the freeze-drying stability. As displayed in Figure 28.a-b, while there was a slight size reduction for both rtPA- and DNase I- loaded Fuco-NPs, the

size and dispersity remained overall stable, indicating that drug loading did not affect the NPs' ability to be freeze-dried.

Nonetheless, the loading and freeze-drying process may affect the drugs' enzymatic activities. Therefore, the amidolytic activity of rtPA after loading was verified with a fluorescent substrate assay (PefaFluor®). As shown in Figure 28.c, the PefaFluor® measured active rtPA LC was no different from the one determined previously by total protein concentration; and freeze-dried Fuco-NP-rtPA also exhibited the same rtPA LC after resuspension, thus validating that the loading and freeze-drying processes did not affect the amidolytic activity of rtPA. On the other hand, the DNase I loading process was performed in harsher acidic conditions. Therefore, we used a fluorescent DNase I activity kit to measure the enzymatic activity of DNase I in acidic conditions, after loading, and after freeze-drying and resuspension (Figure 28.d). Acidic exposure significantly reduced DNase I activity by 12-fold, but surprisingly its activity was partially preserved in Fuco-NP-DNase with only a 2.5-fold reduction in activity. This amounted to an effective LC (measured as [active drug]/{NP]) of 8.3±2.2%. Fuco-NP-DNase freeze-drying further reduced the active drug content, to a corresponding effective LC of 4.7±2.5%. Acidic denaturation of proteins most likely explains the reduced enzymatic activity of free DNase I at pH = 3. However, protein adsorption on various surfaces may affect their conformation and structure [395], and this has been exploited by various hydrogel formulation to stabilize proteins against denaturation (including thermal denaturation) [396,397]: this may shed light on the reduced loss of activity of DNase I when loaded onto Fuco-NPs with acidic conditions, which may be sufficient for further applications. These results therefore validate that Fuco-NPs could load rtPA and DNase I and retain their stability including after freeze-drying and resuspension, with either no loss (rtPA) or reduced (DNase I) enzymatic activity.

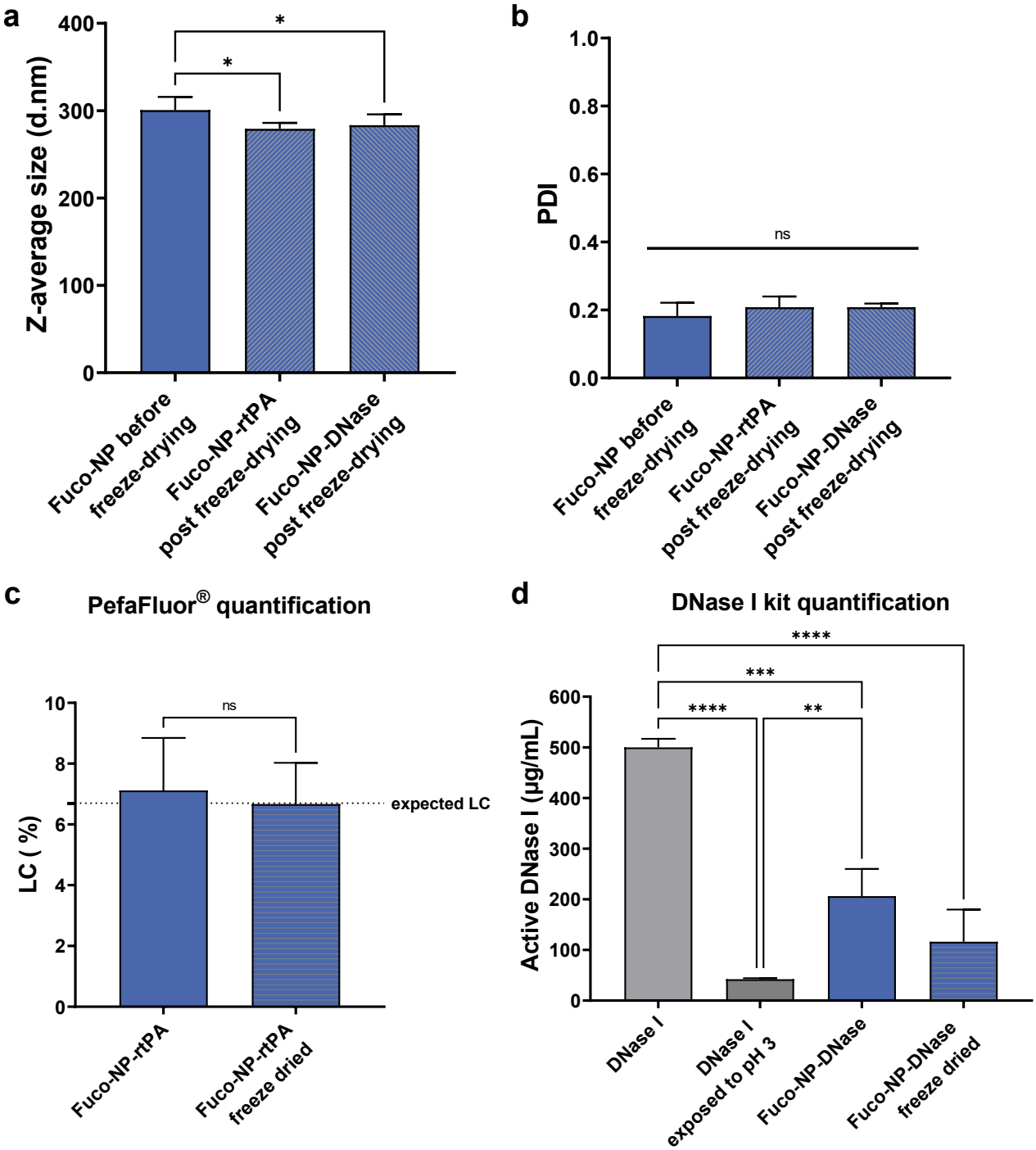


Figure 28: Freeze-drying stability of loaded Fuco-NPs. (a) Z-average size and (b) PDI measured by DLS after Fuco-NP were freeze-dried in 1 wt.% sucrose at -80°C then resuspended. A repeated measures one-way ANOVAs with Tukey's multiple comparison tests were performed (n=3). (c) Quantification of the active rtPA loaded in NPs measured by amidolytic PefaFluor® assay. Fuco-NP-rtPA were compared to Fuco-NP-rtPA freeze-dried in 1% sucrose, after resuspension. The "Expected LC" was taken at 6.7% as determined by prior BCA quantification. A paired t-test was performed (n=3). (d) Quantification of the active DNase I loaded in NPs measured by DNase I activity kit. DNase I is

compared to DNase I exposed to acidic conditions, Fuco-NP-DNase (loaded in acidic conditions) and Fuco-NP-DNase, freeze-dried in 1% sucrose, after resuspension. A one-way ANOVA with Tukey's multiple comparison test was performed (n=3).

Yet, the two quantitative tests used for measuring rtPA and DNase I acitivity relied on fluorescent substrates, and may not reflect the desired physiological activity of these enzymes. Thus, two respective models were designed. On one hand for rtPA, a fibrin agar plate assay (FAPA) was used [391]. The degradation ring's rate of expansion was measured (Figure 29.a) and with a standard range of free rtPA, the active amount of rtPA in a sample could be determined. As shown in Figure 29.b during loading experiments, the amount of active drug loaded in Fuco-NP was measured at 201±23 µg/mL, slightly above the rtPA amount determined by BCA, indicating that the loaded rtPA fully retained its fibrinolytic potential. Most importantly, this FAPA experiment directly measured the fibrinolytic potential of Fuco-NP-rtPA, comparing it to free rtPA standards. It therefore validated the loading on Fuco-NPs as a viable vectorization that did not impede the enzymatic activation of plasminogen by rtPA, and thus the fibrinolysis. On the other hand for DNase I, a NETolysis assay was designed based on previous works [38]. Neutrophils were isolated from human blood then activated with PMA. SytoxGreen and DAPI DNA dyes were used after the various treatments, owing to SytoxGreen lack of intracellular penetration compared to DAPI, to distinguish extracellular DNA (NETs) from nuclear DNA. To validate NET formation, initial staining of $H3_{cit}$ and MPO were also performed. After 4 h activation, the NETs were incubated with the Fuco-NP-DNase samples or with free DNase I. As shown in Figure 29.c top panels, when compared to unactivated neutrophils (left) with small fluorescent areas and DAPI-dominated staining, NETs could be clearly seen after PMA activation (right) with an increased SytoxGreen staining and increased fluorescent area. Notably, extracellular DNA fibers can be observed. NETolysis could be observed in a DNase I concentration-dependent manner, and at equal amounts of DNase I of 0.5 µg/mL, both free DNase I and Fuco-NP-DNase produced similar degradation of the NETs (Fig. Figure 29.c, bottom panels). This validated the NETolysis activity of DNase I on human NETs, but also that despite the reduced DNase I activity after loading, Fuco-NP-DNase retained a NETolytic potential. Thus, the Fuco-NP-rtPA and Fuco-NP-DNase could be used to assess the thrombolytic potential of vectorized rtPA and DNase I with Fuco-NPs.

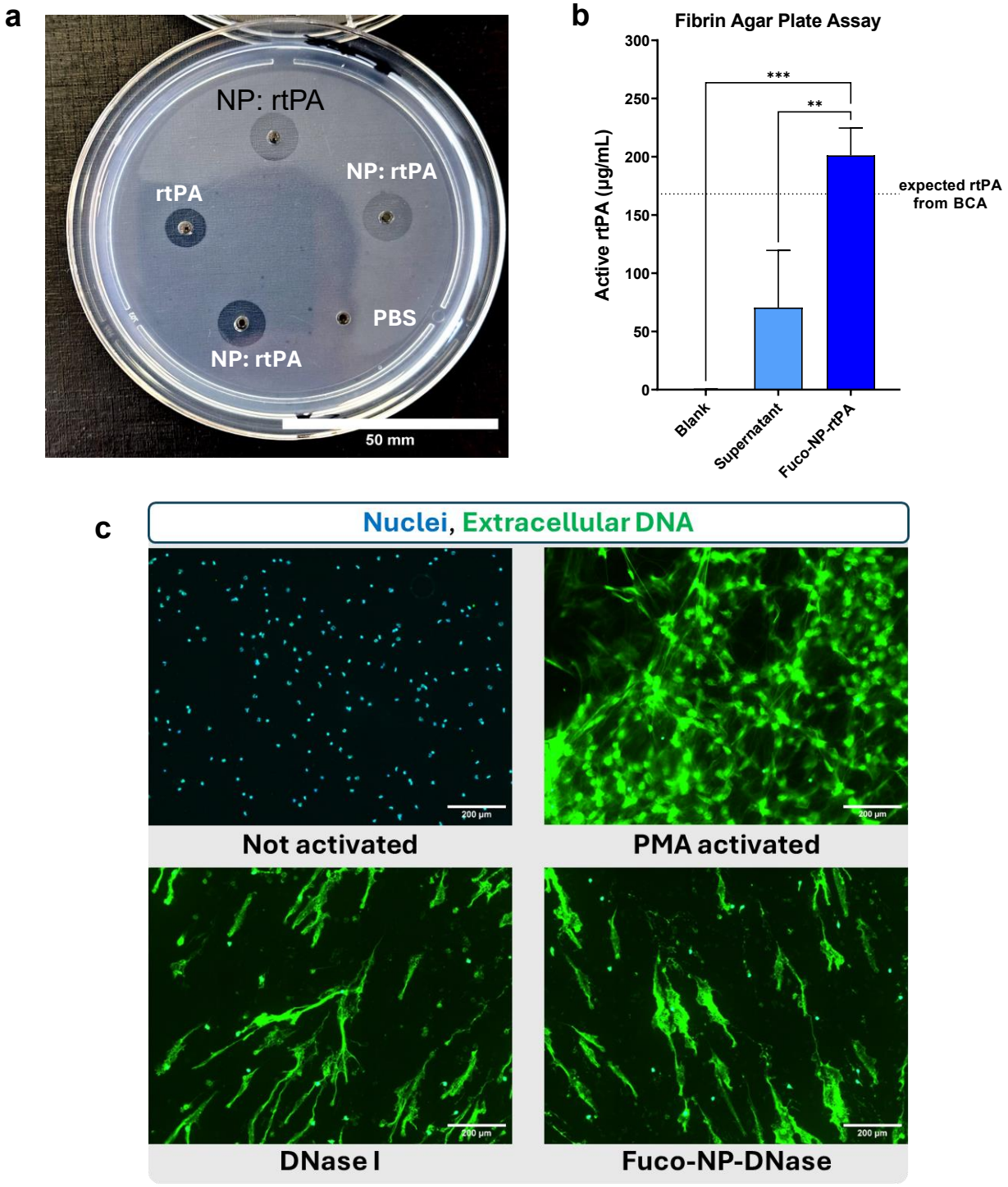


Figure 29: Physiologic activity of Fuco-NP-loaded rtPA and DNase I. (a) Representative fibrin agar plate assay (FAPA) with degradation rings after 8 h incubation at 37°C, with PBS as a control, 1/10th dilution of Fuco-NP-rtPA or rtPA supernatant resulting from a loading experiment (scale bar = 50 mm). (b) FAPA determined concentration of active rtPA in Fuco-NP-rtPA and supernatant resulting from a loading experiment. A one-way ANOVA with Tukey's multiple comparison test was performed. (n=3). (c) NETolysis assay. Neutrophils isolated from human blood were seeded then activated with PMA to release NETs, followed by treatment with DNase I or Fuco-NP-DNase. DAPI and SytoxGreen

were used to differentially stain intra- and extracellular DNA. Top left: neutrophils not exposed to PMA and treatments. Top right: NETs released with PMA but treated with PBS. Bottom left and right: NETs released by PMA and treated with respectively 0.5 mg/mL DNase I or equivalent DNase I concentration in Fuco-NP-DNase (experiment repeated three times) (scale bar = 200 µm).

To validate the fucoidan-mediated targeting capacity of Fuco-NPs, a microfluidic setup was used to assess targeting to activated platelets in simulated blood circulation. Human blood was flown into collagen-coated microfluidic channels at arterial flow rates and the formation of platelet aggregates was observed in real-time. Various NP formulations were then flown into the channels before rinsing with PBS. After rinsing, the fluorescence of NPs and platelets was observed (Figure 30.a). Their colocalization was then calculated with the Pearson's coefficient, as shown in Figure 30.b: Fuco-NPs demonstrated a statistically significant increase in colocalization with platelets when compared to Dex-NPs, as well as a global decrease in TRITC fluorescence (Figure 30.a) validating their targeting capacity. Furthermore, Fuco-NP-rtPA and Fuco-NP-DNase exhibited similar colocalization results as unloaded Fuco-NPs, proving that drug loading did not affect the targeting to aggregated platelets. It was also observed that Fuco-NPs had a superior colocalization to platelets than fucoidan-containing "classical" submicronic particles (Figure 30.c): this may stem from enhanced surface-to-volume ratio thanks to size reduction. Besides, the size of circulating objects can be crucial for their behavior in the blood, due to the margination effects previously mentioned. To verify whether the size reduction from 850 nm to 315 nm could affect the particle distribution profile inside blood vessels, they were flown in blood at venous flow rate in microfluidic channels. As shown in Figure 30.d where fluorescence was measured during blood flow across a cross-section of the microfluidic channel, while 850 nm "classical" particles demonstrated a typical margination to the sides of the channel, the optimized Fuco-NPs presented a homogeneous profile across the microfluidic vessel cross-section. This can help warrant access to the thrombus wherever its location in a blood vessel, and keep NPs in the circulation [128,137]. Thus, these NPs fall in a desirable size range of 150-400 nm in order to avoid extravasation [134] while maintaining them homogeneously distributed in blood flow. In addition to their validated targeting capacity to activated platelet aggregates, this contributes to their potential as circulating drug delivery systems.

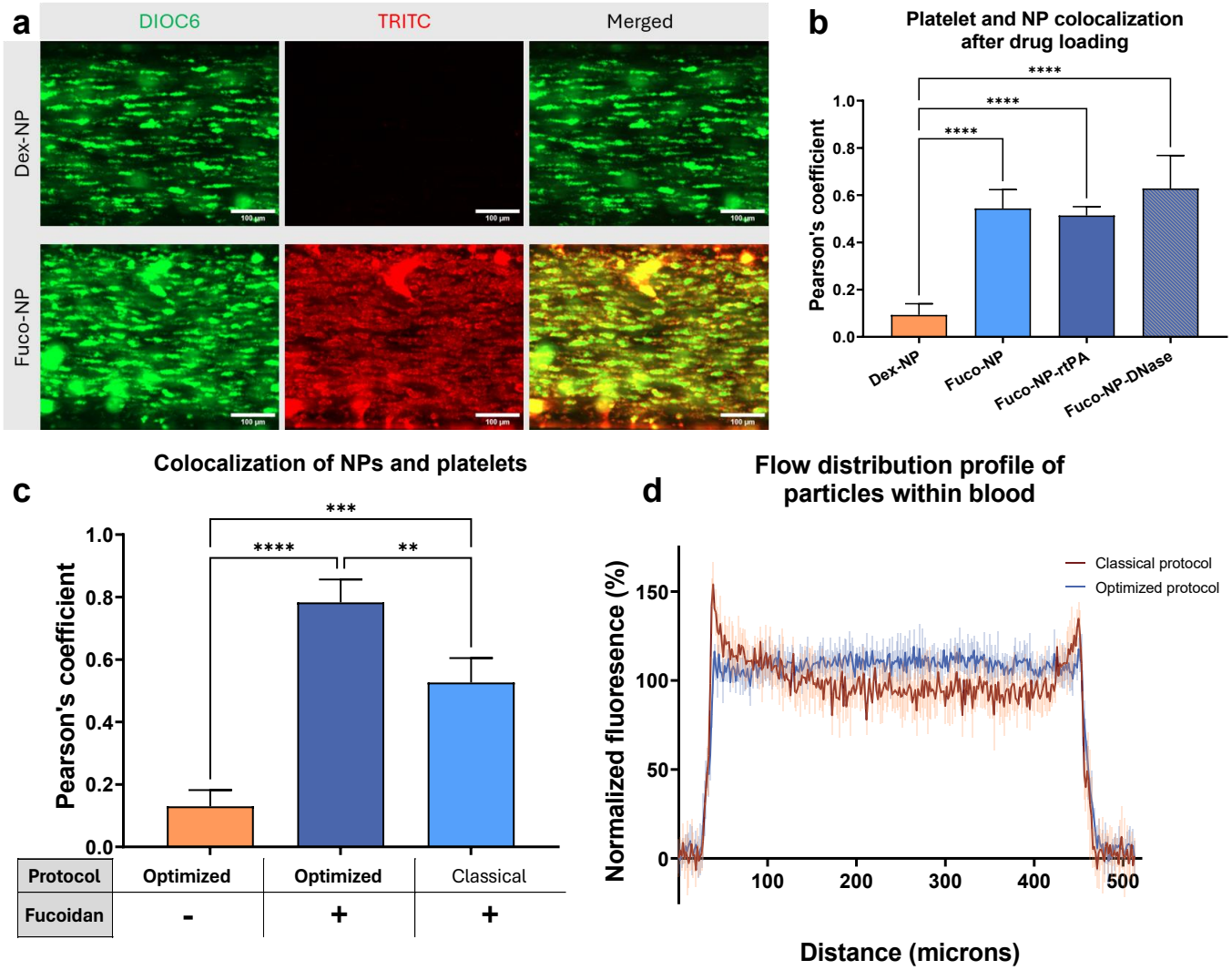


Figure 30: Targeting and flow behavior of Fuco-NPs. (a) Representative final images of the microfluidic targeting experiment on activated platelets. Aggregated platelets labeled with DIOC6 were obtained in microfluidic channels, then 1 mg/mL TRITC-labeled Dex-NPs or Fuco-NPs were flown under arterial flow (to mimic the harshest possible conditions) for 5 min, followed by 5 min rinsing with PBS (scale bar = 100 µm). (b) Resulting colocalization of TRITC and DIOC6 signal after rinsing, measured by Pearson's coefficient for 1 mg/mL Dex-NPs, Fuco-NPs, Fuco-NP-rtPA or Fuco-NP-DNase. A one-way ANOVA with Tukey's multiple comparison test was performed (n=4). (c) Similar targeting experiment to compare classical 850 nm particles to 315 nm Fuco-NP and Dex-NP, at 1 mg/mL. A one-way ANOVA with Tukey's multiple comparison test was performed (n=3). (d) In flow distribution profile comparison of fucoidan containing 850 nm particles, obtained with the classical protocol, with 315 nm Fuco-NPs (optimized protocol). The blood containing 1 mg/mL TRITC-tagged particles is flown at a venous flow rate in a microfluidic channel, and the fluorescence signal across a cross-section of the channel is measured. The X-axis corresponds to the cross-section distance (n=5).

C) Preliminary works and future directions

Therefore, we were able to characterize the NPs' absence of toxicity, measure the targeting potential of Fuco-NPs and investigate the flow behavior subsequent to the size reduction. Moreover, we loaded two different drugs, without affecting the particles' size and targeting properties. Nonetheless, loading could be improved for these drugs, and other therapeutic agents could be explored for application to thrombotic diseases.

C.1) Biological assays

We demonstrated that the NPs formulated by our protocol were nontoxic with a cytotoxicity assay based on the metabolic activity and morphology of HUVECs, an endothelial cell line. In addition, a hemolysis assay demonstrated the lack of hemolytic properties of our NPs. These were expected since the polysaccharides that compose them, dextran and fucoidan, are both nontoxic and were used in clinical applications without toxicity. Nonetheless, there remain some aspects to be investigated. For one, despite initial concerns about antigenicity and immunogenicity with the first dextran-made blood expanders [334–336], optimization of dextran sourcing and production yielded dextrans with low antigenicity [329]. Dextran immunomodulatory and immunosuppressive properties have even been used in biomedical applications [337,398]. However, these aspects should be verified experimentally, with immunization experiments in animals and *in vitro* examination of immune cells' reaction to Dex-NPs and Fuco-NPs. Besides, while dextran and fucoidan are biocompatible materials, crosslinked with a simple, nontoxic phosphate diester bond, their degradation *in vivo* should be investigated. Indeed, dextran has been shown to be degraded by various enzymes in the human body [319,398], however this may be dependent on its degree of substitution [330]. Phosphate diester bonds are common in the human body, and similar hydrogel formation as ours were shown to be biodegradable by enzyme capable of polysaccharide hydrolysis despite STMP crosslinking [301,356,399,400]. Even so, investigation of biodegradability of our NPs is essential, and may be accompanied by *in vivo* long-term toxicity and degradation studies.

Besides, we used two assays to measure the potential of Fuco-NP-rtPA and Fuco-NP-DNase as thrombolytic candidates. For rtPA, we measured the fibrinolytic activity of rtPA in a FAPA experiment, which provided a semi-quantitative measurement of Fuco-NP-rtPA fibrinolysis potential. However, for DNase I, the NETosis protocol remained qualitative as NET degradation by DNase I was nonlinear with a sharp decrease slope for the concentrations

assayed, hence preventing a quantitative assessment with DNase I standards. Modifications of incubation time, DNase I concentration and NETosis conditions should be explored to improve this experiment, since similar protocols have been described [401,33]. However, other assays could be used instead [402], notably with either ELISA [32,403] or surfactant SytoxGreen measurements [402].

C.2) Drug loading

First, rtPA encapsulation was assessed as it is the major fibrinolytic used for thrombolysis. rtPA was successfully loaded in mild, simple conditions by adsorption, reaching a LC of 6.7%. Enzymatic assays demonstrated that rtPA amidolytic and fibrinolytic activity was conserved, and most strikingly, that Fuco-NP-rtPA was freeze-drying compatible, with the resuspended formulation both stable and retaining the drug's activity. Second, DNase I was loaded by adsorption on the NPs, but this step required acidification to allow efficient drug loading. While this acidification was shown to greatly reduce DNase I activity, the loading partially preserved DNase I activity to acceptable levels, and Fuco-NP-DNase I was shown to retain enzymatic and NETolytic activity. On the other hand, freeze-drying Fuco-NP-DNase I, despite conserving the NP's size and dispersion, was associated with a further reduced enzymatic activity of DNase I. The latest assays involved modifying the buffer to increase the enzyme's activity or stabilization (including $CaCl_2$ or $MgCl_2$ for its activation), without discernable improvement. In our protocols however, we used Pulmozyme, a commercial recombinant form of DNase I, in order to be as close as possible to relevant conditions in our experiments by working with products that may be used "as is" in future developments. It is noteworthy that this commercial version of DNase I is conditioned as an already prepared solution, to be stored at 4°C. If this enzyme was easily conditioned by freeze-drying this would most likely have been the case. Thus, we may face difficulties in trying to freeze-dry Pulmozyme after loading in Fuco-NPs. Hence, we should in the future assess different DNase I formulations to verify whether they could be freeze-dried in addition to pursuing assays with the freeze-drying buffers.

Another loading-related aspect that we explored was the co-encapsulation of rtPA and DNase I in the same NPs. Currently, both drug-loaded NPs were prepared separately and pooled together before each relevant experiment. This can be an adequate approach as it allows more flexibility in respective drug concentrations, notably for the thrombolysis experiments below. However, it may be interesting for the simplification of the formulations to load

both agents (or more) in the same NPs. Simultaneous or successive loading of both agents were explored, as shown in Figure 31. Simultaneous loading (protocol A) yielded low encapsulation for both drugs, which was verified by BCA titration. However, when loading the two drugs successively (protocols B and C), rtPA encapsulation always dominated over DNase I, despite intermediate drug titration confirming the loading of either rtPA or DNase I. This could be attributed to rtPA high affinity for fucoidan, favoring its loading compared to DNase I. Overall, no co-encapsulation of rtPA and DNase I was possible in the current drug loading configurations. While it is not necessarily needed for future applications, it may have been useful to simplify logistic considerations.

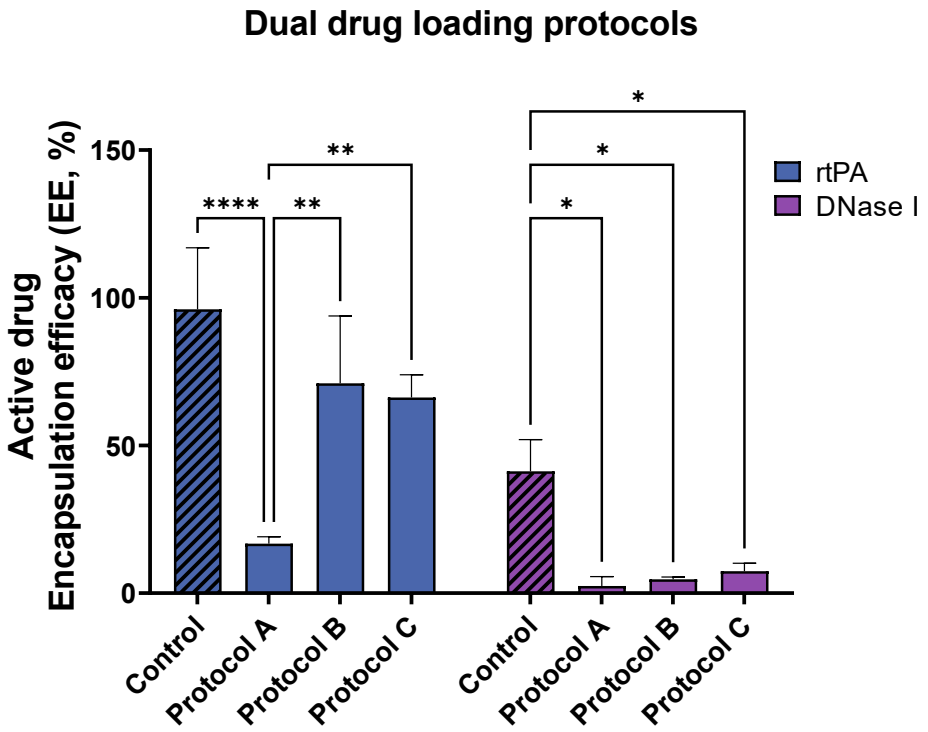


Figure 31: rtPA and DNase I co-encapsulation. Drug concentration was measured by respectively PefaFluor® or DNase I activity kit, and the resulting encapsulation efficacy reported (EE, %). ***Protocol A (Simultaneous)****: 0.25 mg/mL rtPA and 0.5 mg/mL DNase I incubated together with 2.5 mg/mL Fuco-NP at pH=3 for 60 min.* ***Protocol B (rtPA first)****: 0.25 mg/mL rtPA loading in 2.5 mg/mL Fuco-NP for 60 min, followed by ultracentrifugation; then 2.5 mg/mL Fuco-NP-rtPA were exposed to 0.5 mg/mL DNAse I for 60 min at pH=3.* ***Protocol C (DNase I first)****: 0.5 mg/mL DNase I loading in 2.5 mg/mL Fuco-NP for 60 min at pH=3, followed by ultracentrifugation; then 2.5 mg/mL Fuco-NP-DNase were exposed to 0.25 mg/mL rtPA for 60 min. Intermediate rtPA and DNase I contents were also verified, and the controls represent single drug loading conditions. A 2-way ANOVA was performed, with Tukey's multiple comparison test to compare only the differences between loading conditions (n=3).*

In summary, rtPA and DNase I were both loaded in Fuco-NPs. They are not, however, the only drug that could be considered for thrombolytic applications. Indeed, we also investigated the loading of N-acetylcysteine (NAC) as another synergistic therapeutic for thrombotic diseases. This small peptide is a recognized antioxidant and anti-inflammatory molecule, the properties of which have been explored in various diseases, including neurodegenerative ones due to evidence of increased glutathione levels in the brains with NAC administration [404,405]. NAC notably contains a thiol group which may react with cysteines and disulfide bonds, with respectively two described applications. First, NAC has been reported to have mucoadhesive properties cysteines-containing mucus glycoproteins [405,406]. Second, by reducing disulfide bridges, NAC was postulated to be able to reduce these bonds in multimeric proteins, such as VWF. The latter was evoked in “Part One. I. B)Thrombosis pathophysiology” due to its involvement in thrombus formation, composition and possible secondary network which may impede thrombolysis [22]. Accordingly, Martinez de Lizarrondo *et al*. demonstrated in 2017 that NAC could exert thrombolytic effects by reducing VWF multimers in arterial thrombi [407]. In addition, the antioxidant and anti-inflammatory properties of NAC were explored for treatment of ischemia in strokes [408,409], including clinical investigations [410,411]. We therefore tested the loading of NAC in our Fuco-NPs as a candidate for synergic thrombolysis, and eventually management of ischemic damage, but only low amounts could be loaded. Notably, we assayed different pH conditions during loading since NAC has reported negative pKa (2.0), similar to DNase I loading, but this was unsuccessful in raising the encapsulation efficacy (preliminary results). For the sake of furthering the development and testing of Fuco-NP-rtPA and Fuco-NP-DNase, this attempt was arrested at that point. However, future experiments would include N-acetylcysteine amide (NACA) instead of NAC, since this version of NAC showed similar efficacy, but may exhibit improved BBB crossing, and higher pKa (4.6) [412], which might facilitate its loading.

III. Thrombolysis

Once the Fuco-NPs were fully characterized and that their loading of rtPA and DNase quantified, validating the use of Fuco-NP-rtPA and Fuco-NP-DNase as targeted drug delivery systems that may exert their enzymatic activity, the thrombolysis potential of these formulations was explored first *in vitro*, then *in vivo*.

A) Materials and methods

A.1) Materials

Thrombin from human plasma (#T7009), plasminogen from human plasma (#528175), Phorbol 12-myristate 13-acetate (PMA, # P8139-5MG), Iron (III) Chloride hexadydrate ($FeCl_3$, #236489-100G) were purchased from Sigma Aldrich (Saint-Quentin-Fallavier, France). PBS 1X and 10X (#14040133 and #14080055), Rhodamine phalloidin (#R415), DIOC6 (D273), DAPI (#62247), SytoxGreen (#S7020) were purchased from Thermo Fisher Scientific (Massachusetts, United States). Anti-CD68 (#ab283654) antibodies, and IHC detection kit (#ab236468) were purchased from Abcam (Amsterdam, Netherlands). Human whole blood was acquired from EFS (Bichat Hospital, Paris, France), the French blood donation institute, under a research convention, in PPACK, sodium citrate or EDTA collection tubes.

A.2) In vitro *static thrombolysis*

For static thrombolysis assays, two types of blood clots were prepared *in vitro*: “young” and “old” clots. Human whole blood was collected in sodium citrate tubes, and 200 µL blood were added to glass tubes containing 10 µL water with 200 mM $CaCl_2$ and 2 U/mL thrombin. The tubes were closed and incubated at 37°C for 1 h for “young” clots. For “old” clots, 0.2 U/mL thrombin and 24 h incubation were used. The resulting clots were washed four times in PBS, weighted, then washed again three times. The clots were then incubated at 37°C with different conditions (resuspended in PBS, with 0.25 U plasminogen added per clot) for 1 h with slow agitation. The clots were weighted again, and the supernatants were frozen at -20°C for 24 h. Quantification of released hemoglobin (Hb) was performed by thawing the supernatants then mixing twenty volumes of Drabkin’s reagent (200 mg/L potassium ferricyanide, 50 mg/L potassium cyanide, 140 mg/L potassium dihydrogen phosphate, 1% (v/v) Tween 20, pH = 7-7.4) with one volume supernatant. After 10 min incubation in the dark at RT, absorbance is read at 540 nm with a Varioskan LUX multiplate reader

(Thermo Fisher Scientific, Massachusetts, United States). rtPA and DNase I concentrations used were 1 µg/mL and 50 µg/mL respectively. For NET content quantification, untreated “young” and “old” clots were retrieved after the first four PBS washes, then fixed with 4% (v/v) paraformaldehyde for 24 h at 4°C. After washing three times with PBS, then clots were incubated at RT for 30 min with 100 nM SytoxGreen and 1 µg/mL DAPI in PBS, then washed three times before imaging with a Leica Z16 APO macroscope (Leica, Nanterre, France) equipped with an Orca Flash 4.0 LT camera (Hamamatsu, Hamamatsu City, Japan).

A.3) In vivo *$FeCl_3$ mesenteric vein thrombosis model*

Animal studies were performed on 6–8 weeks old C57BL6J mice (Janvier Labs, Le Genest-Saint-Isle, France), with equipartition of males (24.9±2.3 g weight) and females (19.9±2.4 g weight) in each group. All experiment were adapted according to French (Decree 87/848) and European (2010/63/EU) ethical guidelines. The local ethic committee (C2EA-121 Paris Nord, France) and the French Ministère de l’Enseignement Supérieur et de la Recherche approved the fulfilling of the experiments with the reference number APAFIS#49260. After an acclimatation period of one week in an enriched environment, mice received analgesia (subcutaneous injection of buprenorphine 0.05 mg/kg), then were anesthetized for the whole procedure (4% isoflurane inhalation for initiation then continuous 2% isoflurane inhalation). A midline abdominal incision was performed to expose the mesentery, which was gently laid out over a transparent Petri dish and placed under an intravital macroscope: Leica Z16 APO macroscope (Leica, Nanterre, France) equipped with an Orca Flash 4.0 LT camera (Hamamatsu, Hamamatsu City, Japan). A retro-orbital injection of 30 µL DIOC6 50 µM was performed to label leukocytes and platelets. A 1 mm large Whatmann chromatography paper band, previously soaked in 10 wt.% $FeCl_3$ was deposed on a mesentery vein for one minute before removal. The thrombus formation was observed in real time for 10 to 20 min by fluorescence macroscopy. Once the thrombus was formed, images were acquired at 20 s intervals for 30 min. Between the second and third frames, samples were administered with a retro-orbital injection (150 µL injections, in saline suspension). When NPs were used, they were fluorescently labeled with TRITC, and the maximum final concentration of Fuco-NPs in the mice blood was 962±26 µg/mL (obtained for Fuco-NP-rtPA 5 mg/kg and empty Fuco-NPs). At the end of the image acquisition, the animals were sacrificed. Image analysis of thrombi with ImageJ included a SIFT-based alignment with rigid transformation. The thrombus area was measured over time in the DIOC6 channel to create

thrombi binary masks by thresholding and the rate of thrombus degradation was analyzed after the thrombus reached its maximum size in the first 20 frames (7 minutes). For targeting measurements, the mean fluorescence intensity (MFI) was measured in the thrombus for both DIOC6 and TRITC over time, and in particular after 30 min as a ratio of MFI_{TRITC}/MFI_{DIOC6}.

A.4) Biodistribution in mice by histological analysis

For a limited number of animals (n=4) and for the saline and Fuco-NP conditions, organs (liver, spleen, kidney, lung) were harvested after the *in vivo* thrombosis model described above. They were fixed with 4% (v/v) paraformaldehyde for 24 h at 4°C, then transferred in 70% EtOH for storage. The organs were later embedded in paraffin. For each organ, representative slices were stained by hematoxylin-eosin and natural saffron (HES) and Alcian Blue (AB). Furthermore, for one animal for each condition, immunohistochemistry (IHC) was performed. Briefly, after deparaffinization, rehydration, and antigen retrieval (citric acid buffer, pH=6), slides were incubated with a primary anti-CD68 antibody (dilution 1:100) and then the supplier's protocol was followed for the IHC detection kit with horse radish peroxidase (HRP), with an acid Mayer's hemalum counterstaining. Digital slides with tissue slices were acquired using a Nanozoomer (Hamamatsu, Hamamatsu City, Japan). The image analysis was performed by quantifying the positive blue areas with an ImageJ macro listed as "Multi_Alcian_treatment.ijm" (see **ANNEX 14**) based on relative RGB values.

A.5) Image analysis and statistical analysis

Images were analyzed with ImageJ (Fiji), and the macros that were used are made available in **ANNEX 14**. When images are shown, the same contrast values are applied to each channel displayed. Quantitative data were analyzed with the statistical analysis software GraphPad PRISM 9.5.0., with a significance level α taken at 0.05. All presented data consisted of n=3 or more replicates per condition (when not shown on the graphs, replicate number is indicated in the legend). Whenever applicable, presented replicates consist of biological replicates, or, when appropriate, different NP batches. Unless explicitly mentioned, results are presented as mean ± standard deviation. Depending on the design of the experiments, data significance was evaluated with unpaired t-test (two groups, assumed equal variance), unpaired t-test with Welch's correction (two groups, variance not equal), paired t-test (two groups of paired values, with assumed equal variance), one-way ANOVA (one factor explored,

with more than two groups, variances assumed equal) with Tukey's multiple comparison test, one-way Welch's ANOVA (one factor explored, with more than two groups, variances not equal) with Dunnett's T3 multiple comparison test, repeated measures one-way ANOVA (one factor explored, with more than two groups of repeated measures compared to the initial group, variances assumed equal) with Dunnett's multiple comparison test, two-way ANOVA (two factors explored) with Tukey's (comparison of all conditions) or Šidák's (comparison between factors) multiple comparison test. Unless explicitly specified in the legend, unpaired t-tests and ANOVA with Tukey's test are performed. Every p-value below α threshold was represented as follows: * $p < 0.05$; ** $p < 0.01$; *** $p < 0.001$, **** $p < 0.0001$ (ns was indicated for "not significant" if no significant differences are present in the data presented).

B) *In vitro* thrombolysis assays

In order to assess the thrombolytic potential of Fuco-NP-rtPA and Fuco-NP-Dnase, static thrombolysis assays on artificial clots made from human blood were performed. The first formulation of *in vitro* clots, hereafter named "young" clots, were first created by mixing anticoagulated human whole blood (in citrate collection tubes) with 0.1 U/mL thrombin and 10 mM $CaCl_2$ before incubation for 60 min at RT. Then, the thrombi were washed with PBS and weighted, before addition of the various samples and incubation for 60 min with slow agitation. The release of hemoglobin (Hb) and weight decrease were quantified, and the released Hb amount per mass unit of clot was reported. A representative setup of such clots after incubation with different rtPA concentrations is given in Figure 32.a.

First, rtPA-mediated thrombolysis was measured. Both the clot weight reduction (Figure 32.b) and the released hemoglobin are shown (Figure 32.c). Notably, working with weight-normalized hemoglobin release resulted in similar trends as weight reductions, but with clearer outputs and more controlled variations. As can be seen in Figure 32.c, rtPA incubation at 1 µg/mL resulted in significant release of hemoglobin (0.73 ± 0.12 $g.dL^{-1}.mg^{-1}$) when compared to control treatment (PBS). This was correlated with a 30% clot weight reduction. Moreover, the Fuco-NP-rtPA, incubated at equivalent 1 µg/mL rtPA, produced a comparable thrombolysis as free rtPA with 0.73 ± 0.20 $g.dL^{-1}.mg^{-1}$ Hb released per mg of clot. Therefore, Fuco-NP-rtPA retained the same activity as free rtPA in a static thrombolysis model. Since this model was static, without flow, inhibition or rtPA clearance by the liver, no improvement of vectorization was

expected. Nonetheless, this validated that Fuco-NP-rtPA was an adequate method to deliver rtPA so as to having rtPA-mediated thrombolysis.

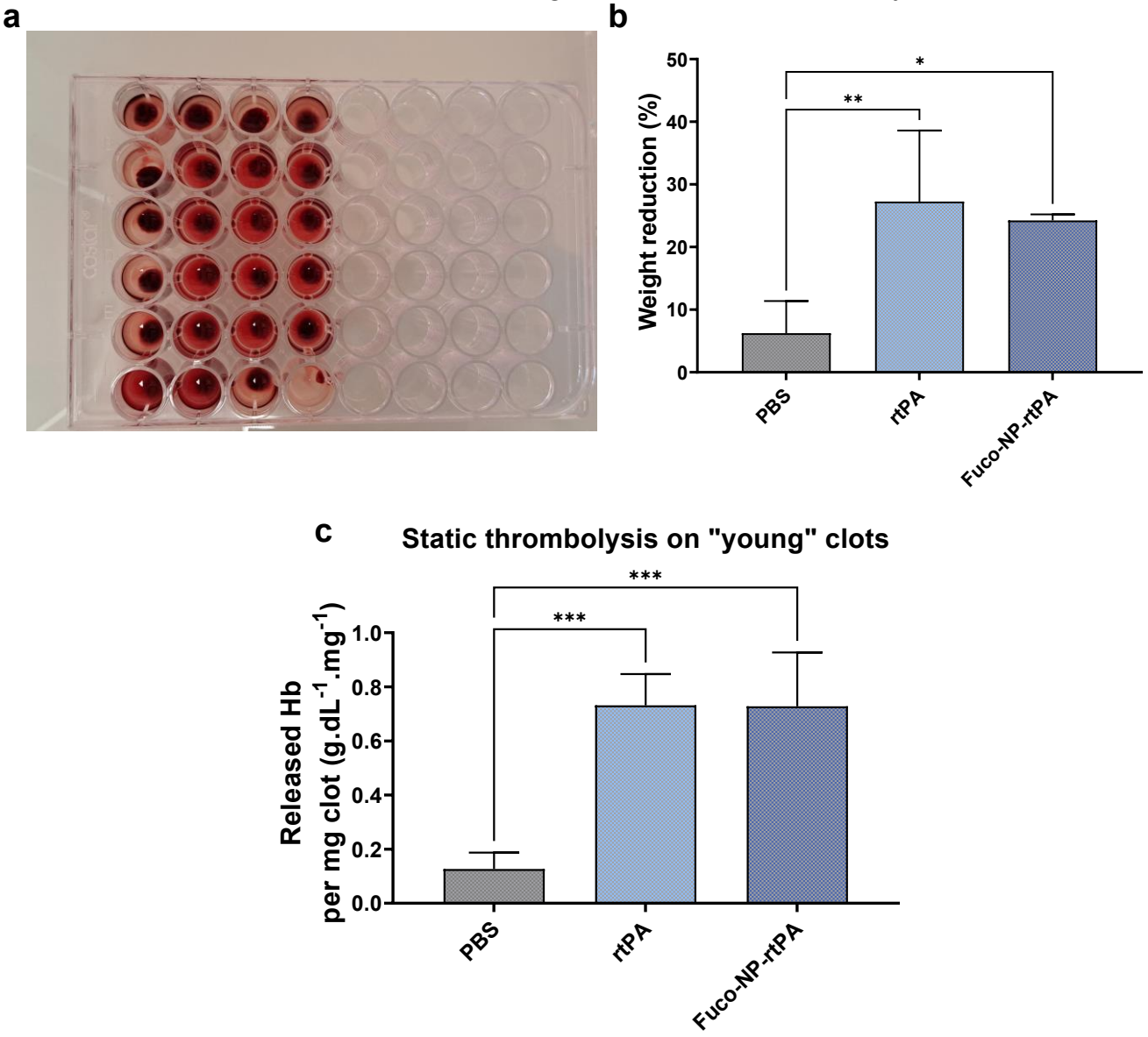


Figure 32: Static thrombolysis by rtPA on "young clots". "Young" clots were obtained after 60 min incubation of whole human blood with 10 mM $CaCl_2$ and 0.1 U/mL thrombin at 37°C. After rinsing, they were weighted and treated with 1 µg/mL rtPA or Fuco-NP-rtPA at the equivalent rtPA dose. (a) Representative clots in a static thrombolysis assay with "young" clots. First row and column (excepted well F1, with rtPA) are different controls without rtPA, while other include various concentrations of rtPA between 1 and 25 µg/mL. The photo was taken after 60 min incubation, before clot weighting. (b) Weight reduction of thrombi in the static thrombolysis assay with "young" clots. A one-way ANOVA with Tukey's multiple comparison test was performed (n=4). (c) Static thrombolysis with "young" clots. The released hemoglobin after 37°C incubation for 1 h was quantified with the Drabkin's reagent and normalized to the initial

clot mass. A one-way ANOVA with Tukey's multiple comparison test was performed (n=4).

However, when considering the combo action of rtPA and DNase I, this model with "young" clots showed no difference between rtPA alone or rtPA combined with DNase I (rtPA at 1 µg/mL, DNase I at 50 µg/mL and equivalent drug concentrations of Fuco-NP-rtPA and Fuco-NP-DNase), as illustrated in Figure 33.a. This was also true across different DNase I concentrations. This could be attributed to the possible absence of NETs in this static thrombus model, since thrombi can have very different compositions [15]. A variation in the protocol for making *in vitro* clots from 1 h incubation to 24 h incubation, combined with a reduced concentration of thrombin, was tested, yielding clots that were hereafter named "old" clots. Based on the SytoxGreen/DAPI differential staining of extracellular and nuclear DNA, some untreated "young" and "old" clots were stained with these two dyes. The total fluorescence ratio of SytoxGreen over DAPI was quantified, and a significant increase in the SytoxGreen over DAPI mean fluorescence intensity ratio was observed (Figure 33.b), ranging from 1.06±0.01 for "young" clots to 1.30±0.05 for "old" clots. This suggested that "old" clots contained more extracellular DNA than "young" ones, likely due to increased NET formation. Thus, the thrombolysis experiment was repeated to evaluate DNase I potentiating action on rtPA on these "old" clots, now comparing rtPA at 1 µg/mL, DNase I at 50 µg/mL and equivalent drug concentrations of Fuco-NP-rtPA and Fuco-NP-DNase (Figure 33.c). In this model, rtPA alone amounted to 0.67±0.10 $g.dL^{-1}.mg^{-1}$ Hb released per mg of clot, while rtPA and DNase free drugs combo achieved 1.10±0.17 $g.dL^{-1}.mg^{-1}$ released Hb per mg clot, thus demonstrating a statistically significant increase in thrombolysis for the rtPA + DNase I combo, while DNase I alone was no different than the control treatment (PBS). Furthermore, the combo of Fuco-NP-rtPA and Fuco-NP-DNase resulted in 1.21±0.08 $g.dL^{-1}.mg^{-1}$ released Hb per mg clot, similar to the free drugs combo, and significantly superior to the rtPA alone condition. The experiment with these two *in vitro* models reflected that like clinical thrombi [16], artificial thrombi could vary in composition, including NET formation. For NET-containing thrombi, DNase I was ineffective alone, but combination with rtPA significantly improved thrombolysis when compared to rtPA alone. Moreover, Fuco-NP-rtPA and Fuco-NP-DNase are viable formulations for delivering the combo of rtPA and DNase I to thrombi.

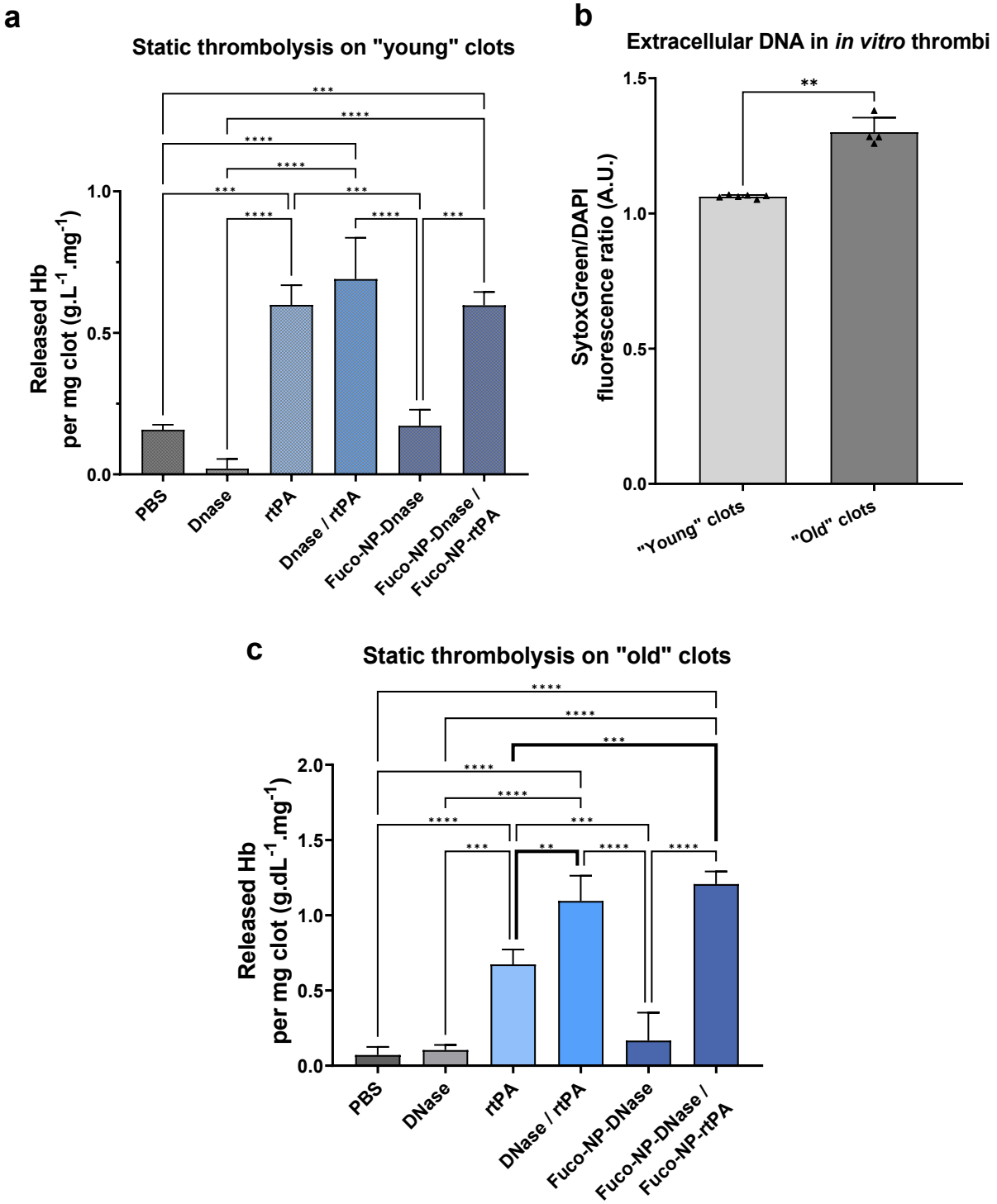


Figure 33: Thrombolysis with DNase I and rtPA. "Old" clots were obtained after 24 h incubation of whole human blood with 10 mM $CaCl_2$ and 0.01 U/mL thrombin at 37°C, then after rinsing they were weighted and treated with 1 µg/mL rtPA, 50 µg/mL DNase I, Fuco-NP-rtPA or Fuco-NP-DNase at the equivalent drug dose. (a) Static thrombolysis with "young" clots. The released hemoglobin after 37°C incubation for 1 h was quantified with the Drabkin's reagent and normalized to the initial clot mass. A one-way ANOVA with Tukey's multiple comparison test was performed (n=4). (b) Fluorescence ratio between

SytoxGreen and DAPI staining of "young" and "old" clots. An unpaired t-test with Welch's correction was performed (young clots: n=6; old clots: n=4). (c) Static thrombolysis with "old" clots. The released hemoglobin after 37°C incubation for 1 h was quantified with the Drabkin's reagent and normalized to the initial clot mass A one-way ANOVA with Tukey's multiple comparison test was performed (n=4).

C) *In vivo* thrombolysis

The *in vivo* thrombosis model was performed as described in Figure 35 with a murine mesenteric vein $FeCl_3$ thrombosis, with male (24.9±2.3 g weight) and female (19.9±2.4 g weight) mice. This model is widely used to create occlusive thrombosis *in vivo,* in both veins and arteries [413,414]. It relies on a vascular injury caused by oxidative damages after $FeCl_3$ application to the outside of blood vessels [415]. Following vascular wall injury, the denudation of the endothelium triggers reliable thrombosis by activating coagulation and platelet aggregation. This model's broad use is related to its simplicity and reliable thrombus formation, as well as generating thrombi that are sensitive to anticoagulant, antiplatelet and fibrinolytic drugs [415], which explains why its implementation (in various vessels from veins to arteries) represents circa 25% of all permanent thrombosis animal models in current nanomedicine preclinical research (see Figure 14). Once the thrombus formation was observed by intravital macroscopy through platelet aggregation, the samples were injected into the retro-orbital vein and continuous imaging was performed for 30 min. Platelet and leukocytes were imaged thanks to DIOC6 labeling, while the NPs were labeled with TRITC. The thrombus area was measured over time, and the rate of thrombus degradation was calculated to account for disparities in thrombi area. Each treatment group contained 10 animals, with equipartition of male and female mice. Saline and empty Fuco-NP (equivalent NP concentration to the Fuco-NP-rtPA 5 mg/kg) were used as negative control treatments, while the 10 mg/kg rtPA injected as a free drug served as the positive control as established before for murine models [393]. Fuco-NP loaded with rtPA alone at 5 mg/kg or 1 mg/kg were compared to free rtPA at the same concentration. The potential synergic effects of DNase I with rtPA were also investigated, with their co-injection as well as the co-injection of Fuco-NP-rtPA 1 mg/kg with Fuco-NP-DNase 5 mg/kg. Overall, the initial clot area was on average 51 795 μm^2.

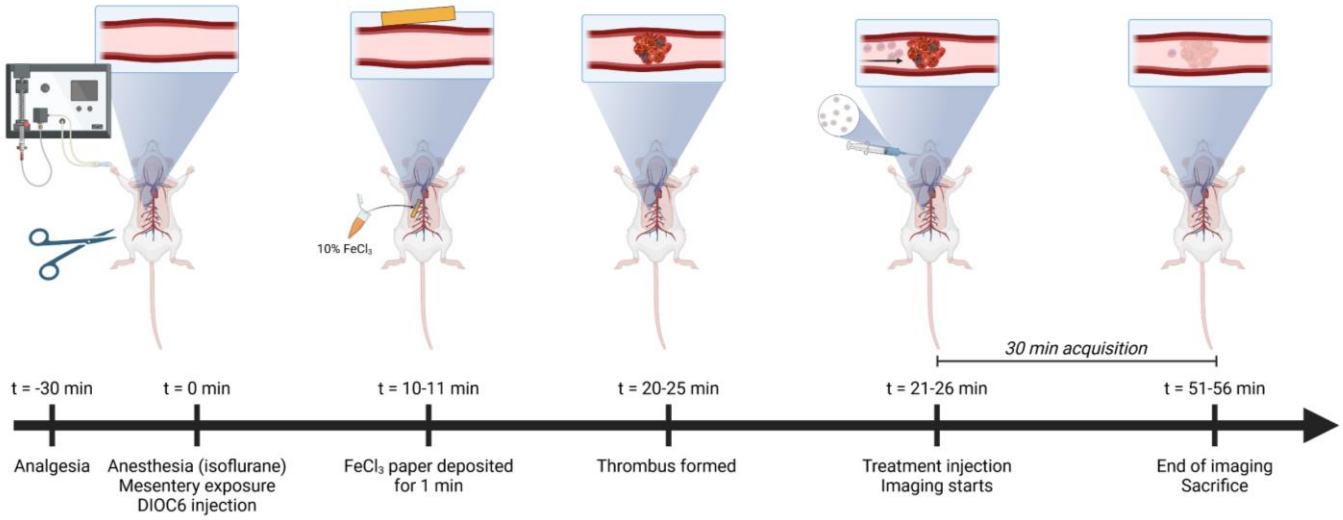


Figure 34: $FeCl_3$ mesenteric vein thrombosis murine model. (a) Schematic timeline of $FeCl_3$ mesenteric vein thrombolysis model. 6-8 weeks male and female mice are used. After analgesia (buprenorphine) and anesthesia with isoflurane, $FeCl_3$ is used to induce thrombosis in a mesenteric vein. Once the thrombus is formed and stable, the various treatments are injected through the retroorbital vein, and thrombus evolution is observed by fluorescence over 30 min before sacrifice. DIOC6 is used to label platelets and leukocytes, and NPs are labeled with TRITC.

Two representative clots are shown in Figure 35.a-b to illustrate the thrombolysis experiments. As can be seen in Figure 35.a, where a mouse was treated with an intravenous administration of saline, the thrombus does not evolve during the 30 min beyond a stabilization in the first minutes. On the other hand, when a mouse is treated with an intravenous administration of Fuco-NP-rtPA 1 mg/kg (Figure 35.b), the accumulation of TRITC-fluorescent Fuco-NPs can be seen. Moreover, the thrombus reduces in size over time, indicating effective thrombolysis. Some animals were injected with empty Dex-NPs and the thrombus mean fluorescence intensity was compared to the saline or empty Fuco-NP administrations. As illustrated in Figure 35.c, TRITC fluorescence increased in both Dex-NPs and Fuco-NPs when compared to saline, indicating that there was some NP accumulation for both formulations at the thrombus. Nonetheless, Fuco-NPs displayed a significantly higher accumulation than Dex-NPs, validating the thrombus targeting properties of fucoidan. The Dex-NPs accumulation likely occurs through unspecific sequestration in the thrombus.

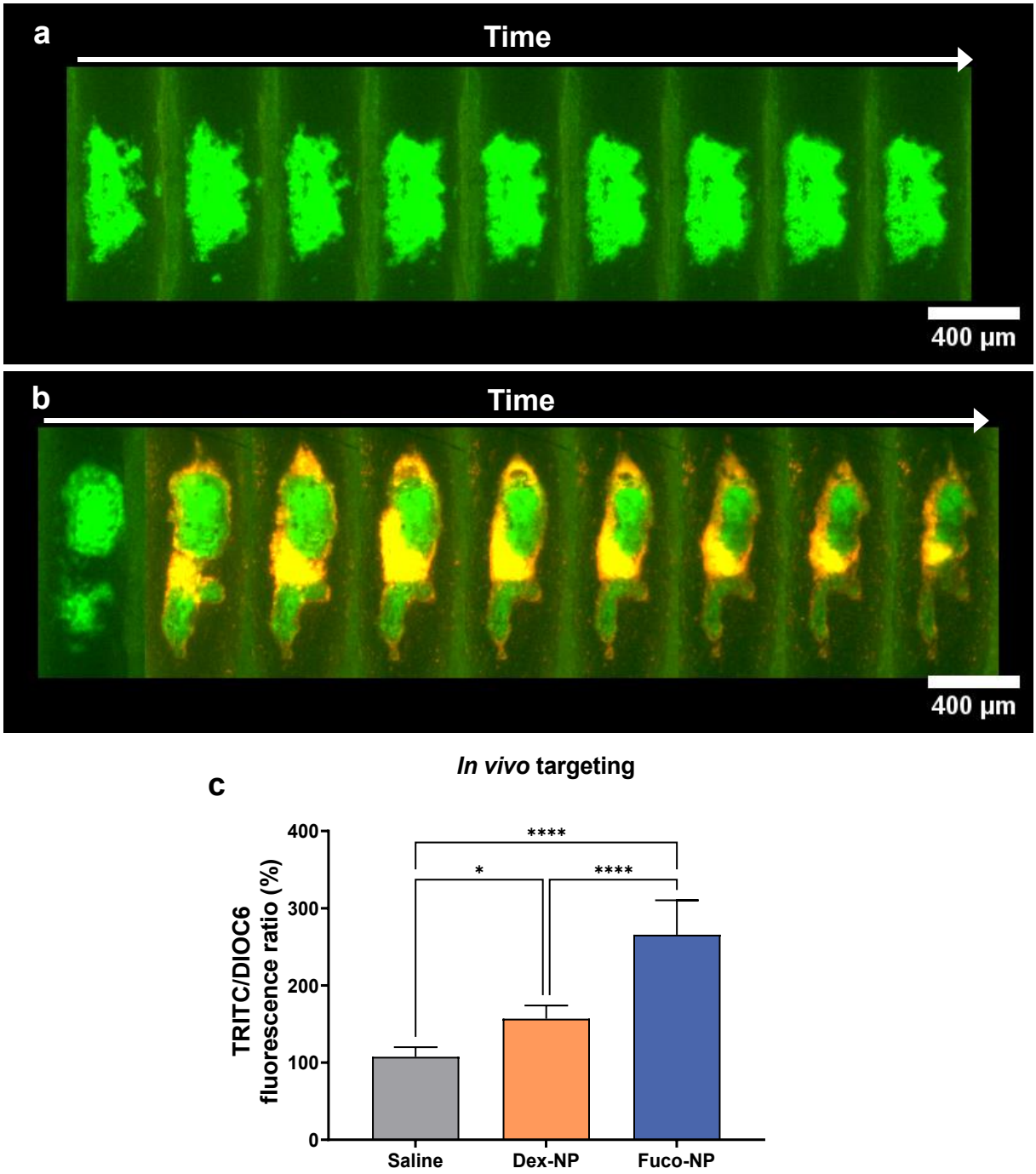


Figure 35: In vivo *thrombus targeting. (a-b) Representative mosaics of two thrombi over time imaged by fluorescence, with one frame extracted every 3 min. DIOC6 (green) colors platelets and leukocytes, and TRITC (red) colors NPs. (a) Thrombus treated with saline, and (b) Thrombus treated by Fuco-NP-rtPA 1 mg/kg (scale bar = 400 µm). (c)* In vivo *targeting. The fluorescence ratio of TRIC-labeled NPs with DIOC6 was compared for non-loaded Dex-NPs and Fuco-NPs. A one-way ANOVA with Tukey's multiple comparison test was performed (Saline, n=10; Dex-NPs, n=4; Fuco-NPs, n=10).*

For quantitative thrombolysis results, the DIOC6 fluorescent images were converted to binary masks allowing for visualization of thrombus area, as shown in Figure 36 after treatment injection for representative clots. The respective clot area evolution curves (on the right of each clot) are also provided. First, the saline treatment demonstrated that the thrombus usually kept growing for a few minutes before reaching a maximum area and stabilizing. Empty Fuco-NPs treatment also resulted in a stable clot. However, when treated with rtPA 10 mg/kg, the thrombi either diminished in size, or showed important remodeling, sometimes followed by clot departure, where the clot is visibly detached whole from the vessel and carried away as shown in Figure 36.

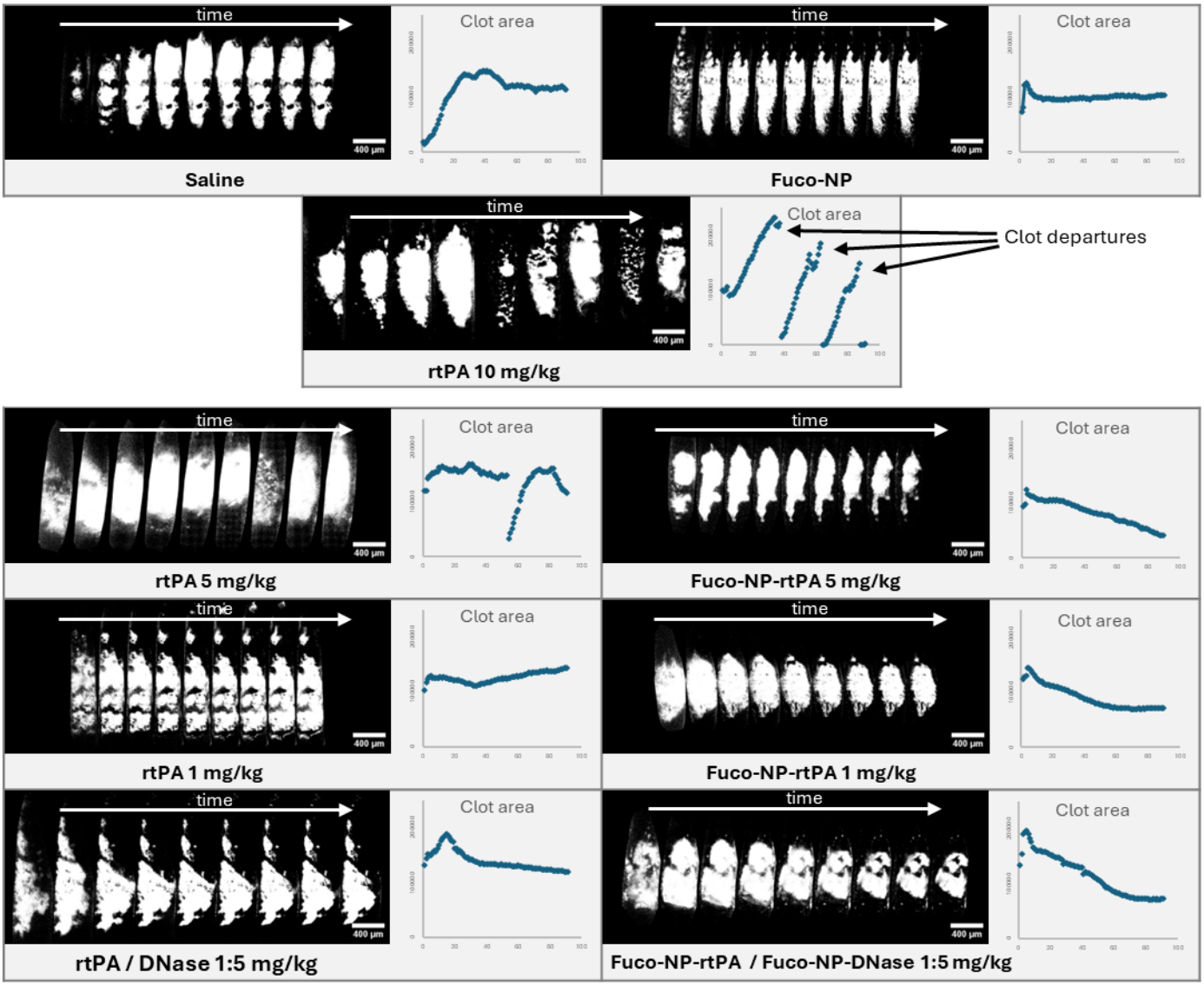


Figure 36: Representative in vivo *thrombi evolutions over time. Each thrombolysis experiment lasted 30 min, and the mosaics shown here are composed of juxtaposed thrombi binary masks acquired every 3 min. Each binary mask is obtained by automated treatment of DIOC6 fluorescence images.*

On the right of each mosaic is drawn the corresponding area evolution curve over 30 min. The top three thrombi correspond to controls (saline, empty Fuco-NPs and rtPA 10 mg/kg), with the black arrow indicating a clot departure for the rtPA 10 mg/kg treatment (scale bar = 400 µm).

These results were recapitulated in Figure 37.a displaying the thrombi area evolution, where departed clots are indicated by orange squares. Removing these departed clots from the analysis yielded the graph in Figure 37.b, which quantified the thrombus area evolution when clots remained attached. Saline and empty Fuco-NP treatments resulted in stable clots (respectively -0.29±0.57 %.min^{-1} and 0.32±0.77 %.min^{-1}). Regarding thrombi treated with empty Fuco-NPs, a slight increase in thrombus area may be observed, which might be due to the added material composed of polysaccharide NPs. However, 6 out of 10 clots treated with rtPA 10 mg/kg were detached (n=6, evolution of 2.98±2.82 %.min^{-1}), and the 4 remaining displayed decreasing clots (n=4, evolution of -1.24±1.17 %.min^{-1}). Diminishing the rtPA concentration reduced how affected the thrombi were: at 5 mg/kg only 3 clot departures and the 7 remaining displaying clot area evolutions of -0.55±1.30 %.min^{-1} in average, while rtPA treatment at 1 mg/kg resulted in stable clots (evolution of -0.00±1.09 %.min^{-1}). Overall, these results demonstrated that, in this thrombosis model, rtPA treatment did not result in systematic thrombus degradation. In some thrombi, a remodeling of the thrombus occurred (mostly at the edges), which resulted in clot departure, where the whole thrombus is detached and flown away. Interestingly, this might shed light on a major limitation of rtPA-based clinical treatment of stroke: a low rate of recanalization, and significantly decreased recanalization when the elapsed time from stroke onset to treatment increases, as explicit in the American guidelines for stroke treatment: “benefit of therapy is time dependent, and treatment should be initiated as quickly as possible” [416,417]. This could indicate that fibrinolysis does not equal thrombolysis, as it is often mistakenly perceived. Some clots, for instance during the early AIS phase, might be more susceptible to rtPA as they are still developing. Another limitation might reside in rtPA mechanism of action by binding to fibrin which could inherently limit its action in the clot [85]; this was also investigated by Bannish *et al*., 2017, who explored how rtPA-mediated fibrinolysis proceeded as a moving front through the clot [418]. This could explain an activity of rtPA limited to the edges or leading edge of a thrombus, thus elucidating its below-ideal efficacy and even why clot departures were seen, eroded from the edges but not destroyed. Most notably, such departed clots are still problematic and could form further emboli in distal

vessels, even if often counted as successful events in *in vivo* studies, which therefore ignore the problematic secondary emboli.

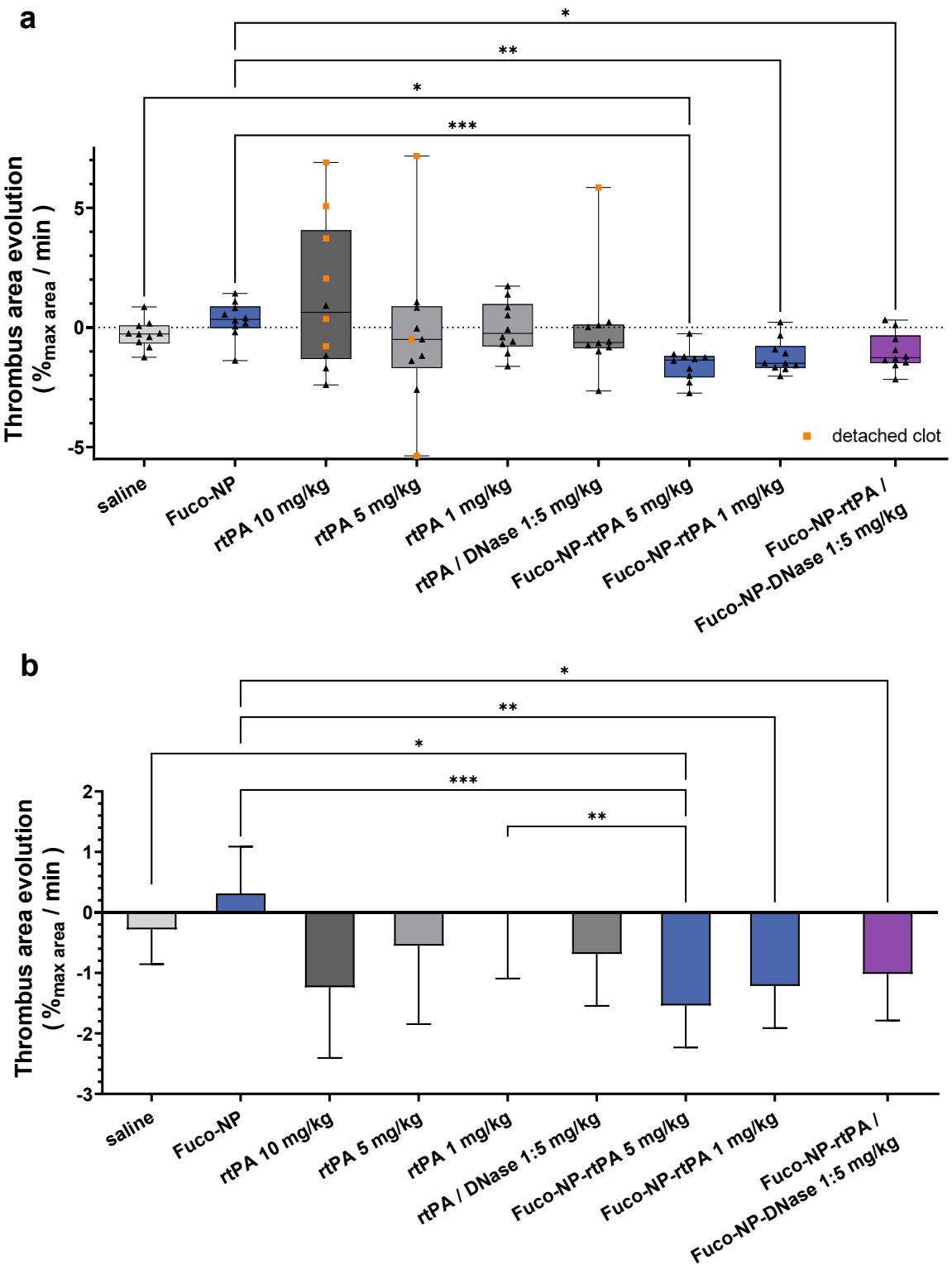


Figure 37: In vivo *thrombus area evolution over various treatments. (a) Each treatment is represented as box and whiskers. Boxes are delimited by 25% and 75% quartiles with median, and whiskers delimit minimum and maximum values.*

Detached clots are marked in orange squares. A one-way Welch's ANOVA with Dunnett's T3 multiple comparison test was performed (n=10). (b) Thrombus area evolution for different treatments, ***without the departed clots****, represented as mean ± standard deviations. A one-way ANOVA with Tukey's multiple comparison test was performed (from left to right, n=10; n=10; n=4; n=7; n=10; n=9; n=10; n=10; n=10).*

Regarding rtPA-loaded NPs, only Fuco-NP-rtPA 5 mg/kg showed statistically significant improvement (evolution of -1.54±0.69 %.min^{-1}) compared to both saline and empty Fuco-NP treatment, with a similar degradation rate to free rtPA 10 mg/kg (undetached clots). As for Fuco-NP-rtPA 1 mg/kg (evolution of -1.21±0.70 %.min^{-1}), it also resulted in a comparable thrombus degradation to free rtPA 10 mg/kg (undetached clots), significantly better than empty Fuco-NPs. To study the combo treatment, the lowest rtPA concentration (1 mg/kg) was chosen and co-administered with DNase I at 5 mg/kg. 1 clot out of 10 departed, and the other displayed relatively stable clots (n = 9, evolution of -0.69±0.86 %.min^{-1}). A non-significant increase in thrombus degradation could be observed when compared to rtPA 1 mg/kg alone (Figure 37.b), which may indicate a slight improvement of the added DNase I. When Fuco-NP-rtPA and Fuco-NP-DNase were co-injected at equivalent drug concentrations, the size of the thrombi decreased (evolution of -1.01±0.77 %.min^{-1}) but without improvement over rtPA alone or Fuco-NP-rtPA treatments.

This demonstrated a benefit in using Fuco-NP-rtPA compared to free rtPA: systematic clot reduction was observed, and the lowering of the rtPA concentration used could reduce associated side effects. While this behavior is not fully understood, the absence of an improved thrombolytic capacity of Fuco-NP-rtPA in static *in vitro* thrombolytic experiments (Figure 32.c) tends to indicate a targeting-related behavior or an unknown *in vivo* biological effect which could only be observed in the *in vivo* experiment. It can be hypothesized that a sustained release over time by Fuco-NPs, attached to the clot, could be more beneficial mechanistically than free rtPA, which would be inhibited faster or lack the improved accumulation imbued by Fuco-NP's targeting.

As for the potentiating effect of DNase I or Fuco-NP-DNase on thrombolysis, no synergistic effect was observed with this *in vivo* model. The concentrations used were 1 mg/mL rtPA (minimum where Fuco-NP-rtPA showed an effect, but where free rtPA was not efficient) with DNase 5 mg/kg (highest dose possible with the constraint of using DNase I formulated at 1 mg/mL). This may indicate that the $FeCl_3$ thrombotic model, which was very relevant to measure Fuco-NP-rtPA-mediated thrombolysis and to observe the mechanistic

differences between free and loaded rtPA, may not be adequate to investigate NET-dependent synergies. On the other hand, using higher DNase I concentrations may be necessary, but was not possible in this setting.

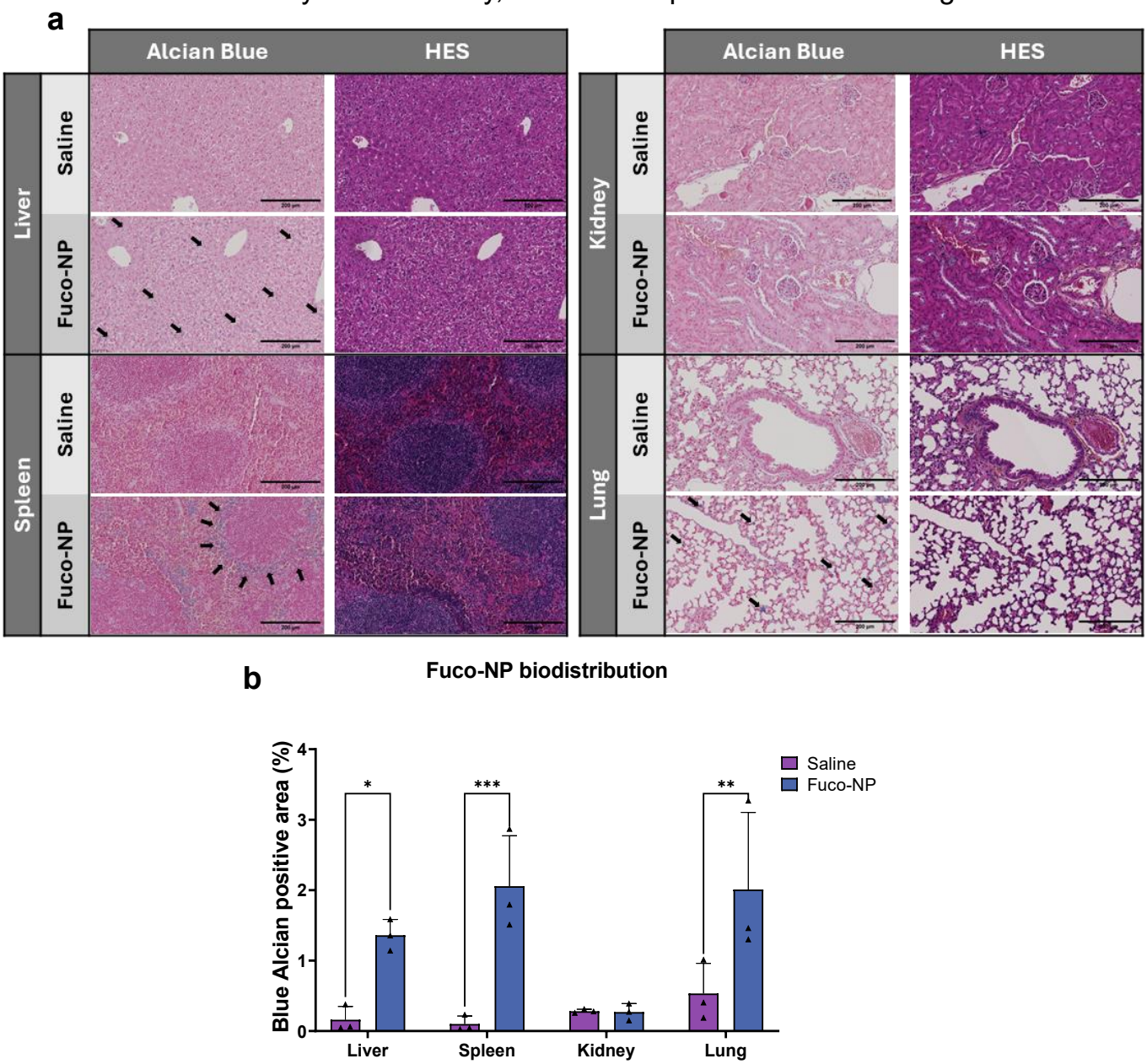


Figure 38: Biodistribution of Fuco-NPs after thrombosis. 3 animals were used for saline or Fuco-NP treatment each. Alcian Blue and HES colorations were obtained for liver, spleen, kidney and lung for each animal. (a) Representative images from different organs of animals treated with saline or Fuco-NP. All slices shown on one line come from the same animal and were aligned (scale bar = 200 µm). (b) Quantification of Blue Alcian positive coloration in each organ for saline or Fuco-NP treatment. The positive blue area was determined by image analysis with RGB relative values with a macro ("Multi_Alcian_treatment.ijm") listed in ANNEX 14. The total area stained in blue was measured for each entire organ slice and divided by the total organ area. A 2-way ANOVA was performed,

with Šidák's multiple comparison test to compare only the differences per organ (n=3).

Fuco-NP accumulation at the thrombus site was clear from *in vivo* acquisition and was quantified with the targeting measurements *in vivo* (Figure 35.b). Nonetheless, NPs fate in living organisms is critical. Therefore, four organs known to be involved in NP circulation removal (liver, spleen, kidney, lung) were harvested at the end of the *in vivo* thrombolysis experiments for the saline and Fuco-NPs treatment. In addition to the classical HES coloration, Alcian Blue (AB) coloration was performed to specifically stain acidic polysaccharides, such as glycosaminoglycans or mucopolysaccharides, but not chromatin DNA [168]. Representative organ histological slices are shown in Figure 38.a. First, based on HES coloration no pathological changes were apparent between animals treated with saline or with Fuco-NPs. Regarding AB coloration, while some blue staining occurred in untreated organs, especially in the kidneys, differential staining was obvious after treatment with Fuco-NPs especially in the liver or the spleen. Based on this differential staining, biodistribution of the Fuco-NPs in the selected organs could be inferred, as determined in Figure 38.b. Increased Fuco-NP presence was evidenced in the liver, spleen and lung with statistical significance (respectively 8-fold increase, 11-fold increase and 4-fold increase over saline treatment) while no difference could be noted in the kidney.

CD68 staining was also performed to compare macrophages localization (Figure 39). Notably, the presence of Fuco-NPs in the various organs followed specific patterns. More precisely, the presence of Fuco-NPs in liver was evidenced in tens of micrometers-sized cellular or sinusoidal shaped areas, homogeneously distributed throughout the organ, following similar patterns as macrophages. In the spleen, Fuco-NPs were localized in specific ring-shaped areas surrounding the lymphoid white pulp, resembling the marginal zone. On the contrary, macrophages were present throughout the red pulp. In the kidney, AB staining was similar in control animals and in Fuco-NP treated animals, corresponding to glomeruli, and showing no increased AB signal between controls and Fuco-NP treated mice, with few macrophages present. In the lung, some staining was evident in the control treated animals, most likely due to the presence of mucosal polysaccharides, but it was strongly enhanced with Fuco-NP treatment, arranged in tens of micrometers-sized cellular shaped areas throughout the whole organ, and following similar patterns as macrophages. The organ distribution is coherent for 315 nm NPs: absence from the kidneys, but evidenced in the liver, spleen and lungs with distribution patterns coherent with

macrophages; however, specific accumulation of Fuco-NPs in the marginal zone of white pulp in the spleen could be seen [419]. This marginal zone is instrumental in building specific responses to phagocytosis-mediated activation of certain cell types. All these elements point towards a mononuclear phagocyte system (MPS)-dependent processing pathway [419,420]. Interestingly, dextran-based materials can be degraded in the human body, notably in the liver and spleen: enzymes capable of hydrolyzing dextrans were found in animal and human tissues [319,330,421]. The presence of phosphate diester bonds, which could hinder this process, may also be hydrolyzed in physiological conditions [330], though it should be experimentally assessed on a case-by-case basis.

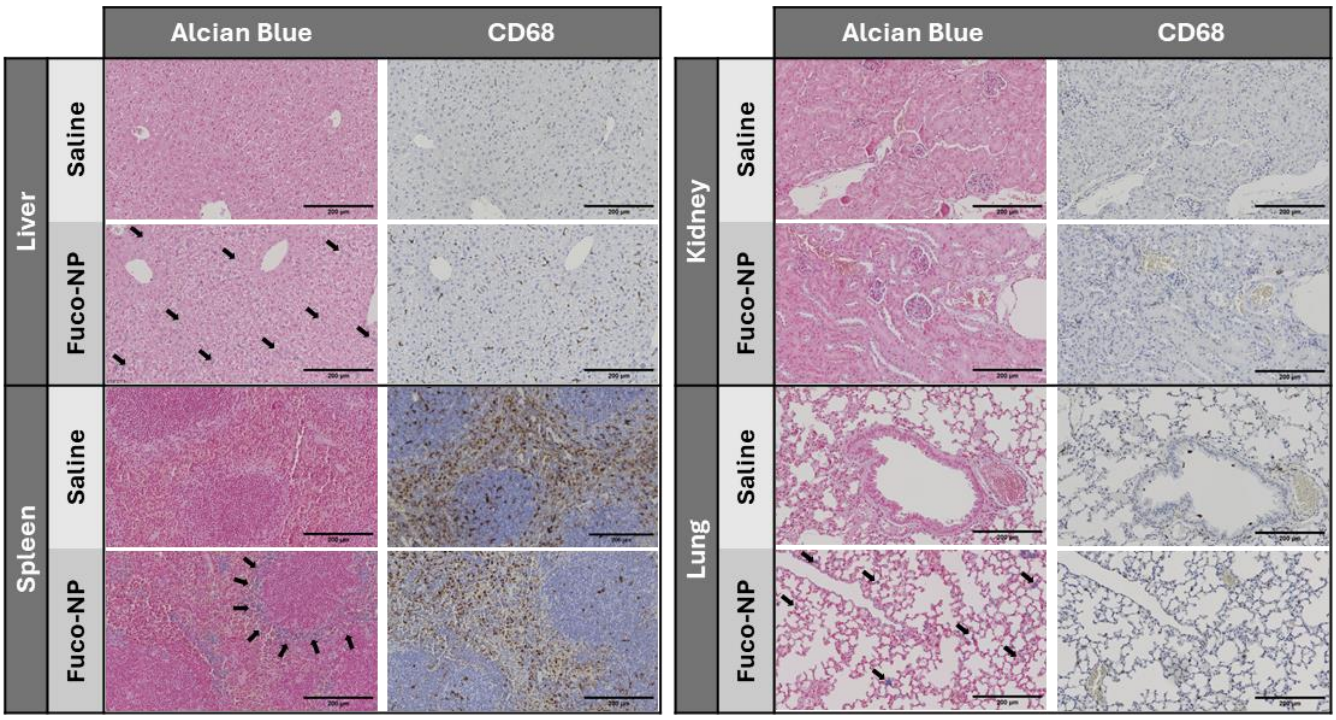


Figure 39: CD68 staining and Fuco-NP biodistribution. 3 animals were used for saline or Fuco-NP treatment each. Alcian Blue and HES colorations were obtained for liver, spleen, kidney and lung for each animal. For one animal per group, a CD68 coloration was also performed. Representative images from different organs of animals treated with saline or Fuco-NP. All slices shown on one line come from the same animal and were aligned (scale bar = 200 µm).

Overall, these *in vivo* results validate the use of Fuco-NPs to deliver therapeutic agents for thrombolysis. They appeared to be safe, displayed targeting capacity towards thrombi and could notably deliver rtPA for an improved thrombolysis at 50% and 10% the usual dose in murine models: strikingly, while the degradation rate was similar for free rtPA-treated animals without clot departure, no such re-embolization risk was observed for Fuco-NP-rtPA as all clots were degraded locally without detachment. While DNase I did

not appear to provide increased thrombolytic capacity in this setting, this should be explored further in other models.

D) Preliminary works and future directions

In summary, we described here how the loading of rtPA did not impair its thrombolytic activity in an artificial thrombus made from whole human blood. We further showed that *in vitro* thrombi differ in composition and hence in their response to potential therapeutic drugs, with for example DNase I demonstrating a synergic increase in rtPA-mediated thrombolysis in one of the two types of artificial thrombus used for static thrombolysis experiments. Furthermore, DNase I activity, despite a reduction shown in Figure 28.d after encapsulation in Fuco-NPs, was sufficient to exert a NETolytic activity (Figure 29.c) and a synergic thrombolytic activity with rtPA or Fuco-NP-rtPA (Figure 33) in NET-containing artificial thrombi.

D.1) An accurate in vitro *AIS thrombolysis model*

Even so, using *in vitro* thrombi presents several challenges, with reproducibility and significance ranking high. Indeed, we showed that modifying two parameters resulted in thrombi that responded differently to a proposed therapeutic mix of rtPA and DNase I. Many different methods for artificial thrombi production were described, with or without using whole blood, recalcification, thrombin addition or not, incubation time and volume, etc. For example, Fitzgerald *et al*. proposed in 2021 a protocol where artificial thrombi were created by mixing different blood fractions (platelets, RBC, plasma, buffy coat) in varying ratios and incubating them after thrombin and $CaCl_2$ addition overnight at RT with agitation. They demonstrated that the resulting blood clots exhibited very different immunohistochemical composition, varying stiffness and response to thrombectomy mimicking assays [16]. This broad variability of thrombus models complicates comparison of efficacy between protocols, while also blurring the mechanistic aspects of thrombosis. Thus, the thrombolysis experiments are difficult to compare, and each conclusion that can be drawn may be very dependent on the chosen thrombus model, not necessarily reflecting pathological thrombi. Moreover, the role of shear rate in thrombus formation, especially for arterial thrombosis, has been described [422].

Therefore, we used an *in vitro* microfluidic thrombosis model that was developed by Astride Perrot and Benoît Ho-Tin-Noé in the laboratory Opten (UMRS 1144 INSERM, UPC). This model relied on the establishment of blood flow in coated microfluidic channels under thrombotic conditions (including

whole human blood recalcification) with various fluorescent biomarkers which allowed the real-time observation of thrombosis. Most notably, this model could be tailored to mimic the formation of AIS thrombi, recapitulating the complete physiological cascade resulting in clot formation. This included platelet aggregation and activation, fibrin network formation and NET release by neutrophils. Commercial fibrinogen tagged with Alexa 594, DIOC6 and DAPI were used to respectively observe fibrin network formation, platelet aggregation, and NET release. Since the NPs were labeled with TRITC which would interfere with Alexa 594, an antibody against fibrin was conjugated to Alexa 647 (α-Fibrin-A647) and verified as shown in Figure 40. 10-20 min flowing of recalcified whole human blood in the microfluidic channels at venous flow rates were usually enough to observe platelet thrombus formation and NET release. This model was set up by Astride Perrot and Benoît Ho-Tin-Noé to provide a first *in vitro* model in flow of AIS blood clots, and accurately observe the different steps and dynamic formation of the latter. In our experiments, we aimed at comparing different treatments for eventual thrombolysis, including Fuco-NP-rtPA and Fuco-NP-DNase.

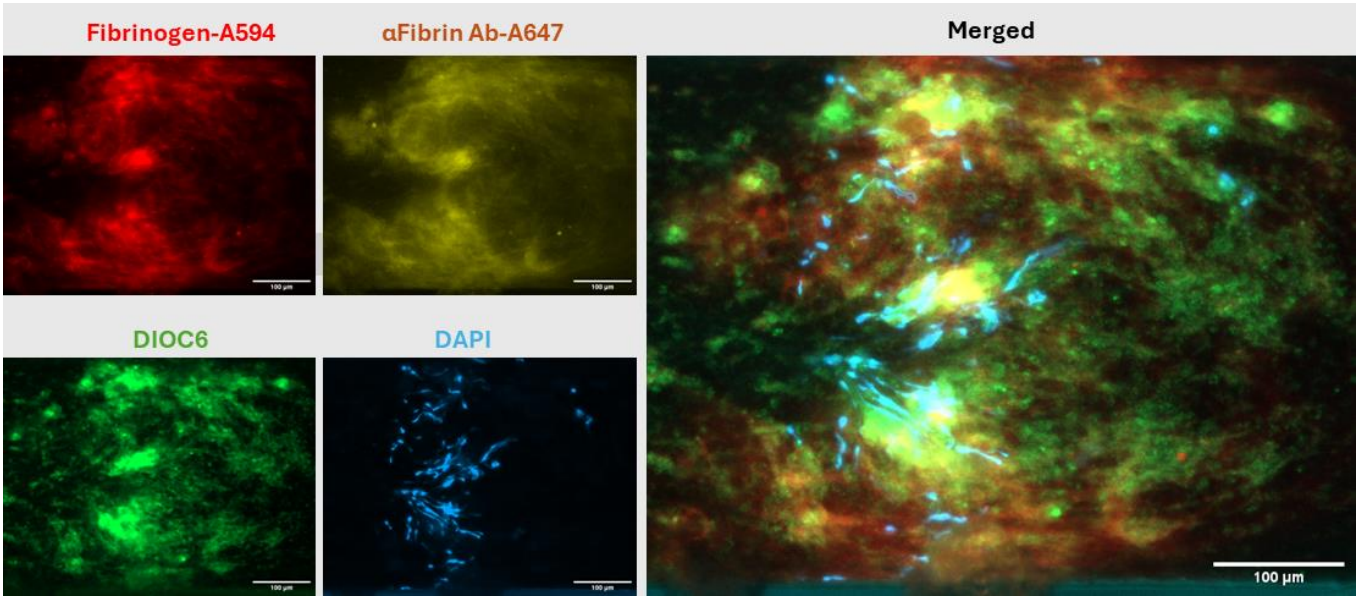


Figure 40: Representative in vitro microfluidic AIS thrombus formation. Thrombi were obtained by flowing recalcified whole human blood in fibrinogen-coated microfluidic channels. A commercial fibrinogen tagged with Alexa 594 and an ad hoc *Alexa 647 conjugated anti-Fibrin antibody were used to label fibrin. DIOC6 was added to observe platelets and leukocytes. DAPI was added to label extracellular DNA. Thrombi were generally obtained 10-20 min after labeled, recalcified whole human blood started flowing in the channels (scale bar = 100 µm).*

Therefore, we trained with this model in order to reliably obtain AIS-mimicking thrombi. A major challenge in this experiment was channel occlusion due to the thrombus formation. Therefore, controlling the thrombosis speed by tuning $CaCl_2$ recalcification levels, and timing of thrombosis and treatment addition were key parameters to ensure that a reliable experiment could be setup. Eventually, we were able to use it and administer rtPA 10 µg/mL, DNase I 50 µg/mL and the Fuco-NP-rtPA and Fuco-NP-DNase formulations at equivalent drug concentration. The evolution of the mean fluorescence of α-Fibrin-A47, DIOC6 and DAPI over 15 min was quantified to respectively measure fibrin degradation, platelet density and NETolysis. As displayed in Figure 41, the fibrin and platelet contents were stable with NaCl or empty Fuco-NP treatments. However, free tPA, the combo of free tPA and DNase I, and the respective Fuco-NP loaded formulation, all significantly reduced the fibrin content of the clots (Figure 41.a). Nonetheless, the overall clot density was not reduced with DIOC6 fluorescence remaining similar or even slightly increasing (Figure 41.b). Regarding NETs, a high variability between samples prevented statistical significance from being observed. Nonetheless, it seemed that DNase and Fuco-NP-DNase cause a slightly stronger decrease in DAPI fluorescence, including when co-administered (Figure 41.c). In order to investigate more finely the NET fluorescence, we verified how the DAPI fluorescence evolved dynamically, as shown in Figure 41.d. For the sake of clarity, only the free drug treatments were shown. It appears that rtPA and DNase I treatments have minimal effect on NET formation. On the contrary, with the combo treatment the NET content increases faster in the first minutes, before falling back again. Therefore, at the assessed concentrations, DNase I did not seem to have an effect by itself on the clot NET content. On the other hand, rtPA successfully reduced the fibrin content of the clots, but this was not followed by clot reduction since the platelet content remained stable. Regarding the combo of rtPA and DNase I, the fibrin network was successfully degraded similar to rtPA, but the NET content was affected, though without overall reduction. The platelet content was not visibly affected. The effects were comparable with the Fuco-NP formulations of rtPA and DNase I, thought the standard deviations were higher. Longer observation periods and increased DNase I concentrations may be necessary to increase the DNase I action on NETs. Interestingly though, DNase I may only have an effect when combined with rtPA as hinted by these results, meaning that the synergic NET degradation offered by DNase I is dependent on rtPA action. Notably, plasmin degrades histones and may free access to DNA, allowing DNase I NETolytic action [34].

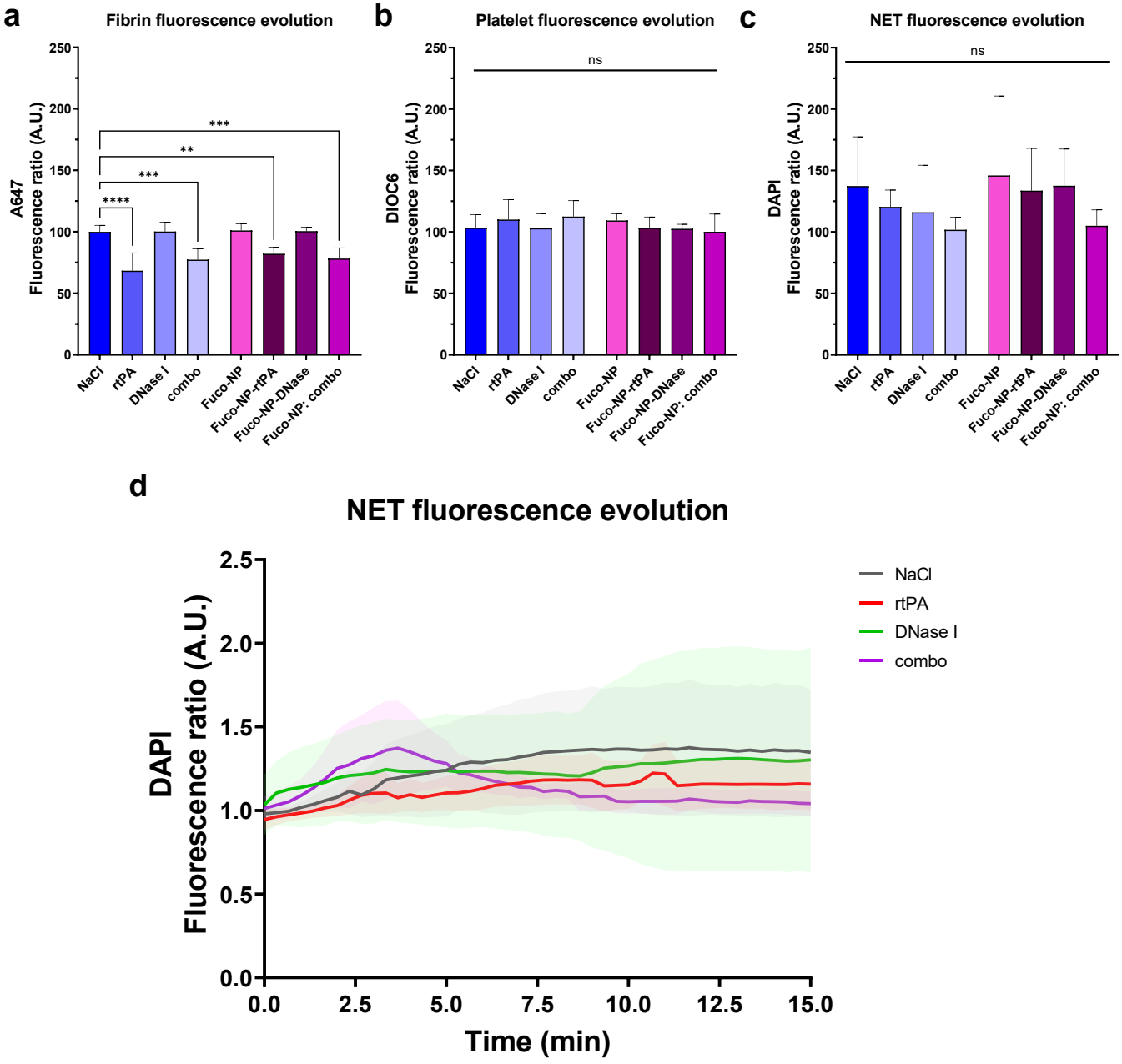


Figure 41: Microfluidic AIS thrombolysis assay. Thrombi were obtained by flowing recalcified whole human blood in fibrinogen-coated microfluidic channels. After NET apparition, the following treatments were added: 0.9% NaCl, rtPA 10 µg/mL, DNase I 50 µg/mL, combo of the two free drugs at the 10 µg/mL and 50 µg/mL respectively, empty Fuco-NPs, Fuco-NP-rtPA and Fuco-NP-DNase formulations at equivalent drug concentration, and combo of Fuco-NP-rtPA with Fuco-NP-DNase at the same equivalent drug concentrations. The fluorescence evolution was observed for 15 min and the ratio between initial and final mean fluorescence intensity reported. (a) An Alexa 647 conjugated anti-Fibrin antibody was used to label fibrin and measure fibrinolysis. (b) DIOC6 was added to observe platelets and leukocytes density. (c) DAPI was added to label extracellular DNA and measure NETolysis. One-way ANOVAs were performed,

with Dunnett's multiple tests to compare every treatment to NaCl (n≥4). (d) Dynamic fluorescence evolution of DAPI over time (relative to initial fluorescence). Only the NaCl, rtPA 10 µg/mL, DNase I 50 µg/mL, and combo of the two free drugs at the 10 µg/mL and 50 µg/mL are shown. The mean curves are shown, with colored areas for the standard deviation. (n≥4).

D.2) In vivo *assays*

Furthermore, we mentioned that DNase I potentiating action was observed only in certain artificial clots. Similarly, even though NETs presence was evidenced in both venous and arterial thrombi [34], even though their action was most thoroughly investigated in arterial thrombi [67,71,72]. Notably, NET contents of clots from different origins may differ, as emerging data seems to indicate that stroke thrombi of cardioembolic origin may contain more DNA than those of large artery atherosclerosis [74]. Therefore, it may be necessary to explore other *in vivo* thrombosis models, which may provide further insights into how various models may respond to different therapies. For example, the $FeCl_3$ murine model of thrombosis involves high ROS concentration, as well as non-classical red blood cells (RBC) involvement in thrombosis [423]. The associated high endothelium damage is not necessarily representative of other thrombosis events. For instance, we performed a preliminary experiment where, during an *in vivo* thrombolysis experiment as described above, SytoxGreen was injected along Rhodamine 6G (instead of DIOC6) in order to visualize extracellular DNA. As shown in Figure 42, a thrombus treated only with saline could be visualized though Rhodamine 6G. However, extracellular DNA staining by SytoxGreen did not reveal obvious NET formation, but it positively stained endothelial cells on the deposition site of the $FeCl_3$ paper: these permanent damages are also responsible for the continuous thrombosis which result in recurrent thrombus formation in this model. Along with other studies dealing with the thrombosis mechanism of $FeCl_3$ models, this helps ascertain the limitations of this model. Therefore, this model may not be adequate to study treatments targeting GPVI for instance, or antioxidant drugs [413]. It remains nonetheless a relevant model due to its reliability and providing a final thrombus which resembles physiological ones, with adequate responses to anticoagulants, antiplatelets or fibrinolytic drugs [75,424]. Even so, other models may be explored, with two notably that may be the most promising in studying fibrinolytic treatments for arterial thrombi. As illustrated in Figure 14, the photothrombotic stroke model currently remains the most investigated permanent ischemia stroke model (31% of the recent preclinical nanomedicine research for AIS). It involves the injection of a photosensitizer (usually Rose Bengal), which after illumination generates ROS:

the subsequent endothelium and blood element peroxidation results in platelet aggregation, and thrombosis [425]. It usually has a lower rate of variability than other protocols, with a relatively simple procedure available in multiple animals and has been extensively used. Even so, it usually exhibits a small penumbra, which limits its use in studying neuroprotection and treatments' neurological effects, and the beneficial effects of treatments are linked to the severity of the induced photochemical damages [425,426]. Another rising stroke (7% of the recent preclinical nanomedicine research for AIS) model is the thrombin injection model in mice or rats [427,428], which benefits from high reliability, good pathophysiological thrombosis and embolization and accurate mimicking of clinical responses. In addition to these *in vivo* efficacy models, which may improve the understanding and selection of potential therapeutics, the safety of these treatments should also be investigated. This would include pharmacokinetics evaluation, biodistribution and clearance investigation [420] in long-term studies, as well as safety. This is especially true since rtPA is associated with severe side effects, notably hemorrhagic transformations after ischemia. Consequently, assessing the potential bleeding, neurotoxicity and hemorrhagic transformation (or lack thereof) in focal ischemia models, for instance with the transient middle cerebral artery occlusion (tMCAO) model, may be necessary to estimate the safety benefits of Fuco-NP-rtPA over free rtPA, including at lower effective drug dose, and other potential treatments.

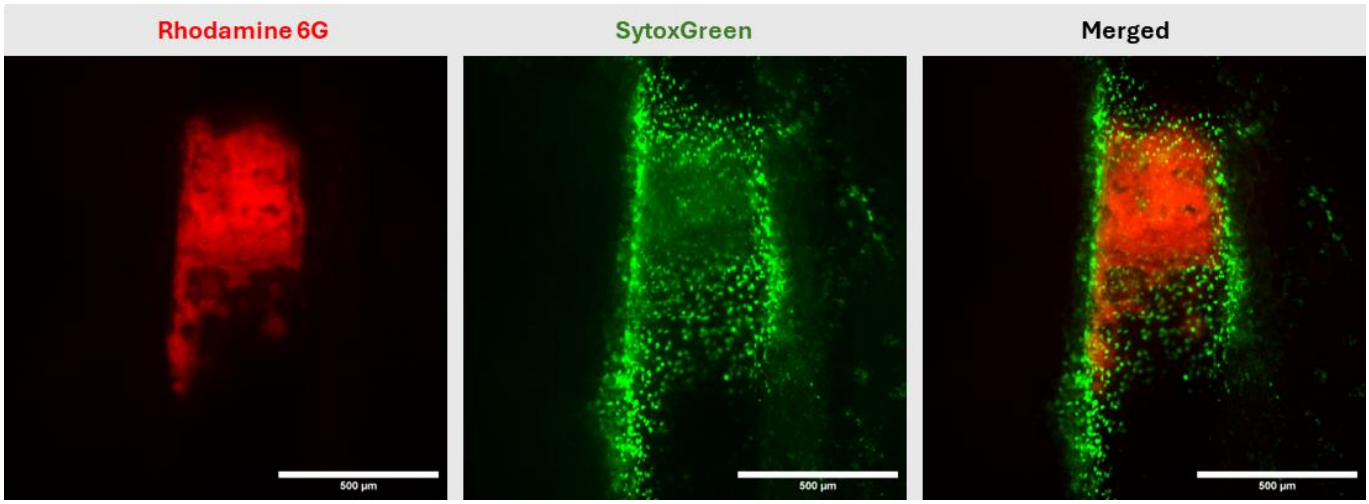


Figure 42: Extracellular DNA in the $FeCl_3$ murine model. Staining of a thrombus obtained in the mesenteric $FeCl_3$ murine model with Rhodamine 6G (platelet staining) and SytoxGreen (extracellular DNA). The image was acquired after 30 min treatment with saline (scale bar = 500 µm).

General discussion

State of thrombotic diseases treatment and nanomedicine

As evoked throughout “Part One. I. Thrombotic diseases: a challenge for human health”, cardiovascular diseases constitute a heavy burden for human health, with thrombotic diseases being preponderant actors as ischemic heart disease and acute ischemic stroke (AIS) [1]. Despite growing evidence that CVD incidence is heavily dependent on external factors, such as environmental, lifestyle and clinical risk factors, efforts to mitigate those have proven insufficient. Regarding lifestyle choices and primary prevention, extensive efforts in the last decades have been undertaken to reduce CVD deaths and are crucial to reduce CVD risk and stopping these preventable deaths [8–10]. Even so, current socioeconomic disparities, both between countries and in the general population, as well as environmental risk factors, may limit the benefits of primary prevention [4].

While the anticoagulants, antiplatelets and fibrinolytics have all demonstrated their importance in the treatment of thrombotic diseases, and new agents are being developed with for example anti-GPVI antibodies [80] or newly developed or rediscovered thrombolytics (urokinase, desmoteplase, tenecteplase, etc.), they still fall short, as evidenced among others by the low rate of recanalization associated to alteplase, the mainly used fibrinolytic for AIS [86]. In addition, there are severe side effects associated with these treatments [78,79,83]. Most importantly, the new therapeutical approaches often come with significant costs and technical difficulties: alteplase is already a drug too expensive to be used in many developing countries [87], and mechanical thrombectomy (MT), the preferred intervention now for MI and AIS when possible, as it offers much greater recanalization perspectives, requires comprehensive intervention centers with cost and accessibility issues [87,115]. As such, there is a need for other approaches that may improve safety, accessibility and efficacy of thrombotic diseases treatment.

Nanomedicine may procure such benefits, as many nanodrugs have already reached the market illustrating the potential of this technology [158]. Nonetheless, despite rich preclinical research on nanomedicine for example for AIS, the clinical translation has so far remained poor, as described in ”Part One. II. D) Applications of nanomedicine for stroke and clinical translation”.

The gap between preclinical nanomedicine research and clinical applications for AIS

With adaptations from:

- **ANNEX 5**: **de La Taille T**, Doukhi D, Mazighi M, Chauvierre C. Ischemic Strokes: Exploring the Challenges of Translating Nanomedicine into Clinical Practice. *Nano Today*, With Editor (2024)

Based on the systematic literature review presented in “Part One. II. B.1) Systematic literature review”, we attempted to identify the obstacles that prevent nanotechnology from bridging the preclinical results with successful clinical applications in the case of AIS research. Among these barriers, we identified intrinsic challenges related to NPs’ characteristics, as well as difficulties in addressing this specific pathology. These hurdles are further compounded by the emergency setting, which demands speed and logistic simplicity.

Consequently, there are intrinsic challenges in implementing nanotechnology for clinical use. Nanoparticle (NP) research typically requires collaboration across various disciplines, including nanotechnology, neurology, pharmacology, and materials science, the coordination of which can be resource intensive, requiring external fundings. Furthermore, characterization of NPs is challenging, with many factors (size, shape, composition) in play. ISO experiments often require long-term safety and efficacy data, which can be challenging to obtain due to the novel nature of nanomedicines. Moreover, long-term studies are critical to understand the chronic effects and potential toxicity of NPs, which interact with biological systems in complex ways, potentially leading to unforeseen side effects [198]. An added hurdle lies in the way that regulatory bodies handle NPs, with categorization as “excipients” or “combination products” not necessarily adequate for NPs characterization, and adding a layer of regulatory challenges [429]. This situation demands more rigorous study designs, especially since common clinical practices like blinding and randomization are not consistently applied. A meta-review from Namiot *et al*. in 2023 revealed that, as of January 2023, 476 clinical trials were underway involving NPs for any medical application, mostly in Phases I and II, with 100 nanomedicines having reached the market, including among others the COVID-19 LNP vaccines [157,158]. This indicates that this technology is still in a relative infancy, with few successful clinical trials to be used as references. In comparison, as of May 2024, 3225 trials of any type have been listed on clinicaltrials.gov for AIS only; yet for small molecules on cancer application, another fast-developing domain, 89 small molecules were approved for

thousands of clinical trials listed [160]. Interestingly, nanomedicine actually seems to fare rather well once it reaches the clinical stage. While it can be hoped that more and more nanomedicine clinical trials succeed in order to build a reference framework, a dialog with regulatory bodies such as the FDA has already started to help clarify the guidelines of using nanotechnology in FDA-regulated products [429].

In order to facilitate the future application of NPs for AIS, the currently proposed preclinical approaches should be designed from the outset with a clinical setting in mind. Notably, while many different affinity moieties are proposed for targeting NPs such as peptides (RGD [239]), polysaccharides (fucoidan [168]) or cell membranes [142], the final choice depends on which specific action is desired: neuroprotection in the ischemic brain, delivery of antiplatelets agents, or of fibrinolytics to the fibrin mesh. This also means using appropriate characterization and *in vivo* modeling. As reported above, few articles report synthesis-related challenges. 21% of investigated articles disclose stability measurements, even though these could be critical both for *in vivo* fate of the NPs, but also for future clinical investigations. Even fewer disclose relevant methods to improve their storage. However, as was seen with the COVID vaccines, logistic criteria can be of paramount importance, especially in developing countries or when speed is necessary [187]. Indeed, the stability of NPs must be ensured during storage as well as within the complex physiological conditions of the human body. In the case of AIS, where early treatment is essential to minimize damage, such formulation issues can thus further delay recovery. This can result from delays related to reconstitution, *in situ* preparation or even procurement of such nanodrugs. A limited number of articles clearly address stability issue: Hoogendijk *et al*. reported in 2020 a continuous flow microfluidic device for production of perfluorocarbon nanoemulsion in order to deliver oxygen to the ischemic tissue [252], while Son *et al*. and Han *et al*. both described 3D methods, thus improving yield and reproducibility, for MSC-derived extracellular vesicles (EV) production: either through micro-patterned wells to form spheroids, or through culture in 3D hydrogels. Both EV formulations were then used for neuroprotection, and characterized for batch-to-batch variability [165,166]. This is critical as the protocols described in articles are not necessarily compatible with scaled-up production, nor with the strict requirements of good manufacturing practices (GMP) which are required for clinical use.

Nonetheless, the primary objective of AIS treatment is to rapidly achieve reperfusion. As previously stated, the two primary reperfusion strategies are thrombolysis and thrombectomy. Despite the significant improvement in recanalization rates that these treatments have brought about, over 50% of patients retain disabilities despite successful recanalization due to the relative inefficacy of the treatments and the associated risks [104]. The use of tPA is constrained by a narrow therapeutic window and hemorrhagic risks. Furthermore, several inherent difficulties are likely to be associated with the nature of ischemic strokes. Indeed, failure to thrombolysis has been shown to be related to the composition of the occluding thrombus, which varies depending on the etiology of the stroke [22]. Vectorizing tPA, using NPs, does not appear to be the only solution for improving recanalization in such situations. Consequently, there is growing interest in identifying new therapeutic targets as alternatives or complements to existing treatments to enhance recanalization success, for example with DNase targeting NETs, N-acetylcysteine, ADAMTS13 targeting von Willebrand factor, and anti-glycoprotein VI, with a potential to enhance recanalization without increasing the hemorrhagic risk [22]. Indeed, thrombi have shown variable behaviors *in vitro*, such as different levels of susceptibility to the synergistic effects of DNase I [72], and *ex vivo*, under conditions mimicking endovascular thrombectomy using human blood clot analogs. This emphasizes the importance of understanding thrombus composition for improving stroke treatment strategies [16].

Importantly, research on NPs in the specific AIS setting for treatment faces several significant challenges. AIS requires immediate intervention to minimize neurological damage within a very narrow therapeutic window. Developing nanoparticle-based therapies that can be administered and effective within this short timeframe is complex. However, a few works mention ways of administration that differ from the usual IV injection: some articles rely on intracisternal, stereotaxic or intracarotid administration, which are more invasive and would face more challenges before clinical acceptance. In contrast, some authors propose intranasal or oral delivery (even though the latter could prove difficult in practice as some stroke patients present dysphagia), which could facilitate treatment access and speed up medical care, such as Yu *et al*. who described in 2023 a multi-drug loaded liposome compatible with intranasal delivery for neuroprotection through anti-inflammation and anti-apoptosis effects [430]. However, these methods have their limitations: specifically, the ability to effectively reach the injured area and the time required for the drug to act. Moreover, in animal models like mice, the shorter distance a drug must travel,

and physiological differences compared to humans can limit the translation of these methods to clinical settings. Consequently, optimizing the pharmacokinetics and biodistribution of NPs to act swiftly within this critical window is essential, yet this aspect is often overlooked in preclinical studies.

Due to the nature of ischemic strokes, the choice of *in vivo* models is critical. The most explored yet, the tMCAO (65% of reported *in vivo* models as evoked above), does not correlate to the current damages that ischemic stroke patients encounter (around 90% of patients admitted with LVO stroke in the US between 2014 and 2015 showed no recanalization) [256]. However, EVT has shown great premises to improve recanalization in patients (up to 90% according to Lapergue *et al*., 2021) [103]. Nonetheless, the rate of EVT-treated patients still represented only 5% of AIS patients in the US up to 2021, with an expected future growth of 5–10%/year for the next several years in performed EVTs [107]. Therefore, choosing a correct model, preferably involving the induction of a thrombus, is paramount to ensure that preclinical results are representative of the clinical fate and to avoid the current overreliance on tMCAO; part of the answer could be the use of *ex vivo* clots retrieved from EVT patients [67] in order to test the various therapies directly on human ischemic stroke thrombi.

Another significant challenge is the safety of reperfusion treatments. Intracranial hemorrhage is a common and serious complication that increases mortality and impairs prognosis. Protecting the vascular endothelium is essential to limit BBB permeability and prevent hemorrhages. Future research should focus on identifying molecular targets that can maintain or restore the BBB integrity. Rather than focusing on the clot exclusively, strategies to protect the endothelium can reduce the risk of barrier rupture and hemorrhagic complications. Interventions aimed at limiting endothelial permeability may include the use of specific molecules that stabilize the endothelium, thereby reducing the risk of hemorrhagic transformation following a stroke [61]. Here, NPs would benefit from the ability to transport various active agents to exert both thrombolysis and protection against subsequent damages.

Overall, NPs represent a potentially powerful therapeutic tool for the acute treatment of stroke. However, it seems important to redefine therapeutic biological targets in alignment with the current needs for improved recanalization and the reduction of hemorrhagic complications associated with existing stroke therapies. Furthermore, the feasibility of using this technology in AIS must be evaluated from the start, as speed is critical for patients' outcome, thus limiting

certain technologies or formulations. Ongoing studies are continually evaluating these aspects to determine the viability and efficacy of nanoparticle-based interventions in acute stroke care, but a rational design of such treatments must take into account the AIS specificity, meaning formulations that can be stored, reconstituted and administered quickly; and key development aspects should be addressed from the start, such as toxicity, biodistribution, feasibility of a scaled-up GMP synthesis, and relevance of *in vivo* experiments. With these considerations, these new treatment options could improve acute stroke patient care.

Developing polysaccharide hydrogel nanoparticles to deliver a combo treatment for thrombotic diseases

In this PhD project, we therefore developed NPs made of polysaccharide hydrogels in order to vectorize one or more drugs, in order to improve the thrombolytic treatment. Inspired by a previous protocol developed in the lab, we aimed at producing 100% polysaccharide particles, with dextran as base material. These particles were loaded with either rtPA or DNase I in order to achieve improved thrombolysis.

Hydrogel-based NPs offer several benefits, including generally good biocompatibility, high water content, and notably soft mechanical properties which bear resemblance to the extracellular matrix. Depending on how they are synthesized, they also exhibit the advantages of polymeric NPs, notably their versatility and high potential for functionalization through fine-tuning of various chemical moieties. Moreover, relying on polysaccharide as building blocks comes with several added benefits. These include general nontoxicity, biocompatibility and/or biodegradability and often innate biological properties. In addition, they are extracted from natural sources which can offer high availability and lower procurement costs. Dextran, notably, is associated with a long biomedical history, making it a reliable biomaterial component with known properties and low immunogenicity. Furthermore, it is a stable polysaccharide in the human body, with high functionalization potential and an especially interesting sourcing opportunity, as this polysaccharide already has broad commercial applications. While other similar nanogels based on polysaccharides were described, including dextran-based NPs for various applications [380,381,384,385], they usually involve different chemical modifications of dextran to achieve their formulation into NPs, like the acetal-modified dextran NPs described by Xu *et al.* in 2019 who used these for thrombus targeting, delivering neuroprotection [231]. The main goal for our

project was therefore to design low-complexity dextran-based hydrogel nanoparticle with minimal modification steps, based on a simple and robust synthesis protocol and involving as much as possible biocompatible and generally recognized as safe (GRAS) or FDA-approved materials status for all intrants. The polysaccharides used were dextran of a pharmaceutical grade, and fucoidan, the GMP formulation of which has been investigated in clinical trials already with good safety results [349]. Regarding the crosslinking, the STMP was chosen as it quickly hydrolyzes in water, and provides simple, physiologically compatible phosphate diester bonds compared to other more toxic crosslinkers (e.g., glutaraldehyde, photocrosslinkers). Moreover, the synthesis itself was a one-pot, simple process which involved sunflower oil as the oil phase instead of other organic solvents, and GRAS surfactants with notably PGPR, commonly used as emulsifier in the food industry. Since no chemical waste was produced with minimal byproducts, this synthesis overall satisfies green chemistry requirements.

Our Team has been working on such biocompatible drug delivery systems with a focus on polysaccharides for many years. Among them, core-shell cyanoacrylate NPs decorated with dextran and fucoidan [167] and fucoidan incorporating cyanoacrylate microbubbles [168,351] were developed and tested for thrombolytic purposes. Moreover, the initial protocol for the synthesis of polysaccharide-based hydrogel drug delivery systems was proposed by Bonnard *et al*. in 2014 [346,347], followed by improvements from Forero Ramirez *et al*. and Zenych *et al*. in 2020 and 2021 [168,352]: these protocols yielded particles ranging from 2.5 µm initially to 800-1500 nm in 2021. Here, we described how we modified this synthesis to reach an adequate size of 315 nm, with key outcomes: simplified protocol, high process robustness with low batch-to-batch variability, removal of the extra filtration steps, high stability without needing surfactant stabilization, and fitting the right size range to achieve homogenous distribution profile in the blood flow while avoiding endothelial internalization. These achievements were partly due to the incorporation of a theoretical framework, the HLD model for microemulsions, in order to achieve a fine control over the emulsion step in the synthesis. Consequently, a patent was filed to protect the resulting NPs and the microemulsion-based control over the emulsification step (application number EP23307118.2, see **ANNEX 4**). Overall, the synthesis was optimized through enhanced control of the crosslinking and emulsification steps. Nonetheless, further optimization to reach different sizes may be possible. For instance, reducing the HLD closer to 0 may achieve even smaller NPs, which may find other useful applications such as endothelium

crossing, stealth from phagocytes, etc. Moreover, despite some improvements to the post-production steps (i.e., purification and isolation), further optimization may be necessary to streamline the synthesis process up to the obtention of purified NPs. The implementation of this protocol in a scaled-up, GMP compliant manner with sterile conditions is also no simple task, requiring additional work to guarantee the NPs properties throughout production adjustments. This also includes cost-effectiveness: while it can be estimated that the current nanoparticle formulation, if formulated to reach the same dose as free rtPA current administration, only costs circa 80 € per patient (1/100th of the rtPA administration), the implementation of good quality control and industrial production may significantly increase this price, notably through the freeze-drying process [431]. Yet for research purposes, the current synthesis method was successful in producing robust batches of NPs with adequate size and low variability, and this stability bodes well for future developments. Hence, we characterized further the resulting NPs properties.

First, the size and stability of the obtained nanoparticles were assessed with Dynamic Light Scattering (DLS). The results demonstrated the improved robustness and stability of these nanoparticles over the previous protocol. Nonetheless, DLS as a single method may report biased results, especially depending on how the raw data is managed to extract the size. Therefore, we relied on Z-average and PDI as key measurements, since other interpolated measures can be misleading [432]. Moreover, we used TEM to verify both the sphericity and the size of the obtained NPs, which showed good adequacy with the DLS measurements. Nevertheless, using different methods to assess the NPs' population distribution may be useful, and, for instance, frit-inlet asymmetrical flow field-flow fractionation (FI-AF4) was described as a technique which explored the precise size distribution of such NPs, which may advantageously be used as a complement to DLS [433]. In addition, the measured zeta potential, representative of surface charge and measured by electrophoretic light scattering, was around -30 mV across a broad pH range: such negative values have been associated with good colloidal stability [377]. Moreover, negatively charged or neutral NPs have been described to exhibit less protein aggregation, cytotoxicity and membrane interaction than cationic NPs [434]. Further characterization included Fourier Transform Infrared (FTIR) and phosphate/sulphate quantification by both total reflection X-ray fluorescence (TXRF) and chemical titration methods, to validate phosphate bonds and fucoidan incorporation. More in-depth chemical characterization may be needed, including nuclear magnetic resonance (NMR) spectra. Notably,

preliminary nitrogen and proton spectra were acquired but the methods need to be refined for polysaccharide NPs. Other characterizations included verifying the re-suspensibility of freeze-dried NPs, their long-term stability and adequate in-flow behavior; we also verified the targeting properties of our NPs after fucoidan incorporation. While the latter was only assessed in this project through platelet aggregation *in vitro* and validated *in vivo*, the specifics of fucoidan targeting through P-selectin interaction in activated platelet and endothelium were investigated elsewhere [222,349,435,436]. Other targeting methods for thrombi have been described, ranging from single molecular target to using cellular membrane coating, while including among others smart targeting moiety with sequential targeting capacities. It could be interesting to compare how each strategy fares in thrombus targeting in the end, but in our case, the fucoidan incorporation as a polysaccharide in the dextran NPs was a simple and straightforward choice, which also provided with a proven and sensible approach for thrombus targeting based on multiple evidence [164,167,222,348,349,352,436].

Furthermore, we were able to vectorize two different drugs in our NPs by simple adsorption. On one hand, rtPA, the major fibrinolytic drug, was used for its thrombolytic potential and its several limitations that may benefit from vectorization and targeted delivery. Moreover, a targeted delivery to the thrombus can increase the local concentration of rtPA at the thrombus, overpowering inhibition and increasing the thrombolytic action at similar, or lower, total administered concentration, while reducing off-target side effects such as bleeding. Therefore, the total amount of injected drug may be lowered, which would reduce other side effects. rtPA was successfully loaded in fucoidan-bearing NPs (Fuco-NPs), while retaining its activity as measured by two concurring assays: the Pefafluor® kit allowed for precise quantification of the amidolytic enzymatic activity, and the fibrin agar plate assay (FAPA) demonstrated that the fibrinolytic activity itself was conserved. On the other hand, we vectorized DNase I in Fuco-NPs as a potential synergic agent with rtPA as described previously for arterial thrombolysis [67,72]. Despite a reduced activity of DNase I after loading in acidic conditions, DNase I, after loading in fucoidan-bearing NPs, retained the capacity to degrade NETs in an *in vitro* assay. Improvements to this loading condition could be made, for instance by performing a gentler loading through continuous acidification with stabilizing agents instead of abrupt pH variation as performed so far. In the future, the loading of other hydrophilic compounds could be investigated, as mentioned with N-acetylcysteine or its modified version, N-acetylcysteine amide, to address

another component of thrombi, the VWF multimers and potentially exert an antioxidant action. As investigated in “Part One. II. D) Applications of nanomedicine for stroke and clinical translation”, many other preclinical approaches (78% of the recent preclinical nanomedicine research for AIS) have favored neuroprotection over thrombolysis, and this may be a sensible approach for thrombotic disease management, as even recanalization is associated with specific damages to the penumbra through ischemia-reperfusion injury [75]. Therefore, assessing the delivery of neuroprotective drugs that may benefit from early targeted administration through P-selectin targeting of activated endothelial cells and platelets by our NPs would be of scientific interest. Nonetheless, recanalization, either spontaneous or through medical intervention, remains low and therefore there should be continuing efforts to improve thrombolysis. Even so, after considering the landscape of fibrinolytic drugs, rtPA (alteplase) may not be the most adequate plasminogen activator to vectorize, due to its cost and limited availability. Urokinase and reteplase for example, which benefit from easier and more cost-effective sourcing while displaying the absence of - or reduced - fibrin specificity, may also benefit from vectorization and offer an interesting alternative to alteplase as currently used.

Besides these characterizations, we verified the lack of toxicity of our NPs. First, this was verified by measuring the metabolic activity of a human endothelial cell line (HUVECs) after Fuco-NPs exposure, as well as with a hemolytic assay. This was in accordance with the lack of mortality during the *in vivo* experiments. While some animals died during the pilot phase, most likely due to the model establishment and anesthesia settings, only one animal died during the experiment out of 101 mice (this animal was treated with Fuco-NPs loaded with rtPA 1 mg/kg). Nonetheless, future developments of these NPs should include other biocompatibility assays. The biodistribution assay that we performed was limited in time and could only be done on animals with induced thrombosis. Therefore, the long-term toxicity and biodistribution should be measured in healthy animals, as well as the lack of immunogenicity and antigenicity with *in vivo* models. The former could be combined with studies to assess the biodegradability of our product, both *in vitro* with various physiological enzymes and *in vivo* or with adequate organ-on-chips. Most importantly, appropriate assays should be designed to specifically verify the reduced toxicity of rtPA loaded in Fuco-NPs compared to the free drug, including at the lower concentrations: these could include working with focal ischemia *in vivo* model, or bleeding-prone animals, to assess the absence of bleeding, neurotoxicity and hemorrhagic transformations.

In addition, we explored the thrombolytic potential of Fuco-NPs loaded with rtPA or DNase I. Starting with a static thrombolysis assay with artificial clots from human blood, we demonstrated that rtPA-loaded Fuco-NP retained the thrombolytic activity of rtPA. Furthermore, we observed that by modifying the artificial clot obtention method, we could either obtain thrombi that were responsive or not to DNase I addition to rtPA. While we verified that DNase I had no sufficient activity on its own as expected, some thrombi displayed increased thrombolysis through the synergy of DNase I and rtPA, which was also confirmed with the Fuco-NP formulations. Notably, the *in vivo* thrombolysis experiment with the $FeCl_3$ mesenteric vein thrombosis model in mice confirmed that, at the tested rtPA and DNase I concentrations, neither the free drugs nor the Fuco-NPs formulations exhibited any synergic action. These results shed further light on DNase I potentiating action through NETolysis in thrombi. While several studies have evidenced the extensive presence of NETs in veinous and arterial thrombi, most notably in the case of AIS thrombi [22,34], there may be differences in how NETs regulate the thrombosis and the final clot stability. Therefore, the synergic action of DNase I that was evidenced for AIS thrombi may not appear for other types of clots, and even the etiology of AIS thrombi may affect this response to a combo treatment [67,22,114]. Thus, it would be interesting to explore the action of Fuco-NP-rtPA and Fuco-NP-DNase in other *in vitro* and *in vivo* thrombi models, Among others, the *in vitro* model of AIS thrombi in a microfluidic setup developed by Astride Perrot and Benoit Ho-Tin-Noé, as evoked in “Experimental results. III. D) Preliminary works and future directions” may help the testing and comprehension of our proposed treatments through nanoparticle vectorization.

Most interestingly, we used the *in vivo* thrombosis model to investigate how the vectorization of rtPA by Fuco-NPs would compare to free rtPA administration. First, we observed no significant difference between saline and empty Fuco-NP treatments; even so, a slight increase in thrombus size with the empty Fuco-NP treatment could be seen, which may be the consequence of the added material content in the thrombus due to NPs targeting and accumulation on the thrombus. On the other hand, we described how the rtPA treatment, at the recommended dose for *in vivo* murine experiments, resulted in a very specific mechanism of action: while some thrombi displayed a size reduction over the observation period, 60% of them were associated with thrombus remodeling, resulting in clot departure from the observed blood vessel area. This phenomenon, which would cause further embolization in distal vessels, may be responsible for the limited efficacy of rtPA as observed in patients, and is

supported by other studies which reported how rtPA mediates thrombus fibrinolysis in a moving front manner [418]. Indeed, this behavior could explain the imperfect recanalization properties of rtPA. Furthermore, some authors may have reported the departure of the clot as a successful thrombolytic event depending on their imaging and analysis methods, which may overestimate the thrombolytic properties of the investigated formulations and neglect this specific mechanism of action. On the other hand, we found that treatment of thrombi with Fuco-NP loaded with rtPA at 5 mg/kg and 1 mg/kg (respectively 1/2 and $1/10^{th}$ of the recommended free rtPA dose) yielded systematic thrombus area reduction in a range similar to the non-departed free rtPA-treated clots, but with no observed departures. This means that both reduced rtPA-loaded Fuco-NPs treatments could reliably degrade the thrombus *in situ*, without displaying the rtPA typical clot departures and emboli risk. Therefore, in this thrombosis model, Fuco-NP loading of rtPA displayed an improved thrombolysis mechanism when compared to free rtPA 10 mg/kg, at 50% and 10% drug concentration. While these results are very promising, they should be validated in other *in vivo* thrombosis models to verify whether this phenomenon is model-dependent or not, and it should be complemented with long-term neurological assessments in order to investigate an eventual beneficial outcome.

General conclusion and Perspectives

Cardiovascular diseases pose an ever-growing burden on human health, responsible for a third of global deaths and are expected to keep increasing due to population aging, degrading environmental factors and the spread of unhealthy lifestyles. While primary prevention is a necessity and may significantly curb the number of premature deaths, this is yet insufficient and there is a dire need for therapeutic care. Acute thrombotic events like myocardial infarction and ischemic strokes are the major culprits of cardiovascular deaths, and despite several pharmaceutical treatments and interventional therapies, recanalization remains scarce with severe consequences. Notably, the main thrombolytic treatment, an intravenous injection of the fibrinolytic rtPA (alteplase), exhibits a limited efficacy as well as severe side effects (e.g., bleeding, neurotoxicity) and a short therapeutic window which limits its utilization. A partial explanation may lie in its short circulation half-life and focus on fibrinolysis to destroy thrombi that have a complex structure and composition. Nanomedicine is a scientific field focusing on ultrasmall objects with very specific properties that may offer alternative or improved thrombolytic treatment, including through targeted local delivery of various drugs.

The objective of this PhD was to develop an innovative targeting nanosized drug delivery system, formulated with biocompatible polysaccharides including dextran as base material for the nanoparticle structure and fucoidan for its affinity to P-selectin. These were capable of delivering several agents to improve the treatment of thrombotic diseases. We were able to successfully tailor the synthesis protocol to render it simpler, more robust and to produce adequately sized nanoparticles through a microemulsion framework, which resulted in a patent submission in 2023. These nanoparticles exhibited remarkable flow behavior and stability, and the fucoidan incorporation was validated, granting the capacity to target activated platelets and endothelium for thrombus targeting. Two different drugs, rtPA and a DNase I, could be loaded in these nanoparticles while retaining their desired enzymatic activity. The lack of toxicity was validated *in vitro* along with preliminary biodistribution results in mice. We investigated the thrombolytic potential of the combo of drugs loaded in nanoparticles *in vitro* and observe how different thrombi exhibited varying responses to treatment, and the *in vivo* results with a murine thrombosis model demonstrated an improved thrombolytic potential of lower doses of rtPA when loaded in fucoidan-containing nanoparticles than the recommended free drug concentration. The loading of other drug candidates as well as the investigation of the differential thrombus response to treatments are key aspects that will be

explored in the future, in addition to improving the formulation for an eventual scale-up and GMP compatible production for potential clinical translation.

Therefore, based on current results, our project with polysaccharide hydrogel NPs displayed promising perspectives for thrombolysis. Nonetheless, it is only a step in the general field of nanomedicine, and for nanomedicine application for thrombotic diseases and AIS management in particular. This project, and this thesis, inscribe themselves in a continuous research flow in our laboratory through the succession of various students and researchers, but also in a larger scheme with the contributions and general scientific advancement of our field. On its own, this project has for perspectives the valorization of the combined experience of our laboratory culminating in the current formulation as well as future developments, with for example the work of Pierre Sarfati, another PhD student working within our Team, who explores the potential vectorization of non-pharmaceutical methods for thrombolysis in similar polysaccharide drug delivery systems. Depending on the future preclinical results through extensive safety and efficacy tests, this valorization may take the form of a clinical study project, supported by the patents and know-how of our Team. However, this represents a long journey, with several hurdles and which will necessitate the involvement of many actors. Nevertheless, the scientific findings in our work may also benefit other teams and other projects, contributing to the general growth of our knowledge and perhaps sustaining other innovations. For example, these polysaccharide-based nanoparticles, and their simple and green chemistry compatible formulation, may open new directions for cost-effective yet efficient drug delivery systems with good biocompatibility. In addition, the example of how we improved the synthesis through the microemulsion framework might be transferred to other objects, such as nanoemulsions, polymerization or other nanoparticle synthesis. Finally, the considerations on thrombolysis through rtPA or DNase I in a combo treatment, the benefits of their vectorization, and the discussion on rtPA limited efficacy evidenced by the thrombus remodeling and departures may participate in future thrombolytic design and applications. There may yet be other developments, in our Teams with future students or outside, which remain to be discovered.

Personal conclusion

This project also opened other scientific perspectives, as I had the opportunity to work with Dr. Louise Fournier on microbubbles, notably through the writing of a review exploring their use for human diagnosis and treatment; and I was also involved in the animal wellness structure of our research unit through an expert mission with Université Paris Cité. In addition to the scientific aspect of this project, this PhD was also an extraordinary opportunity for me. At the beginning of 2021, despite several internships in research laboratories and Biotech companies, I was not sure yet of whether I would like to pursue this demanding but rewarding experience. In the end, I was convinced by several factors, not the least of which being Dr. Cédric Chauvierre's and Pr. Frédéric Chaubet's enthusiasm and trust. What attracted me was the possibility to work on a project focused on bringing concrete answers to theoretical research, and to be part of the whole process, from the synthesis optimization to initial preclinical studies. This was also an opportunity to push myself through these years and several steps, always finding balance between the big picture and the details of one day's work, which was not initially intuitive for me. Moreover, I had the chance of finding out how collaborative and fruitful research can be when you are surrounded by open-minded and benevolent researchers. As an engineer by formation, I did not bring expertise in one specific field, but I found joy in bridging different domains of biology, physics and pharmaceutical formulation together throughout this project, and I can confidently say that each day of this journey I learned something new in the company of amazing people. This PhD also presented with the opportunities to participate in five international conferences, one summer school and two young researchers' conferences, including three oral presentations and three posters, with one of each that were rewarded with a prize (**ANNEX 8** for the poster and **ANNEX 13** for the oral). During this project, I was lucky to be able to participate in the redaction of three reviews (including two as first authors, one of which is currently under review) and two research articles (including one as first author, currently under review), and one patent shared with Dr. Cédric Chauvierre. I could also undertake other responsibilities, including training students, participating in an expert mission for one year in the animal wellness structure of our Unit, and standing as the representative of PhD students at our doctoral school's council. Overall, this adventure was an incredible period of growth and getting to know myself better, surrounded by friends and colleagues, and the opportunity to marvel while doing science. Because in the end, to reference Sally Ride's quote, without curiosity and a certain dose of fun, science would be much less enjoyable and achieve far fewer achievements.

References

1. Global Burden of Disease Collaborative Network. Global Burden of Disease Study 2021 (GBD 2021) Results. [Internet]. Seattle, United States: Institute for Health Metrics and Evaluation (IHME); 2022 [cited 2024 Jul 30]. Available from: https://vizhub.healthdata.org/gbd-results

2. Ferrari AJ, Santomauro DF, Aali A, Abate YH, Abbafati C, Abbastabar H, et al. Global incidence, prevalence, years lived with disability (YLDs), disability-adjusted life-years (DALYs), and healthy life expectancy (HALE) for 371 diseases and injuries in 204 countries and territories and 811 subnational locations, 1990–2021: a systematic analysis for the Global Burden of Disease Study 2021. The Lancet. 2024 May 18;403(10440):2133–61.

3. Martin SS, Aday AW, Almarzooq ZI, Anderson CAM, Arora P, Avery CL, et al. 2024 Heart Disease and Stroke Statistics: A Report of US and Global Data From the American Heart Association. Circulation. 2024 Feb 20;149(8):e347–913.

4. Timmis A, Vardas P, Townsend N, Torbica A, Katus H, De Smedt D, et al. European Society of Cardiology: cardiovascular disease statistics 2021. Eur Heart J. 2022 Feb 21;43(8):716–99.

5. Tsao CW, Aday AW, Almarzooq ZI, Anderson CAM, Arora P, Avery CL, et al. Heart Disease and Stroke Statistics—2023 Update: A Report From the American Heart Association. Circulation. 2023 Feb 21;147(8):e93–621.

6. Folsom AR, Yatsuya H, Nettleton JA, Lutsey PL, Cushman M, Rosamond WD, et al. Community prevalence of ideal cardiovascular health, by the American Heart Association definition, and relationship with cardiovascular disease incidence. J Am Coll Cardiol. 2011 Apr 19;57(16):1690–6.

7. Reamy BV, Williams PM, Kuckel DP. Prevention of Cardiovascular Disease. Prim Care Clin Off Pract. 2018 Mar 1;45(1):25–44.

8. Critchley JA, Capewell S. Substantial potential for reductions in coronary heart disease mortality in the UK through changes in risk factor levels. J Epidemiol Community Health. 2003 Apr 1;57(4):243–7.

9. Ford ES, Ajani UA, Croft JB, Critchley JA, Labarthe DR, Kottke TE, et al. Explaining the Decrease in U.S. Deaths from Coronary Disease, 1980–2000. N Engl J Med. 2007 Jun 7;356(23):2388–98.

10. Capewell S, Ford ES, Croft JB, Critchley JA, Greenlund KJ, Labarthe DR. Cardiovascular risk factor trends and potential for reducing coronary heart

disease mortality in the United States of America. Bull World Health Organ. 2010 Feb;88(2):120–30.

11. Kotseva K, De Backer G, De Bacquer D, Rydén L, Hoes A, Grobbee D, et al. Primary prevention efforts are poorly developed in people at high cardiovascular risk: A report from the European Society of Cardiology EURObservational Research Programme EUROASPIRE V survey in 16 European countries. Eur J Prev Cardiol. 2021 May 8;28(4):370–9.

12. Sundquist K, Winkleby M, Ahlén H, Johansson SE. Neighborhood socioeconomic environment and incidence of coronary heart disease: a follow-up study of 25,319 women and men in Sweden. Am J Epidemiol. 2004 Apr 1;159(7):655–62.

13. Caleyachetty R, Echouffo-Tcheugui JB, Muennig P, Zhu W, Muntner P, Shimbo D. Association between cumulative social risk and ideal cardiovascular health in US adults: NHANES 1999–2006. Int J Cardiol. 2015 Jul 15;191:296–300.

14. Wong ND. Epidemiological studies of CHD and the evolution of preventive cardiology. Nat Rev Cardiol. 2014 May;11(5):276–89.

15. Alkarithi G, Duval C, Shi Y, Macrae FL, Ariëns RAS. Thrombus Structural Composition in Cardiovascular Disease. Arterioscler Thromb Vasc Biol. 2021 Sep;41(9):2370–83.

16. Fitzgerald ST, Liu Y, Dai D, Mereuta OM, Abbasi M, Larco JLA, et al. Novel Human Acute Ischemic Stroke Blood Clot Analogs for In Vitro Thrombectomy Testing. AJNR Am J Neuroradiol. 2021 Jul;42(7):1250–7.

17. Mackman N. Triggers, targets and treatments for thrombosis. Nature. 2008 Feb;451(7181):914–8.

18. Badimon L, Padró T, Vilahur G. Atherosclerosis, platelets and thrombosis in acute ischaemic heart disease. Eur Heart J Acute Cardiovasc Care. 2012 Apr;1(1):60–74.

19. Lippi G, Franchini M, Targher G. Arterial thrombus formation in cardiovascular disease. Nat Rev Cardiol. 2011 Sep;8(9):502–12.

20. Reininger AJ, Bernlochner I, Penz SM, Ravanat C, Smethurst P, Farndale RW, et al. A 2-Step Mechanism of Arterial Thrombus Formation Induced by Human Atherosclerotic Plaques. J Am Coll Cardiol. 2010 Mar 16;55(11):1147–58.

21. Kattula S, Byrnes JR, Wolberg AS. Fibrinogen and fibrin in hemostasis and thrombosis. Arterioscler Thromb Vasc Biol. 2017 Mar;37(3):e13–21.

22. Ho-Tin-Noé B, Desilles JP, Mazighi M. Thrombus composition and thrombolysis resistance in stroke. Res Pract Thromb Haemost. 2023 May 16;7(4):100178.

23. Gunning GM, McArdle K, Mirza M, Duffy S, Gilvarry M, Brouwer PA. Clot friction variation with fibrin content; implications for resistance to thrombectomy. J NeuroInterventional Surg. 2018 Jan 1;10(1):34–8.

24. Tutwiler V, Singh J, Litvinov RI, Bassani JL, Purohit PK, Weisel JW. Rupture of blood clots: Mechanics and pathophysiology. Sci Adv. 2020 Aug 26;6(35):eabc0496.

25. Macrae FL, Duval C, Papareddy P, Baker SR, Yuldasheva N, Kearney KJ, et al. A fibrin biofilm covers blood clots and protects from microbial invasion. J Clin Invest. 2018 Aug 1;128(8):3356–68.

26. Whelihan MF, Zachary V, Orfeo T, Mann KG. Prothrombin activation in blood coagulation: the erythrocyte contribution to thrombin generation. Blood. 2012 Nov 1;120(18):3837–45.

27. Yunoki K, Naruko T, Sugioka K, Inaba M, Iwasa Y, Komatsu R, et al. Erythrocyte-rich thrombus aspirated from patients with ST-elevation myocardial infarction: association with oxidative stress and its impact on myocardial reperfusion. Eur Heart J. 2012 Jun 1;33(12):1480–90.

28. Alapan Y, Little JA, Gurkan UA. Heterogeneous Red Blood Cell Adhesion and Deformability in Sickle Cell Disease. Sci Rep. 2014 Nov 24;4(1):7173.

29. Gelder JM van, Nair CH, Dhall DP. Erythrocyte aggregation and erythrocyte deformability modify the permeability of erythrocyte enriched fibrin network. Thromb Res. 1996 Apr 1;82(1):33–42.

30. Shantsila E, Lip GYH. The role of monocytes in thrombotic disorders. Thromb Haemost. 2009;102(11):916–24.

31. Merza M, Hartman H, Rahman M, Hwaiz R, Zhang E, Renström E, et al. Neutrophil Extracellular Traps Induce Trypsin Activation, Inflammation, and Tissue Damage in Mice With Severe Acute Pancreatitis. Gastroenterology. 2015 Dec;149(7):1920-1931.e8.

32. Rada B. Neutrophil Extracellular Traps. Methods Mol Biol Clifton NJ. 2019;1982:517–28.

33. Dömer D, Walther T, Möller S, Behnen M, Laskay T. Neutrophil Extracellular Traps Activate Proinflammatory Functions of Human Neutrophils. Front Immunol. 2021;12:636954.

34. Laridan E, Martinod K, Meyer SFD. Neutrophil Extracellular Traps in Arterial and Venous Thrombosis. Semin Thromb Hemost. 2019 Feb;45(01):086–93.

35. Martinod K, Wagner DD. Thrombosis: tangled up in NETs. Blood. 2014 May 1;123(18):2768–76.

36. Etulain J, Martinod K, Wong SL, Cifuni SM, Schattner M, Wagner DD. P-selectin promotes neutrophil extracellular trap formation in mice. Blood. 2015 Jul 9;126(2):242–6.

37. Longstaff C, Varjú I, Sótonyi P, Szabó L, Krumrey M, Hoell A, et al. Mechanical Stability and Fibrinolytic Resistance of Clots Containing Fibrin, DNA, and Histones. J Biol Chem. 2013 Mar 8;288(10):6946–56.

38. Jiménez-Alcázar M, Napirei M, Panda R, Köhler EC, Kremer Hovinga JA, Mannherz HG, et al. Impaired DNase1-mediated degradation of neutrophil extracellular traps is associated with acute thrombotic microangiopathies. J Thromb Haemost. 2015 May 1;13(5):732–42.

39. Khan F, Tritschler T, Kahn SR, Rodger MA. Venous thromboembolism. Lancet Lond Engl. 2021 Jul 3;398(10294):64–77.

40. van Moorsel MVA, de Maat S, Vercruysse K, van Leeuwen EM, Jacqmarcq C, Bonnard T, et al. VWF-targeted thrombolysis to overcome rh-tPA resistance in experimental murine ischemic stroke models. Blood. 2022 Dec 29;140(26):2844–8.

41. Ramos-Cabrer P, Campos F, Sobrino T, Castillo J. Targeting the Ischemic Penumbra. Stroke. 2011 Jan;42(1_suppl_1):S7–11.

42. Wolberg AS, Rosendaal FR, Weitz JI, Jaffer IH, Agnelli G, Baglin T, et al. Venous thrombosis. Nat Rev Dis Primer. 2015 May 7;1(1):1–17.

43. Chernysh IN, Nagaswami C, Kosolapova S, Peshkova AD, Cuker A, Cines DB, et al. The distinctive structure and composition of arterial and venous thrombi and pulmonary emboli. Sci Rep. 2020 Mar 20;10:5112.

44. Libby P. The changing landscape of atherosclerosis. Nature. 2021 Apr;592(7855):524–33.

45. Miller M, Stone NJ, Ballantyne C, Bittner V, Criqui MH, Ginsberg HN, et al. Triglycerides and Cardiovascular Disease. Circulation. 2011 May 24;123(20):2292–333.

46. Libby P, Hansson GK. From Focal Lipid Storage to Systemic Inflammation: JACC Review Topic of the Week. J Am Coll Cardiol. 2019 Sep 24;74(12):1594–607.

47. Owsiany KM, Alencar GF, Owens GK. Revealing the Origins of Foam Cells in Atherosclerotic Lesions. Arterioscler Thromb Vasc Biol. 2019 May;39(5):836–8.

48. Zhang F, Guo X, Xia Y, Mao L. An update on the phenotypic switching of vascular smooth muscle cells in the pathogenesis of atherosclerosis. Cell Mol Life Sci CMLS. 2021 Dec 22;79(1):6.

49. Burger PC, Wagner DD. Platelet P-selectin facilitates atherosclerotic lesion development. Blood. 2003 Apr 1;101(7):2661–6.

50. Feske SK. Ischemic Stroke. Am J Med. 2021 Dec 1;134(12):1457–64.

51. Roessler FC, Kalms N, Jann F, Kemmling A, Ribbat-Idel J, Stellmacher F, et al. First approach to distinguish between cardiac and arteriosclerotic emboli of individual stroke patients applying the histological THROMBEX-classification rule. Sci Rep. 2021 Apr 19;11(1):8433.

52. Abbasi M, Fitzgerald S, Ayers-Ringler J, Espina V, Mueller C, Rucker S, et al. Proteomic Analysis of Cardioembolic and Large Artery Atherosclerotic Clots Using Reverse Phase Protein Array Technology Reveals Key Cellular Interactions Within Clot Microenvironments. Cureus. 2021;13(2):e13499.

53. GBD 2019 Stroke Collaborators. Global, regional, and national burden of stroke and its risk factors, 1990-2019: a systematic analysis for the Global Burden of Disease Study 2019. Lancet Neurol. 2021 Oct;20(10):795–820.

54. CDC. Stroke Facts [Internet]. Stroke. 2024 [cited 2024 Aug 26]. Available from: https://www.cdc.gov/stroke/data-research/facts-stats/index.html

55. Chung J, Park SH, Kim N, Kim W, Park JH, Ko Y, et al. Trial of ORG 10172 in Acute Stroke Treatment (TOAST) Classification and Vascular Territory of Ischemic Stroke Lesions Diagnosed by Diffusion-Weighted Imaging. J Am Heart Assoc. 2014 Aug 15;3(4):e001119.

56. Adams HP, Bendixen BH, Kappelle LJ, Biller J, Love BB, Gordon DL, et al. Classification of subtype of acute ischemic stroke. Definitions for use in a multicenter clinical trial. TOAST. Trial of Org 10172 in Acute Stroke Treatment. Stroke. 1993 Jan;24(1):35–41.

57. Campbell BCV, De Silva DA, Macleod MR, Coutts SB, Schwamm LH, Davis SM, et al. Ischaemic stroke. Nat Rev Dis Primer. 2019 Oct 10;5(1):70.

58. Holmstedt CA, Turan TN, Chimowitz MI. Atherosclerotic intracranial arterial stenosis: risk factors, diagnosis, and treatment. Lancet Neurol. 2013 Nov;12(11):1106–14.

59. Velly L, Boumaza D, Simeone P. Cerebral Ischemia: Pathophysiology, Diagnosis, and Management. In: Ichai C, Quintard H, Orban JC, editors. Metabolic Disorders and Critically Ill Patients: From Pathophysiology to Treatment. Cham: Springer International Publishing; 2018. p. 301–25.

60. Candelario-Jalil E, Dijkhuizen RM, Magnus T. Neuroinflammation, Stroke, Blood-Brain Barrier Dysfunction, and Imaging Modalities. Stroke. 2022 May;53(5):1473–86.

61. Okada T, Suzuki H, Travis ZD, Zhang JH. The Stroke-Induced Blood-Brain Barrier Disruption: Current Progress of Inspection Technique, Mechanism, and Therapeutic Target. Curr Neuropharmacol. 2020 Dec;18(12):1187–212.

62. Arba F, Rinaldi C, Caimano D, Vit F, Busto G, Fainardi E. Blood-Brain Barrier Disruption and Hemorrhagic Transformation in Acute Ischemic Stroke: Systematic Review and Meta-Analysis. Front Neurol. 2020;11:594613.

63. Ahn SH, Hong R, Choo IS, Heo JH, Nam HS, Kang HG, et al. Histologic features of acute thrombi retrieved from stroke patients during mechanical reperfusion therapy. Int J Stroke Off J Int Stroke Soc. 2016 Dec;11(9):1036–44.

64. Di Meglio L, Desilles JP, Ollivier V, Nomenjanahary MS, Di Meglio S, Deschildre C, et al. Acute ischemic stroke thrombi have an outer shell that impairs fibrinolysis. Neurology. 2019 Oct 29;93(18):e1686–98.

65. Staessens S, Denorme F, Francois O, Desender L, Dewaele T, Vanacker P, et al. Structural analysis of ischemic stroke thrombi: histological indications for therapy resistance. Haematologica. 2020 Feb 1;105(2):498–507.

66. Laridan E, Denorme F, Desender L, François O, Andersson T, Deckmyn H, et al. Neutrophil extracellular traps in ischemic stroke thrombi. Ann Neurol. 2017;82(2):223–32.

67. Ducroux C, Di Meglio L, Loyau S, Delbosc S, Boisseau W, Deschildre C, et al. Thrombus Neutrophil Extracellular Traps Content Impair tPA-Induced Thrombolysis in Acute Ischemic Stroke. Stroke. 2018 Mar;49(3):754–7.

68. Kang L, Yu H, Yang X, Zhu Y, Bai X, Wang R, et al. Neutrophil extracellular traps released by neutrophils impair revascularization and vascular remodeling after stroke. Nat Commun. 2020 May 19;11(1):2488.

69. Novotny J, Oberdieck P, Titova A, Pelisek J, Chandraratne S, Nicol P, et al. Thrombus NET content is associated with clinical outcome in stroke and myocardial infarction. Neurology. 2020 Jun 2;94(22):e2346–60.

70. Brinjikji W, Mereuta OM, Dai D, Kallmes DF, Savastano L, Liu Y, et al. Mechanisms of fibrinolysis resistance and potential targets for thrombolysis in acute ischaemic stroke: lessons from retrieved stroke emboli. Stroke Vasc Neurol. 2021 Dec 1;6(4).

71. Denorme F, Portier I, Rustad JL, Cody MJ, Araujo CV de, Hoki C, et al. Neutrophil extracellular traps regulate ischemic stroke brain injury. J Clin Invest. 2022 May 16;132(10).

72. Peña-Martínez C, Durán-Laforet V, García-Culebras A, Ostos F, Hernández-Jiménez M, Bravo-Ferrer I, et al. Pharmacological Modulation of Neutrophil Extracellular Traps Reverses Thrombotic Stroke tPA (Tissue-Type Plasminogen Activator) Resistance. Stroke. 2019 Nov;50(11):3228–37.

73. Wang R, Zhu Y, Liu Z, Chang L, Bai X, Kang L, et al. Neutrophil extracellular traps promote tPA-induced brain hemorrhage via cGAS in mice with stroke. Blood. 2021 Jul 8;138(1):91–103.

74. Di Meglio L, Desilles JP, Solonomenjanahary M, Labreuche J, Ollivier V, Dupont S, et al. DNA Content in Ischemic Stroke Thrombi Can Help Identify Cardioembolic Strokes Among Strokes of Undetermined Cause. Stroke. 2020 Sep;51(9):2810–6.

75. Ma R, Xie Q, Li Y, Chen Z, Ren M, Chen H, et al. Animal models of cerebral ischemia: A review. Biomed Pharmacother. 2020 Nov 1;131:110686.

76. Ford G, Xu Z, Gates A, Jiang J, Ford BD. Expression Analysis Systematic Explorer (EASE) analysis reveals differential gene expression in permanent and transient focal stroke rat models. Brain Res. 2006 Feb 3;1071(1):226–36.

77. Rha JH, Saver JL. The impact of recanalization on ischemic stroke outcome: a meta-analysis. Stroke. 2007 Mar;38(3):967–73.

78. Mackman N, Bergmeier W, Stouffer GA, Weitz JI. Therapeutic strategies for thrombosis: new targets and approaches. Nat Rev Drug Discov. 2020 May;19(5):333–52.

79. Watson C, Saaid H, Vedula V, Cardenas JC, Henke PK, Nicoud F, et al. Venous Thromboembolism: Review of Clinical Challenges, Biology, Assessment, Treatment, and Modeling. Ann Biomed Eng. 2024 Mar 1;52(3):467–86.

80. Lebozec K, Jandrot-Perrus M, Avenard G, Favre-Bulle O, Billiald P. Design, development and characterization of ACT017, a humanized Fab that blocks platelet's glycoprotein VI function without causing bleeding risks. mAbs. 2017;9(6):945–58.

81. Eikelboom JW, Connolly SJ, Bosch J, Dagenais GR, Hart RG, Shestakovska O, et al. Rivaroxaban with or without Aspirin in Stable Cardiovascular Disease. N Engl J Med. 2017 Oct 5;377(14):1319–30.

82. Mican J, Toul M, Bednar D, Damborsky J. Structural Biology and Protein Engineering of Thrombolytics. Comput Struct Biotechnol J. 2019 Jul 2;17:917–38.

83. Baig MU, Bodle J. Thrombolytic Therapy. In: StatPearls. Treasure Island (FL): StatPearls Publishing; 2024.

84. Nikitin D, Choi S, Mican J, Toul M, Ryu WS, Damborsky J, et al. Development and Testing of Thrombolytics in Stroke. J Stroke. 2021 Jan;23(1):12–36.

85. Gurewich V. Therapeutic Fibrinolysis: How Efficacy and Safety Can Be Improved. J Am Coll Cardiol. 2016 Nov 8;68(19):2099–106.

86. Bhatia R, Hill MD, Shobha N, Menon B, Bal S, Kochar P, et al. Low Rates of Acute Recanalization With Intravenous Recombinant Tissue Plasminogen Activator in Ischemic Stroke. Stroke. 2010 Oct;41(10):2254–8.

87. de Havenon A, Sheth K, Johnston KC, Delic A, Stulberg E, Majersik J, et al. Acute Ischemic Stroke Interventions in the United States and Racial, Socioeconomic, and Geographic Disparities. Neurology. 2021 Dec 7;97(23):e2292–303.

88. Tsivgoulis G, Katsanos AH, Sandset EC, Turc G, Nguyen TN, Bivard A, et al. Thrombolysis for acute ischaemic stroke: current status and future perspectives. Lancet Neurol. 2023 May 1;22(5):418–29.

89. Gusev EI, Martynov MY, Nikonov AA, Shamalov NA, Semenov MP, Gerasimets EA, et al. Non-immunogenic recombinant staphylokinase versus alteplase for patients with acute ischaemic stroke 4·5 h after symptom onset in Russia (FRIDA): a randomised, open label, multicentre, parallel-group, non-inferiority trial. Lancet Neurol. 2021 Sep;20(9):721–8.

90. Fan G, Wu XG, Jiao WP, Zhang HK, Guo DL. Safety and efficacy of intracoronary recombinant human prourokinase administration in patients with acute myocardial infarction and ST-segment elevation: A meta-analysis of randomized controlled trials. Exp Ther Med. 2022 Nov 30;25(1):40.

91. Song H, Wang Y, Ma Q, Feng W, Liu R, Lv X, et al. Efficacy and Safety of Recombinant Human Prourokinase in the Treatment of Acute Ischemic Stroke Within 4.5 Hours of Stroke Onset. JAMA Netw Open. 2023 Jul 25;6(7):e2325415.

92. Mohammadi E, Seyedhosseini-Ghaheh H, Mahnam K, Jahanian-Najafabadi A, Mir Mohammad Sadeghi H. Reteplase: Structure, Function, and Production. Adv Biomed Res. 2019 Mar 20;8:19.

93. Sailer A, Revzin MV, Pollak J, Ayyagari R, Mojibian HR, Nezami N, et al. Deep Vein Thrombosis: Update on Mechanical Thrombectomy and Intravascular US. RadioGraphics. 2022 Oct;42(6):E184–5.

94. WRITING COMMITTEE MEMBERS, O'Gara PT, Kushner FG, Ascheim DD, Casey DE, Chung MK, et al. 2013 ACCF/AHA Guideline for the Management of ST-Elevation Myocardial Infarction. Circulation. 2013 Jan 29;127(4):e362–425.

95. Lawton JS, Tamis-Holland JE, Bangalore S, Bates ER, Beckie TM, Bischoff JM, et al. 2021 ACC/AHA/SCAI Guideline for Coronary Artery Revascularization: A Report of the American College of Cardiology/American Heart Association Joint Committee on Clinical Practice Guidelines. Circulation. 2022 Jan 18;145(3):e18–114.

96. Ahmad M, Mehta P, Reddivari AKR, Mungee S. Percutaneous Coronary Intervention. In: StatPearls. Treasure Island (FL): StatPearls Publishing; 2024.

97. Berkhemer OA, Fransen PSS, Beumer D, Berg LA van den, Lingsma HF, Yoo AJ, et al. A Randomized Trial of Intraarterial Treatment for Acute Ischemic Stroke. N Engl J Med. 2015 Jan 1;372(1):11–20.

98. Campbell BCV, Mitchell PJ, Kleinig TJ, Dewey HM, Churilov L, Yassi N, et al. Endovascular Therapy for Ischemic Stroke with Perfusion-Imaging Selection. N Engl J Med. 2015 Mar 12;372(11):1009–18.

99. Goyal M, Demchuk AM, Menon BK, Eesa M, Rempel JL, Thornton J, et al. Randomized Assessment of Rapid Endovascular Treatment of Ischemic Stroke. N Engl J Med. 2015 Mar 12;372(11):1019–30.

100. Saver JL, Goyal M, Bonafe A, Diener HC, Levy EI, Pereira VM, et al. Stent-Retriever Thrombectomy after Intravenous t-PA vs. t-PA Alone in Stroke. N Engl J Med. 2015 Jun 11;372(24):2285–95.

101. Jovin TG, Chamorro A, Cobo E, Miquel MA de, Molina CA, Rovira A, et al. Thrombectomy within 8 Hours after Symptom Onset in Ischemic Stroke. N Engl J Med. 2015 Jun 11;372(24):2296–306.

102. Nogueira RG, Jadhav AP, Haussen DC, Bonafe A, Budzik RF, Bhuva P, et al. Thrombectomy 6 to 24 Hours after Stroke with a Mismatch between Deficit and Infarct. N Engl J Med. 2018 Jan 4;378(1):11–21.

103. Lapergue B, Blanc R, Costalat V, Desal H, Saleme S, Spelle L, et al. Effect of Thrombectomy With Combined Contact Aspiration and Stent Retriever vs Stent Retriever Alone on Revascularization in Patients With Acute Ischemic Stroke and Large Vessel Occlusion: The ASTER2 Randomized Clinical Trial. JAMA. 2021 Sep 28;326(12):1158–69.

104. Turc G, Bhogal P, Fischer U, Khatri P, Lobotesis K, Mazighi M, et al. European Stroke Organisation (ESO) - European Society for Minimally Invasive Neurological Therapy (ESMINT) Guidelines on Mechanical Thrombectomy in Acute Ischemic Stroke. J Neurointerventional Surg. 2023 Aug;15(8):e8.

105. Etat des lieux et carte interactive | Société Française de Neuroradiologie [Internet]. 2020 [cited 2024 Sep 7]. Available from: https://www.sfnr.net/neuroradiologie-quotidien/thrombectomie/la-thrombectomie/etat-lieux-carte-interactive

106. Organisation de la prise en charge précoce de l'accident vasculaire cérébral ischémique aigu par thrombectomie mécanique [Internet]. Haute Autorité de Santé. 2018 [cited 2024 Sep 7]. Available from: https://www.has-sante.fr/jcms/c_2757616/fr/organisation-de-la-prise-en-charge-precoce-de-l-accident-vasculaire-cerebral-ischemique-aigu-par-thrombectomie-mecanique

107. Rai AT, Link PS, Domico JR. Updated estimates of large and medium vessel strokes, mechanical thrombectomy trends, and future projections indicate a relative flattening of the growth curve but highlight opportunities for expanding endovascular stroke care. J NeuroInterventional Surg. 2023 Dec 1;15(e3):e349–55.

108. Hacke W, Kaste M, Bluhmki E, Brozman M, Dávalos A, Guidetti D, et al. Thrombolysis with Alteplase 3 to 4.5 Hours after Acute Ischemic Stroke. N Engl J Med. 2008 Sep 25;359(13):1317–29.

109. Thomalla G, Simonsen CZ, Boutitie F, Andersen G, Berthezene Y, Cheng B, et al. MRI-Guided Thrombolysis for Stroke with Unknown Time of Onset. N Engl J Med. 2018 Aug 16;379(7):611–22.

110. Tsivgoulis G, Zand R, Katsanos AH, Goyal N, Uchino K, Chang J, et al. Safety of intravenous thrombolysis in stroke mimics: prospective 5-year study and comprehensive meta-analysis. Stroke. 2015 May;46(5):1281–7.

111. Ali-Ahmed F, Federspiel JJ, Liang L, Xu H, Sevilis T, Hernandez AF, et al. Intravenous Tissue Plasminogen Activator in Stroke Mimics. Circ Cardiovasc Qual Outcomes. 2019 Aug;12(8):e005609.

112. Keselman B, Cooray C, Vanhooren G, Bassi P, Consoli D, Nichelli P, et al. Intravenous thrombolysis in stroke mimics: results from the SITS

International Stroke Thrombolysis Register. Eur J Neurol. 2019 Aug;26(8):1091–7.

113. Yoshimura S, Sakai N, Okada Y, Kitagawa K, Kimura K, Tanahashi N, et al. Efficacy of Endovascular Treatment for Acute Cerebral Large-Vessel Occlusion: Analysis of Nationwide Prospective Registry. J Stroke Cerebrovasc Dis. 2014 May 1;23(5):1183–90.

114. Desilles J, Solo Nomenjanahary M, Consoli A, Ollivier V, Faille D, Bourrienne M, et al. Impact of COVID-19 on thrombus composition and response to thrombolysis: Insights from a monocentric cohort population of COVID-19 patients with acute ischemic stroke. J Thromb Haemost. 2022 Apr 1;20(4):919–28.

115. Kamin Mukaz D, Cushman M. Percutaneous Coronary Intervention in Acute Myocardial Infarction: Community Wealth Matters. J Am Heart Assoc. 2023 Sep 5;12(17):e031415.

116. Kleindorfer D, Broderick J, Demaerschalk B, Saver J. Cost of Alteplase Has More Than Doubled Over the Past Decade. Stroke. 2017 Jul;48(7):2000–2.

117. Khatib R, Arevalo YA, Berendsen MA, Prabhakaran S, Huffman MD. Presentation, Evaluation, Management, and Outcomes of Acute Stroke in Low- and Middle-Income Countries: A Systematic Review and Meta-Analysis. Neuroepidemiology. 2018;51(1–2):104–12.

118. Imaizumi S, Woolworth V, Fishman RA, Chan PH. Liposome-entrapped superoxide dismutase reduces cerebral infarction in cerebral ischemia in rats. Stroke. 1990 Sep;21(9):1312–7.

119. Strebhardt K, Ullrich A. Paul Ehrlich's magic bullet concept: 100 years of progress. Nat Rev Cancer. 2008 Jun;8(6):473–80.

120. Ehrlich P. Experimental Researches on Specific Therapy: On Immunity with special Reference to the Relationship between Distribution and Action of Antigens**[Reprinted (with amendments by the Ed.) from The Harben Lectures for 1907 of the Royal Institute of Public Health, London: Lewis, 1908; cf. Bibl. 200 and 181.]: FIRST HARBEN LECTURE††[Delivered in London, 5 June 1907.]. In: Himmelweit F, editor. The Collected Papers of Paul Ehrlich. Pergamon; 1960. p. 106–17.

121. Bayda S, Adeel M, Tuccinardi T, Cordani M, Rizzolio F. The History of Nanoscience and Nanotechnology: From Chemical–Physical Applications to Nanomedicine. Molecules. 2020 Jan;25(1).

122. Barenholz Y. Doxil®--the first FDA-approved nano-drug: lessons learned. J Control Release Off J Control Release Soc. 2012 Jun 10;160(2):117–34.

123. Zhang C, Yan L, Wang X, Zhu S, Chen C, Gu Z, et al. Progress, challenges, and future of nanomedicine. Nano Today. 2020 Dec 1;35:101008.

124. Blanco E, Shen H, Ferrari M. Principles of nanoparticle design for overcoming biological barriers to drug delivery. Nat Biotechnol. 2015 Sep;33(9):941–51.

125. Sarmah D, Banerjee M, Datta A, Kalia K, Dhar S, Yavagal DR, et al. Nanotechnology in the diagnosis and treatment of stroke. Drug Discov Today. 2021 Feb 1;26(2):585–92.

126. Navya PN, Daima HK. Rational engineering of physicochemical properties of nanomaterials for biomedical applications with nanotoxicological perspectives. Nano Converg. 2016 Feb 1;3:1.

127. Zhao Y, Sultan D, Liu Y. 2 - Biodistribution, Excretion, and Toxicity of Nanoparticles. In: Cui W, Zhao X, editors. Theranostic Bionanomaterials. Elsevier; 2019. p. 27–53. (Micro and Nano Technologies).

128. Hong C, Alser O, Gebran A, He Y, Joo W, Kokoroskos N, et al. Modulating Nanoparticle Size to Understand Factors Affecting Hemostatic Efficacy and Maximize Survival in a Lethal Inferior Vena Cava Injury Model. ACS Nano. 2022 Feb 22;16(2):2494–510.

129. Huang Y, Wang J, Jiang K, Chung EJ. Improving Kidney Targeting: The Influence of Nanoparticle Physicochemical Properties on Kidney Interactions. J Control Release Off J Control Release Soc. 2021 Jun 10;334:127–37.

130. Duan X, Li Y. Physicochemical Characteristics of Nanoparticles Affect Circulation, Biodistribution, Cellular Internalization, and Trafficking. Small. 2013;9(9–10):1521–32.

131. Alexis F, Pridgen E, Molnar LK, Farokhzad OC. Factors Affecting the Clearance and Biodistribution of Polymeric Nanoparticles. Mol Pharm. 2008 Aug 1;5(4):505–15.

132. Longmire M, Choyke PL, Kobayashi H. Clearance Properties of Nano-sized Particles and Molecules as Imaging Agents: Considerations and Caveats. Nanomed. 2008 Oct;3(5):703–17.

133. Navya PN, Daima HK. Rational engineering of physicochemical properties of nanomaterials for biomedical applications with nanotoxicological perspectives. Nano Converg. 2016 Feb 1;3:1.

134. Inggrid Setyawati M, Yong Tay C, Docter D, H. Stauber R, Tai Leong D. Understanding and exploiting nanoparticles' intimacy with the blood vessel and blood. Chem Soc Rev. 2015;44(22):8174–99.

135. Chen Y, Li D, Li Y, Wan J, Li J, Chen H. Margination of Stiffened Red Blood Cells Regulated By Vessel Geometry. Sci Rep. 2017;7.

136. Lee TR, Choi M, Kopacz AM, Yun SH, Liu WK, Decuzzi P. On the near-wall accumulation of injectable particles in the microcirculation: smaller is not better. Sci Rep. 2013 Jun 26;3(1):2079.

137. Müller K, Fedosov DA, Gompper G. Margination of micro- and nano-particles in blood flow and its effect on drug delivery. Sci Rep. 2014 May 2;4(1):4871.

138. D'Apolito R, Tomaiuolo G, Taraballi F, Minardi S, Kirui D, Liu X, et al. Red blood cells affect the margination of microparticles in synthetic microcapillaries and intravital microcirculation as a function of their size and shape. J Control Release Off J Control Release Soc. 2015 Nov 10;217:263–72.

139. Gentile F, Curcio A, Indolfi C, Ferrari M, Decuzzi P. The margination propensity of spherical particles for vascular targeting in the microcirculation. J Nanobiotechnology. 2008 Aug 15;6(1):9.

140. Waris A, Ali A, Khan AU, Asim M, Zamel D, Fatima K, et al. Applications of Various Types of Nanomaterials for the Treatment of Neurological Disorders. Nanomaterials. 2022 Jun 22;12(13):2140.

141. Moore TL, Cook AB, Bellotti E, Palomba R, Manghnani P, Spanò R, et al. Shape-specific microfabricated particles for biomedical applications: a review. Drug Deliv Transl Res. 2022 Aug 1;12(8):2019–37.

142. Ma J, Zhang S, Liu J, Liu F, Du F, Li M, et al. Targeted Drug Delivery to Stroke via Chemotactic Recruitment of Nanoparticles Coated with Membrane of Engineered Neural Stem Cells. Small. 2019;15(35):1902011.

143. Nie S. Understanding and overcoming major barriers in cancer nanomedicine. Nanomed. 2010 Jun;5(4):523–8.

144. Fournier L, de La Taille T, Chauvierre C. Microbubbles for human diagnosis and therapy. Biomaterials. 2023 Mar 1;294:122025.

145. Pellow C, Abenojar EC, Exner AA, Zheng G, Goertz DE. Concurrent visual and acoustic tracking of passive and active delivery of nanobubbles to tumors. Theranostics. 2020;10(25):11690–706.

146. Pellow C, Acconcia C, Zheng G, Goertz DE. Threshold-dependent nonlinear scattering from porphyrin nanobubbles for vascular and extravascular applications. Phys Med Biol. 2018 Oct;63(21):215001.

147. Imamura Y, Yamada S, Tsuboi S, Nakane Y, Tsukasaki Y, Komatsuzaki A, et al. Near-Infrared Emitting PbS Quantum Dots for in Vivo Fluorescence Imaging of the Thrombotic State in Septic Mouse Brain. Molecules. 2016 Aug 18;21(8):1080.

148. Pallavicini P, Chirico G, Taglietti A. Harvesting Light To Produce Heat: Photothermal Nanoparticles for Technological Applications and Biomedical Devices. Chem – Eur J. 2021;27(62):15361–74.

149. Kelly KL, Coronado E, Zhao LL, Schatz GC. The Optical Properties of Metal Nanoparticles: The Influence of Size, Shape, and Dielectric Environment. J Phys Chem B. 2003 Jan 1;107(3):668–77.

150. Khlebtsov NG. Optics and biophotonics of nanoparticles with a plasmon resonance. Quantum Electron. 2008 Jun 30;38(6):504.

151. Singh N, Varma A, Verma A, Maurya BN, Dash D. Relief from vascular occlusion using photothermal ablation of thrombus with a multimodal perspective. Nano Res. 2016 Aug 1;9(8):2327–37.

152. Farinha P, Coelho JMP, Reis CP, Gaspar MM. A Comprehensive Updated Review on Magnetic Nanoparticles in Diagnostics. Nanomaterials. 2021 Dec;11(12):3432.

153. Abenojar EC, Wickramasinghe S, Bas-Concepcion J, Samia ACS. Structural effects on the magnetic hyperthermia properties of iron oxide nanoparticles. Prog Nat Sci Mater Int. 2016 Oct 1;26(5):440–8.

154. Zhang Y, Liu Y, Zhang T, Wang Q, Huang L, Zhong Z, et al. Targeted Thrombolytic Therapy with Metal–Organic-Framework-Derived Carbon Based Platforms with Multimodal Capabilities. ACS Appl Mater Interfaces. 2021 Jun 2;13(21):24453–62.

155. Sarfati P, de La Taille T, Portioli C, Spanò R, Lalatonne Y, Decuzzi P, et al. REVIEW: “ISCHEMIC STROKE: from fibrinolysis to functional recovery” Nanomedicine: emerging approaches to treat ischemic stroke. Neuroscience. 2024 Jul 9;550:102–13.

156. Bernardo-Castro S, Albino I, Barrera-Sandoval ÁM, Tomatis F, Sousa JA, Martins E, et al. Therapeutic Nanoparticles for the Different Phases of Ischemic Stroke. Life. 2021 May 26;11(6):482.

157. Shan X, Gong X, Li J, Wen J, Li Y, Zhang Z. Current approaches of nanomedicines in the market and various stage of clinical translation. Acta Pharm Sin B. 2022 Jul 1;12(7):3028–48.

158. Namiot ED, Sokolov AV, Chubarev VN, Tarasov VV, Schiöth HB. Nanoparticles in Clinical Trials: Analysis of Clinical Trials, FDA Approvals and Use for COVID-19 Vaccines. Int J Mol Sci. 2023 Jan 2;24(1):787.

159. Wong CH, Siah KW, Lo AW. Estimation of clinical trial success rates and related parameters. Biostat Oxf Engl. 2019 Apr;20(2):273–86.

160. Zhong L, Li Y, Xiong L, Wang W, Wu M, Yuan T, et al. Small molecules in targeted cancer therapy: advances, challenges, and future perspectives. Signal Transduct Target Ther. 2021 May 31;6:201.

161. Wang Y, Jian C, Long Y, Xu X, Song Y, Yin Z. H2O2-triggered “off/on signal” nanoparticles target P-selectin for the non-invasive and contrast-enhanced theranostics for arterial thrombosis. Acta Biomater. 2023 Mar 1;158:769–81.

162. Deuchar GA, van Kralingen JC, Work LM, Santosh C, Muir KW, McCabe C, et al. Preclinical Validation of the Therapeutic Potential of Glasgow Oxygen Level Dependent (GOLD) Technology: a Theranostic for Acute Stroke. Transl Stroke Res. 2019 Oct;10(5):583–95.

163. Ye Q, Zheng D, Chen K, Xu H, Yang Z, Wen J, et al. Phase-Change Based Oxygen Carriers Improve Acute Cerebral Hypoxia. Small. 2023;n/a(n/a):2309180.

164. Fournier L, Abioui-Mourgues M, Chabouh G, Aid R, Taille TDL, Couture O, et al. rtPA-loaded fucoidan polymer microbubbles for the targeted treatment of stroke. Biomaterials. 2023 Dec 1;303:122385.

165. Han M, Zhang Z, Liu Z, Liu Y, Zhao H, Wang B, et al. Three-dimensional-cultured MSC-derived exosome with hydrogel for cerebral ischemia repair. Biomater Adv. 2023 Jun 1;149:213396.

166. Son JP, Kim EH, Shin EK, Kim DH, Sung JH, Oh MJ, et al. Mesenchymal Stem Cell-Extracellular Vesicle Therapy for Stroke: Scalable Production and Imaging Biomarker Studies. Stem Cells Transl Med. 2023 Jul 1;12(7):459–73.

167. Juenet M, Aid-Launais R, Li B, Berger A, Aerts J, Ollivier V, et al. Thrombolytic therapy based on fucoidan-functionalized polymer nanoparticles targeting P-selectin. Biomaterials. 2018 Feb 1;156:204–16.

168. Zenych A, Jacqmarcq C, Aid R, Fournier L, Forero Ramirez LM, Chaubet F, et al. Fucoidan-functionalized polysaccharide submicroparticles loaded

with alteplase for efficient targeted thrombolytic therapy. Biomaterials. 2021 Oct 1;277:121102.

169. Colasuonno M, Palange AL, Aid R, Ferreira M, Mollica H, Palomba R, et al. Erythrocyte-Inspired Discoidal Polymeric Nanoconstructs Carrying Tissue Plasminogen Activator for the Enhanced Lysis of Blood Clots. ACS Nano. 2018 Dec 26;12(12):12224–37.

170. Korin N, Kanapathipillai M, Matthews B, Crescente M, Brill A, Mammoto T, et al. Shear-Activated Nanotherapeutics for Drug Targeting to Obstructed Blood Vessels. Science. 2012 Jul 5;337:738–42.

171. Marsh JN, Senpan A, Hu G, Scott MJ, Gaffney PJ, Wickline SA, et al. Fibrin-targeted perfluorocarbon nanoparticles for targeted thrombolysis. Nanomed. 2007 Aug;2(4):533–43.

172. Marsh JN, Hu G, Scott MJ, Zhang H, Goette MJ, Gaffney PJ, et al. A fibrin-specific thrombolytic nanomedicine approach to acute ischemic stroke. Nanomed. 2011 Jun;6(4):605–15.

173. Kawata H, Uesugi Y, Soeda T, Takemoto Y, Sung JH, Umaki K, et al. A new drug delivery system for intravenous coronary thrombolysis with thrombus targeting and stealth activity recoverable by ultrasound. J Am Coll Cardiol. 2012 Dec 18;60(24):2550–7.

174. Wu H, Peng B, Mohammed FS, Gao X, Qin Z, Sheth KN, et al. Brain Targeting, Antioxidant Polymeric Nanoparticles for Stroke Drug Delivery and Therapy. Small. 2022;18(22):2107126.

175. Cheng Y, Cheng A, Jia Y, Yang L, Ning Y, Xu L, et al. pH-Responsive Multifunctional Theranostic Rapamycin-Loaded Nanoparticles for Imaging and Treatment of Acute Ischemic Stroke. ACS Appl Mater Interfaces. 2021 Dec 8;13(48):56909–22.

176. Lee Y, Lee J, Kim M, Kim G, Choi JS, Lee M. Brain gene delivery using histidine and arginine-modified dendrimers for ischemic stroke therapy. J Controlled Release. 2021 Feb 10;330:907–19.

177. Liu Y, Zhang T, Zou X, Yuan Z, Li Y, Zang J, et al. Penumbra-targeted CircOGDH siRNA-loaded nanoparticles alleviate neuronal apoptosis in focal brain ischaemia. Stroke Vasc Neurol. 2023 Jun 16;svn.

178. Tenchov R, Bird R, Curtze AE, Zhou Q. Lipid Nanoparticles─From Liposomes to mRNA Vaccine Delivery, a Landscape of Research Diversity and Advancement. ACS Nano. 2021 Nov 23;15(11):16982–7015.

179. Heeremans JL, Prevost R, Bekkers ME, Los P, Emeis JJ, Kluft C, et al. Thrombolytic treatment with tissue-type plasminogen activator (t-PA)

containing liposomes in rabbits: a comparison with free t-PA. Thromb Haemost. 1995 Mar;73(3):488–94.

180. Kim JY, Kim JK, Park JS, Byun Y, Kim CK. The use of PEGylated liposomes to prolong circulation lifetimes of tissue plasminogen activator. Biomaterials. 2009 Oct;30(29):5751–6.

181. Refaat A, del Rosal B, Palasubramaniam J, Pietersz G, Wang X, Peter K, et al. Smart Delivery of Plasminogen Activators for Efficient Thrombolysis; Recent Trends and Future Perspectives. Adv Ther. 2021;4(6):2100047.

182. Quan X, Liang X, Ding Y, Han Y, Li J, Yuan M, et al. Cryo-Shocked Platelet Coupled with ROS-Responsive Nanomedicine for Targeted Treatment of Thromboembolic Disease. ACS Nano. 2023 Apr 11;17(7):6519–33.

183. Sun S, Lv W, Li S, Zhang Q, He W, Min Z, et al. Smart Liposomal Nanocarrier Enhanced the Treatment of Ischemic Stroke through Neutrophil Extracellular Traps and Cyclic Guanosine Monophosphate-Adenosine Monophosphate Synthase-Stimulator of Interferon Genes (cGAS-STING) Pathway Inhibition of Ischemic Penumbra. ACS Nano. 2023 Sep 26;17(18):17845–57.

184. Ahmad S, Truran S, Karamanova N, Kindelin A, Lozoya M, Weissig V, et al. Nanoliposomes Reduce Stroke Injury Following Middle Cerebral Artery Occlusion in Mice. Stroke. 2022 Feb;53(2):e37–41.

185. Al-Ahmady ZS, Dickie BR, Aldred I, Jasim DA, Barrington J, Haley M, et al. Selective brain entry of lipid nanoparticles in haemorrhagic stroke is linked to biphasic blood-brain barrier disruption. Theranostics. 2022 May 26;12(10):4477–97.

186. Akbarzadeh A, Rezaei-Sadabady R, Davaran S, Joo SW, Zarghami N, Hanifehpour Y, et al. Liposome: classification, preparation, and applications. Nanoscale Res Lett. 2013 Feb 22;8(1):102.

187. Oude Blenke E, Örnskov E, Schöneich C, Nilsson GA, Volkin DB, Mastrobattista E, et al. The Storage and In-Use Stability of mRNA Vaccines and Therapeutics: Not A Cold Case. J Pharm Sci. 2023 Feb 1;112(2):386–403.

188. Ganbold T, Bao Q, Xiao H, Zurgaanjin D, Liu C, Han S, et al. Peptidomimetic Lipid-Nanoparticle-Mediated Knockdown of TLR4 in CNS Protects against Cerebral Ischemia/Reperfusion Injury in Mice. Nanomaterials. 2022 Jan;12(12):2072.

189. Huang G, Zang J, He L, Zhu H, Huang J, Yuan Z, et al. Bioactive Nanoenzyme Reverses Oxidative Damage and Endoplasmic Reticulum

Stress in Neurons under Ischemic Stroke. ACS Nano. 2022 Jan 25;16(1):431–52.

190. Dadfar SM, Roemhild K, Drude NI, von Stillfried S, Knüchel R, Kiessling F, et al. Iron oxide nanoparticles: Diagnostic, therapeutic and theranostic applications. Adv Drug Deliv Rev. 2019 Jan 1;138:302–25.

191. Voros E, Cho M, Ramirez M, Palange AL, De Rosa E, Key J, et al. TPA Immobilization on Iron Oxide Nanocubes and Localized Magnetic Hyperthermia Accelerate Blood Clot Lysis. Adv Funct Mater. 2015;25(11):1709–18.

192. Crist RM, Dasa SSK, Liu CH, Clogston JD, Dobrovolskaia MA, Stern ST. Challenges in the development of nanoparticle-based imaging agents: Characterization and biology. WIREs Nanomedicine Nanobiotechnology. 2021;13(1):e1665.

193. Kim BH, Lee N, Kim H, An K, Park YI, Choi Y, et al. Large-Scale Synthesis of Uniform and Extremely Small-Sized Iron Oxide Nanoparticles for High-Resolution T1 Magnetic Resonance Imaging Contrast Agents. J Am Chem Soc. 2011 Aug 17;133(32):12624–31.

194. Richard S, Eder V, Caputo G, Journé C, Ou P, Bolley J, et al. USPIO size control through microwave nonaqueous sol-gel method for neoangiogenesis T2 MRI contrast agent. Nanomed. 2016 Nov;11(21):2769–79.

195. Portioli C, Benati D, Pii Y, Bernardi P, Crucianelli M, Santucci S, et al. Short-Term Biodistribution of Cerium Oxide Nanoparticles in Mice: Focus on Brain Parenchyma. Nanosci Nanotechnol Lett. 2013 Nov 1;5(11):1174–81.

196. Li X, Han Z, Wang T, Ma C, Li H, Lei H, et al. Cerium oxide nanoparticles with antioxidative neurorestoration for ischemic stroke. Biomaterials. 2022 Dec 1;291:121904.

197. Kim JY, Ryu JH, Schellingerhout D, Sun IC, Lee SK, Jeon S, et al. Direct Imaging of Cerebral Thromboemboli Using Computed Tomography and Fibrin-targeted Gold Nanoparticles. Theranostics. 2015;5(10):1098–114.

198. Soenen S, Rivera Gil P, Montenegro JM, Parak W, De Smedt S, Braeckmans K. Cellular Toxicity of Inorganic Nanoparticles: Common Aspects and Guidelines for Improved Nanotoxicity Evaluation. Nano Today. 2011 Oct 1;6:446–65.

199. Feliu N, Docter D, Heine M, Del Pino P, Ashraf S, Kolosnjaj-Tabi J, et al. In vivo degeneration and the fate of inorganic nanoparticles. Chem Soc Rev. 2016 May 3;45(9):2440–57.

200. Sani A, Cao C, Cui D. Toxicity of gold nanoparticles (AuNPs): A review. Biochem Biophys Rep. 2021 Jul;26.

201. Bhatti R, Shakeel H, Malik K, Qasim M, Khan MA, Ahmed N, et al. Inorganic Nanoparticles: Toxic Effects, Mechanisms of Cytotoxicity and Phytochemical Interactions. Adv Pharm Bull. 2022 Aug;12(4):757–62.

202. Balfourier A, Luciani N, Wang G, Lelong G, Ersen O, Khelfa A, et al. Unexpected intracellular biodegradation and recrystallization of gold nanoparticles. Proc Natl Acad Sci U S A. 2020 Jan 7;117(1):103–13.

203. Ma YH, Wu SY, Wu T, Chang YJ, Hua MY, Chen JP. Magnetically targeted thrombolysis with recombinant tissue plasminogen activator bound to polyacrylic acid-coated nanoparticles. Biomaterials. 2009 Jul;30(19):3343–51.

204. Hu J, Huang S, Zhu L, Huang W, Zhao Y, Jin K, et al. Tissue Plasminogen Activator-Porous Magnetic Microrods for Targeted Thrombolytic Therapy after Ischemic Stroke. ACS Appl Mater Interfaces. 2018 Oct 3;10(39):32988–97.

205. Huang Z, Qian K, Chen J, Qi Y, E Y, Liang J, et al. A biomimetic zeolite-based nanoenzyme contributes to neuroprotection in the neurovascular unit after ischaemic stroke via efficient removal of zinc and ROS. Acta Biomater. 2022 May 1;144:142–56.

206. Sheta M, Taha EA, Lu Y, Eguchi T. Extracellular Vesicles: New Classification and Tumor Immunosuppression. Biology. 2023 Jan 10;12(1):110.

207. Doyle LM, Wang MZ. Overview of Extracellular Vesicles, Their Origin, Composition, Purpose, and Methods for Exosome Isolation and Analysis. Cells. 2019 Jul 15;8(7):727.

208. Zhu ZH, Jia F, Ahmed W, Zhang GL, Wang H, Lin CQ, et al. Neural stem cell-derived exosome as a nano-sized carrier for BDNF delivery to a rat model of ischemic stroke. Neural Regen Res. 2023 Feb;18(2):404.

209. Brown AT, Arthur MC, Nix JS, Montgomery JA, Skinner RD, Roberson PK, et al. Dodecafluoropentane Emulsion (DDFPe) Decreases Stroke Size and Improves Neurological Scores in a Permanent Occlusion Rat Stroke Model. Open Neurol J. 2014;8:27–33.

210. Fitzgerald RT, Ou X, Nix JS, Arthur MC, Brown AT, Skinner RD, et al. Dodecafluoropentane emulsion delays and reduces MRI markers of infarction in a rat stroke model: a preliminary report. Magn Reson Imaging. 2015 Feb;33(2):236–9.

211. Culp WC, Onteddu SS, Brown A, Nalleballe K, Sharma R, Skinner RD, et al. Dodecafluoropentane Emulsion in Acute Ischemic Stroke: A Phase Ib/II Randomized and Controlled Dose-Escalation Trial. J Vasc Interv Radiol JVIR. 2019 Aug;30(8):1244-1250.e1.

212. Cheng HY, Wang YS, Hsu PY, Chen CY, Liao YC, Juo SHH. miR-195 Has a Potential to Treat Ischemic and Hemorrhagic Stroke through Neurovascular Protection and Neurogenesis. Mol Ther - Methods Clin Dev. 2019 Jun 14;13:121–32.

213. Zhong Y, Gong WJ, Gao XH, Li YN, Liu K, Hu YG, et al. Synthesis and evaluation of a novel nanoparticle carrying urokinase used in targeted thrombolysis. J Biomed Mater Res A. 2020;108(2):193–200.

214. Otake H, Yamaguchi M, Ogata F, Deguchi S, Yamamoto N, Sasaki H, et al. Transdermal System Based on Solid Cilostazol Nanoparticles Attenuates Ischemia/Reperfusion-Induced Brain Injury in Mice. Nanomaterials. 2021 Apr;11(4):1009.

215. Zhang S, Peng B, Chen Z, Yu J, Deng G, Bao Y, et al. Brain-targeting, acid-responsive antioxidant nanoparticles for stroke treatment and drug delivery. Bioact Mater. 2022 Oct;16:57–65.

216. Zhou M, Zhang T, Zhang B, Zhang X, Gao S, Zhang T, et al. A DNA Nanostructure-Based Neuroprotectant against Neuronal Apoptosis via Inhibiting Toll-like Receptor 2 Signaling Pathway in Acute Ischemic Stroke. ACS Nano. 2022 Jan 25;16(1):1456–70.

217. Nian K, Harding IC, Herman IM, Ebong EE. Blood-Brain Barrier Damage in Ischemic Stroke and Its Regulation by Endothelial Mechanotransduction. Front Physiol. 2020;11.

218. Yuan J, Li L, Yang Q, Ran H, Wang J, Hu K, et al. Targeted Treatment of Ischemic Stroke by Bioactive Nanoparticle-Derived Reactive Oxygen Species Responsive and Inflammation-Resolving Nanotherapies. ACS Nano. 2021 Oct 26;15(10):16076–94.

219. Knowland D, Arac A, Sekiguchi KJ, Hsu M, Lutz SE, Perrino J, et al. Stepwise Recruitment of Transcellular and Paracellular Pathways Underlies Blood-Brain Barrier Breakdown in Stroke. Neuron. 2014 May 7;82(3):603–17.

220. Liao J, Ren X, Yang B, Li H, Zhang Y, Yin Z. Targeted thrombolysis by using c-RGD-modified N,N,N-Trimethyl Chitosan nanoparticles loaded with lumbrokinase. Drug Dev Ind Pharm. 2019 Jan 2;45(1):88–95.

221. Cao W, Liu Y, Ran P, He J, Xie S, Weng J, et al. Ultrasound-Propelled Janus Rod-Shaped Micromotors for Site-Specific Sonodynamic Thrombolysis. ACS Appl Mater Interfaces. 2021 Dec 15;13(49):58411–21.

222. Bachelet L, Bertholon I, Lavigne D, Vassy R, Jandrot-Perrus M, Chaubet F, et al. Affinity of low molecular weight fucoidan for P-selectin triggers its binding to activated human platelets. Biochim Biophys Acta BBA - Gen Subj. 2009 Feb 1;1790(2):141–6.

223. Pan Y, Ren X, Wang S, Li X, Luo X, Yin Z. Annexin V-Conjugated Mixed Micelles as a Potential Drug Delivery System for Targeted Thrombolysis. Biomacromolecules. 2017 Mar 13;18(3):865–76.

224. Zhao Y, Xie R, Yodsanit N, Ye M, Wang Y, Gong S. Biomimetic fibrin-targeted and H2O2-responsive nanocarriers for thrombus therapy. Nano Today. 2020 Dec 1;35:100986.

225. Seo J, Al-Hilal TA, Jee JG, Kim YL, Kim HJ, Lee BH, et al. A targeted ferritin-microplasmin based thrombolytic nanocage selectively dissolves blood clots. Nanomedicine Nanotechnol Biol Med. 2018 Apr;14(3):633–42.

226. Wang Z, Zhao Y, Jiang Y, Lv W, Wu L, Wang B, et al. Enhanced anti-ischemic stroke of ZL006 by T7-conjugated PEGylated liposomes drug delivery system. Sci Rep. 2015 Jul 29;5(1):12651.

227. Sun M, Miyazawa K, Pendekanti T, Razmi A, Firlar E, Yang S, et al. Combination targeting of ‘platelets + fibrin’ enhances clot anchorage efficiency of nanoparticles for vascular drug delivery. Nanoscale. 2020 Oct 29;12(41):21255–70.

228. Pawlowski CL, Li W, Sun M, Ravichandran K, Hickman D, Kos C, et al. Platelet microparticle-inspired clot-responsive nanomedicine for targeted fibrinolysis. Biomaterials. 2017 Jun;128:94–108.

229. Zhang Y, Zhong Y, Ye M, Xu J, Liu J, Zhou J, et al. Polydopamine-modified dual-ligand nanoparticles as highly effective and targeted magnetic resonance/photoacoustic dual-modality thrombus imaging agents. Int J Nanomedicine. 2019 Sep 3;14:7155–71.

230. Zhao Y, Jiang Y, Lv W, Wang Z, Lv L, Wang B, et al. Dual targeted nanocarrier for brain ischemic stroke treatment. J Controlled Release. 2016 Jul 10;233:64–71.

231. Xu J, Wang X, Yin H, Cao X, Hu Q, Lv W, et al. Sequentially Site-Specific Delivery of Thrombolytics and Neuroprotectant for Enhanced Treatment of Ischemic Stroke. ACS Nano. 2019 Aug 27;13(8):8577–88.

232. Xu J, Zhang Y, Xu J, Liu G, Di C, Zhao X, et al. Engineered Nanoplatelets for Targeted Delivery of Plasminogen Activators to Reverse Thrombus in Multiple Mouse Thrombosis Models. Adv Mater. 2020;32(4):1905145.

233. Yu W, Yin N, Yang Y, Xuan C, Liu X, Liu W, et al. Rescuing ischemic stroke by biomimetic nanovesicles through accelerated thrombolysis and sequential ischemia-reperfusion protection. Acta Biomater. 2022 Mar 1;140:625–40.

234. He W, Mei Q, Li J, Zhai Y, Chen Y, Wang R, et al. Preferential Targeting Cerebral Ischemic Lesions with Cancer Cell-Inspired Nanovehicle for Ischemic Stroke Treatment. Nano Lett. 2021 Apr 14;21(7):3033–43.

235. Li C, Zhao Z, Luo Y, Ning T, Liu P, Chen Q, et al. Macrophage-Disguised Manganese Dioxide Nanoparticles for Neuroprotection by Reducing Oxidative Stress and Modulating Inflammatory Microenvironment in Acute Ischemic Stroke. Adv Sci. 2021 Aug 26;8(20):2101526.

236. Kim HY, Kim TJ, Kang L, Kim YJ, Kang MK, Kim J, et al. Mesenchymal stem cell-derived magnetic extracellular nanovesicles for targeting and treatment of ischemic stroke. Biomaterials. 2020 Jun 1;243:119942.

237. Li M, Li J, Chen J, Liu Y, Cheng X, Yang F, et al. Platelet Membrane Biomimetic Magnetic Nanocarriers for Targeted Delivery and in Situ Generation of Nitric Oxide in Early Ischemic Stroke. ACS Nano. 2020 Feb 25;14(2):2024–35.

238. Shapiro B, Kulkarni S, Nacev A, Muro S, Stepanov PY, Weinberg IN. Open Challenges in Magnetic Drug Targeting. Wiley Interdiscip Rev Nanomed Nanobiotechnol. 2015 May;7(3):446–57.

239. Tian T, Cao L, He C, Ye Q, Liang R, You W, et al. Targeted delivery of neural progenitor cell-derived extracellular vesicles for anti-inflammation after cerebral ischemia. Theranostics. 2021 Apr 19;11(13):6507–21.

240. Goujon G, Baldim V, Roques C, Bia N, Seguin J, Palmier B, et al. Antioxidant Activity and Toxicity Study of Cerium Oxide Nanoparticles Stabilized with Innovative Functional Copolymers. Adv Healthc Mater. 2021;10(11):2100059.

241. Peinado MÁ, Ovelleiro D, del Moral ML, Hernández R, Martínez-Lara E, Siles E, et al. Biological Implications of a Stroke Therapy Based in Neuroglobin Hyaluronate Nanoparticles. Neuroprotective Role and Molecular Bases. Int J Mol Sci. 2022 Jan;23(1):247.

242. Yang H, Luo Y, Hu H, Yang S, Li Y, Jin H, et al. pH-Sensitive, Cerebral Vasculature-Targeting Hydroxyethyl Starch Functionalized Nanoparticles

for Improved Angiogenesis and Neurological Function Recovery in Ischemic Stroke. Adv Healthc Mater. 2021;10(12):2100028.

243. Yu H, Palazzolo JS, Zhou J, Hu Y, Niego B, Pan S, et al. Bioresponsive Polyphenol-Based Nanoparticles as Thrombolytic Drug Carriers. ACS Appl Mater Interfaces. 2022 Jan 26;14(3):3740–51.

244. Zhang H, Zhao Z, Sun S, Zhang S, Wang Y, Zhang X, et al. Molecularly self-fueled nano-penetrator for nonpharmaceutical treatment of thrombosis and ischemic stroke. Nat Commun. 2023 Jan 17;14(1):255.

245. Zhang F, Liu Y, Lei J, Wang S, Ji X, Liu H, et al. Metal–Organic-Framework-Derived Carbon Nanostructures for Site-Specific Dual-Modality Photothermal/Photodynamic Thrombus Therapy. Adv Sci. 2019;6(17):1901378.

246. Shekhar H, Kleven RT, Peng T, Palaniappan A, Karani KB, Huang S, et al. In vitro characterization of sonothrombolysis and echocontrast agents to treat ischemic stroke. Sci Rep. 2019 Jul 9;9:9902.

247. Choi W, Key J, Youn I, Lee H, Han S. Cavitation-assisted sonothrombolysis by asymmetrical nanostars for accelerated thrombolysis. J Controlled Release. 2022 Oct 1;350:870–85.

248. Guan L, Wang C, Yan X, Liu L, Li Y, Mu Y. Author Correction: A thrombolytic therapy using diagnostic ultrasound combined with RGDS-targeted microbubbles and urokinase in a rabbit model. Sci Rep. 2020 Sep 22;10(1):15767.

249. Tang C, Wang Q, Li K, Li X, Wang C, Xue L, et al. A neutrophil-mimetic magnetic nanoprobe for molecular magnetic resonance imaging of stroke-induced neuroinflammation. Biomater Sci. 2021 Jul 27;9(15):5247–58.

250. Yao S, He C, Yuan P, Xu X, Zhou X, Shen L, et al. Real-Time Objective Evaluation of the Ischemic Stroke through pH-Responsive Fluorescence Imaging. Adv Healthc Mater. 2023;12(9):2201981.

251. Debatisse J, Eker OF, Wateau O, Cho TH, Wiart M, Ramonet D, et al. PET-MRI nanoparticles imaging of blood–brain barrier damage and modulation after stroke reperfusion. Brain Commun. 2020 Nov 11;2(2):fcaa193.

252. Hoogendijk E, Swider E, Staal AHJ, White PB, van Riessen NK, Glaßer G, et al. Continuous-Flow Production of Perfluorocarbon-Loaded Polymeric Nanoparticles: From the Bench to Clinic. ACS Appl Mater Interfaces. 2020 Nov 4;12(44):49335–45.

253. Huang L, Wang J, Huang S, Siaw-Debrah F, Nyanzu M, Zhuge Q. Polyacrylic acid-coated nanoparticles loaded with recombinant tissue

plasminogen activator for the treatment of mice with ischemic stroke. Biochem Biophys Res Commun. 2019 Aug 20;516(2):565–70.

254. Fukuta T, Ikeda-Imafuku M, Iwao Y. Development of Edaravone Ionic Liquids and Their Application for the Treatment of Cerebral Ischemia/Reperfusion Injury. Mol Pharm. 2023 Jun 5;20(6):3115–26.

255. Liu S, Xu J, Liu Y, You Y, Xie L, Tong S, et al. Neutrophil-Biomimetic "Nanobuffer" for Remodeling the Microenvironment in the Infarct Core and Protecting Neurons in the Penumbra via Neutralization of Detrimental Factors to Treat Ischemic Stroke. ACS Appl Mater Interfaces. 2022 Jun 22;14(24):27743–61.

256. McBride DW, Zhang JH. Precision Stroke Animal Models: the Permanent MCAO Model Should Be the Primary Model, Not Transient MCAO. Transl Stroke Res. 2017 Oct 1;8(5):397–404.

257. Shi J, Yu W, Xu L, Yin N, Liu W, Zhang K, et al. Bioinspired Nanosponge for Salvaging Ischemic Stroke via Free Radical Scavenging and Self-Adapted Oxygen Regulating. Nano Lett. 2020 Jan 8;20(1):780–9.

258. Tang L, Yin Y, Liu H, Zhu M, Cao Y, Feng J, et al. Blood–Brain Barrier-Penetrating and Lesion-Targeting Nanoplatforms Inspired by the Pathophysiological Features for Synergistic Ischemic Stroke Therapy. Adv Mater. 2024;2312897.

259. Ashafaq M, Intakhab Alam M, Khan A, Islam F, Khuwaja G, Hussain S, et al. Nanoparticles of resveratrol attenuates oxidative stress and inflammation after ischemic stroke in rats. Int Immunopharmacol. 2021 May 1;94:107494.

260. Liao J, Li Y, Fan L, Sun Y, Gu Z, Xu QQ, et al. Bioactive Ceria Nanoenzymes Target Mitochondria in Reperfusion Injury to Treat Ischemic Stroke. ACS Nano. 2024 Jan 24;18(7):5510–29.

261. He L, Huang G, Liu H, Sang C, Liu X, Chen T. Highly bioactive zeolitic imidazolate framework-8-capped nanotherapeutics for efficient reversal of reperfusion-induced injury in ischemic stroke. Sci Adv. 2020 Mar;6(12):eaay9751.

262. Yan BC, Cao J, Liu J, Gu Y, Xu Z, Li D, et al. Dietary Fe3O4 Nanozymes Prevent the Injury of Neurons and Blood–Brain Barrier Integrity from Cerebral Ischemic Stroke. ACS Biomater Sci Eng. 2021 Jan 11;7(1):299–310.

263. Li Y, Liu B, Zhao T, Quan X, Han Y, Cheng Y, et al. Comparative study of extracellular vesicles derived from mesenchymal stem cells and brain endothelial cells attenuating blood–brain barrier permeability via regulating

Caveolin-1-dependent ZO-1 and Claudin-5 endocytosis in acute ischemic stroke. J Nanobiotechnology. 2023 Feb 28;21(1):70.

264. Zhang A, Li J, Wang S, Xu Y, Li Q, Wu Z, et al. Rapid and improved oral absorption of N-butylphthalide by sodium cholate-appended liposomes for efficient ischemic stroke therapy. Drug Deliv. 2021 Jan 1;28(1):2469–79.

265. Woods SD, Skinner RD, Ricca AM, Brown AT, Lowery JD, Borrelli MJ, et al. Progress in Dodecafluoropentane Emulsion as a Neuroprotective Agent in a Rabbit Stroke Model. Mol Neurobiol. 2013 Oct 1;48(2):363–7.

266. Alexandrov AV, Molina CA, Grotta JC, Garami Z, Ford SR, Alvarez-Sabin J, et al. Ultrasound-Enhanced Systemic Thrombolysis for Acute Ischemic Stroke. N Engl J Med. 2004 Nov 18;351(21):2170–8.

267. Ricci S, Dinia L, Del Sette M, Anzola P, Mazzoli T, Cenciarelli S, et al. Sonothrombolysis for acute ischaemic stroke. Cochrane Database Syst Rev. 2012 Jun 13;(6):CD008348.

268. Tsivgoulis G, Eggers J, Ribo M, Perren F, Saqqur M, Rubiera M, et al. Safety and Efficacy of Ultrasound-Enhanced Thrombolysis. Stroke. 2010 Feb;41(2):280–7.

269. Alexandrov AV, Köhrmann M, Soinne L, Tsivgoulis G, Barreto AD, Demchuk AM, et al. Safety and efficacy of sonothrombolysis for acute ischaemic stroke: a multicentre, double-blind, phase 3, randomised controlled trial. Lancet Neurol. 2019 Apr;18(4):338–47.

270. Daffertshofer M, Gass A, Ringleb P, Sitzer M, Sliwka U, Els T, et al. Transcranial Low-Frequency Ultrasound-Mediated Thrombolysis in Brain Ischemia. Stroke. 2005 Jul;36(7):1441–6.

271. Molina CA, Ribo M, Rubiera M, Montaner J, Santamarina E, Delgado-Mederos R, et al. Microbubble Administration Accelerates Clot Lysis During Continuous 2-MHz Ultrasound Monitoring in Stroke Patients Treated With Intravenous Tissue Plasminogen Activator. Stroke. 2006 Feb;37(2):425–9.

272. Nacu A, Kvistad CE, Logallo N, Naess H, Waje-Andreassen U, Aamodt AH, et al. A pragmatic approach to sonothrombolysis in acute ischaemic stroke: the Norwegian randomised controlled sonothrombolysis in acute stroke study (NOR-SASS). BMC Neurol. 2015 Jul 11;15(1):110.

273. Saleh A, Schroeter M, Ringelstein A, Hartung HP, Siebler M, Mödder U, et al. Iron oxide particle-enhanced MRI suggests variability of brain inflammation at early stages after ischemic stroke. Stroke. 2007 Oct;38(10):2733–7.

274. Niu Y, Tan H, Li X, Zhao L, Xie Z, Zhang Y, et al. Protein–Carbon Dot Nanohybrid-Based Early Blood–Brain Barrier Damage Theranostics. ACS Appl Mater Interfaces. 2020 Jan 22;12(3):3445–52.

275. Victor M de S, Barnsley LC, Carugo D, Owen J, Coussios CC, Stride E. Sonothrombolysis with Magnetically Targeted Microbubbles. Ultrasound Med Biol. 2019 May 1;45(5):1151–63.

276. Mei T, Kim A, Vong LB, Marushima A, Puentes S, Matsumaru Y, et al. Encapsulation of tissue plasminogen activator in pH-sensitive self-assembled antioxidant nanoparticles for ischemic stroke treatment – Synergistic effect of thrombolysis and antioxidant –. Biomaterials. 2019 Sep 1;215:119209.

277. Kong J, Zou R, Chu R, Hu N, Liu J, Sun Y, et al. An Ultrasmall Cu/Cu2O Nanoparticle-Based Diselenide-Bridged Nanoplatform Mediating Reactive Oxygen Species Scavenging and Neuronal Membrane Enhancement for Targeted Therapy of Ischemic Stroke. ACS Nano. 2023 Dec 22;

278. Zhang B, Li Q, Jia S, Li F, Li Q, Li J. LincRNA-EPS in biomimetic vesicles targeting cerebral infarction promotes inflammatory resolution and neurogenesis. J Transl Med. 2020 Mar 2;18(1):110.

279. Han R, Lan X, Han Z, Ren H, Aafreen S, Wang W, et al. Improving outcomes in intracerebral hemorrhage through microglia/macrophage-targeted IL-10 delivery with phosphatidylserine liposomes. Biomaterials. 2023 Oct 1;301:122277.

280. Zhao T, He F, Zhao K, Yuxia L, Li H, Liu X, et al. A Triple-Targeted Rutin-Based Self-Assembled Delivery Vector for Treating Ischemic Stroke by Vascular Normalization and Anti-Inflammation via ACE2/Ang1-7 Signaling. ACS Cent Sci. 2023 Jun 28;9(6):1180–99.

281. Chen YY, Gong ZC, Zhang MM, Huang ZH. Brain-Targeting Emodin Mitigates Ischemic Stroke via Inhibiting AQP4-Mediated Swelling and Neuroinflammation. Transl Stroke Res. 2024 Aug 1;15(4):818–30.

282. Kim H, Kim J, Kim J, Oh S, Choi K, Yoon J. Magnetothermal-based non-invasive focused magnetic stimulation for functional recovery in chronic stroke treatment. Sci Rep. 2023 Mar 27;13(1):4988.

283. Yang Y, Fan X, Li L, Yang Y, Nuernisha A, Xue D, et al. Semiconducting Polymer Nanoparticles as Theranostic System for Near-Infrared-II Fluorescence Imaging and Photothermal Therapy under Safe Laser Fluence. ACS Nano. 2020 Feb 25;14(2):2509–21.

284. Hubert V, Hristovska I, Karpati S, Benkeder S, Dey A, Dumot C, et al. Multimodal Imaging with NanoGd Reveals Spatiotemporal Features of

Neuroinflammation after Experimental Stroke. Adv Sci. 2021 Jul 1;8(17):2101433.

285. González-Díaz EC, Varghese S. Hydrogels as Extracellular Matrix Analogs. Gels. 2016 Aug 3;2(3):20.

286. Wichterle O, Lím D. Hydrophilic Gels for Biological Use. Nature. 1960 Jan;185(4706):117–8.

287. Ho TC, Chang CC, Chan HP, Chung TW, Shu CW, Chuang KP, et al. Hydrogels: Properties and Applications in Biomedicine. Molecules. 2022 May 2;27(9):2902.

288. Bashir S, Hina M, Iqbal J, Rajpar AH, Mujtaba MA, Alghamdi NA, et al. Fundamental Concepts of Hydrogels: Synthesis, Properties, and Their Applications. Polymers. 2020 Nov 16;12(11):2702.

289. Saludas L, Pascual-Gil S, Prósper F, Garbayo E, Blanco-Prieto M. Hydrogel based approaches for cardiac tissue engineering. Int J Pharm. 2017 May 25;523(2):454–75.

290. Shi L, Zhang J, Zhao M, Tang S, Cheng X, Zhang W, et al. Effects of polyethylene glycol on the surface of nanoparticles for targeted drug delivery. Nanoscale. 2021 Jun 24;13(24):10748–64.

291. Salimath AS, Phelps EA, Boopathy AV, Che P lin, Brown M, García AJ, et al. Dual Delivery of Hepatocyte and Vascular Endothelial Growth Factors via a Protease-Degradable Hydrogel Improves Cardiac Function in Rats. PLOS ONE. 2012 Nov 30;7(11):e50980.

292. Wang X, Chun YW, Zhong L, Chiusa M, Balikov DA, Frist AY, et al. A temperature-sensitive, self-adhesive hydrogel to deliver iPSC-derived cardiomyocytes for heart repair. Int J Cardiol. 2015 Jul 1;190:177–80.

293. Trombino S, Sole R, Di Gioia ML, Procopio D, Curcio F, Cassano R. Green Chemistry Principles for Nano- and Micro-Sized Hydrogel Synthesis. Mol Basel Switz. 2023 Feb 23;28(5):2107.

294. Toh WS, Loh XJ. Advances in hydrogel delivery systems for tissue regeneration. Mater Sci Eng C. 2014 Dec 1;45:690–7.

295. Eyrich D, Brandl F, Appel B, Wiese H, Maier G, Wenzel M, et al. Long-term stable fibrin gels for cartilage engineering. Biomaterials. 2007 Jan;28(1):55–65.

296. Tamaddon M, Burrows M, Ferreira SA, Dazzi F, Apperley JF, Bradshaw A, et al. Monomeric, porous type II collagen scaffolds promote chondrogenic

differentiation of human bone marrow mesenchymal stem cells in vitro. Sci Rep. 2017 Mar 3;7:43519.

297. Wang J, Viola M, Migliorini C, Paoletti L, Arpicco S, Di Meo C, et al. Polysaccharide-Based Nanogels to Overcome Mucus, Skin, Cornea, and Blood-Brain Barriers: A Review. Pharmaceutics. 2023 Oct 23;15.

298. Alhaique F, Casadei M, Cencetti C, Coviello T, Di Meo C, Matricardi P, et al. From macro to nano polysaccharide hydrogels: An opportunity for the delivery of drugs. J Drug Deliv Sci Technol. 2015 Sep 1;32.

299. Plucinski A, Lyu Z, Schmidt BVKJ. Polysaccharide nanoparticles: from fabrication to applications. J Mater Chem B. 2021 Sep 15;9(35):7030–62.

300. Naderi-Meshkin H, Andreas K, Matin MM, Sittinger M, Bidkhori HR, Ahmadiankia N, et al. Chitosan-based injectable hydrogel as a promising in situ forming scaffold for cartilage tissue engineering. Cell Biol Int. 2014;38(1):72–84.

301. Le Guilcher C, Merlen G, Dellaquila A, Labour MN, Aid R, Tordjmann T, et al. Engineered human liver based on pullulan-dextran hydrogel promotes mice survival after liver failure. Mater Today Bio. 2023 Apr 1;19:100554.

302. Berkovitch Y, Seliktar D. Semi-synthetic hydrogel composition and stiffness regulate neuronal morphogenesis. Int J Pharm. 2017 May 25;523(2):545–55.

303. Bustamante-Torres M, Romero-Fierro D, Arcentales-Vera B, Palomino K, Magaña H, Bucio E. Hydrogels Classification According to the Physical or Chemical Interactions and as Stimuli-Sensitive Materials. Gels. 2021 Oct 25;7(4):182.

304. Aamir R, Fyffe C, Korin N, Lawrence DA, Su EJ, Kanapathipillai M. Heparin and Arginine Based Plasmin Nanoformulation for Ischemic Stroke Therapy. Int J Mol Sci. 2021 Jan;22(21):11477.

305. Monteil V, Bastero A, Mecking S. 1,2-Polybutadiene Latices by Catalytic Polymerization in Aqueous Emulsion. Macromolecules. 2005 Jun 1;38(13):5393–9.

306. Barrère M, Landfester K. Polyester synthesis in aqueous miniemulsion. Polymer. 2003 May 1;44(10):2833–41.

307. Landfester K. Miniemulsion Polymerization and the Structure of Polymer and Hybrid Nanoparticles. Angew Chem Int Ed. 2009 Jun 8;48(25):4488–507.

308. Zhou S, Huang G. Preparation, structure and activity of polysaccharide phosphate esters. Biomed Pharmacother. 2021 Dec 1;144:112332.

309. Kuijpers AJ, van Wachem PB, van Luyn MJ, Engbers GH, Krijgsveld J, Zaat SA, et al. In vivo and in vitro release of lysozyme from cross-linked gelatin hydrogels: a model system for the delivery of antibacterial proteins from prosthetic heart valves. J Control Release Off J Control Release Soc. 2000 Jul 3;67(2–3):323–36.

310. Qazvini NT, Zinatloo S. Synthesis and characterization of gelatin nanoparticles using CDI/NHS as a non-toxic cross-linking system. J Mater Sci Mater Med. 2011 Jan;22(1):63–9.

311. Ottenbrite RM, Park K, Okano T. Biomedical Applications of Hydrogels Handbook. Springer Science & Business Media; 2010. 438 p.

312. Rao JP, Geckeler KE. Polymer nanoparticles: Preparation techniques and size-control parameters. Prog Polym Sci. 2011 Jul 1;36(7):887–913.

313. Kabanov AV, Vinogradov SV. Nanogels as pharmaceutical carriers: finite networks of infinite capabilities. Angew Chem Int Ed Engl. 2009;48(30):5418–29.

314. Vinogradov SV, Bronich TK, Kabanov AV. Nanosized cationic hydrogels for drug delivery: preparation, properties and interactions with cells. Adv Drug Deliv Rev. 2002 Jan 17;54(1):135–47.

315. Akiyoshi K, Deguchi S, Moriguchi N, Yamaguchi S, Sunamoto J. Self-aggregates of hydrophobized polysaccharides in water. Formation and characteristics of nanoparticles. Macromolecules. 1993 Jun 1;26(12):3062–8.

316. Banik BL, Fattahi P, Brown JL. Polymeric nanoparticles: the future of nanomedicine. WIREs Nanomedicine Nanobiotechnology. 2016;8(2):271–99.

317. Allouche J. Synthesis of Organic and Bioorganic Nanoparticles: An Overview of the Preparation Methods. In: Brayner R, Fiévet F, Coradin T, editors. Nanomaterials: A Danger or a Promise? A Chemical and Biological Perspective. London: Springer; 2013. p. 27–74.

318. Gharieh A, Khoee S, Mahdavian AR. Emulsion and miniemulsion techniques in preparation of polymer nanoparticles with versatile characteristics. Adv Colloid Interface Sci. 2019 Jul 1;269:152–86.

319. Maia J, Evangelista M, Gil H, Ferreira L. Dextran-based materials for biomedical applications. In: Carbohydrates Applications in Medicine. M.H. Gil; 2014. p. 31–53.

320. Janovák L, Turcsányi Á, Bozó É, Deák Á, Mérai L, Sebők D, et al. Preparation of novel tissue acidosis-responsive chitosan drug nanoparticles: Characterization and in vitro release properties of Ca2+ channel blocker nimodipine drug molecules. Eur J Pharm Sci. 2018 Oct 15;123:79–88.

321. Tóth OM, Menyhárt Á, Varga VÉ, Hantosi D, Iványkovits-Kiss O, Varga DP, et al. Chitosan nanoparticles release nimodipine in response to tissue acidosis to attenuate spreading depolarization evoked during forebrain ischemia. Neuropharmacology. 2020 Jan 1;162:107850.

322. Moon RJ, Martini A, Nairn J, Simonsen J, Youngblood J. Cellulose nanomaterials review: structure, properties and nanocomposites. Chem Soc Rev. 2011 Jun 20;40(7):3941–94.

323. Vashist A, Atluri V, Raymond A, Kaushik A, Parira T, Huang Z, et al. Development of Multifunctional Biopolymeric Auto-Fluorescent Micro- and Nanogels as a Platform for Biomedical Applications. Front Bioeng Biotechnol. 2020;8:315.

324. Zoratto N, Forcina L, Matassa R, Mosca L, Familiari G, Musaro A, et al. Hyaluronan-Cholesterol Nanogels for the Enhancement of the Ocular Delivery of Therapeutics. Pharmaceutics. 2021 Oct 25;13:1781.

325. Blanco S, Peralta S, Morales ME, Martínez-Lara E, Pedrajas JR, Castán H, et al. Hyaluronate Nanoparticles as a Delivery System to Carry Neuroglobin to the Brain after Stroke. Pharmaceutics. 2020 Jan;12(1):40.

326. Hemshekhar M, Thushara RM, Chandranayaka S, Sherman LS, Kemparaju K, Girish KS. Emerging roles of hyaluronic acid bioscaffolds in tissue engineering and regenerative medicine. Int J Biol Macromol. 2016 May 1;86:917–28.

327. Motwani SK, Chopra S, Talegaonkar S, Kohli K, Ahmad FJ, Khar RK. Chitosan–sodium alginate nanoparticles as submicroscopic reservoirs for ocular delivery: Formulation, optimisation and *in vitro* characterisation. Eur J Pharm Biopharm. 2008 Mar 1;68(3):513–25.

328. Cardia MC, Carta AR, Caboni P, Maccioni AM, Erbì S, Boi L, et al. Trimethyl Chitosan Hydrogel Nanoparticles for Progesterone Delivery in Neurodegenerative Disorders. Pharmaceutics. 2019 Dec;11(12):657.

329. Naessens M, Cerdobbel A, Soetaert W, Vandamme EJ. Leuconostoc dextransucrase and dextran: production, properties and applications. J Chem Technol Biotechnol. 2005;80(8):845–60.

330. Wang R, Dijkstra PJ, Karperien M. Dextran. In: Biomaterials from Nature for Advanced Devices and Therapies. John Wiley & Sons, Ltd; 2016. p. 307–19.

331. Huynh R, Chaubet F, Jozefonvicz J. Anticoagulant properties of dextranmethylcarboxylate benzylamide sulfate (DMCBSu); a new generation of bioactive functionalized dextran. Carbohydr Res. 2001 May 8;332(1):75–83.

332. Frank L, Lebreton-Decoster C, Godeau G, Coulomb B, Jozefonvicz J. Dextran derivatives modulate collagen matrix organization in dermal equivalent. J Biomater Sci Polym Ed. 2006;17(5):499–517.

333. Ikeda Y, Charef S, Ouidja MO, Barbier-Chassefière V, Sineriz F, Duchesnay A, et al. Synthesis and biological activities of a library of glycosaminoglycans mimetic oligosaccharides. Biomaterials. 2011 Jan;32(3):769–76.

334. Kabat EA, Berg D. Dextran—An Antigen in Man1. J Immunol. 1953 Jun 1;70(6):514–32.

335. Kabat EA, Bezer AE. The effect of variation in molecular weight on the antigenicity of dextran in man. Arch Biochem Biophys. 1958 Dec 1;78(2):306–18.

336. Coulson EJ, Stevens H. Some Observations on the Immunochemistry of Dextrans. J Immunol. 1961 Mar 1;86(3):241–52.

337. Soeiro VC, Melo KRT, Alves MGCF, Medeiros MJC, Grilo MLPM, Almeida-Lima J, et al. Dextran: Influence of Molecular Weight in Antioxidant Properties and Immunomodulatory Potential. Int J Mol Sci. 2016 Aug 19;17(8):1340.

338. Simon-Yarza T, Labour MN, Aid R, Letourneur D. Channeled Polysaccharide-Based Hydrogel Reveals Influence of Curvature to Guide Endothelial Cell Arrangement in Vessel-Like Structures. Mater Sci Eng C. 2020 Aug 1;118:111369.

339. Ahmed Omar N, Roque J, Galvez P, Siadous R, Chassande O, Catros S, et al. Development of Novel Polysaccharide Membranes for Guided Bone Regeneration: In Vitro and In Vivo Evaluations. Bioengineering. 2023 Oct 28;10:1257.

340. Pharmacosmos Dextran [Internet]. [cited 2024 Aug 2]. Available from: https://www.dextran.com/about-dextran/dextran-safety/dextran-biodegradation

341. Abbott SJ. Surfactant Science: Principles & Practice. DEStech Publications, Incorporated; 2017. 189 p.

342. Lee JM, Shin ZU, Mavlonov G, Abdurakhmonov I, Yi T. Solid-Phase Colorimetric Method for the Quantification of Fucoidan. Appl Biochem Biotechnol. 2012 Aug 18;168.

343. Haggag YA, Abd Elrahman AA, Ulber R, Zayed A. Fucoidan in Pharmaceutical Formulations: A Comprehensive Review for Smart Drug Delivery Systems. Mar Drugs. 2023 Feb;21(2):112.

344. Kwak KW, Cho KS, Hahn OJ, Lee KH, Lee BY, Ko JJ, et al. Biological effects of fucoidan isolated from Fucus vesiculosus on thrombosis and vascular cells. Korean J Hematol. 2010 Mar 31;45(1):51–7.

345. Shen C, Mackeigan DT, Shoara AA, Xu R, Bhoria P, Karakas D, et al. Dual roles of fucoidan-GPIbα interaction in thrombosis and hemostasis: implications for drug development targeting GPIbα. J Thromb Haemost. 2023 Jan 9;

346. Bonnard T, Serfaty JM, Journé C, Ho Tin Noe B, Arnaud D, Louedec L, et al. Leukocyte mimetic polysaccharide microparticles tracked in vivo on activated endothelium and in abdominal aortic aneurysm. Acta Biomater. 2014 Aug 1;10(8):3535–45.

347. Bonnard T, Yang G, Petiet A, Ollivier V, Haddad O, Arnaud D, et al. Abdominal Aortic Aneurysms Targeted by Functionalized Polysaccharide Microparticles: a new Tool for SPECT Imaging. Theranostics. 2014;4(6):592–603.

348. Ghebouli R, Loyau S, Maire M, Saboural P, Collet JP, Jandrot-Perrus M, et al. Amino-Fucoidan as a Vector for rtPA-Induced Fibrinolysis in Experimental Thrombotic Events. Thromb Haemost. 2018 Jan;118(01):042–53.

349. Zheng KH, Kaiser Y, Poel E, Verberne H, Aerts J, Rouzet F, et al. 99Mtc-Fucoidan As Diagnostic Agent For P-Selectin Imaging: First-In-Human Evaluation (Phase I). Atherosclerosis. 2019 Aug 1;287:e143.

350. Chauvierre C, Aid-Launais R, Aerts J, Chaubet F, Maire M, Chollet L, et al. Pharmaceutical Development and Safety Evaluation of a GMP-Grade Fucoidan for Molecular Diagnosis of Cardiovascular Diseases. Mar Drugs. 2019 Dec;17(12):699.

351. Li B, Aid-Launais R, Labour MN, Zenych A, Juenet M, Choqueux C, et al. Functionalized polymer microbubbles as new molecular ultrasound contrast agent to target P-selectin in thrombus. Biomaterials. 2019 Feb 1;194:139–50.

352. Forero Ramirez LM, Gobin E, Aid-Launais R, Journe C, Moraes FC, Picton L, et al. Gd(DOTA)-grafted submicronic polysaccharide-based particles functionalized with fucoidan as potential MR contrast agent able to target human activated platelets. Carbohydr Polym. 2020 Oct 1;245:116457.

353. Moraes FC, Marcelo Forero Ramirez L, Aid R, Benadda S, Maire M, Chauvierre C, et al. P-selectin targeting polysaccharide-based nanogels for miRNA delivery. Int J Pharm. 2021 Mar 15;597:120302.

354. Xie S, Mo C, Cao W, Xie S, Li S, Zhang Z, et al. Bacteria-propelled microtubular motors for efficient penetration and targeting delivery of thrombolytic agents. Acta Biomater. 2022 Apr 1;142:49–59.

355. Hirsch JB, Kokini JL. Understanding the Mechanism of Cross-Linking Agents (POCl3, STMP, and EPI) Through Swelling Behavior and Pasting Properties of Cross-Linked Waxy Maize Starches. Cereal Chem. 2002;79(1):102–7.

356. Autissier A, Letourneur D, Le Visage C. Pullulan-based hydrogel for smooth muscle cell culture. J Biomed Mater Res A. 2007 Aug;82(2):336–42.

357. Lack S, Dulong V, Picton L, Cerf DL, Condamine E. High-resolution nuclear magnetic resonance spectroscopy studies of polysaccharides crosslinked by sodium trimetaphosphate: a proposal for the reaction mechanism. Carbohydr Res. 2007 May 21;342(7):943–53.

358. Wilson R, Smith M. Human studies on polyglycerol polyricinoleate (PGPR). Food Chem Toxicol Int J Publ Br Ind Biol Res Assoc. 1998 Oct;36(9–10):743–5.

359. Wilson R, Van Schie BJ, Howes D. Overview of the preparation, use and biological studies on polyglycerol polyricinoleate (PGPR). Food Chem Toxicol Int J Publ Br Ind Biol Res Assoc. 1998;36(9–10):711–8.

360. Bastida-Rodríguez J. The Food Additive Polyglycerol Polyricinoleate (E-476): Structure, Applications, and Production Methods. Int Sch Res Not. 2013 Jan 9;2013:e124767.

361. Zembyla M, Murray BS, Sarkar A. Water-in-oil emulsions stabilized by surfactants, biopolymers and/or particles: a review. Trends Food Sci Technol. 2020 Oct 1;104:49–59.

362. Baudron V, Taboada M, Gurikov P, Smirnova I, Whitehouse S. Production of starch aerogel in form of monoliths and microparticles. Colloid Polym Sci. 2020 May 1;298(4):477–94.

363. Raviadaran R, Ng MH, Manickam S, Chandran D. Ultrasound-assisted water-in-palm oil nano-emulsion: Influence of polyglycerol polyricinoleate and NaCl on its stability. Ultrason Sonochem. 2019 Apr 1;52:353–63.

364. Mehrnia MA, Jafari SM, Makhmal-Zadeh BS, Maghsoudlou Y. Crocin loaded nano-emulsions: Factors affecting emulsion properties in spontaneous emulsification. Int J Biol Macromol. 2016 Mar 1;84:261–7.

365. Zhang K, Mao Z, Huang Y, Xu Y, Huang C, Guo Y, et al. Ultrasonic assisted water-in-oil emulsions encapsulating macro-molecular polysaccharide chitosan: Influence of molecular properties, emulsion viscosity and their stability. Ultrason Sonochem. 2020 Jun 1;64:105018.

366. Gupta A, Burak Eral H, Alan Hatton T, S. Doyle P. Nanoemulsions: formation, properties and applications. Soft Matter. 2016;12(11):2826–41.

367. Solans C, Solé I. Nano-emulsions: Formation by low-energy methods. Curr Opin Colloid Interface Sci. 2012 Oct 1;17(5):246–54.

368. Akram S, Anton N, Omran Z, Vandamme T. Water-in-Oil Nano-Emulsions Prepared by Spontaneous Emulsification: New Insights on the Formulation Process. Pharmaceutics. 2021 Jul 7;13(7):1030.

369. Boxall JA, Koh CA, Sloan ED, Sum AK, Wu DT. Droplet Size Scaling of Water-in-Oil Emulsions under Turbulent Flow. Langmuir. 2012 Jan 10;28(1):104–10.

370. Cates ME. Complex Fluids: The Physics of Emulsions. ArXiv12092290 Cond-Mat [Internet]. 2012 Sep 11 [cited 2021 Oct 19]; Available from: http://arxiv.org/abs/1209.2290

371. Tartaro G, Mateos H, Schirone D, Angelico R, Palazzo G. Microemulsion Microstructure(s): A Tutorial Review. Nanomaterials. 2020 Sep;10(9):1657.

372. Mitsou E, Kalogianni EP, Georgiou D, Stamatis H, Xenakis A, Zoumpanioti M. Formulation and Structural Study of a Biocompatible Water-in-Oil Microemulsion as an Appropriate Enzyme Carrier: The Model Case of Horseradish Peroxidase. Langmuir. 2018 Dec 6;

373. Asgari S, Saberi AH, McClements DJ, Lin M. Microemulsions as nanoreactors for synthesis of biopolymer nanoparticles. Trends Food Sci Technol. 2019 Apr 1;86:118–30.

374. Nazari M, Mehrnia MA, Jooyandeh H, Barzegar H. Preparation and characterization of water in sesame oil microemulsion by spontaneous method. J Food Process Eng. 2019;42(4):e13032.

375. Mitsou E, Pletsa V, Sotiroudis GT, Panine P, Zoumpanioti M, Xenakis A. Development of a microemulsion for encapsulation and delivery of gallic acid. The role of chitosan. Colloids Surf B Biointerfaces. 2020 Jun;190:110974.

376. Souguir Z, About-Jaudet E, Picton L, Le Cerf D. Anionic Polysaccharide Hydrogels with Charges Provided by the Polysaccharide or the Crosslinking Agent. Drug Deliv Lett. 2012 Dec 1;2:240–50.

377. Serrano-Lotina A, Portela R, Baeza P, Alcolea-Rodriguez V, Villarroel M, Ávila P. Zeta potential as a tool for functional materials development. Catal Today. 2023 Nov 1;423:113862.

378. Kharlamov A. Plasmonic Photothermal Therapy of Flow-Limiting Atherosclerotic Lesions With Silica-Gold Nanoparticles: a First-in-Man Study. clinicaltrials.gov; 2021 Feb. Report No.: NCT01270139.

379. Miyazawa T, Itaya M, Burdeos GC, Nakagawa K, Miyazawa T. A Critical Review of the Use of Surfactant-Coated Nanoparticles in Nanomedicine and Food Nanotechnology. Int J Nanomedicine. 2021 Jun 9;16:3937–99.

380. Tian H, Yu L, Zhang M, He J, Sun X, Ni P. Dextran-doxorubicin prodrug nanoparticles conjugated with CD147 monoclonal antibody for targeted drug delivery in hepatoma therapy. Colloids Surf B Biointerfaces. 2023 Aug 1;228:113400.

381. Blanco-Cabra N, Movellan J, Marradi M, Gracia R, Salvador C, Dupin D, et al. Neutralization of ionic interactions by dextran-based single-chain nanoparticles improves tobramycin diffusion into a mature biofilm. Npj Biofilms Microbiomes. 2022 Jul 4;8(1):1–12.

382. Bao X, Qian K, Yao P. Insulin- and cholic acid-loaded zein/casein–dextran nanoparticles enhance the oral absorption and hypoglycemic effect of insulin. J Mater Chem B. 2021 Aug 11;9(31):6234–45.

383. Rahimi S, Stumpf S, Grimm O, Schacher FH, Schubert US, Schubert S. Dual Photo- and pH-Responsive Spirooxazine-Functionalized Dextran Nanoparticles. Biomacromolecules. 2020 Sep 14;21(9):3620–30.

384. Maingret V, Courrégelongue C, Schmitt V, Héroguez V. Dextran-Based Nanoparticles to Formulate pH-Responsive Pickering Emulsions: A Fully Degradable Vector at a Day Scale. Biomacromolecules. 2020 Dec 14;21(12):5358–68.

385. Chen C, Wang Z, Zhang J, Fan X, Xu L, Tang X. Dextran-Conjugated Caged siRNA Nanoparticles for Photochemical Regulation of RNAi-Induced Gene Silencing in Cells and Mice. Bioconjug Chem. 2019 May 15;30(5):1459–65.

386. Kumar P, Mittal KL. Handbook of Microemulsion Science and Technology. CRC Press; 1999. 872 p.

387. Prévost S, Gradzielski M, Zemb T. Self-assembly, phase behaviour and structural behaviour as observed by scattering for classical and non-classical microemulsions. Adv Colloid Interface Sci. 2017 Sep 1;247:374–96.

388. Mcclements D. Nanoemulsions versus microemulsions: Terminology, differences, and similarities. Soft Matter. 2012 Jan 18;8:1719–29.

389. Čilek A, Čelebi N, Tirnaksiz F. Lecithin-Based Microemulsion of a Peptide for Oral Administration: Preparation, Characterization, and Physical Stability of the Formulation. Drug Deliv. 2006 Jan 1;13(1):19–24.

390. Chatzidaki MD, Mitsou E, Yaghmur A, Xenakis A, Papadimitriou V. Formulation and characterization of food-grade microemulsions as carriers of natural phenolic antioxidants. Colloids Surf Physicochem Eng Asp. 2015 Oct 20;483:130–6.

391. Wang M, Yang W, Wu Q, Gu H. Modeling of the fibrin agarose plate assay and its application for thrombolytic analysis. Chin Sci Bull. 2012 Aug 1;57.

392. Gruber S, Nickel A. Toxic or not toxic? The specifications of the standard ISO 10993-5 are not explicit enough to yield comparable results in the cytotoxicity assessment of an identical medical device. Front Med Technol. 2023 Jun 14;5:1195529.

393. Orset C, Macrez R, Young AR, Panthou D, Angles-Cano E, Maubert E, et al. Mouse Model of In Situ Thromboembolic Stroke and Reperfusion. Stroke. 2007 Oct;38(10):2771–8.

394. National Institute of Neurological Disorders and Stroke rt-PA Stroke Study Group. Tissue plasminogen activator for acute ischemic stroke. N Engl J Med. 1995 Dec 14;333(24):1581–7.

395. Latour RA. Fundamental Principles of the Thermodynamics and Kinetics of Protein Adsorption to Material Surfaces. Colloids Surf B Biointerfaces. 2020 Jul 1;191:110992.

396. Macdougall LJ, Wechsler ME, Culver HR, Benke EH, Broerman A, Bowman CN, et al. Charged poly(N-isopropylacrylamide) nanogels for the stabilization of high isoelectric point proteins. ACS Biomater Sci Eng. 2021 Sep 13;7(9):4282–92.

397. Marco-Dufort B, Janczy JR, Hu T, Lütolf M, Gatti F, Wolf M, et al. Thermal stabilization of diverse biologics using reversible hydrogels. Sci Adv. 2022 Aug 5;8(31):eabo0502.

398. Petrovici AR, Pinteala M, Simionescu N. Dextran Formulations as Effective Delivery Systems of Therapeutic Agents. Mol Basel Switz. 2023 Jan 21;28(3):1086.

399. Van Tomme SR, Hennink WE. Biodegradable dextran hydrogels for protein delivery applications. Expert Rev Med Devices. 2007 Mar 1;4(2):147–64.

400. Lanouar S, Aid-Launais R, Oliveira A, Bidault L, Closs B, Labour MN, et al. Effect of cross-linking on the physicochemical and in vitro properties of pullulan/dextran microbeads. J Mater Sci Mater Med. 2018 May 29;29(6):77.

401. Teijeira Á, Garasa S, Gato M, Alfaro C, Migueliz I, Cirella A, et al. CXCR1 and CXCR2 Chemokine Receptor Agonists Produced by Tumors Induce Neutrophil Extracellular Traps that Interfere with Immune Cytotoxicity. Immunity. 2020 May;52(5):856-871.e8.

402. Stoimenou M, Tzoros G, Skendros P, Chrysanthopoulou A. Methods for the Assessment of NET Formation: From Neutrophil Biology to Translational Research. Int J Mol Sci. 2022 Dec 13;23(24):15823.

403. Matta B, Battaglia J, Barnes BJ. Detection of neutrophil extracellular traps in patient plasma: method development and validation in systemic lupus erythematosus and healthy donors that carry IRF5 genetic risk. Front Immunol. 2022 Jul 26;13:951254.

404. Markoutsa E, Xu P. Redox potential sensitive N-acetyl cysteine-prodrug nanoparticles inhibit the activation of microglia and improve neuronal survival. Mol Pharm. 2017 May 1;14(5):1591–600.

405. Tardiolo G, Bramanti P, Mazzon E. Overview on the Effects of N-Acetylcysteine in Neurodegenerative Diseases. Molecules. 2018 Dec;23(12):3305.

406. Sheng Y, Sun X, Han J, Hong W, Feng J, Xie S, et al. N-acetylcysteine functionalized chitosan oligosaccharide-palmitic acid conjugate enhances ophthalmic delivery of flurbiprofen and its mechanisms. Carbohydr Polym. 2022 Sep 1;291:119552.

407. Martinez de Lizarrondo S, Gakuba C, Herbig BA, Repessé Y, Ali C, Denis CV, et al. Potent Thrombolytic Effect of N-Acetylcysteine on Arterial Thrombi. Circulation. 2017 Aug 15;136(7):646–60.

408. Turkmen S, Cekic Gonenc O, Karaca Y, Mentese A, Demir S, Beyhun E, et al. The effect of ethyl pyruvate and N-acetylcysteine on ischemia-reperfusion injury in an experimental model of ischemic stroke. Am J Emerg Med. 2016 Sep 1;34(9):1804–7.

409. Liu Y, Liu WC, Sun Y, Shen X, Wang X, Shu H, et al. Normobaric Hyperoxia Extends Neuro- and Vaso-Protection of N-Acetylcysteine in Transient Focal Ischemia. Mol Neurobiol. 2017 Jul 1;54(5):3418–27.

410. Tanen D. Randomized Placebo Controlled Trial of Intravenous N-Acetylcysteine for the Treatment of Acute Ischemic Stroke. clinicaltrials.gov; 2021 Jun. Report No.: NCT04918719.

411. Sabetghadam M, Mazdeh M, Abolfathi P, Mohammadi Y, Mehrpooya M. Evidence for a Beneficial Effect of Oral N-acetylcysteine on Functional Outcomes and Inflammatory Biomarkers in Patients with Acute Ischemic Stroke. Neuropsychiatr Dis Treat. 2020 May 18;16:1265–78.

412. Chen W, Ercal N, Huynh T, Volkov A, Chusuei CC. Characterizing N-acetylcysteine (NAC) and N-acetylcysteine Amide (NACA) Binding for Lead Poisoning Treatment. J Colloid Interface Sci. 2012 Apr 1;371(1):144–9.

413. Eckly A, Hechler B, Freund M, Zerr M, Cazenave JP, Lanza F, et al. Mechanisms underlying FeCl3-induced arterial thrombosis. J Thromb Haemost. 2011;9(4):779–89.

414. Diaz JA, Obi AT, Myers DD, Wrobleski SK, Henke PK, Mackman N, et al. Critical Review of Mouse Models of Venous Thrombosis. Arterioscler Thromb Vasc Biol. 2012 Mar;32(3):556–62.

415. Li W, McIntyre TM, Silverstein RL. Ferric chloride-induced murine carotid arterial injury: A model of redox pathology. Redox Biol. 2013 Jan 26;1(1):50–5.

416. Powers WJ, Rabinstein AA, Ackerson T, Adeoye OM, Bambakidis NC, Becker K, et al. Guidelines for the Early Management of Patients With Acute Ischemic Stroke: 2019 Update to the 2018 Guidelines for the Early Management of Acute Ischemic Stroke: A Guideline for Healthcare Professionals From the American Heart Association/American Stroke Association. Stroke. 2019 Dec;50(12):e344–418.

417. Liu L, Chen W, Zhou H, Duan W, Li S, Huo X, et al. Chinese Stroke Association guidelines for clinical management of cerebrovascular disorders: executive summary and 2019 update of clinical management of ischaemic cerebrovascular diseases. Stroke Vasc Neurol. 2020 Jun 18;5(2):159–76.

418. Bannish BE, Chernysh IN, Keener JP, Fogelson AL, Weisel JW. Molecular and Physical Mechanisms of Fibrinolysis and Thrombolysis from Mathematical Modeling and Experiments. Sci Rep. 2017 Aug 7;7(1):6914.

419. Kraal G, Mebius R. New Insights into the Cell Biology of the Marginal Zone of the Spleen. Int Rev Cytol. 2006;250:175–215.

420. Gustafson HH, Holt-Casper D, Grainger DW, Ghandehari H. Nanoparticle Uptake: The Phagocyte Problem. Nano Today. 2015 Aug;10(4):487–510.

421. Khalikova E, Susi P, Korpela T. Microbial Dextran-Hydrolyzing Enzymes: Fundamentals and Applications. Microbiol Mol Biol Rev. 2005 Jun;69(2):306–25.

422. Casa LDC, Ku DN. Thrombus Formation at High Shear Rates. Annu Rev Biomed Eng. 2017 Jun 21;19(Volume 19, 2017):415–33.

423. Ciciliano JC, Myers DR, Fay ME, Sakurai Y, Li R, Lyon A, et al. New Insights Into The Mechanisms Of Ferric Chloride-Induced Thrombosis: a Reductionist Microfluidic Approach. Blood. 2013 Nov 15;122(21):2308.

424. Li W, Nieman M, Gupta AS. Ferric Chloride-induced Murine Thrombosis Models. J Vis Exp JoVE. 2016;(115).

425. Singh AA, Kharwar A, Dandekar MP. A Review on Preclinical Models of Ischemic Stroke: Insights Into the Pathomechanisms and New Treatment Strategies. Curr Neuropharmacol. 2022 Aug 3;20(9):1667–86.

426. Nagai N, Zhao BQ, Suzuki Y, Ihara H, Urano T, Umemura K. Tissue-type plasminogen activator has paradoxical roles in focal cerebral ischemic injury by thrombotic middle cerebral artery occlusion with mild or severe photochemical damage in mice. J Cereb Blood Flow Metab Off J Int Soc Cereb Blood Flow Metab. 2002 Jun;22(6):648–51.

427. Orset C, Macrez R, Young AR, Panthou D, Angles-Cano E, Maubert E, et al. Mouse Model of In Situ Thromboembolic Stroke and Reperfusion. Stroke. 2007 Oct;38(10):2771–8.

428. Arkelius K, Vivien D, Orset C, Ansar S. Validation of a stroke model in rat compatible with rt-PA-induced thrombolysis: new hope for successful translation to the clinic. Sci Rep. 2020 Jul 22;10(1):12191.

429. Halwani AA. Development of Pharmaceutical Nanomedicines: From the Bench to the Market. Pharmaceutics. 2022 Jan 3;14(1):106.

430. Yu S, Li D, Shi A, Long Y, Deng J, Ma Y, et al. Multidrug-loaded liposomes prevent ischemic stroke through intranasal administration. Biomed Pharmacother. 2023 Jun 1;162:114542.

431. Walters RH, Bhatnagar B, Tchessalov S, Izutsu KI, Tsumoto K, Ohtake S. Next generation drying technologies for pharmaceutical applications. J Pharm Sci. 2014 Sep;103(9):2673–95.

432. Farkas N, Kramar JA. Dynamic light scattering distributions by any means. J Nanoparticle Res. 2021 May 21;23(5):120.

433. Ramirez LMF, Rihouey C, Chaubet F, Le Cerf D, Picton L. Characterization of dextran particle size: How frit-inlet asymmetrical flow field-flow fractionation (FI-AF4) coupled online with dynamic light scattering (DLS) leads to enhanced size distribution. J Chromatogr A. 2021 Sep 13;1653:462404.

434. Blanco E, Shen H, Ferrari M. Principles of nanoparticle design for overcoming biological barriers to drug delivery. Nat Biotechnol. 2015 Sep;33(9):941–51.

435. Zhang H, Qu H, He Q, Gao L, Zhang H, Wang Y, et al. Thrombus-targeted nanoparticles for thrombin-triggered thrombolysis and local inflammatory microenvironment regulation. J Control Release Off J Control Release Soc. 2021 Nov 10;339:195–207.

436. Rouzet F, Bachelet-Violette L, Alsac JM, Suzuki M, Meulemans A, Louedec L, et al. Radiolabeled Fucoidan as a P-Selectin Targeting Agent for In Vivo Imaging of Platelet-Rich Thrombus and Endothelial Activation. J Nucl Med. 2011 Sep 1;52(9):1433–40.

Abstract

Development of natural polysaccharide nanoparticles loaded with a combination of drugs and functionalized with fucoidan to address an efficient targeted treatment of ischemic strokes

Keywords: Polymeric Nanoparticles, Microemulsion, Polysaccharides, Hydrogels, Thrombolysis, Drug Delivery System, Fucoidan, Synthesis

Cardiovascular diseases pose a global threat to human health, with among them thrombotic diseases such as pulmonary embolism, myocardial infarction and acute ischemic stroke as the major killers. Despite the paramount need for primary prevention, population aging and lifestyle changes still contribute to an increasing burden. While various treatments exist, including the fibrinolytic recombinant tissue plasminogen activator (rtPA), the gold standard for treating acute ischemic strokes, they lack efficacy and often are plagued by severe side effects. The goal of this research was therefore to present a nanomedicine-based approach for improved thrombolysis through delivery of multiple therapeutic agents, addressing the complex nature of thrombi.

Consequently, we have developed an innovative synthesis for polysaccharide hydrogel nanoparticles capable of loading rtPA and DNase I, another enzyme, and studied their thrombolytic effect. The former were biocompatible and safe, imbued with a robust synthesis yielding stable colloidal suspensions that were fully characterized. The synthesis notably involved the microemulsion framework to improve the emulsification process. These nanogels also incorporated fucoidan, thus acquiring a targeting capacity of thrombi through the affinity of fucoidan for P-selectin, a marker of activated platelets and endothelium. Hereafter, the successful drug loadings were validated through different assays, culminating in the *in vitro* successful synergic degradation of thrombi. Hence, we explored the thrombolytic properties with a murine *in vivo* thrombosis model, which demonstrated an improved thrombolysis with the loading of rtPA in our nanoparticles, at 50% and 10% the recommended dose. Overall, this work emphasized the potential of fully polysaccharidic polymeric nanoparticles for the targeted treatment of thrombotic diseases.

Résumé

Développement de nanoparticules de polysaccharides naturels, chargées avec une combinaison d'actifs et fonctionnalisées avec du fucoïdane afin de réaliser un traitement ciblé et efficace des accidents vasculaires cérébraux

Mots-clés: Nanoparticules Polymériques, Microémulsion, Polysaccharides, Hydrogels, Thrombolyse, Système d'administration de médicaments, Fucoïdane, Synthèse

Les maladies cardiovasculaires représentent une menace globale pour la santé humaine, avec en particulier les maladies thrombotiques comme l'embolie pulmonaire, l'infarctus du myocarde ou l'accident vasculaire cérébral (AVC) comme principale source de mortalité. Malgré un besoin crucial de prévention, le vieillissement de la population et les changements de mode de vie contribuent toujours plus à ce fardeau croissant. Bien qu'il existe différents traitements dont le fibrinolytique rtPA, le traitement standard pour le traitement des AVC, ceux-ci manquent généralement d'efficacité et s'accompagnent d'effets secondaires importants. Le but de ce projet était donc de présenter une approche reposant sur la nanomédecine pour améliorer la thrombolyse grâce à la délivrance de plusieurs agents thérapeutiques, prenant en compte la complexité des caillots.

Nous avons donc développé une synthèse innovante pour des nanoparticules faites d'hydrogels de polysaccharides, capables de transporter le rtPA et la DNase I, une autre enzyme. Ces particules étaient biocompatibles et non toxiques, et furent obtenues grâce à un protocole robuste produisant des suspensions colloïdales stables que nous avons caractérisées. Cette synthèse a notamment impliqué l'usage de la microémulsion comme cadre théorique pour améliorer l'étape d'émulsion, et les nanogels résultants furent fonctionnalisés avec du fucoïdane, afin de cibler le caillot grâce à l'affinité de ce dernier pour la P-sélectine, un marqueur des plaquettes activées. Nous avons par la suite validé le chargement des médicaments à travers plusieurs méthodes, culminant sur une thrombolyse synergique de caillots *in vitro*. Enfin, nous avons étudié la dégradation de caillots *in vivo* avec un modèle murin de thrombose, démontrant une thrombolyse améliorée pour des nanoparticules contenant 50% et 10% de la dose recommandée de rtPA. Ainsi, ce travail permet de souligner le potentiel de nanoparticules polymériques 100% faites de polysaccharides pour un traitement ciblé des maladies thrombotiques.

Annexes

List of scientific publications as author or co-author

- **ANNEX 1**: Fournier L, **de La Taille T**, Chauvierre C. Microbubbles for human diagnosis and therapy. *Biomaterials*. 2023 Mar 1;294:122025.
- **ANNEX 2**: Fournier L, Abioui-Mourgues M, Chabouh G, Aid R, **de La Taille T**, Couture O, et al. rtPA-loaded fucoidan polymer microbubbles for the targeted treatment of stroke. *Biomaterials*. 2023 Dec 1;303:122385.
- **ANNEX 3**: **de La Taille T**, Sarfati P, Portioli C, Spanò R, Lalatonne Y, Decuzzi P, et al. REVIEW: "ISCHEMIC STROKE: from fibrinolysis to functional recovery" Nanomedicine: emerging approaches to treat ischemic stroke. *Neuroscience*. 2024 Jul 9;550:102–13.
- **ANNEX 4** (Patent): "Crosslinked polysaccharide nanoparticles". EP23307118. 2023 December 1; Inventors: **Thibault de La Taille** and Cédric Chauvierre. Assignee: INSERM Tranfert.
- **ANNEX 5**: **de La Taille T**, Doukhi D, Mazighi M, Chauvierre C. Ischemic Strokes: Exploring the Challenges of Translating Nanomedicine into Clinical Practice. *Nano Today*, With Editor (2024).
- **ANNEX 6**: **de La Taille T**, Sarfati P, Aid R, Fournier L, Pavon-Djavid G, Chaubet F, Chauvierre C. Microemulsion-inspired polysaccharide nanoparticles for an advanced targeted thrombolytic treatment. *ACS Nano*, in revision (2024).

List of international presentations

SF Nano 2022: Annual Conference of the French Society for Nanomedicine (5^{th}-7^{th} December 2022, Strasbourg, France).

- **ANNEX 7**: Poster presentation. *Development of functionalized polysaccharide nanoparticles for a targeted combo treatment of ischemic strokes.* Thibault de La Taille, Louise Fournier, Rachida Aid, Frédéric Chaubet, Cedric Chauvierre.

ECR-ISC 2022: Annual meeting of Cardiovascular Sciences Institute – Young Researchers Meeting (9^{th} December 2022, Paris, France).

- **ANNEX 7**: Poster presentation. *Development of functionalized polysaccharide nanoparticles for a targeted combo treatment of ischemic strokes.* Thibault de La Taille, Louise Fournier, Rachida Aid, Frédéric Chaubet, Cedric Chauvierre.
- **ANNEX 8**: **Prize for the best poster presentation.**

SFB Biomat 2023: Summer school for the French Society of Biomaterials, in partnership with the Swiss Society of Biomaterials (15th-16th June 2023, Zürich, Switzerland).

- **ANNEX 9**: Poster presentation. *Development of functionalized polysaccharide nanoparticles for a targeted treatment of ischemic stroke.* Thibault de La Taille, Rachida Aid, Frédéric Chaubet, Cedric Chauvierre.

SF Nano 2023: Annual Conference of the French Society for Nanomedicine (4th-6th December 2023, Montpellier, France).

- **ANNEX 10**: Oral presentation. *Functionalized polysaccharide nanoparticles for a targeted treatment of ischemic strokes.* Thibault de La Taille, Rachida Aid, Frédéric Chaubet, Cedric Chauvierre.

BIOMAT-MATSAN 2024: Annual Conference of the French Society for Biomaterials and (14th-16th January 2024, Super-Besse, France).

- **ANNEX 11**: Oral presentation. *Functionalized polysaccharide nanoparticles for a targeted treatment of ischemic strokes.* Thibault de La Taille, Pierre Sarfati, Rachida Aid, Frédéric Chaubet, Cédric Chauvierre.

JCBB 2024: Bichat Beaujon Young Researchers' Day (8th October 2024, Strasbourg, France).

- **ANNEX 12**: Oral presentation. *Functionalized polysaccharide nanoparticles for a targeted treatment of ischemic strokes.* Thibault de La Taille, Pierre Sarfati, Rachida Aid, Graciela Pavon Djavid, Frédéric Chaubet, Cédric Chauvierre.
- **ANNEX 13**: **Prize for the best oral presentation.**

Supplementary Materials

- **ANNEX 14**: ImageJ Macros used for image analysis.

ANNEX 1

Biomaterials 294 (2023) 122025

Contents lists available at ScienceDirect

Biomaterials

journal homepage: www.elsevier.com/locate/biomaterials

Microbubbles for human diagnosis and therapy

Louise Fournier, Thibault de La Taille, Cédric Chauvierre *

Université Paris Cité, Université Sorbonne Paris Nord, LVTS, UMRS 1148 INSERM, F- 75018, Paris, France

ARTICLE INFO

Keywords:
Microbubbles
Ultrasound
Molecular imaging
Targeted therapy
Sonothrombolysis
Sonoporation

ABSTRACT

Microbubbles (MBs) were observed for the first time *in vivo* as a curious consequence of quick saline injection during ultrasound (US) imaging of the aortic root, more than 50 years ago. From this serendipitous event, MBs are now widely used as contrast enhancers for US imaging. Their intrinsic properties described in this review, allow a multitude of designs, from shell to gas composition but also from grafting targeting agents to drug payload encapsulation. Indeed, the versatile MBs are deeply studied for their dual potential in imaging and therapy. As presented in this paper, new generations of MBs now opens perspectives for targeted molecular imaging along with the development of new US imaging systems. This review also presents an overview of the different therapeutic strategies with US and MBs for cancer, cardiovascular diseases, and inflammation. The overall aim is to overlap those fields in order to find similarities in the MBs application for treatment enhancement associated with US. To conclude, this review explores the new scales of MBs technologies with nanobubbles development, and along concurrent advances in the US imaging field. This review ends by discussing perspectives for the booming future uses of MBs.

1. Introduction

Conventional therapies are developed in the objective of including as many patients as possible. Therefore, researchers are looking for the best impact with the least adverse effects for their proposed therapies. At the same time, early and precise diagnosis is crucial as it allows early and accurate treatment. High dose injections, necessary for the accumulation of a sufficient drug amount on the pathological site, face major limitations attributed to the high clearance by the reticuloendothelial system (RES) but also potential collateral damages of non-pathological sites (depressed immune system in chemotherapy or collateral bleeding in stroke treatment). The lack of specificity can also be observed for diagnostic strategies where molecular scale observation could help early diagnosis and better understand the pathologies. Those drawbacks led researchers to work on the design and the development of carriers able to specifically targets pathological biomarkers and to encapsulate drugs for the improvement of conventional therapies. This approach was widely studied over the last 20 years at the nano scale with nanoparticles functionalization for various clinical applications [1]. In this review, the focus is on the micro scale with the evaluation of microbubbles (MBs) and their potential application for human therapy and diagnosis. Mostly associated to their response to Ultrasound (US)

Abbreviations: AFM, Atomic Force Microscopy; ARF, Acoustic Radiation Force; BBB, Blood Brain Barrier; BT, Brachytherapy; CNS, Central Nervous System; CO, Carbon Monoxide; CORM, Carbon Monoxide Releasing Molecule; DBCO, Dibenzocyclooctyne-amine; DSPC, (1,2-distearoyl-sn-glycero-3-phosphocholine); DSPE-PEG2000 (1, 2-distearoyl-sn-glycero-3-phosphoethanolamine-N- [amino (polyethylene glycol)-2000]); EDC / NHS, 1-Ethyl-3-(3-dimethylaminopropyl) carbodiimide; N-Hydroxy succinimide, EPR; Enhanced Permeability and Retention, FDA; Food and Drug Administration, FSHR; Follicle Stimulating Hormone Receptor, FUS; Focused Ultrasound, fUSI; Functional Ultrasound Imaging, HA; Hyaluronic Acid, HGN; Hallow Gold Nanoshell, HIFU; High Intensity Focused Ultrasound, GV; Gas Vesicle, HSA; Human Serum Albumin, JAM-A; Junctional Adhesion Molecule A, KDR; Kinase Insert Domain, LPS; Lipopolysaccharide, MB; Microbubble, MI; Mechanical Index, NB; Nanobubble, NCL; Nucleolin, ND; Nanodroplet, NIR; Near Infrared, NO; Nitric Oxide, NP; Nanoparticle, NPMB; Nanoparticles assembled as Microbubble, PALM; Photoactivated Localization Microscopy, PBS; Phosphate Buffer Saline, PCCA; Phase Change Contrast Agent, PEG; Polyethylene Glycol, PFC; Perfluorocarbon, PFD; Perfluorodecalin, PFOB; Perfluoro-octyl-Bromide, PFOC; Perfluorocarbon-based Oxygen Carrier, PSF; Point Spread Function, RES; Reticuloendothelial System, RF; Resonance Frequency, ROS; Reactive Oxygen Species, SH; Subharmonic, sLe^x: Sialyl Lewis X peptide; SPAAC, Strain Promoted Alkyne-Azide Cycloaddition; STAT3, Signal Transducer and Activation of Transcription 3; STORM, Stochastic Optical Reconstruction Microscopy; TCCS, Transcranial Color Doppler Ultrasound; Thyc1, Thymocyte Antigen 1; US, Ultrasound; ULM, Ultrasound Localized Microscopy; VCAM1, Vascular Cell Adhesion Molecule 1; VEGFR2, Vascular Endothelial Growth Factor Receptor 2.

* Corresponding author.
E-mail address: cedric.chauvierre@inserm.fr (C. Chauvierre).

https://doi.org/10.1016/j.biomaterials.2023.122025
Received 31 October 2022; Received in revised form 17 January 2023; Accepted 24 January 2023
Available online 25 January 2023
0142-9612/© 2023 Elsevier Ltd. All rights reserved.

waves, MBs are objects with the capacity to encapsulate various gas, drugs and functionalized with targeting agent. Here, we aimed at painting an overview of the latest published papers on MBs, trying to understand the links between seemingly disconnected fields, like oncology or cardiovascular system. This review aimed at describing the similarities and the differences of application of same echogenic agents in a field where standards have not been established yet. From MBs synthesis to composition characteristics, this work presents the various methods adapted to the microscopic field of imaging and drug delivery. Since MBs are intrinsically US responsive, they hold a considerable advantage over other clinical contrast agents used for diagnosis imaging like PET & SPECT scintigraphy, MRI or X-ray, and also over drug delivery nanoparticles. Here are discussed the advances in the use of MBs for imaging: from commercial MBs to molecular imaging. Among those, the therapeutic approach was studied with the potential of gas and US therapy as well as the synergic effect of the US + MBs system. Finally, this review explores the perspectives that the field offers with new generation of US contrast agent such as nanobubbles (NBs) or nanodrops (NDs) to conclude with the limitation of current US imaging and the latest development of this technique.

2. Microbubbles

MBs are defined as microscale objects composed of a shell and a gas core. They were firstly described in 1968 by Gramiak and Shah [2] as the reason of "ultrasonic contrast in the anatomic identification of the mitral valve" after image analysis. US imaging was poorly resolved and quick saline injection was used to produce "clouds of echoes" [2] contrasting with surrounding tissue. Gramiak and Shah hypothesized that this contrast enhancement was probably caused by "mini bubbles" entering the blood with the saline injection. These first observations led to the perspective for their clinical application. Indeed, a long journey happened since Gramiak and Shah with a focus on criteria validation prior to the injection in living bodies. Some are common to many injectable biomaterials like biocompatibility and biodegradation but MBs also have their specific features. For instance, size has to be controlled under the 10 μm limit to prevent from the obstruction risk in the microvasculature [3] and more preferably in the range of erythrocytes diameter [4]. Those characteristics are defined with the careful choice of gas core, shell composition and surface modification. As presented below, MBs are highly versatile objects that will behave differently *in vivo* depending on their characteristics.

2.1. Synthesis methods for microbubbles generation

Various methods have been developed for the synthesis of microbubbles (Fig. 1) endowing them with different properties. Most of the studied MBs are echogenic liposomes and the main methods for their synthesis consist in the hydration of dried lipids film [5]. It relies on dissolving a mix of lipids into chloroform and using a rotational evaporation system to obtain a thin dried film. The addition of emulsifier (Polyethylene Glycols: PEG) allows the bubble formation and the dried film is hydrated with a buffer solution such as phosphate buffer saline [6]. At last, the solution is heated to its glass transition temperature to help with lipid resuspension [7] and homogenized with US, using a sonicating horn, for several minutes to produce the MBs suspension.

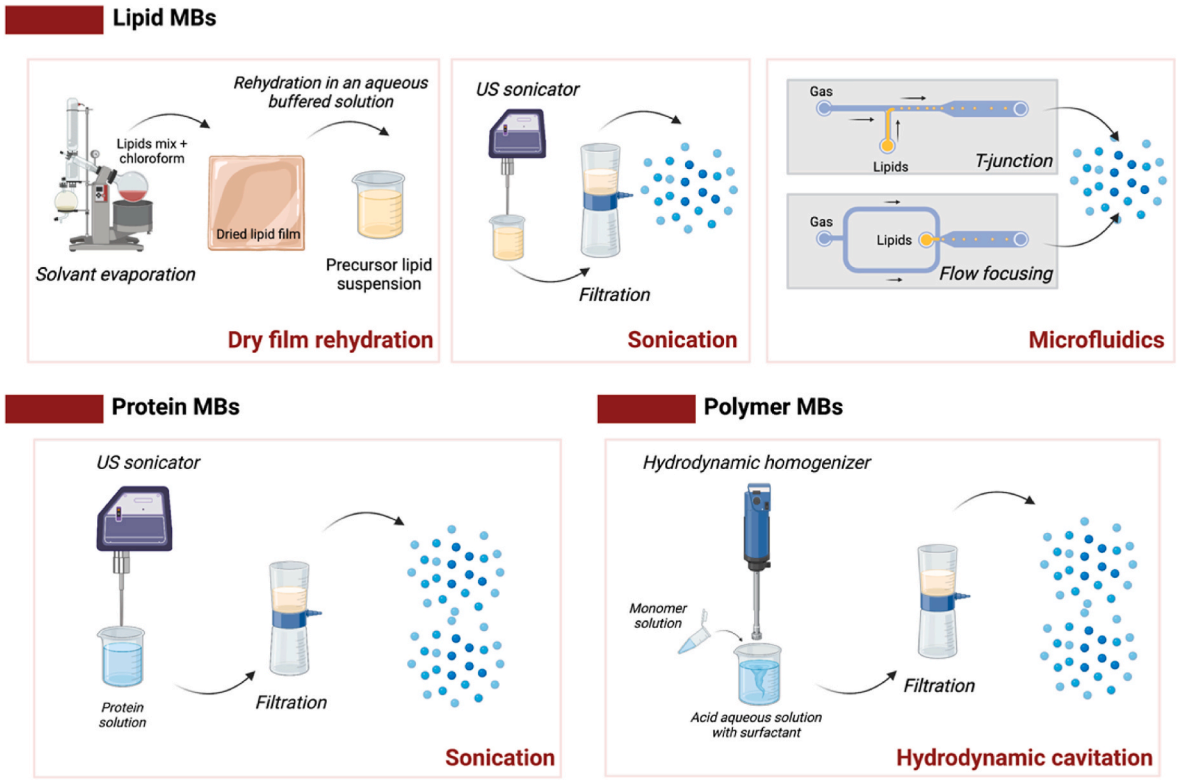


Fig. 1. Methods for Microbubbles synthesis. Lipid MBs are mainly produced following two different methods: Sonication or Microfluidics. The first step consists in dry film rehydration. It requires the solvent evaporation of the lipid + chloroform mix using a rotary evaporator. The obtained film is rehydrated at glass transition temperature and the precursor lipid suspension is homogenized with the help of US sonication. This precursor suspension is either used for a sonication protocol or microfluidics. This method relies on the encounter of the gaseous phase and the lipids phase either with a T-junction or a flow-focusing system. Both allow the generation of highly monodisperse MBs population. Comparing the two methods, dry film rehydration requires day-scale preparation while microfluidics production is obtained in hours scale. Protein MBs are obtained following US insonation of a protein solution followed by filtration of the polydisperse population. Polymer MBs are generated with hydrodynamic cavitation. Monomer solution is incorporated to an acidic aqueous solution under shear stress perturbation. Again, the polydisperse suspension is filtered. Created with BioRender.com.

Lipids dissolution in chloroform and rehydration in phosphate buffered solution constitutes the precursor lipid suspension for all lipid MBs synthesis, and the process can be time-consuming as the chloroform evaporation step can last up to 12 h [8]. Despite the wide practice of this technique, it presents some drawbacks as a complex control on the size distribution. In order to narrow the size dispersity, microfluidics have been a widely explored alternative to obtain reproducible and size tunable protocol. The general idea consists in constraining a liquid flow and/or a gaseous flow into microchannels to generate size monitored MBs. The main advantage is the reduction of reagent volumes meaning a decrease in the total cost of the experiment but also an increased yield of production. Two main systems are leading the field, the T-junction system and the flow focusing setup [9]. Both rely on the convergence of the gas phase and shell material phase with monitored flow rate and optimized channel width to entrap the gas into the shell. Nevertheless, the technology still relies on an advanced miniaturized system with development costs and a time of production slower than other process like sonication or homogenization [10]. A nice review written by Pulsipher et al. presents the various microfluidic technologies developed for MBs generation [9]. Carugo et al. figured out a smart way to overcome the poor production yield without compromising the narrow distribution of microfluidics systems [11]. Instead of direct production of micrometer size MBs, they produce large precursors bubbles with a regular T-junction gas-in-oil system but expose them to a low frequency US field to generates narrow size distribution MBs. This method enables the production of microfluidic-like MBs but with a production yield in the same order of magnitude than conventional batch sonication. Indeed, high yield production methods like hydrodynamic cavitation and sonication have a relatively faster production rate but require post synthesis treatment like filtration to narrow the size distribution. The hydrodynamic cavitation method uses the shear force of a homogenizer in an aqueous solution to induce polymer MBs formation that can be stabilized with the wanted shell component. It briefly consists in the addition of a monomer into an aqueous solution with the constant hydrodynamic stirring of an homogenizer like Ultraturrax for an hour [12]. As for sonication, it is the fastest method and is involved in the generation of the majority of protein shelled MBs [13]. As underlined by Stride et al., sonication is in majority a preparatory step and extensive study about standardization of sonication protocols is not described yet [14]. It consists in the activation of an ultrasonic horn at the solution/air interface causing compression refraction of the liquid [6]. This generation of energy usually creates high local temperature rise and the overall temperature of the solution can be cooled down by placing the setup in ice. Nevertheless, it is known to have strong potential in the obtention of high yield synthesis at low cost and high speed. However, new shell compositions might be studied with this technique to overcome the issue of stability and fast blood clearance known for protein shelled MBs.

Alternative techniques also exists like shaking, used for the synthesis of Definity® MBs by simply shaking a lipid solution in a sealed vial with a shaking device [14]. Moreover, electrohydrodynamic atomization is employed for the generation of lipid MBs by applying a constant electric field on monitored flow rate of a lipid solution in contact with air [15]. Overall, gold standard of MBs synthesis should include the high yield of hydrodynamic cavitation, the size regulation of microfluidic, the fast production time and cost effectiveness of sonication.

2.2. Microbubbles shell composition

The shell integrity of MBs was originally established with albumin polymerization but the resulting MBs quickly showed limitations due to their fast clearance in the body. The most studied protein for MBs application was Human Serum Albumin (HSA) firstly mentioned by Reisner et al. in 1989 [16] and furtherly developed with the addition of additives like Dextrose 5% [17] or fructose 5% [18] through the 90's and 2000's. They had the advantage of providing a sufficient robustness to keep the gas trapped inside and their chemical characteristics implies the possibility to graft targeting or therapeutic agents. The major drawback was attributed to their vulnerability *in vivo*, because of the fast recognition by the patrolling scavenging cells leading to a rapid elimination in the bloodstream [19]. Nowadays, the vast majority of MBs are composed of lipids and a mixture of them arranged as a monolayer [20]. The mixture of phospholipids usually consists of various ratios of DSPC (1,2-distearoyl-sn-glycero-3-phosphocholine) and DSPE-PEG2000 (1, 2-distearoyl-sn-glycero-3-phosphoethanolamine-N- [amino (polyethylene glycol)-2000]). Phosphatidylcholines are a natural component of cell membranes, generally extracted from soybean or egg yolks, and are already used and FDA approved as excipient in various intravenous treatments [21]. The resulting shell is flexible and confers the ability of structural rearrangement. This can be an advantage for an easy reconstitution after freeze drying storage but lipid monolayer reorganization can disservice the overall stability due to weak interaction forces involved in the geometry (hydrophobicity and van der Waals [6]). In consequence, it does not efficiently prevent the gas diffusion and the coalescence. Therefore, lipid shelled MBs strategy relies on the flexible property of lipids and small immunogenicity, as their lipophilic property protect them from reticuloendothelial system clearance [22].

When looking at MBs stability, interaction of MBs between themselves has to be studied. Indeed, during and after their synthesis they will be in close contact as the floatation phenomenon occurs, and unwanted events like the Ostwald ripening or coalescence are more likely to happen [23] (Fig. 2). Ostwald ripening can be defined as the expansion of bigger MBs to the detriment of small and less stable MBs based on thermodynamic equilibrium [24]. This phenomenon can be managed by selecting a low solubility-to-biological-fluid gas and a low solubility-to-biological-fluid shell but also by increasing the stiffness of the shell to prevent exchanges between the surrounding fluid and MBs. In case of lipid shelled MBs, it is recommended to increase the molar volume of the oil phase to reduce their solubility [24]. When two bubbles merge to form a larger bubble, it is called coalescence. It can be prevented by reducing the interaction between MBs using surfactants [25] or by increasing of the synthesis temperature [26]. Hence, MBs shelf stability depends on various parameters like shell and gas composition, shell elasticity, surface tension and viscosity of the aqueous solution. Sridhar et al. [27] proposed a mathematical model to estimate MBs half-life in suspension and focused the attention on shell resistance and the viscosity of the storage solution. Storage stability of MBs in suspension can be extended with stiffer shell material (like polymers) and with the addition of glycerol like ingredient to thicken the aqueous solution [28].

To overcome the shell fragility without compromising the functionalization of the MBs, polymerized cyanoacrylates were introduced as a substitute of lipid shells. Cyanoacrylates are traditionally used in medicine as surgical adhesive for wound closing [29]. They are chemically composed of an ethylene group, a cyano-group and a variable alkyl chain. Initially presented as a monomer solution, their anionic polymerization happens in contact with aqueous media like blood or body tissues conferring adhesive property to the polymer [30]. N-butyl cyanoacrylates are also used in clinics for arterial embolization to prevent from major bleeding in hard to reach regions such as pelvic area [31]. Cyanoacrylate ability to polymerize in water constitutes a new strategy for gas encapsulation in aqueous solution as presented before using hydrodynamic cavitation method. Because of its chemical structure, cyanoacrylate shell are stiffer and thicker (hundreds of nanometers compared to 3–5 nm range for lipid shells [32]) allowing multiple functionalization possibilities including drug loading [33] and targeting peptide grafting [34]. This versatility is accompanied by some drawbacks, the main one relies on the biocompatibility of cyanoacrylate degradation products *in vivo*. Even if the cyanoacrylate glue has been injected in humans [35], it is known that its hydrolysis releases cyanoacetate and formaldehyde which can lead to local ischemia [30].

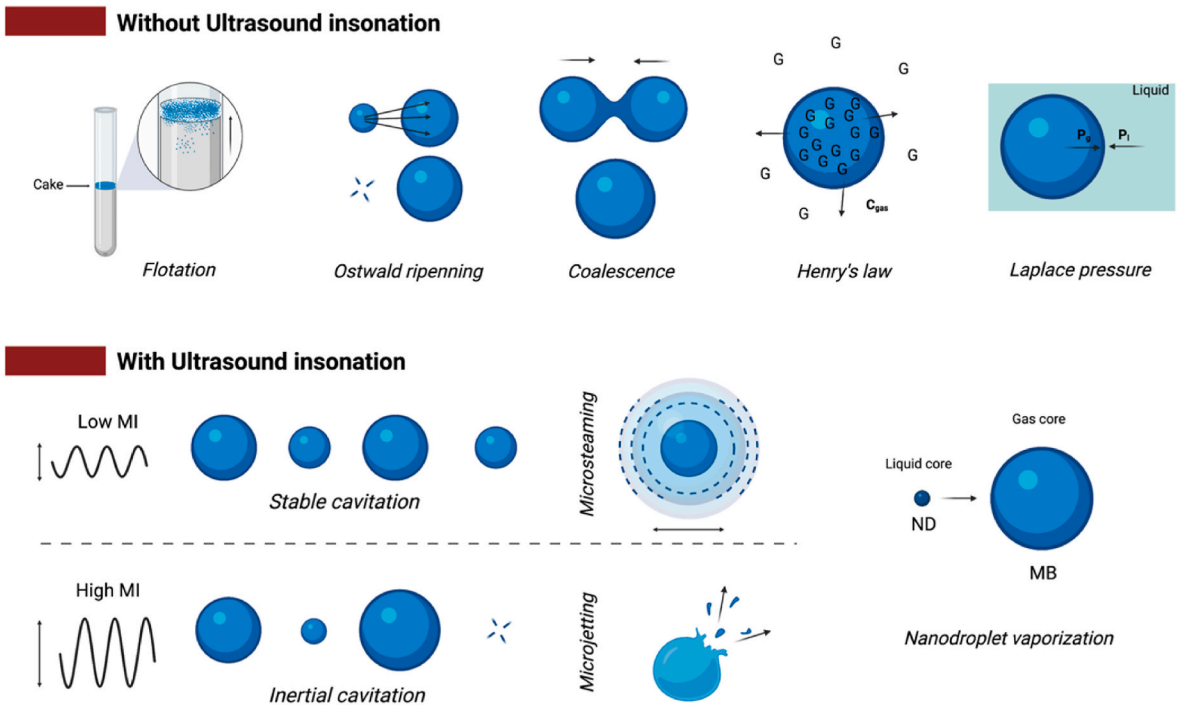


Fig. 2. Microbubbles behavior with their environment and under Us insonation. Microbubbles in static condition will rise to the top of the suspension to form a cake. Depending on the shell properties and surface tension of the MBs/liquid interphase, MBs can undergo Ostwald ripening or coalescence. They are also affected by the gas concentration of their environment according to Henry's Law and to pressure of the surrounding medium according to Laplace's Law. Under US insonation, MBs are distinguished by the US regime. Low intensity US (low Mechanical Index) will induce stable oscillations of the MBs leading to microstreaming. High intensity US (high Mechanical Index) will induce unstable oscillations of the MBs leading to MBs inertial cavitation and microjetting. Also, the liquid core of nanodroplets can undergo vaporization under specific acoustic parameters. ND = Nanodroplets, MB = microbubble, MI = Mechanical Index. Created with BioRender.com.

2.3. Microbubbles surface modification

MBs are now also designed as carriers and they not only need a safe and resistant shell, but also tunability for better biocompatibility, targeting or drug encapsulation. MBs' half-life in the bloodstream is sufficient to perform several rounds in the circulatory system and reach their target but they will get destabilized because of their inevitable gas exchange with the environment. Most lipid MBs are stabilized with PEGs working as a steric shield and avoiding a quick uptake from the reticuloendothelial system and protecting the gas core [36]. Nevertheless, this protection may also lead to generation of anti-polyethylene glycol antibodies with repeated injection [37]. Foreign body recognition can also be limited by fooling the immune system. This interesting approach presented by Yang et al. relies on the surface modification of liposomes by mixing them with platelet membrane [38]. This confers the MBs a safe passage through the blood recognition system because of the incorporation of transmembrane proteins of the platelet membranes. This approach is used here for asepsis induced acute kidney injury diagnosis but is an interesting cloaking strategy also used in nanomedicine for cancer [39] or inflammation [40].

With the acknowledgment that every foreign organism will eventually be discharged, it is also a smart strategy to focus on the targeting of a biomarker rather than the long lasting of MBs *in vivo*. Many innovations are derived from the nanoparticles surface modification [41] with the objective to graft targeting agents for molecular imaging or promoting drug delivery. J. Shue-Min Yeh et al. present a very complete table summarizing the state of the art of surface modification for lipid shell MBs until 2015 [42]. Interestingly out of 94 published papers, 58,5% are based on streptavidin biotin interaction [43,44], 18% on maleimide thiol strategy and the rest are specific lipid-peptide linkage before MBs formulation. Those numbers are interesting because some controversies rely on the immunogenic response to streptavidin in humans due to its bacterial origin. Nevertheless, it remains the strongest non covalent interaction with an affinity constant K_D of 10^{-14} M, shadowing any antibody for antigen recognition. This is why teams are working on improving the immunogenic response [45] and recent work showed great promises about the injection of avidin in humans [46]. This functionalization can be obtained via *in situ* incorporation of streptavidin and with later association of the molecule of interest coupled with biotin, or with chemical incorporation post synthesis of avidin using EDC/NHS (1-Ethyl-3-(3-dimethylaminopropyl) carbodiimide/N-Hydroxy succinimide) coupling [47].

The maleimide thiol bioconjugation strategy relies on the reactivity between maleimides and thiols groups naturally present in biomolecules like cysteines, allowing grafting of fluorochrome, PEGs or proteins [48]. Maleimide groups are added to the structure of the shells and act as an intermediate for drug grafting to the MBs but the chemical reaction has to be monitored because of two competitive reactions. One reversible linkage allowing delivery of agent but easily eliminated in the bloodstream and one irreversible linkage. Therefore, depending on the application and to avoid competition of thiol present in albumin, a fine balance has to be found to improve the stability of this reaction which heavily depends on pH [49].

Covalent bonding of functionalizing agent can be performed via EDC/NHS peptide bond formation. By definition, it allows on the covalent bounding between a carboxymethyl group and a primary amine group [50]. However, standardized protocols are hard to obtain and its accessibility and ease of use does not exclude optimization [51]. A major drawback of this approach is the immobilization of the N-terminus or C-terminus regions of proteins that can be hosting their functional features. Thus, alternative strategies emerged to be more specific regarding the anchoring point. For example, Lui et al. put forward the click chemistry coupling of various desired compounds onto their albumin MBs, conferring a high versatility to the system [52]. Briefly, the method

L. Fournier et al.

Lipids dissolution in chloroform and rehydration in phosphate buffered solution constitutes the precursor lipid suspension for all lipid MBs synthesis, and the process can be time-consuming as the chloroform evaporation step can last up to 12 h [8]. Despite the wide practice of this technique, it presents some drawbacks as a complex control on the size distribution. In order to narrow the size dispersity, microfluidics have been a widely explored alternative to obtain reproducible and size tunable protocol. The general idea consists in constraining a liquid flow with a gaseous flow into microchannels to generate size monitored MBs. The main advantage is the reduction of reagent volumes meaning a decrease in the total cost of the experiment but also an increased yield of production. Two main systems are leading the field, the T-junction system and the flow focusing setup [9]. Both rely on the convergence of the gas phase and shell material phase with monitored flow rate and optimized channel width to entrap the gas into the shell. Nevertheless, using surfactant protein validating the importance of charge on the surface and its environment [56].

Therefore, the balance has to be found for surface modification to obtain weak or strong linkage to functionalizing object, and it must not be forgotten that surface modification has to be strong enough to sustain its functionality in flow condition according to the *in vivo* environment hemodynamics. Moreover, it must not be forgotten that surface modification can influence MBs dynamics, first in term of stability because of Laplace pressure's influence on the MBs but also in terms of acoustic response [58].

US field to generates narrow size distribution MBs. This method enables the production of microfluidic-like MBs but with a production yield in the same order of magnitude than conventional batch sonication. Indeed, high yield production methods like hydrodynamic cavitation and sonication have a relatively faster production rate but require post synthesis treatment like filtration to narrow the size distribution. The hydrodynamic cavitation method uses the shear force of a homogenizer in an aqueous solution to induce polymer MBs formation that can be stabilized with the wanted shell component. It briefly consists in the addition of a monomer into an aqueous solution with the constant hydrodynamic stirring of an homogenizer like Ultraturrax for an hour [12]. As for sonication, it is the fastest method and is involved in the generation of the majority of protein shelled MBs [13]. As underlined by Stride et al., sonication is in majority a preparatory step and extensive study about standardization of sonication protocols is not described yet [14]. It consists in the activation of an ultrasonic horn at the solution air/air interface causing compression retraction of the liquid [6]. This generation of energy usually creates high local temperature rise and the overall temperature of the solution can be cooled down by placing the setup in ice. Nevertheless, it is known to have strong potential in the obtention of high yield synthesis. However, a low control of the MBs dimension, a polydisperse distribution and the formation of non-desirable phases [14] also exist. Like MBs will disappear after synthesis by definitive dissolution of the gas in the liquid medium as saturated with gas [16], this fact is governed by Henry's law (Eq. (2)).

$$C = kP \quad (2)$$

where C is the concentration of a dissolved gas, k a constant and P the pressure of the gas above the suspension or in the MBs [57]. In order to maintain the gas trapped inside it is recommended to have a thicker shell and a stabilizing gas.

2.2. Microbubbles shell composition

An additional strategy to overcome the rapid gas exchange of air between MBs and the surrounding medium resulted in the second generation of MBs where low solubility gas like sulfur hexafluoride (SF_6) or perfluorocarbons (PFCs) replaced the air core. Fluorinated gas and especially perfluorocarbons (PFCs) are now widely used to maintain a longer half-life of the MBs in the blood circulation because of their inert property. Indeed, PFCs are synthetic molecules descending from hydrocarbons where the hydrogen atoms have been substituted by fluorine atoms. They are known to be chemically inert and their intrinsic atomic structure give them the property to be hydrophobic and lipophobic at the same time [23]. Omata et al. studied the effect of the encapsulated gas on their MBs stability and compared lipid based MBs with either SF_6, C_3F_8 or C_4F_{10} [58]. They concluded that PFCs MBs (C_3F_8 and C_4F_{10}) were highly stable *in vitro* compare to the other MBs (including commercial ones) and their half-life *in vivo* was at least two times higher. Those results are strongly correlated to the Ostwald coefficient formula. 2-distearoyl-sn-glycero-3-phosphoethanolamine-N- [amino (polyethylene glycol)-2000]). Phosphatidylcholines are a natural component of cell membranes, generally extracted from soybean or egg yolks, and are already used and FDA approved as excipient in various intravenous treatments [21]. The resulting shell is flexible and confers the ability of structural rearrangement. This can be an advantage for an easy reconstitution after freeze drying storage but rapid monolayer reorganization can disservice the overall stability due to weak interaction forces involved in the geometry (hydrophobicity and van der Waals [57]). In consequence, it does not efficiently prevent the gas diffusion and the coalescence. Therefore, lipid shelled MBs strategy relies on the flexible property of lipids and small immunogenicity, as their biocompatible property protect them from reticuloendothelial system clearance [22].

When looking at MBs stability, interaction of MBs between themselves has to be studied. Indeed, during and after their synthesis they will be in close contact as the floatation phenomenon occurs, and unwanted events like the Ostwald ripening or coalescence are more likely to happen [23] (Fig. 2). Ostwald ripening can be defined as the expansion of bigger MBs to the detriment of small and less stable MBs based on thermodynamic equilibrium [24]. This phenomenon can be managed by selecting a low solubility to biological fluid gas and a low solubility to biological fluid shell but also by increasing the stiffness of the shell to prevent exchanges between the surrounding fluid and MBs. In case of lipid shelled MBs, it is recommended to increase the molar volume of the oil phase to reduce their solubility [24]. When two bubbles merge to form a larger bubble, it is called coalescence. It can be prevented by reducing the interaction between MBs using surfactants [25] or by increasing of the synthesis temperature [26]. Hence, MBs shelf-stability depends on various parameters like shell and gas composition, shell elasticity, surface tension and viscosity of the aqueous solution. Sridher et al. [27] proposed a mathematical model to estimate MBs half-life in suspension and focused the attention on shell resistance and the viscosity of the storage solution. Storage stability of MBs in suspension can be extended with stiffer shell material (like polymers) and with the addition of glycerol like ingredient to thicken the aqueous solution [28].

To overcome the shell fragility without compromising the functionalization of the MBs, polymerized cyanoacrylates were introduced as a substitute of lipid shells. Cyanoacrylates are traditionally used in medicine as surgical adhesive for wound closing [29]. They are chemically composed of an ethylene group, a cyano-group and a variable alkyl chain. Initially presented as a monomer solution, their anionic polymerization happens in contact with aqueous media like blood or body tissues conferring adhesive property to the polymer [30]. N-butyl-cyanoacrylates are also used in clinics for arterial embolization to prevent from major bleeding in hard to reach regions such as pelvic area [31]. Cyanoacrylate ability to polymerize in water constitutes a new strategy for gas encapsulation in aqueous solution as presented before using hydrodynamic cavitation method. Because of its chemical structure, cyanoacrylate shell are stiffer and thicker (hundreds of nanometers compared to 3–5 nm range for lipid shells [32]) allowing multiple functionalization possibilities including drug loading [33] and targeting peptide grafting [34]. This versatility is accompanied by some drawbacks, the main one relies on the biocompatibility of cyanoacrylate degradation products *in vivo*. Even if the cyanoacrylate glue has been injected in humans [35], it is known that its hydrolysis releases cyanoacetate and formaldehyde which can lead to local ischemia [30].

2.3. Microbubbles adapted characterization

Considering their gas core composition, MBs will inevitably rise to the top of the suspension (Fig. 2). This buoyancy phenomenon leads to a cake formation that constantly need to be resuspended to recover a homogeneous suspension. In consequence, most of the characterizations have to be thought differently compared to regular particle analysis where everything is affected by sedimentation. For most applications, alternative approaches exist to overcome this constrain like centrifugating into a syringe to be able to easily discard the infranatant. Eventually, characterization in fluidic condition is more relevant than static condition due to the buoyancy force dominating the sedimentation for MBs, which otherwise dominates in the study of other particles. To overcome the buoyancy issue some adapted characterizations are presented below like acoustic sorting for MBs triage, flow phantoms for US evaluation and atomic force microscopy for mechanical characterization.

As US contrast agents, MBs can be characterized by their resonance frequency (RF) which must match the US transducer frequency to get the best acoustic response. It is highly dependent on the mass of the bubble-liquid system (m) and the stiffness (s) of the shell [62], with the formula:

$$f_r = \frac{1}{2\pi}\sqrt{\frac{s}{m}}$$

Thus, it can be deduced that there is an inversely proportional relationship between the size of the MBs and their resonance frequency. Moreover, an increase in the shell elasticity will increase the magnitude of the backscattered signal [63]. Of course, the surrounding medium plays a role on the resistance and MBs in water won't have the same resonance frequency than MBs in blood. Considering their response to US, acoustic sorting has been a great way to narrow size distribution of the sample. In the theory, since MBs resonance frequency depends on MBs size, their displacement in a microfluidic system under US insonation also depends on their size [64]. Thus, acoustic sorting consists in flow focusing MBs in a microfluidic chip, at a concentration where MBs do not overlap, and inducing the emission of US perpendicularly to the flow. The output of the channel is divided in separated exits where MBs

Lipids dissolution in chloroform and rehydration in phosphate buffered solution constitutes the precursor lipid suspension for all lipid MBs synthesis, and the process can be time consuming as the chloroform evaporation step can last up to 12 h [8]. Despite the wide practice of this technique, it presents some drawbacks as a complex control on the size distribution. In order to narrow the size dispersity, microfluidics have been a widely explored alternative to obtain reproducible and size tunable protocol. The general idea consists in constraining a liquid flow and/or a gaseous flow into microchannels to generate size monitored MBs. The main advantage is the reduction of reagent volumes meaning a decrease in the total cost of the experiment but also an increased yield of production. Two main systems are leading the field, the T-junction system and the flow focusing setup [9]. Both rely on the convergence of the gas phase and shell material phase with *in vitro* monitored flow rate and optimized channel width to entrap the gas into the shell. Nevertheless, disruption threshold as developed by O'Connore et al. [87] starting from home-made agar gels with channel, industrials developed long lasting phantoms with different channel size or morphology for vascular doppler flow (Cirsin®).

Mechanical properties of individual MBs can be hard to determine mainly because of their size but also because of their flotation behavior. Atomic force microscopy (AFM) might be the right alternative to get an idea of MBs mechanical properties [68]. The measurement consists in the immobilization of microbubbles on AFM discs with a specific coating like poly-L-lysine or biotinylated self-assembled monolayer for streptavidin functionalized MBs. Consequently, a tipless cantilever is approached to a single MB and several loads are applied on the MB surface to evaluate the resistance to strain. It has been established with this method that Fe_3O_4 nanoparticles decorated polymer shell MBs had an elastic ratio of 1.0 ± 1.2 GPa [69], thin polymer shell Young's modulus was around 1.5–3 GPa [70] while lipid MBs was lower, around 1.2–2 GPa [71]. This last study also validated that not only the shell composition but also the shell coating can increase this elastic ratio. Similar conclusion was obtained for the stiffness: the more decorated the surface.

As for sonication, it is the fastest method and is involved in the generation of the majority of protein shelled MBs [13]. As underlined by Stride et al., sonication is in majority a preparatory step and extensive study about standardization of sonication protocols is not described yet [14]. If consists in the activation of an ultrasonic horn at the solution/air interface causing compression refraction of the liquid [6]. This generation of energy usually creates high local temperature rise and the overall temperature of the solution can be cooled down by placing the setup in ice. Nevertheless, it is known to have strong potential in the obtention of high yield synthesis at low cost and high speed. However, new shell compositions might be studied with this technique to overcome the issue of stability and fast blood clearance known for protein shelled MBs.

Alternative techniques also exists like shaking used for the synthesis of Definity® MBs by simply shaking a lipid solution in a sealed vial with a shaking device [14]. Moreover, electrohydrodynamic atomization is employed for the generation of lipid MBs by applying a constant electric field on monitored flow rate of a lipid solution in contact with air [15].

On one side, the gas saturation of the environment will influence the hydrodynamic cavitation, the size regulation of microfluidic, the fast production time and cost effectiveness of sonication.

2.2. Microbubbles shell composition

The shell integrity of MBs was originally established with albumin polymerization but the resulting MBs quickly showed limitations due to their fast clearance in the body. The most studied protein for MBs application was Human Serum Albumin (HSA) firstly mentioned by Reisner et al. in 1989 [16] and furtherly developed with the addition of additives like Dextrose 5% [17] or fructose 5% [18] through the 90's and 2000's. They had the advantage of providing a sufficient robustness to keep the gas trapped inside and their chemical characteristics implies the possibility to graft targeting or therapeutic agents. The major drawback was attributed to their vulnerability *in vivo*, because of the fast recognition by the patrolling scavenging cells leading to a rapid elimination in the bloodstream [19]. Nowadays, the vast majority of MBs are composed of lipids and a mixture of them arranged as a monolayer [20]. The mixture of phospholipids usually consists of various ratios of DSPC (1,2-distearoyl-sn-glycero-3-phosphocholine) and DSPE-PEG2000 (1,2-distearoyl-sn-glycero-3-phosphoethanolamine-N-[amino(polyethylene glycol)-2000]). Phosphatidylcholines are a natural component of cell membranes generally extracted from soybean or egg yolks, and are already used and FDA approved as excipient in various intravenous treatments [21]. The resulting shell is flexible and confers the ability of structural rearrangement. This can be an advantage for an easy reconstitution after freeze drying storage but lipid monolayers reorganization can disservice the overall stability due to weak interaction forces involved in the geometry (hydrophobicity and van der Waals [6]). In consequence, it does not efficiently prevent the gas diffusion and the coalescence. Therefore, lipid shelled MBs strategy relies on the flexible property of lipids and small immunogenicity, as their lipophilic property protect them from reticuloendothelial system clearance [22].

When looking at MBs stability, interaction of MBs between themselves has to be studied. Indeed, during and after their synthesis, MBs will be in close contact as the floatation phenomenon occurs, and unwanted events like the Ostwald ripening or coalescence are more likely to happen [23] (Fig. 2). Ostwald ripening can be defined as the expansion of bigger MBs to the detriment of small and less stable MBs based on thermodynamic equilibrium [24]. This phenomenon can be managed by selecting a low solubility to biological fluid gas and a low solubility to biological fluid shell but also by increasing the stiffness of the shell to prevent exchanges between the surrounding fluid and MBs. In case of lipid shelled MBs, it is recommended to increase the molar volume of the oil phase to reduce their solubility [24]. When two bubbles merge to form a larger bubble, it is called coalescence. It can be prevented by reducing the interaction between MBs using surfactants [25], or by increasing of the synthesis temperature [26]. Hence, MBs shelf stability depends on various parameters like shell and gas composition, shell elasticity, surface tension and viscosity of the aqueous solution. Sridhar et al. [27] proposed a mathematical model to estimate MBs half-life in suspension and focused the attention on shell resistance and the viscosity of the storage solution. Storage stability of MBs in suspension can be extended with stiffer shell material (like polymers) and with the addition of glycerol like ingredient to thicken the aqueous solution [28].

Currently available MBs for medical application are mostly lipid shell based and have not yet been put to use as targeting and drug encapsulating agents. Their exclusive function is defined as US contrast enhancers for vascular and cardiac cavity imaging. Nevertheless, the US insonation influence on MBs behavior can promote more than conventional US imaging ability as described below.

2.6. *In vivo behavior of microbubbles*

After all, MBs are meant to be intravenously injected but there is a broad gap between *in vitro* flow phantoms and *in vivo* bodies. Hemodynamically speaking, MBs tend to behave like erythrocytes in the blood as their size is similar. It means that in a bloodstream environment where none of the Virchow's Triad event happens (Stasis, Endothelial injury, Hypercoagulability) [72], the MBs will tend to have a luminal position inside the vessel [73]. Unfortunately, this hemodynamic behavior does not protect them from *in vivo* clearance systems. According to Upadhyay et al., *in vivo* stability of lipids MBs are limited to a maximum of 30 min [6]. Most likely, MBs clearance will occur through two pathways: the inevitable ripening and coalescence of the MBs due to excess of environmental or internal pressure, or the scavenging by macrophages and distribution to the reticuloendothelial systems (RES) organs like spleen, liver, bone marrow or lungs [23].

Overall, gold standard of MBs synthesis should include the high yield of gas exchange between the MBs and the blood and consequently the stability of MBs. For instance, if an animal is under isoflurane anesthesia, the ratio of oxygen in the inhaled gas mixture must be watched or a disequilibrium will appear between dissolved gas in the blood and inhaled air filled MBs. A study on dogs [74] validated that the rapid clearance of albumin air filled MBs depends on the oxygen ratio of the air mixture inhaled by animals: the more oxygen, the more rapid clearance of air filled MBs in US imaging control. On the other side, the main organ involved in the clearance of MBs is the liver. Some MBs can be used to specifically target the liver, like Sonazoid® shell of which is composed of egg phosphatidylserine, a marker externalized by cells undergoing apoptosis and generating phagocytosis induction [75]. This mechanism was studied to evaluate the clearance through liver Kupffer cells *in vivo* microscopy. It was shown that Sonazoid® MBs were almost immediately internalized but survived almost 30 min as MBs inside the macrophage cells of the liver [76]. It validates the possibility of internalization of MBs by macrophages and their survival for several minutes inside the cells before being degraded, allowing potential gas delivery before the gas escape. Biodistribution and liver uptake was also studied with polymer MBs within the work of Warzecha et al. to better understand the impact on liver cell function and viability. First, fluorescence mediated tomography validated that 40% of the MBs uptake was performed by the liver and half of it was still viable after 2 h [77]. An acute reversible hepatocyte dysfunction was observed in the minutes following MBs injection but cell viability was restored after 24 h. Finally, the study validated that even after liver injury with CCl4, the injection of polymer MBs did not affect the injury extent nor compromise the recruitment of inflammatory cells.

Once degraded, MBs debris could also enter the endothelial cells especially their shell is composed of a phospholipid layer. Indeed, those cells would inevitably be the first barrier to be contact with MBs debris. A micro-vessel on a chip study performed by Park et al. highlighted this MBs-to-cells interaction, and especially after stable cavitation of the MBs induced by US insonation [78]. Endothelial cells interaction was also demonstrated with doxorubicin loaded liposomes inducing an increase in the targeted endothelial cells toxicity due to the liposome endocytosis by endothelial cells. We could eventually extrapolate that *in vivo* internalization could be harder to demonstrate according to constant flow and very few studies really explored this pathway [79].

Finally, the major risk after validation of the biocompatibility of the shell and gas, is the occurrence of a micro embolism due to the residual shell aggregating in small vessels. Air embolism is less likely to be a threat as clinical death due to air injection happens with more than 100 mL of injected air [80]. In comparison, considering air injection of MBs of a mean diameter around 3 μm and neglecting the shell width, a standard injection of MBs in humans corresponds to a gas volume in the magnitude of the microliter.

3. Microbubbles for imaging

3.1. *Commercial microbubbles*

Twenty-five years ago, FDA approved the first MBs for contrast enhancement purpose: Albunex® from Molecular Biosystems®. Cyanoacrylate ability to polymerize in water constitutes a new strategy for gas encapsulation in aqueous solution as presented before using hydrodynamic cavitation method. Because of its chemical structure, cyanoacrylate shell are stiffer and thicker (hundreds of nanometers compared to 3–5 nm range for lipid shells [32]) allowing multiple functionalization possibilities including drug loading [33] and targeting peptide grafting [34]. This versatility is accompanied by some drawbacks, the main one relies on the biocompatibility of cyanoacrylate degradation products *in vivo*. Even if the cyanoacrylate glue has been injected in humans [35], it is known that its hydrolysis releases cyanoacetate and formaldehyde which can lead to local ischemia [30].

Albunex® was composed of a human albumin shell and air core [74], which was then slowly replaced by new generations of Albumin MBs like Albumimex® and Optizon®. Sonovue® (BR1) from Bracco is probably the most widely used commercial MBs in research and was approved by the FDA since 2001 [81]. It is a phospholipid shell MB with a sulfur Hexafluoride (SF_6) gas core, employed for cardiac, vascular and hepatic imaging. Definity® from Lantheus Medical Imaging is also frequently described and share the same shell composition as Sonovue®, but with an octafluoropropane (C_3F_8) gas core. In clinical application, it is also approved for cardiac, abdomen and pelvis imaging [82]. Lastly, General Electrics provides two types of clinically approved MBs, Sonazoid® and Optison® with respectively a lipid stabilized shell with perfluorobutane core and an albumin shell with perfluoropropane core. The first one was developed for abdominal imaging while the second one is exclusively used for cardiac application. According to their general guidelines, Sonovue®

L. Fournier et al.

Lipids dissolution in chloroform and rehydration in phosphate buffered solution constitutes the precursor lipid suspension for all lipid MBs synthesis, and the process can be time-consuming as the chloroform evaporation step can last up to 12 h [8]. Despite the wide practice of this technique, it presents some drawbacks as a complex control on the size distribution. In order to narrow the size dispersity, microfluidics have been a widely explored alternative to obtain reproducible and size tunable protocol. The general idea consists in constraining a liquid flow and/or a gaseous flow into microchannels to generate size monitored MBs. The main advantage is the reduction of reagent volumes meaning a decrease in the total cost of the experiment but also an increased yield of production. Two main systems are leading the field, the T-junction system and the flow focusing setup [9]. Both rely on the convergence of the gas phase and shell material phase with monitored flow rate and carrier phase to its strength using research [89], optimized channel width to entrap the gas into the shell. Nevertheless, the technology still relies on an advanced miniaturized system with development costs and a time of production slower than other process like sonication or homogenization [10]. A nice review written by Rubiser et al. presents the various microfluidic technologies developed for MBs generation [9]. Carugo et al. figured out a smart way to overcome the poor production yield without compromising the narrow distribution of microfluidics systems [11]. Instead of direct production, at micrometer size MBs, they produce large precursors bubbles with a regular T-junction gas-in-oil system but expose them to a low frequency US field to generates narrow size distribution MBs. This method enables the production of microfluidic-like MBs but with a production yield in the same order of magnitude than conventional batch sonication. Indeed, high yield production methods like hydrodynamic cavitation and sonication have a relatively faster production rate but require post testing alternative in the contrast agent domains for imaging, we have to better understand the physics behind it. Ultrasound imaging relies on the ability of sound waves to reflect on materials depending on their composition and structure [87]. The rationale of the methods consists on stabilized with the wanted shell component. It briefly consists in the analysis of the acoustic impedance on different tissues, which depends on to the sound waves speed of propagation and tissue density. What is mainly noticeable are the boundaries between soft tissues with different material properties like bone, fat, water and collagen [88]. As for sonication, it is the fastest method and is involved in the generation of the majority of protein shelled MBs. [13]. As underlined by Stride et al., sonication is in majority a preparatory step and extensive study about standardization of sonication protocols is not described yet [14]. It consists in the activation of an ultrasonic horn at the solution/air interface causing compression refraction of the liquid [6]. This generation of energy usually creates high local temperature rise and the overall temperature of the solution can be cooled down by placing the setup in ice. Nevertheless, it is known to have strong potential in the obtention of high yield synthesis at low cost and high speed. However, new shell compositions might be studied with this technique to overcome the issue of stability and fast blood clearance known for protein shelled MBs.

Alternative techniques also exists like shaking, used for the synthesis of Definity® MBs by simply shaking a lipid solution in a sealed vial with a shaking device [14]. Moreover, electrohydrodynamic atomization is employed for the generation of lipid MBs by applying a constant electric field on monitored flow rate of a lipid solution in contact with air [15]. Overall, gold standard of MBs synthesis should include the high yield of production time and cost effectiveness of sonication.

2.2. Microbubbles shell composition

The shell integrity of MBs was originally established with albumin polymerization but the resulting MBs quickly showed limitations due to their fast clearance in the body. The most studied protein for MBs application was Human Serum Albumin (HSA) firstly mentioned by Reisner et al. in 1989 [16] and furtherly developed with the addition of additives like Dextrose 5% [17] or fructose 5% [18] through the 90's and 2000's. They had the advantage of providing a sufficient robustness to keep the gas trapped inside and their chemical characteristics implies dependent on the amplitude of the signal which can be controlled by the voltage. This response is known as subharmonic (SH) emission generated by MBs themselves (rational fraction of the fundamental) after the possibility to graft targeting or therapeutic agents. The major drawback was attributed to their vulnerability *in vivo*, because of the fast recognition by the patrolling scavenging cells leading to a rapid elimination in the bloodstream [19]. Nowadays, the vast majority of MBs are composed of lipids and a mixture of them arranged as a monolayer [20]. The mixture of phospholipids usually consists of various ratios of DSPC (1,2-distearoyl-sn-glycero-3-phosphocholine), and DSPE-PEG2000 (1,2-distearoyl-sn-glycero-3-phosphoethanolamine-N-[amino (polyethylene glycol)-2000]). Phosphatidylcholines are a natural component of cell membranes, generally extracted from soybean, egg yolks, and lizithin. However, their range of creep under the MBs concentration are already used and FDA approved as excipient in various intravenous treatments [21]. The resulting shell is flexible and confers the ability of structural rearrangement. This can be an advantage for an easy reconstitution after freeze drying storage but lipid monolayer reorganizing can disservice the overall stability due to weak interaction forces between MBs induced the increase of their resonance frequency [95]. involved in the geometry (hydrophobicity and van der Waals) [6]). In consequence, it does not efficiently prevent the gas diffusion and the coalescence. Therefore, lipid shelled MBs strategy relies on the flexible property of lipids and small immunogenicity, as their lipophilic property protect them from reticuloendothelial system clearance [22].

When looking at MBs stability interaction of MBs between themselves has to be studied. Indeed during and after their synthesis they will be in close contact as the floatation phenomenon occurs, and unwanted events like the Ostwald ripening or coalescence are more likely to happen [23] (Fig. 2). Ostwald ripening can be defined as the expansion of bigger MBs to the detriment of small and less stable MBs based on thermodynamic equilibrium [24]. This phenomenon can be managed by selecting a low solubility-to-biological-fluid gas and a low solubility-to-biological-fluid shell but also by increasing the stiffness of the shell to prevent exchanges between the surrounding fluid and MBs. In case of lipid shelled MBs, it is recommended to increase the molar volume of the oil phase to reduce their solubility [24]. When two bubbles merge to form a larger bubble, it is called coalescence. It can be prevented by reducing the interaction between MBs using surfactants [25] or by increasing the synthesis temperature [26]. Hence, MBs shelf stability depends on various parameters like shell and gas composition, shell elasticity, surface tension and viscosity of the aqueous solution. Sridhar et al. [27] proposed a mathematical model to estimate MBs half-life in suspension and focused the attention on shell resistance and the viscosity of the storage solution. Storage stability of MBs in suspension can be extended with stiffer shell material (like polymers) and with the addition of glycerol like ingredient to thicken the aqueous solution [28].

To overcome the shell fragility without compromising the functionalization of the MBs, polymerized cyanoacrylates were introduced as a substitute of lipids shells. Cyanoacrylates are traditionally used in medicine as surgical adhesive for wound closing [29]. They are chemically composed of an ethylene group, a cyano-group and a variable alkyl chain. Initially presented as a monomer solution, their anionic polymerization happens in contact with aqueous media like blood or body tissues conferring adhesive property to the polymer [30]. N-butyl cyanoacrylates are also used in clinics for arterial embolization to prevent from major bleeding in hard to reach regions such as pelvic area [31]. Cyanoacrylate ability to polymerize in water constitutes a new strategy for gas encapsulation in aqueous solution as presented before using hydrodynamic cavitation method. Because of its chemical structure, cyanoacrylate shell are stiffer and thicker (hundreds of nanometers compared to 3–5 nm range for lipid shells [32]) allowing multiple functionalization possibilities including drug loading [33] and targeting peptide grafting [34]. This versatility is accompanied by some drawbacks, the main one relies on the biocompatibility of cyanoacrylate degradation products *in vivo*. Even if the cyanoacrylate glue has been injected in humans [35], it is known that its hydrolysis releases cyanoacetate and formaldehyde which can lead to local ischemia [30].

3.2. US insonation's influence on microbubbles

To better understand why microbubbles have been such an interesting contrast agent domains for imaging, we have to better understand the physics behind it. Ultrasound imaging relies on the ability of sound waves to reflect on materials depending on their composition and structure [87]. The rationale of the methods consists on the analysis of the acoustic impedance on different tissues, which depends on to the sound waves speed of propagation and tissue density. As for sonication, it is the fastest method and is involved in the generation of the majority of protein shelled MBs. [13]. As underlined by Harmless, non-invasive and accessible method, it is mostly known for pregnancy follow-up but can bring quick and reliable answers to many more anatomic observation (ligament observation, breast check-up, [14]. It consists in the activation of an ultrasonic horn at the solution/air circulatory system ...). Indeed US imaging can address anatomical examination with B-mode imaging (2D) or functional evaluation with Doppler setting for blood flow monitoring [89]. Ultrasound imaging in clinics is usually performed in a range from 1 to 50 MHz, knowing that the higher the frequency the shorter the tissue penetration will be [87]. High frequencies (over 15 MHz) enable differentiation of objects less than 100 μm apart in depth [90] but are limited to superficial skin and superficial structures. Breast and thyroid can be observed in the range of 10 MHz, deeper organs like general abdomen and gynecological structures are observed around 3.5 MHz and below. Nevertheless, high frequencies are quite frequently used in animal study because it does not require deep tissue penetration and confers a better special resolution than low frequency US. There are some limitations of this imaging modality and especially the difficulty to image small structures like narrow vasculature or delimitations of the heart cavities. According to Yong et al., even in transesophageal echography, up to 15% of cardiac function evaluation fails due to poor contrast delimitation of the heart cavity [91]. Furthermore, US imaging highly depends on the distance to the observed object. In consequence, there has been an interest in the development in contrast enhancing agent capable of a high response to US signal.

Compared to surrounding tissue, MBs response to US stimuli induces an increased contrast. The effect of US waves on MBs is the induction of their oscillation in a non-linear way [92]. The general oscillation of the MBs is not in phase because their response to acoustic stimuli depends on their distance to the source. This non-linear property makes them dependent on the amplitude of the signal which can be controlled by the

insonation which distinguishes them from surrounding tissue, tunable to produce SH [92]. Those harmonics have a lower frequency and are subsequently less attenuated by organs. Sojahrood et al. investigated the conditions for the best signal or SH by insonating MBs and demonstrated that, for a non-destructive regime, the optimum response signal was obtained when the emitted frequency was between 1.5 and 1.8 times the resonance frequency of the MBs [92]. Those particularities adapted enhancement of MBs. Indeed, as a larger MBs can linger in the blood pool and targeted for the imaging of endothelial cells involved in angiogenesis, a key factor in some cancer's growth. With a first introduction of BR55 MBs [84] in the literature in 2010, they completed the first-in-humans injection for the molecular imaging of prostate cancer in 24 patients in 2019 [85]. Using KDR (Kinase Insert Domain) as another targeting agent, BR55 MBs were also injected in humans for the diagnosis of breast and ovarian lesion [86] enhancing US contrast in 93% of the malignant breast lesion and 88% of the ovarian malignant lesion.

plan can play the role as larger MBs can hinder the behavior of smaller MBs. Larger MBs can also be used as contrast enhancer for targeting applications [93]. Nevertheless, MBs range directly with the MBs concentration and are already used and FDA approved as excipient in various intravenous treatments [21]. The resulting shell is flexible and confers the ability of structural rearrangement. This can be an advantage for an easy reconstitution after freeze drying storage but lipid monolayer reorganizing can disservice the overall stability due to weak interaction forces between MBs induced the increase of their resonance frequency [95].

In terms of MBs behavior under US insonation, two categories can be distinguished: stable cavitation and inertial cavitation which differ by the outcome of the mechanical process [18,22]. Stable cavitation of MBs happens at low intensity of US signal allowing stable oscillations of the MBs with an alternance between compression and dilatation episodes without inducing MBs rupture [94]. This behavior is the one observed during US imaging thanks to the emitted subharmonics and ultra-harmonics at low acoustic pressure [95]. Among non-destructive cavitations, microstreaming has been described as the biological effect to happen [23] (Fig. 2). Ostwald ripening can be defined as the expansion of bigger MBs to the detriment of small and less stable MBs based on thermodynamic equilibrium [24]. This phenomenon can be managed by selecting a low solubility-to-biological-fluid gas and a low solubility-to-biological-fluid shell but also by increasing the stiffness of the shell to prevent exchanges between the surrounding fluid and MBs. In case of lipid shelled MBs, it is recommended to increase the molar volume of the oil phase to reduce their solubility [24]. When two bubbles merge to form a larger bubble, it is called coalescence. It can be prevented by reducing the interaction between MBs using surfactants [25] or by increasing the synthesis temperature [26]. Hence, MBs shelf stability depends on various parameters like shell and gas composition, shell elasticity, surface tension and viscosity of the aqueous solution. Sridhar et al. [27] proposed a mathematical model to estimate MBs half-life in suspension and focused the attention on shell resistance and the viscosity of the storage solution. Storage stability of MBs in suspension can be extended with stiffer shell material (like polymers) and with the addition of glycerol like ingredient to thicken the aqueous solution [28].

To overcome the shell fragility without compromising the functionalization of the MBs, polymerized cyanoacrylates were introduced as a substitute of lipids shells. Cyanoacrylates are traditionally used in medicine as surgical adhesive for wound closing [29]. They are chemically composed of an ethylene group, a cyano-group and a variable alkyl chain. Initially presented as a monomer solution, their anionic polymerization happens in contact with aqueous media like blood or body tissues conferring adhesive property to the polymer [30]. N-butyl cyanoacrylates are also used in clinics for arterial embolization to prevent from major bleeding in hard to reach regions such as pelvic area [31]. Cyanoacrylate ability to polymerize in water constitutes a new strategy for gas encapsulation in aqueous solution as presented before using hydrodynamic cavitation method. Because of its chemical structure, cyanoacrylate shell are stiffer and thicker (hundreds of nanometers compared to 3–5 nm range for lipid shells [32]) allowing multiple functionalization possibilities including drug loading [33] and targeting peptide grafting [34]. This versatility is accompanied by some drawbacks, the main one relies on the biocompatibility of cyanoacrylate degradation products *in vivo*. Even if the cyanoacrylate glue has been injected in humans [35], it is known that its hydrolysis releases cyanoacetate and formaldehyde which can lead to local ischemia [30].

3.3. Microbubbles molecular imaging

Molecular imaging represents a new era of early and precise diagnosis that is in development for several imaging techniques from X-ray technology to MRI, including US imaging [88]. Characterized as the merging point between molecular biology and *in vivo* imaging, the goal of molecular imaging is to visualize and quantify biological processes from early stages, end points and sequels. In contrast to other imaging methods, molecular imaging tends to break free from structural imaging to reach a molecular range precision. To that purpose, contrast enhancers must be functionalized with the targeting property toward specific biomarkers.

Early studies used fluorescence microscopy to overcome the lack of

Lipids dissolution in chloroform and rehydration in phosphate buffered solution constitutes the precursor lipid suspension for all lipid MBs synthesis, and the process can be time consuming as the chloroform evaporation step can last up to 12 h [9]. Despite the wide practice of this technique, it presents some drawbacks as a complex control on the size distribution. In order to narrow the size dispersity, microfluidics have been a widely explored alternative to obtain reproducible and size tunable protocol. The general idea consists in constraining a liquid flow and/or a gaseous flow into microchannels to generate size monitored MBs. The main advantage is the reduction of reagent volumes meaning a decrease in the total cost of the experiment but also an increased yield of production. Two main systems are leading the field, the T-junction system and the flow focusing setup [9]. Both rely on the convergence of the gas phase and shell material phase with monitored flow rate and optimized channel width to entrap the gas into the shell. Nevertheless, the technology still relies on an advanced miniaturized system with estimated development costs and a time of production slower than other process like sonication or homogenization [10]. A nice review written by Pu, Tinsley et al. presents the various microfluidic technologies developed for MBs generation [9]. Carugo et al. figured out a smart way to overcome the poor production yield without compromising the narrow distribution of microfluidics systems [11]. Instead of direct production of micrometer size MBs, they produce large precursors bubbles with a regular T-junction gas-in-oil system but expose them to a low frequency US field to generates narrow size distribution MBs. This method enables the production of microfluidic-like MBs but with a production yield in the same order of magnitude than conventional batch sonication. Indeed, high yield production methods like hydrodynamic cavitation and sonication have a relatively faster production rate but require post synthesis treatment like filtration to narrow the size distribution. The hydrodynamic cavitation method uses the shear force of a homogenizer in an aqueous solution to induce polymer MBs formation that can be stabilized with the wanted shell component. It briefly consists in the addition of a monomer into an aqueous solution with the constant hydrodynamic stirring of an homogenizer like Ultraturrax for an hour [12]. As for sonication, it is the fastest method and is involved in the generation of the majority of protein shelled MBs [13]. As underlined by [85,86]. Otherwise, the most accessible animal model remains the Stride et al., sonication is in majority a preparatory step and extensive study about standardization of sonication protocols is not described yet [14]. It consists in the activation of an ultrasonic horn at the solution/air interface causing compression/refraction of the liquid [8]. This generation of energy ustrally creates high local temperature rise and the overall temperature of the solution can be cooled down by placing the setup in ice. Nevertheless, it is known to have strong potential in the obtention of high yield synthesis at low cost and high speed. However, new shell compositions might be studied with this technique to overcome the issue of stability and fast blood clearance known for protein shelled MBs.

Alternative techniques also exists like shaking, used for the synthesis of Definity MBs by simply shaking a lipid solution in a sealed vial with a shaking device [14]. Moreover, electrohydrodynamic atomization is employed for the generation of lipid MBs by applying a constant electric field on monitored flow rate of a lipid solution in contact with air [15]. Overall, gold standard of MBs synthesis should include the high yield of hydrodynamic cavitation, the size regulation of microfluidic, the fast production time and cost effectiveness of sonication.

2.2. Microbubbles shell composition

The shell integrity of MBs was originally established with albumin polymerization but the resulting MBs quickly showed limitations due to their fast clearance in the body. The most studied protein for MBs application was Human Serum Albumin (HSA) firstly mentioned by Feinstein et al. in 1989 [16] and furtherly developed with the addition of additives like Dextrose 5% [17] or fructose 5% [18] through the 90's and 2000 s. They had the advantage of providing a sufficient robustness to keep the gas trapped inside and their chemical characteristics implies the possibility to graft targeting or therapeutic agents. The major drawback was attributed to their vulnerability *in vivo*, because of the fast recognition by the patrolling scavenging cells leading to a rapid elimination in the bloodstream [19]. Nowadays, the vast majority of MBs are composed of lipids and a mixture of them arranged as a monolayer [20]. The mixture of phospholipids usually consists of various ratios of DSPC (1,2-distearoyl-sn-glycero-3-phosphocholine) and DSPE-PEG2000 (1,2-distearoyl-sn-glycero-3-phosphoethanolamine-N- [amino (polyethylene glycol) 2000]). Phosphatidylcholines are a natural component of cell membranes, generally extracted from soybean or egg yolks, and are already used and FDA approved as excipient in various intravenous treatments [21]. The resulting shell is flexible and confers the ability of structural rearrangement. This can be an advantage for an easy reconstitution after freeze drying storage but lipid monolayer reorganization can disservice the overall stability due to weak interaction forces involved in the geometry (hydrophobicity and van der Waals [6]). In consequence it does not efficiently prevent the gas diffusion and the coalescence. Therefore, lipid shelled MBs strategy relies on the flexible property of lipids and small immunogenicity, as their lipophilic property protect them from reticuloendothelial system clearance [22].

4.1. Gas therapy

When looking at MBs stability, interaction of MBs between themselves has to be studied. Indeed, during and after their synthesis they will be in close contact as the floatation phenomenon occurs, and unwanted events like the Ostwald ripening or coalescence are more likely to happen [23] (Fig. 2). Ostwald ripening can be defined as the expansion of bigger MBs to the detriment of small and less stable MBs based on thermodynamic equilibrium [24]. This phenomenon can be managed by selecting a low solubility-to-biological-fluid gas and a low solubility-to-biological-fluid shell but also by increasing the stiffness of the shell to prevent exchanges between the surrounding fluid and MBs. In case of lipid shelled MBs, it is recommended to increase the molar volume of the oil phase to reduce their solubility [24]. When two bubbles merge to form a larger bubble, it is called coalescence. It can be prevented by reducing the interaction between MBs using surfactants [25] or by increasing of the synthesis temperature [26]. Hence, MBs shell stability depends on various parameters like shell and gas composition, shell elasticity, surface tension and viscosity of the aqueous solution. Sridhar et al. [27] proposed a mathematical model to estimate MBs half-life in suspension and focused the attention on shell resistance and the viscosity of the storage solution. Storage stability of MBs in suspension can be extended with stiffer shell material (like polymers) and with the addition of glycerol like ingredient to thicken the aqueous solution [28].

To overcome the shell fragility without compromising the functionalization of the MBs, polymerized cyanoacrylates were introduced as a substitute of lipid shells. Cyanoacrylates are traditionally used in medicine as surgical adhesive for wound closing [29]. They are chemically composed of an ethylene group, a cyano-group and a variable alkyl chain. Initially presented as a monomer solution, their anionic polymerization happens in contact with aqueous media like blood or body tissues conferring adhesive property to the polymer [30]. N-butyl cyanoacrylates are also used in clinics for arterial embolization to prevent from major bleeding in hard to reach regions such as pelvic area [31]. Cyanoacrylate ability to polymerize in water constitutes a new strategy for gas encapsulation in aqueous solution as presented before using hydrodynamic cavitation method. Because of its chemical structure, cyanoacrylate shell are stiffer and thicker (hundreds of nanometers compared to 3–5 nm range for lipid shells [32]) allowing multiple functionalization possibilities including drug loading [33] and targeting peptide grafting [34]. This versatility is accompanied by some drawbacks, the main one relies on the biocompatibility of cyanoacrylate degradation products *in vivo*. Even if the cyanoacrylate glue has been injected in humans [35], it is known that its hydrolysis releases cyanoacetate and formaldehyde that can lead to local ischemia [30,36].

Table 1
Non exhaustive list of targeting ultrasound responsive strategies for molecular imaging since 2015. GPIIb/IIIA = Glycoprotein IIb/IIIa; VCAM-1 = Vascular Cell Adhesion Protein 1; vWF = von Willebrand Factor; JAM-A = Junctional Adhesion Molecule A; VEGFR2 = Vascular Endothelial Growth Factor Receptor 2.

Application	MB composition	Targeting ligand	Biomarker	Clinical advancement	Year	Ref.
Cancer						
Glioma	Lipids	Peptide	VEGFR2	Clinical trials	2017	[84]
Breast and ovarian	Lipids	Peptide	KDR	Clinical trials	2017	[86]
	Lipids	Peptide/Antibody	B7–H3	Mouse model	2020	[108]
	Lipids	Type III fibronectin	VEGFR2	Mouse model	2016	[117]
	Lipids	Antibody	B7–H3	Mouse model	2015	[107]
Pancreas	Lipids	scAntibody	Thy-1	Mouse model	2018	[104]
Colon	Lipids	Peptide	VEGFR1/VEGFR2	Mouse model	2020	[116]
Kidney	Lipids	Peptide	VEGFR2	Mouse model	2016	[118]
Angiogenesis	Lipid	Peptide	Nucleolin	Mouse model	2017	[110]
	Polymer	Peptide	P-selectin	Mouse model	2016	[119]
	Lipids	Peptide	Neuropilin-1	Mouse model	2015	[120]
Thrombosis	Polymer	Fucoidan	P-selectin	Mouse model	2018	[121]
	Lipids	scAntibody	GPIIb/IIIa	Mouse model	2016	[121]
	Lipids	Peptide	Thrombin	*In vitro* model	2017	[122]
Vessel injury	Polymer	Antibody	VCAM-1	Mouse model	2015	[123]
	Polymer	RGD peptide	αvβ3-integrin	Pig model	2016	[124]
Atherosclerosis	MBs	Nanobodies	VCAM-1	Mouse model	2019	[125]
	Lipids	Peptide	VCAM-1/vWF/P-selectin/LOX1	Mouse model	2018	[126]
	Polymer	Antibody	JAM-A	Mouse model	2018	[111]
	Lipids	Antibody/sLe	VCAM-1/ICAM-1/Selectins	Mouse model	2018	[116]
	Lipids	Antibody	JAM-A	Rabbit Model	2016	[113]
Liver injury	Polymer	RGD peptide	Myeloid integrins	Mouse model	2018	[127]
Endothelium	Lipids	Peptide	P-selectin	Dog model	2020	[114]
	Lipids	Peptide/Antibody	P-selectin/VCAM-1/vWF-A1/GPIbα	Mouse model	2018	[126]
Abdominal aorta	Lipids	Antibody	P-selectin/VCAM-1	Mouse model	2017	[127]
Liver fibrosis	Lipids	Antibody	VEGFR2	Rat model	2021	[128]
Bowel	Lipids	Peptide	P and E-selectins	Pig model	2015	[129]

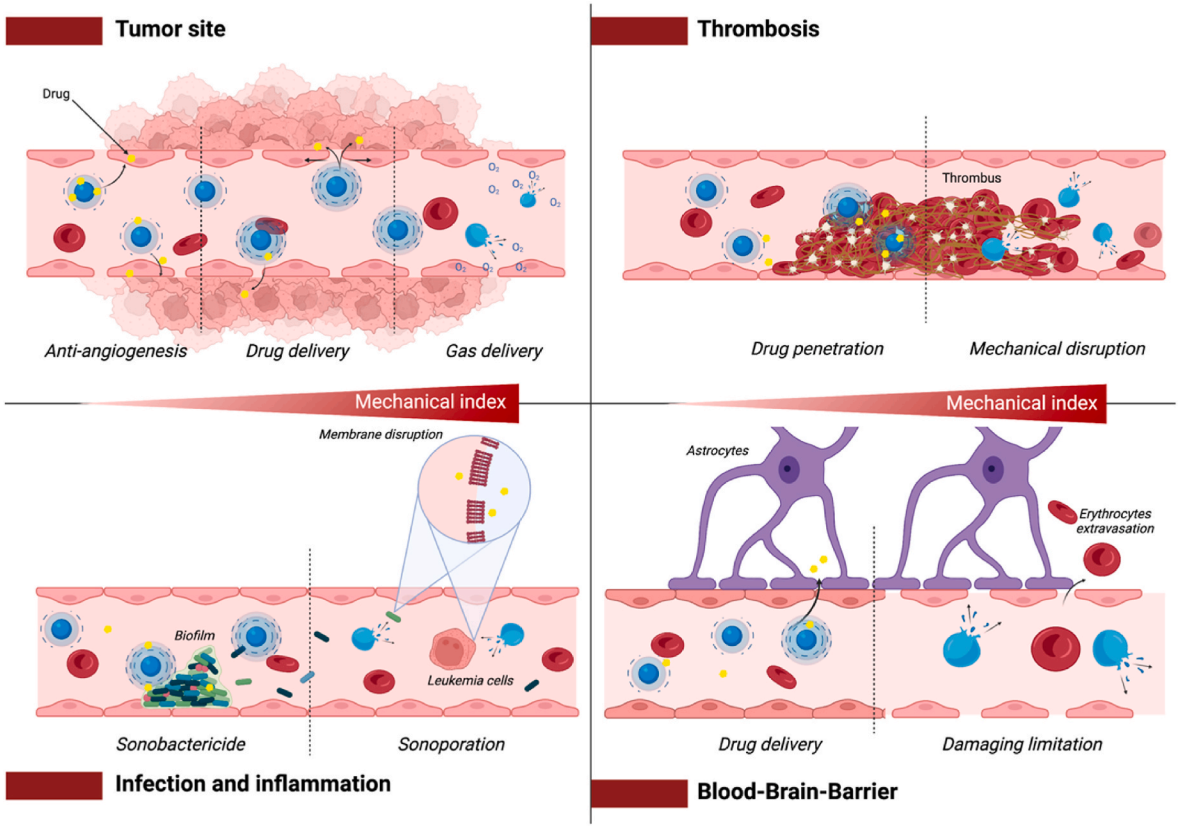


Fig. 3. Therapeutic strategies for tumors, thrombi, infection and Blood-Brain-Barrier. Depending on the mechanical impact of the US signal, MBs therapy can be adapted for different pathologies. Microbubble microstreaming can improve drug delivery to the epithelium and the thrombus. It also destabilizes membrane permeation by fragilizing biofilms and BBB epithelium tight-junctions. The increasing of US mechanical index induces a stronger mechanical impact on the surrounding tissue. Indeed, MBs implosion helps mechanically disrupt thrombi by loosening up the fibrin mesh. This disruption has to be carefully monitored because it promotes cell membrane sonoporation for a therapeutic approach but also vascular permeation causing cerebral hemorrhages. Created with BioRender.com.

it would respond to the oxygen treatment. Unfortunately, most tumors are not accessible for intra-tumoral injection and gas therapy might be delivered via intravenous route. Improvement of radiosensitivity was observed with the intravenous injection of surfactant shelled oxygen MBs on a breast cancer rat model [135]. By increasing tumor oxygenation by 20 mmHg with oxygen MBs, radiosensitivity was almost tripled. This anti-hypoxic treatment leads also to a significant delay in the tumor growth of approximately 30 days compared to radiotherapy only, highlighting great promises for the use of oxygen delivery therapy as a complement of cancer treatment [136]. In order to improve oxygen MBs stability, Peng et al. associated SF_6 to the gas core which showed a 3 times improvement of the circulation half-life *in vivo* [137] (Fig. 4). The study presents lipids O_2SF_6 MBs injected in a nasopharyngeal carcinoma mouse model. Using local US triggered destruction of the MBs, tumor volume significantly dropped from 614 ± 157 mm^3 with regular treatment to 229 ± 31 mm^3. Oxygen therapy is also a promising strategy for wound healing with the embedding of MBs into hydrogels [138].

4.1.2. Nitric oxide

Apart from oxygen therapy, nitric oxide (NO) delivery is a studied strategy because of its function in the regulation of angiogenesis. Thanks to its chemical structure with a very unstable peripherical electron, it is largely used by the cells for signaling and is known for its important role in the promotion of angiogenesis and expending blood vessels [139]. In other words, instead of asphyxiating the tumor, improving its vasculature may overcome the radiotherapy resistance caused by the hypoxic state: it is called tumor vasculature normalization [140]. This hypothesis was studied with the injection of NO micelles combined with radiotherapy [141]. As a result, tumor weight was divided by two compared to the radiotherapy only and survival rate of the mice was also significantly improved. NO is also implicated in the resolution of deep vein thrombosis, by playing a role with the platelets an inflammatory cells aggregation, as well as stimulation the endothelium. Wang et al. injected rats with NO MBs after deep vein thrombosis induction surgery and the resolution of the clot was studied by weighting the clots 8 days later [142]. Interestingly, weight over length ratio of extracted thrombi at day 8 showed a decrease of 40% compared to control group. Compared to anticoagulant therapy this strategy does not involve the risk of collateral bleeding as they measured major indexes of coagulation function. They hypothesized that the antithrombotic effect mainly affected the vessel wall by limiting the leukocyte extravasation (decrease of the expression of VCAM-1 on thrombosis site) and thus maintaining endothelium integrity.

4.1.3. Carbon monoxide

Other gases are potential therapies for cancer such as carbon monoxide (CO) which increases mitochondrial respiration leading to excess production of Reactive Oxygen Species (ROS) and the onset of cell apoptosis [143]. CO also plays a dual role on the nervous central system. Similarly to NO, it is considered as a gasotransmitter in cell signaling and intracellular production of CO can provide neuroprotective effect by upregulating cyclic guanosine phosphate production [144]. Inhalation treatment already proved an infarct volume reduction up to 62.2% in brain ischemia on mice [145]. On the other side, excessive concentration of CO can lead to hypoxia damaging brain cells. Indeed, a strict control of the administered dose creates an unmet medical need for targeted encapsulation of CO as neuroprotective treatment. Looking at another cell signaling pathway, low doses of CO were demonstrated to have an

L. Fournier et al.

Lipids dissolution in chloroform and rehydration in phosphate buffered solution constitutes the precursor lipid suspension for all lipid MBs synthesis, and the process can be time-consuming as the chloroform evaporation step can last up to 12 h [8]. Despite the wide practice of this protocol known a significant accumulation of anti-inflammatory cytokine IL-10 in the tissue with low concentration of CO. Same results briefly observed *in vivo*, allowing interesting perspectives for the role of CO in the regulation of inflammatory response. This treatment strategy would be all the more interesting as intact phages have the ability to perform phagocytosis on circulating elements, hence the MBs. An decrease in the total cost of the experiment but also an increased yield of production. Two main systems are leading the field, the T-junction system and the flow focusing setup [9]. Both rely on the convergence of the gas phase and shell material phase with monitored flow rate and optimized channel width to entrap the gas into the shell. Nevertheless, the technology still relies on an advanced miniaturized system with development costs and a time of production slower than other process like sonication or homogenization [10]. A nice review written by Pulsipher et al. presents the various microfluidic technologies developed for MBs generation [9]. Carugo et al. figured out a smart way to overcome the poor production yield without compromising the narrow distribution of microfluidics systems [11]. Instead of direct production of micrometer size MBs, they produce large precursors bubbles with a regular T-junction gas-in-oil system but expose them to a low-frequency US field to generates narrow size distribution MBs. This method enables the production of microfluidic-like MBs but with a production yield in the same order of magnitude than conventional batch sonication. Indeed, high yield production methods like hydrodynamic cavitation and sonication have a relatively faster production rate but require post synthesis treatment like filtration to narrow the size distribution. The hydrodynamic cavitation method uses the shear force of a homogenizer in an aqueous solution to induce polymer MBs formation that can be stabilized with the wanted shell component. It briefly consists in the addition of a monomer into an aqueous solution with the constant hydrodynamic stirring of an homogenizer like Ultraturrax for an hour [12]. As for sonication, it is the fastest method and is involved in the generation of the majority of protein shelled MBs [13]. As underlined by Stride et al., sonication is in majority a preparatory step and extensive study about standardization of sonication protocols is not described yet [14]. It consists in the activation of an ultrasonic horn at the solution/air interface causing compression refraction of the liquid [6]. This generation of energy usually creates high local temperature rise and the overall temperature of the solution can be cooled down by placing the setup in ice. Nevertheless, it is known to have strong potential in the obtention of high yield synthesis at low cost and high speed. However, new shell compositions might be studied with this technique to overcome the issue of stability and fast blood clearance known for protein shelled MBs.

Alternative techniques also exists like shaking, used for the synthesis of Definity – MBs by simply shaking a lipid solution in a sealed vial with a shaking device [14]. Moreover, electrohydrodynamic atomization is employed for the generation of lipid MBs by applying a constant electric field on monitored flow rate of a lipid solution in contact with air [15]. Overall, gold standard of MBs synthesis should include the high yield of hydrodynamic cavitation, the size regulation of microfluidic, the fast production time and cost effectiveness of sonication.

2.2. Microbubbles shell composition

The shell integrity of MBs was originally established with albumin polymerization but the resulting MBs quickly showed limitations due to their fast clearance in the body. The most studied protein for MBs application was Human Serum Albumin (HSA) firstly mentioned by Reisner et al. in 1989 [16] and furtherly developed with the addition of additives like Dextrose 5% [17] or fructose 5% [18] through the 90's and 2000's. They had the advantage of providing a sufficient robustness to keep the gas trapped inside and their chemical characteristics implies the possibility to graft targeting or therapeutic agents. The major drawback was attributed to their vulnerability *in vivo*, because of the fast recognition by the patrolling scavenging cells leading to a rapid elimination in the bloodstream [19]. Nowadays, the vast majority of MBs are composed of lipids and a mixture of them arranged as a monolayer [20]. The mixture of phospholipids usually consists of various ratios of DSPC (1,2-distearoyl-sn-glycero-3-phosphocholine), and DSPE-PEG2000 (1,2-distearoyl-sn-glycero-3-phosphoethanolamine-N-[amino (polyethylene glycol)-2000]). Phosphatidylcholines are a natural component of cell membranes, generally extracted from soybean or egg yolks, and are already used and FDA approved as excipient in various intravenous treatments [21]. The resulting shell is flexible and confers the ability of structural rearrangement. This can be an advantage for an easy reconstitution after freeze drying storage but lipid monolayer reorganization can dissevice the overall stability due to weak interaction forces involved in the geometry (hydrophobicity and van der Waals [6]). In consequence, it does not efficiently prevent the gas diffusion and the coalescence. Therefore, lipid shelled MBs strategy relies on the flexible property of lipids and small immunogenicity as their lipophilic property protect them from reticuloendothelial system clearance [22].

When looking at MBs stability, interaction of MBs between themselves has to be studied. Indeed, during and after their synthesis they will be in close contact as the floatation phenomenon occurs, and unwanted events like the Ostwald ripening or coalescence are more likely to happen [23] (Fig. 2). Ostwald ripening can be defined as the expansion of bigger MBs to the detriment of small and less stable MBs based on thermodynamic equilibrium [24]. This phenomenon can be managed by selecting a low solubility-to-biological-fluid gas and a low solubility-to-biological-fluid shell but also by increasing the stiffness of confined behavior of MBs differs from unbounded ones and it seems the shell to prevent exchanges between the surrounding fluid and MBs. In case of lipid shelled MBs, it is recommended to increase the molar volume of the oil phase to reduce their solubility [24]. When two bubbles merge to form a larger bubble, it is called coalescence. It can be prevented by reducing the interaction between MBs using surfactants [25] or by increasing of the synthesis temperature [26]. Hence, MBs shelf stability depends on various parameters like shell and gas [158]. *In silico* results assessed that wall shear stress within microvessels could reach 18.3 kPa during MBs expansion and 74 kPa during MB collapse. As constrained MBs behave differently, an *ex vivo* model from perfused rat caecum led to the conclusion that the angle of US insonation on vessels had no impact on the interaction between MBs and the endothelium. It also showed that constrained bubbles in the capillary network had an increased oscillatory lifetime compared to big vessels and that bigger MBs (>4 μm) tend to interact better with the endothelium than very small MBs [159]. Those observed interactions under US insonation consisted in an asymmetrical collapse onto the vessel wall and repeated expansion beyond the vessel limits and the study suggested that the efficacy of ultrasound mediated MBs therapy strongly depends on the MBs concentration and size distribution. On the other hand, *in vitro* vessel phantoms lithotripsy set up with albumin MBs demonstrated that the induced expansion of very large bubble could cause rupture of the vessel wall and therefore pointing out the importance of size dispersity regulation [160]. Those general examples are important to understand the mechanical behavior of MBs. Indeed, despite the wide use of MBs for therapy for cancer, inflammation or thrombotic diseases, some therapeutic strategies are actually very similar. As many innovative therapies, the balance has to be found between the different parameters to get the best advantage over risks ratio. The first parameter that can be monitored is the mechanical index (MI) of the US wave. It is a unitless ratio representing the pic of negative pressure (MPa) over the square root of the frequency (MHz) of the signal [161].

$$MI = \frac{P}{\sqrt{f}}$$

This ratio strongly depends on the US device used and the distance to the object, and it can be measured with an hydrophone calibration [162]. Below 0.1, MI will generate only linear oscillation of the MBs; between 0.1 and 1, these oscillations become non-linear allowing the imaging of the MBs. From 1, inertial cavitation leading to disruption of

4.1.4. Perfluorocarbons

Perfluorocarbons (PFC) do not have direct therapeutic effect, however, they are used as intermediate transporter for oxygen. As mentioned before, O_2 plays an important role in the physiology and consequently in pathologies. PFC in their liquid state like Perfluoro-octyl-bromide (PFOB), or perfluorobutane (PFB) can be employed as O_2, NO and CO carriers [148]. Their very inert property enables the uptake of oxygen. If we compare the capacity of dissolution of oxygen in water or in a PFC, the molar ratio of dissolved O_2 is 1 mol of O_2 in 200 mol of water compared to 1 mol of O_2 in 0.2 mol of Perfluorodecalin (PFD) [23]. Perfluorocarbons-based oxygen carriers (PFOCs) have nicely been reported in the review from Jäger et al., presenting how PFOCs are an innovative tool from cancer therapy to blood substitute [23]. As presented before, the fluorine atomic structure tends to attract electrons from surrounding atoms giving a stiff structure to the molecules that are not aimed to dissolve in aqueous media meaning that PFCs are good candidates as solvent for other gas and especially oxygen, carbon dioxide and nitric oxide [148].

4.2. Ultrasound therapy

US treatments are already widely used without the need of MBs injection. The main advantage of US therapy is the non-invasive characteristic of the method. It is now possible to avoid surgical intervention over kidney stone disease by the use of shock wave lithotripsy [149]. The current use of high peak pressure (up to 100 MPa) and very low rate (2 Hz) safely helps with the resolution of kidney stones [150]. Recent clinical trials of a more efficient burst wave lithotripsy (<12 MPa, <200 Hz) helped to reposition 95% of kidney stones in human [151].

US are also used for ablation therapy without the requirement of surgical intervention. This method called histotripsy uses focused US to destroy tissue, thanks to the induced cavitation, without thermal or ionizing related event [152]. It was first observed as a collateral damaging consequence of lithotripsy, which was finally studied by itself as a new form of non-invasive therapy. Typically used US parameters are performed up to 6 MHz with a high negative pressure up to 15 MPa with low duty cycle to avoid heat generation. Phase 1 clinical trials were conducted on benign prostatic hyperplasia, liver cancer and calcified aortic stenosis [152]. Limitations of US therapy are still attributed to organs containing gas or acoustically unreachable organs because of bone blockage. If recent clinical trials have not confirmed the evidence of US enhanced sonothrombolysis in limb ischemia yet [153], clinical studies are still ongoing to replace invasive mechanical thrombectomy and overcome collateral damages of high dose thrombolytic therapy. This issue can be resolved by using US as an accelerator of thrombolysis, in supplement of drug delivery. Li et al. meta-analysis highlighted that, out of 5 clinical trials, thrombolytic injection associated with US insonation for acute ischemic stroke showed a significant recanalization rate over thrombolytic injection alone [154]. The studied trials had US parameters ranging from 0.5 MHz to 4 MHz over 1 h or US monitoring during a 2 h local treatment, US emitting catheter can be introduced in the popliteal vein along with plasminogen activator for delivery of the treatment [155]. Phosphatidylcholines are a natural component of cell membranes, generally extracted from soybean or egg yolks, and are already used and FDA approved as excipient in various intravenous treatments [21]. The resulting shell is flexible and confers the ability of structural rearrangement. This can be an advantage for an easy reconstitution after freeze drying storage but lipid monolayer reorganization can dissevice the overall stability due to weak interaction forces involved in the geometry (hydrophobicity and van der Waals [6]). In consequence, it does not efficiently prevent the gas diffusion and the coalescence. Therefore, lipid shelled MBs strategy relies on the flexible property of lipids and small immunogenicity as their lipophilic property protect them from reticuloendothelial system clearance [22].

When looking at MBs stability, interaction of MBs between themselves has to be studied. Indeed, during and after their synthesis they will be in close contact as the floatation phenomenon occurs, and unwanted events like the Ostwald ripening or coalescence are more likely to happen [23] (Fig. 2). Ostwald ripening can be defined as the expansion of bigger MBs to the detriment of small and less stable MBs based on thermodynamic equilibrium [24]. This phenomenon can be managed by selecting a low solubility-to-biological-fluid gas and a low solubility-to-biological-fluid shell but also by increasing the stiffness of confined behavior of MBs differs from unbounded ones and it seems the shell to prevent exchanges between the surrounding fluid and MBs. In case of lipid shelled MBs, it is recommended to increase the molar volume of the oil phase to reduce their solubility [24]. When two bubbles merge to form a larger bubble, it is called coalescence. It can be prevented by reducing the interaction between MBs using surfactants [25] or by increasing of the synthesis temperature [26]. Hence, MBs shelf stability depends on various parameters like shell and gas [158]. *In silico* results assessed that wall shear stress within microvessels could reach 18.3 kPa during MBs expansion and 74 kPa during MB collapse. As constrained MBs behave differently, an *ex vivo* model from perfused rat caecum led to the conclusion that the angle of US insonation on vessels had no impact on the interaction between MBs and the endothelium. It also showed that constrained bubbles in the capillary network had an increased oscillatory lifetime compared to big vessels and that bigger MBs (>4 μm) tend to interact better with the endothelium than very small MBs [159]. Those observed interactions under US insonation consisted in an asymmetrical collapse onto the vessel wall and repeated expansion beyond the vessel limits and the study suggested that the efficacy of ultrasound mediated MBs therapy strongly depends on the MBs concentration and size distribution. On the other hand, *in vitro* vessel phantoms lithotripsy set up with albumin MBs demonstrated that the induced expansion of very large bubble could cause rupture of the vessel wall and therefore pointing out the importance of size dispersity regulation [160]. Those general examples are important to understand the mechanical behavior of MBs. Indeed, despite the wide use of MBs for therapy for cancer, inflammation or thrombotic diseases, some therapeutic strategies are actually very similar. As many innovative therapies, the balance has to be found between the different parameters to get the best advantage over risks ratio. The first parameter that can be monitored is the mechanical index (MI) of the US wave. It is a unitless ratio representing the pic of negative pressure (MPa) over the square root of the frequency (MHz) of the signal [161].

$$MI = \frac{P}{\sqrt{f}}$$

This ratio strongly depends on the US device used and the distance to the object, and it can be measured with an hydrophone calibration [162]. Below 0.1, MI will generate only linear oscillation of the MBs; between 0.1 and 1, these oscillations become non-linear allowing the imaging of the MBs. From 1, inertial cavitation leading to disruption of

4.3. Microbubbles as therapeutic tools

The application of MBs for therapy must be preceded by the study of the interaction between vessel wall and MBs interaction. Indeed, if we compare the capacity of dissolution of oxygen in water or in a PFC, reasonably clear that the bioeffect of MBs disruption has to be studied to determine therapeutic boundaries. Known limitations consist in the damage of surrounding tissue attributed to vessel distention or wall impairment due to microjetting (Fig. 2). Mathematical models were established by Hosseinkhah et al. to evaluate the wall shear stress and circumferential stress and have been validated with experimental data [158]. *In silico* results assessed that wall shear stress within microvessels could reach 18.3 kPa during MBs expansion and 74 kPa during MB collapse. As constrained MBs behave differently, an *ex vivo* model from perfused rat caecum led to the conclusion that the angle of US insonation on vessels had no impact on the interaction between MBs and the endothelium. It also showed that constrained bubbles in the capillary network had an increased oscillatory lifetime compared to big vessels and that bigger MBs (>4 μm) tend to interact better with the endothelium than very small MBs [159]. Those observed interactions under US insonation consisted in an asymmetrical collapse onto the vessel wall and repeated expansion beyond the vessel limits and the study suggested that the efficacy of ultrasound mediated MBs therapy strongly depends on the MBs concentration and size distribution. On the other hand, *in vitro* vessel phantoms lithotripsy set up with albumin MBs demonstrated that the induced expansion of very large bubble could cause rupture of tissues conferring adhesive property to the polymer [30]. N-butyl cyanoacrylates are also used in clinics for arterial embolization to prevent tribution regulation [160]. Those general examples are important to from major bleeding in hard to reach regions such as pelvic area [31]. understand the mechanical behavior of MBs. Indeed, despite the wide Cyanoacrylate ability to polymerize in water constitutes a new strategy use of MBs for therapy for cancer, inflammation or thrombotic diseases, for gas encapsulation in aqueous solution as presented before using some therapeutic strategies are actually very similar. As many innovahydrodynamic cavitation method. Because of its chemical structure, tive therapies, the balance has to be found between the different pacyanoacrylate shell are stiffer and thicker (hundreds of nanometers rameters to get the best advantage over risks ratio. The first parameter compared to 3–5 nm range for lipids shells [32]), allowing multiple that can be monitored is the mechanical index (MI) of the US wave. It is a functionalization possibilities including drug loading [33] and targeting unitless ratio representing the pic of negative pressure (MPa) over the peptide grafting [34]. This versatility is accompanied by some drawsquare root of the frequency (MHz) of the signal [161].

$$MI = \frac{P}{\sqrt{f}}$$

backs, the main one relies on the biocompatibility of cyanoacrylate degradation products *in vivo*. Even if the cyanoacrylate glue has been injected in humans [35], it is known that its hydrolysis releases cyanoacetate and formaldehyde which can lead to local ischemia [30].

This ratio strongly depends on the US device used and the distance to

the MBs can be observed [6]. Eventually, these numbers can be adapted to each application but the scientific community and the FDA agreed on the limit of MI to 1.9 in humans to avoid any damaging bioeffect [163] (except for ophthalmological evaluation where the MI is limited to 0.23 [164]).

4.3.1. Thrombosis

As mentioned before, MBs can be triggered to explode by increasing the amplitude of the US signal (Fig. 3). This bursting associated with thrombi therapy is called sonothrombolysis. Basically, sonothrombolysis consists in the use of ultrasound waves and MBs to mechanically disrupt the clot [41]. It can be influenced by the duration of insonation, the composition and the concentration of MBs or the time between pathological incident and treatment. Positive outcomes are evaluated with the recanalization rate [121] or the study of the related ischemic lesion, like presented by Dixon et al. on an ischemic stroke model [10] (Fig. 4). A very complete review from Nederhoed et al. describes the different therapeutic use of MBs and US on peripheral arterial thrombosis based on 26 preclinical studies and 9 clinical ones [165]. They compared the localization of the thrombosis (middle cerebral artery, abdominal aorta, internal carotid artery …), the age of the clot and the number of subjects for preclinical and clinical studies. Recanalization rate was one of the primary outcomes, meaning the ability of the blood flow to be restored after the treatment. There were two ways of quantifying the reperfusion rate: angiography or transcranial Doppler.

Among the *in vivo* preclinical studies (Table 2) using a thrombolytic drug as a control, here are the interesting conclusions: the US settings used for sonothrombolysis were very heterogeneous varying frequency of the transducer from 1 MHz [166] to 6 MHz [167], the MI from 0.2 [168] to 2 [169] and different pulse length [170]. Preferentially, the strategy was to infuse the MBs over several minutes [168,169,171,172] while continuously insonating the clot with different MI. On the other hand, some studies injected the MBs in bolus but always with long treatment insonation [173–175], which is in contradiction with the fact that MBs are relatively quickly cleared out from the blood. The total exposition of clot to the US remains unclear and very heterogeneous to most of the studies. There is a clear need for *in vivo* study to accurately describe the frequency of the probe, the mechanical index, the duty cycle and the total duration of insonation, in order to better establish comparisons. Moreover, lack of control groups using MBs and thrombolytic agent with US insonation has been highlighted as well as lack of comparison with different shell compositions. According to Nederhoed et al., all the studies included for the *in vivo* sonothrombolysis using contrast enhancer agent and a thrombolytic agent presented a minimum recanalization rate of 56% up to 100% while US alone never allow a reperfusion superior to 63% [165]. The lower recanalization rate was attributed to Tomkins et al. because of the platelet rich composition of the clot that responds less efficiently to thrombolytic therapy [172].

Moving on to clinical studies for sonothrombolysis, most of them were performed on ischemic stroke patient with duration therapy from 1 to 2 h with 2 MHz US insonation but with low or non-indicated MI. The biggest clinical study of sonothrombolysis for ischemic stroke patient was performed at the University Hospital of Vall d'Hebron in Barcelona, including 296 patient with acute stroke [176]. After thrombolytic drug bolus, patients received 3 doses of 2.5 g of air-filled galactose-based MBs along with 2 h of transcranial Doppler monitoring. Conclusion of the study was that MBs administration associated with US insonation helped early recanalization without increasing the risk of intracranial hemorrhage. One limitation however remains, since these results were obtained with an operator dependent technique which is the transcranial doppler imaging. The therapeutic window was not meant to be improved in this study but presents potential leads for reduction of thrombolytic drug dose that still can cause collateral hemorrhages. Short pulse duration (<5 μs) is explored in randomized clinical trial to reduce US exposition [177]. In this study, myocardial infarction patients were randomly treated with high MI and Definity® MBs injection before and after undergoing percutaneous coronary intervention. In combination with regular treatment, MBs treatment help doubling the recanalization rate. One key data was the improvement of the systolic function that remained higher with MBs treatment even after 6 months. Consequently, only 5% of the patients required the implantation of a removable defibrillator while 18% of percutaneous coronary only treated patient required one.

The clinical translation of therapeutic MBs still faces obstacles in order to find the right conditions for an efficient sonothrombolysis and standardize the protocols. Furthermore, the actual clinical studies are based on already approved MBs as contrast enhancers, but have not included payload-carrying or targeted MBs yet. Also, as Porter et al. mentioned, one major drawback to overcome with the use of MBs for therapy is the microvascular obstruction after recanalization of myocardial infarction [178]. Despite many strategies evaluated for its resolution, research has failed finding a solution and recanalization of

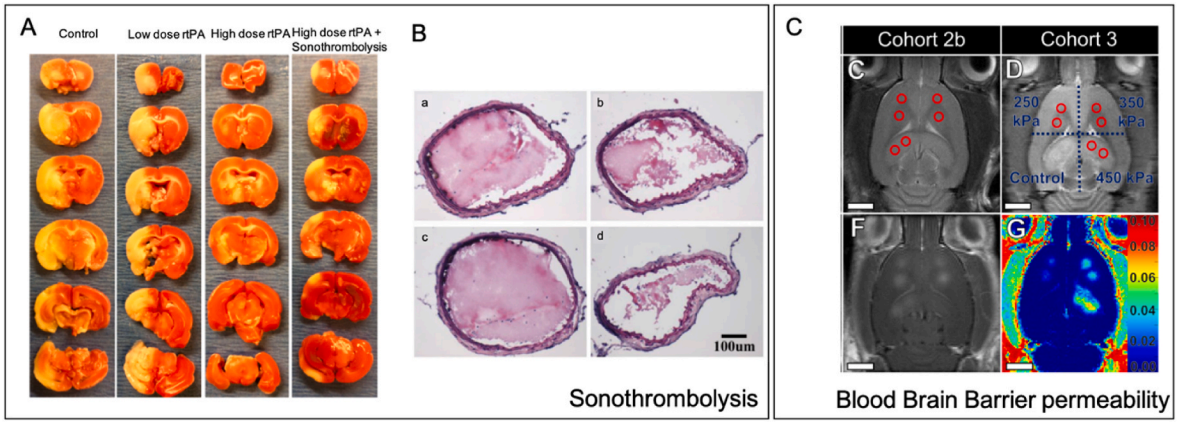


Fig. 4. *MBs and US insonation for sonothrombolysis and Blood Brain Barrier permeability. A) and* ***B)*** *In vivo sonothrombolysis using MBs and US.* ***A)*** *TTC staining of stroke induced cross sectioned brain. Infarct is identified by yellowish areas. Groups are presented as below: control with saline injection; low dose of rtPA (0.09 mg/kg); high dose of rtPA (0.9 mg/kg); low dose of rtPA (0.09 mg/kg) + MBs + US.* ***B)*** *Representative images of hematoxylin and eosin-stained thrombi from mice carotid arteries after different treatments and US imaging. a) Platelet targeted MBs + low dose of rtPA (75 U/g); b) rtPA loaded platelet targeted MBs; c) Platelet targeted MBs + saline; d) Platelet targeted MBs + high dose of rtPA (500U/g).* ***C)*** *MRI images of Targeting Focused US (FUS) on rats. First row red circles represent the MRI guided FUS targets before insonation. Second row corresponds to images after FUS.* ***C–F)*** *Gadolinium contrast enhancement in T1 MRI highlighting BBB permeation on FUS targets.* ***C-G)*** *Dynamic contrast-enhanced-MRI after MBs FUS exposure depending on several US amplitude. TTC = Triphenyltetrazolium Chloride. Adapted with permission from A) [10]; B) [121]; C) [193].* (For interpretation of the references to color in this figure legend, the reader is referred to the Web version of this article.)

L. Fournier et al.

Lipids dissolution in chloroform and rehydration in phosphate buffered solution constitutes the precursor lipid suspension for all lipid MBs synthesis, and the process can be time-consuming as the chloroform evaporation step can last up to 12 h [8]. Despite the wide practice of this technique, it presents some drawbacks as complex control on the size distribution. In order to narrow the size dispersity, microfluidics have been a widely explored alternative to obtain reproducible and size tunable protocol. The general idea consists in constraining a liquid flow and/or a gaseous flow into microchannels to generate size monitored MBs. The main advantage is the reduction of reagent volumes meaning a decrease in the total cost of the experiment but also an increased yield of production. Two main systems are leading the field, the T-junction system and the flow focusing setup [9]. Both rely on the convergence of the gas phase and shell material phase with monitored flow rate and optimized channel width to entrap the gas into the shell. Nevertheless, the technology still relies on an advanced miniaturized system with development costs and a time of production slower than other process like sonication or homogenization [10]. A nice review written by Pulsipher et al. presents the various microfluidic technologies developed for MBs generation [9]. Carugo et al. figured out a smart way to overcome the poor production yield without compromising the narrow distribution of microfluidics systems [11]. Instead of direct production of micrometer size MBs, they produce large precursors bubbles with a regular T-junction gas-in-oil system but expose them to a low frequency US field to generates narrow size distribution MBs. This method enables the production of microfluidic-like MBs but with a production yield in the same order of magnitude than conventional batch sonication. Indeed, high yield production methods like hydrodynamic cavitation and sonication have a relatively faster production rate but require post synthesis treatment like filtration to narrow the size distribution. The hydrodynamic cavitation method uses the shear force of a homogenizer in an aqueous solution to induce polymer MBs formation that can be stabilized with the wanted shell component. It briefly consists in the addition of a monomer into an aqueous solution with the constant hydrodynamic stirring of an homogenizer like Ultraturrax for an hour [12]. As for sonication, it is the fastest method and is involved in the generation of the majority of protein shelled MBs [13]. As underlined by Stride et al., sonication is in majority a preparatory step and extensive study about standardization of sonication protocols is not described yet [14]. It consists in the activation of an ultrasonic horn at the solution/air interface causing compression refraction of the liquid [6]. This generation of energy usually creates high local temperature rise and the overall temperature of the solution can be cooled down by placing the setup in ice. Nevertheless, it is known to have strong potential in the obtention of high yield synthesis at low cost and high speed. However, new shell compositions might be studied with this technique to overcome the issue of stability and fast blood clearance known for protein shelled MBs.

Alternative techniques also exists like shaking, used for the synthesis of Definity MBs by simply shaking a lipid solution in a sealed vial with a shaking device [14]. Moreover, electrohydrodynamic atomization is employed for the generation of lipid MBs by applying a constant electric field on monitored flow rate of a lipid solution in contact with air [15].

2.2. Microbubbles shell composition

The shell integrity of MBs was originally established with albumin polymerization but the resulting MBs quickly showed limitations due to their fast clearance in the body. The most studied protein for MBs application was Human Serum Albumin (HSA) firstly mentioned by Reisner et al. in 1989 [16] and furtherly developed with the addition of additives like Dextrose 5% [17] or fructose 5% [18], through the 90's and 2000's. They had the advantage of providing a sufficient robustness to keep the gas trapped inside and their chemical characteristics implies under US insonation to disturb the surrounding tissue and deliver the oxygenation to overcome the hypoxic state [134], the anti-tumor drug delivery and the anti-angiogenesis strategy [96] (Fig. 3, Table 2).

In terms of drug delivery, biological barriers are a limiting factor, even for nanoparticles (NPs), because of the lack of homogeneity in the tumor vasculature. US assisted delivery with MBs could help drug penetration with the generated microstreaming. This advantage was evaluated by Snipstad et al. in 2017 with polymeric NPs assembled as a MB (NPMBs) [180]. The goal is to take the advantage of MBs behavior under US insonation to disturb the surrounding tissue and deliver the possibility to graft targeting or therapeutic agents. The major drawback was attributed to their vulnerability *in vivo*, because of the fast recognition by the patrolling scavenging cells leading to a rapid elimination in the bloodstream [19]. Nowadays, the vast majority of MBs are composed of lipids and a mixture of them arranged as a monolayer [20]. The mixture of phospholipids usually consists of various ratios of DSPC (1,2-distearoyl-sn-glycero-3-phosphocholine) and DSPE-PEG2000 (1, 2-distearoyl-sn-glycero-3-phosphoethanolamine-N- [amino (polyethylene glycol)-2000]). Phosphatidylcholines are a natural component of cell membranes, generally extracted from soybean or egg yolks, and are already used and FDA approved as excipient in various intravenous treatments [21]. The resulting shell is flexible and confers the ability of structural rearrangement. This can be an advantage for an easy reconstitution after freeze drying storage but lipid monolayer reorganization can disservice the overall stability due to weak interaction forces involved in the geometry (hydrophobicity and van der Waals [6]). In consequence, it does not efficiently prevent the gas diffusion and the coalescence. Therefore, lipid shelled MBs strategy relies on the flexible property of lipids and small immunogenicity, as their lipophilic property protect them from reticuloendothelial system clearance [22].

When looking at MBs stability, interaction of MBs between themselves has to be studied. Indeed, during and after their synthesis they will be in close contact as the flotation phenomenon occurs, and unwanted events like the Ostwald ripening or coalescence are more likely to happen [22,23] (Fig. 2). Ostwald ripening can be defined as the expansion of bigger MBs to the detriment of small and less stable MBs based on thermodynamic equilibrium [24]. This phenomenon can be managed by selecting a low solubility-to-biological-fluid gas and a low solubility-to-biological-fluid shell but also by increasing the stiffness of the shell to prevent exchanges between the surrounding fluid and MBs. In case of lipid shelled MBs, it is recommended to increase the molar volume of the gas phase to reduce their solubility [24]. When two bubbles merge to form a larger bubble, it is called coalescence. It can be prevented by reducing the interaction between MBs using surfactants [25] or by increasing of the synthesis temperature [26]. Hence, MBs shelf stability depends on various parameters like shell and gas composition, shell elasticity, surface tension and viscosity of the aqueous solution. Sridhar et al. [27] proposed a mathematical model to estimate MBs half-life in suspension and focused the attention on shell resistance and the viscosity of the storage solution. Storage stability of MBs in suspension can be extended with stiffer shell material (like polymers) and with the addition of glycerol like ingredient to thicken the aqueous solution [28].

To overcome shell instability while compromising the functionalization of the MBs, polymerized cyanoacrylates were introduced as a substitute of lipid shells. Cyanoacrylates are traditionally used in medicine as surgical adhesive for wound closing [29]. They are chemically composed of an ethylene group, a cyano-group and a variable alkyl chain. Initially presented as a monomer solution, their anionic polymerization happens in contact with aqueous media like blood or body tissues conferring adhesive property to the polymer [30]. N-butyl cyanoacrylates are also used in clinics for arterial embolization to prevent from major bleeding in hard to reach regions such as pelvic area [31]. Cyanoacrylate ability to polymerize in water constitutes a new strategy for gas encapsulation in aqueous solution as presented before using hydrodynamic cavitation method. Because of its chemical structure, cyanoacrylate shell are stiffer and thicker (hundreds of nanometers compared to 3–5 nm range for lipid shells [32]) allowing multiple functionalization possibilities including drug loading [33] and targeting peptide grafting [34]. This versatility is accompanied by some drawbacks, the main one relies on the biocompatibility of cyanoacrylate degradation products *in vivo*. Even if the cyanoacrylate glue has been injected in humans [35], it is known that its hydrolysis releases cyanoacetate and formaldehyde which can lead to local ischemia [30].

The question was addressed on the same protocol, with either drug loaded NPMBs or free drug co-administered with NPMBs to evaluate the true potential of US induced sonopermeation [181]. Interestingly, no

Table 2
Synergic therapies of MBs associated with US and drug for thrombosis and cancer. (No exhaustive list of recent pre-clinical studies evaluating the improvement of drug therapy with MBs. (tPA: tissue plasminogen activator; TCCS: Transcranial Color Doppler Ultrasound; MI: Mechanical Index; Ab: Antibody)

Application	Targeting agent	Drug	Loaded on MBs	Co-injected	US	Outcome	Ref.
Stroke	No	tPA	No	Infusion (NA)	1 MHz, 0.9 MI, 20 min	TCCS + MBs required tPA co-injection for an efficient thrombolysis	[166]
Stroke	No	tPA	No	Infusion (10 mg/kg)	1.3 MHz, 1.2 MI, 10 min	Resistance to tPA thrombolysis for resolution is	[167]
Stroke	No	Urokinase (20,000 U/kg)	No	Infusion	2 MHz, no MI	Synergy in the recanalization rate using co-injection of drug and MBs	[174]
Coronary thrombosis	Yes (IIb/IIIa)	Pro-Urokinase, heparin, Aspirin	No	Infusion (50,000 U/kg)	1.5 MHz, MI 1.9, 30 min	Synergy of clot targeting and high MI	[168]
Coronary thrombosis	No	tPA	No	Infusion (1 or 0.5 mg/kg)	1 MHz, 2.0 MI, 30 min	Synergy of high MI with MBs and low tPA dose	[169]
Coronary and microvascular thrombosis	No	tPA	No	Infusion (1 or 0.5 mg/kg)	1.6 MHz, 1.9 MI, 30 min	Longer duration pulse over higher MI is more efficient	[170]
Abdominal aorta thrombosis	No	tPA	Yes (rehydration with tPA solution, 200 μg/mL)	Control	1.6 MHz, MI 0.4, 30 min	No difference in the US conditions, efficient thrombolysis but no significance difference between co-injection and MBs-loaded MBs	[167]
Limb arterial thrombosis	No	Urokinase (50,000 U/kg)	No	Intra-arterial Infusion	1.6 MHz, 1.2 MI, 60 min	Synergy of US with MBs and low drug dose for faster resolution	[171]
Limb arterial thrombosis	Yes (RGD)	tPA	Yes (rehydration with tPA solution, 200 μg/mL)	Control	1.2 MHz, 0.5 MI, 30 s	Reduced dose of tPA loaded on MBs with US and shell but also by increasing the stiffness of the shell to free tPA regular dose with MBs and US	[172]
Breast cancer	No	Cabazitaxel	Yes, loaded during synthesis (10 mg/kg)	Control	1.1 MHz, 0.5 MI, 2 min	US + encapsulated drug onto MBs resulted in the complete remission in all treated animals	[180]
Anti- angiogenic for breast cancer	Yes (CD105 Ab)	Gene therapy (endostatin)	Yes, loaded during synthesis	No	1 MHz, No MI, 30 s	Tumor volume reduction after targeted gene therapy compared to untargeted MBs	[186]
Anti- angiogenic for breast cancer.	No	Endostan (endostatin)	Yes (avidin-biotin) (10 mg/kg)	Control	1 MHz, 0.5 MI, 30 s	Efficient anti-angiogenesis effect of drug loaded MBs + US compared to group without US insonation.	[187]
Ovarian Cancer	No	Paclitaxel	No	Infusion (10 mg/kg)	1 MHz, 0.4 MI, 1 min	Reversal of drug resistance with the co-injection of MBs and drug	[182]
Prostate cancer	No	Cabazitaxel	Yes, loaded during synthesis	Control	1 MHz, 0.5 MI, 15 min	Efficient reduction of tumor growth with US and either free drug + MBs or drug loaded MBs	[181]
Prostate cancer	No	Oxygen + Doxorubicin	No	Control (7 mg/kg)	2 MHz, 1.4 MI, 30 min	Tumor oxygenation with oxygen MBs assisted with US improved the intratumoral accumulation of anti-cancer drug	[190]
Tumor model	No	Doxorubicin	No	Infusion (6 mg/kg)	1 MHz, 1.0 MI, 10 min	Improved delivery of drug on tumor site with MBs associated with US	[185]
Skin cancer	No	STAT3 decoy	Yes, loaded during synthesis (10 μg)	Control	1.3 MHz, 1.6 MI,125 min	Tumor growth inhibition after the specific delivery of the encapsulated STAT3 decoy	[183]

L. Fournier et al.

Lipids dissolution in chloroform and rehydration in phosphate buffered solution constitutes the precursor lipid suspension for all lipid MBs synthesis, and the process can be time consuming as the chloroform evaporation step can last up to 12 h [8]. Despite the wide practice of this technique, it presents some drawbacks as a complex control on the size distribution. In order to narrow the size dispersity, microfluidics have been a widely explored alternative to obtain reproducible and size tunable protocol. The general idea consists in constraining a liquid flow and/or a gaseous flow into microchannels to generate size monitored MBs. The main advantage is the reduction of reagent volumes meaning a decrease in the total cost of the experiment but also an increased yield of production. Two main systems are leading the field, the T-junction system and the flow focusing setup [9]. Both rely on the convergence of the gas phase and shell material phase with monitored flow rate and optimized channel width to entrap the gas into the shell. Nevertheless, performing during resistant to US insonation. Nevertheless, the technology still relies on an advanced miniaturized system with development costs and a time of production slower than other process like sonication or homogenization [10]. A nice review written by Pulsipher et al. presents the various microfluidic technologies developed for MBs generation [8]. Carugo et al. figured out a smart way to overcome the poor production yield without compromising the narrow distribution of microfluidics systems [11]. Instead of direct production of micrometer size MBs, they produce large precursors bubbles with a regular T-junction gas-in-oil system but expose them to a low frequency US field to generates narrow size distribution MBs. This method enables the production of microfluidic-like MBs but with a production yield in the same order of magnitude than conventional batch sonication. Indeed, high yield production methods like hydrodynamic cavitation and sonication have a relatively faster production rate but require post synthesis treatment like filtration to narrow the size distribution. The hydrodynamic cavitation method uses the shear force of a homogenizer in an aqueous solution to induce polymer MBs formation that can be stabilized with the wanted shell component. It briefly consists in the addition of a monomer into an aqueous solution with the constant hydrodynamic stirring of an homogenizer like Ultraturrax for an hour [12]. As for sonication, it is the fastest method and is involved in the generation of the majority of protein shelled MBs [13]. As underlined by Stride et al., sonication is in majority a preparatory step and extensive study about standardization of sonication protocols is not described yet [14]. It consists in the activation of an ultrasonic horn at the solution/air interface causing compression refraction of the liquid [6]. This generation of energy usually creates high local temperature rise and the overall temperature of the solution can be cooled down by placing the setup in ice. Nevertheless, it is known to have strong potential in the obtention of high yield synthesis at low cost and high speed. However, new shell compositions might be studied with this technique to overcome the issue of stability and fast blood clearance known for protein shelled MBs.

Alternative techniques also exists like shaking, used for the synthesis of Definity®-MBs by simply shaking a lipid solution in a sealed vial with a shaking device [14]. Moreover, electrohydrodynamic atomization is employed for the generation of lipid MBs by applying a constant electric field on monitored flow rate of a lipid solution in contact with air [15]. Overall, gold standard of MBs synthesis should include the high yield of hydrodynamic cavitation, the size regulation of microfluidic, the fast production time and cost effectiveness of sonication.

4.3.3. Blood brain barrier

Major controversy on US associated to MBs treatment is the Blood Brain Barrier (BBB) trespassing. Acting as a highly controlled barrier which limits the penetration of most compound, BBB prevents brain from blood contamination for its owns neuroprotection. Consequently, systemic injection of treatments for Central Nervous System (CNS) pathologies are challenging as only 2% of molecules below 600 Da can cross [191]. As presented before, MBs expansions generated by US insonation can overcome microvasculature elastic limit and cause microvasculature leakage even in very specific tight junction of the cerebral endothelium. Parallelly, human skull (>6 mm) represents a major obstacle for the use of clinical US transducer because of the large absorption of the emitted waves giving a transmission coefficient only estimated of about 14% [191]. Overall, CNS access is limited both to the possibility to graft targeting or therapeutic agents. The major drawback was attributed to their vulnerability *in vivo*, because of the fast recognition by the patrolling scavenging cells leading to a rapid elimination in the bloodstream [19]. Nowadays, the vast majority of MBs are composed of lipids and a mixture of them arranged as a monolayer [20]. The mixture of phospholipids usually consists of various ratios of DSPC (1,2-distearoyl-sn-glycero-3-phosphocholine) and DSPE-PEG2000 (1,2-distearoyl-sn-glycero-3-phosphoethanolamine-N-[amino (polyethylene glycol)-2000]). Phosphatidylcholines are a natural component of cell membranes generally extracted from soybean or egg yolks, and are already used and FDA approved as excipient in various intravenous formulation of BBB permeability modulation [21]. The resulting shell is flexible and confers the ability of structural rearrangement. This can be an advantage for an easy reconstitution of types of injected MBs [22] (Fig. 4). The relevant MBs size distribution plays a role on the inertial cavitation. Polydisperse lipids MBs like Definity® or BG8774 (Bracco®) were less involved in the geometry (hydrophobicity and van der Waals [6]). In consequence, it does not efficiently promote the gas diffusion and the coalescence. Therefore, lipid shelled MBs strategy relies on the flexible property of lipids and small immunogenicity, as their lipophilic property protect them from reticuloendothelial system clearance [22].

When looking at MBs stability, interaction of MBs between themselves has to be studied. Indeed, during and after their synthesis they will be in close contact as the floatation phenomenon occurs, and unwanted events like the Ostwald ripening or coalescence are more likely to happen [23] (Fig. 2). Ostwald ripening can be defined as the expansion of bigger MBs to the detriment of small and less stable MBs based on thermodynamic equilibrium [24]. This phenomenon can be managed by selecting a low solubility biological fluid, gas and a low solubility-to-biological-fluid shell but also by increasing the stiffness of the shell to prevent exchanges between the surrounding fluid and MBs. In case of lipid shelled MBs, it is recommended to increase the molar volume of the oil phase to reduce their solubility [24]. When two bubbles merge to form a larger bubble, it is called coalescence. It can be prevented by reducing the interaction between MBs using surfactants [25] or by increasing of the synthesis temperature [26]. Hence, MBs shelf stability depends on various parameters like shell and gas composition, shell elasticity, surface tension and viscosity of the aqueous solution. Sridhar et al. [27] proposed a mathematical model to estimate MBs half-life in suspension and focused the attention on shell resistance and the viscosity of the storage solution. Storage stability of MBs in suspension can be extended with stiffer shell material (like polymers) and with the addition of glycerol like ingredient to thicken the aqueous solution [28].

Other strategies are emerging by taking all the advantages of US mediated MBs treatment. One major complication observed in clinics are nosocomial infections. Particularly life threatening, biofilms cause majors problems in health care system. Bacteria adhering to tissue or surfaces will develop a protective matrix and behavior limiting the action of antibiotics. *In vitro* proof of concept of sonobactericide potential was presented for the infective endocarditis [200]. Briefly, induced *staphylococcus aureus* biofilms on human blood clots were treated under flow conditions. The major factor identified as contributing to the sonobactericide phenomenon (Fig. 3) was the acoustic streaming produced by insonated MBs. In Lattwein et al. study performed in 2018, US alone did not show any improvement in the infected clot resolution compared to regular treatment (antibiotics + thrombolytic). However, the use of commercial bubbles with US insonation at low frequency parameters (120 kHz, 0.44 MPa) achieve almost 100% of infected clot resolution. This strategy can be applied to several sources of infection like chronic bacterial prostatitis, pneumonia or urinary tract infection [198]. Lattwein et al. study was recently updated by comparing five US parameters from 100 kPa to 400 kPa with different duty cycles [201]. This time, the study of sonoporation by measuring the intake of propidium iodide, which is unable to permeate cell membrane and bacteria dispersion, were mostly observed in the high-pressure US rather than high duty cycles ones. This means that the mechanical index has more influence than the continuity of the emitted US on untargeted MBs for biofilms resolution. Also, this study really demonstrated the key role of US and MBs because no significance in the sonobactericide study was

2.2. Microbubbles shell composition

The shell integrity of MBs was originally established with albumin polymerization but the resulting MBs quickly showed limitations due to their fast clearance in the body. The most studied protein for MBs application was Human Serum Albumin (HSA) firstly mentioned by Reisner et al. in 1989 [16] and furtherly developed with the addition of additives like Dextrose 5% [17] or fructose 5% [18] through the 90's and 2000's. They had the advantage of providing a sufficient robustness to keep the gas trapped inside and their chemical characteristics implies

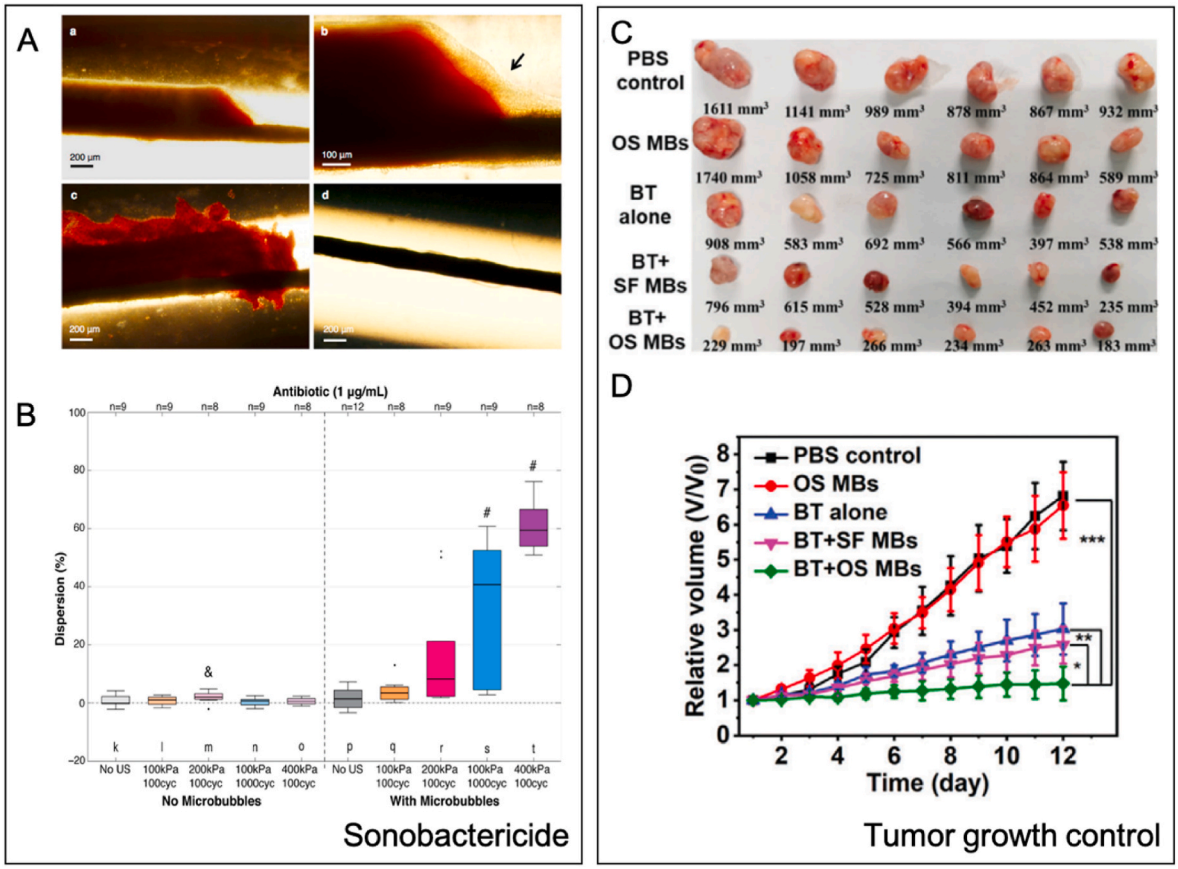


Fig. 5. *MBs and US insonation for sonobactericide and tumor growth control. A) and **B)** In vitro sonobactericide. **A)** Bright-field light microscopy images of infected clots following treatments. Groups are presented as follow: a) plasma control; b) control magnification; c) antibiotic + rtPA; d) antibiotic + rtPA + US + MBs. **B)** Dispersion of bacteria within biofilms with several insonation intensity and duty cycle. Comparing antibiotic treatment with or without MBs (*p < 0.05. or **p < 0.01). **C)** and **D)** In vivo tumor growth evaluation with US and MBs mediated radiotherapy treatment. Groups were defined as follow: administration of PBS (PBS control); administration of Oxygen/SF_6 MBs followed by US activation (OS MBs); Brachytherapy (radiotherapy with 125I seeds) alone (BT alone); Brachytherapy with SF6 MBs followed by US activation (BT + SF MBs); Brachytherapy with Oxygen/SF_6 MBs followed by US activation (BT + OS MBs). **C)** Representative images of ex vivo tumor volumes with different treatments. **D)** Tumor relative volume growth curve of different groups for 12 days (n=6, *p = 0.001, **p = 0.001, and ***p = 0.0004). cyc = cycles; PBS = Phosphate Buffer Saline. Adapted with permission from A)* [200]*; B)* [201]*; C-D)* [137].

shown with the addition of antibiotics (Fig. 5).

Sonoporation induction can also be a strategy for DNA transfection improvement *in vivo* [54]. Ability of MBs to facilitate intracellular delivery by sonoporation has to be further investigated for an innovative gene therapy strategy. Indeed, as mentioned by Duan et al., there is a lack of information about the membrane repair after MBs + US induced sonoporation [202]. They studied the impact on leukemia cells and found that US insonation in presence of untargeted MBs induced the upregulation of cytoprotective gene (heat shock protein) (Fig. 3). In consequence, if a cytoprotective behavior was observed in the first hours, many of them failed to maintain an ordered proliferative cycle and underwent necrosis or apoptosis. Thus, the addition of targeting MBs should improve the selectivity toward leukemia cells before an eventual emergence of new antitumoral treatment. Additionally, endocytosis enhancement was demonstrated by the alteration of clathrin-mediated endocytosis pathway after US microbubble treatment giving more argument for intracellular drug delivery [203].

It can be recapitulated from these different applications that US triggered MBs disruption therapy is not meant to replace drug therapy. Most probably MBs must be used in complement to improve drug efficacy and/or drug delivery. Overall, the use of MBs for therapeutic application is mainly driven by the aim to reduce drug-dose related side effect and improve the treatment outcome (Table 2). The availability of clinically approved microbubbles helped better understand the effect of US with MBs and co-injection of drugs. The latest works now tend to study the synergy of drug loaded targeting MBs and the use of mechanical disruption with US.

5. New scales and technologies

MBs also suffer from several limitations, including their size which limits extravasation of the vascular compartments, as well as a usually short circulation time (in the magnitude of a few minutes [204]). On the other hand, new approaches based on nanotechnologies offer significant advantages such as surface properties, access to the surrounding tissues and longer circulation time thanks to an array of new materials and expertise in various formulations of both organic and inorganic objects [205].

As such, nanobubbles (NBs) were developed as an alternative to ultrasound-active compounds like MBs to achieve extended circulation time, extravasation to surrounding tissue (especially tumor tissue) and potential molecular targeting capacities [206]. New technological developments have also allowed the emergence of more complex acoustically active objects, while also illustrating some limitations and risks of the current nanoscale ultrasound-active approach. Lastly, US imaging in clinical application shows limitation for a more precise imaging leading to the development of innovative ultrafast imaging.

5.1. Nanobubbles

Among the wide use of MBs for clinical imaging application, the existence of NBs themselves was debated for a long time [207], even after being evidenced as existing in commercially available MBs suspensions [208]. For the most part, their stability was not compatible with standard bubble models and as described above, the ultrasound backscatter significantly decreases with the micro/nanobubble size [206], nullifying NB's participation to ultrasound signal. The main takeaway from the literature before 2010 was therefore that NBs, if existing, were present at traces level and would not contribute in any way to a relevant ultrasound contrast enhancement [209]. However, Oeffinger and Wheatley published their work in 2014 with comprehensive description of ultrasound contrast agents with diameters ranging from 400 to 750 nm and formulated from a previously described model of 1.5 μm microbubbles [209,210]. Hereafter, the field started taking off with the emergence of multiple approaches, notably in the field of cancer imaging and therapy.

Typically, NBs consist of similar components as traditional MBs while having a diameter in the range of 100–500 nm [211]. A gaseous core, mostly filled with PFC gas (or mixtures of them) is encapsulated in a shell which, as for the MBs, is often composed of self-assembling lipids. A broad range of phospholipids, either in single or cocktail formulation, have been used over the years while being coupled to various methods of synthesis [212]. Mostly two approaches exist: either isolation from a bulk heterogeneous microbubble suspension [213] (based on centrifugation [214] or filtration [215]), or *ab initio* synthesis with similar techniques as microbubbles with careful optimization of composition and synthesis parameters, such as sonication, mechanical stirring or thin-layer evaporation [211], as well as recently microfluidics [216]. Other interesting NBs have been formulated with different shell formulations, including surfactants [217] or polymers (e.g., organic polymers such as PLGA nanobubbles from Yang et al. [218] or polysaccharide crosslinking as shown by Bhandari et al. [219]). Others have described various synthetic methods for NBs generation [205, 219–221], and since they mostly resemble techniques for MBs synthesis recapitulated above, we will focus in the following discussion on their applications.

First, the advantage of NBs over MBs is their much smaller size, which allows for extravasation in leaky vasculature (Fig. 6). This has been especially investigated in cancer theranostics, with much attention on the Enhanced Permeation and Retention (EPR) effect, associated to leaky endothelium in certain tumors with fenestrations of a few hundreds of nanometers [211]. As such, NBs have an ideal size for specific imaging of tumors with the generally recognized safe and easy-to-implement ultrasound imaging. Several authors described the use of NBs as means of tumor imaging; among them, Zhang et al. showed in 2019 that a carefully controlled preparation method based on differential centrifugation could yield acoustically active NBs with diameters of 475.2 ± 5.7 nm with significant passive targeting of solid tumors *in vivo* when compared to microbubbles [214], as well as similar ultrasound contrast *in vitro* as MBs across a range of 10^5 to 10^9 bubbles/mL. Similar works demonstrated this by various imaging methods [220,222]; however, precise localization of the acoustically active components inside or outside the vasculature was not evident, and mostly macro-imaging methods or efficacy of a fluorophore or drug delivery were often used as endpoint. Therefore, the results from Pellow et al., were particularly interesting as they demonstrated that acoustically active nanobubbles effectively extravasated, and not only fragments and payloads which could have otherwise been detected: they managed this by careful kinetic assessments including destructive cavitation of extravasated NBs [223]. Furthermore, they described an extravasation enhancement with ultrasound stimulation of their NBs, by showing a contrast enhancement of 1.5x the baseline in tumors and 5x when subjected to ultrasound stimulation. Other groups have coupled passive and active targeting of tumors, with for instance by Kumar et al., 2022, who covalently conjugated anti-PD-L1 nanobodies to NBs for molecular imaging of PD-L1 expression in tumors, with promises related to diagnosis and prognosis of multiple cancer types [216].

Moreover, the use of NBs is not limited to cancer imaging, as therapeutics can be delivered with the combined benefits of NBs. The cavitation properties of MBs and NBs can be utilized to improve delivery of gene therapies [222]. In comparison to MBs, NBs benefit from their smaller size for extravasation and tissue penetration [224] and publications from various groups demonstrated the potential of NBs for tissue gene therapy. For example, since 2020 Kida et al. described the optimization of NBs size to improve genetic material delivery [224] and feasibility of *in vivo* gene transfection in mice with a hand-held ultrasound scanner [225]. Such a controlled release is also relevant for drug delivery as shown by Tan et al., among others, who used nanobubbles loaded with an immune checkpoint inhibitor and a sonosensitizer for antitumoral activity in a xenograft mouse model [226]. Interestingly, growing knowledge on the influence of shell properties and NBs size might allow in the future a better controlled acoustic response of NBs, which might allow multiplexing of NBs in the future for differential imaging or therapy [215].

5.2. Beyond nanobubbles

Over the years, more complex approaches have emerged to benefit

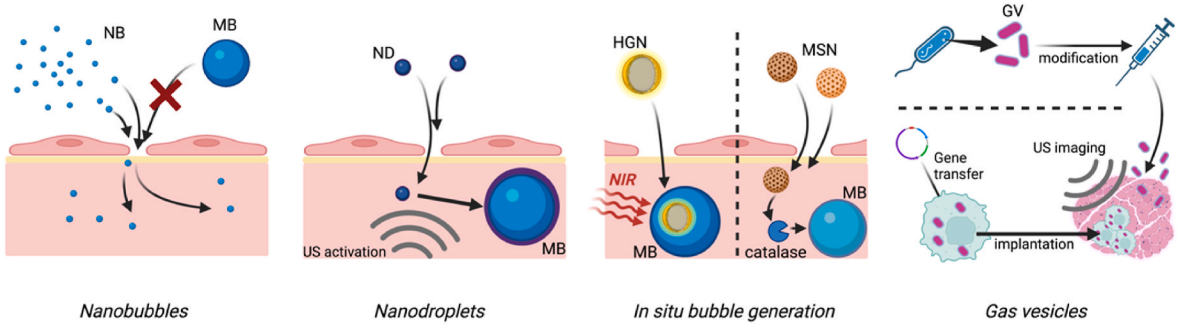


Fig. 6. New scales of US sensitive objects. The rationale behind the different innovations on the nanoscale to MB technologies are represented here. From left to right: NBs are typically smaller than 0.5 μm to allow extravasation, while NDs can be converted from nanosized droplets to MBs to combine NBs and MBs properties. HGNs use plasmonic resonance to locally create vapor MBs, and MSNs can be loaded with enzyme responsible for *in situ* O_2 bubble generation. Finally, gas vesicles can be extracted from bacteria and act as NBs. Otherwise, gas vesicles can be encoded on a genetic cassette, transfected in eukaryotic cells, for the live cell labelling during implantation. *NB = nanobubble, MB = microbubble, ND = nanodroplet, HGN = hollow gold nanoparticle, MSN = mesoporous silica nanoparticle, loaded with the catalase enzyme, GV = gas vesicles.* Created *with* BioRender.com.(For interpretation of the references to color in this figure legend, the reader is referred to the Web version of this article.)

L. Fournier et al.

Lipids dissolution in chloroform and rehydration in phosphate buffered solution constitutes the precursor lipid suspension for all lipid MBs synthesis, and the process can be time-consuming as the chloroform evaporation step can last up to 12 h [8]. Despite the wide practice of this technique, it presents some drawbacks as a complex control on the size distribution. In order to narrow the size dispersity, microfluidics have been a widely explored alternative to obtain reproducible and size tunable protocol. The general idea consists in constraining a liquid flow and/or a gaseous flow into microchannels to generate size monitored MBs. The main advantage is the reduction of reagent volumes meaning a decrease in the total cost of the experiment but also an increased yield of production. Two main systems are leading the field, the T-junction system and the flow focusing setup [9]. Both rely on the convergence of the gas phase and shell material phase with monitored flow rate and optimized channel width to entrap the gas into the shell. Nevertheless, single formulation and focused on fundamental imaging at a classical setting, it pinpoints the extreme care that needs to be taken in formulation, scaling such NBs. It is however interesting to note that NBs were repeatedly shown to have strong nonlinear effects which can be detected [206,207,228]. This recapitulates another limitation of NBs: comparison to MBs is rather complex since imaging modalities differ. While some publications directly compare NBs and MBs with standard ultrasound imaging [210,220,231], rigorous comparison based on volume of molar concentrations equivalence is often lacking. Furthermore, imaging modalities differ especially since several publications using the nonlinearity of Nanodroplets (NDs) response to ultrasound for contrast enhancement, in contrast to MBs. On the other hand, an interesting work by Batchelor et al. in 2020 with NBs nested inside liposomes revealed that in their formulations, both NBs of perfluorobutane (PFB) and PFB droplets were actually present, with the PFB droplets being responsible for the davitation that allowed payload delivery in their liposomes [232]. this pinpointed another rich area of PFC-based acoustically active objects.

Such nanodroplets (NDs) or Phase-Change Contrast Agents (PCCA) have been investigated extensively since 2010 [233,234]. These emulsions of PFC gas in nanoscale droplets can undergo a phase-transition under stimuli to form nano/microbubbles that are acoustically active [235,236]. Interestingly, this shift, which is linked to a vaporization of the majority of protein shelled MBs [13]. As underlined by Stride et al., sonication is in majority a preparatory step and extensive study about standardization of sonication protocols is not described yet [221] or photoacoustically by near-infrared illumination [237]. This [14]. It consists in the activation of an ultrasonic horn at the solution/air interface causing compression refraction of the liquid [6]. This generation of energy usually creates high local temperature rise and the overall temperature of the solution can be cooled down by placing the setup in ice. Nevertheless, it is known to have strong potential in the obtention of high yield synthesis at low cost and high speed. However, new shell compositions might be studied with this technique to overcome the issue of stability and fast blood clearance known for protein shelled MBs.

Alternative techniques also exists like shaking, used for the synthesis of Definity. MBs by simply shaking a lipid solution in a sealed vial with a shaking device [14]. Moreover, electrohydrodynamic atomization is employed for the generation of lipid MBs by applying a constant electric field on monitored flow rate of a lipid solution in contact with air [15]. Overall, gold standard of MBs synthesis should include the high yield of hydrodynamic cavitation, the size regulation of microfluidic, the fast production time and cost effectiveness of sonication.

Recently, super-resolution-based approaches have emerged in photoacoustic imaging with the works from the group of O. Couture starting with the publication of Errico et al., who used MBs to break the diffraction limit in ultrasound imaging [241]; similar work was pursued with both microdroplets [242] for subdiffraction drug delivery control through ultrasound, and later NDs [243] in a photoacoustic setting to reach unequaled spatial resolution in tissue (less than 10 μm spatial resolution). Such NDs therefore show promises in advancing ultrasound contrast agents further into the tissue and therapeutic potency [227].

Other innovative technologies have emerged: *in-situ* generation of nano/microbubbles without PFC gas, with for instance plasmonic nanobubble generation [244] with Hollow Gold Nanoshells (HGN) [245]. In these objects, HGN or simple gold nanoparticles are able under laser excitation to locally heat the surrounding water and create the possibility to graft targeting or therapeutic agents. The major drawback was attributed to their vulnerability *in vivo*, because of the fast recognition by the patrolling scavenging cells leading to a rapid elimination in the bloodstream [246]. Nowadays, the vast majority of MBs are composed of lipids and a mixture of them arranged as a monolayer [20]. The mixture of phospholipids usually consists of various ratios of DSPG (1,2-distearoyl-sn-glycero-3-phosphocholine) and DSPE-PEG2000 (1,2-distearoyl-sn-glycero-3-phosphoethanolamine-N-[amino (polyethylene glycol)-2000]). Phosphatidylcholines are a natural component of cell membranes, generally extracted from soybean or egg yolks, and have been investigated to produce stable microbubbles, by simply tapping these solutions [247]. Another approach relies on nanoemulsion technology and acoustic droplet vaporization (ADV). Nanodroplets, usually composed of PFC gas and a shell material, can be used in a precise delivery of gas and API (Fig. 6). Interestingly, using Nanoshell structure allowed excitation with Near Infrared (NIR) light, therefore enabling this technology to be used *in vivo* thanks to the NIR imaging window [244,248]. As demonstrated by Shin et al. in 2020, a shell tuning of lipid solutes-loaded PFCN based on size, from 10 to 40 nm, or wall thickness and expectation, can be used in a precise delivery of natural and API by Laser pulse, almost in real-time [247]. Other objects have been investigated to produce stable microbubbles, by simply tapping these solutions [247]. Another approach relies on nanoemulsion technology and acoustic droplet vaporization (ADV). Nanodroplets, usually composed of PFC gas and a shell material, can be used in a precise delivery of gas

Table 3
Advantages and limitations of recent contrast agent innovations, based on their imaging, capabilities, circulation properties and tissue penetration.

	Nanobubbles	*Nanodroplets*	In situ *bubble generation: plasmonic effect or enzyme-based*	*Gas vesicles*
Advantages	• Extravasation, tissue penetration • Stability • Nonlinear imaging • EPR effects (tumor passive targeting)	• Extravasation, tissue penetration • Stability • Nonlinear imaging • EPR effects (tumor passive targeting) • MB switching for improved imaging	• Extravasation, tissue penetration • Inorganic (stable, controlled chemistry) • Fine tunability of NP physico-chemical properties • Spatial control, tissue-specific activation	• Extravasation, tissue penetration • Fine size control • Eukaryotic gene reporting • Cell tracking *in vivo* by US imaging
Limits	• Size control can be limited • MB contamination can affect US signal • Modality of imaging is not yet standardized: o Classical mode settings (resonance frequency, intensity) o Nonlinear modes (multiple methods for exploiting nonlinearity, which must be compared)	• Delicate choice of PFC: liquid/gas transition must be fitted to body temperature • Physical activation *in situ* is yet to be mastered (US, light-induced heating) • High pressure/longer pulses are typically required in US activation than usually administered	• No imaging prior activation • Activation control, due to multiple possibilities, is yet to be standardized: o HGN are limited by light penetration and O_2 availability o Enzyme-based NPs require sufficient substrate, ATP and tissue variability can be an issue	• Typically, high concentration is required for similar imaging power as MBs • Differences in imaging with NBs of similar size cannot yet be explained • Nanoengineering capabilities are still recent and requires further refining • *In vivo* cell imaging through gene expression is yet limited to destructive imaging, with possible negative cellular effects

processing units (GPU) that allowed for a software-based parallelization which is especially demanding, in the range of several Gigabytes/s for data transfer to the processing unit, or of 1–2 Gigaflops/s (operations performed by the processing unit) computing power [261]. As explained above, the conventional imaging with an ultrasound probe is based on serialized lines reconstruction by focused beams, and therefore the frame rate is limited by the time to emit, receive, and process the beam on one hand, multiplied by the number of lines necessary for the image [262]; meaning that the building time of an image is directly correlated to the size of the zone being observed with for example at a given depth, an image needing twice more lines will take twice more time to acquire, which either limits the frame rate or the width of the images [261,262]. This can be improved by built-in multiline computation probes, but the serialized design remains the main limitation to the frame rate, typically in the range of 30–100 Hz [261]. On the other hand, in ultrafast imaging the whole process is parallelized, as typically only one (or few) emission is used to simultaneously image the whole region of interest by relying on plane or divergent ultrasound waves [263,264]. All the lines are acquired at once and thus the image frame rate is only limited by the wave time-of-flight, as long as the processing power necessary for data treatment is sufficient. In such ultrafast architectures the image frame rate can reach tens of thousands of Hz [261]. This high frame rate can be

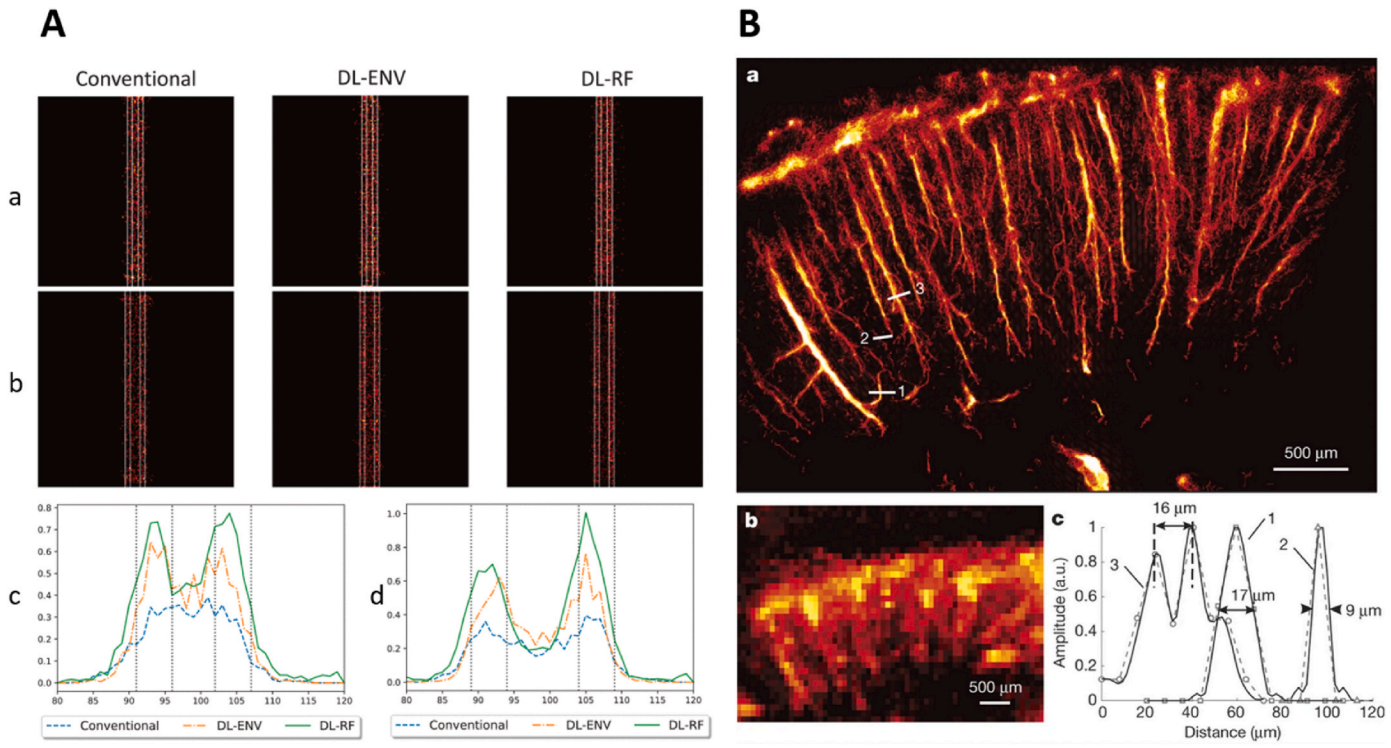


Fig. 7. *Two major applications of Ultrafast Ultrasound imaging: A) Illustration of how different analysis method for MB localization can affect the spatial resolution of ULM. Two deep learning algorithms (DL-ENV and DL-RF) are compared to a conventional localization technique, with (a) and (b), simulated vessels separated by 3.*0 µm *or 4.*9 µm. *Transverse reconstruction with the different methods are respectively shown in (c) and (d).* ***B)*** *Comparison of an Ultrasound Localized Microscopy (ULM) images (a) reconstructed through microbubbles localization (pixel size of 10 × 8 µm), with the same area imaged in conventional power Doppler in (b). Based on the (a) image, a linear intensity projection along the displayed line (from 1 to 3) shows a spatial resolution below* 16 µm. *Adapted from A)* [275]*; B)* [241].

L. Fournier et al.

Lipids dissolution in chloroform and rehydration in phosphate buffered solution constitutes the precursor lipid suspension for all lipid MBs synthesis, and the process can be time-consuming as the chloroform evaporation step can last up to 12 h [8]. Despite the wide practice of this technique, it presents some drawbacks as a complex control on the size distribution. In order to narrow the size dispersity, microfluidics have been a widely explored alternative to obtain reproducible and size tunable protocol. The general idea consists in constraining a liquid flow and/or a gaseous flow into microchannels to generate size monitored MBs. The main advantage is the reduction of reagent volumes meaning a decrease in the total cost of the experiment but also an increased yield of production. Two main systems are leading the field, the T-junction system and the flow focusing setup [9]. Both rely on the convergence of the gas phase and shell material phase with monitored flow rate and optimized channel width to entrap the gas into the shell. Nevertheless, the technology still relies on an advanced miniaturized system with development costs and a time of production slower than other process like sonication or homogenization [10]. A nice review written by Pulsher et al. presents the various microfluidic technologies developed for MBs generation [9]. Carugo et al. figured out a smart way to overcome the poor production yield with no compromising the narrow distribution of microfluidics systems [11]. Instead of direct production of micrometer size MBs, they produce large precursors bubbles with a regular T-junction gas-in-oil system but expose them to a low frequency US field to generates narrow size distribution MBs. This method enables the production of microfluidic-like MBs but with a production yield in the same order of magnitude than conventional batch sonication. Indeed, high yield production methods like hydrodynamic cavitation and sonication have a relatively faster production rate but require post synthesis treatment like filtration to narrow the size distribution. The hydrodynamic cavitation method uses the shear force of a homogenizer in an aqueous solution to induce polymer MBs formation that can be applied in ultrasound imaging of MBs of similar contrast agents stabilized with the wanted shell component. It briefly consists in the addition of a monomer into an aqueous solution with the constant hydrodynamic stirring of an homogenizer like Ultraturrax for an hour [12]. As for sonication, it is the fastest method and is involved in the generation of the majority of protein shelled MBs [13]. As underlined by Stride et al., sonication is in majority a preparatory step and extensive study about standardization of sonication protocols is not described yet [14]. It consists in the activation of an ultrasonic horn at the solution/air interface causing compression refraction of the liquid [6]. This generation of energy usually creates high local temperature rise and the overall temperature of the solution can be cooled down by placing the setup in ice. Nevertheless, it is known to have strong potential in the obtention of high yield synthesis at low cost and high speed. However, new shell compositions might be studied with this technique to overcome the issue of stability and fast blood clearance known for protein shelled MBs.

Alternative techniques also exists like shaking, used for the synthesis of Definity®. MBs by simply shaking a lipid solution in a sealed vial with a shaking device [14]. Moreover, electrohydrodynamic atomization is employed for the generation of lipid MBs by applying a constant electric field on monitored flow rate of a lipid solution in contact with air [15]. Overall, gold standard of MBs synthesis should include the high yield of hydrodynamic cavitation, the size regulation of microfluidic, the fast production time and cost effectiveness of sonication.

2.2. Microbubbles shell composition

The shell integrity of MBs was originally established with albumin polymerization but the resulting MBs quickly showed limitations due to their fast clearance in the body. The most studied protein for MBs application was Human Serum Albumin (HSA), firstly mentioned by Reisner et al. in 1989 [16] and furtherly developed with the addition of additives like Dextrose 5% [17] or fructose 5% [18] through the 90's and 2000's. They had the advantage of providing a sufficient robustness to keep the gas trapped inside and their chemical characteristics implies focused on bridging the gap to the clinical world, with for instance Yan et al., who translated this method to rhesus monkeys and thus opened the way to clinical trials [277], and Demené et al., who first used ULM in human brain without the need for transcranial aperture and with significant improvement in spatial resolution with at least one order of magnitude enhancement at up to 120 mm depth when compared to a typical clinical contrast CT imaging [278], or Errico et al. who recently published a feasibility study in various human organs [279]. The diagnostic potential was also investigated in tumor bearing mice, then in human patients, by the group of Opacic in 2018 and opened new fields of cell membranes, generally extracted from soybean or egg yolks, and are already used and FDA approved as excipient in various intravenous treatments [21]. The resulting shell is flexible and confers the ability of structural rearrangement. This can be an advantage for an easy reconstitution after freeze drying storage but lipid monolayer reorganization can dissipate the overall stability due to weak interaction forces involved in the geometry (hydrophobicity and van der Waals [6]). In consequence, it does not efficiently prevent the gas diffusion and the coalescence. Therefore, lipid shelled MBs strategy relies on the flexible property of lipids and small immunogenicity, as their lipophilic property protect them from reticuloendothelial system clearance [22].

When looking at MBs stability, interaction of MBs between themselves has to be studied. Indeed, during and after their synthesis they will be in close contact as the floatation phenomenon occurs, and unwanted events like the Ostwald ripening or coalescence are more likely to happen [23] (Fig. 2). Ostwald ripening can be defined as the expansion of bigger MBs to the detriment of small and less stable MBs based on thermodynamic equilibrium [24]. This phenomenon can be managed by selecting a low solubility-to-biological-fluid gas and a low solubility-to-biological-fluid shell but also by increasing the stiffness of the shell to prevent exchanges between the surrounding fluid and MBs. In case of lipid shelled MBs, it is recommended to increase the molar volume of the oil phase to reduce their solubility [24]. When two bubbles merge to form a larger bubble, it is called coalescence. It can be prevented by reducing the interaction between MBs using surfactants or NBs or NDs [245,282,]. Functional imaging allowed by targeted MBs [25] or by increasing of the synthesis temperature [26]. Hence, MBs or even NBs to extravasate deeper in tissues might open new insights with improved either temporal or spatial resolution through ultrafast or ULM ultrasound imaging, with encouraging results from already existing (though at a less fine spatial resolution) fUSI in terms of clinical applications. Overall, innovations in the contrast agents field (MBs, NBs, NDs, echogenic NPs, etc …) can converge with advanced imaging methods (Doppler, 3D, ultrafast, ULM, etc …) to improve our exploration of physiology, diagnostics, and therapeutics.

6. Conclusion and perspectives

This work aimed at better understanding the MBs strategies for human treatment and diagnosis. New approaches were described to overcome the unmet medical need for a non-invasive and targeted efficient treatment but also diagnosis tools. Indeed, therapeutic treatments relying on systemic drug injections are still bringing toxicity, collateral damages and uncontrolled pharmacokinetics, such as half-life in circulation or tissue penetration. The use of MBs in clinical application is currently reserved for US imaging thanks to their echogenic properties. Through this review we pointed out the importance of understanding MBs intrinsic characteristics (composition, behavior, stability) to better apprehend their translation to *in vivo* diagnosis and treatment. Secondly, the review focused on the use of commercial MBs for US imaging and the recent prolific development of targeted MBs for molecular imaging that brings a new dimension for early and precise diagnosis. We confronted the applications for cancer, cardiovascular diseases or inflammation to better understand MBs behavior. Depending on their application, MBs can be insonated with US at varying settings to take advantage of different oscillation response. It showed that the frontier between stable cavitation and inertial cavitation *in vivo* is still delicate to establish. According to most pre-clinical studies, it can be concluded that low mechanical index insonation of microbubbles would help mechanically destabilize the surrounding environment. This includes enhancement of drug delivery, biofilms impairment and BBB the possibility to graft targeting or therapeutic agents. The major drawback was attributed to their vulnerability *in vivo*, because of the fast recognition by the patrolling scavenging cells leading to a rapid elimination in the bloodstream [19]. Nowadays, the vast majority of MBs are composed of lipids and a mixture of them arranged as a monolayer [20]. The mixture of phospholipids usually consists of various ratios of DSPC (1,2-distearoyl-sn-glycero-3-phosphocholine) and DSPE-PEG2000 (1,2-distearoyl-sn-glycero-3-phosphoethanolamine-N-[amino (polyethylene glycol)-2000]). Phosphatidylcholines are a natural component of cell membranes, generally extracted from soybean or egg yolks, and are already used and FDA approved as excipient in various intravenous treatments [21]. The resulting shell is flexible and confers the ability of structural rearrangement. This can be an advantage for an easy reconstitution after freeze drying storage but lipid monolayer reorganization can dissipate the overall stability due to weak interaction forces involved in the geometry (hydrophobicity and van der Waals [6]). In consequence, it does not efficiently prevent the gas diffusion and the coalescence. Therefore, lipid shelled MBs strategy relies on the flexible property of lipids and small immunogenicity, as their lipophilic property protect them from reticuloendothelial system clearance [22].

When looking at MBs stability, interaction of MBs between themselves has to be studied. Indeed, during and after their synthesis they will be in close contact as the floatation phenomenon occurs, and unwanted events like the Ostwald ripening or coalescence are more likely to happen [23] (Fig. 2). Ostwald ripening can be defined as the expansion of bigger MBs to the detriment of small and less stable MBs based on thermodynamic equilibrium [24]. This phenomenon can be managed by selecting a low solubility-to-biological-fluid gas and a low solubility-to-biological-fluid shell but also by increasing the stiffness of the shell to prevent exchanges between the surrounding fluid and MBs. In case of lipid shelled MBs, it is recommended to increase the molar volume of the oil phase to reduce their solubility [24]. When two bubbles merge to form a larger bubble, it is called coalescence. It can be prevented by reducing the interaction between MBs using surfactants or NBs or NDs [245,282,]. Functional imaging allowed by targeted MBs [25] or by increasing of the synthesis temperature [26]. Hence, MBs or even NBs to extravasate deeper in tissues might open new insights with improved either temporal or spatial resolution through ultrafast or ULM ultrasound imaging, with encouraging results from already existing (though at a less fine spatial resolution) fUSI in terms of clinical applications. Overall, innovations in the contrast agents field (MBs, NBs, NDs, echogenic NPs, etc …) can converge with advanced imaging methods (Doppler, 3D, ultrafast, ULM, etc …) to improve our exploration of physiology, diagnostics, and therapeutics.

6. Conclusion and perspectives

This work aimed at better understanding the MBs strategies for human treatment and diagnosis. New approaches were described to overcome the unmet medical need for a non-invasive and targeted efficient treatment but also diagnosis tools. Indeed, therapeutic treatments relying on systemic drug injections are still bringing toxicity, collateral damages and uncontrolled pharmacokinetics, such as half-life in circulation or tissue penetration. The use of MBs in clinical application is currently reserved for US imaging thanks to their echogenic properties. Through this review we pointed out the importance of understanding MBs intrinsic characteristics (composition, behavior, stability) to better apprehend their translation to *in vivo* diagnosis and treatment. Secondly, the review focused on the use of commercial MBs for US imaging and the recent prolific development of targeted MBs for molecular imaging that brings a new dimension for early and precise diagnosis. We confronted the applications for cancer, cardiovascular diseases or inflammation to better understand MBs behavior. Depending on their application, MBs can be insonated with US at varying settings to take advantage of different oscillation response. It showed that the frontier between stable cavitation and inertial cavitation *in vivo* is still delicate to establish. According to most pre-clinical studies, it can be concluded that low mechanical index insonation of microbubbles would help mechanically destabilize the surrounding environment. This includes enhancement of drug delivery, biofilms impairment and BBB

opening thanks to microstreaming. In addition, the rise of mechanical index would induce irreversible MBs destruction which can further cause fibrin clot disassembling, cells membrane sonoporation and sometimes vascular leakage with erythrocytes extravasation. Overall, the complete drug-loaded targeting US responsive tools are not yet ready for clinical translation, but the use of clinical MBs co-injected with therapeutic agent and enhanced with US signal showed promising results for the drug doses reduction. In addition, the exact boundaries to avoid damaging features are not established yet except for the FDA fixed 1.9 MI and are highly dependent on MBs intrinsic properties. It has to be understood that MBs mechanical response to US insonation have not been determined completely and a collective effort has to be made to better describe the US transducer parameters (frequency, amplitude, duty cycle) and the set-up characteristics (insonation duration, distance to object, etc.). Due to the broad interest in the MBs potential, there has been multiple advancements and innovations both in designing the right MBs for the right applications, and in adapting the MB rationale to new US contrast agents in order to overcome their limitations. This was described in the last part, including among others the use of nanoscale bubbles and droplets, as well *as in situ* generation of echogenic signals with nanoparticle approaches and new MBs' combined use with recent technologies to breach the physical limits of the US imaging.

In perspective work, it appeared that the emergence of combined technologies could add another dimension to MBs' behavior, including for example photodynamic therapy [283,284], photoacoustic imaging [237,285] or magnetic MBs [286]. Also, the development of US responsive piezoelectric nanomaterial are an interesting new strategy to open the MBs world to cell therapy [287]. As these new therapeutic approaches require the injection of foreign body material, the priority now stands on safety. Clinical trials are widely enrolling patients to established the best parameters for US combination with MBs. These strategies are obviously not meant to replace drug treatments yet but they have the potential to improve their outcome. Since MBs, their applications, and consequent innovations are thriving in multiple fields (oncology, cardiovascular diseases, inflammation), the convergence of expertise and standardization of certain practices are paramount to ensure a quick development and future translation to the clinic.

Authors contribution

Louise FOURNIER: conceptualization, writing and figures development. Thibault DE LA TAILLE: writing, editing and figures development. Cédric CHAUVIERRE: writing, editing, reviewing, supervision and funding acquisition.

Declaration of competing interest

The authors declare that they have no known competing financial interests or personal relationships that could have appeared to influence the work reported in this paper.

Data availability

No data was used for the research described in the article.

Acknowledgment

Authors thank INSERM, Université Paris Cité, Université Sorbonne Paris Nord and the ANR "FightClot" ANR-20-CE18-0005-01 for the financial support.

References

[1] W. Najahi-Missaoui, R.D. Arnold, B.S. Cummings, Safe nanoparticles: are we there yet? Int. J. Mol. Sci. 22 (1) (2021) 1–22, https://doi.org/10.3390/ijms22010385.
[2] R. Gramiak and M. P. Shah, "Echocardiography of the Aortic." .
[3] J. Steinman, M.M. Koletar, B. Stefanovic, J.G. Sled, 3D morphological analysis of the mouse cerebral vasculature: comparison of in vivo and ex vivo methods, PLoS One 12 (10) (2017) 1–17, https://doi.org/10.1371/journal.pone.0186676.
[4] M. Diez-Silva, M. Dao, J. Han, C.T. Lim, S. Suresh, Shape and biomechanics characteristics of human red blood cells in health and disease, MRS Bull. 35 (5) (2010) 382–388, https://doi.org/10.1557/mrs2010.571.
[5] C.I. Ezekiel, A.M. Bapolisi, R.B. Walker, R.W.M. Krause, Ultrasound-triggered release of 5-fluorouracil from soy lecithin echogenic liposomes, Pharmaceutics 13 (6) (2021) 1–14, https://doi.org/10.3390/pharmaceutics13060821.
[6] A. Upadhyay, S.V. Dalvi, Microbubble formulations: synthesis, stability, modeling and biomedical applications, Ultrasound Med. Biol. 45 (2) (2019) 301–343, https://doi.org/10.1016/j.ultrasmedbio.2018.09.022.
[7] T.D. Reusser, K.H. Song, D. Ramirez, R.K.P. Benninger, V. Papadopoulou, M. A. Borden, Phospholipid oxygen microbubbles for image-guided therapy, Nanotheranostics 4 (2) (2020) 83–90, https://doi.org/10.7150/ntno.43808.
[8] D. Liu, et al., Sinapultide-loaded lipid microbubbles and the stabilization effect of sinapultide on the shells of lipid microbubbles, J. Mater. Chem. B 6 (9) (2018) 1335–1341, https://doi.org/10.1039/c7tb02799k.
[9] K.W. Pulsipher, D.A. Hammer, D. Lee, C.M. Sehgal, Engineering theranostic microbubbles using microfluidics for ultrasound imaging and therapy: a review, Ultrasound Med. Biol. 44 (12) (2018) 2441–2460, https://doi.org/10.1016/j.ultrasmedbio.2018.07.026.
[10] A.J. Dixon, J. Li, J.M.R. Rickel, A.L. Klibanov, Z. Zuo, J.A. Hossack, Efficacy of sonothrombolysis using microbubbles produced by a catheter-based microfluidic device in a rat model of ischemic stroke, Ann. Biomed. Eng. (2019), https://doi.org/10.1007/s10439-019-02209-0.
[11] D. Carugo, R.J. Browning, I. Iranmanesh, W. Messaoudi, P. Rademeyer, E. Stride, Scaleable production of microbubbles using an ultrasound-modulated microfluidic device, J. Acoust. Soc. Am. 150 (2) (2021) 1577–1589, https://doi.org/10.1121/10.0005911.
[12] B. Li, et al., Functionalized polymer microbubbles as new molecular ultrasound contrast agent to target P-selectin in thrombus, Biomaterials 194 (2019) (2019) 139–150, https://doi.org/10.1016/j.biomaterials.2018.12.023.
[13] A.H. Liao, H.C. Ho, Y.C. Lin, H.K. Chen, C.H. Wang, Effects of microbubble size on ultrasound-induced transdermal delivery of high-molecular-weight drugs, PLoS One 10 (9) (2015) 1–14, https://doi.org/10.1371/journal.pone.0138500.
[14] E. Stride, et al., Microbubble agents: new directions, Ultrasound Med. Biol. (2020), https://doi.org/10.1016/j.ultrasmedbio.2020.01.027.
[15] U. Farook, E. Stride, M.J. Edirisinghe, Preparation of suspensions of phospholipid-coated microbubbles by coaxial electrohydrodynamic atomization, J. R. Soc. Interface 6 (32) (2009) 271–277, https://doi.org/10.1098/rsif.2008.0225.
[16] S.A. Reisner, et al., Myocardial perfusion imaging by contrast echocardiography with use of intracoronary sonicated albumin in humans, J. Am. Coll. Cardiol. 14 (3) (1989) 660–665, https://doi.org/10.1016/0735-1097(89)90107-1.
[17] S.L. Lin, et al., Left ventricular opacification after peripheral venous injection of a modified albumin solution, Int. J. Card. Imag. 8 (1) (1992) 53–61, https://doi.org/10.1007/BF01137566.
[18] S. Chen, Z. Wang, Y.T. Zhou, P.A. Grayburn, Optimization of the size distribution and myocardial contrast effect of perfluorocarbon-filled albumin microbubbles by lyophilization under continuous negative pressure, J. Am. Soc. Echocardiogr. 13 (8) (2000) 748–753, https://doi.org/10.1067/mje.2000.104644.
[19] A.L. Klibanov, Ultrasound contrast: gas microbubbles in the vasculature, Invest. Radiol. 56 (1) (2021) 50–61, https://doi.org/10.1097/RLI.0000000000000733.
[20] K. Ferrara, R. Pollard, M. Borden, Ultrasound microbubble contrast agents: fundamentals and application to gene and drug delivery, Annu. Rev. Biomed. Eng. 9 (2007) 415–447, https://doi.org/10.1146/annurev.bioeng.8.061505.095852.
[21] P. van Hoogevest, A. Wendel, The use of natural and synthetic phospholipids as pharmaceutical excipients, Eur. J. Lipid Sci. Technol. 116 (9) (2014) 1088–1107, https://doi.org/10.1002/ejlt.201400219.
[22] S. Al-Jawadi, S.S. Thakur, Ultrasound-responsive lipid microbubbles for drug delivery: a review of preparation techniques to optimise formulation size, stability and drug loading, Int. J. Pharm. 585 (2020), 119559, https://doi.org/10.1016/j.ijpharm.2020.119559.
[23] J. Jägers, A. Wrobeln, K.B. Ferenz, Perfluorocarbon-based oxygen carriers: from physics to physiology, Pflugers Arch. Eur. J. Physiol. 473 (2) (2021) 139–150, https://doi.org/10.1007/s00424-020-02482-2.
[24] T.J. Wooster, M. Golding, P. Sanguansri, Impact of oil type on nanoemulsion formation and ostwald ripening stability, Langmuir 24 (22) (2008) 12758–12765, https://doi.org/10.1021/la801685v.
[25] Y. Iida, et al., Bubble population phenomena in sonochemical reactor: II. Estimation of bubble size distribution and its number density by simple coalescence model calculation, Ultrason. Sonochem. 17 (2) (2010) 480–486, https://doi.org/10.1016/j.ultsonch.2009.08.017.
[26] T. Segers, A. Lassus, P. Bussat, E. Gaud, P. Frinking, Improved coalescence stability of monodisperse phospholipid-coated microbubbles formed by flow-focusing at elevated temperatures, Lab Chip 19 (1) (2019) 158–167, https://doi.org/10.1039/c8lc00886h.
[27] S. Sridhar, A. Patel, S.V. Dalvi, Estimation of storage stability of aqueous microbubble suspensions, Colloids Surfaces A Physicochem. Eng. Asp. 489 (Jan. 2016) 182–190, https://doi.org/10.1016/J.COLSURFA.2015.10.044.
[28] R.H. Abou-Saleh, et al., Molecular effects of glycerol on lipid monolayers at the gas-liquid interface: impact on microbubble physical and mechanical properties, Langmuir 35 (31) (2019) 10097–10105, https://doi.org/10.1021/acs.langmuir.8b04130.

L. Fournier et al.

Lipids dissolution in chloroform and rehydration in phosphate buffered solution constitutes the precursor lipid suspension for all lipid MBs synthesis and, the process can be time consuming as the chloroform evaporation step can last up to 12 h [19]. Despite the wide practice of this technique, it presents some drawbacks as a complex control on the size distribution. In order to narrow the size dispersity, microfluidics have been a widely explored alternative to obtain reproducible and size tunable protocol. The general idea consists in constraining a liquid flow and/or a gaseous flow into microchannels to generate size monitored MBs. The main advantage is the reduction of reagent volumes meaning a decrease in the total cost of the experiment but also an increased yield of production. Two main systems are leading the field, the T-junction system and the flow focusing setup [8]. Both rely on the convergence of the gas phase and shell material phase with monitored flow rate and optimized channel width to entrap the gas into the shell. Nevertheless, the technology still relies on an advanced miniaturized system with development costs and a time of production slower than other process like sonication or homogenization [10]. A nice review written by Pulsipher et al. presents the various microfluidic technologies developed for MBs generation [9]. Qiu et al. figured out a smart way to overcome the poor production yield without compromising the narrow distribution of microfluidics systems [11]. Instead of direct production of microbubbles, they produce large precursors bubbles with a regular T-junction gas in oil system but expose them to a low frequency US field to generates narrow size distribution MBs. This method enables the production of microfluidic like MBs but with a production yield in the same order of magnitude than conventional bottom-up sonication. Indeed, high yield production methods like hydrodynamic cavitation and sonication have a relatively faster production rate but require post synthesis treatment like filtration to narrow the size distribution. The hydrodynamic cavitation method uses the shear force of a homogenizer in an aqueous solution to induce polymer MBs formation that can be stabilized with the wanted shell component. It briefly consists in the addition of a protein in an aqueous solution with the constant hydrodynamic stirring of a homogenizer like Ultraturrax for an hour [12]. As for sonication, it is the fastest method and is involved in the generation of the majority of protein shelled MBs [13]. As underlined by Stride et al., sonication is in contrast poorly controlled and extensive study about standardization of sonication protocols is not described yet [14]. It consists in the activation of an ultrasonic horn at the solution/air interface inducing a rapid increase in temperature and the generation of energy usually creates high local temperature is around the overall temperature of the solution which is unfavorable for the stability of ice. Nevertheless, known to have strong potential in the obtention of high yield synthesis at low cost and high speed. However, new shell components might be tested with this technique to overcome the issue of stability and clearance by blood known for protein shelled MBs.

Alternative techniques also exists like shaking, used for the synthesis of Definity® MBs by simply shaking a lipid solution in a sealed vial with a shaker at 4500 rpm for 45 s [15]. More recent, the combination of this method is employed for the generation of lipid MBs by applying a constant flow field on monitored Ultrasonic Volatile Surface Cavitation with air [15]. Overall, similarly to MBs synthesis using mechanical agitation like hydrodynamic cavitation, the size regulation of microfluidic, the fast production time and cost effectiveness of sonication

2.2. Microbubbles shell composition

The shell material is as significant as the gas core. Albumin polymerized MBs were the first generation of MBs approved for clinical application [16]. Nevertheless, their resulting MBs quickly showed limitations due to their fast clearance in the body. The most studied protein for MBs is Albumin, as mentioned by Reisner et al. in 1989 [17] and furthermore developed with the addition of additives like Dextrose 5% [17] or fructose 5% [18] through the 90's and 2000's. They had the advantage of being of excellent robustness to keep the gas trapped inside and their chemical characteristics implied the possibility to graft targeting or therapeutic agents. The major drawback was attributed to their vulnerability *in vivo*, because of the fast recognition by the patrolling scavenging cells leading to a rapid elimination in the bloodstream [19]. Nowadays, the vast majority of MBs are composed of lipids and a mixture of them arranged as a monolayer [20]. The mixture of phospholipids usually consists of various ratios of DSPC (1,2-distearoyl-sn-glycero-3-phosphocholine) and DSPE-PEG2000 (1, 2-distearoyl-sn-glycero-3-phosphoethanolamine-N- [amino (polyethylene glycol)-2000]). Phosphatidylcholines are a natural component of cell membranes, generally extracted from soybean or egg yolk, and are already used and FDA approved as excipient in various intravenous treatments [21]. The resulting shell is flexible and confers the ability of structural rearrangement. This can be an advantage for easy reconstitution after freeze drying storage but lipid monolayer reorganization can disservice the overall stability due to weak interaction forces involving an aqueous environment. Indeed, Sirsi et al. [22] and Kooiman et al. [23] underlined that lipid shelled MBs are more vulnerable to ultrasound exposure and more prone to coalescence. Therefore, lipid shelled MBs strategy relies on the flexible property of lipids and small immunogenicity, as their lipophilic property protect them from the reticuloendothelial system clearance [24].

When loading an MBs stability, interaction of MBs between themselves has to be studied. Indeed, during and after their synthesis they will be in close contact as the formation process occurs, and unwanted events like the Ostwald ripening or coalescence are more likely to happen [24]. Ostwald ripening can be refined as the expansion of bigger MBs to the detriment of small and less stable MBs based on thermodynamic equilibrium [24]. This phenomenon can be managed by selecting a low solubility to biological fluid gas and a low solubility to biological fluid shell but also by increasing the stiffness of the shell to prevent exchanges between the surrounding fluid and MBs. In case of lipid shelled MBs, it is recommended to increase the molar volume of the oil phase to reduce their solubility [24]. When two bubbles merge to form a larger bubble, it is called coalescence. It can be prevented by using surfactants [25] or by increasing of the synthesis temperature [26]. Hence, MBs shelf stability depends on various parameters like shell and gas composition, shell elasticity, surface tension and viscosity of the aqueous solution. Sridhar et al. proposed a mechanical model to estimate MBs half-life in suspension and underlined the attention on shell resistance and the viscosity of the storage solution. Storage stability of MBs is usually improved by adding a stabilizing shell material (like polymers) and/or the addition of glycerol like ingredient to thicken the aqueous solution [27].

To overcome the MBs polymerized cyanoacrylates were introduced as substitute of lipid shells. Cyanoacrylates are traditionally biomedicine substances adhesive for wound closing [29]. They are chemically composed of an ethylene group, a cyano-group and a variable alkyl chain. Initially presented as a monomer solution, their anionic polymerization when put in contact with aqueous media like blood or body tissues conferring adhesive property to the polymer [30]. N-butyl cyanoacrylates are also used in clinics for arterial embolization to prevent from rupture or bleeding in pathologies such as pelvic area [31]. Cyanoacrylate ability to polymerize in water constitutes a new strategy for gas encapsulation in aqueous solution as presented before using hydrodynamic cavitation method. Because of its chemical structure, cyanoacrylate shell are stiffer and thicker (hundreds of nanometers compared to 3–5 nm range for lipid shells [32]) allowing multiple functionalization possibilities including drug loading [33] and targeting peptide grafting [34]. This versatility is compensated by some drawbacks, the main one relies on the biocompatibility of cyanoacrylate degradation products. Indeed, Eisenbrey et al. underlined that when injected in rat models, cyanoacrylate MBs lead to local ischemia [30]. Nevertheless, Wang et al. [35] recently underlined that its hydrolysis releases cyanoacetate and formaldehyde which can lead to local ischemia [30].

[29] S.S. Saluja, J.F. Dillon, J.E. Hollander, The cyanoacrylate topical skin adhesive, Expert Rev. Med. Devices 3 (4) (2006) 419–426, https://doi.org/10.1586/17434440.3.4.419.

[30] D. García Cerda, A.M. Ballester, A. Aliena-Valero, A. Carabén-Redano, J.M. Lloris, T. Sevilla-Lorente, Use of cyanoacrylate glue in peripheral vascular malformations: a case report and review of the literature, Medicina Oral, Patologia Oral y Cirugia Bucal 21 (4) (2016) e496–e501, https://doi.org/10.4317/medoral.21116.

[31] H.S. Cho, Y. Kim, J. Lee, K.S. Yi, C.H. Choi, Use of N-butyl cyanoacrylate in the successful transcatheter arterial embolization of an arteriovenous fistula caused by penetrating trauma, Korean J. Radiol. 9 (Suppl) (2008) S39–S42, https://doi.org/10.3348/kjr.2008.9.s.s39.

[32] S.R. Sirsi, M.A. Borden, Microbubble compositions, properties and biomedical applications, Bubble Sci. Eng. Technol. 1 (1–2) (2009) 3–17, https://doi.org/10.1179/175889709X446507.

[33] M. Lu, et al., Ovalbumin-Loaded, Glucose-Coated, Nanoparticle Vaccine Induces Enhanced Innate and Adaptive Immunity and Tumor Protection, ACS Biomaterials Science & Engineering, 2020, https://doi.org/10.1021/acsbiomaterials.0c00942.

[34] P. Koczera, L. Appold, Y. Shi, M. Liu, A. Dasgupta, PRCA-Based Polymeric Microbubbles for Molecular Imaging and Drug Delivery, 2017, pp. 128–135, https://doi.org/10.1021/acs.molpharmaceut.6b00942.

[35] C. Wang, et al., Efficacy of N-butyl cyanoacrylate glue for non-variceal gastrointestinal bleeding: a systematic review and meta-analysis, Diagn. Interv. Imaging 102 (5) (2021) 293–302, https://doi.org/10.1016/j.diii.2021.01.004.

[36] G. Chen, et al., Erythrocyte exosomes loaded with ultrasmall gold nanozymes for oxidative damage diagnosis and enhanced therapy for acute kidney injury, Nano Today 39 (2021), 101187, https://doi.org/10.1016/j.nantod.2021.101187.

[37] S.M. Fix, G.A. Nyankima, M.D. Mcsweeney, S.K. Tsuruta, S.K. Lai, P.A. Dayton, Accelerated clearance of polyethylene glycol-coated microbubbles after exposure to high-frequency ultrasound, Ultrasound Med. Biol. 176 (1) (2018) 139–148, https://doi.org/10.1016/j.ultrasmedbio.2017.08.1923.

[38] D. Wang, et al., Microbubble functionalization with platelet membrane enables targeting and early detection of sepsis and acute kidney injury, Adv. Healthc. Mater. 10 (23) (2021) 1–14, https://doi.org/10.1002/adhm.202101628.

[39] L. Wang, et al., Platelet-membrane-biomimetic nanoparticles for targeted antitumor drug delivery, J. Nanobiotechnol. 17 (1) (2019) 1–16, https://doi.org/10.1186/s12951-019-0494-0.

[40] Z. Fang, J. Fang, C. Gao, R. Gao, P. Lin, W. Yu, Recent trends in platelet membrane-coated nanoparticles for application of inflammatory diseases, Drug Deliv. 29 (1) (2022) 2805–2814, https://doi.org/10.1080/10717544.2022.2114254.

[41] A. Zervich, J. Fournier, C. Chauvierre, Nanomedicine progress in thrombolytic therapy, Biomaterials 258 (January 2020), https://doi.org/10.1016/j.biomaterials.2020.120269.

[42] J.M. Warram, A.G. Sorace, R. Saini, H.R. Umphrey, K.R. Zinn, K. Hoyt, A triple-targeted ultrasound contrast agent provides improved localization to tumor vasculature and data standardization in response to vascular endothelial growth factor receptor 2 blockade, Ultrasound Med. Biol. 40 (8) (2014) 1838–1851, https://doi.org/10.1016/j.ultrasmedbio.2014.03.009.

[43] J.M. Warram, A.G. Sorace, R. Saini, H.R. Umphrey, K.R. Zinn, K. Hoyt, A triple-targeted ultrasound contrast agent provides improved localization to tumor vasculature and data standardization in response to vascular endothelial growth factor receptor 2 blockade, Ultrasound Med. Biol. 40 (8) (2014) 1838–1851, https://doi.org/10.1016/j.ultrasmedbio.2014.03.009.

[44] B. Wu, et al., Preparation of novel targeting nanobubbles conjugated with small interfering RNA for concurrent molecular imaging and gene therapy in vivo, PLoS One 10 (7) (2015) 1–23, https://doi.org/10.1371/journal.pone.0129681.

[45] K. Yamura, et al., Mutation of tyrosine residues in streptavidin: impact on the structure and function of core streptavidin, Protein Sci. 22 (2) (2013) 213–221, https://doi.org/10.1002/pro.2203.

[46] J. Strozzelli, et al., Therapeutic use of avidin is not hampered by anti-avidin antibodies in human, Cancer Biother. Radiopharm. 25 (5) (2010) 563–570, https://doi.org/10.1089/cbr.2010.0797.

[47] S. Fokong, et al., Image-guided, targeted and triggered drug delivery to tumors using polymer-based microbubbles, J. Contr. Release 165 (1) (2012) 75–81, https://doi.org/10.1016/j.jconrel.2012.10.017.

[48] K. Renault, W. Fredy, P.Y. Renard, C. Sabot, Covalent modification of biomolecules through maleimide-based labeling strategies, Bioconjugate Chem. 29 (8) (2018) 2497–2513, https://doi.org/10.1021/acs.bioconjchem.8b00252.

[49] M. Monsigny, A.C. Roche, P. Midoux, R. Mayer, Glycoconjugates as carriers for specific delivery of therapeutic drugs and genes, Adv. Drug Deliv. Rev. 14 (1) (1994) 1–24, https://doi.org/10.1016/0169-409X(94)90002-7.

[50] N.J. de Mol, M.J.E. Fischer, Amide coupling through EDC/NHS: a practical approach, Methods Mol. Biol. 627 (2010) 273–290, https://doi.org/10.1007/978-1-60761-670-2_20.

[51] Y. Zhang, J.L. Xu, Z.H. Yuan, W. Qi, Y.Y. Liu, M.C. He, Artificial intelligence techniques to optimize the EDC/NHS-mediated immobilization of cellulase on Eudragit L-100, Int. J. Mol. Sci. 13 (7) (2012) 7952–7962, https://doi.org/10.3390/ijms13077952.

[52] X. Liu, et al., Fast functionalization of ultrasound-responsive bubbles using strain-promoted click chemistry, Biomater. Sci. 6 (3) (2018) 623–632, https://doi.org/10.1039/c8bm00004h.

[53] S. Stride, et al., Characterization of positively charged lipid shelled microbubbles with ultrasonic pulse sensing, IEEE Int. Ultrason. Symp. IUS (2014) 1–4, https://doi.org/10.1109/ULTSYM.2014.0001.

[54] C.M. Lange, et al., Ultrasound-mediated gene delivery with cationic versus neutral microbubbles: effect of DNA and microbubble data on in vitro transfection efficiency, Theranostics 2 (11) (2012) 1078–1091, https://doi.org/10.7150/thno.4290.

[55] S.R. Sirsi, C. Fung, S. Garg, M.Y. Tianning, P.A. Mountford, M.A. Borden, Lung surfactant microbubbles increase lipophilic drug payload for ultrasound-targeted delivery, Theranostics 3 (6) (2013) 419–433, https://doi.org/10.7150/thno.5964.

[56] E. Stride, The influence of surface adsorption on microbubble dynamics, Philos. Trans. R. Soc. A Math. Phys. Eng. Sci. 366 (1873) (2008) 2103–2115, https://doi.org/10.1098/rsta.2008.0014.

[57] S. Omata, et al., Effects of encapsulated gas on stability of lipid-based nanobubble technology for water treatment, Chemosphere 84 (9) (2011) 1175–1180, https://doi.org/10.1016/j.chemosphere.2011.05.054.

[58] S. Omata, et al., Effects of encapsulated gas on stability of lipid-based microbubbles as generated from soybean and egg yolk lecithins, and their relationship with ultrasound imaging, Biochim. Biophys. Acta Biomembr. 1860 (9) (2018) 65–78, https://doi.org/10.1016/j.bbamem.2018.08.023.

[59] R. Battino, The Ostwald coefficient of gas solubility, Fluid Phase Equil. 15 (3) (1984) 231–240, https://doi.org/10.1016/0378-3812(84)87009-0.

[60] A. Kabalnov, et al., Dissolution of multicomponent microbubbles in the blood stream: 2. Experiment, Ultrasound Med. Biol. 24 (5) (1998) 751–760, https://doi.org/10.1016/S0301-5629(98)00034-9.

[61] A. Kabalnov, et al., Dissolution of multicomponent microbubbles in the blood stream: 1. Theory, Ultrasound Med. Biol. 24 (5) (1998) 739–749, https://doi.org/10.1016/S0301-5629(98)00033-7.

[62] N. De Jong, A. Bouakaz, P. Frinking, Basic acoustic properties of microbubbles, Echocardiography 19 (3) (2002) 229–240, https://doi.org/10.1046/j.1540-8175.2002.00229.x.

[63] D. Chen, et al., Biomimetic cascade hydrogel sequentially blocks colorectal cancer self-seeding and distant dissemination, Sci. Adv. 6 (2020) 1–15, https://doi.org/10.1126/sciadv.aaz0774.

[64] E. Segers, M. Versluis, Acoustic bubble sorting for ultrasound contrast agent enrichment, Lab Chip 14 (10) (2014) 1705–1709, https://doi.org/10.1039/c4lc00185f.

[65] T. Segers, N. de Jong, M. Versluis, Uniform scattering and attenuation of subharmonically sorted ultrasound contrast agent bubbles, J. Acoust. Soc. Am. 140 (6) (2016) 2506–2517, https://doi.org/10.1121/1.4964370.

[66] D.I. Nikitichev, A. Barburas, K. McPherson, J.M. Mari, S.J. West, A.E. Desjardins, Construction of 3-dimensional printed ultrasound phantoms with wall-less vessels, J. Ultrasound Med. 35 (9) (2016) 1933–1939, https://doi.org/10.7863/ultra.15.09019.

[67] O. Couture, S. Bannouf, G. Montaldo, J.F. Aubry, M. Fink, M. Tanter, Ultrafast imaging of ultrasound contrast agents, Ultrasound Med. Biol. 35 (11) (2009) 1908–1916, https://doi.org/10.1016/j.ultrasmedbio.2009.05.020.

[68] J. Feshitan, C. Chen, J. Kwan, M. Borden, Microbubble size isolation by differential centrifugation, J. Colloid Interface Sci. 329 (2) (2009) 316–324, https://doi.org/10.1016/j.jcis.2008.10.018.

[69] X. Chu, et al., Mechanical properties of sub-microbubbles with a nanoparticle-stabilized shell, Langmuir 30 (19) (2014) 5557–5563, https://doi.org/10.1021/la404804u.

[70] E. Glynos, V. Sboros, V. Koutsos, Polymeric thin shells: measurement of elastic properties at the nanometer scale using atomic force microscopy, Mater. Sci. Eng. B Solid-State Mater. Adv. Technol. 168 (1–3) (2010) 143–147, https://doi.org/10.1016/j.mseb.2009.08.016.

[71] R.H. Abou-Saleh, S.A. Peyman, K. Critchley, S.D. Evans, N.H. Thomson, Nanomechanics of lipid encapsulated microbubbles with functional coatings, Langmuir 29 (12) (2013) 4096–4105, https://doi.org/10.1021/la400010k.

[72] D.D. Monard, R.P. Bell, Pathogenesis of thrombosis: cellular and pharmacogenetic contributions, Cardiovasc. Diagn. Ther. 7 (Suppl 3) (2017) S291–S298, https://doi.org/10.21037/cdt.2017.09.11.

[73] W. Wiedeman, Z. Likyova, H. Basas, Y. Poulikakos, V. Kuteifan, The breakup of interfacial lipid shells: dynamics and stylization, Biomech. Model. Mechanobiol. 16 (2) (2017) 611–624, https://doi.org/10.1007/s10237-016-0840-2.

[74] J.H. Wible, J.K. Wojdyla, G.L. Bakes, W.N. McMullen, L.A. Geiser, D.D. Buss, Initially presented as a monomer solution, their anionic polymerization does not occur in contact with aqueous media like blood or body tissues conferring adhesive property to the polymer, N-butyl cyanoacrylates are also used in clinics for arterial embolization to prevent from rupture or bleeding in pathologies such as pelvic area, Chem. Res. Toxicol. 13 (11) (2000) 1175–1185, https://doi.org/10.1021/tx000163u.

[75] R.B. Birge, et al., Phosphatidylserine is a global immunosuppressive signal in efferocytosis, infectious disease, and cancer, Cell Death Differ. 23 (6) (2016) 962–978, https://doi.org/10.1038/cdd.2016.11.

[76] R. Watanabe, M. Matsumura, T. Munemasa, M. Fujimaki, M. Suematsu, Mechanism of hepatic parenchyma-specific contrast of microbubble-based sonography in rats, Acad. Radiol. 19 (2) (2012) 227–236, https://doi.org/10.1016/j.acra.2011.09.024.

[77] K.T. Warzecha, et al., Targeting and modulation of liver myeloid immune cells by shell microbubbles, Adv. Biosyst. 2 (5) (2018), https://doi.org/10.1002/adbi.201800016.

[78] Y.C. Park, et al., Microvessels-on-a-chip to assess targeted ultrasound-assisted drug delivery, ACS Appl. Mater. Interfaces 8 (46) (2016) 31541–31549, https://doi.org/10.1021/acsami.6b09671.

[79] A. Pitson, et al., Endothelial cell activation and antigen expression induced by ultrasound-assisted ultrasound, Ultrasound Med. Biol. 46 (7) (2020) 1565–1583, https://doi.org/10.1016/j.ultrasmedbio.2020.03.013.

[80] N. Malik, et al., Air embolism: diagnosis and management, Future Cardiol. 13 (4) (2017) 365–378, https://doi.org/10.2217/fca-2017-0015.

[81] K. Seitz, D. Strobel, A. Milestone, Approval of CEUS for diagnostic liver imaging in adults and children in the USA, Ultraschall der Med. 37 (3) (2016) 229–232, https://doi.org/10.1055/s-0042-107411.

L. Fournier et al.

Lipids dissolution in chloroform and rehydration in phosphate buffered solution constitutes the precursor lipid suspension for all lipid MBs synthesis, and the process can be time-consuming as the chloroform evaporation step can last up to 12 h [88]. Despite the wide practice of this technique, it presents some drawbacks as a complex control on the size distribution. In order to narrow the size dispersity, microfluidics have been a widely explored alternative to obtain reproducible and size tunable protocol. The general idea consists in constraining a liquid flow and/or a gaseous flow into microchannels to generate size monitored MBs. The main advantage is the reduction of reagent volumes necessary and a decrease in the total cost of the experiment but also an increased yield of production. Two main systems are leading the field, the T-junction system and the flow focusing system [9]. Both rely on the convergence of the gas phase and shell material phase with monitored flow rate and optimized channel width to entrap the gas into the shell. Nevertheless, the technology still relies on an advanced miniaturized system with development costs and a time of production slower than other process like sonication or homogenization [10]. A nice review written by Pulsipher et al. presents the various microfluidic technologies developed for MBs generation [89]. Carugo et al. figured out a smart way to overcome the poor production yield without compromising the narrow distribution of microfluidics systems [11]. Instead of direct production of microbubbles, they produced large effect emulsion of double regular T-junction gas-in-oil system but expose them to a low frequency US field to generates narrow size distribution MBs. This method enables the production of microfluidic like MBs but with a production yield in the same order of magnitude than conventional batch sonication. Indeed, high yield production methods like hydrodynamic cavitation and sonication are relatively faster production rate but require post synthesis treatment like filtration to narrow the size distribution. The hydrodynamic cavitation method uses the shear force of a homogenizer in an aqueous solution to produce polymer MBs formation that can be stabilized with the wanted shell component. It briefly consists in the addition of a monomer into an aqueous solution with the constant hydrodynamic stirring of a homogenizer like Ultraturrax for an hour [12]. As for sonication, it is the fastest method and is involved in the generation of the majority of protein shelled MBs [13]. As underlined by Stride et al., sonication is a relatively easy procedure and extensive study about standardization of sonication protocols is not described yet [14]. It consists in the activation of an ultrasonic horn in the bulk of air interface source (generally referring to a tissue-mimicking material, Ultrasound Med. Biol. 27 (10) (2001) 1399–1412, https://doi.org/10.1016/S0301-5629(01)00438-0.) of energy usually creates high local temperature rise and the overall temperature rise of the medium. Often driven by placing the setup in ice. Nevertheless, it is known to have a high potential in the obtention of high yield synthesis at low cost and high speed. However, new shell compositions might be studied with this technique to overcome the issue of stability and fast blood clearance of protein shelled MBs.

Alternative techniques also exists like shaking, used for the synthesis of Definity® MBs by simply shaking a lipid solution at a scale of vial with a shaking machine [15]. Moreover, recently established cavitation is employed for the generation of lipid MBs by applying a constant electric field on a microfluidic flow rate of a lipid solution in contact with air [16]. Overall, a robust MBs synthesis should include the high yield of hydrodynamic cavitation, the size regulation of microfluidic, the fast production time and cost effectiveness of sonication.

2.2. Microbubbles shell composition

The shell integrity of MBs was originally established with albumin polymer, leading to the resulting MBs circulating time extension due to their fast clearance in the body. The most studied protein for MBs application is human serum albumin (HSA) [17] or bovine serum albumin (BSA) [18] through the 90's and 2000's. They hold the advantage of providing sufficient robustness to keep the shell integrity and unique biochemical characteristics implies the possibility to graft targeting or therapeutic agents. The major drawback was attributed to their vulnerability *in vivo*, because of the fast recognition by the patrolling scavenging cells leading to a rapid elimination in the bloodstream [19]. Nowadays, the vast majority of MBs are composed of lipids and a mixture of them arranged as a monolayer [20]. The mixture of phospholipids usually consists of various ratios of DSPC (1,2-distearoyl-sn-glycero-3-phosphocholine) and DSPE-PEG2000 (1,2-distearoyl-sn-glycero-3-phosphoethanolamine-N-[amino(polyethylene glycol)-2000]). Phosphatidylcholines are a natural component of cell membranes. Commercially extracted from soybean or egg yolks, they are already used and FDA approved as excipient in various intravenous treatments [21]. The resulting shell is flexible and confers the ability of structural rearrangement. This can be an easy reconstitution after freeze drying storage but lipid monolayer reorganization can dissevice the overall stability due to weak interaction forces involved in the geometry, hydrophobicity and van der Waals [6]. In consequence, it does not efficiently prevent the gas diffusion and the coalescence. Therefore, lipid shelled MBs strategy relies on the flexible property of lipids and small amount activity as the polymer property protect them from reticuloendothelial system clearance [22].

When looking at MBs stability, interaction of MBs between themselves has to be studied. Indeed, during and after their synthesis they will be in close contact as the flotation phenomenon occurs for easy and unwanted events like the Ostwald ripening or coalescence are more likely to happen [23] (Fig. 2). Ostwald ripening can be defined as the expansion of bigger MBs to the detriment of small and less stable MBs based on thermodynamic equilibrium [24]. This phenomenon can be managed by selecting a low soluble-to-biological-fluid gas and a low solubility to biological fluid shell but also by increasing the stiffness of the shell to prevent exchanges between the surrounding fluid and MBs. In case of lipid shelled MBs, it is recommended to increase the molar volume of the phase to reduce their solubility [24]. When two bubbles merge to form a larger bubble, it is called coalescence. It can be prevented by reducing the interaction between MBs using surfactants [25] or by increasing of the synthesis temperature [26]. Hence, MBs shelf stability depends on various parameters like shell and gas composition, shell elasticity, surface tension and viscosity of the aqueous solution. Srinivasan et al. proposed a mathematical model to estimate MBs half-life in suspension and focused the attention on shell resistance and the viscosity of the storage solution. Storage stability of MBs is also extended using polymers and with the addition of glycerol like ingredient to thicken the aqueous solution [27].

To enhance the shell fragility without compromising the functionalization of the MBs, polymerized cyanoacrylates were introduced as substitute of lipid shelled MBs. Cyanoacrylate is traditionally used in medicine as surgical adhesive for tissue repair and closing [29]. They are chemically composed of an ethylene group, a cyano-group, and a variable alkyl chain, initially presented as monomer solution, their anionic polymerization is spontaneous in aqueous media like blood or body tissues conferring adhesive property to the polymer [30]. N-butyl cyanoacrylates are also used in clinics for arterial embolization to prevent from massive bleeding [31]. Cyanoacrylate adhesive property in water constitutes a new strategy for gas encapsulation in aqueous solution as presented before using hydrodynamic cavitation. Because of its chemical structure, cyanoacrylate shell are stiffer and thicker (hundreds of nanometers compared to 3–5 nm range for lipid shells [32]) allowing multiple functionalization possibilities with targeting ligands like antibodies or peptide grafting [34]. This versatility is accompanied by some drawbacks, the main one relies on the biocompatibility of cyanoacrylate degradation products. Indeed, as already mentioned, Bolinger et al. injected cyanoacrylate [35], it is known that its hydrolysis releases cyanoacetate and formaldehyde which can lead to local ischemia [30].

[82] C.M. Moran, J.V. Hannah, Single-pass versus recirculation during sonothrombolysis in vitro, Eur. Heart J. 25 (2) (2004) 157–164, https://doi.org/10.1016/j.ehj.2003.10.029.

[83] J.M. Hwelin, et al., Use of ultrasound contrast agent microbubbles in preclinical research : recommendations for small animal imaging, Invest. Radiol. 48 (8) (2013) 555–567, https://doi.org/10.1097/RLI.0b013e31828a0fbf.

[84] A. Bouakaz, et al., Nonlinear detection of ultrasound contrast agents with particular emphasis on chirp excitation, IEEE Trans. Ultrason. Ferroelectrics Freq. Control 52 (9) (2005) 1491–1504, https://doi.org/10.1109/TUFFC.2005.1516019.

[85] M. Smeenge, et al., Novel hybrid contrast agent for ultrasound molecular imaging of prostate cancer: safety and feasibility study, Invest. Radiol. 52 (7) (2017) 419–427, https://doi.org/10.1097/RLI.0000000000000362.

[86] J.K. Willmann, et al., Ultrasound molecular imaging with BR55 in patients with breast and ovarian lesions: first-in-human results, J. Clin. Oncol. 30 (31) (2012) 3872–3879, https://doi.org/10.1200/JCO.2012.42.3273.

[87] S. Wang, J.A. Hossack, A.L. Klibanov, Targeting of microbubbles: contrast agents for ultrasound molecular imaging, J. Drug Target. 26 (5–6) (2018) 420–434, https://doi.org/10.1080/1061186X.2017.1394161.

[88] S. Stride, N. Edirisinghe, Novel microbubble preparation technologies, Soft Matter 4 (12) (2008) 2341–2349, https://doi.org/10.1039/b805257a.

[89] A. Rix, A. Curaj, E. Liehn, F. Kiessling, Ultrasound microbubbles for diagnosis and therapy: advances in multimodality imaging probes and translational studies, Methods Mol. Biol. 1816 (2018) 1–28, https://doi.org/10.1007/978-1-4939-8597-5_1.

[90] V.S. Lucas, R.S. Burk, S. Grechan, M.J. Grap, Utility of high frequency ultrasound: moving beyond the surface to detect changes in skin integrity, Plast. Surg. Nurs. 33 (3) (2013) 125–131, https://doi.org/10.1097/PSN.0b013e3182a0b1f4.

[91] D. Feng, et al., Diagnostic accuracy and large effect emission of double regular T-junction gas-in-oil system but expose them to a low frequency US field to generates narrow size distribution MBs. This method enables the production of microfluidic like MBs but with a production yield in the same order of magnitude than conventional batch sonication. Indeed, high yield production methods like hydrodynamic cavitation and sonication are relatively faster production rate but require post synthesis treatment like filtration to narrow the size distribution. The hydrodynamic cavitation method uses the shear force of a homogenizer in an aqueous solution to produce polymer MBs formation that can be stabilized with the wanted shell component. It briefly consists in the addition of a monomer into an aqueous solution with the constant hydrodynamic stirring of a homogenizer like Ultraturrax for an hour [12]. As for sonication, it is the fastest method and is involved in the generation of the majority of protein shelled MBs [13]. As underlined by Stride et al., sonication is a relatively easy procedure and extensive study about standardization of sonication protocols is not described yet [14]. It consists in the activation of an ultrasonic horn in the bulk of air interface source (generally referring to a tissue-mimicking material, Ultrasound Med. Biol. 27 (10) (2001) 1399–1412, https://doi.org/10.1016/S0301-5629(01)00438-0.) of energy usually creates high local temperature rise and the overall temperature rise of the medium. Often driven by placing the setup in ice. Nevertheless, it is known to have a high potential in the obtention of high yield synthesis at low cost and high speed. However, new shell compositions might be studied with this technique to overcome the issue of stability and fast blood clearance of protein shelled MBs.

Alternative techniques also exists like shaking, used for the synthesis of Definity® MBs by simply shaking a lipid solution at a scale of vial with a shaking machine [15]. Moreover, recently established cavitation is employed for the generation of lipid MBs by applying a constant electric field on a microfluidic flow rate of a lipid solution in contact with air [16]. Overall, a robust MBs synthesis should include the high yield of hydrodynamic cavitation, the size regulation of microfluidic, the fast production time and cost effectiveness of sonication.

2.2. Microbubbles shell composition

The shell integrity of MBs was originally established with albumin polymer, leading to the resulting MBs circulating time extension due to their fast clearance in the body. The most studied protein for MBs application is human serum albumin (HSA) [17] or bovine serum albumin (BSA) [18] through the 90's and 2000's. They hold the advantage of providing sufficient robustness to keep the shell integrity and unique biochemical characteristics implies the possibility to graft targeting or therapeutic agents. The major drawback was attributed to their vulnerability *in vivo*, because of the fast recognition by the patrolling scavenging cells leading to a rapid elimination in the bloodstream [19]. Nowadays, the vast majority of MBs are composed of lipids and a mixture of them arranged as a monolayer [20]. The mixture of phospholipids usually consists of various ratios of DSPC (1,2-distearoyl-sn-glycero-3-phosphocholine) and DSPE-PEG2000 (1,2-distearoyl-sn-glycero-3-phosphoethanolamine-N-[amino(polyethylene glycol)-2000]). Phosphatidylcholines are a natural component of cell membranes. Commercially extracted from soybean or egg yolks, they are already used and FDA approved as excipient in various intravenous treatments [21]. The resulting shell is flexible and confers the ability of structural rearrangement. This can be an easy reconstitution after freeze drying storage but lipid monolayer reorganization can dissevice the overall stability due to weak interaction forces involved in the geometry, hydrophobicity and van der Waals [6]. In consequence, it does not efficiently prevent the gas diffusion and the coalescence. Therefore, lipid shelled MBs strategy relies on the flexible property of lipids and small amount activity as the polymer property protect them from reticuloendothelial system clearance [22].

When looking at MBs stability, interaction of MBs between themselves has to be studied. Indeed, during and after their synthesis they will be in close contact as the flotation phenomenon occurs for easy and unwanted events like the Ostwald ripening or coalescence are more likely to happen [23] (Fig. 2). Ostwald ripening can be defined as the expansion of bigger MBs to the detriment of small and less stable MBs based on thermodynamic equilibrium [24]. This phenomenon can be managed by selecting a low soluble-to-biological-fluid gas and a low solubility to biological fluid shell but also by increasing the stiffness of the shell to prevent exchanges between the surrounding fluid and MBs. In case of lipid shelled MBs, it is recommended to increase the molar volume of the phase to reduce their solubility [24]. When two bubbles merge to form a larger bubble, it is called coalescence. It can be prevented by reducing the interaction between MBs using surfactants [25] or by increasing of the synthesis temperature [26]. Hence, MBs shelf stability depends on various parameters like shell and gas composition, shell elasticity, surface tension and viscosity of the aqueous solution. Srinivasan et al. proposed a mathematical model to estimate MBs half-life in suspension and focused the attention on shell resistance and the viscosity of the storage solution. Storage stability of MBs is also extended using polymers and with the addition of glycerol like ingredient to thicken the aqueous solution [27].

To enhance the shell fragility without compromising the functionalization of the MBs, polymerized cyanoacrylates were introduced as substitute of lipid shelled MBs. Cyanoacrylate is traditionally used in medicine as surgical adhesive for tissue repair and closing [29]. They are chemically composed of an ethylene group, a cyano-group, and a variable alkyl chain, initially presented as monomer solution, their anionic polymerization is spontaneous in aqueous media like blood or body tissues conferring adhesive property to the polymer [30]. N-butyl cyanoacrylates are also used in clinics for arterial embolization to prevent from massive bleeding [31]. Cyanoacrylate adhesive property in water constitutes a new strategy for gas encapsulation in aqueous solution as presented before using hydrodynamic cavitation. Because of its chemical structure, cyanoacrylate shell are stiffer and thicker (hundreds of nanometers compared to 3–5 nm range for lipid shells [32]) allowing multiple functionalization possibilities with targeting ligands like antibodies or peptide grafting [34]. This versatility is accompanied by some drawbacks, the main one relies on the biocompatibility of cyanoacrylate degradation products. Indeed, as already mentioned, Bolinger et al. injected cyanoacrylate [35], it is known that its hydrolysis releases cyanoacetate and formaldehyde which can lead to local ischemia [30].

[92] V.S. Lucas, R.S. Burk, S. Grechan, M.J. Grap, Utility of high frequency ultrasound: moving beyond the surface to detect changes in skin integrity, Plast. Surg. Nurs. 33 (3) (2013) 125–131, https://doi.org/10.1097/PSN.0b013e3182a0b1f4.

[93] D. Feng, et al., Diagnostic accuracy and large effect emission of double regular T-junction gas-in-oil system but expose them to a low frequency US field to generates narrow size distribution MBs. This method enables the production of microfluidic like MBs but with a production yield in the same order of magnitude than conventional batch sonication. Indeed, high yield production methods like hydrodynamic cavitation and sonication are relatively faster production rate but require post synthesis treatment like filtration to narrow the size distribution. The hydrodynamic cavitation method uses the shear force of a homogenizer in an aqueous solution to produce polymer MBs formation that can be stabilized with the wanted shell component. It briefly consists in the addition of a monomer into an aqueous solution with the constant hydrodynamic stirring of a homogenizer like Ultraturrax for an hour [12]. As for sonication, it is the fastest method and is involved in the generation of the majority of protein shelled MBs [13]. As underlined by Stride et al., sonication is a relatively easy procedure and extensive study about standardization of sonication protocols is not described yet [14]. It consists in the activation of an ultrasonic horn in the bulk of air interface source (generally referring to a tissue-mimicking material, Ultrasound Med. Biol. 27 (10) (2001) 1399–1412, https://doi.org/10.1016/S0301-5629(01)00438-0.) of energy usually creates high local temperature rise and the overall temperature rise of the medium. Often driven by placing the setup in ice. Nevertheless, it is known to have a high potential in the obtention of high yield synthesis at low cost and high speed. However, new shell compositions might be studied with this technique to overcome the issue of stability and fast blood clearance of protein shelled MBs.

Alternative techniques also exists like shaking, used for the synthesis of Definity® MBs by simply shaking a lipid solution at a scale of vial with a shaking machine [15]. Moreover, recently established cavitation is employed for the generation of lipid MBs by applying a constant electric field on a microfluidic flow rate of a lipid solution in contact with air [16]. Overall, a robust MBs synthesis should include the high yield of hydrodynamic cavitation, the size regulation of microfluidic, the fast production time and cost effectiveness of sonication.

2.2. Microbubbles shell composition

The shell integrity of MBs was originally established with albumin polymer, leading to the resulting MBs circulating time extension due to their fast clearance in the body. The most studied protein for MBs application is human serum albumin (HSA) [17] or bovine serum albumin (BSA) [18] through the 90's and 2000's. They hold the advantage of providing sufficient robustness to keep the shell integrity and unique biochemical characteristics implies the possibility to graft targeting or therapeutic agents. The major drawback was attributed to their vulnerability *in vivo*, because of the fast recognition by the patrolling scavenging cells leading to a rapid elimination in the bloodstream [19]. Nowadays, the vast majority of MBs are composed of lipids and a mixture of them arranged as a monolayer [20]. The mixture of phospholipids usually consists of various ratios of DSPC (1,2-distearoyl-sn-glycero-3-phosphocholine) and DSPE-PEG2000 (1,2-distearoyl-sn-glycero-3-phosphoethanolamine-N-[amino(polyethylene glycol)-2000]). Phosphatidylcholines are a natural component of cell membranes. Commercially extracted from soybean or egg yolks, they are already used and FDA approved as excipient in various intravenous treatments [21]. The resulting shell is flexible and confers the ability of structural rearrangement. This can be an easy reconstitution after freeze drying storage but lipid monolayer reorganization can dissevice the overall stability due to weak interaction forces involved in the geometry, hydrophobicity and van der Waals [6]. In consequence, it does not efficiently prevent the gas diffusion and the coalescence. Therefore, lipid shelled MBs strategy relies on the flexible property of lipids and small amount activity as the polymer property protect them from reticuloendothelial system clearance [22].

When looking at MBs stability, interaction of MBs between themselves has to be studied. Indeed, during and after their synthesis they will be in close contact as the flotation phenomenon occurs for easy and unwanted events like the Ostwald ripening or coalescence are more likely to happen [23] (Fig. 2). Ostwald ripening can be defined as the expansion of bigger MBs to the detriment of small and less stable MBs based on thermodynamic equilibrium [24]. This phenomenon can be managed by selecting a low soluble-to-biological-fluid gas and a low solubility to biological fluid shell but also by increasing the stiffness of the shell to prevent exchanges between the surrounding fluid and MBs. In case of lipid shelled MBs, it is recommended to increase the molar volume of the phase to reduce their solubility [24]. When two bubbles merge to form a larger bubble, it is called coalescence. It can be prevented by reducing the interaction between MBs using surfactants [25] or by increasing of the synthesis temperature [26]. Hence, MBs shelf stability depends on various parameters like shell and gas composition, shell elasticity, surface tension and viscosity of the aqueous solution. Srinivasan et al. proposed a mathematical model to estimate MBs half-life in suspension and focused the attention on shell resistance and the viscosity of the storage solution. Storage stability of MBs is also extended using polymers and with the addition of glycerol like ingredient to thicken the aqueous solution [27].

To enhance the shell fragility without compromising the functionalization of the MBs, polymerized cyanoacrylates were introduced as substitute of lipid shelled MBs. Cyanoacrylate is traditionally used in medicine as surgical adhesive for tissue repair and closing [29]. They are chemically composed of an ethylene group, a cyano-group, and a variable alkyl chain, initially presented as monomer solution, their anionic polymerization is spontaneous in aqueous media like blood or body tissues conferring adhesive property to the polymer [30]. N-butyl cyanoacrylates are also used in clinics for arterial embolization to prevent from massive bleeding [31]. Cyanoacrylate adhesive property in water constitutes a new strategy for gas encapsulation in aqueous solution as presented before using hydrodynamic cavitation. Because of its chemical structure, cyanoacrylate shell are stiffer and thicker (hundreds of nanometers compared to 3–5 nm range for lipid shells [32]) allowing multiple functionalization possibilities with targeting ligands like antibodies or peptide grafting [34]. This versatility is accompanied by some drawbacks, the main one relies on the biocompatibility of cyanoacrylate degradation products. Indeed, as already mentioned, Bolinger et al. injected cyanoacrylate [35], it is known that its hydrolysis releases cyanoacetate and formaldehyde which can lead to local ischemia [30].

[94] C. Claussen, D. Dollet, C. Dauliac, J. Coupier, Spherical oscillations of microbubbles in viscoelastic fluids: influence of the interfacial rheological properties, J. Acoust. Soc. Am. 149 (2) (2021) 1240–1257, https://doi.org/10.1121/10.0003500.

[95] P. Martínez, N. Bottenus, M. Bowden, Cavitation characterization of size-isolated sonothrombolysis microbubbles, Ultrasound Med. Biol. 49 (9) (2022), https://doi.org/10.3390/pharmaceutics14091925.

[96] K. Kooiman, et al., Ultrasound-responsive cavitation nuclei for therapy and drug delivery, Ultrasound Med. Biol. (2020), https://doi.org/10.1016/j.ultrasmedbio.2020.07.001.

[97] R.G. Holt, R.A. Roy, Measurements of bubble-enhanced heating from focused, MHz-frequency ultrasound in a tissue-mimicking material, Ultrasound Med. Biol. 27 (10) (2001) 1399–1412, https://doi.org/10.1016/S0301-5629(01)00438-0.

[98] S. Wang, et al., Accelerating thrombolysis using a precision and clot-penetrating drug delivery strategy by nanoparticle-shelled microbubbles, Sci. Adv. 6 (31) (2020), https://doi.org/10.1126/sciadv.aaz8204.

[99] H. Yu, S. Chen, A model to calculate microstreaming shear stress generated by oscillating microbubbles on the cell membrane in sonoporation, Bio Med. Mater. Eng. 24 (1) (2014) 861–868, https://doi.org/10.3233/BME-130879.

[100] Y.H. Chuang, P.W. Cheng, P.C. Li, Combining radiation force with cavitation for enhanced sonothrombolysis, IEEE Trans. Ultrason. Ferroelectrics Freq. Control 60 (1) (2013) 97–104, https://doi.org/10.1109/TUFFC.2013.2547.

[101] A. Goyal, et al., Inertial cavitation ultrasound with microbubbles improves fibrinolysis and tissue plasminogen activator in an in vitro model of microvascular obstruction, Ultrasound Med. Biol. 43 (7) (2017) 1391–1400, https://doi.org/10.1016/j.ultrasmedbio.2017.02.013.

[102] Y. Lin, et al., Effect of acoustic parameters on the cavitation behavior of SonoVue microbubbles induced by pulsed ultrasound, Ultrason. Sonochem. 35 (2017) 176–184, https://doi.org/10.1016/j.ultsonch.2016.09.015.

[103] N. Kudo, K. Okada, K. Yamamoto, Sonoporation by single-shot pulsed ultrasound with microbubbles adjacent to cells, Biophys. J. 96 (12) (2009) 4866–4876, https://doi.org/10.1016/j.bpj.2009.02.080.

[104] M.W. Keller, S.B. Segall, S. Kaul, S. Duling, The behavior of sonicated albumin microbubbles within the microcirculation: a basis for their use during myocardial contrast echocardiography, Circ. Res. 65 (2) (1989) 458–467, https://doi.org/10.1161/01.RES.65.2.458.

[105] P.N. Burns, et al., Harmonic imaging of contrast agents, Ultrasonics 32 (3) (1994) 185–192, https://doi.org/10.1016/0041-624X(94)90006-X.

[106] M.W. Keller, S.B. Segall, S. Kaul, S. Duling, Profile of contrast-mediated albumin microbubble destruction and fragment formation, J. Am. Soc. Echocardiogr. 3 (1) (1990) 49–58, https://doi.org/10.1016/S0894-7317(14)80358-X.

[107] S.M. Rychak, K.G. Hensel, K.E. Wilson, L. Tian, M.W. Lutz, E.K. Willmann, Breast cancer detection by B7-H3-targeted ultrasound molecular imaging, Cancer Res. 95 (6) (2015) 1338–1356, https://doi.org/10.1158/0008-5472.CAN-14-3361.

[108] H. Bom, et al., Early detection of breast cancer using targeted nanobubbles and ultrasound, Int. J. Cancer 140 (9) (2017) 2140–2150, https://doi.org/10.1158/1078-0432.CCR-19-1655.Efficacy.

[109] L. Abou-Elkacem, et al., Thy1-targeted microbubbles for ultrasound molecular imaging of tumor angiogenesis, Clin. Cancer Res. 24 (12) (2018) 2874–2883, https://doi.org/10.1158/1078-0432.CCR-17-3412.

[110] H. Zhang, et al., In vitro characterization and in vivo ultrasound molecular imaging of nucleolin-targeted microbubbles, Biomaterials 118 (2017) 63–73, https://doi.org/10.1016/j.biomaterials.2016.11.020.

[111] T. Tinkov, et al., Ultrasound molecular imaging of early-stage atherosclerosis in advanced glycation end product-receptor axis activated vasculature with a clinical translatable microbubble targeted to murine and human VCAM-1, Int. J. Nanomed. 14 (2019) 1–15, https://doi.org/10.2147/IJN.S181512.

[112] M. Kaneko, et al., Preparation of a novel microbubble containing a gene and cationic lipid for ultrasound-mediated gene delivery, Biochem. Biophys. Res. Commun. 364 (3) (2007) 592–597, https://doi.org/10.1016/j.bbrc.2007.10.046.

[113] L. Abou-Elkacem, et al., Ultrasound molecular imaging of the breast cancer neovasculature using engineered fibronectin scaffold ligands: a novel class of targeted contrast agent, Theranostics 6 (11) (2016) 1740–1752, https://doi.org/10.7150/thno.15169.

[114] A. Luong, et al., Development of a translatable ultrasound molecular imaging agent for cardiovascular inflammation, Ann. Biomed. Eng. 48 (2) (2020) 796–806, https://doi.org/10.1007/s10439-019-02413-8.

[115] A. Ingels, et al., Ultrasound molecular imaging of renal cell carcinoma: VEGFR targeted therapy monitored with VEGFR1 and FSHR targeted microbubbles, Sci. Rep. 10 (1) (2020) 1–8, https://doi.org/10.1038/s41598-020-61512-2.

[116] P. van Elsen, C. Ultrasound molecular imaging of atherosclerosis: clinical applications, Ultrasound Med. Biol. 46 (2020) 1–15, https://doi.org/10.1016/j.ultrasmedbio.2019.09.009.

[117] L. Abou-Elkacem, et al., Dual-modality endoglin antibody conjugated microbubbles for quantification of tumor angiogenesis with clinical ultrasound imaging and high-resolution optical imaging, Contrast Media Mol. Imaging 2017 (2017), https://doi.org/10.1155/2017/4784195.

[118] J. Zhou, et al., Target-targeted three-dimensional ultrasound imaging can predict therapeutic outcome of anti-angiogenic therapy in preclinical models of colon cancer, Cancer Res. 76 (14) (2016) 4081–4089, https://doi.org/10.1158/0008-5472.CAN-15-3201.

[119] T. Spivak, et al., Low-dose molecular ultrasound imaging with E-selectin-targeted microbubbles for monitoring inflammation in a rat model of myocardial ischemia-reperfusion injury, Int. J. Cardiovasc. Imaging 32 (10) (2016) 1501–1510, https://doi.org/10.1007/s10554-016-0904-9.

[120] H. Zhang, et al., Ultrasound molecular imaging of tumor angiogenesis with a neuropilin-1-targeted microbubble, Biomaterials 176 (12) (2015) 139–148, https://doi.org/10.1016/j.biomaterials.2018.05.049.

[121] X. Wang, et al., Thrombus-targeted theranostic microbubbles: a new technology towards concurrent rapid ultrasound diagnosis and bleeding-free fibrinolytic treatment of thrombosis, Theranostics 6 (5) (2016) 726–738, https://doi.org/10.7150/thno.14441.

[122] J. Lux, et al., Thrombin-activatable microbubbles as potential ultrasound contrast agents for the detection of acute thrombosis, ACS Appl. Mater. Interfaces 9 (43) (2017) 37587–37596, https://doi.org/10.1021/acsami.7b10592.

[123] A. Curaj, et al., Noninvasive molecular ultrasound monitoring of vessel healing after intravascular surgical procedures in a preclinical setup, Arterioscler. Thromb. Vasc. Biol. 35 (6) (2015) 1366–1373, https://doi.org/10.1161/ATVBAHA.114.304857.

[124] A. Rix, et al., Molecular imaging of VEGF receptor 2 expression in arterial tumors of rabbits: implications for the anti-angiogenic therapy, Invest. Radiol. 51 (12) (2016) 767–775, https://doi.org/10.1097/RLI.0000000000000282.

[125] F. Moccetti, et al., Ultrasound molecular imaging of atherosclerosis using small-peptide targeting ligands against endothelial markers of inflammation and neovascularization, Ultrasound Med. Biol. 44 (6) (2018) 1155–1163, https://doi.org/10.1016/j.ultrasmedbio.2018.01.004.

[126] F. Moccetti, et al., Myocardial infarction produces sustained pro-inflammatory endothelial activation in remote arteries, J. Am. Coll. Cardiol. 176 (1) (2018) 1–10, https://doi.org/10.1016/j.ijcard.2014.06.038.

[127] S. Wang, S. Ramkishman, E.B. Herbst, A.L. Klibanov, F.W. Mauldin, J.A. Hossack, Ultrasound molecular imaging of inflammation in mouse abdominal aorta, Invest. Radiol. 176 (1) (2017) 439–148, https://doi.org/10.1097/RLI.0000000000000338.

[128] Q. Qin, et al., VEGFR2-targeted ultrasound molecular imaging of angiogenesis to evaluate liver allograft fibrosis, Biomater. Sci. 9 (17) (2021) 5802–5811, https://doi.org/10.1039/d1bm00100k.

[129] H. Wang, et al., US molecular imaging of acute ischemic anti-inflammatory treatment response postulated with targeted microbubbles in a preclinical model, Radiology 289 (1) (2018) 90–100, https://doi.org/10.1148/radiol.2018172600.

[130] G. Rose, M. Barguzyte, F. Kiessling, Molecular ultrasound imaging, Nanomaterials 1 (10) (2020) 1–28, https://doi.org/10.3390/nano10101950.

[131] A. Ingels, et al., Ultrasound molecular imaging of cardiovascular diseases, Front. Cardiovasc. Med. 7 (2020) 1–9, https://doi.org/10.3389/fcvm.2020.00214.

[132] P. Vaupel, M. Höckel, A. Mayer, Detection and characterization of tumor hypoxia using pO2 histography, Antioxidants Redox Signal. 9 (8) (2007) 1221–1235, https://doi.org/10.1089/ars.2007.1628.

[133] H.E. Barker, J.T.E. Paget, A.A. Khan, K.J. Harrington, Barker HE_tumour microenvironment after IRR_cancer reviews 2015.pdf, Nat. Publ. Gr. 15 (7) (2016) 409–425, https://doi.org/10.1038/nrc3958.The.

opening thanks to microstreaming. In addition, the rise of mechanical index would induce irreversible MBs destruction which can further cause fibrin clot disassembling, cells membrane sonoporation and sometimes vascular leakage with erythrocytes extravasation. Overall, the complete drug-loaded targeting US responsive tools are not yet ready for clinical translation but the use of clinical MBs co-injected with therapeutic agents and enhanced with US signal showed promising results for the drug doses reduction. In addition, the exact boundaries to avoid damaging features are not established yet except for the FDA fixed 1.9 MI range although dependent on MBs formulation. It has to be understood that MBs' mechanical response to US insonation have not been determined completely and a collective effort has to be made to better describe the US transducer parameters (frequency, amplitude, duty cycle) and the set-up characteristics (insonation duration, distance to object etc.). Due to the broad interest in the MBs potential, there has been multiple advancements and innovations noted in designing promising MBs for the right applications, and in adapting the MBs rationale to new US contrast agents in order to overcome their limitations. This was described in the last part, including among others the use of nanoscale bubbles and droplets, as well as *in situ* generation of echogenic signals with nanoparticle approaches and new MBs' combined use with recent technologies to breach the physical limits of the US imaging.

In perspective of these works, it appeared that the emergence of combined technologies could add another dimension to MBs' behavior, including for example phoretodynamic therapy [283,284], photoacoustic imaging [237,285], or magnetic MBs [286]. Also, the development of US responsive piezoelectric nanomaterial are an interesting new strategy to open the MBs world to cell therapy [287]. As these new therapeutic approaches require the injection of foreign body material, the priority now stands on safety. Clinical trials are widely enrolling patients to established the best parameters for US combination with MBs. These strategies are obviously not meant to replace drug treatments yet but they have the potential to improve their outcomes. Since MBs, they are applications, and consequent innovations are thriving in multiple fields (oncology, cardiovascular diseases, inflammation), the convergence of expertise and standardizations of certain practices appear paramount to ensure a quick development and future translation to the clinic.

CRediT author statement

Louise FOURNIER: conceptualization, writing and figures development. Thibault DE LA TAILLE: writing, editing and figures development. Cedric CHAVENTRE: writing, editing, reviewing, supervision and funding acquisition.

Declaration of competing interest

The authors declare that they have no known competing financial interests or personal relationships that could have appeared to influence the work reported in this paper.

Data availability

No data was used for the research described in the article.

Acknowledgments

Authors thank INSERM, Universite Paris Cite, Universite Sorbonne Paris Nord, Labex Inflamex, Fondation Bettencourt Schueller for their financial support.

[1] W. Najahi-Missaoui, R.D. Arnold, B.S. Cummings, Safe nanoparticles: are we there yet? Int. J. Mol. Sci. 22 (1) (2021) 1–22, https://doi.org/10.3390/ijms22010385.

[2] R. Gramiak and M. P. Shah, "Echocardiography of the Aortic ...

[3] J. Steinman, M.M. Koletar, B. Stefanovic, J.G. Sled, 3D morphological analysis of the mouse cerebral vasculature: comparison of in vivo and ex vivo methods, PLoS One 12 (10) (2017) 1–17, https://doi.org/10.1371/journal.pone.0186676.

[4] M. Ding, M.L. Palmeri, N. Haystead, C.M. Haystead, K.R. Nightingale, Quantifying inflammatory biomarkers in chronic liver disease with ultrasound shear wave elastography, Ultrasound Med. Biol. 43 (10) (2017) 2416–2425, https://doi.org/10.1016/j.ultrasmedbio.2017.06.005.

[5] C.J. Ezekiel, A.M. Bapoliši, R.B. Walker, R.O. Mkhize, Ultrasound-triggered release of antibiotics from microbubbles for ultrasonic chemotherapy, Pharmaceutics 13 (6) (2021) 1–16, https://doi.org/10.3390/pharmaceutics13060882.

[6] A. Upadhyay, S.V. Dalvi, Microbubble formulations: synthesis, stability, modeling and biomedical applications in therapy and diagnosis, Chem. Eng. Res. Des. 91 (12) (2013) 2874–2909, https://doi.org/10.1016/j.cherd.2013.07.018.

[7] D. Ramirez, R.K.P. Benninger, V. Papadopoulou, M. Ramachandran, C. Ma, J. Souquet, P. Hoffman, A. Bernier, P. Hébert, J. Hingot, Y. Zhou, Simultaneous ultrasound localization microscopy and Doppler for characterization of microbubble dynamics in a microvascular network, Ultrasound Med. Biol. 47 (10) (2021) 2821–2838, https://doi.org/10.1016/j.ultrasmedbio.2021.06.009.

[8] R. Li, Y. Song, L. Wang, Z. Wang, Y. Zhang, Y. Zhang, Y. Zh

J. Cancer Res. Clin. Oncol. 145 (5) (2019) 1191–1200, https://doi.org/10.1007/s00432-019-02866-7.
[188] D. Hong, J. Yang, J. Guo, Y. Zhang, Z. Chen, Ultrasound-targeted microbubble destruction enhances inhibitory effect of Apatinib on angiogenesis in triple negative breast carcinoma xenografts, Anal. Cell Pathol. 2021 (2021), https://doi.org/10.1155/2021/8837950.
[189] C. Viallard, B. Larrivée, Tumor angiogenesis and vascular normalization: alternative therapeutic targets, Angiogenesis 20 (4) (2017) 409–426, https://doi.org/10.1007/s10456-017-9562-9.
[190] Y.J. Ho, et al., Normalization of tumor vasculature by oxygen microbubbles with ultrasound, Theranostics 9 (24) (2019) 7370–7383, https://doi.org/10.7150/thno.37750.
[191] J. Deprez, G. Lajoinie, Y. Engelen, S.C. De Smedt, I. Lentacker, Opening doors with ultrasound and microbubbles: beating biological barriers to promote drug delivery, Adv. Drug Deliv. Rev. 172 (2021) 9–36, https://doi.org/10.1016/j.addr.2021.02.015.
[192] M.A. O'Reilly, A. Muller, K. Hynynen, Ultrasound insertion loss of rat parietal bone appears to Be proportional to animal mass at submegahertz frequencies, Ultrasound Med. Biol. 37 (11) (2011) 1930–1937, https://doi.org/10.1016/j.ultrasmedbio.2011.08.001.
[193] D. McMahon, A. Lassus, E. Gaud, V. Jeannot, K. Hynynen, Microbubble formulation influences inflammatory response to focused ultrasound exposure in the brain, Sci. Rep. 10 (1) (2020) 1–15, https://doi.org/10.1038/s41598-020-78657-9.
[194] O. Vince, et al., Microbubbles containing lysolipid enhance ultrasound-mediated blood–brain barrier breakdown in vivo, Adv. Healthc. Mater. 10 (3) (2021) 1–11, https://doi.org/10.1002/adhm.202001343.
[195] K.T. Chen, K.C. Wei, H.L. Liu, Focused ultrasound combined with microbubbles in central nervous system applications, Pharmaceutics 13 (7) (2021) 1–22, https://doi.org/10.3390/pharmaceutics13071084.
[196] Y. Shen, et al., Ultrasound with microbubbles improves memory, ameliorates pathology and modulates hippocampal proteomic changes in a triple transgenic mouse model of alzheimer's disease, Theranostics 10 (25) (2020) 11794–11819, https://doi.org/10.7150/thno.44152.
[197] Y. Huang, R.M. Jones, L.M. Oliveira, B. Davidson, A. Bethune, P. Maralani, Putaminal Recombinant Glucocerebrosidase Delivery with Magnetic Resonance – Guided Focused Ultrasound in Parkinson ' s Disease : A Phase I Study (2022) 1–7, https://doi.org/10.1002/mds.29190.
[198] K.F. Timbie, B.P. Mead, R.J. Price, Drug and gene delivery across the blood-brain barrier with focused ultrasound, J. Contr. Release 176 (1) (2015) 139–148, https://doi.org/10.1016/j.jconrel.2015.08.059 (Drug).
[199] Z.I. Kovacsa, et al., Disrupting the blood-brain barrier by focused ultrasound induces sterile inflammation, Proc. Natl. Acad. Sci. U.S.A. 114 (1) (2017) E75–E84, https://doi.org/10.1073/pnas.1614777114.
[200] K.R. Lattwein, et al., An in vitro proof-of-principle study of sonobactericide, Sci. Rep. 8 (1) (Dec. 2018) 1–12, https://doi.org/10.1038/s41598-018-21648-8.
[201] K.R. Lattwein, et al., Dispersing and sonoporating biofilm-associated bacteria with sonobactericide, Pharmaceutics 14 (6) (2022), https://doi.org/10.3390/pharmaceutics14061164.
[202] X. Duan, Q. Zhou, J.M.F. Wan, A.C.H. Yu, Sonoporation generates downstream cellular impact after membrane resealing, Sci. Rep. 11 (1) (2021) 1–12, https://doi.org/10.1038/s41598-021-84341-3.
[203] F. Fekri, R.C. Delos Santos, R. Karshafian, C.N. Antonescu, Ultrasound microbubble treatment enhances clathrin-mediated endocytosis and fluid-phase uptake through distinct mechanisms, PLoS One 11 (6) (2016) 1–22, https://doi.org/10.1371/journal.pone.0156754.
[204] K.E. Landmark, P.W. Johansen, J.A. Johnson, B. Johansen, S. Uran, T. Skotland, Pharmacokinetics of perfluorobutane following intravenous bolus injection and continuous infusion of sonazoid in healthy volunteers and in patients with reduced pulmonary diffusing capacity, Ultrasound Med. Biol. 34 (3) (Mar. 2008) 494–501, https://doi.org/10.1016/j.ultrasmedbio.2007.09.019.
[205] M.J. Mitchell, M.M. Billingsley, R.M. Haley, M.E. Wechsler, N.A. Peppas, R. Langer, Engineering precision nanoparticles for drug delivery, Nat. Rev. Drug Discov. 20 (2) (Feb. 2021) 101–124, https://doi.org/10.1038/s41573-020-0090-8.
[206] A.A. Exner, M.C. Kolios, Bursting microbubbles: how nanobubble contrast agents can enable the future of medical ultrasound molecular imaging and image-guided therapy, Curr. Opin. Colloid Interface Sci. 54 (2021), 101463, https://doi.org/10.1016/j.cocis.2021.101463.
[207] M. Alheshibri, J. Qian, M. Jehannin, V.S.J. Craig, A history of nanobubbles, Langmuir 32 (43) (Nov. 2016) 11086–11100, https://doi.org/10.1021/acs.langmuir.6b02489.
[208] C.T. Chin, P.N. Burns, Predicting the acoustic response of a microbubble population for contrast imaging in medical ultrasound, Ultrasound Med. Biol. 26 (8) (Oct. 2000) 1293–1300, https://doi.org/10.1016/S0301-5629(00)00299-4.
[209] P.C. Sontum, J. Østensen, K. Dyrstad, L. Hoff, Acoustic properties of NC100100 and their relation with the microbubble size distribution, Invest. Radiol. 34 (4) (Apr. 1999) 268.
[210] B.E. Oeffinger, M.A. Wheatley, Development and characterization of a nano-scale contrast agent, Ultrasonics 42 (1) (Apr. 2004) 343–347, https://doi.org/10.1016/j.ultras.2003.11.011.
[211] C. Su, et al., Current advances in ultrasound-combined nanobubbles for cancer-targeted therapy: a review of the current status and future perspectives, RSC Adv. 11 (21) (May 2021) 12915–12928, https://doi.org/10.1039/D0RA08727K.
[212] N. Güvener, et al., Recent advances in ultrasound-based diagnosis and therapy with micro- and nanometer-sized formulations, Methods 130 (Nov. 2017) 4–13, https://doi.org/10.1016/j.ymeth.2017.05.018.
[213] E.C. Abenojar, et al., Effect of bubble concentration on the in vitro and in vivo performance of highly stable lipid shell-stabilized micro- and nanoscale ultrasound contrast agents, Langmuir 35 (31) (2019) 10192–10202, https://doi.org/10.1021/acs.langmuir.9b00462.
[214] J. Zhang, et al., The optimized fabrication of a novel nanobubble for tumor imaging, Front. Pharmacol. 10 (May 2019) 610, https://doi.org/10.3389/fphar.2019.00610.
[215] A. Jafari Sojahrood, et al., Toward precisely controllable acoustic response of shell-stabilized nanobubbles: high yield and narrow dispersity, ACS Nano 15 (3) (2021) 4901–4915, Aug, https://doi.org/10.1021/acsnano.0c09701.
[216] U.S. Kumar, A. Natarajan, T.F. Massoud, R. Paulmurugan, FN3 linked nanobubbles as a targeted contrast agent for US imaging of cancer-associated human PD-L1, J. Contr. Release 346 (Jun. 2022) 317–327, https://doi.org/10.1016/j.jconrel.2022.04.030.
[217] Z. Xing, et al., The fabrication of novel nanobubble ultrasound contrast agent for potential tumor imaging, Nanotechnology 21 (14) (Apr. 2010) 145607, https://doi.org/10.1088/0957-4484/21/14/145607.
[218] H. Yang, et al., Multifunctional PLGA nanobubbles as theranostic agents: combining doxorubicin and P-gp siRNA Co-delivery into human breast cancer cells and ultrasound cellular imaging, J. Biomed. Nanotechnol. 11 (12) (2015) 2124–2136, https://doi.org/10.1166/jbn.2015.2168.
[219] P. Bhandari, X. Wang, J. Irudayaraj, Oxygen nanobubble tracking by light scattering in single cells and tissues, ACS Nano 11 (3) (Mar. 2017) 2682–2688, https://doi.org/10.1021/acsnano.6b07478.
[220] M.A. Wheatley, F. Forsberg, N. Dube, M. Patel, B.E. Oeffinger, Surfactant-stabilized contrast agent on the nanoscale for diagnostic ultrasound imaging, Ultrasound Med. Biol. 32 (1) (Jan. 2006) 83–93, https://doi.org/10.1016/j.ultrasmedbio.2005.08.009.
[221] P.S. Sheeran, et al., Methods of generating submicrometer phase-shift perfluorocarbon droplets for applications in medical ultrasonography, IEEE Trans. Ultrason. Ferroelectrics Freq. Control 64 (1) (2017) 252–263, https://doi.org/10.1109/TUFFC.2016.2619685.
[222] Y. Endo-Takahashi, Y. Negishi, Microbubbles and nanobubbles with ultrasound for systemic gene delivery, Pharmaceutics 12 (10) (2020) 1–14, https://doi.org/10.3390/pharmaceutics12100964.
[223] C. Pellow, E.C. Abenojar, A.A. Exner, G. Zheng, D.E. Goertz, Concurrent visual and acoustic tracking of passive and active delivery of nanobubbles to tumors, Theranostics 10 (25) (2020) 11690–11706, https://doi.org/10.7150/thno.51316.
[224] H. Kida, et al., Nanobubble mediated gene delivery in conjunction with a hand-held ultrasound scanner, Front. Pharmacol. 11 (Apr. 2020) 363, https://doi.org/10.3389/fphar.2020.00363.
[225] H. Kida, L.B. Feril, Y. Irie, H. Endo, K. Itaka, K. Tachibana, Influence of nanobubble size distribution on ultrasound-mediated plasmid DNA and messenger RNA gene delivery, Front. Pharmacol. 13 (2022).
[226] Y. Tan, et al., Nanobubbles containing sPD-1 and Ce6 mediate combination immunotherapy and suppress hepatocellular carcinoma in mice, Int. J. Nanomed. 16 (2021) 3241–3254, https://doi.org/10.2147/IJN.S305857.
[227] A. Yildirim, N. Blum, A. Goodwin, Colloids, nanoparticles, and materials for imaging, delivery, ablation, and theranostics by focused ultrasound (FUS), Theranostics 9 (Apr. 2019) 2572–2594, https://doi.org/10.7150/thno.32424.
[228] J.M. Gorce, M. Arditi, M. Schneider, Influence of bubble size distribution on the echogenicity of ultrasound contrast agents: a study of SonoVue, Invest. Radiol. 35 (11) (2000) 661–671, https://doi.org/10.1097/00004424-200011000-00003.
[229] L. Hoff, Acoustic Characterization of Contrast Agents for Medical Ultrasound Imaging, Springer Netherlands, Dordrecht, 2001.
[230] J.Z. Myers, J.A. Navarro-Becerra, M.A. Borden, Nanobubbles are non-echogenic for fundamental-mode contrast-enhanced ultrasound imaging, *Bioconjug. Chem.*, Apr. (2022), https://doi.org/10.1021/acs.bioconjchem.2c00155.
[231] W. Bin Cai, et al., The optimized fabrication of nanobubbles as ultrasound contrast agents for tumor imaging, Sci. Rep. 5 (1) (Sep. 2015) 13725, https://doi.org/10.1038/srep13725.
[232] D.V.B. Batchelor, R.H. Abou-Saleh, P.L. Coletta, J.R. McLaughlan, S.A. Peyman, S. D. Evans, Nested nanobubbles for ultrasound-triggered drug release, ACS Appl. Mater. Interfaces 12 (26) (Jul. 2020) 29085–29093, https://doi.org/10.1021/acsami.0c07022.
[233] P.S. Sheeran, P.A. Dayton, Phase-change contrast agents for imaging and therapy, Curr. Pharmaceut. Des. 18 (15) (2012) 2152–2165.
[234] N. Rapoport, Phase-shift, stimuli-responsive perfluorocarbon nanodroplets for drug delivery to cancer, WIREs Nanomedicine and Nanobiotechnology 4 (5) (2012) 492–510, https://doi.org/10.1002/wnan.1176.
[235] N. Rapoport, et al., Ultrasound-mediated tumor imaging and nanotherapy using drug loaded, block copolymer stabilized perfluorocarbon nanoemulsions, J. Control. Release Off. J. Control. Release Soc. 153 (1) (Jul. 2011) 4–15, https://doi.org/10.1016/j.jconrel.2011.01.022.
[236] K.-H. Nam, N.Y. Rapoport, Stable Nanoemulsions for Ultrasound-Mediated Drug Delivery and Imaging, Apr-2014 no. US8709451B2.
[237] M. Kuriakose, M.A. Borden, Microbubbles and Nanodrops for photoacoustic tomography, Curr. Opin. Colloid Interface Sci. 55 (2021), 101464, https://doi.org/10.1016/j.cocis.2021.101464.
[238] L.C. Moyer, K.F. Timbie, P.S. Sheeran, R.J. Price, G.W. Miller, P.A. Dayton, High-intensity focused ultrasound ablation enhancement in vivo via phase-shift nanodroplets compared to microbubbles, J. Ther. Ultrasound 3 (2015) 7, https://doi.org/10.1186/s40349-015-0029-4.

[239] D. Qin, et al., A highly efficient one-for-all nanodroplet for ultrasound imaging-guided and cavitation-enhanced photothermal therapy, Int. J. Nanomed. 16 (2021) 3105–3119, https://doi.org/10.2147/IJN.S301734.
[240] A. Ishijima, et al., Selective intracellular delivery of perfluorocarbon nanodroplets for cytotoxicity threshold reduction on ultrasound-induced vaporization, Cancer Rep 2 (4) (2019) e1165, https://doi.org/10.1002/cnr2.1165.
[241] C. Errico, et al., Ultrafast ultrasound localization microscopy for deep super-resolution vascular imaging, Nature 527 (7579) (Nov. 2015) 499–502, https://doi.org/10.1038/nature16066.
[242] V. Hingot, et al., Subwavelength far-field ultrasound drug-delivery, Appl. Phys. Lett. 109 (Nov. 2016) 194102, https://doi.org/10.1063/1.4967009.
[243] G. Zhang, et al., Photoacoustic super-resolution imaging using laser activation of low-boiling-point dye-coated nanodroplets in vitro and in vivo, in: IEEE International Ultrasonics Symposium, IUS, 2019, pp. 944–947, https://doi.org/10.1109/ULTSYM.2019.8926179, 2019-Octob.
[244] S.-Y. Yu, C.-H. Tu, J.-W. Liaw, M.-K. Kuo, Laser-induced plasmonic nanobubbles and microbubbles in gold nanorod colloidal solution, Nanomaterials 12 (7) (Jan. 2022) 1154, https://doi.org/10.3390/nano12071154.
[245] A. Veeren, M.O. Ogunyankin, J.E. Shin, J.A. Zasadzinski, Liposome-tethered gold nanoparticles triggered by pulsed NIR light for rapid liposome contents release and endosome escape, Pharmaceutics 14 (4) (Apr. 2022) 701, https://doi.org/10.3390/pharmaceutics14040701.
[246] M.O. Ogunyankin, J.E. Shin, D.O. Lapotko, V.E. Ferry, J.A. Zasadzinski, Optimizing the NIR fluence threshold for nanobubble generation by controlled synthesis of 10 - 40 nm hollow gold Nanoshells, Adv. Funct. Mater. 28 (10) (Mar. 2018) 1705272, https://doi.org/10.1002/adfm.201705272.
[247] J.E. Shin, M.O. Ogunyankin, J.A. Zasadzinski, Near infrared-triggered liposome cages for rapid, localized small molecule delivery, Sci. Rep. 10 (Feb. 2020) 1706, https://doi.org/10.1038/s41598-020-58764-3.
[248] J.J. Kwan, et al., Ultrasound-propelled nanocups for drug delivery, Small 11 (39) (Oct. 2015) 5305–5314, https://doi.org/10.1002/smll.201501322.
[249] T. Liu, et al., Endogenous catalytic generation of O2 bubbles for in situ ultrasound-guided high intensity focused ultrasound ablation, ACS Nano 11 (9) (Sep. 2017) 9093–9102, https://doi.org/10.1021/acsnano.7b03772.
[250] X. Cui, X. Han, L. Yu, B. Zhang, Y. Chen, Intrinsic chemistry and design principle of ultrasound-responsive nanomedicine, Nano Today 28 (2019), 100773, https://doi.org/10.1016/j.nantod.2019.100773 xxxx.
[251] F. Pfeifer, Distribution, formation and regulation of gas vesicles, Nat. Rev. Microbiol. 10 (10) (Oct. 2012) 705–715, https://doi.org/10.1038/nrmicro2834.
[252] M.G. Shapiro, et al., Biogenic gas nanostructures as ultrasonic molecular reporters, Nat. Nanotechnol. 9 (4) (Apr. 2014) 311–316, https://doi.org/10.1038/nnano.2014.32.
[253] G. Wang, et al., Surface-modified GVs as nanosized contrast agents for molecular ultrasound imaging of tumor, Biomaterials 236 (Apr. 2020) 119803, https://doi.org/10.1016/j.biomaterials.2020.119803.
[254] A. Farhadi, G.H. Ho, D.P. Sawyer, R.W. Bourdeau, M.G. Shapiro, Ultrasound imaging of gene expression in mammalian cells, Science 365 (6460) (Sep. 2019) 1469–1475, https://doi.org/10.1126/science.aax4804.
[255] R. Gao, et al., Biosynthetic nanobubble-mediated CRISPR/Cas9 gene editing of Cdh2 inhibits breast cancer metastasis, Pharmaceutics 14 (7) (Jul. 2022) 1382, https://doi.org/10.3390/pharmaceutics14071382.
[256] B. Delannoy, et al., Acoustical image reconstruction in parallel-processing analog electronic systems, JAPCA 50 (5) (1979) 3153–3159, https://doi.org/10.1063/1.326397.
[257] R. Torguet, C. Bruneel, E. Bridoux, J.M. Rouvaen, B. Nongaillard, Ultrafast echotomographic system using optical processing of ultrasonic signals, Acoust. Hologr. (1977) 79–85, https://doi.org/10.1007/978-1-4757-0653-6_6.
[258] D. Shattuck, M.D. Weinshenker, S.W. Smith, O.T. von Ramm, Explososcan: a parallel processing technique for high speed ultrasound imaging with linear phased arrays, J. Acoust. Soc. Am. 75 (4) (1984) 1273–1282, https://doi.org/10.1121/1.390734.
[259] L. Sandrin, S. Catheline, M. Tanter, X. Hennequin, M. Fink, Time-resolved pulsed elastography with ultrafast ultrasonic imaging, Ultrason. Imag. 21 (4) (1999) 259–272, https://doi.org/10.1177/016173469902100402.
[260] M. Tanter, J. Bercoff, L. Sandrin, M. Fink, Ultrafast compound imaging for 2-D motion vector estimation: application to transient elastography, IEEE Trans. Ultrason. Ferroelectrics Freq. Control 49 (10) (Oct. 2002) 1363–1374, https://doi.org/10.1109/TUFFC.2002.1041078.
[261] J. Bercoff, Ultrafast ultrasound imaging, Ultrasound Imaging - Med. Appl. (Aug. 2011), https://doi.org/10.5772/19729.
[262] A. Ng, J. Swanevelder, Resolution in ultrasound imaging, Cont. Educ. Anaesth. Crit. Care Pain 11 (5) (Oct. 2011) 186–192, https://doi.org/10.1093/BJACEACCP/MKR030.
[263] H. Hasegawa, C.L. de Korte, Ultrafast ultrasound imaging, Ultrafast Ultrasound Imaging (Sep. 2018), https://doi.org/10.3390/BOOKS978-3-03897-128-3.
[264] G. Montaldo, M. Tanter, J. Bercoff, N. Benech, M. Fink, Coherent plane-wave compounding for very high frame rate ultrasonography and transient elastography, IEEE Trans. Ultrason. Ferroelectrics Freq. Control 56 (3) (Mar. 2009) 489–506, https://doi.org/10.1109/TUFFC.2009.1067.
[265] A. Ozturk, J.R. Grajo, M. Dhyani, B.W. Anthony, A.E. Samir, Principles of ultrasound elastography, Abdom. Radiol. 43 (4) (Feb. 2018) 773–785, https://doi.org/10.1007/S00261-018-1475-6, 2018 434.
[266] J. Bercoff, et al., Ultrafast compound Doppler imaging: providing full blood flow characterization, IEEE Trans. Ultrason. Ferroelectrics Freq. Control 58 (1) (Jan. 2011) 134–147, https://doi.org/10.1109/TUFFC.2011.1780.
[267] C. Demene, et al., Functional ultrasound imaging of brain activity in human newborns, Sci. Transl. Med. 9 (411) (Oct. 2017), https://doi.org/10.1126/SCITRANSLMED.AAH6756/SUPPL_FILE/AAH6756_VIDEO_S2.MP4.
[268] O. Couture, M. Tanter, M. Fink, PROCEDE et dispositif D'IMAGERIE ULTRASONORE, Eur. Pat. Off. (Jun. 2012) no. PCT/FR2011/052810.
[269] O. Couture, V. Hingot, B. Heiles, P. Muleki-Seya, M. Tanter, Ultrasound localization microscopy and super-resolution: a state of the art, IEEE Trans. Ultrason. Ferroelectrics Freq. Control 65 (8) (Aug. 2018) 1304–1320, https://doi.org/10.1109/TUFFC.2018.2850811.
[270] K. Christensen-Jeffries, R.J. Browning, M.X. Tang, C. Dunsby, R.J. Eckersley, In vivo acoustic super-resolution and super-resolved velocity mapping using microbubbles, IEEE Trans. Med. Imag. 34 (2) (Feb. 2015) 433–440, https://doi.org/10.1109/TMI.2014.2359650.
[271] V. Hingot, A. Chavignon, B. Heiles, O. Couture, Measuring image resolution in ultrasound localization microscopy, IEEE Trans. Med. Imag. 40 (12) (2021) 3812–3819, Dec, https://doi.org/10.1109/TMI.2021.3097150.
[272] A. Chavignon, V. Hingot, C. Orset, D. Vivien, O. Couture, 3D transcranial ultrasound localization microscopy for discrimination between ischemic and hemorrhagic stroke in early phase, Sci. Rep. 12 (1) (Aug. 2022) 1–11, https://doi.org/10.1038/S41598-022-18025-X, 2022 121.
[273] S.B. Andersen, et al., Super-resolution ultrasound imaging can quantify alterations in microbubble velocities in the renal vasculature of rats, Diagnostics 12 (5) (May 2022), https://doi.org/10.3390/DIAGNOSTICS12051111.
[274] M.R. Lowerison, et al., Super-resolution Ultrasound Imaging of Cerebrovascular Impairment in a Mouse Model of Alzheimer's Disease, bioRxiv, Oct. 2022, p. 2022, https://doi.org/10.1101/2022.10.05.511008, 10.05.511008.
[275] X. Chen, M.R. Lowerison, Z. Dong, A. Han, P. Song, Deep learning-based microbubble localization for ultrasound localization microscopy, IEEE Trans. Ultrason. Ferroelectrics Freq. Control 69 (4) (Apr. 2022) 1312–1325, https://doi.org/10.1109/TUFFC.2022.3152225.
[276] B. Heiles, A. Chavignon, V. Hingot, P. Lopez, E. Teston, O. Couture, Performance benchmarking of microbubble-localization algorithms for ultrasound localization microscopy, Nat. Biomed. Eng. (2022), https://doi.org/10.1038/S41551-021-00824-8.
[277] L. Yan, et al., Study on the application of super-resolution ultrasound for cerebral vessel imaging in rhesus monkeys, Front. Neurol. 12 (Nov. 2021), https://doi.org/10.3389/FNEUR.2021.720320/PDF.
[278] C. Demené, et al., Transcranial ultrafast ultrasound localization microscopy of brain vasculature in patients, Nat. Biomed. Eng. 5 (3) (Mar. 2021) 219–228, https://doi.org/10.1038/S41551-021-00697-X.
[279] C. Huang, et al., Super-resolution ultrasound localization microscopy based on a high frame-rate clinical ultrasound scanner: an in-human feasibility study, Phys. Med. Biol. 66 (8) (Apr. 2021), https://doi.org/10.1088/1361-6560/ABEF45.
[280] T. Opacic, et al., Motion model ultrasound localization microscopy for preclinical and clinical multiparametric tumor characterization, Nat. Commun. 9 (1) (Apr. 2018) 1–13, https://doi.org/10.1038/S41467-018-03973-8, 2018 91.
[281] A. Sun, et al., Evaluation of visible NIR-I and NIR-II light penetration for photoacoustic imaging in rat organs, Opt Express 28 (6) (Mar. 2020) 9002–9013, https://doi.org/10.1364/OE.389714, vol. 28, no. 6, pp. 9002–9013.
[282] H. Yoon, K.A. Hallam, C. Yoon, S.Y. Emelianov, Super-resolution imaging with ultrafast ultrasound imaging of optically triggered perfluorohexane nanodroplets, IEEE Trans. Ultrason. Ferroelectrics Freq. Control 65 (12) (Dec. 2018) 2277–2285, https://doi.org/10.1109/TUFFC.2018.2829740.
[283] Y. Jang, et al., Development of an ultrasound triggered nanomedicine-microbubble complex for chemo-photodynamic-gene therapy, Nanomed. Nanotechnol. Biol. Med. 27 (2020), 102194, https://doi.org/10.1016/j.nano.2020.102194.
[284] H. Li, et al., Instant ultrasound-evoked precise nanobubble explosion and deep photodynamic therapy for tumors guided by molecular imaging, ACS Appl. Mater. Interfaces 13 (18) (2021) 21097–21107, https://doi.org/10.1021/acsami.1c05517.
[285] R. Chen, et al., Photoacoustic molecular imaging-escorted adipose photodynamic–browning synergy for fighting obesity with virus-like complexes, Nat. Nanotechnol. 16 (4) (2021) 455–465, https://doi.org/10.1038/s41565-020-00844-6.
[286] M. de Saint Victor, L.C. Barnsley, D. Carugo, J. Owen, C.C. Coussios, E. Stride, Sonothrombolysis with magnetically targeted microbubbles, Ultrasound Med. Biol. 45 (5) (2019) 1151–1163, https://doi.org/10.1016/j.ultrasmedbio.2018.12.014.
[287] A. Marino, G.G. Genchi, E. Sinibaldi, G. Ciofani, Piezoelectric effects of materials on bio-interfaces, ACS Appl. Mater. Interfaces 9 (21) (2017) 17663–17680, https://doi.org/10.1021/acsami.7b04323.

ANNEX 2

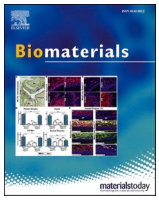
Biomaterials 303 (2023) 122385



Contents lists available at ScienceDirect

Biomaterials

journal homepage: www.elsevier.com/locate/biomaterials





rtPA-loaded fucoidan polymer microbubbles for the targeted treatment of stroke

Louise Fournier [a], Myriam Abioui-Mourgues [b], Georges Chabouh [c], Rachida Aid [a,d], Thibault De La Taille [a], Olivier Couture [c], Denis Vivien [b,e], Cyrille Orset [b], Cédric Chauvierre [a,*]

[a] Université Paris Cité, Université Sorbonne Paris Nord, UMR-S U1148 INSERM, Laboratory for Vascular Translational Science (LVTS), F-75018, Paris, France
[b] Normandie University, UNICAEN, INSERM UMR-S U1237, Physiopathology and Imaging of Neurological Disorders (PhIND), GIP Cyceron, Institut Blood and Brain @ Caen-Normandie (BB@C), Caen, France
[c] Sorbonne Université, CNRS, INSERM, Laboratoire d'Imagerie Biomédicale, Paris, France
[d] Université Paris Cité, UMS 34, Fédération de Recherche en Imagerie Multi-modalité (FRIM), F-75018, Paris, France
[e] Department of Clinical Research, Caen-Normandie University Hospital, Caen, France

ARTICLE INFO

Keywords:
Microbubbles
Fucoidan
Fibrinolytic
Ultrasound
Targeted thrombolysis
Stroke

ABSTRACT

Systemic injection of thrombolytic drugs is the gold standard treatment for non-invasive blood clot resolution. The most serious risks associated with the intravenous injection of tissue plasminogen activator-like proteins are the bleeding complication and the dose related neurotoxicity. Indeed, the drug has to be injected in high concentrations due to its short half-life, the presence of its natural blood inhibitor (PAI-1) and the fast hepatic clearance (0.9 mg/kg in humans, 10 mg/kg in mouse models). Overall, there is a serious need for a dose-reduced targeted treatment to overcome these issues. We present in this article a new acoustic cavitation-based method for polymer MBs synthesis, three times faster than current hydrodynamic-cavitation method. The generated MBs are ultrasound responsive, stable and biocompatible. Their functionalization enabled the efficient and targeted treatment of stroke, without side effects. The stabilizing shell of the MBs is composed of Poly-Isobutyl Cyanoacrylate (PIBCA), copolymerized with fucoidan. Widely studied for its targeting properties, fucoidan exhibit a nanomolar affinity for activated endothelium and activated platelets (P-selectins). Secondly, the thrombolytic agent (rtPA) was loaded onto microbubbles (MBs) with a simple adsorption protocol. Hence, the present study validated the *in vivo* efficiency of rtPA-loaded Fuco MBs to be over 50 % more efficient than regular free rtPA injection for stroke resolution. In addition, the relative injected rtPA grafted onto targeting MBs was 1/10th of the standard effective dose (1 mg/kg in mouse). As a result, no hemorrhagic event, BBB leakage nor unexpected tissue distribution were observed.

1. Introduction

The global burden of cardiovascular diseases (CVD) places them as the leading cause of mortality around the world. Among them, thrombotic diseases including ischemic heart disease and stroke are the most prevalent and described as the main cause of disability [1]. Every year, 15 million new cases of stroke are reported according to the World Health Organization (WHO). The prevalence of stroke increases with age, with the highest rates typically occurring in people over the age of 75. Stroke is also more common in women, and is more prevalent in certain regions of the world, such as Southeast Asia and sub-Saharan Africa, compared to other regions [2]. Overall, the prevalence of stroke is expected to continue to increase in the coming years due to the aging of global population and the increase of risk factors such as high blood pressure, diabetes, and obesity. In medical terms, ischemic stroke is defined as the obstruction of vasculature in the brain caused by a thrombus. Those blood clots are highly heterogenous and composed of a variety of cell types [3] including erythrocytes, immune cells and platelets, with the addition of Von Willebrand Factor (VWF) and Neutrophil Extracellular Traps (NETs), tied together by a strong fibrin mesh [4]. Physiologically needed to repair impaired vessel walls, their pathological formation and their circulation in the bloodstream can lead to flow obstruction and distal tissue ischemia if the vessel recanalization is not quickly supported. Patients undergoing stroke events are treated with the gold standard systemic injection of a thrombolytic drug [5] in

* Corresponding author.
E-mail address: cedric.chauvierre@inserm.fr (C. Chauvierre).

https://doi.org/10.1016/j.biomaterials.2023.122385
Received 15 September 2023; Received in revised form 27 October 2023; Accepted 2 November 2023
Available online 8 November 2023
0142-9612/© 2023 The Authors. Published by Elsevier Ltd. This is an open access article under the CC BY-NC-ND license (http://creativecommons.org/licenses/by-nc-nd/4.0/).

Abbreviations

BBB	Blood Brain Barrier
BCA	Bicinchoninic Acid Assay
CMDex	CarboxyMethyl Dextran
CVD	CardioVascular Disease
DMEM	Dulbecco's Modified Eagle Medium
ESEM	Environmental Scanning Electron Microscopy
FIB	Focused Ion Beam
FTIR	Fourier-Transform InfraRed spectroscopy
GA	Gadoteric Acid
HUVEC	Human Umbilical Vein Endothelial Cell
LDH	Lactate DeHydrogenase
MB	Microbubble
MCA	Middle Cerebral Artery
MI	Mechanical Index
MTT	3-(4,5-dimethyl-2thiazolyl)-2,5-diphenyl-2H-tetrazolium bromide
NET	Neutrophil Extracellular Trap
PAI-1	Plasminogen Activator Inhibitor-1
PFA	ParaFormAldehyde
PFB	PerFluoroButane
PIBCA	Poly-IsoButyl CyanoAcrylate
PRF	Pulse Repetition Frequency
PSGL-1	P-Selectin Glycoprotein Ligand 1
RBC	Red Blood Cell
ROI	Region Of Interest
rtPA	recombinant tissue Plasminogen Activator
SD	Standard Deviation
TX	Texas Red
US	UltraSound
VWF	Von Willebrand Factor
WB	Working Buffer
WHB	Whole Human Blood
WHO	World Health Organization
WL	White Light
3T3	Fibroblasts

order to disassemble the fibrin mesh. There are several different types of "clot busters" used depending on their application (myocardial infarction, pulmonary embolism, stroke …) but they are mainly plasminogen activators like (Alteplase: rtPA, Reteplase: rPA, Tenecteplase: TNK) [6]. Indeed, this serine protease is naturally present in the body [7] allowing the cleavage of plasminogen into plasmin, responsible for fibrin degradation in homeostatic regulation. This thrombolytic injection can also be associated to mechanical thrombectomy [8] with the limitation of it being an invasive procedure. In addition, the systemic injection of the thrombolytic drug brings several drawbacks like hemorrhagic transformation [9] and neurotoxicity [10] with a recanalization rate below 50 % [11]. To overcome those issues, the strategy to encapsulate rtPA has been explored with different carriers from nanoparticles [6] to microbubbles [12] with the common objective to reduce drug doses and improve the treatment efficiency. Besides drug encapsulation, nanomedicine is also focusing on targeted drug delivery on identified biomarkers. In thrombotic diseases, they are mainly described on activated platelets [13] with P-selectins, GPIIb/IIIa integrins and phosphatidylserines or with circulating molecules like Factor XIII, VWF and fibrin [6]. We focused here on the highly specific interaction between P-selectins expressed on activated platelets or activated endothelium [14] and a sulfated polysaccharide: the fucoidan [15,16]. Indeed, fucoidan has been studied for a few decades because of its structural similarities with PSGL-1 (P-Selectin Glycoprotein Ligand 1) [17], natural ligand of P-selectins. Fucoidan nanomolar affinity [17] for P-selectins, makes the fucoidan a very promising targeting agent for thrombotic diseases and already showed its performance *in vivo* [18,19] and is already in clinical trials [20]. The present strategy relies on polymer microbubbles (MBs) for their carrier ability but also their imaging property and treatment enhancement perspectives. Indeed, microbubbles are widely used as clinical contrast agent (Definity®, Sonovue® …) for US imaging due to their intrinsic echogenic properties [21] and have also been of main interest for the development of sonothrombolysis [22]. Also compared to nanoparticles and smaller systems [23], their micrometric size suggests a similar behavior in the blood compartment as erythrocytes and limits their extravasation [24]. We present in this work, the innovative synthesis of polymer microbubbles via acoustic cavitation recently patented (PCT/FR2022/050309). Indeed, the use of US for MBs generation was only used for protein shelled MBs [25] or as a side step for lipid shell MBs [26]. This new method improved the yield of polymer MBs synthesis and reduce the synthesis time by three compared to standard polymer MBs synthesis with hydrodynamic cavitation.

Functionalized with fucoidan as a targeting agent and rtPA-loaded, these fully competent MBs were studied for the targeted treatment of stroke (Fig. 1). We characterized these new MBs in terms of stability, biocompatibility, echogenicity, targeting property and thrombolytic activity. Then, in order to validate the efficacy of the treatment, we performed a mouse stroke model and compared gold standard treatment to drug-loaded targeted MBs by measuring the ischemic lesion reduction after 24 h with MRI imaging. Overall, this paper gives interesting perspectives for the use of drug-loaded targeted polymer MBs for the treatment of thrombotic diseases.

2. Materials and methods

Materials: Isobutyl cyanoacrylate (IBCA) monomers were purchased from Afinitica Technologies (Barcelona, Spain). Carboxymethyl dextran 40 (CMDex) was provided from TdB Labs (Uppsala Sweden). Sulfated polysaccharide fucoidan (Mn = 18 kDa Mw = 104 kDa) was obtained from Algues et Mer (Ouessant, France). Surfactant Tween 20 was purchased from Sigma Aldrich as well as the Rhodamine B fluorochrome. Perfluorobutane (PFB) was obtained from F2 Chemicals (Preston, UK).

2.1. Polymer MBs synthesis

Poly-isobutyl cyanoacrylate (PIBCA) microbubbles were obtained from the anionic polymerization of IBCA monomer at the water gas interface. Briefly, 50 ml of an aqueous solution was prepared with HCl 1 M to reach a pH of 2.5. This solution was saturated with perfluorobutane for 10 min and put into a freezer for 15 min to cool it down. Meanwhile, 700 μl of IBCA solution was loaded into a 1 ml syringe and placed onto a syringe pump (AL-300, World Precision Instrument, Florida, USA). The aqueous solution was then placed on ice, under the microtip of the Sonifier (SFX 550, BRANSON Ultrasonic Corp, Danbury, USA) so the tip is centered and half of a centimeter plunged into the aqueous solution. The organic solution and the PFB tank were connected into the aqueous solution with polyethylene catheters (Bioseb Lab Instrument, Salon de Provence, France). Just before the insonation, 500 μl of Tween 20 detergent was added drop by drop into the aqueous phase. The Sonifier was turned on for 20 min at 30 % of amplitude and the IBCA was injected at a controlled speed of 0.45 ml/min. For the MBs containing polysaccharide, 1 g (2 % w/w) was dissolved at the first step of synthesis into the aqueous solution giving fucoidan MBs (Fuco MBs) or carboxymethyl dextran MBs (CMDex MBs) used here as a non-targeting polysaccharide control. Similarly, for the fluorescent MBs, 500 μg of Rhodamine B was added in the first step of the aqueous phase preparation.

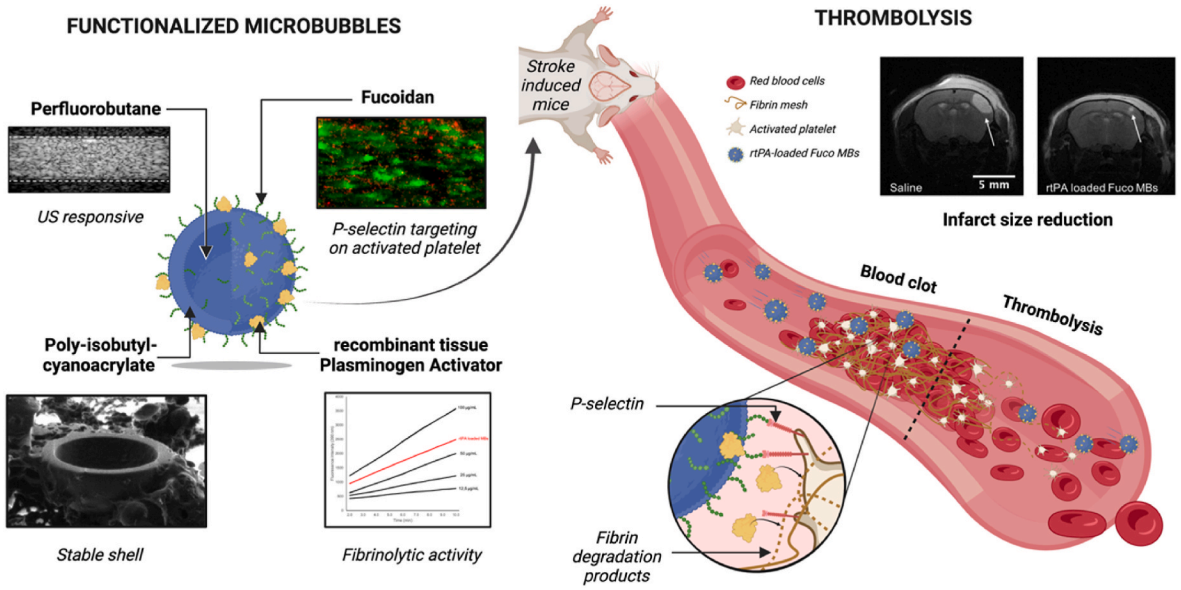


Fig. 1. Graphical abstract of functionalized MBs for the treatment of stroke. MBs are composed of a stable poly-isobutyl cyanoacrylate (PIBCA) shell with a perfluorobutane (PFB) gas core enabling US imaging. Their functionalization was validated for P-selectin targeting with fucoidan and for thrombolytic activity with recombinant tissue Plasminogen Activator (rtPA) loading. After *in vitro* validation, rtPA-loaded targeting MBs were injected in a mouse stroke model to improve thrombolysis recanalization compared to systemic injection of the drug. Fucoidan targeting onto activated platelet P-selectins allowed a specific delivery of rtPA to induce local fibrin degradation. The targeted delivery improved the treatment outcome by reducing the infarcted area after 24 h as observed with MRI imaging.

The obtained foam was centrifuged 3 times at 0.1 g in 50 ml falcon tubes for 20 min, and a solution of 0.02 % Tween 20 was used to resuspend the floating MBs. MBs are then filtered through a 5 μm sieve using a sieve shaker. The obtained suspension was stored at 5 °C in a 0.02 % Tween 20 solution. For all experiment requiring fluorescence microscopy visualization, MBs were labelled with Rhodamine B.

2.2. MBs concentration, size and zeta potential measurements

MBs concentration is expressed in MBs/ml and measured with image analysis. Briefly, a diluted suspension of MBs was injected into a Malassez cell and imaged with an optical microscope (10× objective, Axio Observer, Zeiss). Counting was performed with ImageJ thresholding of MBs signal allowing an evaluation of the mean concentration with count extrapolation. MBs' size was measured with a Mastersizer 3000 (Malvern Instruments, UK), in water and flow speed of 1500 rpm. For each sample the 10th, 50th and 90th percentile of size in volume (Dv10; Dv50; Dv90) were collected. The measurements were reproduced over the weeks to validate the shelf stability. Zeta potential was measured with electrophoretic light scattering method (Nano ZS, Malvern Instrument, UK). Briefly, MBs were diluted to 1/10 in a KCl 1 mM solution and added to the chamber allowing surface charge measurement, each sample was measured three times and averaged.

2.3. FTIR analysis

Fourier-transform infrared spectroscopy (FTIR) spectrums were measured using a Thermo Nicolet AVATAR 370 FTIR spectrometer (Thermo Electron Corporation, Waltham, MA). The lyophilized samples were blended with KBr (1 % mass) and compressed to obtain a pellet. Transmission spectra were acquired between 4000 cm^{-1} and 400 cm^{-1}.

2.4. Confocal imaging and Scanning Electron Microscopy

Confocal imaging was performed with Zeiss LSM 780 microscope in phase contrast or filtered for Rhodamine B MBs observation. Environmental Scanning Electron Microscopy (ESEM, Philips XL30, ESEM-FEG, Amsterdam, Netherland) images were performed with the following parameters: HV 10 kV, WD 13.7 mm, pressure 2.5e^{-4} Pa and magnification from 2500 to 10,000 x. To evaluate the internal structure of the MBs, Focused Ion Beam (FIB) assisted Scanning Electron Microscopy (SEM, Aquilos™ Cryo-FIB, Thermofisher Scientific) was used to cut through the MBs. Samples were deposited onto the SEM grid and dried with paper. The FIB parameters were defined with: HV 30 kV, current 0.10 nA and pressure 1.66e^{-4} Pa.

2.5. Fucoidan quantification with methylene blue dosage

Fucoidan sulfated groups can be recognized by methylene blue colorimetric assay like previously described [27]. On a grade 1 chromatography paper (Whatman®, GE Healthcare), squares of 1 cm^2 were drawn to delimit the samples. Standard solutions of fucoidan MMW (Algues & Mer, France) were prepared with a serial dilution from 0.5 to 0.3125 mg/ml and the negative control was prepared with a suspension of CMDex MBs. MBs suspension were hydrolyzed with an alkaline solution of NaOH (0.1 M) until no further accumulation at the surface. MBs suspension at a concentration of 1 × 10^{10} MB/ml and standard samples were successively deposited 5 times 2 μl with an intermediate drying step at 50 °C for 10min. Once dry, the paper was treated with a solution of Methanol/Acetone (6:4) for 3 min, then treated with the Methylene blue solution of Methanol/Acetone/Water (6:4:15) containing 0.1 % (w/w) methylene blue and 50 mM HCl (1 M) for 10 min. The paper was then washed with several bath of washing solution (Acetic acid/-Methanol/Acetone/Water, 5:6:4:75) until the bath remains translucid. To help with the paper manipulation, it was left to dry under the hood. The drawn squared were then cut and placed in 1.5 ml Eppendorf tubes. 500 μl of 2 % SDS methanol solution was incubated with the cut papers at 50 °C for 15 min. Then, 200 μl of the tainted solution was then extracted to a 96 well plate and the absorbance was read at 663 nm. Fucoidan final concentration was determined with the linear regression of the standard solution curve.

2.6. US phantom model, US burst model, US imaging in vivo

In vitro echogenic MBs properties were studied through a home-made setup. The US phantom employed was a tissue mimicking Doppler flow

phantom (ATS Laboratories, CIRS) with a wall-less channel of 8 mm in diameter at 20 mm depth. US imaging was conducted using a medical probe, GE-L3-12-D (General Electrics; 256 elements, 0.2 mm pitch size) connected to a research ultrasound scanner, Vantage 256 (Verasonics, Kirkland, USA) and driven at 5 MHz center frequency. The amplitude modulation sequence used here (checkerboard) was programmed with Matlab (The MathWorks, Inc., Natick, MA). The *in vitro* acquisition consisted of 3 blocks of 200 images each, using a compounded framerate of 150 Hz and five angles (−4°; −2°; 0°; 2°; 4°) with a pulse repetition frequency (PRF) of 3 kHz. Prior to the experiments, the emitted pressures of the probe were measured and calibrated using a 0.2 mm needle hydrophone (Precision Acoustic, UK). Flow rate was modulated using butterfly valves to stop the flow. The probe was positioned on top of wall-less phantom and various amplitude of signal (from 8 V to 17 V corresponding to Mechanical Index from 0.23 to 0.60) were evaluated to establish the burst threshold of the MBs, with a constant duty cycle of 67 %. In that manner, MBs suspension flow was stopped to evaluate the signal before and after US insonation. The signal intensity was measured by image analysis with background noise subtraction. *In vivo* US acquisitions were then performed with a 256-channel Verasonics® and an 8 MHz multiplexed matrix probe. Five hundred blocks were acquired, with 200 images per block and a frame rate of 250 Hz; each image being the result of a compounding of 5 plane waves oriented according to ±5° (in the elevation axis and in the lateral axis). The sequence was decomposed according to a "light" sequence [28], and lasted for 6 min with an injection of MBs at 50 μl/min. The data were then reconstructed on a [98.5, 150, 150] μm grid.

2.7. rtPA incorporation onto MBs

An adsorption method was performed by increasing the pH of the MBs suspension to 10 with NaOH 1 M. 2 ml of suspension containing 10^{10} MBs at pH 10 was gently mixed with 500 μg of rtPA (Actilyse®, Boehringer) for 2 h at 5 °C. The mix was then placed in a 5 ml syringe with a closing cap and centrifuged for 20 min at 0.1 g. The undernatent was discharged and the mix was rinsed with the storage solution (0.02 % Tween 20 solution at physiological pH), 3 times. The stability of the incorporated drug was measured with the enzyme activity evaluation over 4 days with a washing step between each day.

2.8. Amidolytic activity of incorporated rtPA with PefaFluor® assay

The amidolytic activity of rtPA-loaded MBs was measured by recording the fluorescent signal of the degradation product of PefaFluor® in contact with the serine protease. Briefly, 2.5 μl of the rtPA-loaded MBs were put in contact with 97.5 μl of working buffer (0.1 M HEPES, 0.05 % BSA, 0.9 % NaCl) in a 96 well plate. 10 μl of PefaFluor® (Interchim, France) solution (1 M) was added with a multi pipette and measurement of the fluorescence was performed with monochromatic spectrophotometer (TECAN, Infinite M200 PRO) at $\lambda_{em} = 390$ nm, $\lambda_{ex} = 440$ nm during 70 min. A standard range was obtained by serial dilution of rtPA (Actilyse®, Boehringer) from 400 μg/ml to 6.25 μg/ml and a negative control was obtained with Tween 0.02 % solution. The kinetics of the fluorescent substrate generation is proportional to the concentration of the enzyme. The leading coefficients of the linear part of the standard curves were then used to established the linear regression of the concentration.

2.9. rtPA release in vitro

In vitro release was performed by adding 0.3 ml of 10^{10} MB/ml suspension to 2.2 ml of PBS 1X at 37 °C for different durations (5, 10, 15, 30, 45, 60 min). The tubes were centrifuged to separate the MBs from unloaded rtPA, 10 min at 0.3 g rtPA was then measured in the undernatent compared to non-centrifuged rtPA-loaded MBs, using the PefaFluor® assay. The release percentage was calculated as followed: (quantity of rtPA in the undernatent/quantity of rtPA on loaded MBs) * 100. The control group corresponds to the undernatent of centrifuged rtPA-loaded Fuco MBs in 0.02 % Tween 20 storage solution.

2.10. Fibrinolytic activity

rtPA ability to lyse fibrin was evaluated *in vitro*, comparing free rtPA to rtPA-loaded MBs on a fibrin gel model. The gel was prepared by mixing a fibrinogen solution and a thrombin solution. A TRIS buffer (TRIS 0.1 M, NaCl 0.9 %, pH 7.6) was prepared to mix the different component of the solutions. In two separated water baths, 5 ml of the fibrinogen solution (5 mg/ml, from Human plasma, Sigma Aldrich) was heated to 37 °C while 5 ml of 3 % low melting agarose (Thermo Scientific) was heated to 65 °C. Once agarose has reached its melting temperature, the solution was cooled down to 37 °C and 2.5 U of thrombin (from Human plasma, Sigma Aldrich) was added. The two solutions were mixed and quickly poured into a 9 cm Petri dish plate and left to gel 30 min at 5 °C. Holes were defined with a 3 mm punch and 5 μl of samples diluted to 1/15 were dropped where the gel was extracted. The set-up was placed at 37 °C overnight and fibrin degradation rings were measured with Fiji software.

2.11. In vitro targeting flow experiment on human platelet aggregates

The specific binding of Fuco MBs on P-selectins expressed on activated platelet was evaluated with a microfluidic model [29]. Using the Vena8 Fluoro^{+} biochip (Cellix Ltd, Ireland). Microchannels were coated overnight with a 200 μg/ml solution of collagen type I at 4 °C (equine tendon collagen, Collagen Reagens HORM®, Takeda). Whole Human Blood (WHB) was collected from healthy volunteers in 75 mM PPACK tubes, and platelets were stained with a DIOC6 solution of 50 μg/ml right before injection into the channel. DIOC6 specifically stains mitochondria membranes in living cells [30], excluding erythrocytes staining. For each channel, the following sequence was performed: channel washing with saline solution (NaCl 0.9 %) for 3 min at arterial flow rate (60 μl/min), WHB with DIOC6 injection at arterial flow rate up to 5 min until platelet aggregates start to appear without obstructing the channel; WHB washing with saline solution (NaCl 0.9 %) for 5 min; Rhodamine B stained Fuco MBs injection at venous flow rate (4 μl/min) for 5 min; Washing of Rhodamine B Fuco MBs with saline solution (NaCl 0.9 %) at venous flow rate (4 μl/min) until no more free MBs were circulating. A microscopy image (Axio Observer, Zeiss) was taken between each step to control the platelet aggregates and the targeting properties of the MBs. A negative control was obtained with the injection of CMDex MBs. Quantification was established by measuring the amount of MBs colocalized on platelet aggregates after the final rinsing and normalized to the size of the aggregates using Fiji thresholding analysis.

2.12. Cytotoxicity assays

The evaluation of cytotoxicity was performed with a LDH (Lactate Dehydrogenase) mortality assay and MTT [3-(4,5-dimethyl-2thiazolyl)-2,5-diphenyl-2H-tetrazolium bromide] viability assay. Both HUVECs (Human Umbilical Vein Endothelial Cells, CRL-1730, ATCC) and BALB/3T3 (mouse embryo fibroblast, clone A31, CCL-163, ATCC) were cultured until confluency, at 37 °C in a 5 % CO_2 incubator, with Dulbecco's Modified Eagle Medium (DMEM) with 10 % (v/v) fetal bovine medium, 4 mmol of L-glutamine, 1 % (v/v) of penicillin and 1 % (v/v) of streptomycin. For LDH mortality assay (Cytotoxicity detection kit PLUS, Roche), HUVECs and BALB/3T3 were culture in 96 wells plates. Briefly, after incubation with various concentrations of MBs diluted in cell culture medium (10^8, 10^7, 10^6, 10^5 and 10^4 MB/ml), supernatants were recovered either after 2, 4 or 6 h. The recovered culture medias were incubated with LDH reaction mix according to the supplier guidelines for 15 min at room temperature. After addition of the stop solution, the absorbance of the samples was read at 492 and 690 nm (control

wavelength). The cell cytotoxicity was then determined by subtracting the control wavelength to the absorbance at 492 nm and normalized to dead cell absorbance: Cell mortality = [(Abs of the sample - Abs of culture medium)/(Abs of 100 % of dead cells - Abs of culture medium) x 100].

For the MTT assay, cells were seeded in 24 well plates. This assay was performed with cell culture insert (Falcon®, 1 μm of mesh diameter) to avoid the sedimentation of MBs residues onto the cells, allowing the focus on the degradation product toxicity rather than cell asphyxia in static conditions. Indeed, due to the experimental conditions, 37 °C for 6 h, we expected MBs burst and consequently MBs residues sedimentation rather than intact MBs floating property. Cell culture medium was discharged and replaced by 300 μl of new medium, inserts were placed in each well and 300 μl of MBs diluted in cell culture medium were added inside the inserts for a final MBs concentration of 10^8, 10^7, 10^6, 10^5 and 10^4 MB/ml. After 6 h of incubation, cells insert and medium were replaced by 300 μl of MTT solution (0.05 % in PBS 1X) and incubated for 3 h at 37 °C in dark environment. The medium was removed by gentle plate reversal on dry paper and the 300 μl of isopropanol was added to each well. After 1 h at room temperature, absorbance was measured at 490 nm in a TECAN (Infinite M200 PRO) plate reader. The cell viability was measured as: Cell viability = [(Abs of sample - Abs of dead cells control)/(Abs of living cells control - Abs of dead cells control) x 100].

2.13. Hemolysis evaluation

Whole Human Blood from healthy volunteers was centrifuged 5 min at 500 g to isolate Red Blood Cells (RBC) in 25 μM PPACK tube to avoid coagulation. Hematocrit and plasma level were labelled on the tube, plasma phase was aspirated and replaced by 0.9 % saline solution twice. Then 0.9 % NaCl was replaced by PBS 1X. The final RBC suspension was diluted to 1/50 in PBS 1X. In a V-bottom 96 well plate, 10 μl of MBs suspension was added at different concentration (from 0.125×10^8 to 10^8 MB/ml). 190 μl of previously prepared RBC suspension was added to the wells and incubated at 37 °C for 1 h on an orbital shaker. Plates were centrifuged to the same conditions to recover the RBC pellet. Supernatant was then transferred into a clean flat bottomed 96-well plate and absorbance was measured at 450 nm with a monochromator (TECAN, Infinite M200 PRO). Positive control was obtained with Triton 10X allowing a complete lysis of the RBCs and negative control was performed with PBS 1X. Percentage of hemolysis was obtained with the following formula: Hemolysis = [(Abs of sample - Abs of negative control)/(Abs of positive control - Abs of negative control) x 100].

2.14. In vivo stroke model

Animal studies were performed on 6–8 weeks old (30–40 g) Swiss wild type male (Janvier Labs, Le Genest-Saint-Isle, France). All experiment were adapted according to French (Decree 87/848) and European (2010/63/EU) ethical guidelines. The local committee of Normandy (CENOMEXA) approved the fulfilling of the experiments with the reference number APAFIS#44566. Mice were anesthetized with 5 % of isoflurane inhalation and maintained to 2 % during the entire procedure. As analgesic, they subcutaneously received buprenorphine (0.1 mg/kg) and ear local anesthesia with lidocaine spay. Mice heads were stabilized in a stereotaxic platform and a catheter was placed in the tail vein for the treatment injection. After a local craniotomy on top of the Middle Cerebral Artery (MCA), the dura mater was excised to expose the MCA bifurcation. Precise pneumatical injection of 1 μl of murine thrombin (1 IU, Stago BNL) was carried out by elongated glass capillaries in the MCA to induce fibrin rich thrombus formation [31]. The treatment procedures were performed intravenously, 30 min after thrombin injection with either, free rtPA (Actilyse®, Boehringer) at 1 mg/kg in infusion (300 μl, 10 % bolus + 90 % infusion for 40 min, N = 20); rtPA-loaded Fuco MBs at 1 mg/kg equivalence in bolus (300 μl, 3×10^9 MBs, N = 18); Fuco MBs in bolus (300 μl, 3×10^9 MBs, N = 18) or saline in infusion (300 μl, 10 % bolus + 90 % infusion for 40 min, N = 19).

2.15. Speckle imaging

Monitoring of the *in vivo* brain perfusion was obtained with Laser Speckle Contrast Imager (MOOR FLPI-2, Moor Instruments), allowing the visualization of blood figurative elements. Speckle images were taken before and after the stroke induction as well as before and after the treatment to control the occlusion. The quantification of the flow mean was generated by comparing stroke Region of Interest (ROI) to the same region on the contralateral hemisphere, before and after treatment. In case of no ischemic lesion, mice with pre-stroke contrast difference in both hemisphere and mice with complete reperfusion right after treatment were excluded from the study. For the first scenario, it was not possible to define if the clot was ever obtained. For the second scenario, it was not possible to attest if the clot was not formed correctly or completely dissolved by the treatment.

2.16. Magnetic resonance imaging and BBB permeability

24 h after treatment, mice brains were imaged with MRI to measure the size of the infarcted areas. Briefly, mice were anesthetized with 5 % of isoflurane inhalation and maintained to 2 % during the acquisitions. All acquisitions were obtained with a Pharmascan 7 T (Bruker Biospin, France), T2 sequence (echo time 39.9 ms, repetition time 3500 ms, 2 averages) were used for ischemic lesion visualization and T2 Star sequence (echo time 8.7 ms, repetition time 500 ms, 2 averages) were used for hemorrhagic lesion visualization. Lesion volumes were quantified with image analysis of the hyper signal cut off area on all the brain slices (0.5 mm thickness) with the formula: Ischemic lesion volume = $(\sum ischemic\ areas)x0.5$.

For the evaluation of Blood Brain Barrier (BBB) permeability, Gadoteric Acid (GA, Clariscan Gé, GE Healthcare) was injected intravenously in the tail vein (200 μl at 0.75 mmol/kg). After 15 min, three dimensional T1 Flash acquisition (echo time 4.4 ms, repetition time 15 ms, 3 averages) was recorded and white hyper signal volume was quantified as BBB leakage of GA compared to acquisition before injection, using Fiji software using the same formula as for ischemic lesion volume.

2.17. In vivo fluorescence imaging

The observation of florescent Fuco MBs targeting was performed using a modular stereo microscope (Leica Microsystems MZ10 F). As previously described, ischemic stroke was induced by thrombin injection in the right MCA under the stereo-microscope. Centrifuged ultrasound gel and a microscope slide were applied onto the MCA to facilitate imaging. Acquisitions were performed using both white light (WL) and a Texas Red (TX) filter, 30 min after the stroke, before and after Fuco MBs injection (300 μl, 3×10^9 MBs, N = 1).

2.18. Ex vivo fluorescence biodistribution on complete or sectioned organs

Organs from previously described procedures were harvested 2 h (Fuco MBs: N = 3), 8 h (Fuco MBs: N = 3) or 24 h (Fuco MBs: N = 7, rtPA-loaded Fuco MBs: N = 5) after treatment. Biodistribution of the Fuco MBs was imaged by near-infrared fluorescence imaging (IVIS® Lumina III, PerkinElmer, USA). The imaging of complete organs was performed on brain, liver, lungs, bladder, spleen, intestines and kidney right after euthanasia without PFA fixation. The quantification of fluorescence intensities (λ_{Ex} = 550 nm, λ_{Em} = 620 nm) in regions of interest (ROIs) were analyzed using Living Image® software. For histology analysis, mice received buprenorphine (0.1 mg/kg) and were deeply anesthetized with 5 % of isoflurane inhalation before procedure. After a thoracotomy, a cannula was inserted into the left ventricle, and the right atrium was incised to rinse the circulatory system. Transcardiac

perfusion was then performed with 50 ml of heparinized saline (0.5 ml/L) followed by 30 ml of 4 % paraformaldehyde (PFA) at a constant speed of 14 ml/min. Organs were post-fixed in 4 % PFA overnight at 4 °C then plunged in cryoprotective solution (20 % sucrose in PBS 1X) overnight before to be stored at −80 °C. Organs were subsequently sliced with a cryostat at a 10 µm thickness. Slices were stained with DAPI mounting medium (ABCAM) for nucleus recognition and with rat anti-mouse CD68 primary antibody (Biolegend) followed by a FITC secondary antibody (Biolegend) to highlight tissue macrophages.

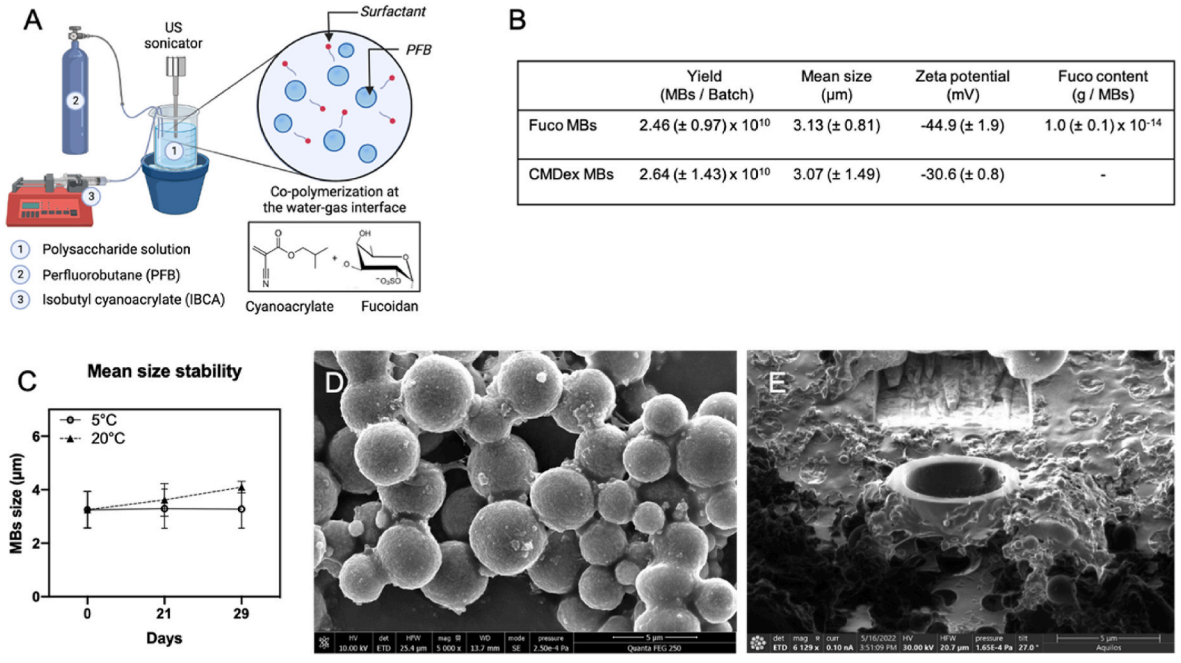
2.19. Statistical analysis

Quantitative data underwent the statistical analysis of GraphPad PRISM 8 with a 95 % confidence level. All presented data are means of at least triplicates expressed with their standard deviation (SD). Normality test were performed using Kolmogorov-Smirnov test and if needed outliers were identified and excluded with ROUT method (1 % of aggressivity of the Gaussian distribution). Depending on the design of the experiment and after normality validation, data were evaluated with unpaired *t*-test (two groups) or ANOVA (more than two groups) in association with multiple comparison in between groups (Tukey's test). P-values were represented as followed, and deemed significant below the 0.05 threshold: *p < 0.05; **p < 0.01; ***p < 0.001, ****p < 0.0001.

3. Results

3.1. Polymer MBs synthesis and characterization

MBs synthesis was inspired by the well-described hydrodynamic cavitation method like recently published by Bo Li. et al. [19]. In this work, the cavitation energy was replaced by ultrasonic insonation into the polysaccharide solution. This recently patented acoustic cavitation method enabled the production of polymer MBs within 20 min (Fig. 2A) (PCT/FR2022/050309). The set-up was placed on ice to regulate the synthesis temperature rise and perfluorobutane (PFB) was constantly injected into the polysaccharide solution. The entrapped gas helped for the stability of the anionic copolymerization between cyanoacrylate monomer and polysaccharide chains. Fucoidan (Fuco) was used here as the targeting agent and so carboxymethyl dextran (CMDex) was used as the control polysaccharide for untargeted MBs. Comparing Fuco MBs and CMDex MBs (Fig. 2B), it was demonstrated that the amount of MBs produced was independent from the polysaccharide composition with a yield around 2.5 × 10^{10} MBs per batch. The mean size after sieve filtration was measured at 3.13 (±0.81) µm for Fuco MBs and 3.07 (±1.49) µm for CMDex MBs, showing no significant difference depending on the shell compositions, in accordance with the close size range of both polysaccharides (Fig. S1A). The evaluation of the surface charge was shown negative with a zeta potential close to −45 mV for Fuco MBs and close to −30 mV for CMDex MBs, also in accordance with the negatively charged groups in fucoidan and carboxymethyl dextran (Fig. S1B). The size stability was monitored over a month by measuring the size of the MBs. A slight size augmentation would be attributed to shell destabilization leading to MBs aggregation detected by the apparatus as bigger MBs. In Fig. 2C, the shelf stability was measured right after synthesis, after 3 and 4 weeks (independently of their incorporated polysaccharide). MBs were either placed at −5 °C or 20 °C to establish the best storage conditions for MBs suspension. It has been demonstrated that 5 °C was the best storage temperature as the mean MBs was stable at 3.27 (±0.71) µm for 4 weeks. Room temperature storage showed a slight increased mean size to 4.09 (±0.22) µm after 4 weeks, which is still in the range for possible animal injection. The whole size distribution presenting the Dv10, Dv50, Dv90 are plotted on Fig. S1C, highlighting



	Yield (MBs / Batch)	Mean size (µm)	Zeta potential (mV)	Fuco content (g / MBs)
Fuco MBs	2.46 (± 0.97) x 10^{10}	3.13 (± 0.81)	-44.9 (± 1.9)	1.0 (± 0.1) x 10^{-14}
CMDex MBs	2.64 (± 1.43) x 10^{10}	3.07 (± 1.49)	-30.6 (± 0.8)	-

Fig. 2. Functionalized polymer MBs characterization. A) Innovative synthesis method. Monomer of isobutyl cyanoacrylate (IBCA) was injected with a needle pusher into the acidic aqueous polysaccharide solution while constant bubbling of perfluorobutane was ongoing. US sonicator was immerged inside the aqueous solution and generates continuous signal for 20 min at 30 % of amplitude. The system is placed on ice to avoid temperature rising. Due to high hydrophobicity, IBCA will tend to polymerized at the water-gas interface, copolymerizing with polysaccharides dissolved into the solution and entrapping PFB. B) Summary of principal physico-chemical characterization depending on the incorporated polysaccharide. Yield was measured with MBs counting on Malassez cell, mean size was measured with laser diffraction granulometry, zeta potential was obtained with electrophoretic light scattering and fucoidan content was dosed with methylene blue colorimetric assay. C) Mean size of MBs suspension over a month measured with laser diffraction granulometry, comparing 5 °C and 20 °C for shelf storage. D) Environmental Scanning Electron Microscopy (ESEM) image of MBs pointing out their homogenous rounded shape. Scale bar is 5 µm. E) Focus Ion Beam (FIB) cut through a single polymer MBs pointing out the hollow structure and the thick shell around 500 nm thick. Scale bar is 5 µm. (For interpretation of the references to color in this figure legend, the reader is referred to the Web version of this article.)

the size stability after 4 weeks. In complement to this size distribution study, we validated that the incorporation of rtPA presented below did not affect the mean size of the MBs (*Fig. S1D*).

The characterization of fucoidan content was obtained with the quantification of sulfated groups as presented in the Supplementary data (Fig. S2A-B-C). This colorimetric method based on Methylene Blue staining pointed out the presence of the sulfated polysaccharide in the range of 1×10^{-14} g/MB using CMDex MBs as negative control. Environmental Scanning Electron Microscopy (ESEM) images presented in Fig. 2D validated the rounded shape of MBs as well as the short polydispersity after filtration. To ensure the hollow structure of the MBs observed in confocal imaging (Fig. S3A), Focused Ion Beam (FIB) technology was used to cut through individual MBs (Fig. 2E). The shell homogeneity was then demonstrated and an estimation of the shell thickness was measured in the range of 500 nm, subsequently emphasized with confocal fluorescence imaging (Fig. S3B-C-D).

3.2. Echogenicity of MBs

One intrinsic property of MBs is their ability to respond to an ultrasound signal [32,33]. Indeed, microbubbles are now widely used in clinic as US contrast agents for US imaging. Their ability to resonate under US creates bright signal compared to surrounding tissues in cardiac echography for example. The proposed agent can be an answer for the problem of specificity in diagnostic or treatment thanks to its precise targeting. To ensure the echogenic properties of those newly synthetized MBs, a home-made *in vitro* model was established to determine the burst threshold of MBs in function of the intensity of the signal (Fig. 3A). Intensities varied from 8 V, 9 V 10 V, 11 V, 12 V, 13 V, 14 V and 17 V corresponding respectively to the following mechanical index 0.230 (±0.002), 0.270 (±0.003), 0.310 (±0.004), 0.350 (±0.002), 0.390 (±0.003), 0.430 (±0.003), 0.470 (±0.002) and 0.600 (±0.001). The imaging sequences were measured with a 2 V signal before and after 2 sequences of the burst periods (Fig. 3B). The signal was normalized to water and to MBs insonated with 2 V all along. The intensity rise at the beginning of each burst sequence corresponds to a "blinking" phenomenon of MBs before ongoing inertial cavitation. The last part of the graph displays the loss of signal due to some MBs implosion. The difference between the initial intensity signal and the final intensity one in plotted on Fig. 3C as the disruptive ratio. This ratio determines the amount of disrupted MBs and clearly states that over 10 V (Mechanical Index = 0.31) more than 50 % of MBs underwent inertial cavitation. This is illustrated with Fig. 3D, displaying the US images of the channels before and after 8 V or 17 V US insonation. In addition, *in vivo US* imaging was performed as presented on Fig. S4. The matrix represents an US image of a mouse brain on the Bregma 0 2D section. On the left we can observe the US signal before MBs injection and on the right the accentuated contrast after MBs injection. This figure validates MBs survival *in vivo* through their contrast enhancer property.

3.3. Drug loading and targeting of MBs

MBs were functionalized with rtPA (Actilyse®), the recombinant tissue Plasminogen Activator used for human treatment. The incorporation was obtained with an adsorption protocol (Fig. 4A) where the pH rising of the MBs suspension allowed the incorporation of the protein within 2 h, followed by several washing steps with the storage solution at physiological pH. To evaluate the amount of incorporated rtPA, the protein activity was measured, ensuring that its incorporation did not affect its enzymatic activity. Primarily noticed result was the high number of incorporated proteins onto Fuco MBs compared to CMDex MBs (Fig. 4B). This specific incorporation is believed to be related to the

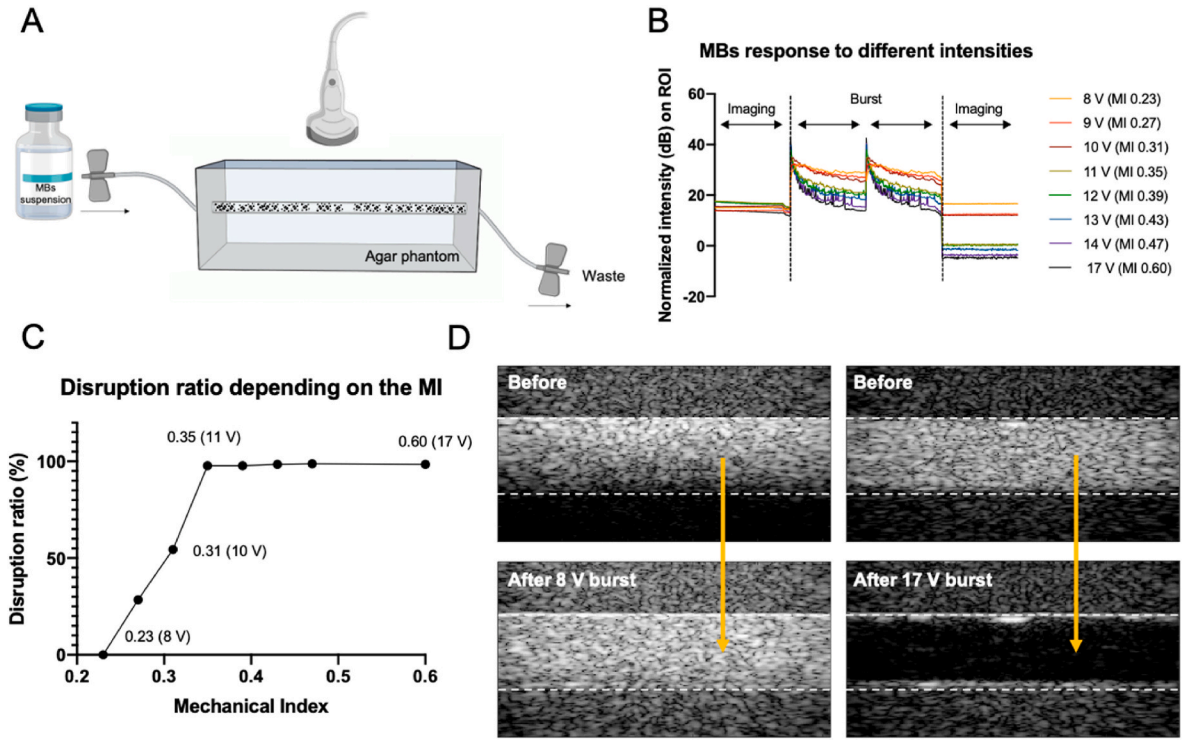


Fig. 3. Ecogenicity characterization of MBs. A) Flow phantom setup mimicking blood vessel circulation. The flow can be monitored with a butterfly closure system and the US transducer is placed on top of the phantom. B) Echogenic response of MBs at 5 MHz frequency and different intensities in volt (from 8 to 17). The curve is composed of 4 sequences: 1 imaging at 2 V, 2 burst sequences depending on the different intensities and 1 more imaging sequence at 2 V to compare before and after bursting signal. C) Disruptive ratio calculated from the normalized intensity difference before and after burst sequence. Mechanical Index 0.230 (±0.002), 0.270 (±0.003), 0.310 (±0.004), 0.350 (±0.002), 0.390 (±0.003), 0.430 (±0.003), 0.470 (±0.002) and 0.600 (±0.001)) correspond to the voltage signal of 8 V–17 V. D) US images from phantom setup before and after 8 V burst and before and after 17 V burst. The channel is highlighted with a dotted line and MBs signal is visible in white contrast.

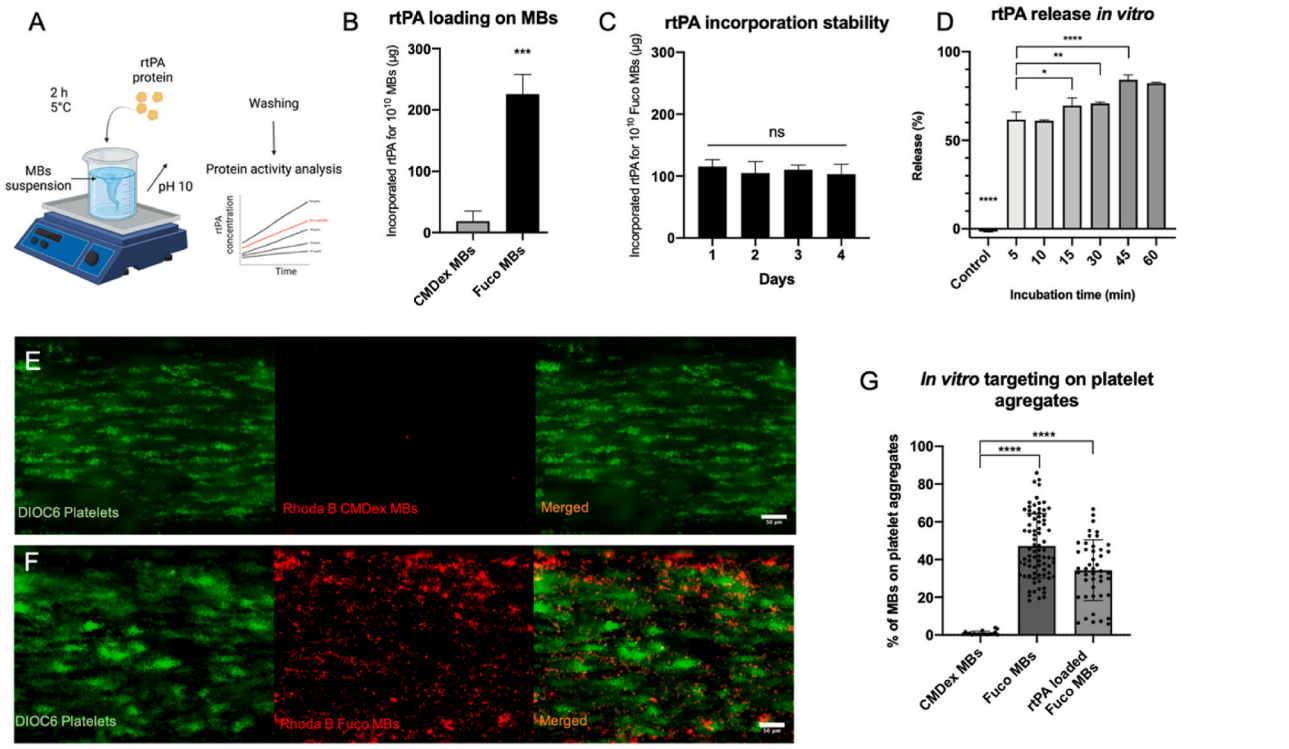


Fig. 4. Functionalization of MBs. A-B-C-D) Drug loading and validation of the rtPA activity after incorporation. A) Drug loading adsorption protocol. Briefly, 500 µg of rtPA in solution was added to a MBs suspension from which the pH has been risen to 10 with NaOH. The mix was left for 2 h under gentle agitation and then rinsed 3 times by centrifugation and discharge of the undernantent. The protein activity is then monitored on drug-loaded MBs with a kinetic substrate degradation assay (PefaFluor ®). B) Protein incorporation determined from protein activity assay of rtPA onto either Fuco MBs or CMDex MBs after 3 centrifugation basing step. C) Stability of rtPA incorporation onto Fuco MBs over 4 days with washing centrifugation step in between days. D) In vitro release of rtPA in PBS 1X at 37 °C from 5 to 60 min rtPA was quantified in the undernatent after MBs suspension centrifugation and compared to the total amount of loaded rtPA. Control group corresponds to Fuco MBs incubated in 0.02 % Tween 20 storage solution. E-F-G) In vitro flow targeting. E-F) Microscopy images of Vena8 Fluoro^{+} microchannels. Platelets from Whole Human Blood were labelled with DIOC6 and MBs were synthesized with Rhodamine B, the last image is a merge of both DIOC6 and Rhodamine B channels. Images are taken under venous flow indicating that stopped MBs are attached to platelet aggregates. E) is the control group of CMDex MBs and F) is the result of Fuco MBs. Scale bar is 50 µm. G) Quantification of MBs targeting on platelet aggregates normalized to the size of the aggregates. The evaluation of rtPA-loaded Fuco MBs targeting confirmed that the drug loading did not compromise the effective targeting on P-selectins.

interaction with activated sulfated groups of fucoidan [34]. Indeed, Fucoidan MBs were able to incorporate 226 ± 32 µg of rtPA for 10^{10} MBs compared to 19 ± 16 µg of rtPA for 10^{10} MBs onto CMDex MBs. Then, rtPA incorporation stability was evaluated over 4 days with centrifugation washing between each day (Fig. 4C), pointing out a stable incorporation threshold of 108 ± 5 µg of rtPA for 10^{10} MBs from day 1 to day 4. This stable incorporated score was observed after the 4th centrifugation washing step on day 1 and stable after the next washing steps. With the aim of producing reproducible results, the stable quantity of incorporated rtPA onto Fuco MBs was set to 100 µg/10^{10} MBs. The fibrinolytic activity of incorporated rtPA was validated with a fibrin agar assay (Fig. S5A) by measuring the degradation area of the gel after 2, 5 and 24 h at 37 °C. This semi quantitative method demonstrated that the fibrinolytic activity was maintained when rtPA was encapsulated compared to free rtPA (Fig. S5B). For further *in vivo* translation, release profile was performed by incubating rtPA-loaded MBs in PBS 1X at 37° from 5 to 60 min (Fig. 4D). It was demonstrated that more than 62 ± 4 % of release happened in the first 5 min of incubation and after 60 min of incubation up to 82 ± 1 % of rtPA was released in PBS 1X.

The targeting property of Fuco MBs were evaluated in fluidic conditions mimicking *in vivo* blood circulation (Fig. 4E–G). Platelet aggregates formation on collagen coating is highly dependent to flow rate (60 µl/min) [35] and was monitored with fluorescent microscopy to avoid channel cloaking. Fuco MBs targeting was measured with Fiji image analysis after rinsing the channel with saline solution and normalized to the platelet aggregate size. Previous work validated the specificity of fucoidan for P-selectins over E and L-selectins [18], here the focus was on expressed P-selectins by activated human platelets. The targeting (Fig. 4G) was highly significant (P Value < 0.0001) comparing CMDex MBs (Fig. 4E) to Fuco MBs (Fig. 4F). Also, the drug-loaded MBs were still able to target activated platelets with a significant difference to control CMDex MBs (P Value < 0.0001). This targeting assay validated that *ex vivo* platelet targeting was highly efficient and that rtPA incorporation did not prohibit MBs targeting despite rtPA interaction with the targeting agent. *In vivo* targeting was also evaluated with fluorescence microscopy on the stroke region (Fig. S6). Briefly, 30 min after stroke induction fluorescent MBs were injected in the tail vain and before (Fig. S6A) and after (Fig. S6B) shot were taken. The fluorescence is nicely located on the MCA bifurcation (highlighted in white) validating the affinity of Fuco MBs for the inflammatory signal of stroke *in vivo*.

3.4. Biocompatibility of MBs

Before *in vivo* injection, cytotoxicity towards Red Blood Cells (RBC), endothelial cells (HUVEC) and fibroblast (3T3) were assessed (Fig. 5). Lactate Dehydrogenase (LDH) is a cytoplasmic enzyme, thus its presence in the culture medium is a marker of cell membrane rupture. This mortality assay was performed on two cell types likely to encounters MBs *in vivo*. Mortality tests on endothelial cells were on average of 4.73 (±2.07) % all conditions reunited (Fig. 5A) while fibroblasts showed a mortality of 7.9 (±3.5) % independently of the condition (Fig. 5B). Overall, no mortality was measured (above 30 % threshold), neither for HUVECs and 3T3 nor 2 h, 4 h or 6 h times points and likewise for increasing MBs concentrations. The second cytocompatibility evaluation

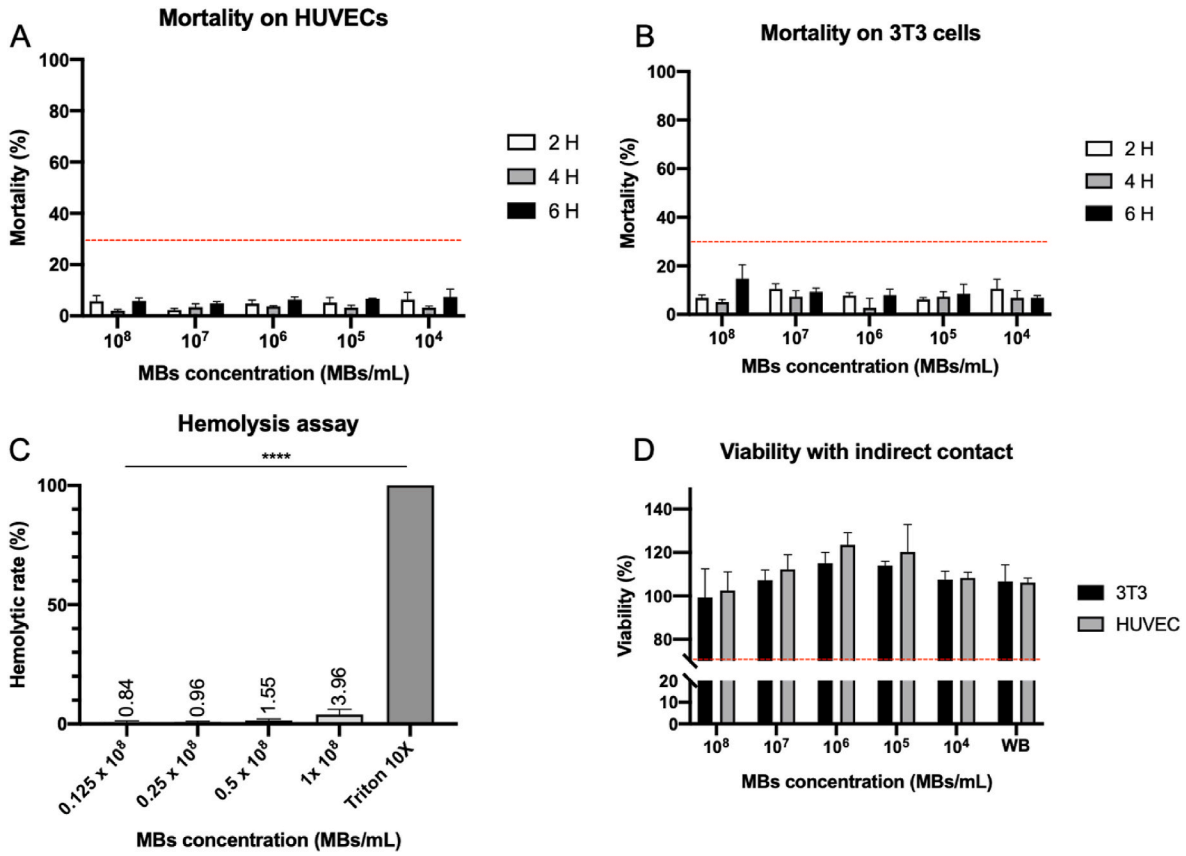


Fig. 5. Biocompatibility study of Fuco MBs on different cell types. A-B) LDH quantification assay on endothelial cells (A) and fibroblasts (B) for increasing concentration of MBs and different time points. LDH is a cytoplasmic enzyme only present in the culture medium if cells undergo apoptosis. Here, none of the concentrations or time of contact induced a mortality above the red dotted line of 30 % indicating the biocompatibility of Fuco MBs. C) Hemolysis assay of Fuco MBs on human Red Blood Cells. The time of contact here was 1 h and showed less that 4 % of hemolysis at the highest MBs concentration (10^8 MB/ml) compared to Triton 10X. D) MTT assay with indirect contact of Fuco MBs on endothelial cells and fibroblasts for 6 h. The MBs suspension was added on top of a cell culture insert with 1 μm mesh to avoid the asphyxia of cells due to MBs debris sedimentation after long contact time in culture medium. The same Fuco MBs concentration was used as the mortality assay and 0.02 % Tween Working Buffer (WB) was also put to the test. Again, no condition induced a viability below 70 % (red dotted line). (For interpretation of the references to color in this figure legend, the reader is referred to the Web version of this article.)

was performed on RBC by the measurement of hemoglobin release in the supernatant also marker of cell lysis (Fig. 5C). Normalized to Triton 10X lysis, MBs incubation with RBC for 1 h did not induce cell lysis even at 10^8 MB/ml (<4 %). Lastly, viability assay was performed for 6 h with MTT assay. To prevent from cell asphyxia because of MBs debris sedimentation (caused by the assay temperature and time conditions), the MBs suspension was added on top of a 1 μm cell culture insert. The MTT assay evaluates the cell metabolic activity by the reduction of MTT to formazan with mitochondrial reductases. After 6 h of incubation, none of the conditions showed a diminution in the cell's metabolic activity for HUVECs or 3T3 (Fig. 5D) with a mean survival rate above 100 % compared to MBs control cells cultured without MBs. The 0.02 % Tween Working Buffer (WB) did not influence the cell viability either. Images of formazan crystals were also taken with optical microscopy comparing the highest concentration (10^8 MB/ml) to cells that were not in contact with MBs (Fig. S7). Those pictures highlighted the healthy phenotypes of cells and the correct metabolization of MTT. Therefore, no cytotoxicity was demonstrated on three different cell types in contact high concentrations of MBs, using three different assays.

3.5. *In vivo* stroke model

The *in vivo* stroke model was performed as presented in Fig. 6A. After a local craniotomy over the MCA, thrombin injection generated fibrin rich clot formation. Speckle imaging was performed before and after each step to validate the reduction of blood flow in the region of the stroke (Fig. 6B). Speckle imaging enabled the visualization of the perfusion on each hemisphere and was quantified with image analysis as presented in Fig. 6C. Low signal in blue was observed in all groups (Fig. 6B), with a reduction of perfusion close to 40 % without significative difference in between groups, 30 min after the thrombin injection. Then, the treatment was carried out with intravenous tail vein injection. The final checkup was obtained at 24 h with MRI image analysis of the ischemic region. The MRI images displayed on Fig. 6D were taken 24 h after the treatment, and the white region pointed by an arrow represents the ischemic region on successive planes of mouse brains for the three groups. In pre-clinical application, the treatment for an efficient thrombolysis using rtPA injection in mice models is usually performed with 10 mg/kg ratio while we set the threshold here to 1 mg/kg of rtPA for both free rtPA and rtPA-loaded MBs [31]. In consequence, there is no significant difference in the ischemic lesion volume between the saline group (N = 19, 10.99 ± 4.83 mm^3), the free rtPA group (N = 20, 8.26 ± 5.75 mm^3) and neither control Fuco MBs (N = 18, 13.70 ± 5.80 mm^3). Nevertheless, the rtPA-loaded Fuco MBs treatment significantly reduced the infarcted area by more than 50 % (N = 18, 3.83 ± 3.55 mm^3) compared to free rtPA treatment (Fig. 6E). In addition, we compared the infarct size prevalence in each group (Fig. 6F) by defining 4 groups: no lesion (0 mm^3), small lesion (<5 mm^3), medium lesions (from 5 to 10 mm^3) and large lesions (>10 mm^3). Large lesions were only observed once in rtPA-loaded Fuco MBs treatment with a majority of small lesion (N = 9). On the contrary, saline group and Fuco MBs group presented a majority of large lesion (N = 11 and N = 12 respectively). Free rtPA

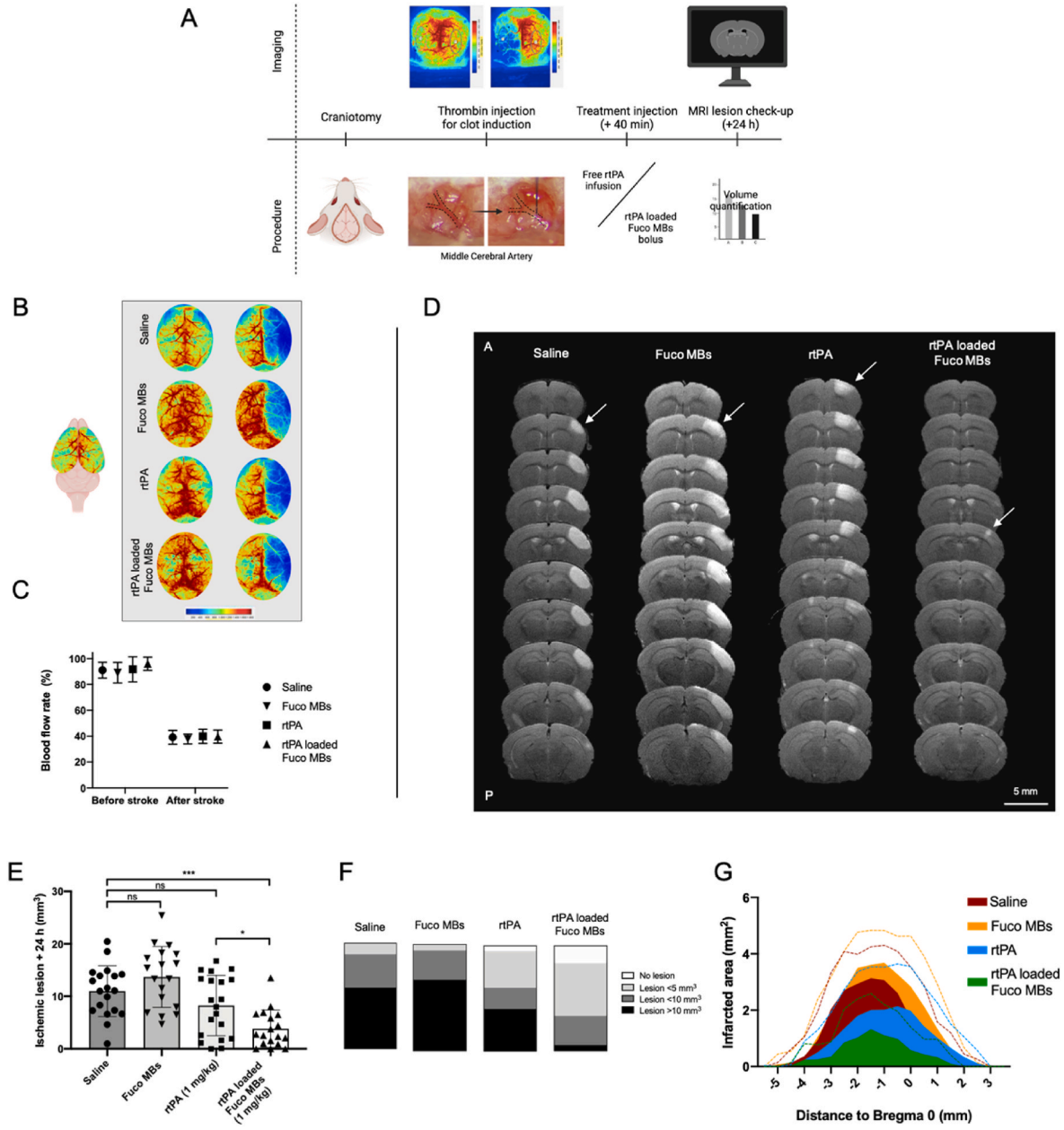


Fig. 6. In vivo stroke model study on mice comparing rtPA-loaded Fuco MBs treatment to systemic injection of rtPA. A) Graphical abstract of the experimental setup. Briefly, mice were anesthetized and placed onto a stereotaxic platform. A craniotomy allowed the direct access to the Middle Cerebral Artery (MCA) to inject thrombin. After 40 min, either saline infusion, Fuco MBs bolus, free rtPA infusion or rtPA-loaded Fuco MBs bolus were used as stroke treatment. The MRI images of the mouse brain were taken 24 h after the treatement to evaluate the infarcted area volume. B) Validation of the partial occlusion after stroke induction with laser Speckle acquisition for each group. C) Flow rates quantification from laser Speckle imaging comparing the right hemisphere to the contralateral one for each group. D) MRI images of mouse brains +24 h after the three treatment conditions from antero (A) to posterior position (P). The white arrows point out the infarcted area and the scale bar is 5 mm. Those images are representative of each group lesions. E) Lesions volumes quantification from MRI images. Volumes were measured with the Fiji software by compiling areas of all brain slices for saline, drug free Fuco MBs, free rtPA and rtPA-loaded Fuco MBs treatment. F) Lesion distribution according to their severity from: no lesion, small lesion (<5 mm^3), medium lesion (>5; <10 mm^3) to large lesion (>10 mm^3) depending on the treatment. G) Ischemic lesion distribution means in the brain for the different groups (dotted lines represent the standard deviation). Bregma plan is considered at the plan 0 for all conditions.

group presented a reduced amount of large lesion (N = 8) but still had a majority of medium lesion and above. Another representation of ischemic lesions is presented on Fig. 6G displaying the mean lesion size distribution in the different planes of the brain using the Bregma as the zero position. The doted lines represent the standard deviations associated to each treatment. The extent of distribution remains similar to all the groups (from −4 to +2 mm) but the size of the lesions on individual segment is largely reduced with rtPA-loaded Fuco MBs treatment in green.

Since MBs treatment involves micron size bubbles, we also monitored the Blood Brain Barrier (BBB) permeability (Figs. S8A–B). By injecting Gadoteric Acid (GA) intravenously, the leakage of BBB permeability can be observed with T1 MRI acquisition as white spots around the infarcted areas (Fig. S8A). Nevertheless, this test showed no evidence of BBB impairment comparing saline, Fuco MBs, free rtPA and rtPA-loaded Fuco MBs groups (Fig. S8B). Some spots were identified with saline treatment but isolated events could also be the consequence of the surgery itself. Overall, the targeted treatment with rtPA-loaded

Fuco MBs was significantly more efficient than gold standard treatment and neither collateral hemorrhage or BBB leakage was observed.

3.6. *Ex vivo fluorescence biodistribution on sectioned or complete organs*

The biodistribution of rtPA-loaded Fuco MBs has been studied with organ fluorescence macroscopy (Fig. 7A-B-C). *Ex vivo* organ macroscopy was performed 24 h after treatment (Fig. 7A and B) on brain, lungs, liver, kidney, spleen, bladder and intestine compared to saline groups. As MBs were labelled with Rhodamine B, the fluorescence residues of MBs can be observed with an excitation wavelength of 550 nm (Fig. 7A). Normalized to the size of the organ, fluorescence count (Fig. 7B) gives a qualitative evaluation of MBs biodistribution in the body. The majority of fluorescence was observed in the brain for each Fuco MBs ($1.4 \pm 0.2 * 10^6$ count/cm^2/s) and rtPA-loaded Fuco MBs ($1.1 \pm 0.4 * 10^6$ count/cm^2/s), validating the targeting property *in vivo* but also the targeting property conservation despite rtPA loading. Then lungs and liver displayed fluorescence fulfilling their function of blood detoxification. No fluorescence was observed neither in the kidney, spleen, bladder or intestine. We also followed the fluorescence of Fuco MBs at 2 h and 8 h post treatment in the organs (Fig. 7C) without significant difference but interestingly the specific fluorescence in the stroke area was still observed after 24 h. It enhanced the validation of Fuco MBs targeting capacity *in vivo* but also brings new insights for the P-selectins expression on activated endothelium, after clot resolution and thus interesting perspectives for molecular imaging. In regards to those results, the histology study was performed on liver explanted 2 h after Fuco MBs injection, to assess their uptake by resident macrophages. In Fig. 7D, cell nuclei were colored with DAPI and macrophages were labelled in green with an antibody against CD68 biomarker. Rhodamine B Fuco MBs residues were observed to be colocalized with macrophages biomarker CD68 indicating a potential internalization by the scavenger cells.

4. Discussion

Thrombotic diseases are life threatening conditions. Despite the

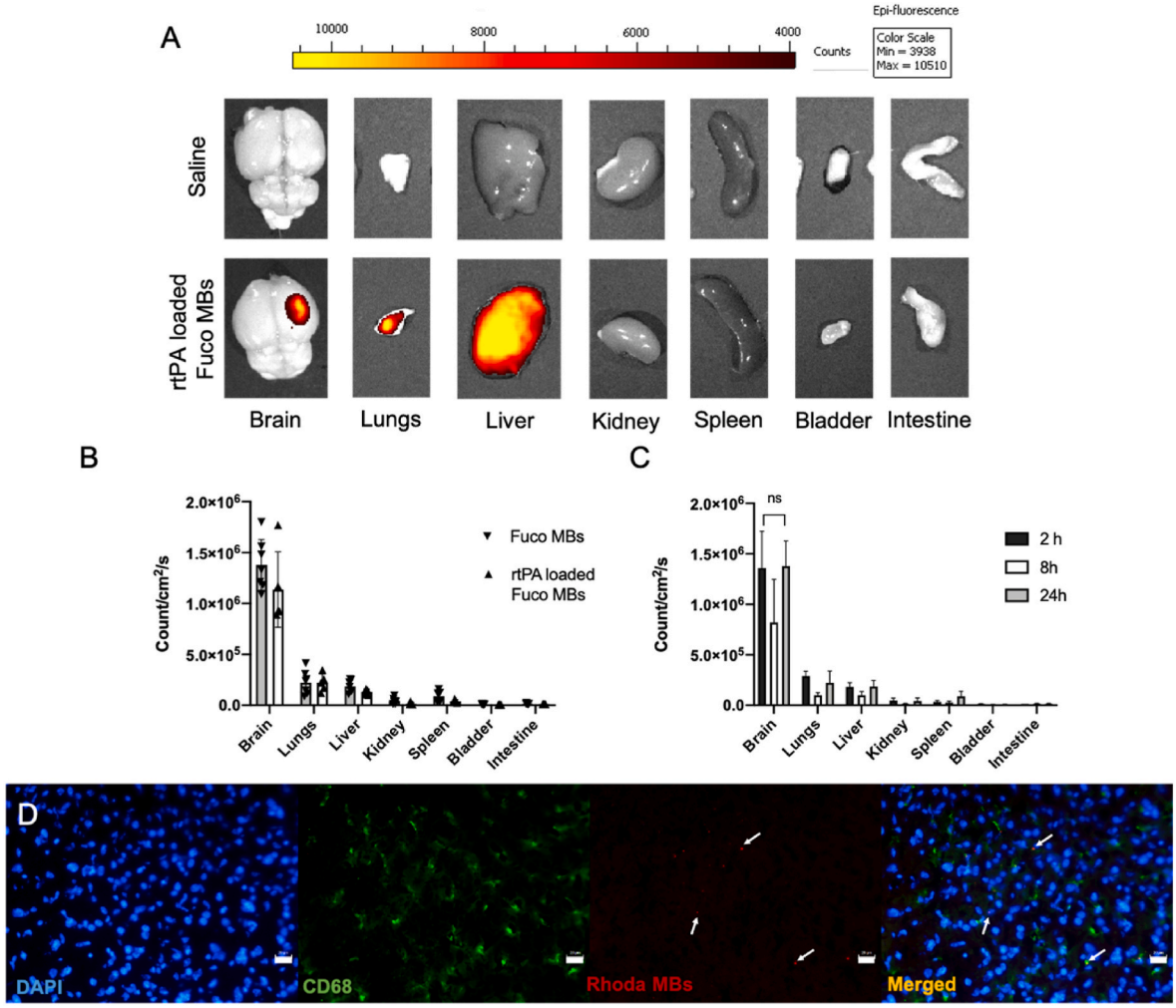


Fig. 7. Biodistribution of fluorescent MBs and MBs residues in mice. A-B-C) Ex vivo fluorescence macroscopy quantification of MBs outcome in brain, lungs, liver, kidney, spleen, bladder and intestine. A) Fluorescence macroscopy images of various organs 24 h after stroke treatment (saline: top row, rtPA-loaded Fuco MBs: bottom row). Organs were retrieved 24 h after treatment and imaged without tissue fixation. The epi fluorescence scale was set between 3938 and 10510 counts. Specific targeting of MBs to the stroke area was still visible after 24 h and liver and lungs were fulfilling their blood cleaning property as the rest of the fluorescence was observed in those two organs. B–C) Quantification of the fluorescence in each organ in counts/cm^2/s. B) Comparison of Fuco MBs (N = 7) and rtPA-loaded Fuco MBs (N = 5) residues of fluorescence 24 h after stroke. C) Comparison of Fuco MBs fluorescence residues at 2 h (N = 3), 8 h (N = 3) and 24 h (N = 7) after stroke. D) Histology coloration of liver tissue 2 h after injection of Rhodamine B Fuco MBs in mice. From left to right, DAPI coloration of cell nuclei, CD68 immunostaining of macrophages, Rhodamine B Fuco MBs, Merged image. The white arrows point out the MBs fluorescent residues in red and scale bar is 20 μm. MBs residues were found in liver tissue after 2 h and some of them seemed to be internalized in liver macrophages. (For interpretation of the references to color in this figure legend, the reader is referred to the Web version of this article.)

availability of thrombolytic drugs, there are still a number of unmet medical needs for more effective and safer treatments. We presented in this study a drug-loaded targeting polymer MBs for the improvement of stroke treatment. The development of a new synthesis protocol was driven by an ambition to simplify polymer MBs production and also avoid toxic solvent and time-consuming protocols of phospholipid MBs synthesis. The stability of polymer MBs was validated over 4 weeks in suspension (Fig. S1C) and their biodistribution aligns with the liver primary function to detoxify the blood. In addition, the shell composition did not affect the shelf stability (Fig. S1D) allowing data compilation. Cyanoacrylate are strong adhesives commonly used in surgical procedures for wound closure but are also injected in humans to seal blood vessels [36]. Fucoidans on the other hand are derived from brown algae [16] and were injected in humans with NANO-ATHERO project (NCT03422055) [16,30]. Thereby, this easy to make and scalable acoustic cavitation protocol draws new perspectives for the development of biocompatible acoustic microbubbles. The shell composition was validated by Fourier Transform Infrared (FTIR) as presented on Fig. S9, displaying the characteristic pics of ester bound around 1750 and 2250 cm^{-1} for cyanoacrylate. However, the polysaccharide incorporation with either fucoidan or carboxymethyl dextran was challenging to identify given the small amount of it. This quantification was better performed with sulfate dosage (Figs. S2A–B) and fucoidan targeting properties (Fig. 4E-F-G). In addition, the use of whole Human Blood rather than P-selectin coating for the evaluation of targeting properties is a much more accurate model for *in vivo* translation and was indeed validated with fluorescence microscopy on the stroke area (Fig. S6). The micron size of MBs helped for imaging characterization with ESEM (Fig. 2D), confocal (Fig. S3A) and FIB (Fig. 2E; Fig. S3D) imaging. In that manner, we were able to estimate the shell thickness by two methods (FIB and confocal fluorescence) to 518 ± 116 nm (Fig. S3B-C-D). The wide standard deviation is also the consequence of the FIB sample preparation that affected the MBs integrity limiting the sample number (N = 4). After validation of MBs physicochemical properties, rtPA incorporation was obtained with a simple adsorption protocol using no additive chemical and no critical temperature. We validated the rtPA activity through two enzymatic assays, the fibrinolytic activity on agar gel (Figs. S5A–B) and the amidolytic activity on fluorescent substrate (Fig. 4 A-B). Regular protein quantification with copper reduction (BCA assay) was not possible due to the reactivity of MBs without any incorporated drug. The incorporation was also validated by the shift in the surface charge of rtPA-loaded Fuco MBs compared to Fuco MBs (Fig. S1A). Lastly, the activity of the incorporated protein was stable over 4 days (Fig. 4C) with no shift in the mean size of the MBs (Fig. S1D). Therefore, to ensure the effectiveness and the quality of the treatment, rtPA-loaded MBs were not use after 4 days for *in vivo* injection.

MBs are of main interest because of their acoustic property in US imaging also validated here with a homemade US setup. Establishing echogenic evaluation is not standardized yet and it mainly relies on contrast enhancement validation. Moreover, the system is highly setup dependent (distance, probe, medium) and required probe calibration. The test was computer driven with different voltage but, in order to translate to Mechanical Index, a hydrophone calibration was performed to measure the negative pressure of the signal. Nevertheless, it gives good insights for *in vivo* translation. We wanted to determine the threshold of MBs stability for US imaging but also the disruptive ratio of MBs for later sonothrombolysis experimentation. Indeed, many teams [20–22] have been exploring the impact of bursting MBs with US for the mechanical impairment of blood clots. No standards have been determined yet, except for bio-damaging boundaries of high Mechanical Index (MI, 1.9) [37]. A better understanding of MBs response to US signal *in vivo* is a key element to perform safe and monitored sonothrombolysis. In any case, US signal was validated *in vivo (Fig. S4) giving those newly synthetized MBs the property of US contrast enhancer agents.*

Before in vivo injection, we validated the in vitro biocompatibility of cyanoacrylate degradation products [38] *with mortality (*Fig. 5A and B) and viability (Fig. 5D) assays on endothelial cells and fibroblasts, and hemolytic tests (Fig. 5C). The safety of MBs was demonstrated for each cell type independently from the MBs concentration (up to 1×10^8 MB/ml) or the duration of the experiment (from 2 h to 6 h). The assays durations were selected according to the fact that MBs are not designed to be circulating after a few hours in the bloodstream. Overall, in accordance with the International Standard (ISO 10993–5) the 70 % viability and 30 % for mortality threshold were not exceeded. Thus, the safety of polymer MBs allowed the translation to the animal stroke model.

Thrombin injection triggers the formation of fibrin rich clot compared to ferric chloride model [39] that induces platelet rich thrombi. In consequence, thrombin-induced clots are more likely to respond to rtPA treatment. In this study rtPA was injected to 1/10th of the treatment usually used in mice [40]. This choice was driven by the ultimate goal to limit rtPA dose related side effects. This constrain did not prevent from an efficient clot resolution thanks to the specific targeting of rtPA-loaded Fuco MBs. Indeed, 1 mg/kg injection of rtPA loaded onto targeting MBs, reduced by more than 50 % the volume of the ischemic lesion for 18 animals (Fig. 6E-F-G). The prevalence of small (<5 mm^3) and no lesion (0 mm^3) was considerably improved compared to free rtPA treatment (Fig. 6F) as well as the small extend of lesion in the different plans of the brain (Fig. 6G). While previous study showed the efficacy of rtPA targeted delivery at a reduced dose in a femoral artery clamping model [41], we have demonstrated that our newly designed system achieved competitive results in an minimally invasive arterial model, that physiologically reproduce an ischemic stroke event. The drug encapsulation was efficient protecting the protein and the specific clot targeting lead to the treatment improvement, as we demonstrated that Fuco MBs alone did not have any therapeutic properties. This result is even more promising as free rtPA treatment at the same concentration was not significantly more efficient than treatment with saline. In consequence, we can hypothesize about the synergic action of rtPA loaded onto Fucoidan MBs for a successful thrombolysis. The specific targeting of fucoidan may also be enhanced with the known affinity of rtPA for fibrin [42] and consequently improve the precise drug delivery. The targeting strategy at a molecular scale overcome the limitations that can be observed with magnetic targeting [43] considering the complex 3D vasculature of the brain. Finally, this efficient targeted drug delivery treatment gets in the range of human recommended dose of 0.9 mg/kg (according to the National Institute of Neurological disorders and Stroke), suggesting that lower dosage of encapsulated rtPA could have beneficial outcomes and reduce dose related side effects in humans too.

No animal was harmed with the injection of rtPA-loaded MBs and we aimed at reducing the number of animals. Hence, control conditions like rtPA-loaded CMDex MBs and free rtPA at 10 mg/kg for stroke treatment were not explored. Firstly, rtPA-loaded CMDex MBs treatment evaluation could highlight the importance of targeting for the clot resolution. However, efficient rtPA loading on CMDex MBs was not possible as presented in Fig. 4B. Secondly, free rtPA treatment validation of 10 mg/kg efficient thrombolysis on thrombin clot mouse model was largely studied [31], suggesting the real advantage of our dose reduced treatment.

We also studied the outcome and clearance process of MBs after stroke treatment. The circulation time of polymer MBs in the body depends on a number of factors, including size of the MBs, type of polymer, and the density of the gas core [44]. In addition, the circulation time can be influence by the presence of blood proteins that can bind to the surface of MBs and alter their movement through the body. Overall, circulation time is widely dependent of the MBs composition but is usually ranging from minutes to tens of minutes, long enough for conventional diagnosis or therapeutic methods. The biodistribution study was performed at 2 h after injection in the liver tissue with immunolabelling of resident macrophages to evaluate the early blood detoxification in the liver (Fig. 7D). In addition, the biodistribution on *ex vivo* organs revealed the final whereabout of MBs in the body with the

expected contrast in liver and lungs (Fig. 7A) without significant difference at 2 h, 8 h or 24 h after the treatment. The residual fluorescence of rtPA-loaded Fuco MBs was also observed in the stroke region after 24 h (Fig. 7A) validating the specific targeting of fucoidan on P-selectin but also pointed out the long-term expression of the biomarker after the treatment by activated endothelial cells. This suggests an interesting insight for further molecular imaging of thrombotic diseases resolution. Especially since the residual fluorescence is not due to BBB permeability as demonstrated with Gadoteric Acid (GA) injection (Figs. S8A–B). P-selectin is a known endothelial-related inflammation biomarker [45] and an increase in its concentration within 72 h could predict the incidence of post stroke infection [46]. Nevertheless, some controversies still remain in the significance of P-selectin expression in stroke versus non stroke patients [47] and molecular imaging could be an alternative way to set the debate. In that manner the study of thrombo-inflammation with Fuco MBs may be investigated over different time points with either fluorescent microscopy or US imaging.

5. Conclusion

In the present study, we developed ultrasound responsive microbubbles for the targeted treatment of stroke. Acoustic cavitation synthesis was optimized for the production of targeting polymer MBs, firstly described here in the literature. This innovative protocol reduced the production time by three compared to gold standard hydrodynamic cavitation. The physicochemical properties and biocompatibility assessments were intensively evaluated to conclude on their contrast enhancement with US signal, effective targeting of P-selectins, and fibrinolytic potential. The *in vivo* evaluation on mice stroke model demonstrated the efficiency of rtPA-loaded Fuco MBs over clinical systemic injection of the drug. Indeed, we observed a volume reduction of the brain injury by more than 50 % with a 1/10th lower dose of rtPA than recommended in mice. No BBB permeability or hemorrhagic complication was observed and expected biodistribution was found in detoxification organs including lungs and liver, indicating a high potentiality for a safe and scalable treatment. Our finding now rises new possibilities for the application of drug-loaded targeting MBs in ischemic stroke treatment.

The main perspectives of this work now rely on the US responsive property of MBs. The ischemic memory observed after 24 h on the stroke region with residual fluorescence on activated endothelium, allowed us to think about the potential of Fuco MBs for molecular imaging [48]. We demonstrated the contrast enhancement capacity of MBs for US signal *in vivo* and targeted imaging with US is an active research field. Indeed, US technology is a non-invasive, safe for pregnant patients and less expensive method compared to other imaging modalities. With the recent advances in stroke US imaging in rats [28], P-selectin targeted MBs present new possibilities for the early diagnosis and clot resolution follow-up of stroke events. Also, chemical thrombolysis alone only achieve good outcomes for 40 % of patients [5] and clot migration can cause a variety of serious problems including distal vessels obstruction. The need for non-invasive clot damaging treatment led the scientific community to study microbubble-assisted US clot bursting: the sonothrombolysis. Especially since tissue plasminogen treatment is less efficient on distal occlusions [11], sonothrombolysis could mechanically disrupt the clot [8] in addition to fibrinolysis. Despite the fact that it is an area of active research [49], these therapies are not yet widely available or fully understood. Few boundaries are nevertheless already established, including Mechanical Index threshold of 1.9 and the need of biocompatible MBs. Our technology is then a great candidate for the development of targeted sonothrombolysis for stroke resolution.

Credit author statement

Louise FOURNIER: Conceptualization, Investigation, Experimental work, Data analysis, Writing, Visualization.; Myriam ABIOUI-MOURGUES: Investigation (Animal model main investigator), Data validation.; Georges CHABOUH: Investigation, Data validation.; Rachida AID: Methodology.; Thibault DE LA TAILLE: Investigation.; Olivier COUTURE: Conceptualization, Methodology.; Denis VIVIEN: Review and Editing.; Cyrille ORSET: Conceptualization, Methodology.; Cédric CHAUVIERRE: Conceptualization, Review and Editing, Supervision, Project administration, Funding acquisition. All the authors approved the final revised version of the manuscript.

Declaration of competing interest

The authors declare the following financial interests/personal relationships which may be considered as potential competing interests: Cedric CHAUVIERRE reports financial support was provided by French National Research Agency. Olivier COUTURE reports a relationship with Resolve Stroke company that includes: board membership. Cedric CHAUVIERRE has patent pending to INSERM Transfert. Louise FOURNIER has patent pending to INSERM Transfert.

Data availability

Data will be made available on request.

Acknowledgments

Authors thank INSERM, Université Paris Cité, Université Sorbonne Paris Nord, the ANR “FightClot” ANR-20-CE18-0005-01, and ANR “FucoChem” ANR-13-LAB1-0005-01 for the financial support. We express our gratitude to Algues & Mer for the supplying of fucoidan. The authors would like to acknowledge Christine CHOQUEUX for the ESEM images performed at Université de Technologie de Compiègne (France). We kindly thank Stephane TACHON from the Nanoimagerie department of Institut Pasteur (France) for the FIB assisted SEM images. We also thank Véronique OLLIVIER and Stéphane LOYAU for their help and expertise on the *in vitro* targeting experiment. The confocal images were also performed with the help of Camille LE GUILCHER and Chloé DUJARDIN, we also thank her and Graciela PAVON-DJAVID for their support in cell culture experiments. The illustrations were designed with BioRender online software (biorender.com).

Appendix A. Supplementary data

Supplementary data to this article can be found online at https://doi.org/10.1016/j.biomaterials.2023.122385.

References

[1] G.A. Roth, et al., GBD-NHLBI-JACC Global Burden of Cardiovascular Diseases Writing Group. Global burden of cardiovascular diseases and risk factors, 1990-2019: update from the GBD 2019 study, J. Am. Coll. Cardiol. 76 (25) (2020) 2982–3021.
[2] C.W. Tsao, et al., Heart disease and stroke statistics-2022 update: a report from the american heart association, Circulation 145 (8) (2022).
[3] G. Alkarithi, C. Duval, Y. Shi, F.L. Macrae, R.A.S. Ariëns, Thrombus structural composition in cardiovascular disease, Arterioscler. Thromb. Vasc. Biol. 41 (9) (2021) 2370–2383, https://doi.org/10.1161/ATVBAHA.120.315754.
[4] P. Jolugbo, R.A.S. Ariëns, Thrombus composition and efficacy of thrombolysis and thrombectomy in acute ischemic stroke, Stroke (2021) 1131–1142, https://doi.org/10.1161/STROKEAHA.120.032810, no. March.
[5] S. Prabhakaran, I. Ruff, R.A. Bernstein, Acute stroke intervention: a systematic review, JAMA, J. Am. Med. Assoc. 313 (14) (2015) 1451–1462, https://doi.org/10.1001/jama.2015.3058.
[6] A. Zenych, L. Fournier, C. Chauvierre, Nanomedicine progress in thrombolytic therapy, Biomaterials 258 (2020), https://doi.org/10.1016/j.biomaterials.2020.120297. January.
[7] D. Vivien, Can the benefits of rtPA treatment for stroke be improved? Rev. Neurol. 173 (9) (2017) 566–571, https://doi.org/10.1016/j.neurol.2017.07.003.
[8] A. Chang, E. Beheshtian, E.J. Llinas, O.R. Idowu, E.B. Marsh, Intravenous tissue plasminogen activator in combination with mechanical thrombectomy: clot migration, intracranial bleeding, and the impact of ‘drip and ship’ on effectiveness and outcomes, Front. Neurol. 11 (2020) 1–10, https://doi.org/10.3389/fneur.2020.585929. December.

[9] C. Liu, et al., Hemorrhagic transformation after tissue plasminogen activator treatment in acute ischemic stroke, Cell. Mol. Neurobiol. 42 (3) (2022) 621–646, https://doi.org/10.1007/s10571-020-00985-1.

[10] G.W.J. Harston, B.A. Sutherland, J. Kennedy, A.M. Buchan, The contribution of L-arginine to the neurotoxicity of recombinant tissue plasminogen activator following cerebral ischemia: a review of rtPA neurotoxicity, J. Cerebr. Blood Flow Metabol. 30 (11) (2010) 1804–1816, https://doi.org/10.1038/jcbfm.2010.149.

[11] M. Gomis, A. Dăvalos, Recanalization and reperfusion therapies of acute ischemic stroke: what have we learned, what are the major research questions, and where are we headed? Front. Neurol. 5 (2014) 1–12, https://doi.org/10.3389/fneur.2014.00226. November.

[12] A. Rix, A. Curaj, E. Liehn, F. Kiessling, Ultrasound microbubbles for diagnosis and treatment of cardiovascular diseases, Semin. Thromb. Hemost. (2019), https://doi.org/10.1055/s-0039-1688492.

[13] E. Falk, Pathogenesis of atherosclerosis, J. Am. Coll. Cardiol. 47 (8 SUPPL) (2006), https://doi.org/10.1016/j.jacc.2005.09.068, 0–5.

[14] L.A. Perkins, C.J. Anderson, E.M. Novelli, Targeting P-selectin adhesion molecule in molecular imaging: P-selectin expression as a valuable imaging biomarker of inflammation in cardiovascular disease, J. Nucl. Med. 60 (12) (2019) 1691–1697, https://doi.org/10.2967/jnumed.118.225169.

[15] F. Rouzet, et al., Radiolabeled fucoidan as a P-selectin targeting agent for in vivo imaging of platelet-rich thrombus and endothelial activation, J. Nucl. Med. 52 (9) (2011) 1433–1440, https://doi.org/10.2967/jnumed.110.085852.

[16] C. Chauvierre, et al., Pharmaceutical development and safety evaluation of a GMP-grade fucoidan for molecular diagnosis of cardiovascular diseases, Mar. Drugs 17 (12) (2019), https://doi.org/10.3390/md17120699.

[17] L. Bachelet, et al., Affinity of low molecular weight fucoidan for P-selectin triggers its binding to activated human platelets, Biochim. Biophys. Acta Gen. Subj. 1790 (2) (2009) 141–146, https://doi.org/10.1016/j.bbagen.2008.10.008.

[18] A. Zenych, et al., Fucoidan-functionalized polysaccharide submicroparticles loaded with alteplase for efficient targeted thrombolytic therapy, Biomaterials 277 (August) (2021), https://doi.org/10.1016/j.biomaterials.2021.121102.

[19] B. Li, et al., Functionalized polymer microbubbles as new molecular ultrasound contrast agent to target P-selectin in thrombus, Biomaterials 194 (2019) 139–150, https://doi.org/10.1016/j.biomaterials.2018.12.023, 2019.

[20] K.H. Zheng, et al., 99Mtc-Fucoidan as diagnostic agent for P-selectin imaging: first-in-human evaluation (phase I), Atherosclerosis 287 (2019) e143, https://doi.org/10.1016/j.atherosclerosis.2019.06.425, 2019.

[21] G. Chabouh, B. Dollet, C. Quilliet, G. Coupier, Spherical oscillations of encapsulated microbubbles: effect of shell compressibility and anisotropy, J. Acoust. Soc. Am. 149 (2) (2021) 1240–1257, https://doi.org/10.1121/10.0003500.

[22] L. Auboire, et al., Microbubbles combined with ultrasound therapy in ischemic stroke: a systematic review of in-vivo preclinical studies, PLoS One 13 (2) (2018) 1–19, https://doi.org/10.1371/journal.pone.0191788.

[23] R. Ghebouli, et al., Amino-fucoidan as a vector for rtPA-induced fibrinolysis in experimental thrombotic events, Thromb. Haemostasis 118 (1) (2018) 42–53, https://doi.org/10.1160/TH17-02-0132.

[24] L. Fournier, T.D. La Taille, Microbubbles for human diagnosis and therapy, Biomaterials 294 (2023), https://doi.org/10.1016/j.biomaterials.2023.122025. January.

[25] A.L. Klibanov, Ultrasound contrast: gas microbubbles in the vasculature, Invest. Radiol. 56 (1) (2021) 50–61, https://doi.org/10.1097/RLI.0000000000000733.

[26] A. Upadhyay, S.V. Dalvi, Microbubble formulations: synthesis, stability, modeling and biomedical applications, Ultrasound Med. Biol. 45 (2) (2019) 301–343, https://doi.org/10.1016/j.ultrasmedbio.2018.09.022.

[27] J.M. Lee, Z.U. Shin, G.T. Mavlonov, I.Y. Abdurakhmonov, T.H. Yi, Solid-phase colorimetric method for the quantification of fucoidan, Appl. Biochem. Biotechnol. 168 (5) (2012) 1019–1024, https://doi.org/10.1007/s12010-012-9837-y.

[28] A. Chavignon, V. Hingot, C. Orset, D. Vivien, O. Couture, 3D transcranial ultrasound localization microscopy for discrimination between ischemic and hemorrhagic stroke in early phase, Sci. Rep. 12 (1) (Aug. 2022) 1–11, https://doi.org/10.1038/S41598-022-18025-X.

[29] B. Li, et al., Development of polymer microcapsules functionalized with fucoidan to target P-selectin overexpressed in cardiovascular diseases, Adv. Healthcare Mater. 6 (4) (2017), https://doi.org/10.1002/adhm.201601200.

[30] A.J. Koning, P.Y. Lum, J.M. Williams, R. Wright, DiOC6 staining reveals organelle structure and dynamics in living yeast cells, Cell Motil Cytoskeleton 25 (2) (1993) 111–128, https://doi.org/10.1002/cm.970250202.

[31] C. Orset, et al., Mouse model of in situ thromboembolic stroke and reperfusion, Stroke 38 (10) (2007) 2771–2778, https://doi.org/10.1161/STROKEAHA.107.487520.

[32] O. Couture, S. Bannouf, G. Montaldo, J.F. Aubry, M. Fink, M. Tanter, Ultrafast imaging of ultrasound contrast agents, Ultrasound Med. Biol. 35 (11) (2009) 1908–1916, https://doi.org/10.1016/j.ultrasmedbio.2009.05.020.

[33] O. Couture, M. Fink, M. Tanter, Ultrasound contrast plane wave imaging, IEEE Trans. Ultrason. Ferroelectrics Freq. Control 59 (12) (2012) 2676–2683, https://doi.org/10.1109/TUFFC.2012.2508.

[34] K. Renault, J.W. Fredy, P.Y. Renard, C. Sabot, Covalent modification of biomolecules through maleimide-based labeling strategies, Bioconjugate Chem. 29 (8) (2018) 2497–2513, https://doi.org/10.1021/acs.bioconjchem.8b00252.

[35] L.D.C. Casa, D.N. Ku, Thrombus Formation at high shear rates, Annu. Rev. Biomed. Eng. 19 (2017) 415–433, https://doi.org/10.1146/annurev-bioeng-071516-044539.

[36] O. Chevallier, et al., Efficacy, safety and outcomes of transcatheter arterial embolization with N-butyl cyanoacrylate glue for non-variceal gastrointestinal bleeding: a systematic review and meta-analysis, Diagn. Interv. Imaging 102 (7–8) (2021) 479–487, https://doi.org/10.1016/j.diii.2021.03.004.

[37] Y. Deng, M.L. Palmeri, N.C. Rouze, G.E. Trahey, C.M. Haysteas, K.R. Nightingale, Quantifying image quality improvement using elevated acoustic output in B-mode harmonic imaging, Ultrasound Med. Biol. 43 (10) (2017) 2416–2425, https://doi.org/10.1016/j.ultrasmedbio.2017.06.024.QUANTIFYING.

[38] D. García Cerdá, A.M. Ballester, A. Aliena-Valero, A. Carabén-Redaño, J.M. Lloris, Use of cyanoacrylate adhesives in general surgery, Surg. Today 45 (8) (2015) 939–956, https://doi.org/10.1007/s00595-014-1056-4.

[39] X. Lin, et al., Establishment of a modified and standardized ferric chloride-induced rat carotid artery thrombosis model, ACS Omega 7 (10) (2022) 8919–8927, https://doi.org/10.1021/acsomega.1c07316.

[40] C. Orset, et al., Efficacy of Alteplase® in a mouse model of acute ischemic stroke : a Retrospective Pooled Analysis, Stroke 47 (5) (2016) 1312–1318, https://doi.org/10.1161/STROKEAHA.116.012238.Efficacy.

[41] X. Hua, et al., In vivo thrombolysis with targeted microbubbles loading tissue plasminogen activator in a rabbit femoral artery thrombus model, J. Thromb. Thrombolysis 38 (1) (2014) 57–64, https://doi.org/10.1007/s11239-014-1071-8.

[42] A. Zhu, P. Rajendram, E. Tseng, S.B. Coutts, A.Y.X. Yu, Alteplase or tenecteplase for thrombolysis in ischemic stroke: an illustrated review, Res. Pract. Thromb. Haemost. 6 (6) (2022) 1–13, https://doi.org/10.1002/rth2.12795.

[43] S. Wang, et al., Accelerating thrombolysis using a precision and clot-penetrating drug delivery strategy by nanoparticle-shelled microbubbles, Sci. Adv. 6 (31) (2020), https://doi.org/10.1126/sciadv.aaz8204.

[44] E. Stride, et al., Microbubble agents: new directions, Ultrasound Med. Biol. (2020), https://doi.org/10.1016/j.ultrasmedbio.2020.01.027.

[45] D.D. Zhang, et al., Inflammatory biomarkers and cerebral small vessel disease: a community-based cohort study, Stroke Vasc. Neurol. 7 (4) (2022) 302–309, https://doi.org/10.1136/svn-2021-001102.

[46] G. Pusch, et al., Early dynamics of P-selectin and interleukin 6 predicts outcomes in ischemic stroke, J. Stroke Cerebrovasc. Dis. 24 (8) (2015) 1938–1947, https://doi.org/10.1016/j.jstrokecerebrovasdis.2015.05.005.

[47] S. Wiseman, F. Marlborough, F. Doubal, D.J. Webb, J. Wardlaw, Blood markers of coagulation, fibrinolysis, endothelial dysfunction and inflammation in lacunar stroke versus non-lacunar stroke and non-stroke: systematic review and meta-analysis, Cerebrovasc. Dis. 37 (1) (2014) 64–75, https://doi.org/10.1159/000356789.

[48] G. Köse, M. Darguzyte, F. Kiessling, Molecular ultrasound imaging, Nanomaterials 10 (10) (2020) 1–28, https://doi.org/10.3390/nano10101935.

[49] T. Porter, P. Zeng, F. Xie, Advances in ultrasound therapeutics, Curr. Cardiol. Rep. 23 (10) (2021) 4–11, https://doi.org/10.1007/s11886-021-01563-7.

ANNEX 3

Neuroscience 550 (2024) 102–113

Contents lists available at ScienceDirect

Neuroscience

journal homepage: www.elsevier.com/locate/nsc

REVIEW: "ISCHEMIC STROKE: From Fibrinolysis to Functional Recovery" Nanomedicine: emerging approaches to treat ischemic stroke

Pierre Sarfati [a,†], Thibault De La Taille [a,†], Corinne Portioli [b,†], Raffaele Spanò [b,†], Yoann Lalatonne [a,c], Paolo Decuzzi [b,‡], Cédric Chauvierre [a,‡,*]

[a] Université Paris Cité, Université Sorbonne Paris Nord, UMR-S U1148 INSERM, Laboratory for Vascular Translational Science (LVTS), F-75018 Paris, France
[b] Laboratory of Nanotechnology for Precision Medicine, Fondazione Istituto Italiano di Tecnologia, Via Morego 30, 16163 Genova, Italy
[c] Département de Biophysique et de Médecine Nucléaire, Assistance Publique-Hôpitaux de Paris, Hôpital Avicenne, F-93009 Bobigny, France

ARTICLE INFO

Key words:
ischemic stroke
nanomedicine
targeted treatment
thrombolytics
molecular imaging
clinical trials

ABSTRACT

Stroke is responsible for 11% of all deaths worldwide, the majority of which are caused by ischemic strokes, thus making the need to urgently find safe and effective therapies. Today, these can be cured either by mechanical thrombectomy when the thrombus is accessible, or by intravenous injection of fibrinolytics. However, the latter present several limitations, such as potential severe side effects, few eligible patients and low rate of partial and full recovery. To design safer and more effective treatments, nanomedicine appeared in this medical field a few decades ago. This review will explain why nanoparticle-based therapies and imaging techniques are relevant for ischemic stroke management. Then, it will present the different nanoparticle types that have been recently developed to treat this pathology. It will also study the various targeting strategies used to bring nanoparticles to the stroke site, thereby limiting side effects and improving the therapeutic efficacy. Finally, this review will present the few clinical studies testing nanomedicine on stroke and discuss potential causes for their scarcity.

Relevance of nanomedicine

Cardiovascular diseases account for approximately a third of global mortality, with stroke alone causing over 10% of annual deaths worldwide (Institute for Health Metrics and Evaluation, 2022). In most cases, the so-called ischemic stroke is triggered by the formation of a blood clot (thrombus) (Feske, 2021), which restricts blood flow to the brain. The thrombus formation is a complex phenomenon which involves multiple players, from cellular (such as platelets, red blood cells, and neutrophils) to molecular elements (such as fibrin and Von

Abbreviations: VWF, Von Willebrand Factor; EVT, Endovascular therapy; PA, Plasminogen activators; rtPA, Recombinant tissue plasminogen activators; sICH, Symptomatic intracerebral hemorrhage; NP, Nanoparticle; MRI, Magnetic resonance imaging; CT, Computed tomography; PET, Positron emission tomography; BBB, Blood–brain barrier; QDs, Quantum dots; LSPR, Localized surface plasmon resonance; PEG, Polyethylene glycol; EL, Echogenic liposomes; CsPLTs, Cryo-shocked platelets; ROS, Reactive oxygen species; NET, Neutrophil extracellular traps; PAD4, Peptidylarginine deiminase 4; MCAO/R, Middle cerebral artery occlusion and reperfusion; cGAS-STING, Cyclic guanosine monophosphate-adenosine monophosphate synthase-stimulator of interferon genes; OGD/R, Oxygen-glucose deprivation-reoxygenation; PNPs, Polymeric NPs; RREP, Redox radical emulsion polymerization; Fuco-NPs, Fucoidan-functionalized dextran particles; DPNs, Discoidal polymeric nanoconstructs; PLGA, Poly(lactic-co-glycolic acid); SA-NTs, Shear-activated nanotherapeutics; SK, Streptokinase; PTT, Poly(2,2′-thiodiethylene 3,3′-thiodipropionate; ASPTT, AMD3100-conjugated shrinkable PTT NPs; RAPA, Rapamycin; RAPA/Gd^{3+}@NPs, pH-sensitive theranostic rapamycin (RAPA)-loaded NP system; HO-1, Heme oxygenase-1; HSA-Mn_3O_4, Mn_3O_4 nanoenzymes stabilized by human serum albumin; ER, Endoplasmic reticulum; Glycol-chitosan-coated gold NPs, conjugated to fibrin-targeting peptides (fib-GC-AuNP); IONPs, Iron oxide NPs; rtPA-NCs, Clusters of iron oxide nanocubes, coated and stabilized by rtPA; SPIO, Superparamagnetic IONPs; USPIOs, Ultrasmall superparamagnetic iron oxide NPs; ESIONs, Extremely small-sized iron oxide NPs; NSC, Neural stem cells; CDs, Carbon dots; NBP-CeO_2 NPs, CeO_2 NPs loaded with dl-3-n-butylphthalide; BMVECs, Brain microvascular endothelial cells; NEs, Nanoemulsions; DDFPe, Dodecafluoropentane nanoemulsion; BA, Betulinic acid; BAM, Betulinic amine; EVs, Extracellular vesicles; ADSC-Exo, Exosomes released from adipose-derived mesenchymal stem cells; MSC, Mesenchymal Stem Cells; LK, Lumbrokinase; SLe x, Sialyl Lewis x; PBP, Platelet-binding peptides; FBP, Fibrin-binding peptides; SHp, Stroke homing peptide; PcNP, Polymeric NPs coated with murine platelet membrane; RcNP, Erythrocyte-membrane coated polymeric NPs; HLA, Human leukocyte antigen; PAA–MNP, Polyacrylic acid-coated magnetite NPs; rtPA-MRs, rtPA-coated iron oxide microrods; RMF, Rotating magnetic field; GRAS, Generally Recognized As Safe.

* Corresponding author.
E-mail address: cedric.chauvierre@inserm.fr (C. Chauvierre).
† Contributed equally.
‡ Share the last authorship.

https://doi.org/10.1016/j.neuroscience.2023.11.035
Received 7 September 2023; Accepted 30 November 2023
Available online 4 December 2023
0306-4522/© 2023 IBRO. Published by Elsevier Ltd. All rights reserved.

Willebrand Factor (VWF)). Consequences may be severe if the vascular occlusion is not addressed promptly, thus demanding a rapid and efficient therapeutic intervention to alleviate possible permanent damages resulting from ischemic strokes. However, pharmacological and surgical treatment options for ischemic strokes are limited. On one hand, mechanical intervention through surgical thrombectomy (endovascular therapy, or EVT) is not always possible depending on thrombus accessibility and availability of competent surgeons and infrastructure. On the other hand, pharmaceutical action can be achieved mostly through fibrinolytic drugs (plasminogen activators (PA)), as well as anticoagulants and antiplatelets for the prevention of secondary strokes (Feske, 2021). However, these fibrinolytic treatments are intravenously injected and therefore have body-wide side effects and limited thrombolysis efficiency. For instance, the gold standard treatment, Alteplase® (a recombinant tissue PA, rtPA), suffers from low circulation half-life, risks of symptomatic intracerebral hemorrhage (sICH), neurotoxicity, and overall cannot achieve full recanalization in all the patients (only in 30%) (Bhatia et al., 2010; Mosconi and Paciaroni, 2022).

In summary, stroke treatments are not always administered (e.g., around 10% of ischemic stroke patients in the United States received rtPA in 2018) (de Havenon et al., 2021), partly due to a very short therapeutic window (4.5 hours from stroke onset), often with major side effects through systemic activity and lack of efficacy, thus requiring new directions to improve patients' outcome.

To overcome these limitations, nanomedicine applied to stroke treatment has been investigated for several years. In the early 19th century, the German Nobel prize Paul Ehrlich created the concept of "magic bullet" specifically directed against pathogens in the organism, like bullets fired from a gun that hit a specific target (Strebhardt and Ullrich, 2008). New treatments were inspired by this concept and are now designed to bring an active drug with poor availability and adverse toxicity profile to a specific target by encapsulating it into a controlled vector - the nanoparticle (NP). In this context, the encapsulation and targeted delivery of thrombolytic agents would benefit from: (i) protection from the physiological environment, thus increasing the agent's half-life; (ii) limitation of systemic adverse effects; (iii) improvement in therapeutic efficacy by increasing its accumulation at the thrombus site (Blanco et al., 2015). This concept has also been adapted to stroke diagnosis. Indeed, instead of bringing an active drug to the targeted thrombus, nanoscale objects such as NPs can be used directly as contrast agents (e.g., iron oxide NPs for magnetic resonance imaging (MRI) or to transport imaging compounds such as radioactive markers). Thanks to their targeting capacity, they can accumulate at the cerebral blood clot and enhance the imaging signal of the stroke that can be obtained with MRI, computed tomography (CT), positron emission tomography (PET) or doppler ultrasonography (Sarmah et al., 2021).

In addition to resolving the thrombus and restore blood flow, neuroprotection is essential to limit tissue damage resulting from ischemia (Ghozy et al., 2022). This is why NP-based treatments are promising as they have the potential to simultaneously deliver both neuroprotective and thrombolytic agents and enhance overall therapeutic outcomes (Vos et al., 2022). In particular, NPs benefit from very specific characteristics due to their size which can be useful for imaging as well as therapeutic activity. First of all, their small size allows access to areas not available to other objects, such as the intracellular compartment or the crossing of the blood–brain barrier (BBB). Indeed, the BBB crossing capacity of NP has been largely documented in the case of brain tumors as well as for the treatment of various neurological disorders, including Krabbe, Alzheimer's or Parkinson's diseases (Waris et al., 2022; Moore et al., 2023), and this property can be essential for treating the insulted tissue post-ischemia (Ma et al., 2019).

Operating at the nanometric scale induces specific advantages in the circulation, as the vascular margination of blood-borne objects varies based on their size and shape (Lee et al., 2013; Müller et al., 2014). It has also been stated that NPs above 10 nm avoid the kidneys' filtration, and for those below the micron scale, clearance by phagocytosis is hindered: thus, NPs in a 10 nm - few hundreds of nm size window benefit from good circulation, though it also varies with material, shape, or coating (Duan and Li, 2013). Moreover, this size reduction is accompanied by an increasing surface/volume ratio, which plays a critical role in functionalization, target recognition, as well as surface exchange for drug release (Navya and Daima, 2016). There is increasing evidence that at such scale NPs' behavior is critically affected by their shape, with consequences on cell interaction for instance (Navya and Daima, 2016). Modified responses to exogenous stimuli can also appear, which is for instance the case for ultrasound contrast enhancement upon ultrasound imaging (Pellow et al., 2018). Regarding inorganic NPs, specific properties emerge. For instance, quantum dots (QDs) present strong luminescence with tunable absorption and emission wavelengths, notably through NP size control. They can therefore be useful for imaging, as shown with the near-infrared emitting QDs for thrombus imaging from Imamura's group (Imamura et al., 2016). Plasmonic NPs such as gold materials can absorb light at different wavelengths depending on their size through localized surface plasmon resonance (LSPR), which emerges from the classical surface plasmon resonance at nano scales. This has been used in a proof-of-concept photothermal thrombolytic system based on gold NPs in 2016 (Singh et al., 2016). At the nanoscale, similar NPs show great thermal conversion properties due to their naturally high thermal conductivity combined to increased surface/volume ratio, which has allowed the development of such a photothermal approach (Pallavicini et al., 2021). In addition, ferro/ferrimagnetic NPs undergo a superparamagnetism phenomenon: when they are small enough, each NP is made of only one magnetic domain. Thus, in the absence of an external magnetic field, the magnetic moments of all NPs are differently oriented, as dictated by Néel relaxation, leading to zero magnetization. In the presence of an external magnetic field, instead, superparamagnetic NPs exhibit a stronger magnetization than paramagnetic ones (Farinha et al., 2021). Additionally, through their Néel and Brownian relaxation processes, under stimulation of an alternating magnetic field, superparamagnetic NPs can also be used to produce heat in order to help the dissolution of the clot (Abenojar et al., 2016; Zhang et al., 2021b).

Finally, NPs exhibit high versatility as carriers capable of delivering various drugs to a wide range of tissues. Their ability to either remain in the vascular compartment or cross the BBB depending on their size and shape provides great flexibility and a tailored approach to tackle the different phases of ischemic stroke. For example, during the hyperacute phase of stroke (first 6 hours), when the BBB becomes leaky in the ischemic area, thrombolysis and neuroprotection will be the main therapeutic objectives. NPs enable the targeting of the blood clot for thrombolytics delivery or to reach the ischemic tissue through the more permeable BBB to limit neuronal damage with neuroprotectants. In the subacute and chronic phases (>48 hours after stroke onset), neoangiogenesis and neurogenesis will be the main targeted processes. Thus, growth factors or miRNAs will be delivered to the infarcted region, notably via targeting agents on the NPs surface that promote the passage of BBB, which is less permeable than in the early stage of ischemic stroke (Bernardo-Castro et al., 2021).

Nanotechnological platforms developed to tackle stroke

Over the last two decades, different nanotechnologies have been proposed in combination with tPA or other therapeutics, to broaden the portfolio of stroke treatments and diagnostic tools. Here are described the diverse nanotechnological platforms that have been tested: liposomes, polymeric NPs, inorganic NPs, and miscellaneous NPs (Fig. 1).

Liposomes

Liposomes are nano-micrometer sized particles, made of a phospholipid bilayer which encloses a hydrophilic core, that can be loaded with both hydrophobic and/or hydrophilic molecules. For stroke applications, thrombolytic drugs or contrast agents were principally incorporated in the hydrophilic region. This idea was applied successfully in the work of Heeremans et al. in 1995, where rt-PA (Actilyse®) loaded liposomes showed a significantly higher thrombolytic efficacy than free rt-PA. However, the incomplete and suboptimal encapsulation efficiency led to a fast removal of more than 50% of the circulating drug (Heeremans et al., 1995).

To further increase the systemic circulation of the thrombolytic agents, Kim *et al.* tested polyethylene glycol (PEG)-ylated liposomes to conceal the particles from the innate body defense. Both *in vitro* and *in vivo* rtPA release rates were slower and more sustained in the presence of the PEG, with a significant improvement (up to 20-times) of the drug half-life. Furthermore, rtPA entrapment efficiency was constant over 45 days of storage at 4 °C (Kim et al., 2009). Echogenic liposomes (EL), carrying gas in the core, are ultrasound-responsive, and were tested as contrast and thrombolytic agents, alone or in combination with tPA. The selective and controlled release of the liposome content was driven by ultrasonic pulses that trigger cavitation and the destruction of gas bubbles, thus further affecting clot integrity and tissue permeability. These advantages were confirmed in several studies, where rtPA-loaded EL showed an increased thrombolytic activity in presence of ultrasound, compared to the free drug (Refaat et al., 2021). Nonetheless, several studies highlighted that the rtPA encapsulation efficiency was limited in this technology, in addition to the limited targeting properties. Overall, further optimization steps are needed before reaching a clinically valuable product (Wang et al., 2020).

By using different lipids and their relative ratios, the liposome composition can be tailored, for instance, with the addition of surface targeting moieties or stimulus responsive molecules to increase selectivity. Furthermore, the possibility to load multiple and different types of drugs allows one to combine the thrombolytic function with neuroprotection. An example is given by the design developed by Quan and colleagues who encapsulated tPA and aspirin (anti-inflammatory drug) in liposomes associated to cryo-shocked platelets (CsPLTs). In this novel approach, the binding of CsPLTs with liposomes was mediated by an “host–guest” interaction between adamantane, a reactive oxygen species (ROS)-responsive molecule on the liposomes, and cucurbit[7]uril on the platelet membrane. This technology showed high affinity with clots as demonstrated *in vitro* and *in vivo* in a murine model of mesenteric artery thrombosis. *In vivo*, in a stroke mouse model induced via photothrombosis, a significant improvement of neurological scoring, volume of stroke damage, and BBB leakage was documented. This technology showed a safe profile with no negative effects as assessed by histological analyses, coagulation molecular indicators, liver and kidney functions (Quan et al., 2023). In 2023, Sun *et al.* proposed a smart liposomal nanocarrier, aiming to tackle neutrophil extracellular traps (NET) formation (NETosis): this phenomenon, that occurs in several pathological conditions including

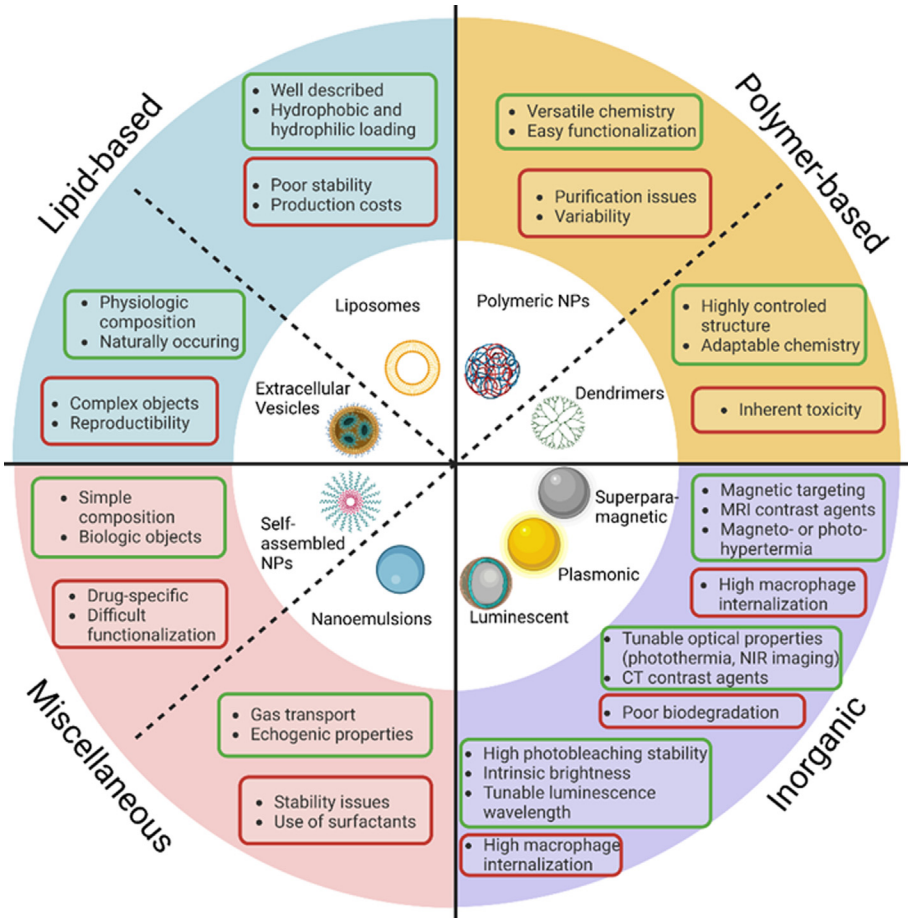


Fig. 1. Main NP types used for stroke treatment and imaging, and the associated advantages (green frame)/drawbacks (red frame). NP: nanoparticles; MRI: magnetic resonance imaging; CT: computer tomography; NIR: near infrared. Respective examples of superparamagnetic, plasmonic and luminescent NPs are iron oxide NPs, gold NPs and quantum dots.

stroke, is regulated by the neutrophils and is responsible for the immune system overactivation in the brain. Their liposomal system (C-Lipo/CA) was intercalated with ROS-responsive polymers (for ROS scavenging and drug release) and coated with CREKA peptide sequences (for fibrin binding). C-Lipo/CA were loaded with Cl-amidine, a peptidylarginine deiminase 4 (PAD4) enzyme inhibitor, to block the NETosis process. *In vitro*, C-Lipo/CA showed efficient binding to microthrombi. *In vivo* experiments displayed a good safety profile, with no impairments in organ architecture and biochemical indicators. In addition, biodistribution tests displayed high retention of the particles in the ischemic brain area. In the middle cerebral artery occlusion and reperfusion (MCAO/R) stroke animal model, C-Lipo/CA showed positive effects on animal behavior, a lesion size reduction from 46.7% (saline group) to 12.1%, and BBB leakage, resulting from the suppression of NETosis and the cyclic guanosine monophosphate-adenosine monophosphate synthase-stimulator of interferon genes (cGAS-STING) pathway, both overactivated in ischemic area (Sun et al., 2023).

Interestingly, empty liposomes with a specific lipid composition, but without any encapsulated drug, could also be effective. A brief report published in 2022 explained that empty nanoliposomes (<100 nm size) made of phosphatidylcholine, cholesterol and monosialogangliosides, have a positive effect against stroke. The authors showed an antioxidant protective response *in vitro* on human neuroblastoma (SH-SY5Y) and human microvascular endothelial cells exposed to oxygen-glucose deprivation-reoxygenation (OGD/R). Similarly, nanoliposomes improved neurological scoring, reduced infarct, and edema size in MCAO mice model (Ahmad et al., 2022).

Noteworthy, Al-Ahmady *et al.* found two temporal windows to maximize liposomes localization into the brain after stroke: during the hyperacute phase (0.5 h post-stroke), and the sub-acute/chronic phase (48 h post-stroke). This discovery has opened up new avenues for the development of therapeutic options, allowing for the targeting of various aspects of the pathology (Al-Ahmady et al., 2019).

Taking into consideration all these studies, drug encapsulation into liposomes increases efficacy, stability, and therapeutic index of the thrombolytic treatment, reducing at the same time toxic and off-site effects. Adverse effects can be further reduced by adding stimulus-responsive molecules to the liposome composition, thus releasing the drug only at the thrombus site. Nevertheless, their use is still limited due to high production costs, poor stability and short half-life after administration or during the storage (Akbarzadeh et al., 2013).

Polymeric nanoparticles

Polymeric NPs (PNPs) are versatile drug delivery systems made of particulate dispersions of polymers and have a size range between 10 and 1,000 nm. Their size, shape and mechanical properties can be precisely designed, thanks to several easy fabrication techniques, and a wide list of natural or synthetic biocompatible and biodegradable monomers/polymers that can be used as brick for their synthesis. PNP surface can be tailored with the insertion of targeting moieties, to increase the particle selectivity to the therapeutic target. For these reasons, PNPs were suggested for different biomedical applications, including stroke treatment. Chauvierre's group in 2018 developed fucoidan-labeled PNPs carrying rtPA adsorbed on the surface. PNPs were made of polysaccharide-poly(isobutylcyanoacrylate) by a redox radical emulsion polymerization (RREP). With RREP, the polysaccharides were distributed on the surface of the PNPs to allow rtPA (Actilyse®) adsorption. The addition of dextran modified with amino groups increased the stability of the drug. This technology showed, both *in vitro* and *in vivo,* increased affinity to blood clot and enhanced thrombolytic efficacy (Juenet et al., 2018). Lately, the same research group developed and tested other PNPs named fucoidan-functionalized dextran particles (Fuco-NPs). These PNPs were obtained by green chemistry starting from FDA-approved biodegradable and biocompatible polysaccharides. They were successfully loaded with rtPA, with high encapsulation efficiency of about 65% and 80% for control-NPs and Fuco-NPs, respectively. *In vivo*, Fuco-NPs loaded with rtPA could improve the angiographic scores in murine stroke models: Fuco-NPs loaded with rtPA showed a 67% total recanalization rate versus only 33% for free rtPA treated mice (Zenych et al., 2021).

PNPs shape can be finely tailored, to enable specific hemo-dynamic performance after systemic administration. For example, Moore *et al.* designed discoidal polymeric nanoconstructs (DPNs) that have a diameter of 1,000 nm and a height of 400 nm, and are composed with a mixture of poly(lactic-co-glycolic acid) (PLGA) and PEG. DPNs were successfully tested *in vitro* and *in vivo* for vascular delivery of imaging and therapeutic molecules against tumors (Moore et al., 2022). Colasuonno *et al.* tested rtPA-loaded DPNs as a thrombolytic agent, demonstrating a clot lytic activity similar to the free drug in static experimental conditions, while it was increased in microfluidic experiments with dynamic conditions. *In vivo* experiments on the mouse mesenteric vein thrombosis model confirmed the clot lytic efficacy, where rtPA-DPN outperformed free rtPA for occlusion resolution (Colasuonno et al., 2018). Another approach based on hemodynamic performance was proposed by Korin *et al.*, in 2012. Shear-activated nanotherapeutics (SA-NTs) produced by spray-drying concentrated solutions of small PLGA NPs (~180 nm) to form microaggregates (~3.8 μm). These microaggregates are stable in aqueous solution due to the PLGA NPs' hydrophobicity and remain intact under physiological blood flow conditions. Interestingly, they break when exposed to high shear stress, similarly to what occurs in proximity to an occluded vessel, enabling the release of tPA near the occlusion. *In vitro,* in presence of a simulated clot, SA-NTs showed increased thrombolytic activity in comparison to free tPA. *In vivo*, SA-NTs induced progressive thrombolysis, increased efficacy, and animal survival in two different preclinical animal models (Korin et al., 2012).

A combined approach mixing targeting, thrombolytics and ultrasound sensitivity was proposed by Marsh *et al.*, in 2007. They tested a fibrin-specific liquid perfluorocarbon (perfluoro-octylbromide) NP loaded with the thrombolytic agent streptokinase (SK). Perfluoro-octylbromide is a biocompatible molecule with echogenic properties. The authors confirmed the efficacy of this technology as an acoustic contrast agent, useful for clot imaging and volumetric analysis. Furthermore, the clot lysis was efficaciously increased in comparison to free SK thanks to the NPs' targeting ability, and could be monitored through ultrasound visualization (Marsh et al., 2007). Similarly, Kawata *et al.,* combined basic gelatin and zinc ions to carry and control the activity of rtPA Monteplase (Cleactor®). In this complex, rtPA activity is reduced to 45%, but it can be fully restored after ultrasound exposure. This approach allowed the rtPA protection from serum proteins inactivation, and the control of off-site effects of the treatment (*i.e.*, hemorrhagic transformation). rtPA-loaded gelatin-zinc particles have an intrinsic targeting ability due to the affinity between gelatin and VWF, as highlighted by *in vitro* and *in vivo* experiments in the mouse arterial thrombosis model. Animal experiments confirmed the efficacy of the treatment and the survival rate dramatically increased in comparison to free-rtPA treatment in the swine acute myocardial infarction model (Kawata et al., 2012).

Multifunctional polymers with specific features, such as microenvironment responsiveness, were adopted for PNP crafting. An example is given by the technology proposed by Wu *et al.* in 2022: PNP made with a modified version of poly(ethylene glycol) (PEG), having in the structure a ROS-degradable poly(2,2′-thiodiethylene 3,3′-thiodipropionate or PTT) polymer with an antioxidant activity, and a thrombin-cleavable peptide (NH2-norleucine-TPRSFL-C-SH). This tailored polymer is cleaved in the presence of thrombin, with a resulting particle rearrangement and shrinkage, to improve brain penetration. The synthesized particles made with a modified co-polymer (PTT NP) showed in biodistribution experiments the efficient localization into the

ischemic area 24 h after stroke induction and treatment. PTT NPs showed positive effect in the MCAO/R mouse model, with a reduction of the infarct area from about 60% (PBS group) to 30% (PTT NPs). To further increase the brain penetration, the surface of the PTT NPs was decorated with AMD3100 for its specific affinity with a chemokine receptor, CXCR4, particularly expressed in the ischemic tissue. The conjugation with AMD3100 enabled a significant enhancement in NP localization into the ischemic area, as confirmed by whole-animal fluorescence analysis. Lastly, AMD3100-conjugated shrinkable PTT NPs (ASPTT) were loaded with glyburide, an anti-edema drug useful in stroke condition, as determined in the clinical trial GAMES-RP, where its administration resulted in an increased patient survival (Sheth et al., 2016). ASPTT-glyburide showed a controlled release of the drug, which happens only in presence of thrombin and ROS. *In vivo*, in the MCAO/R model, ASPTT-glyburide outperformed the control conditions (ASPTT NPs without glyburide or free glyburide) in terms of reduced infarcted area, neurological scoring, survival and BBB leakage (Wu et al., 2022).

Similarly, Cheng *et al.* tested a pH-sensitive theranostic rapamycin (RAPA)-loaded NP system (RAPA/Gd^{3+}@NPs), able to selectively release the payload (drug and contrast agent) in the ischemic tissue. RAPA/Gd^{3+}@NPs were synthetized by self-assembly of the pH-sensitive amphiphilic block copolymer (mPEG-b-P(DPA-co-HEMA)-Ce6) in aqueous solution with RAPA and Gd^{3+}, obtaining spherical particles with a mean diameter of 20–30 nm. The biodistribution in the MCAO/R rat model showed high accumulation of RAPA/Gd^{3+}@NPs inside the ischemic area 6 h-post administration, as displayed by MR T1-imaging and ex-vivo NIR fluorescence imaging. Also, neurological and behavioral tests showed an amelioration of ~50% of the scores after treatment with RAPA/Gd^{3+}@NPs, in comparison to the saline control group. Similar benefits were found evaluating lesion size and BBB integrity. BBB integrity was also preserved with a significant edema reduction in the ischemic hemisphere. The molecular analysis of inflammatory markers (IL-6 and TNF-α) suggested the neuroprotective role of these NPs by helping the BBB heal after the ischemic event. Finally, these technologies showed a good safety profile, with no obvious damage detected by histological analysis of the main organs (Cheng et al., 2021).

A subtype of highly ordered multibranched polymeric NPs, called dendrimers, has also been investigated for drug deployment in stroke, as it is possible to precisely tune their size distribution, architecture, and functionalization. For example, Lee *et al.* described early-generation polyamidoamine dendrimers (PG2HR), which have been tested as gene carriers in MCAO/R stroke animal models and injected together with heme oxygenase-1 (HO-1) plasmid. The complex pHO-1/PG2HR reduced apoptosis and infarct sizes (from 40% to 30% total infarct brain area) in ischemic brains, suggesting a potential use as gene therapy of inflammatory diseases including ischemic stroke, also due to the high gene delivery efficiency and low cytotoxicity (Lee et al., 2021).

Even though PNPs have a great potential as nanomedicines due to their versatility, highly controlled chemistry, tunable architecture, and the broad range of drugs and targeting moieties they can be equipped with, several limitations remain to be overcome. PNPs synthesis often requires the use of catalyzers, organic solvents, photo-polymerizers, which are all potentially toxic reagents for cells and tissues. Therefore, extensive purification steps are needed to limit the presence of impurities. Several biocompatible and biodegradable polymers have a limited use due to batch-to-batch variations. Finally, to assure suitability for biomedical application, it is crucial to outline a standardized array of characterization techniques in order to guarantee a complete quantitative analysis.

Inorganic nanoparticles

Inorganic NPs have been investigated for their intrinsic material features, such as catalytic, magnetic, thermal or optical properties, which sustained their application as a diagnostic and therapeutic tool, notably for stroke application. Among them, Mn_3O_4 nanoenzymes stabilized by human serum albumin (HSA-Mn_3O_4) have been studied as an antioxidative treatment to address ischemic stroke reperfusion injury. Mn_3O_4 NPs can release manganese ions in circulation, which promotes the activity of superoxide dismutase 2 in the body. The positive *in vitro* results against oxygen-glucose deprivation, endoplasmic reticulum (ER) damage and cell apoptosis were further confirmed in animal investigations. The presence of the HSA on the surface enabled prolonged circulation time (~72 h), preserving the ROS scavenging ability from off-site activation. *In vivo*, HSA-Mn_3O_4 showed a strong neuroprotective effect, with reduction in stroke volume and improvement in behavioral score. In addition, the highest dose of HSA-Mn_3O_4 (0.4 mg/kg) reversed the ER stress pathways activation to normal level, counteracting the activation of pro-apoptotic signals (Huang et al., 2022).

Inorganic NPs also enable theranostic approaches, as shown by Kim *et al.*, with glycol-chitosan-coated gold NPs, conjugated to fibrin-targeting peptides (fib-GC-AuNP). Gold NPs especially show desirable optical properties due to the surface plasmon resonance effect, enabling photothermal treatment. This optical effect is localized from the visible to the infrared region, depending on the particle size, shape, and structure (Khlebtsov, 2008). The particles from Kim's group hold targeting features and the capacity to visualize cerebrovascular thrombi by CT-based imaging. Thus, fib-GC-AuNP allowed quantification of cerebral thrombi over the tPA treatment to directly evaluate its thrombolytic effect. Remarkably, fib-GC-AuNP acted as CT contrast agent and enabled the image analysis on recurrent thrombosis by mCT for up to 3 weeks, with a single administration and without neurobehavioral or systemic toxicity (Kim et al., 2015).

Among magnetic NPs, iron oxide NPs (IONPs), made of magnetite (Fe_3O_4), maghemite (γ-Fe_2O_3) or mixed ferrites (MFe_2O_4 where M = Co, Mn, Ni or Zn) have been proposed and tested for several different applications. IONPs are non-toxic, biodegradable, can modulate cell differentiation and eventually become a source for *in vivo* iron supplements, useful as anemia treatment (Dadfar et al., 2019). A clear example is the approach proposed by Voros *et al.*, that aimed to increase thrombolytic activity of rtPA (Alteplase®). They tested clusters of iron oxide nanocubes, coated and stabilized by rtPA (rtPA-NCs), to have a combined pharmacological and thermal therapy of blood clots. Thermal therapy is a strategy already approved by the FDA against cancer, to increase the efficacy of chemotherapy. For stroke, this strategy involves heating local areas through magnetic hyperthermia, in order to improve rtPA clot lysis. *In vitro*, rtPA-NCs showed higher dissolution rates compared to free rtPA, in absence of heating (around 100 times). The exposure to thermal treatment increased even more the efficacy of the rtPA-NCs (10 times) compared to unexposed NPs. *In vivo* experiments on the mouse mesenteric thrombosis model confirmed rtPA-NCs efficacy, leading to a complete clot dissolution in less than 3 min, while the same concentration of free-rtPA was ineffective even after 60 min. Noteworthy, rtPA-NCs displayed high values of transverse relaxivity, suggesting the possible application of these particles for MRI imaging and magnetic targeting of the clot (Voros et al., 2015).

Similarly, nanoscale superparamagnetic IONPs (SPIO), with a 20–50 nm core size, were already exploited as a contrast agent for T2 weighted MRI. Further investigations on IONP magnetic properties revealed that by reducing the NP size, the longitudinal T1 relaxation effect was enhanced. For this reason, ultrasmall superparamagnetic iron oxide NPs (USPIOs), and extremely small-sized iron oxide NPs (ESIONs) characterized by a core size below 4 nm and a paramagnetic behavior, were suggested as T1 contrast agents for MRI (Kim et al., 2011). This is mainly due to the high surface-to-volume ratio of the NPs and the predominance of a magnetically disordered spin-canted shell (Richard et al., 2016).

Another approach appraised in the last decade consists of labeling cells with NPs for *in vivo* tracking of the transplanted cells by imaging

techniques (e.g., MRI, CT, and bioluminescence BMI). This has been applied to stem cells which represent a promising therapy for different pathologies, including stroke, but lack a way for *in vivo* tracking (Bliss et al., 2007). Wen and collaborators tested the efficacy of NPs to track neural stem cells (NSC) in presence of stroke: before injection, the cells were labeled with nano-sized cationic polymersomes loaded with SPION and QDs. QDs are 1–10 nm sized nanocrystals with enhanced optical properties. Their first generation has a core made of elements from groups II to VI of the periodic table, surrounded by a second semiconductor, usually zinc sulfide, making them brighter and much more stable than common fluorophores. Labeled cells were effectively visualized *in vivo* by dual-modal imaging (magnetic resonance and fluorescence imaging). In the rat stroke model, NPs-labeled NSC were detected by T2- and T2*-weighted MRI, until 6 weeks post-injection. In fluorescence imaging, the signal was recorded 1 week after transplantation, with a gradual decline until 5 weeks (Wen et al., 2014). These QDs were followed by the development of next-generation structures, such as carbon dots (CDs), which are useful as MRI and optical probes. Nanohybrids, formed by the covalent linkage between thrombolytic agents and CDs, have been reported to emit a fluorescence signal in the brain of transient MCAO murine models and for retaining PA activity. Such nanohybrids could also be a promising indicator of early BBB damages and intracranial hemorrhage after thrombolysis, favoring early intervention (Niu et al., 2020).

Inorganic NPs were also applied as agents or carriers of neuroprotective drugs. For instance, Cerium oxide (CeO_2) NPs have several intrinsic antioxidant and neuroprotective effects, in addition to BBB crossing, and were therefore already proposed as drug delivery systems for neurological disorders (Portioli et al., 2013). For instance, Li *et al.* investigated CeO_2 NPs loaded with dl-3-n-butylphthalide (NBP-CeO_2 NPs). NBP acts on the ischemic area microcirculation promoting angiogenesis, neurogenesis and neuroplasticity, reducing inflammation and apoptosis, with overall neuroprotective effects. For these reasons, it was FDA-approved for a phase II trial in the treatment of ischemic stroke. Here, NBP-CeO_2 NPs reduced ROS levels in brain microvascular endothelial cells (BMVECs) and hippocampal neurons after OGD/R. In the MCAO/R mouse model, NBP-CeO_2 NPs preserved BBB integrity and reduced lesion volume in comparison to control conditions (damaged area of 39.8% in the saline treated group, reduced to 10.6% in the NBP-CeO_2 NPs group). Neuroinflammation was also reduced in the NBP-CeO_2 group, in comparison to the saline condition. Interestingly, empty CeO_2 NPs also showed positive effects on BBB leakage, lesion size reduction and neuroinflammation, supporting the development of this nanotechnology for new stroke therapies (Li et al., 2022b).

Even though possible toxicity issues related to inorganic NPs have been highlighted and debated (Soenen et al., 2011), the literature still does not offer a definitive conclusion on this matter (Sani et al., 2021; Bhatti et al., 2022). Like organic nanomaterials, their biodegradation depends mostly on NP material and coating, and for instance, clear degradation issues have been shown with certain inorganic nanomaterials such as gold (Balfourier et al., 2020). Other inorganic technologies showed good biocompatibility and reduced risk of toxic effects (Ma et al., 2009; Kim et al., 2015; Hu et al., 2018; Huang et al., 2022). All things considered, further pre-clinical and clinical investigations focusing more on safety and toxicological aspects will be needed to elucidate the potential risks for human health.

Miscellaneous nanoparticles

Nanoemulsions

Nanoemulsions (NEs) are dispersions of small droplets in the range of 0.1–100 μm, generated with two immiscible phases (liquid in liquid emulsions), and stabilized by emulsifying agents (surfactants and cosurfactants). The size of the droplets depends on the composition of the system and the homogenization method. Among NEs, dodecafluoropentane nanoemulsion (DDFPe) is a neuroprotectant perfluorocarbon that was initially proposed as ultrasound contrast agent. Additional investigations highlighted the *in vivo* potential as oxygen and carbon dioxide cargo. Preclinical studies in the rabbit embolic stroke model demonstrated >80% reduction in acute infarction. Further, the repeated administration of DDFPe over a 24-hour period showed positive improvement in vital signs and cerebral tissue, as highlighted by histological analysis. Different MRI markers of infarct improved in the early hours following vascular occlusion (Brown et al., 2014; Fitzgerald et al., 2015), with extension in the time window for tPA intervention (Culp et al., 2015).

Natural compound-derived nanoparticles

Several natural compound-derived NPs were tested against stroke, with the advantage of using natural materials with intrinsic therapeutic effects, combined to an efficient brain delivery. Zhang *et al.* screened a collection of natural nanomaterials, identifying betulinic acid (BA) as a preferential compound against stroke. BA has intrinsic antioxidant properties, useful to counteract the reperfusion injury damage and oxidative stress triggered by stroke. A chemically modified form of BA, named betulinic amine (BAM), was used for the NP preparation. BAM NPs were synthesized using a standard emulsion procedure, with solvent evaporation over the emulsion. After the purification, BAM NPs were conjugated to AMD3100, a CXCR4 antagonist, which increased the brain penetration of the particles. Intravenous administration showed an increased survival of mice, reduced infarct volume by 57%, and improved neurological scores. Furthermore, the neuroprotective peptide NA1, already in clinical trial (phase III) for its neuroprotective activity against NMDA receptor-mediated toxicity, was bound on the surface of BAM NPs. The additional conjugation of NA1 further increased the mice survival and reduced the infarct volume by 69.8%, in comparison to the control condition (Zhang et al., 2022).

Extracellular vesicles

Extracellular vesicles (EVs) are released by living cells and transfer lipids, nucleic acids, proteins, and metabolites within and between organs in an endocrine process. The heterogeneous population of EVs produced *in vivo* play crucial roles in physiological and pathogenetic mechanisms. EVs include exosomes produced through the endosome pathway and released into the extracellular space, and ectosomes formed by directly budding of the cell plasma membrane (Cocucci and Meldolesi, 2015). Wang *et al.* observed that serum exosomes from young healthy rats, administered into aged ischemic rats, improved short- and long-term functional outcomes, and reduced synaptic loss. Conversely, exosomes from aged healthy rats did not have positive effects (Wang et al., 2023). In the work of Zhang *et al.*, they observed that the levels of pro-inflammatory mediators in serum exosomes increase with age. This mechanism is associated with worsened stroke outcomes, through excessive activation of C3aR-dependent microglial phagoptosis (Zhang et al., 2021a). Recent discoveries showed the therapeutic potential of EVs from specific cell types. Exosomes released from adipose-derived mesenchymal stem cells (ADSC-Exo) were tested against cerebral ischemia/reperfusion injury. ADSC-Exo carried miR-760-3p (miRNA) which inhibits with high efficiency the CHAC1 gene expression, upregulated by ischemic stroke ferroptosis. *In vivo*, intranasal administration of ADSC-Exo improved mice neurobehavior after ischemia/reperfusion injury (Wang et al., 2023). Similarly, cortical astrocytic derived EVs accelerated recovery after stroke, in the rat ischemia/reperfusion model after a single intracerebroventricular administration (Heras-Romero et al., 2022). EVs exert neuroprotective effects, modulating the recruitment of circulating immune cells into the damaged area. In Han *et al.* study, small EVs obtained from Mesenchymal Stem Cells (MSC), after intravenous administration in young and aged ischemic mice, reduced neurological deficits, infarct volume, brain edema, and neuronal injury,

with a decreased count of immune cells in the ischemic brain of aged mice (Han et al., 2023).

Targeting strategies

While the structure and composition of NPs can vary considerably, most recent nanoplatforms include some sort of targeting. Indeed, this is critical to ensure that the payload, or desired effect, can be delivered at the expected location: namely, the clot itself or the ischemic tissue. As discussed above, the main explored class of thrombolytics and the only approved one for ischemic stroke is formed by plasminogen activators (PAs), which suffer from limited recanalization rate and high deleterious side effects (Zenych et al., 2020). Thus, targeting the drug delivery only to the thrombus can limit systemic side effects, while ensuring a local high concentration of active agents. Here are described various targeting strategies, from the single molecular targeting to multiple molecular targeting methods, as well as magnetic and passive targeting (Fig. 2). Notably, we focused on quantification of targeting capacities rather than therapeutic efficacy to illustrate the potential of the various methods described hereafter.

Single molecular targeting

Multiple biomarkers have been identified to recognize either the blood clot, or the ischemic region. Regarding the former, some NPs aim to target activated platelets. The peptide cRGD is among the well-known binding motifs used for NPs, as it was characterized for stroke application, to bind the GPIIb/IIIa receptor, which is expressed on platelets, and play a critical role during their activation and aggregation through fibrinogen and VWF binding (Liao et al., 2019). For instance, Liao *et al.* described in 2018 a trimethyl chitosan NP, loaded with lumbrokinase (LK) and functionalized with cRGD. This system showed improved thrombolysis *in vitro* and *in vivo* on rat thrombus models, compared to free drug (around 60% reduction in clot weight for targeted NPs vs. no difference for untargeted NPs) (Liao et al., 2019). More complex designs were also described, such as the Janus-rod micromotors from Cao *et al.*, in 2021, in which the cRGD targeting allowed the US-responsive objects to accumulate at the thrombus (3.4-fold improved accumulation at the thrombus vs. no cRGD), where enhanced penetration and thrombolysis (74%) was achieved (Cao et al., 2021). Other biomarkers exist for activated platelets, such as the P-selectin, a transmembrane protein expressed on activated platelets and endothelium, which mediates leukocyte adhesion through the Sialyl Lewis x (SLe x) motif on PSLG-1 ligand. A natural polysaccharide, fucoidan, was found to mimic this motif with high affinity and specificity (Bachelet et al., 2009), and can thus be used as targeting moiety: for instance, the technology developed in 2021 by Zenych *et al.* used it as a targeting agent. Here, fucoidan was cross-linked to PNPs, and the resulting Fuco-NPs could effectively target P-selectin and aggregated platelets *in vitro,* with a significant increase in aggregated platelets' targeting in a microfluidic setup compared to untargeted NPs (Zenych et al., 2021). Interestingly, some authors took into account the time-wise development of thrombi in their targeting, such as Pan *et al.* who described in 2017 micelles which could be loaded with LK and functionalized with Annexin V. Annexin V have high affinity for phosphatidylserine, a lipid presented on the exterior membrane of apoptotic cells, as well as on platelets during their activation. This allowed a significant accumulation of targeted micelles to the clots (compared to non-targeted) and significantly enhanced thrombolysis in $FeCl_3$ murine thrombosis model, when compared to free LK or non-targeted micelles (Pan et al., 2017).

Other groups chose to target components of the thrombus, such as the fibrin molecule. For instance, Marsh *et al.* described in 2011 SK-loaded perfluorocarbon NPs decorated with *ad hoc* antibodies against fibrin (10^{-10} M affinity, with no reactivity toward fibrinogen). These NPs retained good SK-mediated *in vitro* thrombolysis (20–30% increase in clot dissolution when compared to empty NPs). Moreover, in the canine thrombosis model, an accumulation of targeted NPs into clots was observed when compared to the non-targeted NPs. However, they lack evidence of enhanced thrombolysis *in vivo* (Marsh et al., 2011). Recent literature focused on small peptides to target fibrin, notably CREKA (Zhao et al., 2020), or interestingly *ad hoc* designed peptides (Seo et al., 2018). For example, Seo *et al.* leveraged peptides, selected through phage display, that could only recognize fibrin-

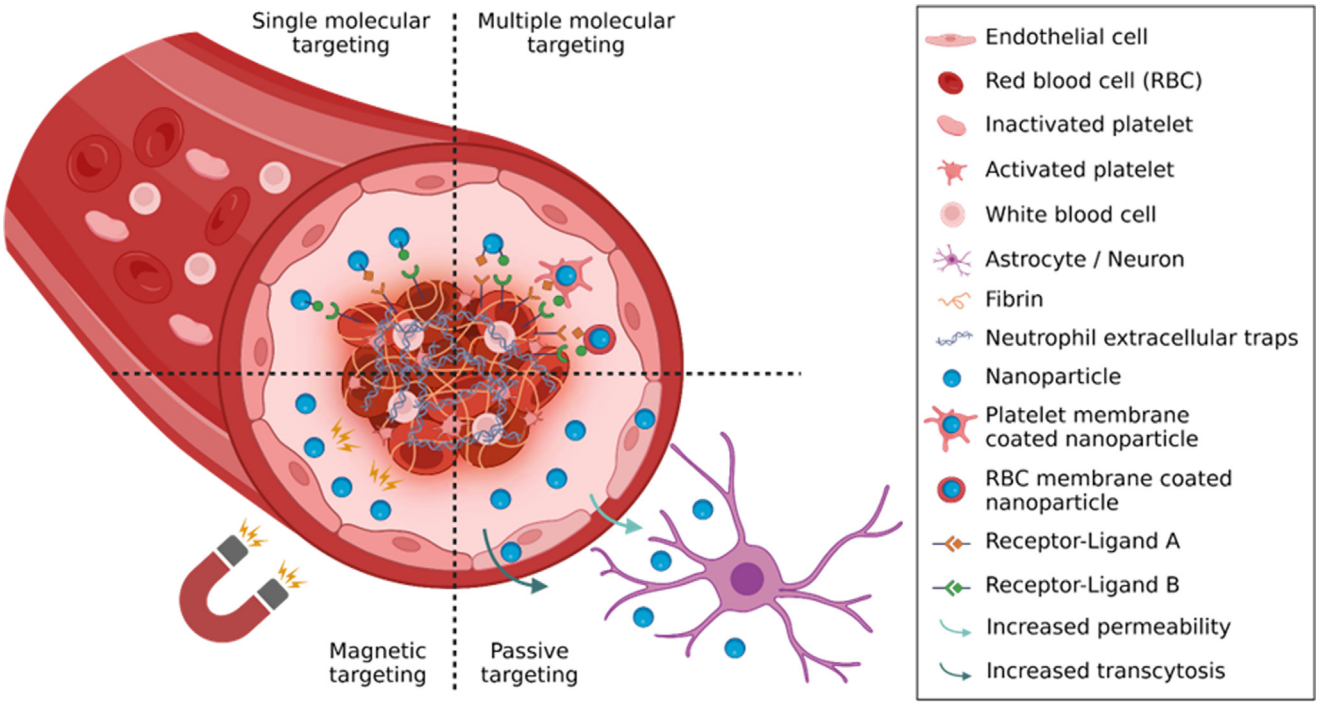


Fig. 2. The different targeting strategies for NP-related stroke treatment and diagnosis.

fibronectin complexes (and not fibrin alone), to allow the specific targeting of thrombi. This was incorporated in a transferrin-based nanocage to deliver C-terminal encoded microplasmin (and produced thanks to a single transgene expression). This system was validated *in vitro* for their clot-binding properties. In the murine arterial thrombus or deep vein thrombosis models, they showed a 50% reduction of thrombosis, in comparison to non-targeted, non-loaded nanocages, or targeted microplasmin without the nanocage construct (Seo et al., 2018).

Nevertheless, some approaches aim not at dissolving the clot, but rather alleviating the damage of ischemia, therefore requiring targeting to the ischemic tissue. While the leakiness of the BBB can be exploited to deliver certain drugs with NPs (Yuan et al., 2021), some authors increase the specificity of drug delivery to the damaged tissue by adding targeting moieties to ischemic regions (Wang et al., 2015), such as Zhang *et al.* who described in 2022 antioxidant NPs targeting CXCR4, a biomarker of ischemic cells in the brain, thanks to a small antagonist molecule, AMD3100. The resulting NPs were shown to significantly accumulate in the ischemic region with high reduction (50%) of the infarct region and significant neurological recovery compared to non-targeted NPs in mice stroke models (Zhang et al., 2022).

Therefore, there is no single gold standard biomarker for thrombus targeting. Instead, multiple biomarkers have been identified. Appropriate targeting strategies should be carefully chosen by identifying the target area: the clot itself, the ischemic tissue, or a single cell type for example.

Multiple molecular targeting

Multiple molecule grafting

All the targeting strategies mentioned above involve only one targeting agent and one biomarker. However, recent papers proposed alternative strategies, including grafting more than one targeting moiety at the NP surface to increase either their specificity or their accumulation at the thrombus site (Fig. 2*)*. Sun *et al.* designed liposomes coated with either platelet-binding peptides (PBP), fibrin-binding peptides (FBP) or a combination of them (PBP + FBP), to compare their thrombus targeting efficacy (Sun et al., 2020). *In vitro,* and on the mouse carotid artery thrombus model, they showed that with a lower total peptide concentration, combination targeting allowed a greater accumulation to the clot than targeting with PBP or FBP only, which can be explained by the possible multiple interaction with receptors or clot components. This approach may also enhance the targeting specificity to acute ischemic stroke thrombi which are made up of a dense outer shell containing mainly fibrin, VWF, and aggregated platelets (Di Meglio et al., 2019). In addition, their results proved that targeting can be impaired when ligand density is too high, and they suggested a role of the steric hindrance between the targeting agent and its target. Rather than targeting different components of the thrombus, several articles proposed to target only platelets with two different peptides grafted, RGD (GPIIb/IIIa binding) and EWVDV (P-selectin binding). In two different articles for respectively thrombus treatment and thrombus imaging, the combination of these peptides increased the accumulation of NPs at the thrombus site, compared to RGD or EWVDV decoration only (Pawlowski et al., 2017; Zhang et al., 2019). Indeed, Pawlowski *et al.* demonstrated *in vitro* in a microfluidic dynamic flow experiment that the peptide combination enhanced the targeting to platelet-rich thrombus, doubling the retention onto platelets, compared to either one (Pawlowski et al., 2017). However, instead of targeting platelet-rich clots, fibrin or erythrocyte-targeted NPs would be preferable in the case of stroke, considering they are the major components of the associated clots (Jolugbo and Ariëns, 2021; Mereuta et al., 2021).

Grafting several molecules can also be a strategy to sequentially reach different targets in ischemic stroke (Zhao et al., 2016; Xu et al., 2019). For instance, by decorating liposomal nanocarriers with T7 peptide and stroke homing peptide (SHp), Zhao *et al.* aimed to cross the BBB, and then target ischemic neurons to deliver ZL006, a novel promising neuroprotective agent (Zhao et al., 2016). Their coating combination enabled nanocarriers to accumulate 1.5 times more in the ischemic brain than with T7 alone and reduced the infarction volume by approximately 30% compared to coating with T7 or SHp alone, in a MCAO/R model on rats.

All things considered, grafting several targeting molecules can be performed to improve thrombus homing, to selectively select certain thrombi, or reach sequentially different targets.

Cellular membrane coating

Some groups have described a simple solution for NP targeting without having to settle for one or more biomarkers: by leveraging the cellular membrane of critically chosen cells, they addressed both the circulation stabilization (stealth) of their NPs and homing to the clot or the ischemic area.

Based on the process behind platelet aggregation and clot formation, the platelet membrane coating of NPs was assessed (Xu et al., 2019, 2020; Yu et al., 2022). For instance, Xu *et al.* described polymeric NPs coated with murine platelet membrane to deliver rtPA (PcNP) and compared them to erythrocyte-membrane coated control NPs (RcNP). They showed clear thrombus targeting of PcNPs vs. RcNPs in multiple murine thrombotic disease models, e.g., evidenced in a pulmonary embolism model with a significant fluorescence accumulation to the lungs compared to RcNPs. Moreover, they evidenced that while rtPA alone had a similar thrombolysis rate to their rtPA-loaded PcNP in mesenteric artery thrombosis mice models during thrombus formation, only the targeted NPs could elicit thrombolysis once the clot was fully formed. Finally, they demonstrated a clear enhancement of neurological and survival outcomes of PcNP-PA in comparison to free rtPA in transient stroke murine models (Xu et al., 2020). Others took advantage of the homing properties of platelet membranes to accumulate at the stroke site. Xu *et al.* developed in 2019 a nanoconstruct where rtPA was delivered after the thrombin-mediated cleavage of its linker to the NP, which in turn facilitated the exposure of the Tat peptide, secondary targeting of the endothelium, and crossing of the BBB for the antioxidant delivery. These NPs consisted of neuroprotectant (ZL006e) and dextran. It was shown that these NPs could accumulate on blood clots and have *in vitro* and *in vivo* enhanced thrombolysis compared to free drugs: the infarct volume was reduced to 20% compared to approximately 60% for non-cleavable NPs or free drug. Furthermore, the sequential targeting and thrombin dependent delivery significantly reduced the infarct area in mice stroke models in comparison to the free drugs (Xu et al., 2019).

Notably, other cellular coatings could be used to reach different targets. For instance, Ma *et al.* described in 2019 polymeric NPs coated with neural stem cell (NSC) membrane to deliver an anti-edema drug through the BBB membrane at the stroke site. However, they further strengthened the design by using CXCR4-overexpressing NSCs membranes and showed that it relied on the interaction between CXCR4 and SDF-1 (enriched in the ischemic microenvironment) to further enhance drug delivery and improve neurological recovery in a mouse stroke model compared to classic NSC membrane-coated NPs (Ma et al., 2019). Comparable approaches relied for example on cellular membrane from highly brain-metastatic tumor 4T1 cells (from a breast tumor cell line) to target the brain ischemic tissue and noted a significant neurological improvement, in comparison to non-membrane-coated NPs in murine models. These coated NPs accumulated three times more in the brain ischemic region than untargeted NPs (He et al., 2021). Macrophage membrane coating has also been used to increase targeting and disguise from immune system cells. For instance, macrophage membrane coated manganese dioxide NPs targeted endothelial cell adhesion molecules, thus allowing ROS scavenging, neuroprotection, and macrophage-type polarization (Li et al., 2021).

However, key aspects must be taken into account when resorting to cellular targeting: as discussed by Xu *et al.*, provenance of the cell membrane can play a major role in their tolerability by the host body, and human leukocyte antigen (HLA) matching could be an issue for scaling-up these therapies (Xu et al., 2020). On the other hand, using platelet membrane to deliver NPs with platelet-affecting drugs can prove ineffective: as demonstrated by Yi *et al.* in 2020, who had to use erythrocyte membrane functionalized with CREKA peptide (for fibrin targeting) instead of platelet membrane since they aimed at delivering tirofiban, a GPIIb/IIIa antagonist which prevents platelets aggregation in thrombi and thus impaired the targeting of platelet membrane coated NPs (Zhao et al., 2020).

Magnetic targeting

Over the past two decades, magnetic NPs have been increasingly used for biomedical applications (Fig. 2). This can be explained by their numerous interesting properties, including their magnetic manipulability. Indeed, by applying an external magnetic field near the brain ischemic region, the circulating magnetic NPs can accumulate there. Ma *et al.* tested the effects of rtPA linked through carbodiimide-mediated amide bound to polyacrylic acid-coated magnetite (PAA–MNP) NPs. Positive results were obtained *in vitro* and *in vivo*, in a rat embolic model of iliac artery occlusion. The PAA–MNP–rtPA under magnetic guidance along the artery restored the iliac blood flow, while control groups and free rtPA showed no improvement on hemodynamics (Ma et al., 2009). Hu *et al.* designed rtPA-coated iron oxide microrods (rtPA-MRs) to target the cerebral thrombus and dissolve it through combined fibrinolysis and mechanical stimulation by an external rotating magnetic field (RMF) (Hu et al., 2018). On a distal MCAO stroke mouse model, the authors found that the microrods could efficiently target the brain clot by placing a magnet near the distal middle cerebral artery area. Further, the blood flow was restored in 25 minutes with rtPA-MRs at 0.13 mg/kg rtPA accompanied by RMF, compared to the 85 minutes needed with free rtPA at 10 mg/kg. Thus, their nanosystem could perform a more efficient thrombolysis with approximately 100 times fewer rtPA. In addition to fibrinolytic agents, magnetic guidance can be used to deliver neuroprotectants to the stroke region and thus limit the cerebral infarction. In their work, Kim *et al.* tested MSC-derived nanovesicles encapsulating iron oxide NPs (IONPs) (Kim et al., 2020). In MCAO/R rat models, they obtained a 5.1-fold higher accumulation of their NPs at the ischemic lesion by magnetic stimulation in comparison to unstimulated ones. Furthermore, IONPs enabled a significant reduction of the infarcted volume through the angiogenic, anti-apoptotic and anti-inflammation properties of the MSC nanovesicles. Nonetheless, the clinical translatability of this approach needs further improvements: in this study, the helmet which enabled the magnetic guidance was kept 3 days on mice. Consequently, it is essential to refine and enhance this technique before considering its application in human use. To further increase the targeting efficacy to stroke lesions, Li's group loaded IONPs and L-arginine (for stimulation of NO generation) in platelet-membrane-based nanovesicles. Their results on a Rose Bengal induced mouse stroke model demonstrated that the magnetic guidance of NPs could increase the targeting compared to platelet membrane alone and allowed a faster blood flow recovery through NO-mediated vasodilation (Li et al., 2020). Despite the efficacy of magnetic targeting, one should be aware of the remaining challenges for the transfer to humans: for example, the type of magnet to use and how to implement its use with the human body. Optimized magnets and mathematical models are necessary to predict the movement of magnetic NPs in biological fluids, besides the regulatory approvals that will be required (Shapiro et al., 2015).

Passive targeting

In most stroke patients, there is a loss of the BBB integrity due to damaged tight junctions, which results in enhanced BBB permeability (Nian et al., 2020). This pathological state can be used to increase the BBB crossing of circulating NPs in the ischemic region compared to the healthy one. This is the case in Yuan *et al.* study, where they showed a 33% higher accumulation of oligosaccharide NPs in the ischemic brain than in the healthy tissue in a MCAO/R mouse model, only through passive targeting (Yuan et al., 2021) (Fig. 2). This strategy is particularly interesting to deliver neuroprotective agents.

In addition to this enhanced permeability, the BBB presents a higher rate of transcytosis in stroke conditions which can additionally enhance the passive targeting of ischemia (Knowland et al., 2014; Yuan et al., 2021). Although these strategies are less effective than active targeting, they don't require any specific coating, thus limiting the complexity of the nanosystem injected to the patient and making their production and approval easier.

Clinical studies

As described above, there is a broad amount of *in vitro* and preclinical studies using therapeutic agents combined with NPs, to tackle ischemic stroke (Blanco et al., 2015; Sarmah et al., 2021). However, to our knowledge, only clinical studies based on the use of USPIOs have been performed as detectors of stroke lesions compared to the conventional gadolinium-enhanced MRI (Saleh et al., 2004; Tang et al., 2009). Based on their size, SPIOs are phagocytosed by cells of the reticuloendothelial system in the liver and the spleen leading to rapid clearance from the peripheral circulation, while USPIOs are taken up by cells of the mononuclear phagocyte system and can circulate longer, promoting the interaction with phagocyte populations in the blood and lymph nodes. Among USPIOs' specificities, one can also mention T2-weighted tissue hypo-enhancement and the possibility to localize in macrophage-mediated inflamed areas, increasing the potential use in targeted imaging of inflammatory disease states (Farinha et al., 2021). USPIOs as contrast agents have been tested to enhance MRI for macrophage imaging in human ischemic stroke lesions (Saleh et al., 2004). USPIOs were infused one week after symptom onset, and 2 follow-up scans were performed 24 hours and 48 hours post-infusion. The presence of USPIOs in macrophages allowed the visualization of MRI signal variations such as vessel changes (signal loss in T2 images) and brain parenchymal enhancement (T1 images). USPIO-enhanced MRI may provide an *in vivo* indication of cellular inflammation in stroke and other neuroinflammatory diseases, with neurological effects, that involve microglial activation and blood macrophage recruitment. Another clinical trial tested the effects of 2 doses (10 mg and 80 mg) of atorvastatin on carotid plaque inflammation, determined by USPIO-enhanced carotid MRI (Tang et al., 2009). Patients with carotid stenosis and intraplaque accumulation of USPIO on MRI were treated with atorvastatin daily for 12 weeks. The primary endpoint was represented by a change from baseline in MRI signal intensity at 6 and 12 weeks. A significant reduction in USPIO-defined inflammation was observed in the 80 mg group at both time points. Additionally, this dose significantly reduced total cholesterol and low-density lipoproteins at 12 weeks. These trials support the USPIO-enhanced MRI methodology as a successful and timely imaging detection for stroke diagnosis with the first trial, and for the screening and assessment of the therapeutic response to anti-inflammatory interventions in patients with atherosclerotic lesions, typical in stroke patients.

With the goal of improving functional recovery and limiting ischemic damage, clinical trials for stroke patients tested the potential neuroprotection of DDFPe for hemorrhagic shock and/or traumatic brain injury (Li et al., 2022a). After promising results obtained in preclinical studies in rat and rabbit stroke models (Culp et al., 2015; Fitzgerald et al., 2015), DDFPe was intravenously injected in acute ischemic stroke patients, starting within 12 hours of symptom onset, and appeared to be safe at all doses tested. Although earlier DDFPe

treatment seemed promising and clinical outcomes were observed, the small sample size limited the significance of differences (Culp et al., 2019).

Other clinical trials on stroke focused on EVs as potential biomarkers (Gualerzi et al., 2021; Bang et al., 2022; 2023). The detection of cell-derived structures, such as EVs, is based on the application of surface plasmon resonance imaging-based biosensors. Blood EVs from stroke patients could reveal differences in cell types and may be useful to identify new biomarkers for the profiling of stroke patients with the final aim of reaching a rehabilitation and regenerative personalized therapy (Gualerzi et al., 2021; Bang et al., 2023). Investigating the composition of EVs from stroke patients could also fuel the improvement and the characterization of targeting moieties for NPs, reducing the immune system trapping and increasing the half-life of drugs (Duong et al., 2023).

Recent clinical trials investigated tenecteplase, the emergency treatment of myocardial infarction and pulmonary emboli, as potential stroke therapy. Interestingly, compared to the approved form alteplase, already used for ischemic stroke, it has a longer half-life, higher fibrin specificity, less systemic depletion of circulating fibrinogen, and higher resistance to plasminogen activator inhibitor (see for e.g. (Bivard et al., 2022; Li et al., 2022a; Rehman et al., 2023)). In further studies, since it may be soon approved for stroke therapy, tenecteplase could be a promising agent for the development of new nanomedicines that must meet quality and safety requirements before definition and starting of clinical trials.

Nanomedicine appears suited to answer the current limitations in the clinical care for stroke patients. Over the years, multiple approaches have demonstrated how a broad range of NPs could be manufactured with different configurations, including inorganic and organic materials, as well as biologically derived components, and boost imaging efficiency and therapeutic efficacy in thrombolysis and neuroprotection. However, to date, these promising results remain mostly limited to preclinical studies with few successful translations to clinical trials. From the articles described here, some key aspects seem to emerge and may be taken into account to overcome this gap. Standardization of both efficacy and biosafety assessments might improve visibility among the numerous approaches explored. For the former, several groups resort to simple, non-brain specific animal models such as the mouse mesenteric vein, while the objective is to prove efficacy for stroke application, where some more adequate models exist. As for biosafety, it draws major challenges related to NPs' degradation and accumulation in the body, especially since NPs often form complexes which might be more difficult to bring through clinical approval than simpler designs. Consequently, in order to breach these obstacles, NPs with robust production pathways, scalable and made using GRAS (Generally Recognized As Safe) materials, while preferring green chemistry when possible, may have the best chances to finally reach clinical applications.

Ethics statement

The authors Pierre Sarfati, Thibault De La Taille, Corinne Portioli, Raffaele Spanò, Yoann Lalatonne, Paolo Decuzzi, and Cédric Chauvierre have read and have abided by the statement of ethical standards for manuscripts submitted to Neuroscience.

Declaration of competing interest

The authors declare that they have no known competing financial interests or personal relationships that could have appeared to influence the work reported in this paper.

CRediT authorship contribution statement

Pierre Sarfati: Conceptualization. **Thibault De La Taille:** Conceptualization. **Corinne Portioli:** Conceptualization. **Raffaele Spanò:** Conceptualization. **Yoann Lalatonne:** Advising for inorganic nanoparticle application. **Paolo Decuzzi:** Supervision, Funding acquisition. **Cédric Chauvierre:** Supervision, Funding acquisition.

Acknowledgements

Authors thank INSERM, Université Paris Cité, Université Sorbonne Paris Nord, the ANR "FightClot" ANR-20-CE18-0005-01; the Fondazione Istituto Italiano di Tecnologia in Genova (Italy), and the Marie Sklodowska-Curie Action COFUND - 2018 "MINDED" (Award Number: 754490) for the financial support.

References

Abenojar, E.C., Wickramasinghe, S., Bas-Concepcion, J., Samia, A.C.S., 2016. Structural effects on the magnetic hyperthermia properties of iron oxide nanoparticles. Prog Nat Sci Mater Int 26, 440–448.

Ahmad, S., Truran, S., Karamanova, N., Kindelin, A., Lozoya, M., Weissig, V., Emerson, H., Griffiths, D.R., Vail, T., Lifshitz, J., Ducruet, A.F., Migrino, R.Q., 2022. Nanoliposomes reduce stroke injury following middle cerebral artery occlusion in mice. Stroke 53, 2023.

Akbarzadeh, A., Rezaei-Sadabady, R., Davaran, S., Joo, S.W., Zarghami, N., Hanifehpour, Y., Samiei, M., Kouhi, M., Nejati-Koshki, K., 2013. Liposome: classification, preparation, and applications. Nanoscale Res Lett 8, 102.

Al-Ahmady, Z.S., Jasim, D., Ahmad, S.S., Wong, R., Haley, M., Coutts, G., Schiessl, I., Allan, S.M., Kostarelos, K., 2019. Selective liposomal transport through blood brain barrier disruption in ischemic stroke reveals two distinct therapeutic opportunities. ACS Nano 13, 12470–12486.

Bachelet, L., Bertholon, I., Lavigne, D., Vassy, R., Jandrot-Perrus, M., Chaubet, F., Letourneur, D., 2009. Affinity of low molecular weight fucoidan for P-selectin triggers its binding to activated human platelets. Biochim Biophys Acta 1790, 141–146.

Balfourier, A., Luciani, N., Wang, G., Lelong, G., Ersen, O., Khelfa, A., Alloyeau, D., Gazeau, F., Carn, F., 2020. Unexpected intracellular biodegradation and recrystallization of gold nanoparticles. Proc Natl Acad Sci U S A 117, 103–113.

Bang, O.Y., Kim, E.H., Cho, Y.H., Oh, M.J., Chung, J.-W., Chang, W.H., Kim, Y.-H., Yang, S.W., Chopp, M., 2022. Circulating extracellular vesicles in stroke patients treated with mesenchymal stem cells: a biomarker analysis of a randomized trial. Stroke 53, 2276–2286.

Bang, O.Y., Kim, E.H., Oh, M.J., Yoo, J., Oh, G.S., Chung, J.-W., Seo, W.-K., Kim, G.-M., Ahn, M.-J., Yang, S.W., Investigators of the OASIS-CANCER Study, 2023. Circulating extracellular-vesicle-incorporated microRNAs as potential biomarkers for ischemic stroke in patients with cancer. J Stroke 25, 251–265.

Bernardo-Castro, S., Albino, I., Barrera-Sandoval, Á.M., Tomatis, F., Sousa, J.A., Martins, E., Simões, S., Lino, M.M., Ferreira, L., Sargento-Freitas, J., 2021. Therapeutic nanoparticles for the different phases of ischemic stroke. Life 11, 482.

Bhatia, R., Hill, M.D., Shobha, N., Menon, B., Bal, S., Kochar, P., Watson, T., Goyal, M., Demchuk, A.M., 2010. Low rates of acute recanalization with intravenous recombinant tissue plasminogen activator in ischemic stroke. Stroke 41, 2254–2258.

Bhatti, R., Shakeel, H., Malik, K., Qasim, M., Khan, M.A., Ahmed, N., Jabeen, S., 2022. Inorganic nanoparticles: toxic effects, mechanisms of cytotoxicity and phytochemical interactions. Adv Pharm Bull 12, 757–762.

Bivard, A. et al, 2022. Tenecteplase versus Alteplase for Stroke Thrombolysis Evaluation Trial in the Ambulance (Mobile Stroke Unit-TASTE-A): protocol for a prospective randomised, open-label, blinded endpoint, phase II superiority trial of tenecteplase versus alteplase for ischaemic stroke patients presenting within 4.5 hours of symptom onset to the mobile stroke unit. BMJ Open 12, e056573.

Blanco, E., Shen, H., Ferrari, M., 2015. Principles of nanoparticle design for overcoming biological barriers to drug delivery. Nat Biotechnol 33, 941–951.

Bliss, T., Guzman, R., Daadi, M., Steinberg, G.K., 2007. Cell transplantation therapy for stroke. Stroke 38, 817–826.

Brown, A.T., Arthur, M.C., Nix, J.S., Montgomery, J.A., Skinner, R.D., Roberson, P.K., Borrelli, M., Culp, W.C., 2014. Dodecafluoropentane Emulsion (DDFPe) decreases stroke size and improves neurological scores in a permanent occlusion rat stroke model. Open Neurol J 8, 27–33.

Cao, W., Liu, Y., Ran, P., He, J., Xie, S., Weng, J., Li, X., 2021. Ultrasound-propelled Janus rod-shaped micromotors for site-specific sonodynamic thrombolysis. ACS Appl Mater Interfaces 13, 58411–58421.

Cheng, Y., Cheng, A., Jia, Y., Yang, L., Ning, Y., Xu, L., Zhong, Y., Zhuang, Z., Guan, J., Zhang, X., Lin, Y., Zhou, T., Fan, X., Li, J., Liu, P., Yan, G., Wu, R., 2021. pH-responsive multifunctional theranostic rapamycin-loaded nanoparticles for imaging and treatment of acute ischemic stroke. ACS Appl Mater Interfaces 13, 56909–56922.

Cocucci, E., Meldolesi, J., 2015. Ectosomes and exosomes: shedding the confusion between extracellular vesicles. Trends Cell Biol 25, 364–372.

Colasuonno, M., Palange, A.L., Aid, R., Ferreira, M., Mollica, H., Palomba, R., Emdin, M., Del Sette, M., Chauvierre, C., Letourneur, D., Decuzzi, P., 2018. Erythrocyte-inspired discoidal polymeric nanoconstructs carrying tissue plasminogen activator for the enhanced lysis of blood clots. ACS Nano 12, 12224–12237.

Culp, W.C., Brown, A.T., Lowery, J.D., Arthur, M.C., Roberson, P.K., Skinner, R.D., 2015. Dodecafluoropentane emulsion extends window for tPA therapy in a rabbit stroke model. Mol Neurobiol 52, 979–984.

Culp, W.C., Onteddu, S.S., Brown, A., Nalleballe, K., Sharma, R., Skinner, R.D., Witt, T., Roberson, P.K., Marsh, J.D., 2019. Dodecafluoropentane emulsion in acute ischemic stroke: a phase Ib/II randomized and controlled dose-escalation trial. J Vasc Interv Radiol JVIR 30, 1244–1250.e1.

Dadfar, S.M., Roemhild, K., Drude, N.I., von Stillfried, S., Knüchel, R., Kiessling, F., Lammers, T., 2019. Iron oxide nanoparticles: Diagnostic, therapeutic and theranostic applications. Adv Drug Deliv Rev 138, 302–325.

de Havenon, A., Sheth, K., Johnston, K.C., Delic, A., Stulberg, E., Majersik, J., Anadani, M., Yaghi, S., Tirschwell, D., Ney, J., 2021. Acute ischemic stroke interventions in the United States and racial, socioeconomic, and geographic disparities. Neurology 97, e2292–e2303.

Di Meglio, L., Desilles, J.-P., Ollivier, V., Nomenjanahary, M.S., Di Meglio, S., Deschildre, C., Loyau, S., Olivot, J.-M., Blanc, R., Piotin, M., Bouton, M.-C., Michel, J.-B., Jandrot-Perrus, M., Ho-Tin-Noé, B., Mazighi, M., 2019. Acute ischemic stroke thrombi have an outer shell that impairs fibrinolysis. Neurology 93, e1686–e1698.

Duan, X., Li, Y., 2013. Physicochemical characteristics of nanoparticles affect circulation, biodistribution, cellular internalization, and trafficking. Small 9, 1521–1532.

Duong, A., Parmar, G., Kirkham, A.M., Burger, D., Allan, D.S., 2023. Registered clinical trials investigating treatment with cell-derived extracellular vesicles: a scoping review. Cytotherapy 25, 939–945.

Farinha, P., Coelho, J.M.P., Reis, C.P., Gaspar, M.M., 2021. A comprehensive updated review on magnetic nanoparticles in diagnostics. Nanomaterials 11, 3432.

Feske, S.K., 2021. Ischemic stroke. Am J Med 134, 1457–1464.

Fitzgerald, R.T., Ou, X., Nix, J.S., Arthur, M.C., Brown, A.T., Skinner, R.D., Borrelli, M.J., Culp, W.C., 2015. Dodecafluoropentane emulsion delays and reduces MRI markers of infarction in a rat stroke model: a preliminary report. Magn Reson Imaging 33, 236–239.

Ghozy, S., Reda, A., Varney, J., Elhawary, A.S., Shah, J., Murry, K., Sobeeh, M.G., Nayak, S.S., Azzam, A.Y., Brinjikji, W., Kadirvel, R., Kallmes, D.F., 2022. Neuroprotection in acute ischemic stroke: a battle against the biology of nature. Front Neurol 13, 870141.

Gualerzi, A., Picciolini, S., Rodà, F., Bedoni, M., 2021. Extracellular vesicles in regeneration and rehabilitation recovery after stroke. Biology 10, 843.

Han, M., Zhang, Z., Liu, Z., Liu, Y., Zhao, H., Wang, B., Zhang, C., Shang, H., Li, Y., Wang, S., Xin, T., 2023. Three-dimensional-cultured MSC-derived exosome with hydrogel for cerebral ischemia repair. Biomater Adv 149, 213396.

He, W., Mei, Q., Li, J., Zhai, Y., Chen, Y., Wang, R., Lu, E., Zhang, X.-Y., Zhang, Z., Sha, X., 2021. Preferential targeting cerebral ischemic lesions with cancer cell-inspired nanovehicle for ischemic stroke treatment. Nano Lett 21, 3033–3043.

Heeremans, J.L., Prevost, R., Bekkers, M.E., Los, P., Emeis, J.J., Kluft, C., Crommelin, D. J., 1995. Thrombolytic treatment with tissue-type plasminogen activator (t-PA) containing liposomes in rabbits: a comparison with free t-PA. Thromb Haemost 73, 488–494.

Heras-Romero, Y., Morales-Guadarrama, A., Santana-Martínez, R., Ponce, I., Rincón-Heredia, R., Poot-Hernández, A.C., Martínez-Moreno, A., Urrieta, E., Bernal-Vicente, B.N., Campero-Romero, A.N., Moreno-Castilla, P., Greig, N.H., Escobar, M.L., Concha, L., Tovar-Y-Romo, L.B., 2022. Improved post-stroke spontaneous recovery by astrocytic extracellular vesicles. Mol Ther 30, 798–815.

Hu, J., Huang, S., Zhu, L., Huang, W., Zhao, Y., Jin, K., ZhuGe, Q., 2018. Tissue plasminogen activator-porous magnetic microrods for targeted thrombolytic therapy after ischemic stroke. ACS Appl Mater Interfaces 10, 32988–32997.

Huang, G., Zang, J., He, L., Zhu, H., Huang, J., Yuan, Z., Chen, T., Xu, A., 2022. Bioactive nanoenzyme reverses oxidative damage and endoplasmic reticulum stress in neurons under ischemic stroke. ACS Nano 16, 431–452.

Imamura, Y., Yamada, S., Tsuboi, S., Nakane, Y., Tsukasaki, Y., Komatsuzaki, A., Jin, T., 2016. Near-infrared emitting PbS quantum dots for in vivo fluorescence imaging of the thrombotic state in septic mouse brain. Molecules 21, 1080.

Institute for Health Metrics and Evaluation, 2022. GBD Results. Inst Health Metr Eval. Available at: https://www.healthdata.org/data-visualization/gbd-results [Accessed May 2, 2023].

Jolugbo, P., Ariëns, R.A.S., 2021. Thrombus composition and efficacy of thrombolysis and thrombectomy in acute ischemic stroke. Stroke 52, 1131–1142.

Juenet, M., Aid-Launais, R., Li, B., Berger, A., Aerts, J., Ollivier, V., Nicoletti, A., Letourneur, D., Chauvierre, C., 2018. Thrombolytic therapy based on fucoidan-functionalized polymer nanoparticles targeting P-selectin. Biomaterials 156, 204–216.

Kawata, H., Uesugi, Y., Soeda, T., Takemoto, Y., Sung, J.-H., Umaki, K., Kato, K., Ogiwara, K., Nogami, K., Ishigami, K., Horii, M., Uemura, S., Shima, M., Tabata, Y., Saito, Y., 2012. A new drug delivery system for intravenous coronary thrombolysis with thrombus targeting and stealth activity recoverable by ultrasound. J Am Coll Cardiol 60, 2550–2557.

Khlebtsov, N.G., 2008. Optics and biophotonics of nanoparticles with a plasmon resonance. Quantum Electron 38, 504.

Kim, B.H., Lee, N., Kim, H., An, K., Park, Y.I., Choi, Y., Shin, K., Lee, Y., Kwon, S.G., Na, H.B., Park, J.-G., Ahn, T.-Y., Kim, Y.-W., Moon, W.K., Choi, S.H., Hyeon, T., 2011. Large-scale synthesis of uniform and extremely small-sized iron oxide nanoparticles for high-resolution T1 magnetic resonance imaging contrast agents. J Am Chem Soc 133, 12624–12631.

Kim, H.Y., Kim, T.J., Kang, L., Kim, Y.-J., Kang, M.K., Kim, J., Ryu, J.H., Hyeon, T., Yoon, B.-W., Ko, S.-B., Kim, B.-S., 2020. Mesenchymal stem cell-derived magnetic extracellular nanovesicles for targeting and treatment of ischemic stroke. Biomaterials 243, 119942.

Kim, J.-Y., Kim, J.-K., Park, J.-S., Byun, Y., Kim, C.-K., 2009. The use of PEGylated liposomes to prolong circulation lifetimes of tissue plasminogen activator. Biomaterials 30, 5751–5756.

Kim, J.-Y., Ryu, J.H., Schellingerhout, D., Sun, I.-C., Lee, S.-K., Jeon, S., Kim, J., Kwon, I. C., Nahrendorf, M., Ahn, C.-H., Kim, K., Kim, D.-E., 2015. Direct imaging of cerebral thromboemboli using computed tomography and fibrin-targeted gold nanoparticles. Theranostics 5, 1098–1114.

Knowland, D., Arac, A., Sekiguchi, K.J., Hsu, M., Lutz, S.E., Perrino, J., Steinberg, G.K., Barres, B.A., Nimmerjahn, A., Agalliu, D., 2014. Stepwise recruitment of transcellular and paracellular pathways underlies blood-brain barrier breakdown in stroke. Neuron 82, 603–617.

Korin, N., Kanapathipillai, M., Matthews, B., Crescente, M., Brill, A., Mammoto, T., Ghosh, K., Jurek, S., Bencherif, S., Bhatta, D., Coşkun, A., Feldman, C., Wagner, D., Ingber, D., 2012. Shear-activated nanotherapeutics for drug targeting to obstructed blood vessels. Science 337, 738–742.

Lee, T.-R., Choi, M., Kopacz, A.M., Yun, S.-H., Liu, W.K., Decuzzi, P., 2013. On the near-wall accumulation of injectable particles in the microcirculation: smaller is not better. Sci Rep 3, 2079.

Lee, Y., Lee, J., Kim, M., Kim, G., Choi, J.S., Lee, M., 2021. Brain gene delivery using histidine and arginine-modified dendrimers for ischemic stroke therapy. J Control Release Off J Control Release Soc 330, 907–919.

Li, M., Li, J., Chen, J., Liu, Y., Cheng, X., Yang, F., Gu, N., 2020. Platelet membrane biomimetic magnetic nanocarriers for targeted delivery and in situ generation of nitric oxide in early ischemic stroke. ACS Nano 14, 2024–2035.

Li, S., Campbell, B.C.V., Schwamm, L.H., Fisher, M., Parsons, M., Li, H., Pan, Y., Wang, Y., TRACE II investigators, 2022a. Tenecteplase Reperfusion therapy in Acute ischaemic Cerebrovascular Events-II (TRACE II): rationale and design. Stroke Vasc Neurol 7, 71–76.

Li, X., Han, Z., Wang, T., Ma, C., Li, H., Lei, H., Yang, Y., Wang, Y., Pei, Z., Liu, Z., Cheng, L., Chen, G., 2022b. Cerium oxide nanoparticles with antioxidative neurorestoration for ischemic stroke. Biomaterials 291, 121904.

Li, Y., Liu, B., Chen, Y., Quan, X., Han, Y., Zheng, Y., Zhao, Y., 2021. Extracellular vesicle application as a novel therapeutic strategy for ischemic stroke. Transl Stroke Res.

Liao, J., Ren, X., Yang, B., Li, H., Zhang, Y., Yin, Z., 2019. Targeted thrombolysis by using c-RGD-modified N,N,N-trimethyl chitosan nanoparticles loaded with lumbrokinase. Drug Dev Ind Pharm 45, 88–95.

Ma, J., Zhang, S., Liu, J., Liu, F., Du, F., Li, M., Chen, A.T., Bao, Y., Suh, H.W., Avery, J., Deng, G., Zhou, Y., Wu, P., Sheth, K., Wang, H., Zhou, J., 2019. Targeted drug delivery to stroke via chemotactic recruitment of nanoparticles coated with membrane of engineered neural stem cells. Small 15, 1902011.

Ma, Y.-H., Wu, S.-Y., Wu, T., Chang, Y.-J., Hua, M.-Y., Chen, J.-P., 2009. Magnetically targeted thrombolysis with recombinant tissue plasminogen activator bound to polyacrylic acid-coated nanoparticles. Biomaterials 30, 3343–3351.

Marsh, J.N., Hu, G., Scott, M.J., Zhang, H., Goette, M.J., Gaffney, P.J., Caruthers, S.D., Wickline, S.A., Abendschein, D., Lanza, G.M., 2011. A fibrin-specific thrombolytic nanomedicine approach to acute ischemic stroke. Nanomed 6, 605–615.

Marsh, J.N., Senpan, A., Hu, G., Scott, M.J., Gaffney, P.J., Wickline, S.A., Lanza, G.M., 2007. Fibrin-targeted perfluorocarbon nanoparticles for targeted thrombolysis. Nanomed 2, 533–543.

Mereuta, O.M. et al, 2021. Characterization of the 'white' appearing clots that cause acute ischemic stroke. J Stroke Cerebrovasc Dis 30, 106127.

Moore, T.L., Cook, A.B., Bellotti, E., Palomba, R., Manghnani, P., Spanò, R., Brahmachari, S., Di Francesco, M., Palange, A.L., Di Mascolo, D., Decuzzi, P., 2022. Shape-specific microfabricated particles for biomedical applications: a review. Drug Deliv Transl Res 12, 2019–2037.

Moore, T.L., Pannuzzo, G., Costabile, G., Palange, A.L., Spanò, R., Ferreira, M., Graziano, A.C.E., Decuzzi, P., Cardile, V., 2023. Nanomedicines to treat rare neurological disorders: The case of Krabbe disease. Adv Drug Deliv Rev 203, 115132.

Mosconi, M.G., Paciaroni, M., 2022. Treatments in ischemic stroke: current and future. Eur Neurol 85, 349–366.

Müller, K., Fedosov, D.A., Gompper, G., 2014. Margination of micro- and nano-particles in blood flow and its effect on drug delivery. Sci Rep 4, 4871.

Navya, P.N., Daima, H.K., 2016. Rational engineering of physicochemical properties of nanomaterials for biomedical applications with nanotoxicological perspectives. Nano Converg 3, 1.

Nian, K., Harding, I.C., Herman, I.M., Ebong, E.E., 2020. Blood-brain barrier damage in ischemic stroke and its regulation by endothelial mechanotransduction. Front Physiol 11.

Niu, Y., Tan, H., Li, X., Zhao, L., Xie, Z., Zhang, Y., Zhou, S., Qu, X., 2020. Protein-carbon dot nanohybrid-based early blood-brain barrier damage theranostics. ACS Appl Mater Interfaces 12, 3445–3452.

Pallavicini, P., Chirico, G., Taglietti, A., 2021. Harvesting light to produce heat: photothermal nanoparticles for technological applications and biomedical devices. Chem – Eur J 27, 15361–15374.

Pan, Y., Ren, X., Wang, S., Li, X., Luo, X., Yin, Z., 2017. Annexin V-conjugated mixed micelles as a potential drug delivery system for targeted thrombolysis. Biomacromolecules 18, 865–876.

Pawlowski, C.L., Li, W., Sun, M., Ravichandran, K., Hickman, D., Kos, C., Kaur, G., Sen Gupta, A., 2017. Platelet microparticle-inspired clot-responsive nanomedicine for targeted fibrinolysis. Biomaterials 128, 94–108.

Pellow, C., Acconcia, C., Zheng, G., Goertz, D.E., 2018. Threshold-dependent nonlinear scattering from porphyrin nanobubbles for vascular and extravascular applications. Phys Med Biol 63, 215001.
Portioli, C., Benati, D., Pii, Y., Bernardi, P., Crucianelli, M., Santucci, S., Bentivoglio, M., Passacantando, M., 2013. Short-term biodistribution of cerium oxide nanoparticles in mice: focus on brain parenchyma. Nanosci Nanotechnol Lett 5, 1174–1181.
Quan, X., Liang, X., Ding, Y., Han, Y., Li, J., Yuan, M., Li, Y., Yuan, Z., Wang, R., Zhao, Y., 2023. Cryo-shocked platelet coupled with ROS-responsive nanomedicine for targeted treatment of thromboembolic disease. ACS Nano 17, 6519–6533.
Refaat, A., Del Rosal, B., Palasubramaniam, J., Pietersz, G., Wang, X., Peter, K., Moulton, S.E., 2021. Smart delivery of plasminogen activators for efficient thrombolysis; recent trends and future perspectives. Adv Ther 4, 2100047.
Rehman, A.U., Mohsin, A., Cheema, H.A., Zahid, A., Rehman, M.E.U., Ameer, M.Z., Ayyan, M., Ehsan, M., Shahid, A., Aemaz Ur Rehman, M., Shah, J., Khawaja, A., 2023. Comparative efficacy and safety of tenecteplase and alteplase in acute ischemic stroke: A pairwise and network meta-analysis of randomized controlled trials. J Neurol Sci 445, 120537.
Richard, S., Eder, V., Caputo, G., Journé, C., Ou, P., Bolley, J., Louedec, L., Guenin, E., Motte, L., Pinna, N., Lalatonne, Y., 2016. USPIO size control through microwave nonaqueous sol-gel method for neoangiogenesis T2 MRI contrast agent. Nanomed 11, 2769–2779.
Saleh, A., Schroeter, M., Jonkmanns, C., Hartung, H.-P., Mödder, U., Jander, S., 2004. In vivo MRI of brain inflammation in human ischaemic stroke. Brain J Neurol 127, 1670–1677.
Sani, A., Cao, C., Cui, D., 2021. Toxicity of gold nanoparticles (AuNPs): A review. Biochem Biophys Rep 26.
Sarmah, D., Banerjee, M., Datta, A., Kalia, K., Dhar, S., Yavagal, D.R., Bhattacharya, P., 2021. Nanotechnology in the diagnosis and treatment of stroke. Drug Discov Today 26, 585–592.
Seo, J., Al-Hilal, T.A., Jee, J.-G., Kim, Y.-L., Kim, H.-J., Lee, B.-H., Kim, S., Kim, I.-S., 2018. A targeted ferritin-microplasmin based thrombolytic nanocage selectively dissolves blood clots. Nanomed Nanotechnol Biol Med 14, 633–642.
Shapiro, B., Kulkarni, S., Nacev, A., Muro, S., Stepanov, P.Y., Weinberg, I.N., 2015. Open challenges in magnetic drug targeting. Wiley Interdiscip Rev Nanomed Nanobiotechnol 7, 446–457.
Sheth, K.N., Elm, J.J., Beslow, L.A., Sze, G.K., Kimberly, W.T., 2016. Glyburide advantage in malignant edema and stroke (GAMES-RP) trial: Rationale and design. Neurocrit Care 24, 132–139.
Singh, N., Varma, A., Verma, A., Maurya, B.N., Dash, D., 2016. Relief from vascular occlusion using photothermal ablation of thrombus with a multimodal perspective. Nano Res 9, 2327–2337.
Soenen, S., Rivera Gil, P., Montenegro, J.M., Parak, W., De Smedt, S., Braeckmans, K., 2011. Cellular toxicity of inorganic nanoparticles: common aspects and guidelines for improved nanotoxicity evaluation. Nano Today 6, 446–465.
Strebhardt, K., Ullrich, A., 2008. Paul Ehrlich's magic bullet concept: 100 years of progress. Nat Rev Cancer 8, 473–480.
Sun, M., Miyazawa, K., Pendekanti, T., Razmi, A., Firlar, E., Yang, S., Shokuhfar, T., Li, O., Li, W., Gupta, A.S., 2020. Combination targeting of 'platelets + fibrin' enhances clot anchorage efficiency of nanoparticles for vascular drug delivery. Nanoscale 12, 21255–21270.
Sun, S., Lv, W., Li, S., Zhang, Q., He, W., Min, Z., Teng, C., Chen, Y., Liu, L., Yin, J., Zhu, B., Xu, M., Dai, D., Xin, H., 2023. Smart liposomal nanocarrier enhanced the treatment of ischemic stroke through neutrophil extracellular traps and cyclic guanosine monophosphate-adenosine monophosphate synthase-stimulator of interferon genes (cGAS-STING) pathway inhibition of ischemic penumbra. ACS Nano 17, 17845–17857.
Tang, T.Y., Howarth, S.P.S., Miller, S.R., Graves, M.J., Patterson, A.J., U-King-Im, J.-M., Li, Z.Y., Walsh, S.R., Brown, A.P., Kirkpatrick, P.J., Warburton, E.A., Hayes, P.D., Varty, K., Boyle, J.R., Gaunt, M.E., Zalewski, A., Gillard, J.H., 2009. The ATHEROMA (Atorvastatin Therapy: Effects on Reduction of Macrophage Activity) Study. Evaluation using ultrasmall superparamagnetic iron oxide-enhanced magnetic resonance imaging in carotid disease. J Am Coll Cardiol 53, 2039–2050.
Voros, E., Cho, M., Ramirez, M., Palange, A.L., De Rosa, E., Key, J., Garami, Z., Lumsden, A.B., Decuzzi, P., 2015. TPA immobilization on iron oxide nanocubes and localized magnetic hyperthermia accelerate blood clot lysis. Adv Funct Mater 25, 1709–1718.
Vos, E.M., Geraedts, V.J., van der Lugt, A., Dippel, D.W.J., Wermer, M.J.H., Hofmeijer, J., van Es, A.C.G.M., Roos, Y.B.W.E.M., Peeters-Scholte, C.M.P.C.D., van den Wijngaard, I.R., 2022. Systematic review - combining neuroprotection with reperfusion in acute ischemic stroke. Front Neurol 13, 840892.
Wang, C., Sun, J., Chen, Q., Chen, J., Wan, H., Ni, Q., Yuan, H., Wu, J., Wang, Y., Sun, B., 2023. Application of nanotechnology-based products in stroke. ACS Chem Neurosci 14, 2405–2415.
Wang, S., Guo, X., Xiu, W., Liu, Y., Ren, L., Xiao, H., Yang, F., Gao, Y., Xu, C., Wang, L., 2020. Accelerating thrombolysis using a precision and clot-penetrating drug delivery strategy by nanoparticle-shelled microbubbles. Sci Adv 6, eaaz8204.
Wang, Z., Zhao, Y., Jiang, Y., Lv, W., Wu, L., Wang, B., Lv, L., Xu, Q., Xin, H., 2015. Enhanced anti-ischemic stroke of ZL006 by T7-conjugated PEGylated liposomes drug delivery system. Sci Rep 5, 12651.
Waris, A., Ali, A., Khan, A.U., Asim, M., Zamel, D., Fatima, K., Raziq, A., Khan, M.A., Akbar, N., Baset, A., Abourehab, M.A.S., 2022. Applications of various types of nanomaterials for the treatment of neurological disorders. Nanomaterials 12, 2140.
Wen, X., Wang, Y., Zhang, F., Zhang, X., Lu, L., Shuai, X., Shen, J., 2014. In vivo monitoring of neural stem cells after transplantation in acute cerebral infarction with dual-modal MR imaging and optical imaging. Biomaterials 35, 4627–4635.
Wu, H., Peng, B., Mohammed, F.S., Gao, X., Qin, Z., Sheth, K.N., Zhou, J., Jiang, Z., 2022. Brain targeting, antioxidant polymeric nanoparticles for stroke drug delivery and therapy. Small 18, 2107126.
Xu, J., Wang, X., Yin, H., Cao, X., Hu, Q., Lv, W., Xu, Q., Gu, Z., Xin, H., 2019. Sequentially site-specific delivery of thrombolytics and neuroprotectant for enhanced treatment of ischemic stroke. ACS Nano 13, 8577–8588.
Xu, J., Zhang, Y., Xu, J., Liu, G., Di, C., Zhao, X., Li, X., Li, Y., Pang, N., Yang, C., Li, Y., Li, B., Lu, Z., Wang, M., Dai, K., Yan, R., Li, S., Nie, G., 2020. Engineered nanoplatelets for targeted delivery of plasminogen activators to reverse thrombus in multiple mouse thrombosis models. Adv Mater 32, 1905145.
Yu, W., Yin, N., Yang, Y., Xuan, C., Liu, X., Liu, W., Zhang, Z., Zhang, K., Liu, J., Shi, J., 2022. Rescuing ischemic stroke by biomimetic nanovesicles through accelerated thrombolysis and sequential ischemia-reperfusion protection. Acta Biomater 140, 625–640.
Yuan, J., Li, L., Yang, Q., Ran, H., Wang, J., Hu, K., Pu, W., Huang, J., Wen, L., Zhou, L., Jiang, Y., Xiong, X., Zhang, J., Zhou, Z., 2021. Targeted treatment of ischemic stroke by bioactive nanoparticle-derived reactive oxygen species responsive and inflammation-resolving nanotherapies. ACS Nano.
Zenych, A., Fournier, L., Chauvierre, C., 2020. Nanomedicine progress in thrombolytic therapy. Biomaterials 258, 120297.
Zenych, A., Jacqmarcq, C., Aid, R., Fournier, L., Forero Ramirez, L.M., Chaubet, F., Bonnard, T., Vivien, D., Letourneur, D., Chauvierre, C., 2021. Fucoidan-functionalized polysaccharide submicroparticles loaded with alteplase for efficient targeted thrombolytic therapy. Biomaterials 277, 121102.
Zhang, H., Lin, S., McElroy, C.L., Wang, B., Jin, D., Uteshev, V.V., Jin, K., 2021a. Circulating pro-inflammatory exosomes worsen stroke outcomes in aging. Circ Res 129, e121–e140.
Zhang, S., Peng, B., Chen, Z., Yu, J., Deng, G., Bao, Y., Ma, C., Du, F., Sheu, W.C., Kimberly, W.T., Simard, J.M., Coman, D., Chen, Q., Hyder, F., Zhou, J., Sheth, K.N., 2022. Brain-targeting, acid-responsive antioxidant nanoparticles for stroke treatment and drug delivery. Bioact Mater 16, 57–65.
Zhang, Y., Liu, Y., Zhang, T., Wang, Q., Huang, L., Zhong, Z., Lin, J., Hu, K., Xin, H., Wang, X., 2021b. Targeted thrombolytic therapy with metal–organic-framework-derived carbon based platforms with multimodal capabilities. ACS Appl Mater Interfaces 13, 24453–24462.
Zhang, Y., Zhong, Y., Ye, M., Xu, J., Liu, J., Zhou, J., Wang, S., Guo, D., Wang, Z., Ran, H., 2019. Polydopamine-modified dual-ligand nanoparticles as highly effective and targeted magnetic resonance/photoacoustic dual-modality thrombus imaging agents. Int J Nanomed 14, 7155–7171.
Zhao, Y., Jiang, Y., Lv, W., Wang, Z., Lv, L., Wang, B., Liu, X., Liu, Y., Hu, Q., Sun, W., Xu, Q., Xin, H., Gu, Z., 2016. Dual targeted nanocarrier for brain ischemic stroke treatment. J Controlled Release 233, 64–71.
Zhao, Y., Xie, R., Yodsanit, N., Ye, M., Wang, Y., Gong, S., 2020. Biomimetic fibrin-targeted and H_2O_2-responsive nanocarriers for thrombus therapy. Nano Today 35, 100986.

ANNEX 4

Europäisches Patentamt | European Patent Office | Office européen des brevets

Acknowledgement of receipt

We hereby acknowledge receipt of your request for grant of a European patent as follows:

Submission number	1000514279	
Application number	EP23307118.2	
File No. to be used for priority declarations	EP23307118	
Date of receipt	01 December 2023	
Your reference	B2302827EP	
Applicant	Institut National de la Santé et de la Recherche Médicale	
Country	FR	
Title	Crosslinked polysaccharide nanoparticles	
Documents submitted	package-data.xml	ep-request.xml
	application-body.xml	ep-request.pdf (5 p.)
	SPECEPO-1.pdf\CHIM23270 CHAUVIERRE - Draft_20231201.pdf (23 p.)	
Submitted by	CN=Catherine Touati 8517	
Method of submission	Online	
Date and time receipt generated	01 December 2023, 15:05:27 (CET)	
Official Digest of Submission	D6:8D:36:84:66:2E:BA:A1:9E:04:4E:83:88:8E:9A:55:37:06:1F:71	

/INPI, section dépôt/

Crosslinked polysaccharide nanoparticles

Technical domain

The present disclosure relates to crosslinked polysaccharide nanoparticles obtained via an emulsion.

Background

Cardiovascular diseases are held responsible for a third of all deaths worldwide, leading with heart attacks and strokes, among which the latter is responsible for over 12.2 million cases each year. Notably, around 80 % of strokes are of ischemic nature, and the recommended care for this pathological blood clot (thrombus) is the quick systemic injection of a fibrinolytic drug, rtPA, which suffers from severe side effects, offers a short therapeutic window, and does not guarantee recanalization. It was also shown that the more complex nature of thrombi impedes their lysis.

It is therefore an object of the present disclosure to provide a biocompatible nanosystem targeting the thrombus, to deliver drugs for improved blood clot bursting and improved recovery.

Document WO2021249974A1 discloses cross-linked polysaccharide particles that may be functionalized with fucoidan and loaded with rtPA.

The particles described in WO2021249974A1 are biocompatible particles, prepared by the inverse emulsion / crosslinking method. When these particles were functionalized with fucoidan, a polysaccharide, which was demonstrated to have high affinity to P-selectin, a marker of activated platelets and endothelial cells, they could be used for thrombus targeting. It was shown in WO2021249974A1, that rtPA could be loaded in the particles, and its amidolytic and fibrinolytic activities were maintained *in vitro* and *in vivo*. Thrombus targeting potential of these particles was validated in microfluidic assay under arterial and venous blood shear rates on recombinant P-selectin and activated platelet aggregates. The thrombolytic efficacy of the particles was tested in a murine model of acute ischemic stroke, revealing faster Middle Cerebral Artery recanalization and reduction in the brain infarct volume and blood-brain barrier permeability post-stroke, evidenced by laser speckle contrast imaging and MRI. Collectively, this proof-of-concept study demonstrated the potential of these particles for the precise treatment of acute thrombotic events.

However, the particles of WO2021249974A1 had several drawbacks. The size of the particles of WO2021249974A1 varied noticeably depending on the salinity of the dispersion medium and the particles were stable in a saline solution only if a surfactant was added to the saline solution. In WO2021249974A1 the sizes disclosed corresponds to measurements made in a saline solution in the presence of a surfactant. Particles sizes were higher when measured in pure water or in a saline solution

devoid of a surfactant (in this latter case, moreover, the particles were unstable). It was in fact not possible to obtain particles with an average size below 500 nm as measured in pure water or in a saline solution devoid of surfactant.

For therapeutic applications, however, smaller particles are advantageous as they allow better targeting and drug delivery (because of the higher surface over volume ratio). Due to margination of blood-borne objects in blood vessels, particles with size below 500 nm are also desired. Moreover, it is preferable that the particles are stable in saline conditions and in the absence of a surfactant.

Aiming to provide improved cross-linked polysaccharide particles that may be used as a drug delivery system, in particular for thrombus targeting and thrombolysis, the present disclosure provides novel particles with a smaller size. Moreover, it has been observed that the size of the particles does not vary depending on the ionic strength of the aqueous solution in which they are dispersed. Moreover, the particles are reliably obtained with a low polydispersity.

Summary

The method of the invention relies on the selection of a particular mix of surfactants that allows the formation of a suitable emulsion, that in its turn yields particles comprising a cross-linked polysaccharide matrix with a smaller size than in the prior art. Moreover, it has been observed that the size of the particles does not vary depending on the ionic strength of the aqueous solution in which they are dispersed and that the particles are stable in a saline aqueous solution even in the absence of added surfactant. Moreover, the particles are reliably obtained with a low polydispersity.

As such the present invention relates to the following item:

Item 0: Method for the preparation of particles comprising a cross-linked polysaccharide matrix, said method comprising the following steps:

a) providing an aqueous phase comprising the polysaccharide and a salt;

b) providing an oil phase comprising an oil as a solvent;

c) mixing the aqueous phase and the oil phase in presence of a mixture of a surfactant A and a surfactant B so as to obtain a water/oil (w/o) emulsion;

d) crosslinking the polysaccharide comprised in the dispersed aqueous phase to obtain the particles, wherein the crosslinking comprises the reaction between a crosslinking agent and the polysaccharide to obtain the polysaccharide matrix;

e) recovering the particles;

wherein the surfactant A is a nonionic surfactant comprising:

as a hydrophilic group, a polyethyleneglycol or a polyglycerol chain,

as a hydrophobic group, a polyester of a monohydroxylated fatty acid,

for example, surfactant A is polyglycerol polyricinoleate; and

wherein the surfactant B has a negative Cc value, for example, surfactant B is a nonionic surfactant having a negative Cc value, for example surfactant B is a nonionic ethoxylated surfactant having a negative Cc value, for example surfactant B is a polysorbate having a negative Cc value, for example surfactant B is polyoxyethylene (20) sorbitan monooleate.

Item 1: Method for the preparation of particles comprising a cross-linked polysaccharide matrix, said method comprising the following steps:

a) providing an aqueous phase comprising the polysaccharide and a salt;

b) providing an oil phase comprising an oil as a solvent;

c) mixing the aqueous phase and the oil phase in presence of a surfactant so as to obtain a water/oil (w/o) emulsion;

d) crosslinking the polysaccharide comprised in the dispersed aqueous phase to obtain the particles, wherein the crosslinking comprises the reaction between a crosslinking agent and the polysaccharide to obtain the polysaccharide matrix;

e) recovering the particles;

wherein the concentration of the salt in the aqueous phase, the oil, and the surfactant are selected so that the HLD at a temperature of 25°C is of 0 to 3, for example of 0 to 2.5, for example of 1 to 2.5.

Item 2: the method of item 0 or 1, wherein step c) comprises stirring the oil phase using a rotor-stator homogenizer.

Item 3: the method of any one of items 0 to 2, wherein step c) comprises adding the aqueous phase dropwise to the oil phase, while stirring the oil phase, for example while stirring the oil phase using a rotor-stator homogenizer.

Item 4: the method of any one of items 0 to 3, wherein the surfactant is a non-ionic surfactant.

Item 5: the method of any one of items 1 to 4, wherein the surfactant is a mixture of at least two different surfactants.

Item 6: the method of item 5, wherein the mixture of surfactants comprises a surfactant A, which is a nonionic surfactant comprising:

as a hydrophilic group, a polyethyleneglycol or a polyglycerol chain,

as a hydrophobic group, a polyester of a monohydroxylated fatty acid,

for example comprises polyglycerol polyricinoleate as the surfactant A.

Item 7: the method of item 6, wherein the mixture is a mixture of surfactant A and surfactant B having a negative Cc value, for example, surfactant B is a nonionic surfactant having a negative Cc value, for example surfactant B is a nonionic ethoxylated surfactant having a negative Cc value, for example

surfactant B is a nonionic polysorbate having a negative Cc value, for example surfactant B is polyoxyethylene (20) sorbitan monooleate.

Item 8: the method of any one of items 0 to 7, wherein the mass of surfactant A represents less than 70%, for example between 50% and 70% of the mass of the surfactant mixture.

Item 9: the method of item 8, wherein the rest of the surfactant mixture is surfactant B.

Item 10: the method of any one of items 0 to 9, wherein the aqueous phase is devoid of alcohols of formula R-OH, wherein R is a hydrocarbon chain.

Item 11: the method of any one of items 0 to 10, wherein the surfactant is dissolved in the oil phase before step c).

Item 12: the method of any one of items 0 to 11, wherein the amount of surfactant is of 5 to 200 g/L of the oil phase, for example of 10 to 100 g/L of the oil phase.

Item 13: the method of any one of items 0 to 12, wherein the amount of surfactant is of 0.3 to 7.5 g/mL of the aqueous phase, for example of 0.5 to 5 g/mL of the aqueous phase.

Item 14: the method of any one of items 0 to 13, wherein the cross-linking agent is added to the aqueous phase before step c), for example between 1 and 6 minutes before step c).

Item 15: the method according to any one of items 0 to 14, wherein the cross-linking results in the formation of phosphodiester bonds between the polysaccharide chains.

Item 16: the method of item 15, wherein the cross-linking agent is trisodium trimetaphosphate (STMP).

Item 17: the method of any one of items 0 to 16, wherein the cross-linking agent is added to the aqueous phase before step c) in an amount of 5 to 100 g / 100 g of polysaccharide, for example of 10 to 50 g / 100 g of polysaccharide.

Item 18: the method of any one of items 0 to 17, wherein, a base is added to the aqueous phase before step c).

Item 19: the method of any one of items 0 to 18, wherein the base is added before the cross-linking agent.

Item 20: the method of item 18 or 19, wherein the base is a strong base.

Item 21: the method of item 20, wherein the strong base is NaOH.

Item 22: the method of any one of items 18 to 21, wherein the pH of the aqueous phase is of at least 10, for example at least 11, for example at least 12, for example at least 13.

Item 23: the method of any one of items 0 to 22, wherein, after adding the cross-linking agent, the temperature is kept below 20°C and wherein cross-linking comprises maintaining the emulsion at a temperature of 30°C to 90°C for at least 10 minutes.

Item 24: the method of item 23, wherein cross-linking comprises maintaining the emulsion at a temperature of 40°C to 80°C, for at least 15 minutes.

Item 25: the method of any one of items 0 to 24, wherein the concentration of the salt in the aqueous phase is of at least 1 mol/L, for example of 2 to 10 mol/L.

Item 26: the method of any one of items 0 to 25, wherein the salt is a monovalent salt.

Item 27: the method of any one of items 0 to 25, wherein the salinity of the aqueous phase is of 10 to 30 g_{NaCl} / 100 mL of the solution.

Item 28: the method of any one of items 0 to 27, wherein the volume of the aqueous phase at step c) represents 1 to 10% of the volume of the oil phase at step c).

Item 29: the method of any one of items 0 to 28, wherein the solvent of the oil phase is a vegetable oil.

Item 30: the method of item 29, wherein the vegetable oil is sunflower oil.

Item 31: the method of any one of items 0 to 30, wherein the concentration of the polysaccharide in the aqueous phase at step a) is of 60 g/L to 1500 g/L, for example of 100 to 900 g/L.

Item 32: the method of any one of items 0 to 31, wherein the polysaccharide consists of only one polysaccharide.

Item 33: the method of any one of items 0 to 31, wherein the polysaccharide consists of a mixture of polysaccharides.

Item 34: the method of any one of items 0 to 33, wherein the polysaccharide comprises dextran.

Item 35: the method of item 34, wherein the dextran has a weight average molar mass of 5000 to 200000 g/mol, for example of 10000 to 80000 g/mol, for example of 35000 to 45000 g/mol.

Item 36: the method of any one of items 0 to 35, wherein the polysaccharide comprises fucoidan.

Item 37: the method of any one of items 0 to 36, wherein recovering the particles comprises separating the particles from the oil phase by at least one centrifugation step, wherein after the centrifugation step, the supernatant is discarded, and the particles are resuspended in an aqueous solution.

Item 38: the method of any one of items 0 to 37, further comprising a step of loading the particles with a water-soluble active compound, for example a water-soluble drug, for example a fibrinolytic agent or a thrombolytic agent.

Item 39: the method of item 38, wherein the loading comprises:

- suspending the particles in an aqueous solution of the active compound to obtain particles loaded with the active compound, and
- recovering the loaded particles.

Item 40: the method of item 38 or 39, wherein the active compound is a protein.

Item 41: the method of item 40, wherein the protein is a globular protein.

Item 42: the method of item 40 or 41, wherein the protein has a mass of 10000 Da to 200000 Da.

Item 43: the method of any one of items 40 to 42, wherein the protein is a tissue-type plasminogen activator (tPA) or a deoxyribonuclease I (DNase I).

Item 44: the method of any one of items 40 to 43, wherein the loading comprises:

- suspending the particles in an aqueous solution of the protein to obtain particles loaded with the protein, and
- recovering the loaded particles,

and wherein the pH of the aqueous solution of the protein is below the isoelectric point of the protein.

Item 45: particles obtainable by the method of any one of items 0 to 44.

Item 46: particles comprising a cross-linked polysaccharide matrix, having a hydrodynamic size of below 500 nm, for example of 150 nm to 400 nm, as measured by Dynamic Light Scattering in a 0.9 wt% NaCl in water solution.

Item 47: the particles of item 46, further characterized in that they are spherical.

Item 48: the particles of item 46 or 47, further characterized in that they have a polydispersity index of below 0.2, as measured by Dynamic Light Scattering in a 0.9 wt% NaCl in water solution.

Item 49: the particles of any one of items 46 to 48, further characterized in that they have a Zeta potential of -40 to -20 mV for a pH of 4 to 10, for example for a pH of 2 to 12.

Item 50: the particles of any one of items 46 to 49, further comprising a releasable water-soluble active compound, for example a water-soluble drug, for example a fibrinolytic agent.

Item 51: the particles of item 50, wherein the active compound is a protein.

Item 52: the particles of item 51, wherein the protein is a globular protein.

Item 53: the particles of item 50 or 51, wherein the protein has a mass of 10000 Da to 200000 Da.

Item 54: the particles of any one of items 51 to 53, wherein the protein is a tissue-type plasminogen activators (tPA) or a deoxyribonuclease I (DNase I).

Item 55: the particles of any one of items 46 to 54, wherein the polysaccharide consists of only one polysaccharide.

Item 56: the particles of any one of items 46 to 54, wherein the polysaccharide consists of a mixture of polysaccharides.

Item 57: the particles of any one of items 46 to 56, wherein the polysaccharide comprises dextran.

Item 58: the particles of item 57, wherein the dextran has a weight average molar mass of 5000 to 200000 g/mol, for example of 10000 to 80000 g/mol, for example of 35000 to 45000 g/mol.

Item 59: the particles of any one of items 46 to 58, wherein the polysaccharide comprises fucoidan.

Item 60: the particles of any one of items 46 to 59, wherein the polysaccharide molecules are crosslinked via phosphodiester bonds.

Item 61: the particles of item 60, comprising a phosphorus content of 5 to 15 µg/mg of particle.

Brief description of the drawings

Fig. 1 Stability of nanoparticles of the present invention (Final protocol) compared to submicroparticles (Initial protocol) as disclosed in the prior art. Both samples were subjected to solvent exchanges and size and PDI were verified by DLS after 6 h. N = 3 batches per condition.

Fig. 2 Z-average hydrodynamic diameter and polydispersity (PDI) determined by DLS for nanoparticles of the present invention (Final protocol) compared to submicroparticles (Initial protocol) as disclosed in the prior art. Each triangle represents a different production batch.

Fig. 3 (Left) Loading of rtPA in particles of the invention determined by BCA (BiCinchoninic acid Assay). (Right) Release of rtPA after 1 h incubation at 37°C in PBS 1X determined by BCA.

Fig. 4 (Left) Fibrin agar plate assay (FAPA) representative picture after 6 h. (Right) Amount of active rtPA loaded in nanoparticles of the present invention quantified by the FAPA assay.

Fig. 5 (Left) Representative in flow targeting under arterial shear stress of platelet aggregates (**green**) by nanoparticles of the present invention (**red**). (Right) Colocalization of empty or rtPA-loaded nanoparticles of the present invention and aggregates from inflow targeting assays measured by Pearson's coefficient.

Detailed description

The method of the invention relies on the selection of a particular mix of surfactants that allows the formation of a suitable emulsion, that in its turn yields particles comprising a cross-linked polysaccharide matrix with a smaller size than in the prior art. Moreover, it has been observed that the size of the particles does not vary depending on the ionic strength of the aqueous solution in which they are dispersed and that the particles are stable in a saline aqueous solution even in the absence of added surfactant. Moreover, the particles are reliably obtained with a low polydispersity.

Hydrophilic-lipophilic difference (HLD)

As defined herein, the term emulsion encompasses both unstable and metastable emulsions and microemulsions. Microemulsions are thermodynamically stable emulsions.

HLD, the hydrophilic-lipophilic difference, is a well-known parameter in the art of emulsions. Systems with positive HLD generally form w/o emulsions, whereas systems with negative HLD generally form o/w emulsions. Moreover, systems having HLD close to 0 can form microemulsions.

More detailed information about the HLD can be found, for example, in the book *Surfactant Science: Principles and Practice*, by Prof Steven Abbott, available online at https://www.stevenabbott.co.uk/practical-surfactants/the-book.php or in Salager, Jean-Louis, Antón,

Raquel, Andérez, José, Aubry, Jean-Marie. (2001). *Formulation des micro-émulsions par la méthode HLD*. Techniques de l'Ingénieur. 1-20. DOI:10.51257/a-v1-j2157.

The HLD can be calculated as follows:

$$HLD = F(S) - k.EACN - \alpha(T-25) + Cc,$$

Wherein:

S is the salinity of the aqueous phase expressed in g_{NaCl} / 100 mL of aqueous phase. Expressing the salinity in g_{NaCl} / 100 mL means for example that, for monovalent salts $S = m_{salt} \times (58/M_{salt})$ g / 100 mL. For divalent and trivalent salts the value of S is changed via the ionic strength according to corrections known of the skilled person (equivalent S for multivalent salts can be calculated e.g. at this URL: https://www.stevenabbott.co.uk/practical-surfactants/hld-expert.php).

In the present disclosure, S is calculated for a hypothetical solution that comprises the same salt and amount of salt as the aqueous phase but ignoring the contribution of the base, the cross-linking agent and of the polysaccharide.

$F(S) = 0.13 \times S$ when the surfactant is nonionic and $F(S) = \ln(S)$ when the surfactant is ionic.

EACN, the Effective Alkane Carbon Number, is characteristic of the oil. EACN values are tabulated or can be measured, for example according to the procedure below.

The EACN scaling factor, k, is characteristic of the surfactant. It is tabulated or can be measured.

T is the temperature.

α is characteristic of the surfactant. α values are tabulated.

In the present disclosure, the HLD is calculated with T taken to be 25°C, so that the temperature term vanishes.

Cc, the Characteristic Curvature, is characteristic of the surfactant. Cc values are tabulated or can be measured, for example according to the procedure below.

EACN determination

EACN of an oil is determined by screenings of tubes with varying Cc. Centrifugation tubes are set as Cc screening range with varying mix of surfactants with known Cc. 750 µL of the oil is mixed with 90 mg surfactant mix for one hour. Then, 750 µL ultrapure water is gently added, and followed by three quick

inversions by hand. Then the tubes are set to rest at RT for at least 2 h. Visual inspection allows to identify which tubes contained a o/w emulsion (phase I), a w/o emulsion (phase II), or a microemulsion (phase III). The EACN value for the oil is determined as the value that would result in the same pattern of tubes. This can be repeated with various known surfactants depending on the accuracy needed.

Cc determination

Cc of a surfactant is determined by screenings of tubes with varying Cc. Centrifugation tubes are set as Cc screening range with varying mix of a surfactant with known Cc and the surfactant whose Cc is determined. 750 µL of an oil of known EACN is mixed with 90 mg surfactant mix for one hour. Then, 750 µL ultrapure water is gently added, and followed by three quick inversions by hand. Then the tubes are set to rest at RT for more than 2 h. Visual inspection allowed to identify which tubes contained a o/w emulsion (phase I), a w/o emulsion (phase II), or a microemulsion (phase III). The Cc value for the surfactant is determined as the value that would result in the same pattern of tubes. This can be repeated with various known surfactants depending on the accuracy needed.

Surfactant

As defined herein, and unless specified otherwise, a surfactant can be a mixture of surfactants.

Surfactants with negative Cc values are more hydrophilic surfactants, whereas surfactants with positive Cc values are more lipophilic.

The Cc of a mixture of surfactants can be computed from the parameter Cc/k of the mixture. The Cc of a mixture of surfactants over the k of said mixture is the sum of the Cc/k of the surfactants in the mixture weighted by their molar fraction in the mixture of surfactants and the k a mixture of surfactants is the sum of the k of the surfactants in the mixture weighted by their molar fraction in the mixture of surfactants.

An example of a surfactant A comprising a polyethyleneglycol chain and a polyester of a monohydroxylated fatty acid is PEG-30 dipolyhydroxystearate.

As defined herein, an ethoxylated surfactant is a surfactant whose hydrophilic part comprises polymers or oligomers of ethylene glycol (the repeated unit is $-CH_2-CH_2-O-$).

Examples of nonionic polysorbate having a negative Cc value comprise Tween 60 (polyoxyethylene (20) sorbitan monostearate) and Tween 80 (polyoxyethylene (20) sorbitan monooleate).

Alcohols are often used as co-surfactant for formulating emulsions. However, the presence of alcohols can lead to the precipitation of the polysaccharide.

Oil phase

The oil phase is a hydrophobic and lipophilic liquid phase

Cross-linking agent

The timing of the addition of the cross-linking agent and the control of the temperature of the mix is useful to avoid unwanted cross-linking before the cross-linking step d).

Examples of crosslinking agents that result in the formation of phosphodiester bond between the polysaccharide chains comprise STMP or $POCl_3$.

A phosphodiester bond liking two groups R has the following formula: R-O-P(=O)(-O^-)-O-R.

The base facilitates the cross-linking of the polysaccharide.

Salt

Adding a salt to the aqueous phase helps stabilizing the emulsion formed and facilitates reactions between species of the same charge, if any, during the crosslinking step, by screening the charges. Such species can be, for example, the cross-linking agent, the polysaccharide chains in the presence of the base, partially crosslinked polysaccharide chains when the crosslinking results in conferring a charge to the polysaccharide. This is the case, for example, when STMP is used as the cross-linking agent.

As defined herein, a monovalent salt is an ion pair wherein the anion has a charge of -1 and the cation has a charge of +1.

Polysaccharide

As defined herein, and unless specified otherwise, a polysaccharide can be a mixture of polysaccharides.

As used herein, a particle comprising a cross-linked polysaccharide matrix is a particle wherein the cross-linked polysaccharide is the substance in which the other constituents of the particles are fixed, buried etc., in other words the cross-linked polysaccharide constitutes the backbone of the particle.

Particles comprising a cross-linked polysaccharide matrix, such as the particles of the present disclosure, are often referred to as hydrogel particles.

Active agent

As defined herein, an active compound can be a drug or a contrast agent.

As defined herein, tissue type plasminogen activator and deoxyribonuclease I comprise recombinant tissue type plasminogen activator and recombinant deoxyribonuclease I.

For negatively charged particles, lowering the pH of the aqueous solution of the protein below the isoelectric point of the protein favors the loading of the protein.

Characteristics of the particles

The hydrodynamic size (also called Z-average size) is measured in a 0.9 wt% NaCl in water solution by dynamic light scattering (DLS), for example using an instrument such as a Zetasizer Nano ZS (Malvern Instruments, 30 Orsay, France).

A 0.9 wt% NaCl in water solution designates a solution comprising only water and the 0.9wt% NaCl. A 0.9 wt% NaCl in water solution does not comprise a surfactant.

The hydrodynamic size and the polydispersity index (PDI) are defined by the ISO norms: ISO 22412:2017 and ISO 22412:2017.

Particles obtained by an emulsion method are generally spherical since surface tension imposes a spherical shape for the droplets of the emulsion used to produce the particles.

Zeta potential is measured by Electrophoretic Light Scattering (ELS), for example using a Zetasizer Nano ZS (Malvern Instruments, Orsay, France). Samples are diluted in 1 mM KCl.

Zeta potential is defined by ISO norms ISO 13099-2:2012 and ISO 13099-1:2012.

A releasable compound is a compound that is not covalently linked to the particle and that can be released from the particle when the particle is diluted in physiologically relevant conditions, for example in phosphate-buffered saline (PBS 1X) at 37°C.

Examples

Materials

Dextran 40 kDa was purchased from Pharmacosmos (Holbæk, Danemark, #5510 0040 1007); FITC-Dextran 40 kDa and TRITC-Dextran 40 kDa were purchased from TDB Consultancy (Uppsala, Sweden, #FD40 and #TD40). Fucoidan (Mn = 18 kDa/Mw = 104 kDa) was a gift from Algues & Mer (Ouessant, France, #MMWFSA14093). Vegetable sunflower oil (Lesieur - Huile Coeur de Tournesol, Lesieur S.A.S, Asnieres-sur-Seine, France) was purchased from a local supermarket (Monoprix, Paris, France). Polyglycerol polyricinoleate (PGPR) was kindly supplied by Palsgaard (Lyon, France, # PGPR 4150). Fetal bovine serum (FBS) was purchased from Pan-Biotech (Aidenbach, Germany, #P30-3306). HUVEC cells line (ATCC, Manassas, Virginie, #ATCC-CRL-1730) was used at fewer than 40 passages. Tween 80 (#P1754), Trisodium trimetaphosphate (STMP, #T5508), Sodium Dodecyl Sulfate (SDS,

#L3771), Sucrose (#S7903), fibrinogen type I from human plasma (#F3879), thrombin from human plasma (#T7009), plasminogen from human plasma (#528175) were purchased from Sigma Aldrich (Saint-Quentin-Fallavier, France). DMEM, low glucose, pyruvate (#31885049), Antibiotic Antimycotic solution (#15240062), PBS 1X and 10X (#14040133 and #14080055), Rhodamine phalloidin (#R415), low melting point agarose (#R0801), DIOC6 (D273) were purchased from Thermo Fisher Scientific (Massachusetts, United States). Horm® collagen type I was purchased from Takeda Pharmaceutical (Tokyo, Japan). rtPA (alteplase) was purchased from Boehringer Ingelheim (Ingelheim am Rhein, Germany, # Actilyse®). DNase I (dornase alfa) was purchased from Roche – Genentech (San Francisco, United States, #Pulmozyme® 2500 U/2,5 mL).

Methods

Nanoparticle synthesis according to the invention: polysaccharide nanoparticles (NPs) were obtained through a water-in-oil (w/o) microemulsion, with chemical crosslinking in the aqueous phase. A polysaccharide solution (300 g/L polysaccharide, 6 M NaCl) was prepared; The polysaccharide was either pure Dextran 40 or Dextran 40 in a 90% w/w ratio with fucoidan at a 10% w/w ratio. For fluorescent NPs, a 5:95 mass mixture of TRITC-Dextran 40 or FITC-Dextran 40 with Dextran 40 was used. 15 mL organic phase composed of sunflower oil and 6% w/v surfactant (60:40 PGPR and Tween 80) was cooled at -20°C for 30 min. Meanwhile, 1200 mg of the polysaccharide solution is mixed with 60 µL of 10 M NaOH for 10 min. 240 µL of 30 % w/v STMP solution was added before quick mixing for 1 min. 600 µL of this aqueous mix are then added dropwise to the organic phase under dispersion with a stand-disperser (Polytron PT 3100, dispersing aggregate PT-DA 07/2 EC-B101, Kinematica, Luzern, Switzerland) for 2 min 30 s at 30'000 rpm on ice. The resulting emulsion was incubated at 50°C for 20 min before successive purification by ultracentrifugation (50'000 g, 30 min) then resuspending the pellets with SDS 0.04 % w/v four times, then with ultrapure water three times. The resulting NPs were stored at 4°C in ultrapure water. Concentration of NPs could be performed with ultracentrifugation devices with size cutoff of 300'000 Da (Vivaspin, Dutscher, Issy-les-Moulineaux, France). Stable freeze-dried NPs were obtained with the LyoVac GT2 freeze dryer (SRK Systemtechnik, Riedstadt, Allemagne) after -20 °C freezing for 1 h in a 1 % sucrose solution. Notably, stable freeze-dried NPs were obtained for rtPA loaded NPs. Pure Dextran NPs and Fucoidan-containing NPs are respectively abbreviated Dex-NPs and Fuco-NPs.

Comparative submicroparticle synthesis: Polysaccharide submicroparticles (SPs) were obtained via a water-in-oil (w/o) emulsification combined with a crosslinking process. Polysaccharide solution (300 mg/ml, 6 M NaCl) was prepared. The polysaccharide was Dextran 40 in a 90% w/w ratio with fucoidan at a 10% w/w ratio. The same procedure as for the NPs is used except that the surfactant was PGPR only (dissolved in the organic phase at a concentration 6% w/v).

HLD calculations

A Cc of 4 was determined for PGPR. For Tween 80, Cc is tabulated at -3.7.

A k of 0.16 is taken both for PGPR and for Tween 80.

EACN for sunflower oil was determined at 16.
Both for the NPs and for the SPs, the salinity (ignoring the STMP and any charged polysaccharide) is of 18.8 g_{NaCl} / 100 mL of aqueous phase.

For the NPs, the molar fraction of PGPR is 0.79 (taking a molar mass of 521 g/mol for PGPR) and the molar fraction of Tween 80 is 0.21 (taking a molar mass of 1310 for Tween 80).

$HLD_{NP} = 0.13*18.8 – 0.16*16 + 0.79*4 + 0.21*(-3.7) = 2.27$

$HLD_{SP} = 0.13*18.8 – 0.16*16 + 4 = 3.88$

Physico-chemical characterization: The particles formulations were studied for particle morphology, size and zeta potential distributions, mass concentration, and elemental composition. Particle morphology was visualized by Transmission Electron Microscopy (TEM) (Philips FEI Tecnai 12, Amsterdam, Netherlands), negatively stained with 1% (w/v) uranyl acetate for 5 min. Hydrodynamic size (diameter), polydispersity (PDI) and Zeta potential (ζ-potential) were measured by Dynamic Light Scattering (DLS) and Electrophoretic Light Scattering (ELS), respectively (Zetasizer Nano ZS, Malvern Instruments, Orsay, France). Samples were diluted in distilled water, 0.9% NaCl or PBS 1X for size, and in 1 mM KCl for ζ-potential determination. All runs were performed at 25°C in triplicate. Mass concentration was determined by freeze-drying. Elemental composition was assessed by total reflection X-ray fluorescence spectroscopy (TXRF) technique to quantify the phosphorus and sulfur content (S2 PICOFOX Bruker, Massachusetts, United States). The stability of Fuco-NPS and compared submicroparticles (SPs) in various solvents (ultrapure water, 0.9% NaCl, 0.9% NaCl and 0.02% Tween 20) was evaluated 6 h after solvent exchange.

Sulfate and fucoidan quantification: The sulfate content of fucoidan was determined by a semi-quantitative solid-phase colorimetric assay. Briefly, 12.5 µg of Fuco-NPs in suspension at a concentration of around 1 mg/mL were added by 5 µL drops on a piece of Whatman Chromatography paper grade 1 with drying between each drop addition. The paper was first soaked into a methanol/acetone (6:4) solution for 3 min and then into a methanol/acetone/water (6:4:15) solution with 50 mM HCl and 0.1% w/w methylene blue for 10 min. Finally, the paper was extensively washed with acetic acid/methanol/acetone/water (5:6:4:85) until no coloration was detected in the washing solution. The paper was then transferred to the Eppendorf, containing 0.5 mL methanol with 2% w/v SDS, and incubated for 15 min at 50°C. 0.2 mL of the extracted dye was placed in a 96-well plate, and its concentration was determined by reading absorbance at 663 nm with a Varioskan LUX multiplate reader (Thermo Fisher Scientific, Massachusetts, United States). Standard curves were obtained from fucoidan in solution with known concentrations.

Cell culture and cytotoxicity assay: To evaluate the cytotoxicity of the SPs, Fluorometric Cell Viability Assay (#TOX-8 kit, Sigma Aldrich, Saint-Quentin-Fallavier, France) was used on confluent Human

Umbilical Vein Endothelial Cells (HUVECs). The cells were cultured in low glucose DMEM supplemented with 10 % (v/v) FBS and 1 % antibiotic-antimycotic; the cells were kept in an incubator at 37°C in a humidified atmosphere of 5 % CO_2. Cells were seeded into 96-well plates with 30,000 cells per well. Following 24 h of incubation, the medium was changed to Fuco-NPs resuspended in culture medium in a range of 100 mg/L to 1 g/L, and the cells were cultured for another 24 h. Cells cultured with equivalent PBS 1X medium dilution were set as control. Negative controls were culture medium only, and positive controls were 1 % Triton X-100 in culture medium for 15 min. Then the medium was replaced with 100 µL 10 % Resazurin solution in culture medium, and the plates were covered in foil and incubated for another 2 h. The Resazurin 's absorbance signals were monitored at 570 nm and 590 nm wavelengths with a Varioskan LUX multiplate reader. The corrected absorbance values were blank corrected: $A' = A_{570\ nm} - A_{590\ nm}$, and the relative cell viability was expressed as $(A' - A'_{neg}) / (A'_{pos} - A'_{neg}) \times 100$ %, with the negative and positive control absorbances respectively averaged in the control wells as detailed above. To examine possible cell morphology changes after co-incubation with Fuco-NPs, HUVECs cells were seeded in 8-wells Lab-Tek II Chamber Slide w/Cover (Thermo Fischer Scientific, Massachusetts, United States) with 10,000 cells per well. The medium was changed 24 h to Fuco-NPs resuspended in culture medium in a range of 100 mg/L to 1 g/L, and the cells were cultured for another 24 h. Cells cultured with equivalent PBS 1X medium dilution were set as control. Next, cells were fixed with 4% paraformaldehyde for 30 min at 4°C. After rinsing with PBS, cells were permeabilized with Triton X-100 0.1 % in PBS for 5 min at room temperature (RT), then washed twice with PBS before incubation for 60 min at RT with 1 % Phalloidin-Rhodamine in PBS. After two PBS washes, the slides are mounted with a Mounting Medium with DAPI. Visualization was performed with a confocal microscope (Zeiss LSM 780, Iena, Germany).

Drug loading: rtPA was loaded onto the NPs by adsorption. 50 µL of NPs (5 mg/mL) were mixed with 50 µL rtPA (1 mg/mL) in ultrapure water then incubated for 15 min. Free unabsorbed rtPA was removed by ultracentrifugation (15 min, 15'000 g). The rtPA loaded NPs were resuspended in ultrapure water, and rtPA encapsulation was determined as described below by BCA and PefaFluor® tPA assays. DNase I was loaded onto the NPs by adsorption in acidic conditions. 50 µL of NPs (5 mg/mL) were mixed with 25 µL DNase I (1 mg/mL), 5 µL of HCl ($2x10^{-2}$ M) and 20 µL ultrapure water then incubated for 15 min. Free unabsorbed DNase I was removed by ultracentrifugation (15 min, 15'000 g). The DNase I loaded NPs were resuspended in ultrapure water and DNase I encapsulation was determined as described below by BCA and a fluorescent substrate DNAse detection kit assays.

Drug encapsulation efficiency: The amount of drug (rtPA or DNase I) loaded on the NPs was measured using the Pierce BCA protein assay kit (Life Technologies SAS, Courtaboeuf, France). Briefly, 200 µL of working reagent was added to 25 µL of each sample in 96 wells multiplate. The absorbance at 562 nm was read with a Varioskan LUX multiplate reader after 30 min incubation at 37°C. The concentration of the drug was extrapolated by a calibration curve prepared with different concentrations of rtPA or DNase I respectively. The encapsulation efficacy (EE) was calculated as EE (%) = 100% x $[Drug]_{loaded}/[Drug]_{initial}$ and the loading capacity (LC) was calculated as LC (%) = 100% x $[Drug]_{loaded}/[NP]$.

Fibrin Agar Plate Assay (FAPA): To assess the fibrinolytic activity of rtPA-loaded NPs, a fibrinolysis experiment was performed. 5 mL of TBS Buffer (0.1 M Tris, 0.8 % NaCl, 0.02 % KCl, pH = 7.4) with 3% w/v low melting agarose were heated above 65°C. 5 mL of TBS buffer with 25 mg fibrinogen and 1 U plasminogen was slowly heated to 37°C. Once the agarose solution reached 65 ◦C, it was cooled to 37°C, and 2 U of thrombin were added. Next, the two solutions were slowly mixed, then poured into a 9 cm Petri dish and incubated at 37°C for 2 h (gels can be kept a few days at 4°C). On the solidified agarose gel, round wells were formed using a 3 mm punch as sample reservoirs. 5 µL of each NPs sample (diluted 1:10) was dropped into the wells and incubated at 37°C in a humid environment. Pictures were taken every hour for 8 h. The degree of fibrin lysis was quantified with ImageJ by comparing the rate of fibrinolysis between samples and free rtPA standards.

In flow platelet aggregates targeting assay: An *in vitro* flow adhesion assay was performed to evaluate the targeting of Fuco-NPs with to activated platelets. Micro-channels of Vena8 Fluoro+ chambers (width: 0.04 cm, height: 0.01 cm, and length: 2.8 cm; Cellix Ltd, Dublin, Ireland) were coated overnight with fibrillar type I collagen (50 µg/ml) overnight at 4°C and rinsed with NaCl 0.9 % before use. Human whole blood (EFS, Bichat Hospital, Paris, France), collected in the PPACK tubes and labeled with 5 µM DIOC6 (to image platelets), was perfused at arterial shear stress for 5 min to induce platelet activation and aggregation. Platelet aggregation through contact with collagen was visualized in real-time with phase-contrast microscopy (Axio Observer, Carl Zeiss Microscopy, Oberkochen, Germany). After rinsing with NaCl 0.9 %, fluorescent Dex-NPs or Fuco-NPs (unloaded or loaded with rtPA) resuspended in 0.9 % NaCl at 1 mg/mL, were injected into the channels for 5 min. Their accumulation onto activated aggregates was monitored in real time. Channels were then washed for 5 min with NaCl 0.9%. Finally, quantification of bound NPs to aggregated platelets were performed with ImageJ by measuring total fluorescence intensity and colocalization with the Pearson's coefficient.

Results

Fig. 1 compares the size and stability in various solutions of the comparative SPs and of the Fuco-NPs of the invention. On the figure, "Initial protocol" designates the comparative SPs and "Final protocol" designates the Fuco-NPs of the invention. It can be seen that the comparative SPs have an increased PDI in 0.9% NaCl, which indicates that the particles were destabilized and that aggregation took place.

Fig. 2 compares the reliability of the synthesis of the comparative SPs and of the Fuco-NPs of the invention. Size and polydispersity were measured in pure water. It can be seen that the size and polydispersity of the comparative SPs is much more variable from batch to batch than the size and polydispersity of the Fuco-NPs of the invention.

Fig. 3 shows that the particles of the invention are able to load and release tPA efficiently.

Fig. 4 shows the efficiency of the particles of the invention as particles for drug delivery since there is no loss of fibrinolytic activity of the tPA that has been loaded and released.

Fig. 5 shows that the addition of fucoidan in the particles of the invention helps targeting platelet aggregates and thus should allow thrombus targeting. Moreover, targeting capacity is retained when the Fuco-NPs are loaded with rtPA.

Claims

1. Method for the preparation of particles comprising a cross-linked polysaccharide matrix, said method comprising the following steps:

a) providing an aqueous phase comprising the polysaccharide and a salt;

b) providing an oil phase comprising an oil as a solvent;

c) mixing the aqueous phase and the oil phase in presence of a surfactant so as to obtain a water/oil (w/o) emulsion;

d) crosslinking the polysaccharide comprised in the dispersed aqueous phase to obtain the particles, wherein the crosslinking comprises the reaction between a crosslinking agent and the polysaccharide to obtain the polysaccharide matrix;

e) recovering the particles;

wherein the concentration of the salt in the aqueous phase, the oil, and the surfactant are selected so that the HLD at a temperature of 25°C is of 0 to 3, for example of 0 to 2.5, for example of 1 to 2.5.

2. The method of claim 1, wherein the mixture of surfactants comprises a surfactant A, which is a nonionic surfactant comprising:

as a hydrophilic group, a polyethyleneglycol or a polyglycerol chain,

as a hydrophobic group, a polyester of a monohydroxylated fatty acid,

for example, one said surfactant A is polyglycerol polyricinoleate.

3. The method of claim 2, wherein the mixture is a mixture of surfactant A and a surfactant B having a negative Cc value, for example, surfactant B is a nonionic surfactant having a negative Cc value, for example surfactant B is a nonionic polysorbate having a negative Cc value, for example surfactant B is polyoxyethylene (20) sorbitan monooleate.

4. The method of claim 2 or 3, wherein the mass of surfactant A represents less than 60%, for example between 50% and 60% of the mass of the surfactant mixture.

5. The method of claim 4, wherein the rest of the surfactant mixture is surfactant B.

6. The method of claim 5, wherein the cross-linking results in the formation of phosphodiester bonds between the polysaccharide chains, for example the cross-linking agent is trisodium trimetaphosphate (STMP).

7. The method of any one of claims 1 to 6, wherein the volume of the aqueous phase at step c) represents 1 to 10% of the volume of the oil phase at step c).

8. The method of any one of claims 1 to 7, wherein the solvent of the oil phase is a vegetable oil, for example sunflower oil.

9. The method of any one of claims 1 to 8, wherein the polysaccharide comprises dextran, for example a dextran having a weight average molar mass of 10000 to 80000 g/mol, for example of 10000 to 60000 g/mol, for example of 35000 to 45000 g/mol.

10. The method of any one of claims 1 to 9, wherein the polysaccharide comprises fucoidan.

11. The method of any one of claims 1 to 10, further comprising a step of loading the particles with a water-soluble active compound, for example a water-soluble drug, for example a fibrinolytic agent or a thrombolytic agent.

12. Particles obtainable by the method of any one of claims 1 to 11.

13. Particles comprising a cross-linked polysaccharide matrix, having a hydrodynamic size of below 500 nm, for example of 150 nm to 400 nm, as measured by Dynamic Light Scattering in a 0.9 wt% NaCl in water solution.

14. The particles of claim 13, further characterized in that they have a polydispersity index of below 0.2, as measured by Dynamic Light Scattering in a 0.9 wt% NaCl in water solution.

15. The particles of claim 13 or 14, further comprising a releasable water-soluble active compound, for example a water-soluble drug, for example a fibrinolytic or a thrombolytic agent.

Abstract

The present invention relates to cross-linked polysaccharide nanoparticles, which can be used as drug delivery systems. The herein disclosed cross-linked polysaccharide nanoparticles are obtained via an emulsion cross-linking process. The careful choice of the surfactants used for forming the emulsion allows to reliably obtain small particles with a low polydispersity. Moreover, these particles are stable in saline solutions. The cross-linked polysaccharide nanoparticles can be loaded with proteinaceous fibrinolytic or thrombolytic agents and could be used as drug delivery systems for the treatment of thrombosis.

Figures

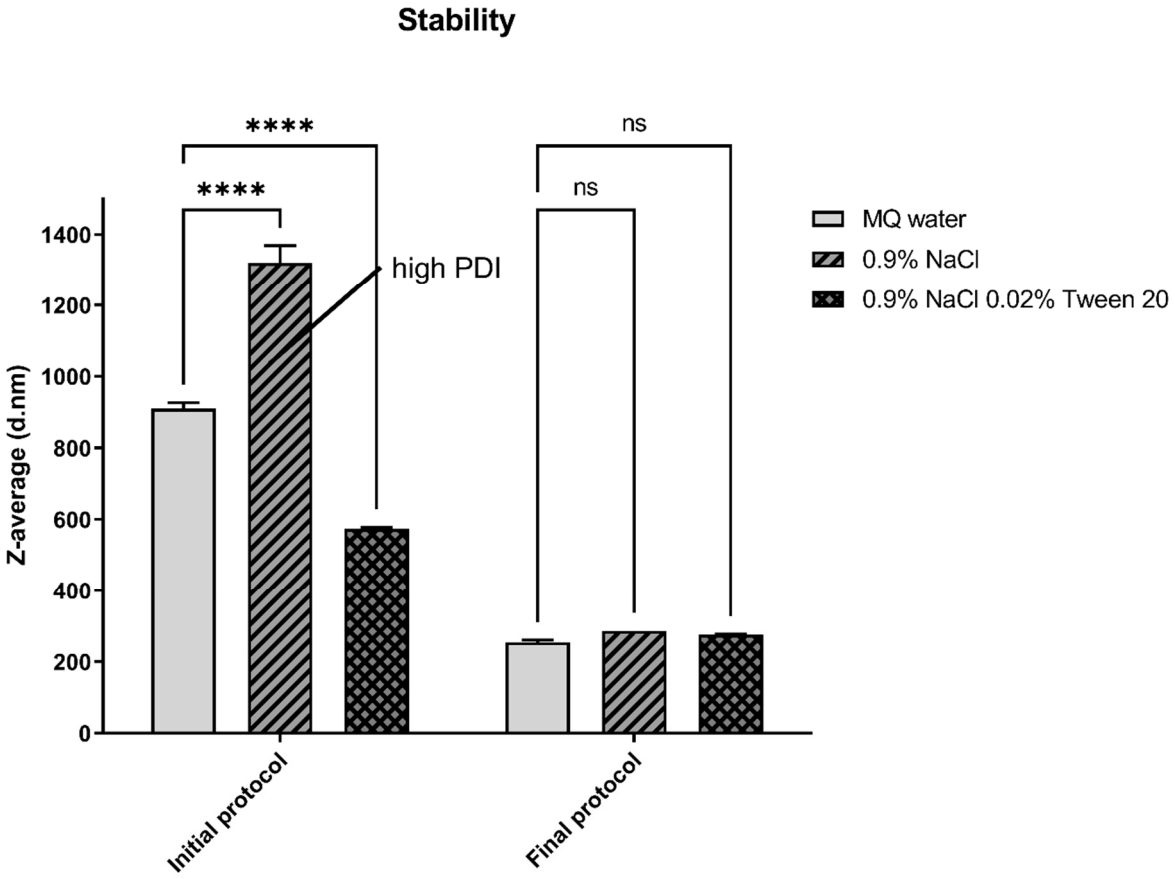


Fig. 1

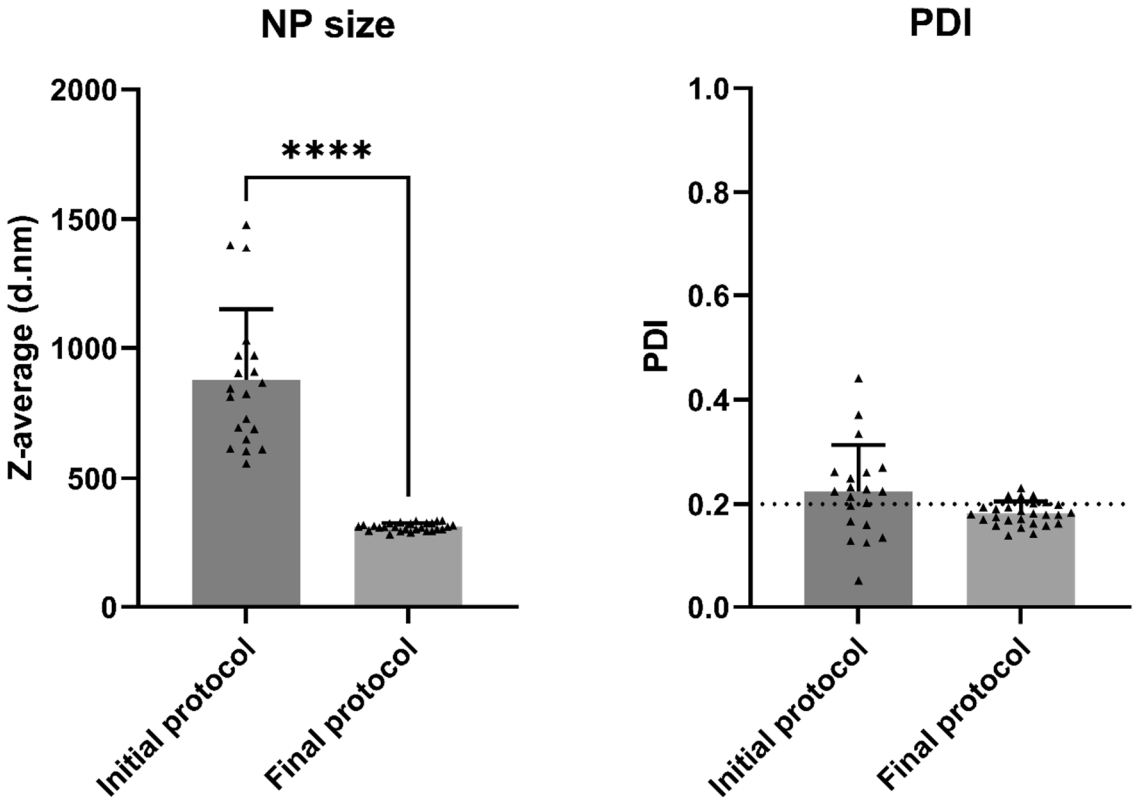

NP size
Z-average (d.nm)
2000
1500
1000
500
0
****
Initial protocol
Final protocol
PDI
PDI
1.0
0.8
0.6
0.4
0.2
0.0
Initial protocol
Final protocol

Fig. 2

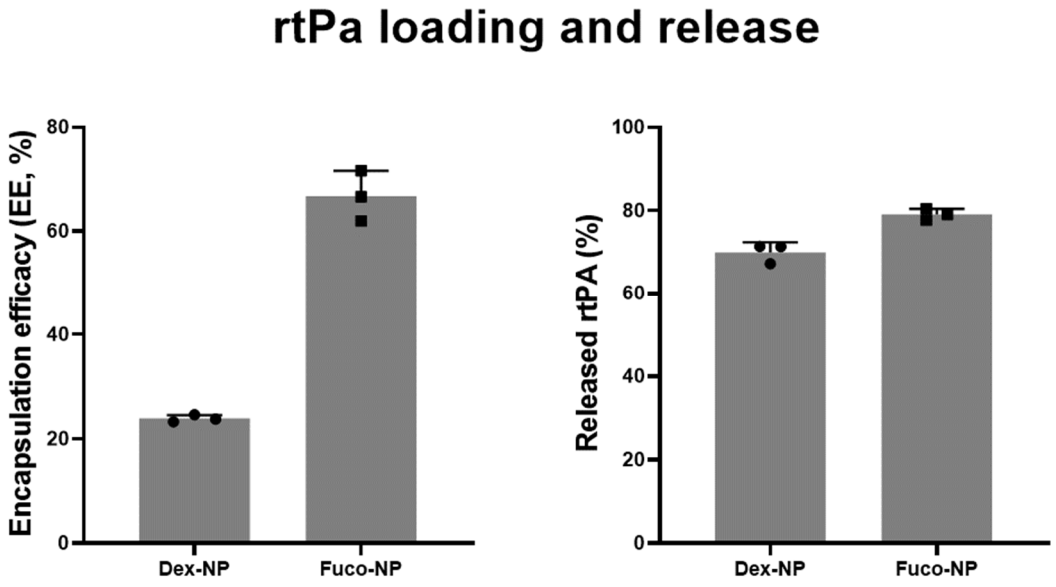

rtPa loading and release
Encapsulation efficacy (EE, %)
80
60
40
20
0
Dex-NP
Fuco-NP
Released rtPA (%)
100
80
60
40
20
0
Dex-NP
Fuco-NP

Fig. 3

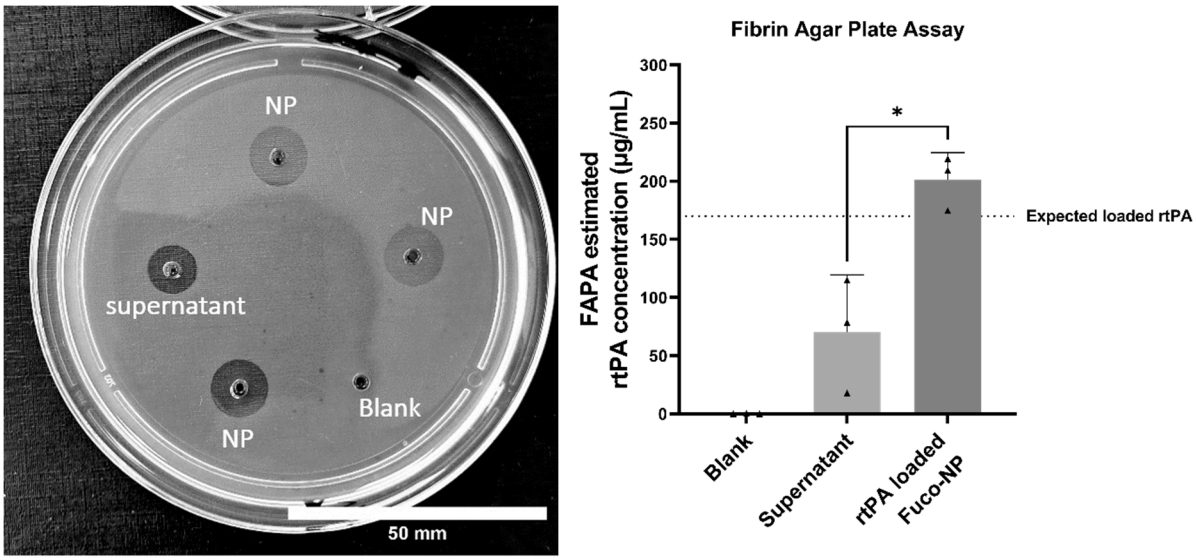


Fig. 4

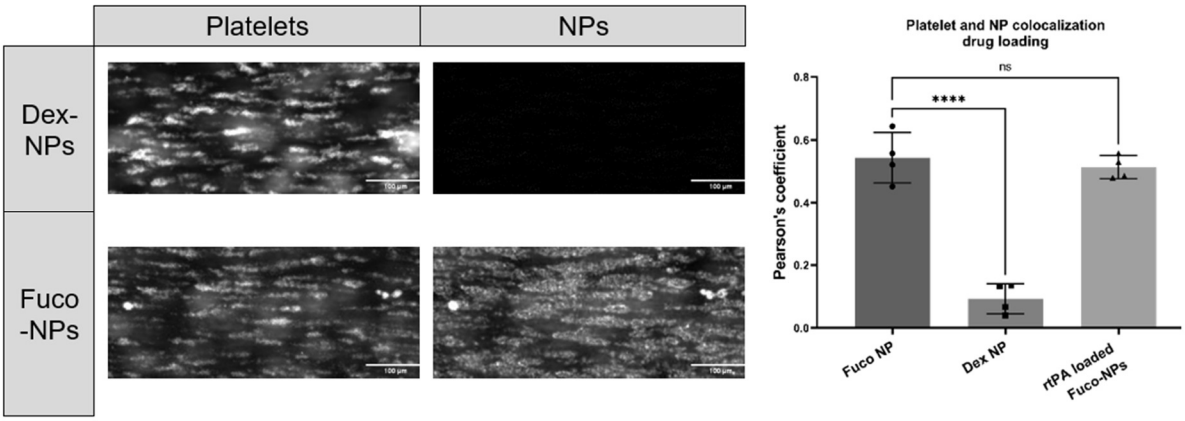


Fig. 5

ANNEX 5

Ischemic Strokes: Exploring the Challenges of Translating Nanomedicine into Clinical Practice

Authors: Thibault De La Taille, MSc[a,b,c] *; Diana Doukhi, MD[d,e,f] *; Mikael Mazighi, MD PhD[b,d,e,f]†; Cédric Chauvierre, PhD[a,b,c] †

[a] Université Sorbonne Paris Nord, 93430 Villetaneuse, France

[b] Université Paris Cité, 75006 Paris, France

[c] INSERM U1148, Hôpital Bichat, 46 rue Henri Huchard, 75018 Paris, France

[d] Department of Neurology, Hôpital Lariboisiere, 2 rue Ambroise-Paré, 75010 Paris, France

[e] FHU NeuroVasc, 2 rue Ambroise Paré, 75010 Paris, France

[f] INSERM U1144, Faculté de Pharmacie de Paris, 4, avenue de l'observatoire, 75006 Paris, France

(*contributed equally; † corresponding authors, share last authorship)

Corresponding authors:

- Cédric Chauvierre (cedric.chauvierre@inserm.fr), INSERM U1148 (LVTS), X. Bichat Hospital, 46 rue H. Huchard, 75018 Paris, France
- Mikael Mazighi (mikael.mazighi@inserm.fr), Hôpital Lariboisière, 2 rue Ambroise-Paré, 75010 Paris, France

Abstract

Acute ischemic strokes (AIS) represent a major health concern with more than 12 million deaths per year. Despite the establishment of intravenous thrombolysis as the main line of treatment three decades ago, and the subsequent advent of endovascular therapy, most patients remain disabled. While nanomedicine has shown considerable promise in the management of strokes over the years, there remains a gap between the numerous preclinical studies and the paucity of related clinical trials. In the last five years, around 250 articles described preclinical nanomedicine-based approaches to tackle AIS. These articles explore multiple directions to alleviate AIS, including firstly neuroprotection, followed by the use of thrombolysis through various approaches. Notably, they show a broad variety in the *in vivo* model choice as well as key readouts, making comparison across protocols difficult. Moreover, relevant data for clinical translation is often lacking, such as biodistribution, pharmacokinetics, or stability of the proposed nanomaterials. On the other hand, only a few clinical trials have involved nanoparticles, with mixed results. Thus, it can be proposed that among the obstacles hindering the clinical application of the often-promising nanomaterials, the major challenges are the insufficient characterization of nanomaterials including storage, stability, biodistribution and pharmacokinetics; diversity of *in vivo* protocols, hyper-focused ischemia-reperfusion damages compared to thrombolysis; and a necessity to acknowledge the complexity of AIS thrombi when designing a therapeutic approach. However, ongoing research considering the speed and feasibility requirements for AIS might result in future improvement in patient care.

Keywords

- Acute stroke
- Nanomedicine
- Thrombolysis
- Neuroprotectants
- Nanoparticles

Abbreviations

- AIS: acute ischemic stroke
- EVT: endovascular therapy
- IVT: intravenous thrombolysis
- tPA: tissue plasminogen activator
- IV: intravenous
- LVO: large vessel occlusion
- IONP: iron oxide nanoparticle
- MRI: magnetic resonance imaging
- NP: nanoparticle
- BBB: blood-brain barrier
- PNP: polymeric nanoparticle
- PLGA: poly(lactic-co-glycolic acid)
- EV: extracellular vesicle
- AV: apoptotic vesicle
- LNP: lipid nanoparticle
- NE: nanoemulsion
- NB/MB: nano/microbubble
- US: ultrasound
- PET: positron emission tomography

1. Introduction

Stroke is a major public health concern, being the second leading cause of death and the third leading cause of death and disability combined [1]. Since the introduction of thrombolysis in 1995 [2] and endovascular therapy (EVT) therapy twenty years later [3–7], acute ischemic stroke (AIS) management has undergone a revolutionary change. In 1995, intravenous thrombolysis (IVT) with alteplase was shown to be effective in improving clinical outcomes at three months when administered within three hours of the onset of AIS [2]. Alteplase is a recombinant human tissue plasminogen activator (tPA) administered as a 10% bolus followed by a 1-hour continuous infusion at a dose of 0.9 mg/kg. A second trial also demonstrated efficacy when administered between 3 and 4.5 hours after symptom onset[8]. Therefore, international guidelines recommend using alteplase as a first-line treatment for AIS when administered within 4.5 hours of onset [9,10]. Recently, the indication for IVT has been expanded to include selected patients with acute stroke of unknown onset [11], and those within 9 hours of stroke onset or wake-up strokes, when salvageable brain is identified based on advanced cerebral imaging [12]. Tenecteplase (0.25 mg/kg) is an alternative to alteplase with higher fibrin affinity and longer half-life. It can be administered in a single intravenous (IV) bolus injection and is indicated for patients with AIS within 4.5 hours duration and with large vessel occlusion (LVO) who are candidates for EVT [13]. However, only a small percentage of patients are eligible for IVT [14]. This is due to the limited time window and the many contraindications, which are partially related to the increased risk of symptomatic intracranial hemorrhage. Additionally, the efficacy of the treatment is often limited, with recanalization rates less than 30%, which varies depending on the occlusion site. LVOs have been observed to have the worst recanalization rates [15]. This point is critical as functional outcome is driven by recanalization success. In 2015, five trials (MR CLEAN, SWIFT PRIME, REVASCAT, ESCAPE, EXTEND IA) [3–7] demonstrated that EVT provides clinical benefits in cases of AIS with LVO of the internal carotid or middle cerebral artery, in addition to IVT, within 6 hours of onset. The efficacy of EVT has been extended to patients with AIS within 16 hours of onset, who have a perfusion mismatch[16], and/or within 24 hours of onset, who have a mismatch between clinical deficit and infarct identified with brain imaging [17]. Unfortunately, despite these techniques, over half of patients remain functionally dependent at 3 months [18].

Modern advances in the field of nanotechnology offer new means to overcome the limitations of current AIS therapy. The underlying principle of a so-called “magic bullet” was first coined by Pr. Paul Ehrlich at the beginning of the 20th century [19] and laid the ground for the receptor concept in immunology, then cancer chemotherapies and in a broader sense, modern pharmaceutical research: in a few words, designing a drug to specifically target the cause of the disease (initially, bacteria or cancer cells). The development of nanomedicine therefore developed with this mindset: how can nanosized objects be used to exert a specific action at only a desired locus in the body (organ, cell type, cellular compartment, etc.)? Most often, nanomedicine is thus used to protect an active compound, then deliver it only where needed to improve local efficacy and reduce systemic side effects. Notably, this can be used to improve imaging capacities, with for instance iron oxide nanoparticles (IONP), used as magnetic resonance imaging (MRI) contrast agents, or to improve the circulation and half-life of poor water-soluble drugs until it reaches its target [20]. Key aspects of nanomedicine’s benefits rely on the possibility to increase solubility and transport of certain compounds,

shield them from circulation, present multiple moieties on a single nanoparticle (NP) in order to incorporate targeting, “smart” capacities such as controlled release or degradation, or to combine effects with multiple drug loading or theranostics [21]. Other size-dependent effects exist such as increased surface-to-volume ratio, vascular margination of blood-borne objects due to size and shape [21], or the emergence of specific properties like localized surface plasmon resonance or superparamagnetism [22].

AIS management can benefit from nanomedicine in several ways. On one hand, the delivery of thrombolytic agents directly to the thrombus could circumvent their severe side effects. Moreover, addressing therapies to the ischemic brain across the blood-brain barrier (BBB) can be achieved by specific vectorization with NPs and help reduce the lasting damages of ischemia. Finally, NPs can also be used as contrast agents with different imaging modalities to specifically locate and assess the thrombus formation and ischemic lesion, and can even be used in a theranostic manner to couple imaging with controlled IVT [23].

2. Preclinical developments

Thus, we analyzed articles published in the last five years (2019-May 2024) referenced on PubMed with the keywords [“stroke”] and either [“nanoparticle”], [“nano”], [“liposome”], or [“lipo” AND “nano”]. The research yielded 856 articles, 440 of which were not retained (outside scope, retracted articles). Of the selected 416 articles, 169 were reviews. The remaining 247 articles were analyzed for their use of NPs in addressing AIS (including 10 which are related to hemorrhagic stroke, but with methods which could also be relevant for ischemic stroke treatment), as well as their relevance towards clinical translation. Notably, their use of *in vivo* models and results regarding scalability (storage, stability, etc.) was assessed. The results are recapitulated in Fig. 1. It is worth mentioning that 15% of the articles report nanoplatforms for imaging of the ischemic area through various modes (MRI, ultrasound (US), near-infrared (NIR) luminescence, etc.), and a third of these report theranostic approaches, with for instance the H_2O_2-triggered polymeric nanoparticle (PNP) developed in 2023 by Wang *et al.*, which had antithrombotic capacities *in vivo* coupled with imaging of the clot region through photoacoustic tomography [24]. We will focus here however on therapeutic approaches.

Over the last five years, a strong focus was brought upon using nanomedicine for delivering some form of neuroprotection to the ischemic area (194 articles), compared to 37 articles aiming for IVT. Regarding the latter, most approaches relied on vectorising tPA or an enzyme with similar activity (e.g., urokinase, streptokinase, or directly plasmin). However, some resort to nonchemical thrombolysis, such as magnetic hyperthermia [25], photodynamic/photothermal therapies [26,27], or notably sonothrombolysis, where ultrasound waves are used to induce mechanical forces to disrupt the clot thanks to echogenic NPs [28,29]. One such nonchemical approach was presented by Zhang *et al.* in 2023, with molecular self-assembled NPs, based on two molecules: DiR, a photosensitizer, and BNN6, a photothermally activatable NO donor, which together could under NIR irradiation induce mechanical (with NO-induced propulsion) and photothermal thrombolytic effects. Notably, stability, both in biological fluids and long-term, was assessed, as well as organ toxicity, pharmacokinetics and biodistribution [26]. As an example of NP-mediated tPA delivery, Xu *et al*. described in 2020 self-assembled poly(lactic-co-glycolic acid) (PLGA) PNPs coated with

platelet membrane for shielding and targeting of the thrombus. These NPs were loaded with tPA and demonstrated promising results in two *in vivo* models, while showing no organ toxicity nor changes in blood coagulation parameters. Moreover, pharmacokinetic and biodistribution studies were performed [30]. In contrast, only 50% of the articles mentioning any form of thrombolysis presented biodistribution results, and only 15 described toxicity assessments in organs.

Regarding the 194 articles mentioning neuroprotection, bringing antioxidant therapies as well as modulating inflammation appear as the two most explored ways to tackle ischemic damage. For example, Li *et al*. presented in 2021 a manganese oxide NP coated with macrophage cell membrane to target the ischemic site [31]. These NPs could exert antioxidant activity due to the manganese oxide itself, but also incorporated fingolimod, a drug that could reprogram macrophages from M1 to M2 phenotype to alleviate inflammation. Interestingly, in this article the authors addressed translatability of their NPs, by checking their stability in fetal bovine serum supplemented medium, their pharmacokinetic properties in the blood as well as biodistribution and organ toxicity. In some instances, the authors resort to innate capacities of the nanoparticles to exert a therapeutic effect, with for instance Tian *et al*. who described in 2021 extracellular vesicles (EVs) isolated from a human neural progenitor cell line and modified them to display RGD peptide as a targeting moiety. They studied how these modified EVs reduced inflammation in a murine ischemia-reperfusion model, but they also investigated organ toxicity, blood parameters, and biodistribution of these IV administered EVs [32]. However, for neuroprotection as well, such in-depth studies are not the norm; for instance, only 30% of articles display biodistribution results, and 29% with organ toxicity analysis. To sum up, on average 90% of both thrombolysis and neuroprotection-oriented papers present *in vivo* results, but less than 40% display certain key aspects of technology translation such as biodistribution and organ toxicity data.

Besides, the wide array of *in vivo* models used can make comparison challenging. For instance, 14 different ischemic stroke models can be identified, with 159 temporary occlusions and 64 permanent ones. A visual representation is provided in Fig.2. Among the permanent occlusion models, 54 involve some sort of clot formation or introduction, making these models relevant for thrombolysis evaluation: the most common are the photothrombotic stroke model (with Rose Bengal injection) [33] or the $FeCl_3$ (applied to various blood vessels, from the middle cerebral artery [34] to the carotid arteries [24]); notably, newly developed models include thrombin injection to the middle cerebral artery [35]. Regarding these clot models, their variety can make comparison of efficacy results challenging, and even more so since AIS clot composition has been shown to be peculiar [36,37], with notably a core-shell structure and neutrophil-derived NETs (neutrophil extracellular traps) [37]. Thus, there is no clear consensus appearing over the last five years regarding thrombosis models for nanoparticle therapeutic development, especially since the model choice can depend on the physiopathological path targeted by treatment. On the other hand, the most common model used for tackling stroke-related ischemic damage or microcirculation damage is the transient middle cerebral artery occlusion (tMCAO), accounting for 65% of all *in vivo* ischemic stroke models. Relying on the temporary occlusion of a blood vessel with a filament retracted after some varying time [38–40], this model is well-described and very useful for the investigation of ischemia-induced brain damages and appropriate candidate drugs. However, its regular implementation (artery choice, time of occlusion for instance) still leaves a clear room for improvement [41]. Most notably, the relevance of an ischemia/reperfusion model is debatable as most patients

(around 90% of patients admitted with LVO stroke in the US between 2014 and 2015) never presented a recanalization, and that permanent occlusion damages differ from those of ischemia/reperfusion, however, as discussed below, EVT could significantly change this rate [42]. Therefore, there remains a broad range of *in vivo* models with no obvious best-in-class model, while the most used, tMCAO, remains relevant for investigation on microcirculation and ischemia-reperfusion damages, but its overuse does not correlate to the current low proportion of recanalized patients [42]. Overall, the variety of *in vivo* models prevents comparison between efficacy results, especially given that ensuing pathological behavior can differ: for instance, ischemia-reperfusion (tMCAO) damages are very different from total ischemia (permanent occlusions such as pMCAO) [42].

Moreover, for technology evaluation, storage stability as well as stability in bodily fluids are key criteria that should be investigated. Among the 247 articles analyzed, only 21% mention any form of such stability investigation. Overall, the suspension media vary widely, from ultrapure water [43], saline or phosphate-buffered saline [26], to cell culture medium [44] or serum [45]. Though it may not be easy to measure the stability of NPs in complex bodily fluids, this is a critical parameter to consider as stability in storage "clean" media such as saline or water does not necessarily equate to colloidal stability in blood. Furthermore, long-term stability assessment is necessary to make sure that the described NPs can be successfully stored and used by clinicians. Here again, no clear measurement window is defined as some authors investigate stability only for a few days [46] while others report months-long stability [47]. Obviously, differences arise based on the material considered (as extracellular vesicles for instance might not be stable in storage as inorganic NPs) but should be discussed with regards to potential applications. Interestingly, 12% of articles have disclosed freeze-drying as a means to store their NPs for long-term storage [48], or other forms of drying [49,50] or precipitation[51]. Not only must the storage be questioned, but delivery methods can also be critical: while most authors rely on IV injections, 8 articles mention an oral or nasal delivery which could be favored as fast and easy delivery methods [52]; whereas 14 describe administration methods (stereotaxic, cisternal or intracarotid injections) that might be less suitable to clinical use.

Finally, the articles analyzed here also represent a wide range of materials, NP types and provenance, as displayed in Fig. 1-a. Among them, PNPs account for the most studied material (34%), with PLGA the most represented polymer used (31% of PNPs) due to its self-assembling properties. As for lipid-based materials (30% of articles), half of them is composed of the well-described liposomes, but also include lipid nanoparticles or nanovesicles such as EVs. Finally, inorganics and other types of NPs (nanoemulsions [53], nano-microbubbles [46,54], etc.) represent the last third. This diversity illustrates how researchers can use specific qualities of certain NPs to aim towards various ways of dealing with ischemic strokes (innate properties, tunable chemistry, etc.). However, 15% of these NPs incorporate cellular elements (membrane-derived coatings [55] mostly, or EVs [56]), with specific challenges related to sourcing, biological characterization and safety. Nonetheless, some authors have already addressed these, such as Son *et al.*, which described in 2024 EVs sourced from 3D cultured mesenchymal stem cells (MSC) for ischemic tissue regeneration with large-scale production in mind and evaluated batch-to-batch variability [57].

3. Clinical advancement

Therefore, the current preclinical nanomedicine research on AIS treatment is rich, diverse and promising, though clinical translation remains rare, possibly due to the aspects investigated above.

As previously mentioned, IV nanoemulsions have been described as potential neuroprotectants, including dodecafluoropentane emulsion (DDFPe) which has demonstrated neuroprotective effects in animal models of AIS by improving oxygen transport in the ischemic zones [58]. Preclinical studies have also shown the safety of this strategy[59]. Based on this, Culp *et al*. conducted a phase Ib/II randomized, placebo-controlled, double-blind, dose-escalation trial in 24 AIS patients to further establish the safety of DDFPe (NuvOx Pharma, LLC) [60]. Patients were randomly assigned to receive either DDFPe or a placebo every 90 minutes, starting within 12 hours of symptom onset. The study results indicate that there were no significant differences in adverse events between the treatment and placebo groups. Additionally, the high-dose DDFPe group exhibited better outcomes on the modified Rankin scale (mRS) at 1 and 3 months. Two additional clinical trials are currently underway. One is a phase 2 study on DDFPe (NuvOx LLC) for LVO stroke is ongoing (ClinicalTrials.gov ID: NCT05389748), while the other is a phase 2 study using another perfluorocarbon, ABL-101 (Aurum Biosciences) (ClinicalTrials.gov ID: NCT03463551).

Few clinical trials have shown particular interest in sonothrombolysis with mixed results. The initial trials focused on ultrasound use - without the injection of nanoparticles - in conjunction with standard treatment, to produce cavitation and fluid motion into the thrombus. The CLOTBUST trial involved 126 patients presenting with AIS consecutive to middle cerebral artery occlusion treated with IV tPA. They were randomly assigned to receive either adjunctive continuous high-frequency (2 MHz) transcranial Doppler ultrasound or a placebo. The study found that the ultrasound group had a significantly higher incidence of complete recanalisation or early or dramatic clinical recovery at 2 hours, with a non-significant trend towards an increased rate of stroke recovery compared to the placebo [61]. Smaller trials and meta-analyses [62,63] have confirmed better early recanalisation without improvement in outcome at 3 months. However, the CLOTBUST-ER trial, a large, phase 3, multicentre, double-blind, randomized controlled trial, enrolling 676 AIS patients receiving IV alteplase with or without ultrasound, was stopped early due to futility [64]. The primary outcome was functional autonomy assessed by mRS at 90 days, and there was no increased risk of symptomatic intracerebral hemorrhage compared with tPA alone [61–64]. On the contrary, exposure to tPA plus low-frequency ultrasound (300 Hz) showed an increased rate of cerebral hemorrhage in a trial including 26 patients [65]. Nonetheless, microbubbles were postulated to reduce the energy required for cavitation by acting as cavitation nuclei. Their administration in conjunction with ultrasound demonstrated a significant improvement in two-hour recanalisation in a study of 111 AIS patients consecutive to middle cerebral artery occlusion treated with IV tPA [66]. The NOR-SASS study investigated contrast-enhanced sonothrombolysis with Sonovue® in an unselected AIS population, with or without occlusion, receiving tPA, but showed no significant clinical effect [67]. Another technique for targeting thrombus involves using magnetic nanoparticles under external magnetic force irradiation. The Pulse NanoMED System (Euphrates Vascular) is currently undergoing testing (ClinicalTrials.gov ID: NCT06052969 and NCT03098732). It combines an external rotating magnet with IV administered iron-oxide nanoparticles to enhance flow near the occlusion,

facilitating the delivery of tPA to the clot.

Finally, nanoparticles could be interesting for diagnosing AIS. Saleh *et al*. used IV ultrasmall IONPs in conjunction with multimodal stroke imaging to track macrophage recruitment into ischemic brain lesions, which reflects the inflammatory component of stroke damage [68]. The authors observed different patterns of macrophage infiltration during the early stages of AIS. This suggests that anti-inflammatory treatment could be tailored to the stroke profile. Iv *et al.* planned to use IONPs to measure inflammation in patients with brain tumors or other conditions of the central nervous system, including ischemic stroke, to help with diagnostic and potential treatments. However, the trial was stopped after only 10 patients over 120 were enrolled, all of whom had glioma (ClinicalTrials.gov ID: NCT02452216). The challenge of diagnosing AIS before brain imaging has triggered many research studies, but finding a biomarker has been unsuccessful so far.

4. Discussion

This review shows that there is no shortage of promising preclinical nanomedicine projects for the AIS diagnosis and treatment. However, this broad array of nanoparticles displayed in recent research articles varies widely in terms of maturity, feasibility and cannot most of the times be easily compared. This can be explained by the disparity in measurable readouts, *in vivo* models and often absence of certain key aspects towards future translation, such as storage viability or biodistribution data. Additionally, the methods used to obtain these data—such as fluorescence, radiotracing, or mass spectrometry—may not always be directly comparable. Conversely, only a few projects have reached the clinical stage, despite research on nanoparticles to treat AIS ongoing for more than three decades[69]. Current trials are underway to study the potential of nanoparticles in the AIS setting, to facilitate a more accurate and rapid diagnosis and to improve the efficacy of standard drug delivery, in order to enhance reperfusion and improve functional outcome.

Therefore, the current situation raises the question of which obstacles prevent nanotechnology from bridging the preclinical results with successful clinical applications. Among these obstacles, we identified intrinsic challenges related to nanoparticles' characteristics, as well as difficulties in addressing this specific pathology. These hurdles are further compounded by the emergency setting, which demands speed and logistic simplicity.

Consequently, there are intrinsic challenges in implementing nanotechnology for clinical use. Nanoparticle research typically requires collaboration across various disciplines, including nanotechnology, neurology, pharmacology, and materials science, the coordination of which can be resource-intensive. These resources are often scarce in public settings, making external funding crucial for clinical translation; however, securing such funding is frequently a complex process for researchers. Furthermore, characterization of NPs is challenging, with many factors (size, shape, composition) in play. ISO experiments often require long-term safety and efficacy data, which can be challenging to obtain due to the novel nature of nanomedicines. Long-term studies are essential to understand the chronic effects and potential toxicity of nanoparticles. Moreover, nanoparticles interact with biological systems in complex ways, potentially leading to unforeseen side effects [70]. An added hurdle lies in

the way that regulatory bodies handle NPs, with categorization as “excipients” or “combination products” not necessarily adequate for NPs characterization, and adding a layer of regulatory challenges [71]. This situation demands more rigorous study designs, especially since common clinical practices like blinding and randomization are not consistently applied. A meta-review from Namiot et al. in 2023 revealed that, as of January 2023, 476 clinical trials were underway involving nanoparticles for any medical application, mostly in Phase I and II, with 100 nanomedicines having reached the market, including among others the COVID-19 LNP vaccines. [72,73]. This indicates that this technology is still in a relative infancy, with few successful clinical trials to be used as references. In comparison, as of May 2024, 3225 trials of any type have been listed on clinicaltrials.gov for AIS only; however, for small molecules on cancer application, another fast-developing domain, 89 small molecules were approved for thousands of clinical trials listed [74]. Interestingly, nanomedicine actually seems to fare rather well once it reaches the clinical stage. While it can be hoped that more and more nanomedicine clinical trials succeed in order to build a reference framework, a dialog with regulatory bodies such as the FDA has already started to help clarify the guidelines of using nanotechnology in FDA-regulated products [71].

In order to facilitate the future application of nanoparticles for AIS, the currently proposed preclinical approaches should be designed from the outset with a clinical setting in mind. Notably, while many different affinity moieties are proposed for targeting NPs such as peptides (RGD [32]), polysaccharides (fucoidan [35]) or cell membranes [55], the final choice depends on which specific action is desired: neuroprotection in the ischemic brain, delivery of antiplatelets agents, or of fibrinolytics to the fibrin mesh. This also means using appropriate characterization and *in vivo* modeling. As reported above, few articles report synthesis-related challenges. 21% of investigated articles disclose stability measurements, even though these could be critical both for *in vivo* fate of the nanoparticles, but also for formulation prior patient administration. Even fewer disclose drying methods to improve their storage. However, as was seen with the COVID vaccines, logistic criteria can be of paramount importance, especially in developing countries or when speed is necessary [75]. The stability of nanoparticles must be ensured during storage and within the complex physiological conditions of the human body. Nanoparticles are prone to aggregation or degradation over time, which can alter their intended function and reduce their therapeutic potential. In the case of AIS, where early treatment is essential to minimize damage, such formulation issues can thus further delay recovery. This can result from delays related to reconstitution, *in situ* preparation or even procurement of such nanodrugs. A limited number of articles clearly address stability issue: Hoogendijk *et al*. reported in 2020 a continuous flow microfluidic device for production of perfluorocarbon nanoemulsion in order to deliver oxygen to the ischemic tissue [76], while Son *et al*. and Han *et al*. both described 3D methods, thus improving yield and reproducibility, for MSC-derived EV production: either through micro-patterned wells to form spheroids, or through culture in 3D hydrogels. Both EV formulations were then used for neuroprotection, and characterized for batch-to-batch variability [56,57]. This is critical as the protocols described in articles are not necessarily compatible with scaled-up production, nor with the strict requirements of good manufacturing practices (GMP) which are required for clinical use.

Nonetheless, the primary objective of AIS treatment is to rapidly achieve reperfusion. As previously stated, the two primary reperfusion strategies are thrombolysis and thrombectomy. Despite the significant improvement in recanalization rates that these

treatments have brought about, over 50% of patients retain disabilities despite successful recanalization due to the relative inefficacy of the treatments and the associated risks [18]. The use of tPA is constrained by a narrow therapeutic window and hemorrhagic risks. Furthermore, several inherent difficulties are likely to be associated with the nature of ischemic strokes. Indeed, failure to thrombolysis has been shown to be related to the composition of the thrombus causing the occlusion, which varies depending on the etiology of the stroke [37]. Vectorising tPA, using nanoparticles, does not appear to be the only solution for improving recanalization in such situations. Consequently, there is growing interest in identifying new therapeutic targets in stroke composition as alternatives or complements to existing treatments to enhance recanalization success, for exempla with DNase targeting NETs, N-acetylcysteine, ADAMTS13 targeting von Willebrand factor, and anti-glycoprotein VI, with a potential to enhance recanalization without increasing the hemorrhagic risk [37]. Indeed, thrombi have shown variable behaviors in vitro, such as different levels of susceptibility to the synergistic effects of DNase I [77], and ex vivo, under conditions mimicking endovascular thrombectomy using human blood clot analogs. This emphasizes the importance of understanding thrombus composition for improving stroke treatment strategies [78].

Importantly, research on nanoparticles in the specific AIS setting for treatment faces several significant challenges. AIS requires immediate intervention to minimize neurological damage within a very narrow therapeutic window. Developing nanoparticle-based therapies that can be administered and effective within this short timeframe is complex. However, a few researchers mention ways of administration that differ from the usual IV injection: some articles rely on intracisternal, stereotaxic or intracarotid administration, which are more invasive and would face more challenges before clinical acceptance. In contrast, some authors propose intranasal or oral delivery (even though the latter could prove difficult in practice as some stroke patients present dysphagia), which could facilitate treatment access and speed up medical care, such as Yu et al. who described in 2023 a multi-drug loaded liposome compatible with intranasal delivery for neuroprotection through anti-inflammation and anti-apoptosis effects [79]. However, these methods have their limitations: specifically, the ability to effectively reach the injured area and the time required for the drug to act. Moreover, in animal models like mice, the shorter distance a drug must travel, and anatomical differences compared to humans can limit the translation of these methods to clinical settings. Consequently, optimizing the pharmacokinetics and biodistribution of nanoparticles to act swiftly within this critical window is essential, yet this aspect is often overlooked in preclinical studies.

Moreover, due to the nature of ischemic strokes, the choice of *in vivo* models is critical. The most explored yet, the tMCAO (65% of reported *in vivo* models as evoked above), does not correlate to the current damages that ischemic stroke patients encounter (around 90% of patients admitted with LVO stroke in the US between 2014 and 2015 showed no recanalization) [42]. However, EVT has shown great premises to improve recanalization in patients (up to 90% according to Lapergue *et al.*, 2021) [80]. Nonetheless, the rate of EVT-treated patients still represented only 5% of AIS patients in the US up to 2021, with an expected future growth of 5–10%/year for the next several years in performed EVTs [81]. Therefore, choosing a correct model, preferably involving the induction of a thrombus, is paramount to ensure that preclinical results are representative of the clinical fate and to avoid

the current overreliance on tMCAO; part of the answer could be the use of ex vivo clots retrieved from EVT patients [82] in order to test the various therapies directly on human ischemic stroke thrombi.

Another significant challenge is the safety of reperfusion treatments. Intracranial hemorrhage is a common and serious complication that increases mortality and impairs prognosis. Protecting the vascular endothelium is essential to limit BBB permeability and prevent hemorrhages. Future research should focus on identifying molecular targets that can strengthen the BBB integrity. Rather than focusing on the clot exclusively, strategies to protect the endothelium can reduce the risk of barrier rupture and hemorrhagic complications. Interventions aimed at limiting endothelial permeability may include the use of specific molecules that stabilize the endothelium, thereby reducing the risk of hemorrhagic transformation following a stroke [83]. Here, nanoparticles could benefit from the ability to transport various active agents to exert both thrombolysis and protection against subsequent damages.

Finally, precision medicine represents a promising avenue for research into the treatment of AIS. The identification of specific biomarkers would allow for the development of personalized treatments and optimized clinical outcomes. The measurement of circulating free DNA, an indicator of NETosis, could enable more effective targeting of patients with molecules inhibiting this process. The use of biomarkers can also help determine the presence and activity of specific biological targets, thereby better selecting patients for available therapies. The use of biomarkers to rapidly assess the extent of ischemia and potential treatment response could allow clinicians to tailor therapeutic strategies in real time, thereby improving recovery chances and reducing adverse effects.

Nanoparticles represent a potentially powerful therapeutic tool for the acute treatment of stroke. However, it seems important to redefine therapeutic biological targets in alignment with the current needs for improved recanalization and the reduction of hemorrhagic complications associated with existing stroke therapies. Furthermore, the feasibility of using this technology in AIS must be evaluated from the start, as speed is critical for patients' outcome, thus limiting certain technologies or formulations. Ongoing studies are continually evaluating these aspects to determine the viability and efficacy of nanoparticle-based interventions in acute stroke care, but a rational design of such treatments must take into account the AIS specificity, meaning formulations that can be stored, reconstituted and administered quickly; and key development aspects should be addressed from the start, such as toxicity, biodistribution, feasibility of a scaled-up GMP synthesis, and relevance of *in vivo* experiments. With these considerations, these new treatment options could improve acute stroke patient care.

Sources of Funding

This work was supported by INSERM, Université Paris Cité, Université Sorbonne Paris Nord and the ANR "FightClot" (ANR-20-CE18-0005-01).

Declaration of Competing Interest

The authors declare that they have no known competing financial interests or personal

relationships that could have appeared to influence the work reported in this paper.

Supplementary Material

Bibliography of all 247 experimental papers used in this analysis.

CRediT

Thibault de La Taille: Conceptualization, Data curation, Investigation, Methodology, Visualization, Writing – original draft ; **Diana Doukhi**: Data curation, Investigation, Writing – original draft; **Mikael Mazighi**: Formal analysis, Funding acquisition, Project administration, Resources, Supervision, Validation, Writing – review and editing; **Cédric Chauvierre**: Conceptualization, Formal analysis, Funding acquisition, Project administration, Resources, Supervision, Validation, Writing – review and editing.

References

[1] GBD 2019 Stroke Collaborators. Global, regional, and national burden of stroke and its risk factors, 1990-2019: a systematic analysis for the Global Burden of Disease Study 2019. Lancet Neurol 2021;20:795–820. https://doi.org/10.1016/S1474-4422(21)00252-0.

[2] National Institute of Neurological Disorders and Stroke rt-PA Stroke Study Group. Tissue plasminogen activator for acute ischemic stroke. N Engl J Med 1995;333:1581–7. https://doi.org/10.1056/NEJM199512143332401.

[3] Goyal M, Demchuk AM, Menon BK, Eesa M, Rempel JL, Thornton J, et al. Randomized Assessment of Rapid Endovascular Treatment of Ischemic Stroke. N Engl J Med 2015;372:1019–30. https://doi.org/10.1056/NEJMoa1414905.

[4] Berkhemer OA, Fransen PSS, Beumer D, Berg LA van den, Lingsma HF, Yoo AJ, et al. A Randomized Trial of Intraarterial Treatment for Acute Ischemic Stroke. N Engl J Med 2015;372:11–20. https://doi.org/10.1056/NEJMoa1411587.

[5] Saver JL, Goyal M, Bonafe A, Diener H-C, Levy EI, Pereira VM, et al. Stent-Retriever Thrombectomy after Intravenous t-PA vs. t-PA Alone in Stroke. N Engl J Med 2015;372:2285–95. https://doi.org/10.1056/NEJMoa1415061.

[6] Jovin TG, Chamorro A, Cobo E, Miquel MA de, Molina CA, Rovira A, et al. Thrombectomy within 8 Hours after Symptom Onset in Ischemic Stroke. N Engl J Med 2015;372:2296–306. https://doi.org/10.1056/NEJMoa1503780.

[7] Campbell BCV, Mitchell PJ, Kleinig TJ, Dewey HM, Churilov L, Yassi N, et al. Endovascular Therapy for Ischemic Stroke with Perfusion-Imaging Selection. N Engl J Med 2015;372:1009–18. https://doi.org/10.1056/NEJMoa1414792.

[8] Hacke W, Kaste M, Bluhmki E, Brozman M, Dávalos A, Guidetti D, et al. Thrombolysis with Alteplase 3 to 4.5 Hours after Acute Ischemic Stroke. N Engl J Med 2008;359:1317–29. https://doi.org/10.1056/NEJMoa0804656.

[9] Powers WJ, Rabinstein AA, Ackerson T, Adeoye OM, Bambakidis NC, Becker K, et al. Guidelines for the Early Management of Patients With Acute Ischemic Stroke: 2019 Update to the 2018 Guidelines for the Early Management of Acute Ischemic Stroke: A Guideline for Healthcare Professionals From the American Heart Association/American Stroke Association. Stroke 2019;50:e344–418. https://doi.org/10.1161/STR.0000000000000211.

[10] Berge E, Whiteley W, Audebert H, De Marchis GM, Fonseca AC, Padiglioni C, et al. European Stroke Organisation (ESO) guidelines on intravenous thrombolysis for acute ischaemic stroke. Eur Stroke J 2021;6:I–LXII. https://doi.org/10.1177/2396987321989865.

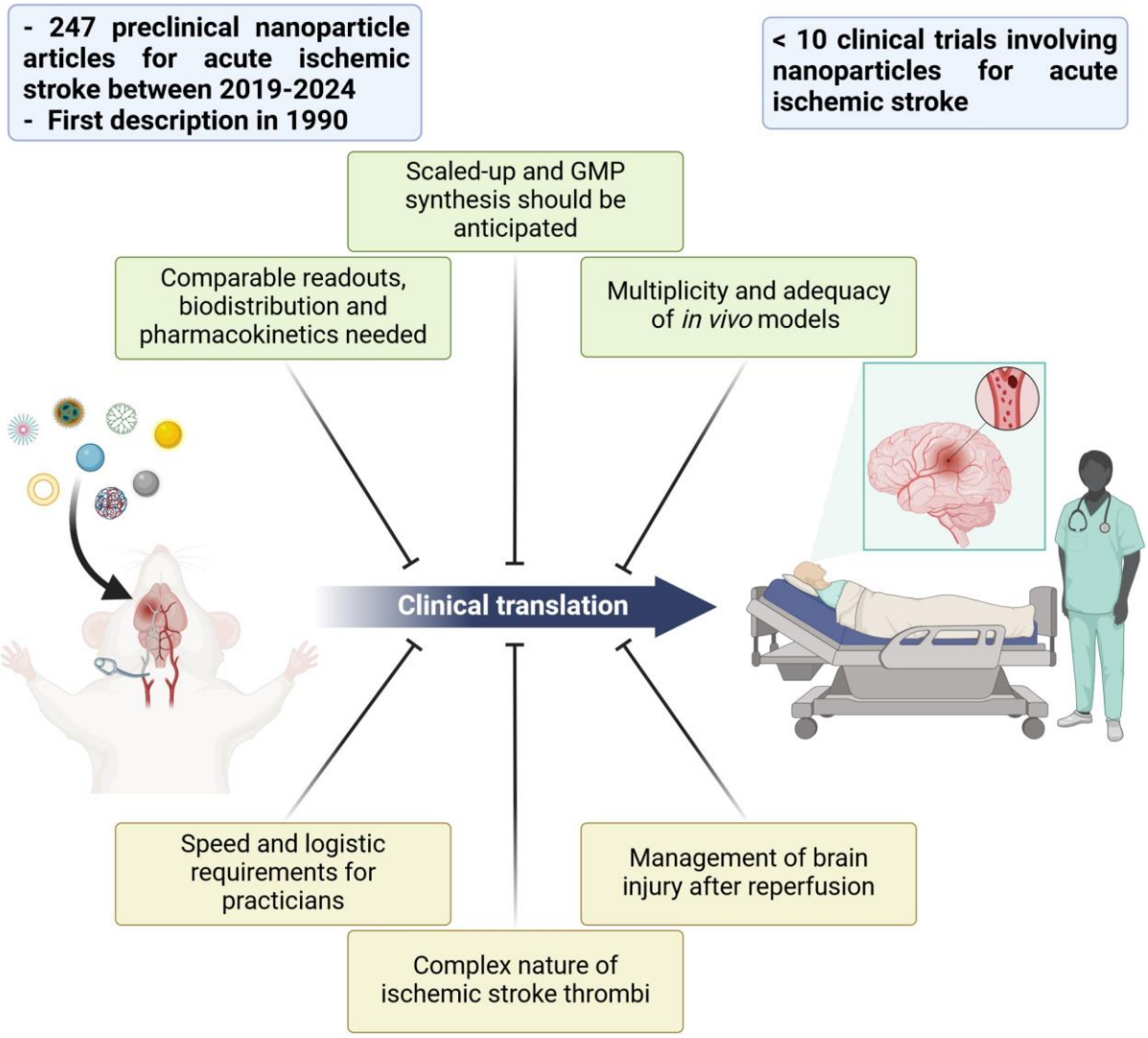
[11] Thomalla G, Simonsen CZ, Boutitie F, Andersen G, Berthezene Y, Cheng B, et al. MRI-Guided Thrombolysis for Stroke with Unknown Time of Onset. N Engl J Med 2018;379:611–22. https://doi.org/10.1056/NEJMoa1804355.
[12] Ma H, Campbell BCV, Parsons MW, Churilov L, Levi CR, Hsu C, et al. Thrombolysis Guided by Perfusion Imaging up to 9 Hours after Onset of Stroke. N Engl J Med 2019;380:1795–803. https://doi.org/10.1056/NEJMoa1813046.
[13] Alamowitch S, Turc G, Palaiodimou L, Bivard A, Cameron A, De Marchis GM, et al. European Stroke Organisation (ESO) expedited recommendation on tenecteplase for acute ischaemic stroke. Eur Stroke J 2023;8:8–54. https://doi.org/10.1177/23969873221150022.
[14] de Havenon A, Sheth K, Johnston KC, Delic A, Stulberg E, Majersik J, et al. Acute Ischemic Stroke Interventions in the United States and Racial, Socioeconomic, and Geographic Disparities. Neurology 2021;97:e2292–303. https://doi.org/10.1212/WNL.0000000000012943.
[15] Seners P, Turc G, Maïer B, Mas J-L, Oppenheim C, Baron J-C. Incidence and Predictors of Early Recanalization After Intravenous Thrombolysis. Stroke 2016;47:2409–12. https://doi.org/10.1161/STROKEAHA.116.014181.
[16] Albers GW, Marks MP, Kemp S, Christensen S, Tsai JP, Ortega-Gutierrez S, et al. Thrombectomy for Stroke at 6 to 16 Hours with Selection by Perfusion Imaging. N Engl J Med 2018;378:708–18. https://doi.org/10.1056/NEJMoa1713973.
[17] Nogueira RG, Jadhav AP, Haussen DC, Bonafe A, Budzik RF, Bhuva P, et al. Thrombectomy 6 to 24 Hours after Stroke with a Mismatch between Deficit and Infarct. N Engl J Med 2018;378:11–21. https://doi.org/10.1056/NEJMoa1706442.
[18] Turc G, Bhogal P, Fischer U, Khatri P, Lobotesis K, Mazighi M, et al. European Stroke Organisation (ESO) - European Society for Minimally Invasive Neurological Therapy (ESMINT) Guidelines on Mechanical Thrombectomy in Acute Ischemic Stroke. J Neurointerventional Surg 2023;15:e8. https://doi.org/10.1136/neurintsurg-2018-014569.
[19] Ehrlich P. Experimental Researches on Specific Therapy: On Immunity with special Reference to the Relationship between Distribution and Action of Antigens**[Reprinted (with amendments by the Ed.) from The Harben Lectures for 1907 of the Royal Institute of Public Health, London: Lewis, 1908; cf. Bibl. 200 and 181.]: FIRST HARBEN LECTURE††[Delivered in London, 5 June 1907.]. In: Himmelweit F, editor. Collect. Pap. Paul Ehrlich, Pergamon; 1960, p. 106–17. https://doi.org/10.1016/B978-0-08-009056-6.50015-4.
[20] Blanco E, Shen H, Ferrari M. Principles of nanoparticle design for overcoming biological barriers to drug delivery. Nat Biotechnol 2015;33:941–51. https://doi.org/10.1038/nbt.3330.
[21] Navya PN, Daima HK. Rational engineering of physicochemical properties of nanomaterials for biomedical applications with nanotoxicological perspectives. Nano Converg 2016;3:1. https://doi.org/10.1186/s40580-016-0064-z.
[22] Müller K, Fedosov DA, Gompper G. Margination of micro- and nano-particles in blood flow and its effect on drug delivery. Sci Rep 2014;4:4871. https://doi.org/10.1038/srep04871.
[23] Sarfati P, de La Taille T, Portioli C, Spanò R, Lalatonne Y, Decuzzi P, et al. REVIEW: “ISCHEMIC STROKE: from fibrinolysis to functional recovery” Nanomedicine: emerging approaches to treat ischemic stroke. Neuroscience 2024;550:102–13. https://doi.org/10.1016/j.neuroscience.2023.11.035.
[24] Wang Y, Jian C, Long Y, Xu X, Song Y, Yin Z. H2O2-triggered “off/on signal” nanoparticles target P-selectin for the non-invasive and contrast-enhanced theranostics for arterial thrombosis. Acta Biomater 2023;158:769–81. https://doi.org/10.1016/j.actbio.2022.12.026.
[25] Zhang Y, Liu Y, Zhang T, Wang Q, Huang L, Zhong Z, et al. Targeted Thrombolytic Therapy with Metal–Organic-Framework-Derived Carbon Based Platforms with Multimodal Capabilities. ACS Appl Mater Interfaces 2021;13:24453–62. https://doi.org/10.1021/acsami.1c03134.

[26] Zhang H, Zhao Z, Sun S, Zhang S, Wang Y, Zhang X, et al. Molecularly self-fueled nano-penetrator for nonpharmaceutical treatment of thrombosis and ischemic stroke. Nat Commun 2023;14:255. https://doi.org/10.1038/s41467-023-35895-5.
[27] Zhang F, Liu Y, Lei J, Wang S, Ji X, Liu H, et al. Metal–Organic-Framework-Derived Carbon Nanostructures for Site-Specific Dual-Modality Photothermal/Photodynamic Thrombus Therapy. Adv Sci 2019;6:1901378. https://doi.org/10.1002/advs.201901378.
[28] Shekhar H, Kleven RT, Peng T, Palaniappan A, Karani KB, Huang S, et al. In vitro characterization of sonothrombolysis and echocontrast agents to treat ischemic stroke. Sci Rep 2019;9:9902. https://doi.org/10.1038/s41598-019-46112-z.
[29] Choi W, Key J, Youn I, Lee H, Han S. Cavitation-assisted sonothrombolysis by asymmetrical nanostars for accelerated thrombolysis. J Controlled Release 2022;350:870–85. https://doi.org/10.1016/j.jconrel.2022.09.008.
[30] Xu J, Zhang Y, Xu J, Liu G, Di C, Zhao X, et al. Engineered Nanoplatelets for Targeted Delivery of Plasminogen Activators to Reverse Thrombus in Multiple Mouse Thrombosis Models. Adv Mater 2020;32:1905145. https://doi.org/10.1002/adma.201905145.
[31] Li C, Zhao Z, Luo Y, Ning T, Liu P, Chen Q, et al. Macrophage-Disguised Manganese Dioxide Nanoparticles for Neuroprotection by Reducing Oxidative Stress and Modulating Inflammatory Microenvironment in Acute Ischemic Stroke. Adv Sci 2021;8:2101526. https://doi.org/10.1002/advs.202101526.
[32] Tian T, Cao L, He C, Ye Q, Liang R, You W, et al. Targeted delivery of neural progenitor cell-derived extracellular vesicles for anti-inflammation after cerebral ischemia. Theranostics 2021;11:6507–21. https://doi.org/10.7150/thno.56367.
[33] Yu W, Yin N, Yang Y, Xuan C, Liu X, Liu W, et al. Rescuing ischemic stroke by biomimetic nanovesicles through accelerated thrombolysis and sequential ischemia-reperfusion protection. Acta Biomater 2022;140:625–40. https://doi.org/10.1016/j.actbio.2021.12.009.
[34] Huang L, Wang J, Huang S, Siaw-Debrah F, Nyanzu M, Zhuge Q. Polyacrylic acid-coated nanoparticles loaded with recombinant tissue plasminogen activator for the treatment of mice with ischemic stroke. Biochem Biophys Res Commun 2019;516:565–70. https://doi.org/10.1016/j.bbrc.2019.06.079.
[35] Zenych A, Jacqmarcq C, Aid R, Fournier L, Forero Ramirez LM, Chaubet F, et al. Fucoidan-functionalized polysaccharide submicroparticles loaded with alteplase for efficient targeted thrombolytic therapy. Biomaterials 2021;277:121102. https://doi.org/10.1016/j.biomaterials.2021.121102.
[36] Lippi G, Franchini M, Targher G. Arterial thrombus formation in cardiovascular disease. Nat Rev Cardiol 2011;8:502–12. https://doi.org/10.1038/nrcardio.2011.91.
[37] Ho-Tin-Noé B, Desilles J-P, Mazighi M. Thrombus composition and thrombolysis resistance in stroke. Res Pract Thromb Haemost 2023;7:100178. https://doi.org/10.1016/j.rpth.2023.100178.
[38] Fukuta T, Ikeda-Imafuku M, Iwao Y. Development of Edaravone Ionic Liquids and Their Application for the Treatment of Cerebral Ischemia/Reperfusion Injury. Mol Pharm 2023;20:3115–26. https://doi.org/10.1021/acs.molpharmaceut.3c00103.
[39] Liu S, Xu J, Liu Y, You Y, Xie L, Tong S, et al. Neutrophil-Biomimetic “Nanobuffer” for Remodeling the Microenvironment in the Infarct Core and Protecting Neurons in the Penumbra via Neutralization of Detrimental Factors to Treat Ischemic Stroke. ACS Appl Mater Interfaces 2022;14:27743–61. https://doi.org/10.1021/acsami.2c09020.
[40] Huang Z, Qian K, Chen J, Qi Y, E Y, Liang J, et al. A biomimetic zeolite-based nanoenzyme contributes to neuroprotection in the neurovascular unit after ischaemic stroke via efficient removal of zinc and ROS. Acta Biomater 2022;144:142–56. https://doi.org/10.1016/j.actbio.2022.03.018.
[41] Ma R, Xie Q, Li Y, Chen Z, Ren M, Chen H, et al. Animal models of cerebral ischemia: A review. Biomed Pharmacother 2020;131:110686. https://doi.org/10.1016/j.biopha.2020.110686.

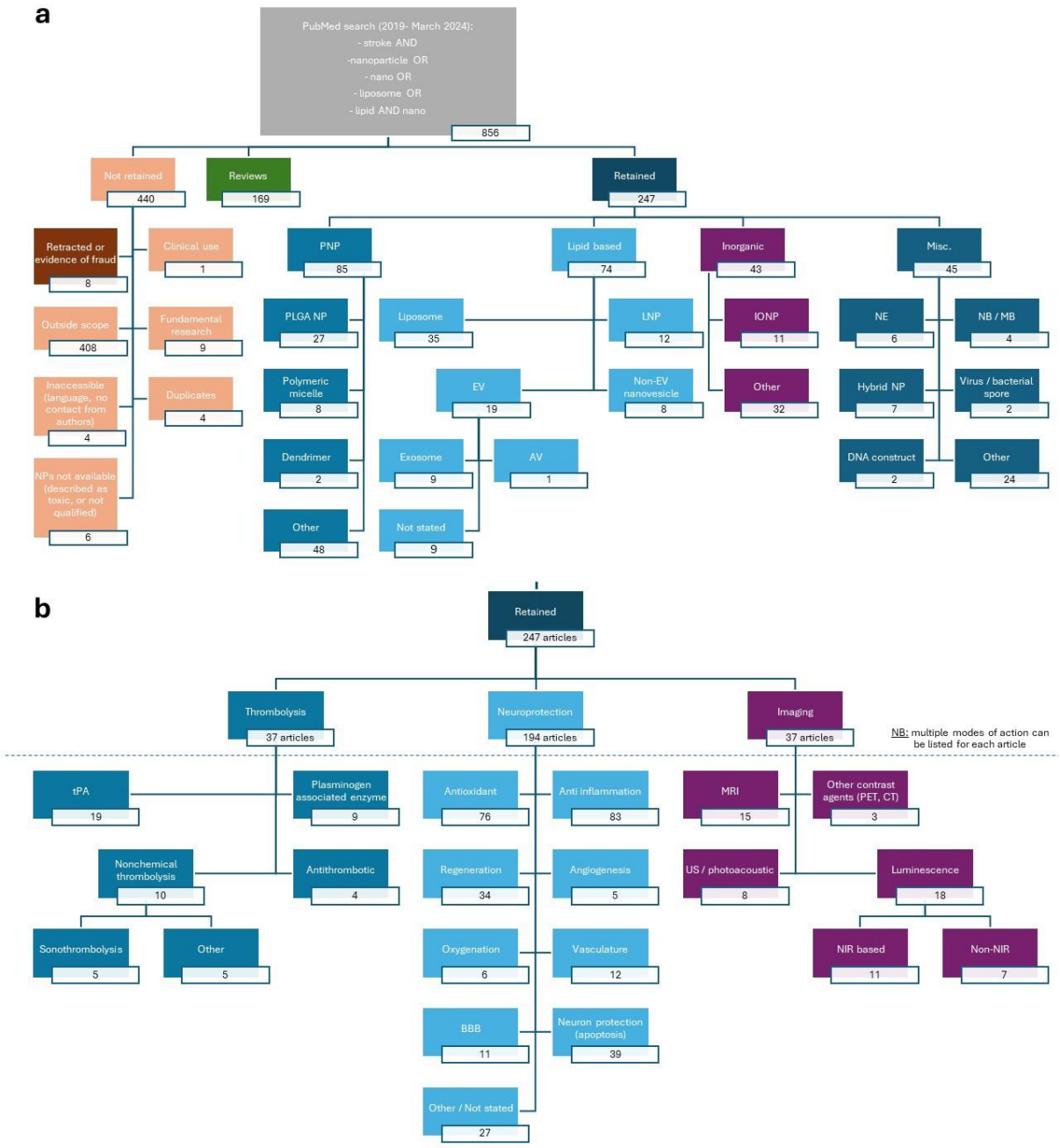
[42] McBride DW, Zhang JH. Precision Stroke Animal Models: the Permanent MCAO Model Should Be the Primary Model, Not Transient MCAO. Transl Stroke Res 2017;8:397–404. https://doi.org/10.1007/s12975-017-0554-2.
[43] Shi J, Yu W, Xu L, Yin N, Liu W, Zhang K, et al. Bioinspired Nanosponge for Salvaging Ischemic Stroke via Free Radical Scavenging and Self-Adapted Oxygen Regulating. Nano Lett 2020;20:780–9. https://doi.org/10.1021/acs.nanolett.9b04974.
[44] Tang L, Yin Y, Liu H, Zhu M, Cao Y, Feng J, et al. Blood–Brain Barrier-Penetrating and Lesion-Targeting Nanoplatforms Inspired by the Pathophysiological Features for Synergistic Ischemic Stroke Therapy. Adv Mater 2024:2312897. https://doi.org/10.1002/adma.202312897.
[45] Zhou M, Zhang T, Zhang B, Zhang X, Gao S, Zhang T, et al. A DNA Nanostructure-Based Neuroprotectant against Neuronal Apoptosis via Inhibiting Toll-like Receptor 2 Signaling Pathway in Acute Ischemic Stroke. ACS Nano 2022;16:1456–70. https://doi.org/10.1021/acsnano.1c09626.
[46] Ye Q, Zheng D, Chen K, Xu H, Yang Z, Wen J, et al. Phase-Change Based Oxygen Carriers Improve Acute Cerebral Hypoxia. Small 2023;n/a:2309180. https://doi.org/10.1002/smll.202309180.
[47] Ashafaq M, Intakhab Alam M, Khan A, Islam F, Khuwaja G, Hussain S, et al. Nanoparticles of resveratrol attenuates oxidative stress and inflammation after ischemic stroke in rats. Int Immunopharmacol 2021;94:107494. https://doi.org/10.1016/j.intimp.2021.107494.
[48] Liao J, Li Y, Fan L, Sun Y, Gu Z, Xu Q-Q, et al. Bioactive Ceria Nanoenzymes Target Mitochondria in Reperfusion Injury to Treat Ischemic Stroke. ACS Nano 2024;18:5510–29. https://doi.org/10.1021/acsnano.3c10982.
[49] He L, Huang G, Liu H, Sang C, Liu X, Chen T. Highly bioactive zeolitic imidazolate framework-8-capped nanotherapeutics for efficient reversal of reperfusion-induced injury in ischemic stroke. Sci Adv 2020;6:eaay9751. https://doi.org/10.1126/sciadv.aay9751.
[50] Yan BC, Cao J, Liu J, Gu Y, Xu Z, Li D, et al. Dietary Fe3O4 Nanozymes Prevent the Injury of Neurons and Blood–Brain Barrier Integrity from Cerebral Ischemic Stroke. ACS Biomater Sci Eng 2021;7:299–310. https://doi.org/10.1021/acsbiomaterials.0c01312.
[51] Li Y, Liu B, Zhao T, Quan X, Han Y, Cheng Y, et al. Comparative study of extracellular vesicles derived from mesenchymal stem cells and brain endothelial cells attenuating blood–brain barrier permeability via regulating Caveolin-1-dependent ZO-1 and Claudin-5 endocytosis in acute ischemic stroke. J Nanobiotechnology 2023;21:70. https://doi.org/10.1186/s12951-023-01828-z.
[52] Zhang A, Li J, Wang S, Xu Y, Li Q, Wu Z, et al. Rapid and improved oral absorption of N-butylphthalide by sodium cholate-appended liposomes for efficient ischemic stroke therapy. Drug Deliv 2021;28:2469–79. https://doi.org/10.1080/10717544.2021.2000678.
[53] Deuchar GA, van Kralingen JC, Work LM, Santosh C, Muir KW, McCabe C, et al. Preclinical Validation of the Therapeutic Potential of Glasgow Oxygen Level Dependent (GOLD) Technology: a Theranostic for Acute Stroke. Transl Stroke Res 2019;10:583–95. https://doi.org/10.1007/s12975-018-0679-y.
[54] Fournier L, Abioui-Mourgues M, Chabouh G, Aid R, Taille TDL, Couture O, et al. rtPA-loaded fucoidan polymer microbubbles for the targeted treatment of stroke. Biomaterials 2023;303:122385. https://doi.org/10.1016/j.biomaterials.2023.122385.
[55] Ma J, Zhang S, Liu J, Liu F, Du F, Li M, et al. Targeted Drug Delivery to Stroke via Chemotactic Recruitment of Nanoparticles Coated with Membrane of Engineered Neural Stem Cells. Small 2019;15:1902011. https://doi.org/10.1002/smll.201902011.
[56] Han M, Zhang Z, Liu Z, Liu Y, Zhao H, Wang B, et al. Three-dimensional-cultured MSC-derived exosome with hydrogel for cerebral ischemia repair. Biomater Adv 2023;149:213396. https://doi.org/10.1016/j.bioadv.2023.213396.
[57] Son JP, Kim EH, Shin EK, Kim DH, Sung JH, Oh MJ, et al. Mesenchymal Stem Cell-Extracellular Vesicle Therapy for Stroke: Scalable Production and Imaging Biomarker Studies. Stem Cells Transl Med 2023;12:459–73. https://doi.org/10.1093/stcltm/szad034.

[58] Brown AT, Arthur MC, Nix JS, Montgomery JA, Skinner RD, Roberson PK, et al. Dodecafluoropentane Emulsion (DDFPe) Decreases Stroke Size and Improves Neurological Scores in a Permanent Occlusion Rat Stroke Model. Open Neurol J 2014;8:27–33. https://doi.org/10.2174/1874205X01408010027.
[59] Woods SD, Skinner RD, Ricca AM, Brown AT, Lowery JD, Borrelli MJ, et al. Progress in Dodecafluoropentane Emulsion as a Neuroprotective Agent in a Rabbit Stroke Model. Mol Neurobiol 2013;48:363–7. https://doi.org/10.1007/s12035-013-8495-6.
[60] Culp WC, Onteddu SS, Brown A, Nalleballe K, Sharma R, Skinner RD, et al. Dodecafluoropentane Emulsion in Acute Ischemic Stroke: A Phase Ib/II Randomized and Controlled Dose-Escalation Trial. J Vasc Interv Radiol JVIR 2019;30:1244-1250.e1. https://doi.org/10.1016/j.jvir.2019.04.020.
[61] Alexandrov AV, Molina CA, Grotta JC, Garami Z, Ford SR, Alvarez-Sabin J, et al. Ultrasound-Enhanced Systemic Thrombolysis for Acute Ischemic Stroke. N Engl J Med 2004;351:2170–8. https://doi.org/10.1056/NEJMoa041175.
[62] Ricci S, Dinia L, Del Sette M, Anzola P, Mazzoli T, Cenciarelli S, et al. Sonothrombolysis for acute ischaemic stroke. Cochrane Database Syst Rev 2012:CD008348. https://doi.org/10.1002/14651858.CD008348.pub2.
[63] Tsivgoulis G, Eggers J, Ribo M, Perren F, Saqqur M, Rubiera M, et al. Safety and Efficacy of Ultrasound-Enhanced Thrombolysis. Stroke 2010;41:280–7. https://doi.org/10.1161/STROKEAHA.109.563304.
[64] Alexandrov AV, Köhrmann M, Soinne L, Tsivgoulis G, Barreto AD, Demchuk AM, et al. Safety and efficacy of sonothrombolysis for acute ischaemic stroke: a multicentre, double-blind, phase 3, randomised controlled trial. Lancet Neurol 2019;18:338–47. https://doi.org/10.1016/S1474-4422(19)30026-2.
[65] Daffertshofer M, Gass A, Ringleb P, Sitzer M, Sliwka U, Els T, et al. Transcranial Low-Frequency Ultrasound-Mediated Thrombolysis in Brain Ischemia. Stroke 2005;36:1441–6. https://doi.org/10.1161/01.STR.0000170707.86793.1a.
[66] Molina CA, Ribo M, Rubiera M, Montaner J, Santamarina E, Delgado-Mederos R, et al. Microbubble Administration Accelerates Clot Lysis During Continuous 2-MHz Ultrasound Monitoring in Stroke Patients Treated With Intravenous Tissue Plasminogen Activator. Stroke 2006;37:425–9. https://doi.org/10.1161/01.STR.0000199064.94588.39.
[67] Nacu A, Kvistad CE, Logallo N, Naess H, Waje-Andreassen U, Aamodt AH, et al. A pragmatic approach to sonothrombolysis in acute ischaemic stroke: the Norwegian randomised controlled sonothrombolysis in acute stroke study (NOR-SASS). BMC Neurol 2015;15:110. https://doi.org/10.1186/s12883-015-0359-4.
[68] Saleh A, Schroeter M, Ringelstein A, Hartung H-P, Siebler M, Mödder U, et al. Iron oxide particle-enhanced MRI suggests variability of brain inflammation at early stages after ischemic stroke. Stroke 2007;38:2733–7. https://doi.org/10.1161/STROKEAHA.107.481788.
[69] Imaizumi S, Woolworth V, Fishman RA, Chan PH. Liposome-entrapped superoxide dismutase reduces cerebral infarction in cerebral ischemia in rats. Stroke 1990;21:1312–7. https://doi.org/10.1161/01.str.21.9.1312.
[70] Soenen S, Rivera Gil P, Montenegro JM, Parak W, De Smedt S, Braeckmans K. Cellular Toxicity of Inorganic Nanoparticles: Common Aspects and Guidelines for Improved Nanotoxicity Evaluation. Nano Today 2011;6:446–65. https://doi.org/10.1016/j.nantod.2011.08.001.
[71] Halwani AA. Development of Pharmaceutical Nanomedicines: From the Bench to the Market. Pharmaceutics 2022;14:106. https://doi.org/10.3390/pharmaceutics14010106.
[72] Namiot ED, Sokolov AV, Chubarev VN, Tarasov VV, Schiöth HB. Nanoparticles in Clinical Trials: Analysis of Clinical Trials, FDA Approvals and Use for COVID-19 Vaccines. Int J Mol Sci 2023;24:787. https://doi.org/10.3390/ijms24010787.
[73] Shan X, Gong X, Li J, Wen J, Li Y, Zhang Z. Current approaches of nanomedicines in the market and various stage of clinical translation. Acta Pharm Sin B 2022;12:3028–48. https://doi.org/10.1016/j.apsb.2022.02.025.

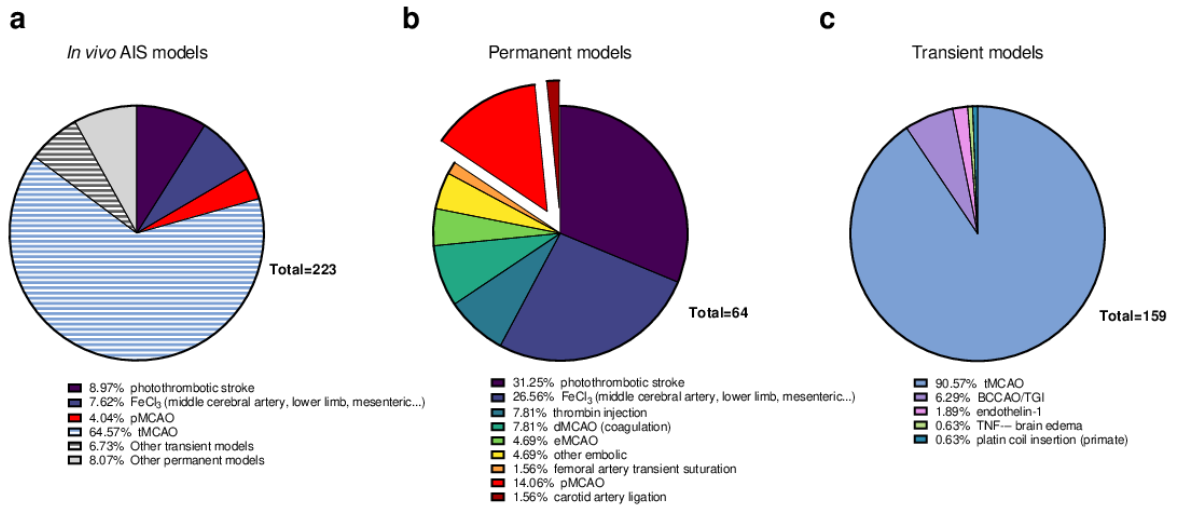
[74] Zhong L, Li Y, Xiong L, Wang W, Wu M, Yuan T, et al. Small molecules in targeted cancer therapy: advances, challenges, and future perspectives. Signal Transduct Target Ther 2021;6:201. https://doi.org/10.1038/s41392-021-00572-w.
[75] Oude Blenke E, Örnskov E, Schöneich C, Nilsson GA, Volkin DB, Mastrobattista E, et al. The Storage and In-Use Stability of mRNA Vaccines and Therapeutics: Not A Cold Case. J Pharm Sci 2023;112:386–403. https://doi.org/10.1016/j.xphs.2022.11.001.
[76] Hoogendijk E, Swider E, Staal AHJ, White PB, van Riessen NK, Glaßer G, et al. Continuous-Flow Production of Perfluorocarbon-Loaded Polymeric Nanoparticles: From the Bench to Clinic. ACS Appl Mater Interfaces 2020;12:49335–45. https://doi.org/10.1021/acsami.0c12020.
[77] Peña-Martínez C, Durán-Laforet V, García-Culebras A, Ostos F, Hernández-Jiménez M, Bravo-Ferrer I, et al. Pharmacological Modulation of Neutrophil Extracellular Traps Reverses Thrombotic Stroke tPA (Tissue-Type Plasminogen Activator) Resistance. Stroke 2019;50:3228–37. https://doi.org/10.1161/STROKEAHA.119.026848.
[78] Fitzgerald ST, Liu Y, Dai D, Mereuta OM, Abbasi M, Larco JLA, et al. Novel Human Acute Ischemic Stroke Blood Clot Analogs for In Vitro Thrombectomy Testing. AJNR Am J Neuroradiol 2021;42:1250–7. https://doi.org/10.3174/ajnr.A7102.
[79] Yu S, Li D, Shi A, Long Y, Deng J, Ma Y, et al. Multidrug-loaded liposomes prevent ischemic stroke through intranasal administration. Biomed Pharmacother 2023;162:114542. https://doi.org/10.1016/j.biopha.2023.114542.
[80] Lapergue B, Blanc R, Costalat V, Desal H, Saleme S, Spelle L, et al. Effect of Thrombectomy With Combined Contact Aspiration and Stent Retriever vs Stent Retriever Alone on Revascularization in Patients With Acute Ischemic Stroke and Large Vessel Occlusion: The ASTER2 Randomized Clinical Trial. JAMA 2021;326:1158–69. https://doi.org/10.1001/jama.2021.13827.
[81] Rai AT, Link PS, Domico JR. Updated estimates of large and medium vessel strokes, mechanical thrombectomy trends, and future projections indicate a relative flattening of the growth curve but highlight opportunities for expanding endovascular stroke care. J NeuroInterventional Surg 2023;15:e349–55. https://doi.org/10.1136/jnis-2022-019777.
[82] Ducroux C, Di Meglio L, Loyau S, Delbosc S, Boisseau W, Deschildre C, et al. Thrombus Neutrophil Extracellular Traps Content Impair tPA-Induced Thrombolysis in Acute Ischemic Stroke. Stroke 2018;49:754–7. https://doi.org/10.1161/STROKEAHA.117.019896.
[83] Okada T, Suzuki H, Travis ZD, Zhang JH. The Stroke-Induced Blood-Brain Barrier Disruption: Current Progress of Inspection Technique, Mechanism, and Therapeutic Target. Curr Neuropharmacol n.d.;18:1187–212. https://doi.org/10.2174/1570159X18666200528143301.



<u>Graphical abstract:</u> The gap between a rich preclinical research and low clinical translation of nanomedicine for acute ischemic strokes. The blunt-headed arrows represent hindrance to the development of clinical applications. Created with BioRender.com.



<u>Fig. 1:</u> Selection process of articles published in the last five years regarding the use of nanoparticles for stroke treatment. (a) Full selection including causes of rejection, and classification by NP type. (b) Classification of NPs by mechanism of action. AV: apoptotic vesicle. LNP: lipid nanoparticle. NE: nanoemulsion. NB/MB: nano-microbubble. PET: positron emission tomography. CT: computed tomography.



<u>Fig. 2:</u> Repartition of preclinical in vivo *models of AIS. (a) Repartition between permanent models (full slices) and transient models (hacked slices). (b) Repartition of the various permanent models, all composed of clots except the pMCAO and carotid artery ligation. (c) Repartition of the various transient models. pMCAO: permanent middle cerebral occlusion. dMCAO: distal middle cerebral occlusion. eMCAO: embolic middle cerebral occlusion. BCCAO/TGI: bilateral common carotid artery occlusion/transient global ischemia.*

ANNEX 6

Microemulsion-inspired polysaccharide nanoparticles for an advanced targeted thrombolytic treatment

*Thibault de La Taille [a], Pierre Sarfati [a], Rachida Aid [a, b], Louise Fournier [a], Graciela Pavon-Djavid [a], Frédéric Chaubet [a], Cédric Chauvierre [a,]**

[a] Université Paris Cité, Université Sorbonne Paris Nord, UMR-S U1148 INSERM, Laboratory for Vascular Translational Science (LVTS), F-75018, Paris, France

[b] Université Paris Cité, UMS 34, Fédération de Recherche en Imagerie Multi-modalité (FRIM), F-75018, Paris, France

* Corresponding author. E-mail address: cedric.chauvierre@inserm.fr (C. Chauvierre).

- Polysaccharides
- Polymeric nanoparticles
- Thrombotic diseases
- Targeted thrombolysis
- Drug delivery

Abstract

Among cardiovascular diseases, thrombotic diseases such as ischemic heart diseases and acute ischemic strokes are the most lethal, responsible by themselves for a quarter of worldwide deaths. While surgical treatments exist, they may not be used in all situations and systemic thrombolytic drug injection, such as recombinant tissue plasminogen activators (rtPA), often remain necessary, despite serious limitations including short therapeutic window, severe side effects and failure to address the complex nature of thrombi. This prompted intense research into alternative thrombolytics or delivery methods, including nanomedicine. However, most nanoparticles face issues of stability, biocompatibility or synthesis robustness; among them, polymeric nanoparticles, though usually versatile and biocompatible, sometimes lack robustness and may involve toxic or complex synthesis. Here, we present polysaccharide hydrogel nanoparticles, designed with an improved microemulsion-based approach which allowed a critical size reduction from microparticles to 315 nm nanoparticles. They were decorated with fucoidan, a sulfated polysaccharide capable of high affinity binding to P-selectin, a thrombi biomarker. These nanoparticles exhibited remarkable stability, adequate size, biocompatibility and targeting capacity, and could be loaded with two different drugs, rtPA (fibrin degradation) or DNase I (degradation of neutrophil extracellular traps, or NETs), to exert thrombolysis. Notably, improved thrombolysis was demonstrated on NET-containing thrombi, while *in vivo* thrombolysis shed light into improved thrombolysis of rtPA-loaded nanoparticles at 50% and 10% the recommended dose without secondary embolization. These safe, robust and easy-to-make nanoparticles could provide new effective delivery strategies for thrombolytic treatments, while demonstrating the potential of polysaccharide nanoparticles as drug delivery agents.

Cardiovascular diseases (CVDs) have been responsible for the most deaths worldwide in recent years, causing around 20 million deaths in 2021 alone [1]. Thrombotic diseases such as ischemic heart diseases (IHD) and acute ischemic strokes (AIS) are the two top killers among them, and they remain respectively at the second and fourth place (behind COVID19 pandemic) in leading causes for disability-adjusted life years (DALYs) worldwide in 2021. There are multiple factors that can explain recent increasing trends in CVDs, including diabetes, high blood pressure, population aging, and health inequities among others. The burden of AIS and IHDs is generally expected to continue increasing, making both prevention and improving therapeutic treatment critical. For ischemic diseases such as IHD and AIS, the insufficient blood flow causes tissue infarction and usually results from thrombi (blood clots) occluding blood vessels in the heart (myocardial infarction, MI) or the brain (AIS) [2]. While the exact composition of these thrombi can vary widely depending on the etiology and site of occlusion, they contain mostly fibrin, which is essential for the thrombus formation and mechanical strength, as well as various cell types including erythrocytes, immune cells or platelets [2]. However, other components were shown to be critical, such as Von Willebrand Factor (VWF) or neutrophil extracellular traps (NETs), which are DNA and protein networks released by neutrophils through a specific form of cell death known as NETosis [3].

Several "clot busters" thrombolytic drugs exist. In the case of AIS, intravenous thrombolysis was introduced in 1995 [4]: a recombinant tissue plasminogen activator (rtPA) enzyme, alteplase, is intravenously administered in order to activate plasminogen into plasmin, which will degrade fibrin in the thrombus. Despite its current place as a golden standard treatment, the drug half-life in circulation is less than 10 minutes, recanalization is low (around 20%) [5] and due to severe side effects (e.g., neurotoxicity, hemorrhagic transformations) and a short therapeutic window, only few patients are eligible: less than 10% AIS patients were treated with rtPA in the US in 2018 [6]. Since 2015, endovascular therapy (EVT) was introduced and demonstrated promising results, with a reported recanalization of more than 90% in certain patients [7]; however, it remains currently limited to large and medium vessel occlusions and therefore only 5% of all AIS patients in the US received EVT up to 2021, with few potentially eligible [8]. Furthermore, it has been recently advanced that the complex composition and structure of thrombi might impair thrombolytic approaches [3], with the extensive presence of NETs in AIS thrombi linked to rtPA resistance [9].

Thus, multiple nanomedicine approaches have been reported to improve thrombotic disease treatment [10,11]. Indeed, the vectorization of certain drugs through nanoparticles (NPs) directly to the thrombus could increase drug circulation time, avoid systemic side effects and reduce the total drug amount to be delivered. Interestingly, the size and shape of NPs can affect their distribution inside the blood flow due to margination effects. In blood vessels, erythrocytes and similarly sized objects tend to circulate in the center, while smaller objects are pushed to the sides ("marginate"). However, below a size threshold in the hundreds of nanometers, nanoparticles follow a plasma-like homogeneous flow distribution [12–14]. In contrast, below 100 nm NPs are generally most likely to extravasate or be internalized by endothelial cells, thus leaving the blood vessel [15,16] . Such behaviors could be used to either aim particles to the sides or to the center of the flow in blood

vessels. Other NPs innate properties can be useful, including increased surface-to-volume ratio, or emergence of certain physical properties (e.g., superparamagnetism, localized surface plasmon resonance) [11]. Moreover, the targeting of such NPs to the thrombus is paramount to ensure a reduced drug use and a local increased activity. For blood clots, multiple biomarkers and adequate targeting moieties have been identified, including the RGD peptide for GPIIb-IIIa platelet receptors [17], the CREKA peptide for fibrin [18], or platelet membrane coating to mimic platelet recruitment to the clot [19]. Besides, the use of nanoplatforms also opens the way for multiple drug delivery, as explored by Xu *et al*., 2019, who co-delivered rtPA and a neuroprotection agent to the ischemic brain area [20], theranostics with fluorescent nanoparticles with thrombolytic delivery from Niu *et al.*, 2020 [21], or simultaneous enzymatic and mechanical thrombolysis with the use of sonothrombolysis coupled with thrombolytic delivery through echogenic microbubbles [22].

While multiple NP formulations exist, from inorganic particles to dendrimers or lipid-based, choosing one design is not straightforward. For instance inorganic NP are usually very stable and reproductible, but their degradation and excretion can be problematic; dendrimers are multivalent tools useful for drug delivery, but have been burdened with toxicity issues; lipid-based materials such as liposomes or lipid nanoparticles are very promising, but they involve complex mix of lipids, sometimes chemically modified, with reproducibility issues and high production costs [11,23]. On the other hand, polymeric particles are interesting because of their versatility and broad available materials, but can also face reproducibility and toxicity issues, due to the polymerizing or crosslinking agents, and eventual organic solvents involved in synthesis [11].

To propose a new nanomedicine-based approach for thrombolysis, we designed targeted polysaccharide NPs that can be loaded with rtPA and DNase I. These particles are composed of polysaccharide hydrogels, and their synthesis through a novel microemulsion-inspired process yielded 315 nm NPs, while the one-pot synthesis was simple and involved only cost-effective, FDA-compliant reagents which satisfied green chemistry criteria. Notably, they were stable, composed of biodegradable materials, and exhibited remarkable robustness throughout batch production. The targeting moiety was the fucoidan, a sulfated polysaccharide with nanomolar affinity for P-selectin, which is expressed on activated platelets and endothelium, and was demonstrated to be safe in human with GMP formulation [24–26]. These nanoparticles were fully characterized, including composition, stability, biocompatibility, targeting, the loading of two different drugs, rtPA and DNase I, and subsequent thrombolytic capacities, both *in vitro* and with a murine thrombosis model. Overall, these findings demonstrated the potential of new polysaccharide NPs to deliver drugs to thrombi, validated the microemulsion-inspired framework for emulsion-based synthesis and open perspectives for drug delivery through biocompatible polysaccharide nanoparticles.

Results and Discussion

Nanoparticle synthesis

The synthesis consisted of a one-pot, two-steps simple synthesis with robust production of uniformly sized NPs. It was inspired by previous protocols (referred to as “classical”) for

formulating particles made up of polysaccharide hydrogels [27,28]. Notably, this protocol combines the chemical crosslinking of dextran with sodium trimetaphosphate (STMP) under alkaline conditions to form hydrogels, which was described elsewhere [29], with the formation of stable water-in-oil (w/o) emulsion where water droplets serve as small reactors for hydrogel particle synthesis, as described in Fig.1.a; the crosslinking bonds with STMP are phosphate diesters. Improvements were made by delaying the crosslinking reaction and, most importantly, by using the microemulsion (i.e., a thermodynamically stable emulsion) conceptualization of emulsions [30,31] to improve the w/o emulsion stability and diminish the water droplet size, thus reducing the resulting NP size. The Hydrophilic Lipophilic Difference (HLD) equation was used as presented by Abbott [30]:

$$(1) \qquad HLD = F(S) - k.EACN - \alpha.(T-25) + Cc$$

where F(S) represents a function of salinity S in the aqueous phase, EACN is the Effective Alkane Carbon Number determining the "oiliness" of oils, T is the temperature, Cc the characteristic value of the surfactant, and k and α fixed constants. When the HLD value is close to 0, the mixture obtained presents a balance between hydrophilic and lipophilic tendencies with extremely low interfacial tension, resulting in Type III Winsor emulsions. When HLD < 0, we obtain Winsor Type I oil-in-water (o/w) emulsions, and with HLD > 0, we obtain Winsor Type II w/o emulsions (Fig.1.b). In practice, these values can be determined from tables or determined experimentally, as shown in Fig.1.c, where a gradient in Cc values with two surfactants was prepared, thus obtaining a range of tubes displaying o/w emulsions (tubes 1 to 8, Fig.1.c), microemulsions (tubes 9 and 10, Fig.1.c) and w/o emulsions (tube 11, Fig.1.c). To form stable w/o emulsions, a strictly positive HLD value close to 0 was chosen. Through this framework, an adequate surfactant mix was determined to improve the emulsion step, with Cc = 2.39 and HLD = 0.80 (see HLD parameters in Sup.Fig.1). This synthesis yielded full dextran NPs, named Dex-NPs, and 5 wt.% fucoidan-incorporating dextran NPs, named Fuco-NPs, to serve as targeting NPs. The Z-average hydrodynamic diameter was respectively 313.7±14.4 nm and 316.5±15.3 nm, with low dispersity (polydispersity index, or PDI, considered as monodisperse below 0.2) as measured by Dynamic Light Scattering (DLS), without significant differences between both formulations (Sup.Fig.2). When comparing the former "classical" formulation to the microemulsion-based optimized formulation, the synthesis yielded batches in a robust manner with narrow Z-average size distribution which retained the same dispersity throughout batches (Fig.1.d-e, Sup.Fig.3), with an overall size reduction from around 850 nm to 315 nm. Size distribution and sphericity were also confirmed by TEM (Sup.Fig.3). Furthermore, a major challenge with NPs remains their stability in various colloidal suspensions, with stabilizing agents often used. As shown in Fig.1.f, with the "classical" submicronic particles, size increase through aggregation and sedimentation is seen when resuspended in saline without addition of the surfactant Tween 20; in contrast, with the optimized protocol, the Fuco-NPs do not show any significant differences in size in ultrapure water, saline, or saline with a stabilizer. These results validate the use of a microemulsion model to improve the formulation: a significant size reduction of NPs was obtained while using a similar protocol similar to the "classical" one which previously yielded micron-sized particles [27,28]. It also

guaranteed a robust process with low inter-batch variability. Interestingly, the protocol improvement also resulted in increased stability of NPs without using stabilizing agents and without significant size variation even when the solvent ionic strength increases, in contrast to the previous "classical" particles.

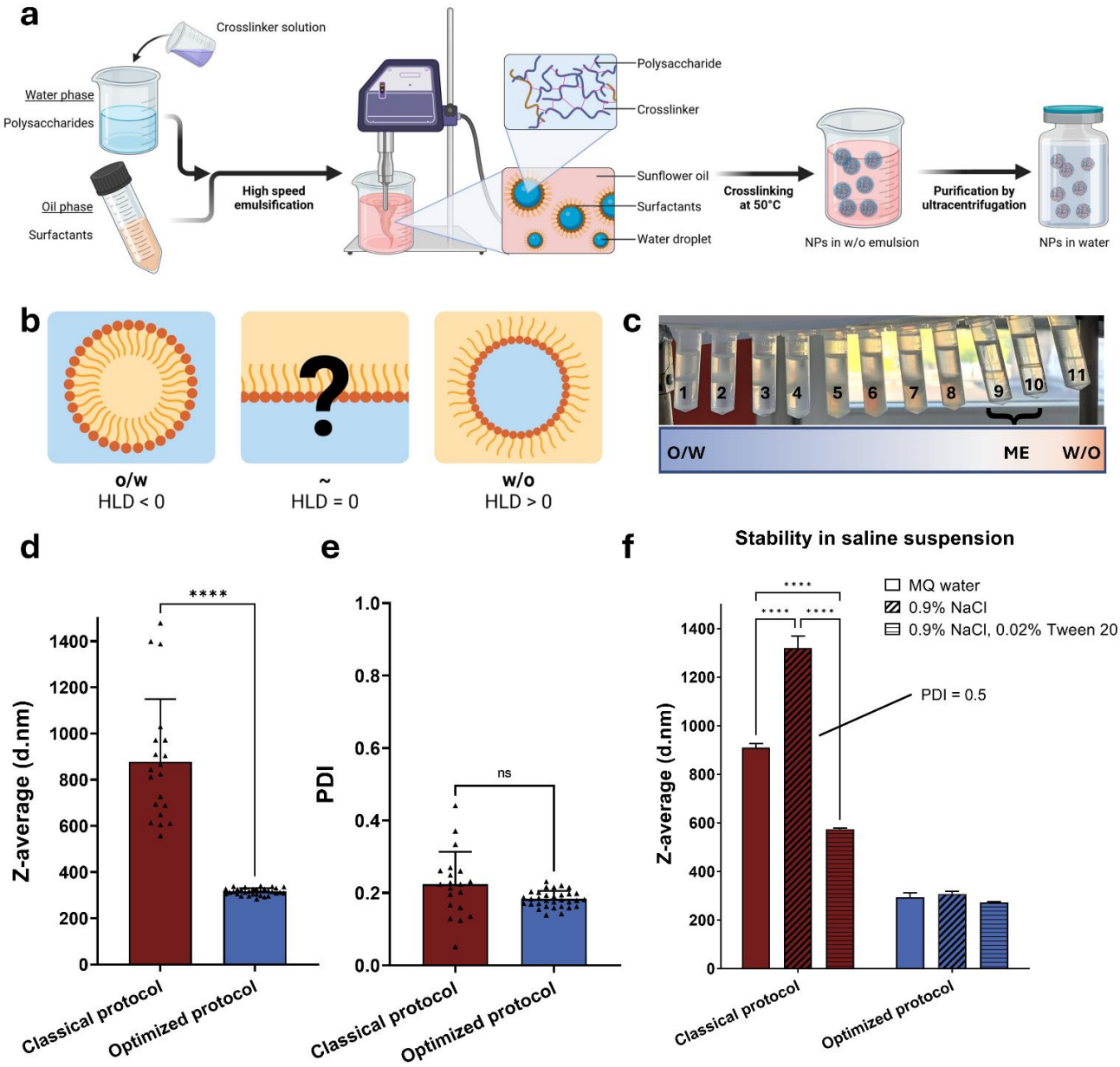


Figure 1. Synthesis of Dex-NPs and Fuco-NPs. (a) Description of the one-pot synthesis process. A water phase containing the polysaccharides, NaCl and NaOH, is mixed with the STMP crosslinker, then added dropwise in the oil phase constituted of sunflower oil and surfactants. The emulsification is performed with a high-speed homogenizer at 30'000 rpm on ice for 2.5 min followed by transfer in a 50°C oven for crosslinking. The resulting nanoparticles (NP) are purified and isolated by multiple rounds of ultracentrifugation. (b) Thermodynamic emulsion behavior of

water and oil depending on Hydrophilic Lipophilic Difference (HLD) values (right). (c) Representative microemulsion scan based on sunflower oil, water, and a mix of surfactants displaying a microemulsion (ME) in tubes 9 and 10. The surfactant mix is performed such as the HLD is increasing from left to right. (d-e) Comparison of particle size (d) and dispersity (e) between the classical (n=21) and final (n=32) protocols. (f) Size comparison of fucoidan containing particles between classical particles and Fuco-NPs in water, saline or saline with 0.02% Tween 20 as surfactant. When not indicated, PDI was below 0.2. A two-way ANOVA was performed, with Tukey's multiple comparison test to compare only the suspension medium effects (n=3).

Nanoparticle characterization

The size and PDI of Dex-NPs and Fuco-NPs are recapitulated in Fig.2.a and were obtained in similar yields. The surface charge of NPs was measured as it often plays a major role in colloidal stability. Across a broad pH range, the Zeta potential measured by Electrophoretic Light Scattering (ELS) was below -20 mV for Dex-NPs and below -25 mV for Fuco-NPs (Sup.Fig.4), with specifically the Zeta potential at neutral pH of -25.9±1.2 mV for Dex-NPs and -32.2±1.8 mV for Fuco-NPs. The phosphorus and sulfur content were measured by TXRF, which respectively validated the incorporation of phosphorus through the phosphate diester crosslinking bonds, and incorporation of sulfate-containing fucoidan in Fuco-NPs. Similar FTIR spectra (Sup.Fig.4) also demonstrated that Dex-NPs and Fuco-NPs were both fully constituted of polysaccharides (fucoidan being mostly indistinguishable from dextran by FTIR). Being made of dextran, a neutral polysaccharide, the low Zeta potential of NPs also clearly indicated the incorporation of negatively charged components: the phosphate diester crosslinking bonds, and fucoidan; such negative surface charges are generally considered low enough to impart electrostatic colloidal stability. This was verified by the storage stability of Fuco-NPs evaluated by size measurements over a year at 4°C (Fig.2.b). Besides, freeze-drying of Fuco-NPs in 1% sucrose was possible without loss in size or dispersity as verified in Sup.Fig.6. This long-term cold storage and freeze-drying capacity are especially interesting for logistic and pharmaceutical purposes. Furthermore, the size of circulating objects can be crucial for their behavior in the blood, due to the margination effects previously mentioned. To verify whether the size reduction from 850 nm to 315 nm could affect the particle distribution profile inside blood vessels, they were flown in blood at venous flow rate in microfluidic channels. As shown in Fig.2.c, while 850 nm "classical" particles demonstrated a typical margination to the sides of the channel, the optimized Fuco-NPs presented a homogeneous profile across the microfluidic vessel cross-section. This can help warrant access to the thrombus wherever its location in a blood vessel, and keep NPs in the circulation [13,32]. Thus, these NPs fall in a desirable size range of 150-400 nm in order to avoid extravasation [16] while maintaining them homogeneously distributed in blood flow [13,32]. To further validate the use of these NPs, their biocompatibility was assessed. As they are meant to interact in the circulation, cytotoxicity was evaluated by measuring the metabolic activity by resazurin reduction after 24 h incubation of HUVEC endothelial cells in contact with the Fuco-NPs, as shown in Fig.2.d, where all concentrations assayed displayed a viability above the 70% threshold (decided as per ISO 10993-5

[33]), with notably the highest assayed concentration, 1000 µg/mL Fuco-NPs, displaying a 92.8±5.7% viability. PBS was used as a control to compare effects of the different medium dilutions. Moreover, HUVEC cell morphology was verified after incubation of 100, 400, 800 (not shown) and 1000 µg/mL Fuco-NPs for 24h (Fig.2.e): the cells retained the cobblestone aspect and preservation of the actin cytoskeleton when comparing PBS exposure to Fuco-NPs. Finally, since the Fuco-NPs are meant to be circulating, the absence of hemolytic properties was essential. Both Dex-NPs and Fuco-NPs showed no hemolytic properties when incubated with human erythrocytes (10% being the threshold for nonhemolytic, and >25% for hemolytic risk [34]) as shown in Sup.Fig.7.

a

	Z-average size (d.nm)	PDI	Concentration post synthesis (g/L)	Zêta potential at pH = 7 (mV)	Fucoidan content (wt.%)	Phosphorus content (wt.%)
Dex-NPs	313.7 ± 14.4	0.18 ± 0.02	1.4 ± 1.0	- 25.9 ± 1.2	-	1.0 ± 0.3
Fuco-NPs	316.5 ± 15.3	0.18 ± 0.03	1.8 ± 0.8	- 32.2 ± 1.8	4.4 ± 2.0	1.3 ± 0.4

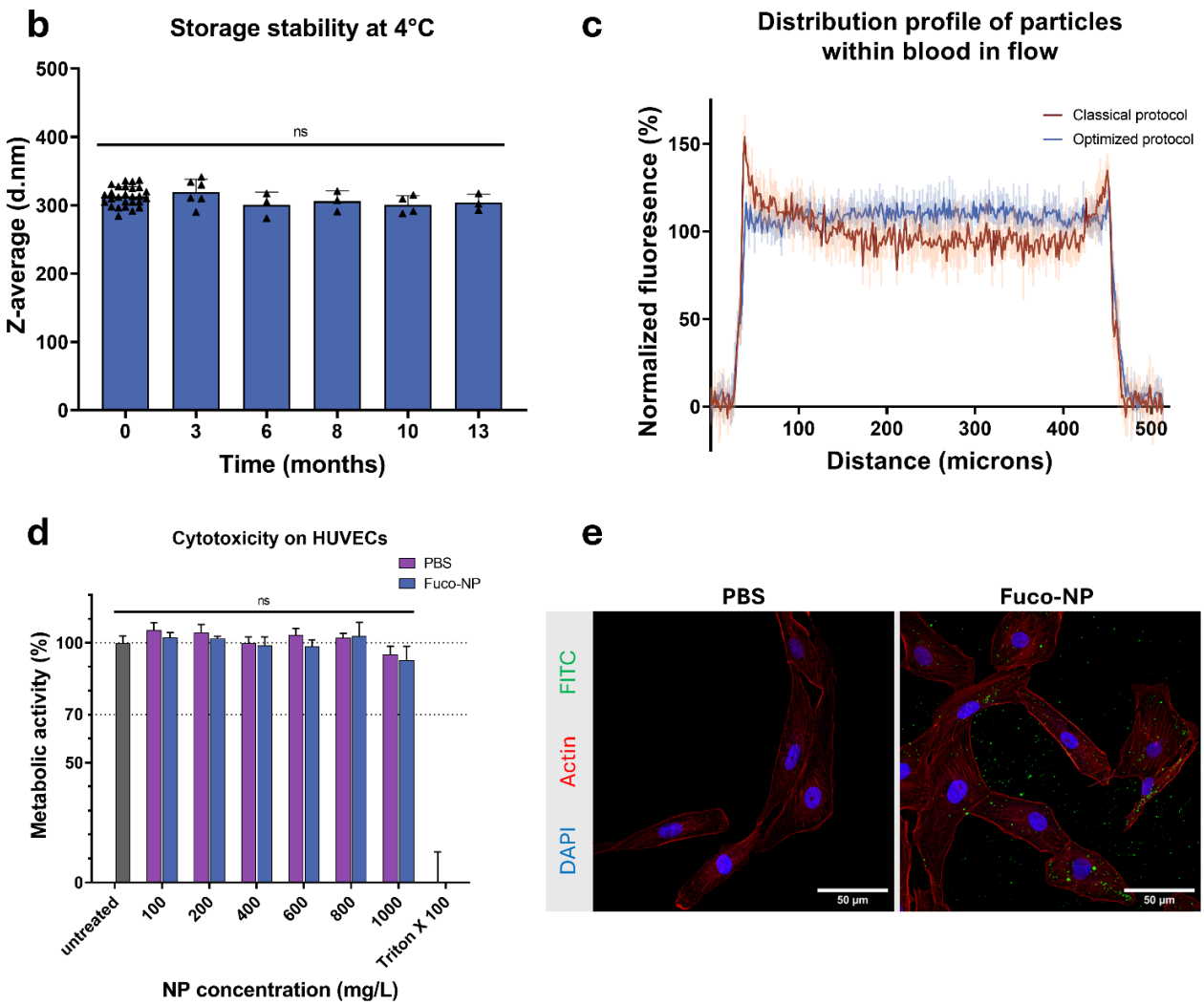


Figure 2. Characterization of NPs. (a) Major physico-chemical characteristics of Dex-NPs and Fuco-NPs. The fucoidan and phosphate content presented were obtained by TXRF. (b) Z-average evolution measured by DLS over storage time at 4°C. One-way ANOVA with Dunnett's multiple comparison test to compare every column to t=0 was performed (n≥3). (c) In flow behavior comparison of fucoidan containing 850 nm particles, obtained with the classical protocol, with 315 nm Fuco-NPs (optimized protocol). The blood containing 1 mg/mL TRITC-tagged particles is flown at a venous flow rate in a microfluidic channel, and the fluorescence signal across a cross-section of the channel is measured. The X-axis corresponds to the cross-section distance (n=5). (d) Cytotoxicity test performed by measuring HUVECs viability through the metabolic activity by resazurin after 24 h incubation with Fuco-NPs or PBS (similar medium dilution as a control). Triton X-100 1% for 15 min served as a positive control, was significantly different with all others (not shown for clarity); the analysis was a 2-way ANOVA with Tukey's multiple comparison test to compare only the differences between PBS and Fuco-NP (n=4). e) HUVEC morphology after 24 h incubation with 1 mg/mL FITC-labeled Fuco-NPs visualized with the nuclei (DAPI) and actin (Rhodamine phalloidin) (scale bar = 50 µm).

Drug loading

Once the NPs were fully characterized, the loading of various drugs by simple adsorption, including rtPA and DNase I, was investigated. Notably, the loading capacity (LC (%) = [drug loaded]/[NP]) was measured by BCA (total protein quantification) across various rtPA and Fuco-NP concentrations, as displayed in Fig.3.a. For a fixed 2.5 mg/mL Fuco-NP concentration, co-incubation with 0.25 mg/mL rtPA yielded the highest LC. This loading condition was kept in all further experiments, and the resulting loaded NPs designed as Fuco-NP-rtPA, with a LC of 6.7±0.6% (Fig.3.c). Interestingly, it was observed that, in similar loading conditions, rtPA loading was significantly increased in Fuco-NPs, due to an previously undescribed affinity of rtPA to fucoidan [35], compared to Dex-NPs (Fig.3.c). Moreover, the release of rtPA was investigated in PBS at 37°C, at a dilution corresponding to the injection of a 1 mg/kg rtPA dose in mice (10 times lower than the effective dose usually used [36]) or equivalent to 0.9 mg/kg dose of rtPA in humans, the current clinical recommendation for AIS treatment [4]. As shown in Fig.3.d, a release curve illustrative of a burst release in the first 15 min and reaching a complete release after 60 min was obtained. The amidolytic activity of rtPA after loading was validated with a fluorescent substrate assay (PefaFluor®) as shown in Sup.Fig.8, and was retained after freeze-drying and resuspension without destabilizing the Fuco-NPs, with only a minor size decrease (Sup.Fig.8 and Sup.Fig.10). However, in the same loading conditions, barely any DNase I was loaded in Fuco-NPs. The isoelectric point of rtPA is around 7.5, while the isoelectric point of Pulmozyme® (the DNase I used) is reported at 4.6, meaning that at neutral pH, rtPA is either neutral or slightly positively charged, while DNase I is negatively charged, which could prevent loading onto Fuco-NPs by electrostatic repulsion. As the latter remained negative across a broad pH range (Sup.Fig.4), loading at different pH values was tested (see Sup.Fig.9.a), demonstrating a successful adsorption of DNase I at pH = 3. Based on this acidic condition, various DNase I and Fuco-NP conditions were tested, with notably the incubation of 0.5 mg/mL DNase I with 2.5 mg/mL Fuco-NP yielding

the highest LC (Fig.3.b). This condition was used in all following experiments and labeled Fuco-NP-DNase: the LC of DNase I was 16.9±0.4%. This LC remained similar for both Dex-NP-DNase and Fuco-NP-DNase (Fig.3.e), with a similar release profile as rtPA (Fig.3.f). However, such acidic conditions could denature DNase I, and therefore a fluorescent DNA substrate kit was used to measure the DNase I activity after loading onto Fuco-NPs and in acidic conditions (Sup.Fig.9.b). This demonstrated that while acidic exposure significantly reduced DNase I activity by 12-fold, activity was partially preserved in Fuco-NP-DNase with only a 2.5-fold reduction in activity. This amounted to an effective LC (measured as [active drug]/{NP]) of 8.3±2.2%. Fuco-NP-DNase freeze-drying further reduced the active drug content (Sup.Fig.9.b), to a corresponding effective LC of 4.7±2.5%, but Fuco-NP-DNase remained stable, with only a minor size decrease (Sup.Fig.10). Co-loading rtPA and DNase I in the same NPs was tested with no success, as rtPA loading always prevailed on DNase I (Sup.Fig.11), and thus Fuco-NP-rtPA and Fuco-NP-DNase were prepared separately and assembled immediately before each further experiment. Even though the rtPA and DNase I enzymatic activity were assessed with fluorescent substrate assays, it did not necessarily guarantee that they can still fulfill their fibrinolytic or NETolytic activity. Thus, two respective models were designed. On one hand for rtPA, a fibrin agar plate assay (FAPA) was used [37]. The degradation ring's rate of expansion was measured (Sup.Fig.12) and with a standard range of free rtPA, the active amount of rtPA in a sample could be determined. As shown in Fig.3.g during loading experiments, the amount of active drug loaded in Fuco-NP was measured at 201±23 µg/mL, slightly above the rtPA amount determined by BCA, indicating that the loaded rtPA retained its fibrinolytic potential. On the other hand for DNase I, a NETolysis assay was designed based on previous works [38]. Neutrophils were isolated from human blood then activated with PMA. SytoxGreen and DAPI DNA dyes were used after the various treatments, owing to SytoxGreen lack of intracellular penetration compared to DAPI, to distinguish extracellular DNA (NETs) from nuclear DNA. After 4 h activation, the NETs were incubated with the Fuco-NP-DNase samples or with free DNase I. As shown in Fig.3.h top panels, NETs could be clearly seen after PMA activation. NETolysis could be observed in a DNase I concentration-dependent manner, and at equal amounts of DNase I of 0.5 µg/mL, both free DNase I and Fuco-NP-DNase produced similar degradation of the NETs (Fig.3h bottom panels). This validated the NETolysis activity of DNase I on human NETs, but also confirmed the retained activity of DNase I after loading in Fuco-NPs.

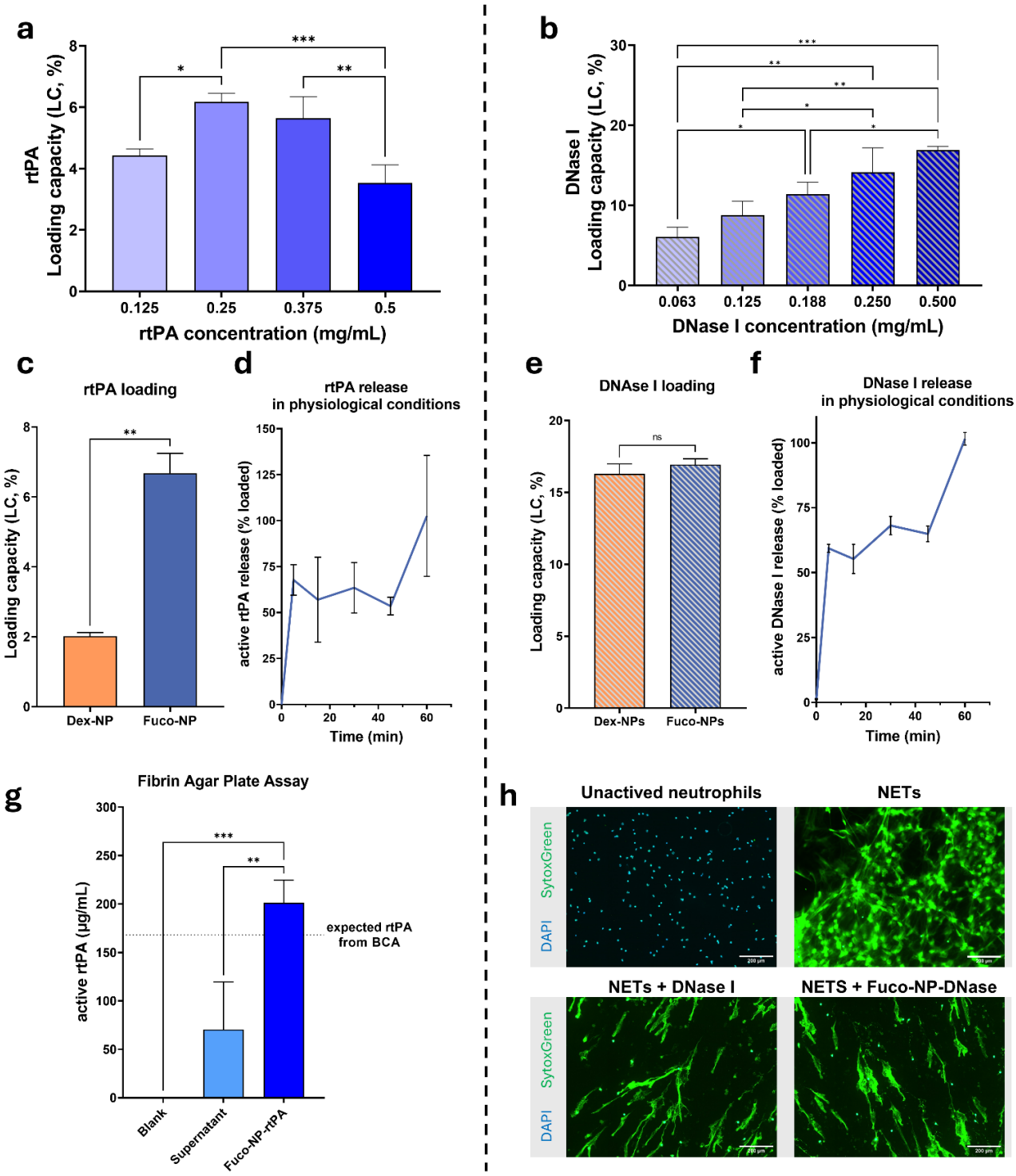


Figure 3. Drug loading in NPs (rtPA left column, DNase I right column). (a) rtPA loading capacity in Fuco-NPs 2.5 mg/mL for various rtPA concentrations, measured by BCA (n=3). (b) DNase I loading concentration in Fuco-NPs 2.5 mg/mL at pH=3 for various DNase I concentrations, measured by BCA (n=3). (c) Comparison of rtPA loading capacity in Dex-NPs and Fuco-NPs by BCA ([rtPA]=0.25 mg/mL, [NP]=2.5 mg/mL) (n=3). (d) rtPA release in PBS at 37°C with a

dilution equivalent to 1 mg/kg in mice or 0.9 mg/kg in human measured by PefaFluor (n=3). (e) Comparison of DNase I loading capacity in Dex-NPs and Fuco-NPs by BCA ([DNase I]=0.5 mg/mL, [NP]=2.5 mg/mL) (n=3). (f) DNase I release in PBS at 37°C with a dilution equivalent to 5 mg/kg in mice measured by DNase I kit (n=3). (g) FAPA determined concentration of active rtPA in Fuco-NP-rtPA and supernatant resulting from a loading experiment (n=3). (h) NETolysis assay. Neutrophils isolated from human blood were seeded then activated with PMA to release NETs, followed by treatment with DNase I or Fuco-NP-DNase. DAPI and SytoxGreen were used to differentially stain intra- and extracellular DNA. Top left: neutrophils not exposed to PMA and treatments. Top right: NETs released with PMA but treated with PBS. Bottom left and right: NETs released by PMA and treated with respectively 0.5 mg/mL DNase I or equivalent DNase I concentration in Fuco-NP-DNase (experiment repeated three times) (scale bar = 200 µm).

Aggregated platelets targeting

To validate that fucoidan-mediated targeting capacity of Fuco-NPs, a microfluidic setup was used to assess targeting to activated platelets in simulated blood circulation. Human blood is flown into collagen-coated microfluidic channels at arterial flow rates and the formation of platelet aggregates are observed in real-time. Various NP formulations were then flown into the channels before rinsing with PBS (see Sup.Fig.13.a and Sup.Movies 1-5). After rinsing, the fluorescence of NPs and platelets was measured (Fig.4.a). Their colocalization was then calculated with the Pearson's coefficient, as shown in Fig.4.b: Fuco-NPs demonstrated a statistically significant increase in colocalization with platelets when compared to Dex-NPs, as well as a global decrease in TRITC fluorescence (Fig.4.a) validating their targeting capacity. Furthermore, Fuco-NP-rtPA and Fuco-NP-DNase exhibited similar colocalization results as unloaded Fuco-NPs, proving that drug loading did not affect the targeting to aggregated platelets. It was also observed that Fuco-NPs had a superior colocalization to platelets than fucoidan-containing "classical" submicronic particles (Sup.Fig.13.b): this may stem from enhanced surface-to-volume ratio thanks to size reduction. Besides, this targeting was further quantified by *in vivo* targeting of thrombi (Sup.Fig.13.c), validating the aggregated platelet targeting through P-selectin/fucoidan interaction to target thrombi.

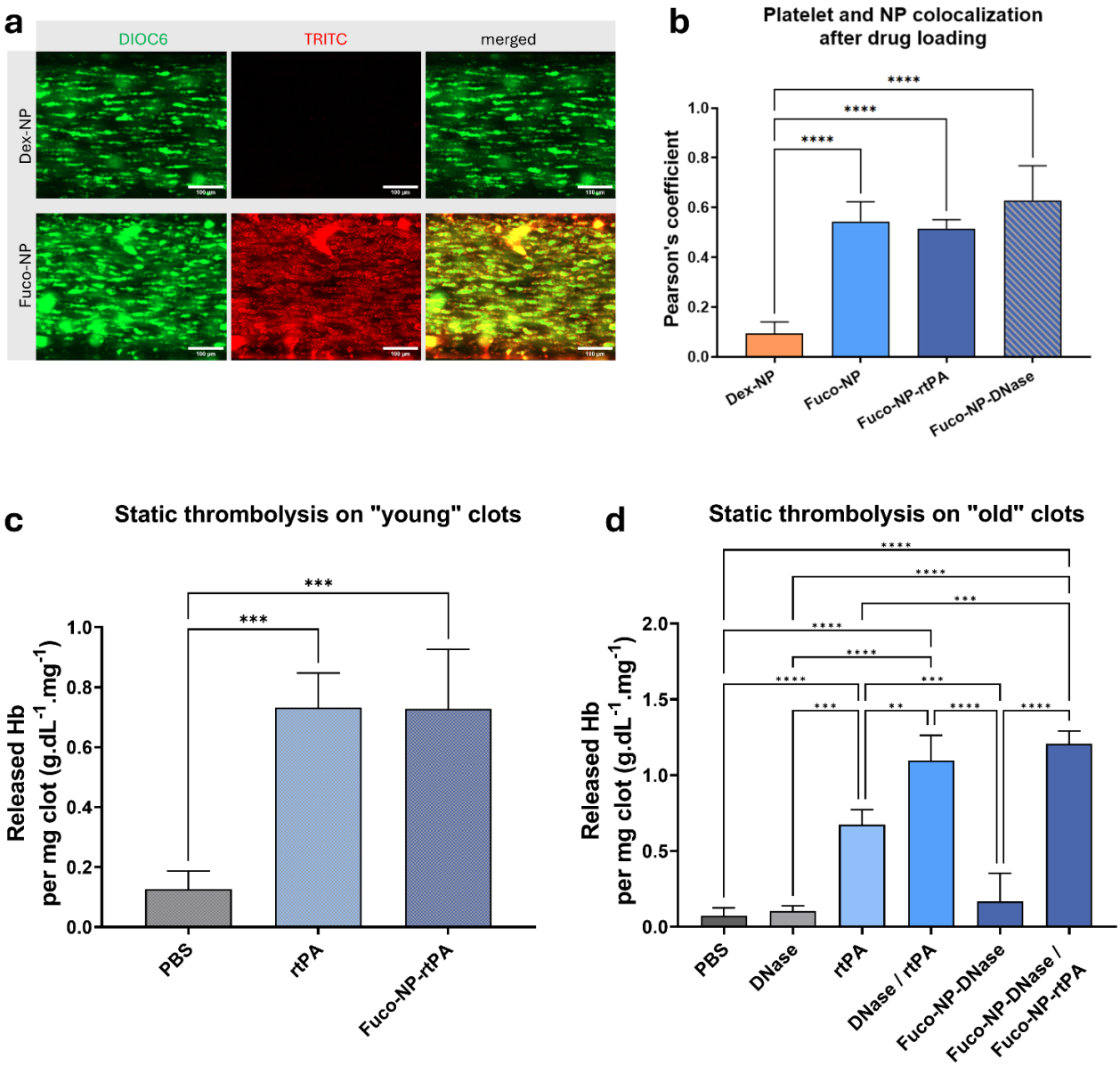


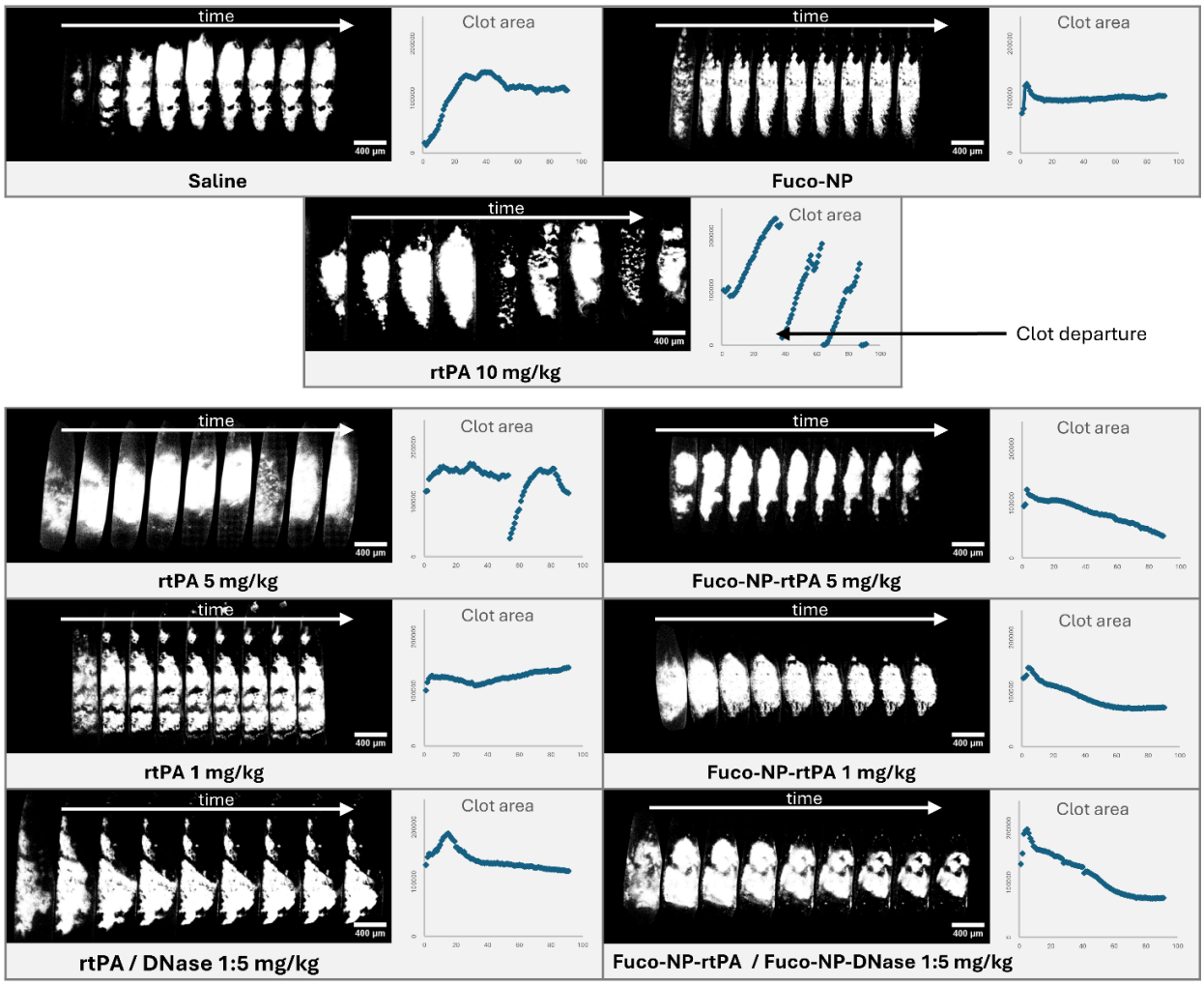
Figure 4. Validation of targeting and thrombolytic properties. (a) Representative final images of the microfluidic targeting experiment on activated platelets. Aggregated platelets labeled with DIOC6 were obtained in microfluidic channels, then 1 mg/mL TRITC-labeled Dex-NPs or Fuco-NPs were flown under arterial flow for 5 min, followed by 5 min rinsing with PBS (scale bar = 100 µm). (b) Resulting colocalization of TRITC and DIOC6 signal after rinsing, measured by Pearson's coefficient for 1 mg/mL Dex-NPs, Fuco-NPS, Fuco-NP-rtPA or Fuco-NP-DNase (n=4). (c) Static thrombolysis with "young" clots. "Young" clots were obtained after 60 min incubation of whole human blood with 10 mM CaCl2 and 0.1 U/mL thrombin at 37°C. After rinsing, they were weighted and treated with 1 µg/mL rtPA or Fuco-NP-rtPA at the equivalent rtPA dose. The released hemoglobin after 37°C incubation for 1 h was quantified with the Drabkin's reagent and normalized to the initial clot mass (n=4). (d) Static thrombolysis with "old" clots. "Old" clots

were obtained after 24 h incubation of whole human blood with 10 mM CaCl2 and 0.01 U/mL thrombin at 37°C, then after rinsing they were weighted and treated with 1 µg/mL rtPA, 50 µg/mL DNase I, Fuco-NP-rtPA or Fuco-NP-DNase at the equivalent drug dose. The released hemoglobin after 37°C incubation for 1 h was quantified with the Drabkin's reagent and normalized to the initial clot mass (n=4).

Static thrombolysis

Once Fuco-NP characterization, drug loading and targeting capacity were evaluated, static thrombolysis was assayed in static conditions on thrombi from human blood. The first formulation of *in vitro* clots, hereafter named "young" clots, were first created by mixing anticoagulated human whole blood with thrombin and $CaCl_2$ at 37°C, then they were incubated with rtPA or Fuco-NP-rtPA. The release of hemoglobin (Hb) and weight decrease were quantified, and the released Hb amount per mass unit of clot is reported. As can be seen in Fig.4.c, rtPA incubation at 1 µg/mL resulted in significant release of hemoglobin (0.73 ± 0.12 $g.dL^{-1}.mg^{-1}$) when compared to control treatment (PBS, which was correlated with a clot weight reduction. Moreover, the Fuco-NP-rtPA, incubated at equivalent 1 µg/mL rtPA, produced a comparable thrombolysis as free rtPA with 0.73 ± 0.20 $g.dL^{-1}.mg^{-1}$ Hb released per mg of clot. Thus, Fuco-NP-rtPA retained the same activity as free rtPA in a static thrombolysis model. However, when considering the combo action of rtPA and DNase I, this model with "young" clots showed no difference between rtPA alone or rtPA combined with DNase I (Sup.Fig.14.a), even with different DNase I concentrations. This could be attributed to the possible absence of NETs in this static thrombus model, since thrombi can have very different compositions [2]. A variation in the protocol for making *in vitro* clots from 1 h incubation to 24 h incubation, combined with a reduced concentration of thrombin, was tested, yielding clots that were named "old" clots. Based on the SytoxGreen/DAPI differential staining of extracellular and nuclear DNA, "young" and "old" clots were stained and the total fluorescence ratio of SytoxGreen over DAPI was quantified: a significant increase in the SytoxGreen and DAPI mean fluorescence intensity ratio from 1.06 ± 0.01 to 1.30 ± 0.05 was observed, indicating that "old" clots contained more extracellular DNA than "young" ones (Sup.Fig.14.b), likely due to increased NET formation. The thrombolysis experiment was repeated to evaluate DNase potentiating action on rtPA on these "old" clots, now comparing rtPA at 1 µg/mL, DNase I at 50 µg/mL and equivalent drug concentrations of Fuco-NP-rtPA and Fuco-NP-DNase (Fig.4.d). In this model, rtPA alone amounted to 0.67 ± 0.10 $g.dL^{-1}.mg^{-1}$ Hb released per mg of clot, while rtPA and DNase free drugs combo achieved 1.10 ± 0.17 $g.dL^{-1}.mg^{-1}$ released Hb per mg clot, thus demonstrating a statistically significant increase in thrombolysis for the rtPA + DNase I combo, while DNase I alone was no different than the control treatment (PBS). Furthermore, the combo of Fuco-NP-rtPA and Fuco-NP-DNase resulted in 1.21 ± 0.08 $g.dL^{-1}.mg^{-1}$ released Hb per mg clot, similar to the free drugs combo, and significantly superior to the rtPA alone condition. This experiment reflected that like clinical thrombi [39], artificial thrombi could vary in composition, including NET formation; but for NET-containing thrombi, DNase I (ineffective alone) can improve thrombolysis with rtPA; and that Fuco-NP-rtPA and Fuco-NP-DNase are viable formulations for delivering these active drugs.

a


time
Clot area
400 µm
Saline
Fuco-NP
rtPA 10 mg/kg
Clot departure
rtPA 5 mg/kg
Fuco-NP-rtPA 5 mg/kg
rtPA 1 mg/kg
Fuco-NP-rtPA 1 mg/kg
rtPA / DNase 1:5 mg/kg
Fuco-NP-rtPA / Fuco-NP-DNase 1:5 mg/kg

b

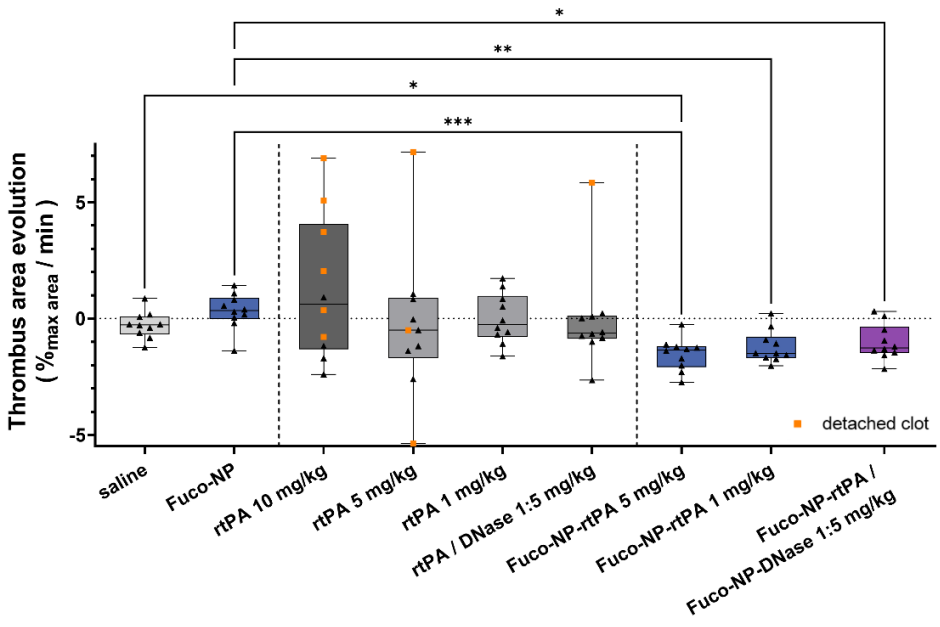

Thrombus area evolution
(%max area / min)
5
0
-5
*
**
*
***
detached clot
saline
Fuco-NP
rtPA 10 mg/kg
rtPA 5 mg/kg
rtPA 1 mg/kg
rtPA / DNase 1:5 mg/kg
Fuco-NP-rtPA 5 mg/kg
Fuco-NP-rtPA 1 mg/kg
Fuco-NP-rtPA / Fuco-NP-DNase 1:5 mg/kg

Figure 5. In vivo thrombolysis in the FeCl3 mesenteric vein model. (a) Representative thrombi evolutions over time. Each thrombolysis experiment lasted 30 min, and the mosaics shown here are composed of juxtaposed thrombi binary masks acquired every 3 min. On the right of each mosaic is drawn to corresponding area evolution curve over 30 min. The top three thrombi correspond to controls (saline, empty Fuco-NPs and rtPA 10 mg/kg) (scale bar = 400 µm). (b) In vivo thrombus area evolution over various treatments, represented as box and whiskers. Boxes are delimited by 25% and 75% quartiles and whiskers delimit minimum and maximum values. Detached clots are marked in orange squares. Statistical analysis was performed with one way Welch's ANOVA with Dunnett's T3 multiple comparison test (n=10).

In vivo thrombolysis

The *in vivo* thrombosis model was performed as described in Sup.Fig.15 with a murine mesenteric vein $FeCl_3$ thrombosis, with male (24.9±2.3 g weight) and female (19.9±2.4 g weight) mice. Once the thrombus formation was observed by intravital macroscopy through platelet aggregation, the samples were injected into the retro-orbital vein and continuous imaging was performed for 30 min (Sup.Movies 6-14). The thrombus area was measured over time, and the rate of thrombus degradation was calculated to account for disparities in thrombi area. Each treatment group contained 10 animals, with equipartition of male and female mice. Saline and empty Fuco-NP (equivalent NP concentration to the Fuco-NP-rtPA 5 mg/kg) were used as negative control treatments, while the 10 mg/kg rtPA injected as a free drug served as the positive control as established before for murine models [36]. Fuco-NP loaded with rtPA alone at 5 mg/kg or 1 mg/kg were compared to free rtPA at the same concentration. The potential synergic effects of DNase I with rtPA were also investigated, with their co-injection as well as the co-injection of Fuco-NP-rtPA 1 mg/kg with Fuco-NP-DNase 5 mg/kg. Representative clot evolutions over time are shown in Fig.5.a after treatment injection, with the respective clot area evolution curves (on the right of each clot). First, the saline treatment demonstrated that the thrombus keeps growing for a few minutes before reaching a maximum area before stabilizing. Empty Fuco-NPs treatment also resulted in a stable clot. However, when treated with rtPA 10 mg/kg, the thrombi either diminished in size, or showed important remodeling, sometimes followed by clot departure, where the clot is visibly detached whole from the vessel and carried away. These results were recapitulated in Fig.5.b displaying the thrombi area evolution: while saline and empty Fuco-NP treatments resulted in stable clots (respectively -0.29±0.57%.min^{-1} and 0.32±0.77%.min^{-1}), 6 out of 10 clots treated with rtPA 10 mg/kg were detached (n = 6, evolution of 2.98±2.82%.min^{-1}), and the 4 remaining displayed decreasing clots (n = 4, evolution of -1.24±1.17%.min^{-1}). Diminishing the rtPA concentration reduced how affected the thrombi were: at 5 mg/kg only 3 clot departures and the 7 remaining displaying clot area evolutions of -0.55±1.30%.min^{-1} in average, while rtPA treatment at 1 mg/kg resulted in stable clots (evolution of -0.00±1.09%.min^{-1}). Interestingly, this might shed light on a major limitation of rtPA-based clinical treatment of stroke: a low rate of recanalization, and significantly decreased recanalization when the elapsed time from stroke onset to treatment increases, as explicit in the American guidelines for stroke treatment: "benefit of therapy is time dependent, and treatment should be initiated as quickly as possible" [40,41]. This could

indicate that fibrinolysis does not equal thrombolysis, as it is often mistakenly perceived. Some clots, for instance during the early AIS phase, might be more susceptible to rtPA as they are still developing. Another limitation might reside in rtPA mechanism of action by binding to fibrin which could inherently limit its action in the clot [42]; this was also investigated by Bannish *et al*., 2017, who explored how rtPA-mediated fibrinolysis proceeded as a moving front through the clot [43]. It could explain an activity of rtPA limited to the edges or leading edge of a thrombus, thus elucidating its below-ideal efficacy and even why clot departures were seen, eroded from the edges but not destroyed. Most notably, such departed clots are still problematic and could form further emboli in distal vessels, even if often counted as successful events in *in vivo* studies, which therefore ignore the problematic secondary emboli. Regarding rtPA loaded NPs, only Fuco-NP-rtPA 5 mg/kg showed statistically significant improvement (evolution of $-1.54\pm0.69\%.min^{-1}$) compared to both saline and empty Fuco-NP treatment, with a similar degradation rate to free rtPA 10 mg/kg (undetached clots). As for Fuco-NP-rtPA 1 mg/kg (evolution of $-1.21\pm0.70\%.min^{-1}$), it also resulted in a comparable thrombus degradation to free rtPA 10 mg/kg (undetached clots), significantly better than empty Fuco-NPs. To study the combo treatment, the lowest rtPA concentration (1 mg/kg) was chosen and combined with DNase I at 5 mg/kg. 1 clot out of 10 departed, and the other displayed relatively stable clots ($n = 9$, evolution of $-0.69\pm0.86\%.min^{-1}$). When Fuco-NP-rtPA and Fuco-NP-DNase were co-injected at equivalent drug concentrations, the size of the thrombi decreased (evolution of $-1.01\pm0.77\%.min^{-1}$) but without improvement over rtPA alone or Fuco-NP-rtPA treatments. Thrombus area evolutions quantified without the departed clots are shown in Sup.Fig.16. This demonstrated a benefit in using Fuco-NP-rtPA compared to free rtPA: systematic clot reduction was observed, and the lowering of the rtPA concentration used could reduce associated side effects. While this behavior is not fully understood, the absence of an improved thrombolytic capacity of Fuco-NP-rtPA in static *in vitro* experiments (Fig.4) tends to indicate a targeting-related behavior or an unknown *in vivo* biological effect which could only be observed in the *in vivo* experiment. It can be hypothesized that a sustained release over time by Fuco-NPs, attached to the clot, could be more beneficial mechanistically than free rtPA, which could be inhibited faster or lack the improved accumulation imbued by Fuco-NP's targeting. As for the potentiating effect of DNase I or Fuco-NP-DNase on thrombolysis, no synergistic effect was observed. The concentrations used were 1 mg/mL rtPA (minimum where Fuco-NP-rtPA showed an effect, but where free rtPA was not efficient) with DNase 5 mg/kg (highest dose possible with the constraint of using DNase I formulated at 1 mg/mL). This indicated that the $FeCl_3$ thrombotic model, which was very relevant to measure Fuco-NP-rtPA-mediated thrombolysis and to observe the mechanistic differences between free and loaded rtPA, may not be adequate to investigate NET-dependent synergies.

Biodistribution

Fuco-NP accumulation at the thrombus site is clear from *in vivo* acquisition and was quantified with the targeting measurements *in vivo* (Sup.Fig.13.c). Nonetheless, NPs fate in living organisms is critical. Therefore, four organs known to be involved in NP circulation removal (liver, spleen, kidney, lung) were harvested at the end of the *in vivo* thrombolysis experiments for the saline and

Fuco-NPs treatment. In addition to the classical HES coloration, Alcian Blue (AB) coloration was performed to specifically stain acidic polysaccharides, such as glycosaminoglycans or mucopolysaccharides, but not chromatin DNA [28]. Representative organ histological slices are shown in Fig.6.a. First, based on HES coloration no pathological changes were apparent between animals treated with saline or with Fuco-NPs. Regarding AB coloration, while some blue staining occurred in untreated organs, especially in the kidneys, differential staining was obvious after treatment with Fuco-NPs especially in the liver or the spleen. Based on this differential staining, biodistribution of the Fuco-NPs in the selected organs could be inferred, as determined in Fig.6.b. Increased Fuco-NP presence was evidenced in the liver, spleen and lung with statistical significance (respectively 8-fold increase, 11-fold increase and 4-fold increase over saline treatment) while no difference could be noted in the kidney. CD68 staining was also performed to compare macrophages localization (Sup.Fig.17). Notably, the presence of Fuco-NPs in the various organs followed specific patterns, as seen at lower magnification in Sup.Fig.18. More precisely, the presence of Fuco-NPs in liver was evidenced in tens of micrometers-sized cellular or sinusoidal shaped areas, homogeneously distributed throughout the organ, following similar patterns as macrophages. In the spleen, Fuco-NPs were localized in specific ring-shaped areas surrounding the lymphoid white pulp, resembling the marginal zone. On the contrary, macrophages were present throughout the red pulp. In the kidney, AB staining was similar in control animals and in Fuco-NP treated animals, corresponding to glomeruli, and showing no increased AB signal between controls and Fuco-NP treated mice, with few macrophages present. In the lung, some staining was evident in the control treated animals, most likely due to the presence of mucosal polysaccharides, but it was strongly enhanced with Fuco-NP treatment, arranged in tens of micrometers-sized cellular shaped areas throughout the whole organ, and following similar patterns as macrophages. The organ distribution is coherent for 315 nm NPs: absence from the kidneys, but evidenced in the liver, spleen and lungs with distribution patterns coherent with macrophages; however, specific accumulation of Fuco-NPs in the marginal zone of white pulp in the spleen could be seen [44]. This marginal zone is instrumental in building specific responses to phagocytosis-mediated activation of certain cell types. All these elements point towards a mononuclear phagocyte system (MPS)-dependent processing pathway [44,45]. Interestingly, dextran-based materials can be degraded in the human body, notably in the liver and spleen: enzymes capable of hydrolyzing dextrans were found in animal and human tissues [46–48]. The presence of phosphate diester bonds, which could hinder this process, may also be hydrolyzed in physiological conditions [48], though it should be experimentally assessed on a case-by-case basis.

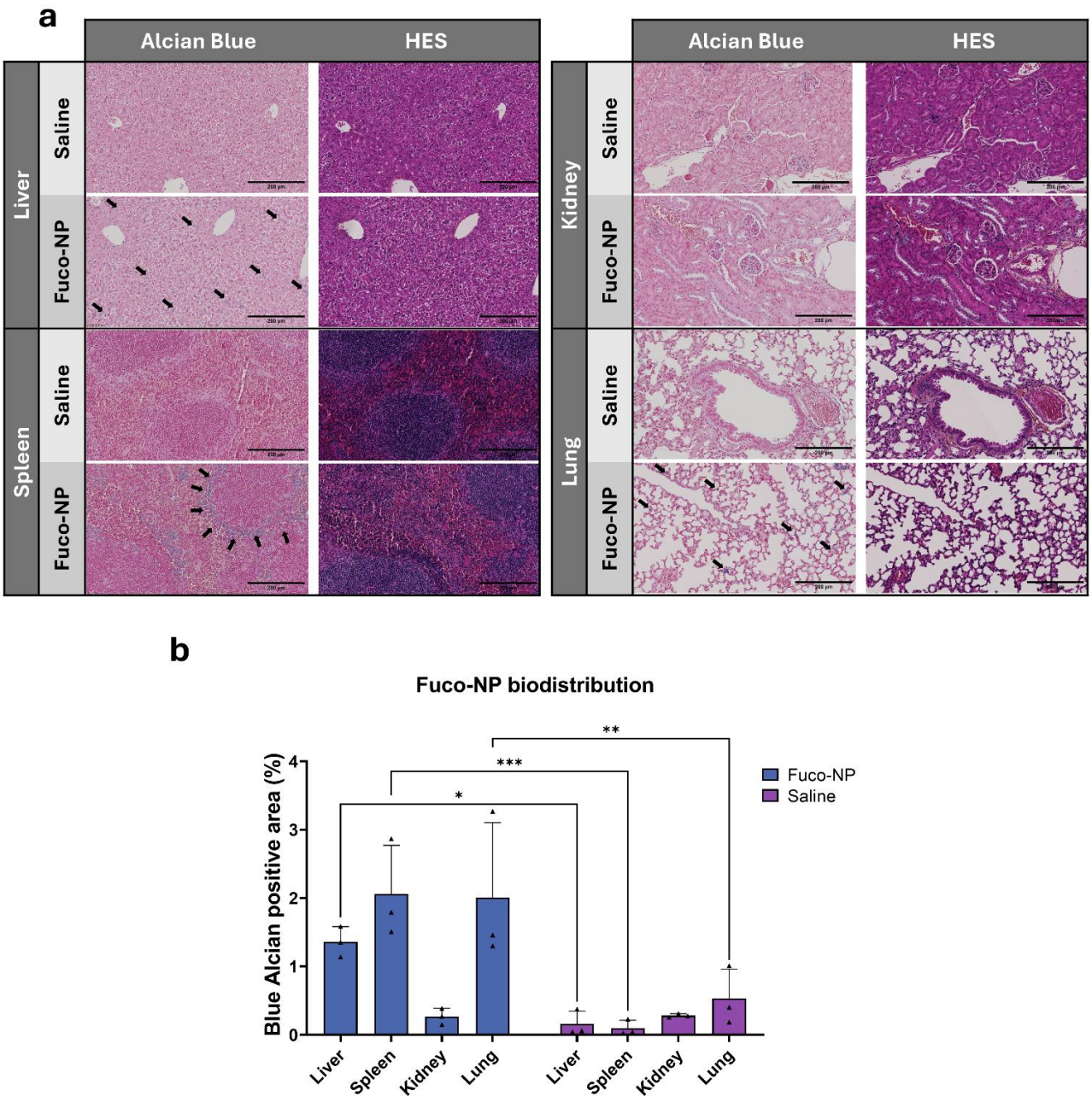


Figure 6. Biodistribution of Fuco-NPs in mice after thrombosis experiment. 3 animals were used for saline or Fuco-NP treatment each. Alcian Blue and HES colorations were obtained for liver, spleen, kidney and lung for each animal. (a) Representative images from different organs of animals treated with saline or Fuco-NP (representative Fuco-NP staining was indicated by black arrows). All slices shown on one line come from the same animal and were aligned (scale bar = 200 µm). (b) Quantification of Blue Alcian positive coloration in each organ for Fuco-NP (blue) or saline (purple) treatment. The total area stained in blue was measured for each entire organ

slice and divided by the total organ area. A 2-way ANOVA was performed, with Tukey's multiple comparison test to compare only the differences per organ (n=3).

Conclusion

In this study, we presented innovative full polysaccharide nanoparticles which could be used for targeted thrombolytic treatment. These were designed with a simple and robust protocol which was developed with the help of a valuable microemulsion theoretical framework, which allowed a significant size reduction and a remarkable robustness for a protocol initially designed for microparticle synthesis [27,28]. The resulting 315 nm NPs fell in a desired size window of 150-400 nm to remain in the circulation, and were fully characterized, including good stability and freeze-drying capacities, which are especially interesting for future developments. Their biocompatibility and safety were assessed *in vitro* with cytotoxicity and hemolysis assays, and explored *in vivo* with biodistribution in the liver, spleen, kidney and lung. They demonstrated their ability to specifically accumulate at the thrombi site *in vivo* through fucoidan targeting of P-selectin on activated platelets. Furthermore, the loading of rtPA and DNase I by adsorption was successfully optimized and ensured that enzymatic and thrombolytic activities were retained after loading, which was demonstrated *in vitro* on artificial thrombi, while validating that DNase I could potentiate rtPA action on certain blood clots. Besides, qualifying the action of Fuco-NP-rtPA and Fuco-NP-DNase over various subtypes of thrombi, would eventually help pinpoint which combinations would be best suited for different thrombotic pathologies, and thus potentially help improve the standard of care for patients. *In vivo,* efficient thrombolysis of Fuco-NP-rtPA was demonstrated at 50% and 10% of the recommended free rtPA dose in mice. Strikingly, this improved thrombolysis was accompanied by a systematic *in situ* clot reduction instead of having clot detachments, as was the case with the free rtPA. Future development of these Fuco-NPs should include scaled-up production in a GMP setting, and a more complete *in vivo* exploration of their behavior and clearance in living organisms, validating the absence of toxicity and the safety improvement by working with these formulations. The *in vivo* degradability of these materials should also be assessed. The microemulsion-based approach is especially interesting as it led to enhanced storage stability (including freeze-drying capacity) and critical size reduction of polymeric hydrogel nanoparticles. The implementation of this concept over various protocols might improve robustness and ease the design of emulsion-involving synthesis. Finally, these Fuco-NPs, which could be loaded with rtPA or other drugs, show promising results towards an application for thrombotic diseases.

Materials and Methods

Materials

Dextran 40 kDa was purchased from Pharmacosmos (Holbæk, Denmark, #5510 0040 1007); FITC-Dextran 40 kDa and TRITC-Dextran 40 kDa were purchased from TDB Consultancy (Uppsala, Sweden, #FD40 and #TD40). Fucoidan (Mn = 18 kDa/Mw = 104 kDa) was a gift from Algues & Mer (Ouessant, France, #MMWFSA14093). Vegetable sunflower oil (Lesieur - Huile

Coeur de Tournesol, Lesieur S.A.S, Asnieres-sur-Seine, France) was purchased from a local supermarket (Monoprix, Paris, France). Polyglycerol polyricinoleate (PGPR) was kindly supplied by Palsgaard (Lyon, France, # PGPR 4150). Fetal bovine serum (FBS) was purchased from Pan-Biotech (Aidenbach, Germany, #P30-3306). HUVEC cells line (ATCC, Manassas, Virginie, #ATCC-CRL-1730) was used at fewer than 40 passages. Tween 80 (#P1754), Trisodium trimetaphosphate (STMP, #T5508), Sodium Dodecyl Sulfate (SDS, #L3771), Sucrose (#S7903), fibrinogen type I from human plasma (#F3879), thrombin from human plasma (#T7009), plasminogen from human plasma (#528175), Phorbol 12-myristate 13-acetate (PMA, # P8139-5MG), Iron (III) Chloreide hexadydrate ($FeCl_3$, # 236489-100G) were purchased from Sigma Aldrich (Saint-Quentin-Fallavier, France). DMEM, low glucose, pyruvate (#31885049), Antibiotic Antimycotic solution (#15240062), PBS 1X and 10X (#14040133 and #14080055), Rhodamine phalloidin (#R415), low melting point agarose (#R0801), DIOC6 (D273), DAPI (#62247), SytoxGreen (#S7020) were purchased from Thermo Fisher Scientific (Massachusetts, United States). Horm® collagen type I was purchased from Takeda Pharmaceutical (Tokyo, Japan). rtPA (alteplase) was purchased from Boehringer Ingelheim (Ingelheim am Rhein, Germany, # Actilyse®). DNase I (dornase alfa) was purchased from Roche – Genentech (San Francisco, United States, #Pulmozyme® 2500 U/2,5 mL). The PefaFluor® kit (#CG8433) for rtPA titration was purchased from Interchim (Montluçon, France). The DNase I detection kit (#JE-PP-410L) was purchased from Euromedex (Souffelweyersheim, France). Polymorphprep (#1114683) was purchased from Proteogenix (Schiltigheim, France). Anti-H3 (#ab5103), anti-MPO (#ab90810), anti-CD68 (#ab283654) antibodies, and IHC detection kit (#ab236468) were purchased from Abcam (Amsterdam, Netherlands). Human whole blood was acquired from EFS (Bichat Hospital, Paris, France), the French blood donation institute, under a research convention, in fePPACK, sodium citrate or EDTA collection tubes.

Nanoparticle synthesis

Polysaccharide nanoparticles (NPs) were obtained through a water-in-oil (w/o) microemulsion, with chemical crosslinking in the aqueous phase. A polysaccharide solution (300 g/L dextran, 6 M NaCl) was prepared; for fluorescent NPs, a 5:95 mass mixture of TRITC-Dextran 40 or FITC-Dextran 40 with Dextran 40 was used. For targeting NPs, fucoidan was substituted to dextran at a 10 wt.% ratio. 15 mL organic phase composed of sunflower oil and 6 wt.% surfactant (60:40 PGPR and Tween 80) was cooled at -20°C for 30 min. Meanwhile, 1200 mg of the polysaccharide solution is mixed with 60 µL of 10 M NaOH for 10 min. 240 µL of 30 wt.% STMP solution was added before quick mixing for 1 min. 600 µL of this aqueous mix are then added dropwise to the organic phase under dispersion with a stand-disperser (Polytron PT 3100, dispersing aggregate PT-DA 07/2 EC-B101, Kinematica, Luzern, Switzerland) for 2 min 30 s at 30’000 rpm on ice. The resulting emulsion was incubated at 50°C for 20 min before successive purification by ultracentrifugation (50’000 g, 30 min): the pellets were resuspended first with SDS 0.04 wt.% four times, then with ultrapure water three times. The resulting NPs were stored at 4°C in ultrapure water. Further concentrating of NPs could be performed with ultracentrifugation devices with size cutoff of 300’000 Da (Vivaspin, Dutscher, Issy-les-Moulineaux, France). Stable

freeze-dried NPs were obtained with the LyoVac GT2 freeze dryer (SRK Systemtechnik, Riedstadt, Allemagne) after -80 °C freezing for 1 h in a 1 wt.% sucrose solution. Submicroparticles (SPs) for comparison were synthesized as per Zenych et al., 2021 [28].

HLD screening

HLD screenings were performed by mixing surfactants together for a total of 90 mg in centrifuge tubes, then adding oil phase (750 µL sunflower oil) with agitation for 1 h. Then water phase is then added (750 µL ultrapure water, saline solutions, or aqueous phase from the NP synthesis) slowly. A gentle agitation by three up-and-down inversion is performed then the tubes are left to incubate at RT for more than 1 h, before they are observed and photographed. Surfactant gradients were used to determine unknown parameters as described by Abbott [30]: two known surfactants (Tween 80 and Span 80) to determine sunflower oil EACN, then Tween 80 with PGPR in sunflower oil were used to determine PGPR Cc. HLD was found to be independent of salinity for PGPR. Constants used: k = 0.16, F(S) = 0.13*S, and α was ignored by working at 25°C (RT). Known values were: $Cc_{Tween80} = -3.7$, $Cc_{Span80} = 3.1$. Determined values were: $Cc_{PGPR} = 4$, $EACN_{sunflower\ oil} = 16$.

Physico-chemical characterization

The NPs formulations were studied for particle morphology, size and zeta potential distributions, mass concentration, and elemental composition. Particle morphology was visualized by Transmission Electron Microscopy (TEM) (Philips FEI Tecnai 12, Amsterdam, Netherlands), negatively stained with 1 wt.% uranyl acetate for 5 min. Hydrodynamic size (diameter), polydispersity (PDI) and Zeta potential (ζ-potential) were measured by Dynamic Light Scattering (DLS) and Electrophoretic Light Scattering (ELS), respectively (Zetasizer Nano ZS, Malvern Instruments, Orsay, France). Samples were diluted in distilled water, 0.9 wt.% NaCl or PBS 1X for size, and in 1 mM KCl for ζ-potential determination. All runs were performed at 25°C in triplicate. Mass concentration (yield) was determined by freeze-drying. Elemental composition was assessed by total reflection X-ray fluorescence spectroscopy (TXRF) technique to quantify the phosphorus and sulfur content (S2 PICOFOX Bruker, Massachusetts, United States). Fourier transform infrared spectroscopy (FTIR) spectra were obtained after drying and inclusion in KBr pellets (Thermo Nicolet AVATAR 370 FTIR spectrometer, Thermo Electron Corporation, Waltham, MA). The stability of Fuco-NPs and compared submicroparticles (SPs) in various solvents (ultrapure water, 0.9 wt.% NaCl, PBS 1X) was evaluated 6 h after solvent exchange, or after various timepoints after storage at 4°C or at 37°C.

Fucoidan and phosphate chemical quantification

The fucoidan content of NPs was determined by a semi-quantitative solid-phase colorimetric assay for sulfate titration [49]. Briefly, 12.5 µg of Fuco-NPs in suspension at a concentration of around 1 mg/mL were added by 5 µL drops on a piece of Whatman Chromatography paper grade 1 with drying between each drop addition. The paper was first soaked into a methanol/acetone (6:4) solution for 3 min and then into a methanol/acetone/water (6:4:15) solution with 50 mM HCl and 0.1 wt.% methylene blue for 10 min. Finally, the paper was extensively washed with acetic acid/methanol/acetone/water (5:6:4:85) until no coloration was detected in the washing solution.

The paper was then transferred to the Eppendorf, containing 0.5 mL methanol with 2 wt.% SDS, and incubated for 15 min at 50°C. 0.2 mL of the extracted dye was placed in a 96-well plate, and its concentration was determined by reading absorbance at 663 nm with a Varioskan LUX multiplate reader (Thermo Fisher Scientific, Massachusetts, United States). Standard curves were obtained from fucoidan in solution with known concentrations. The phosphate content of NPs was determined by a colorimetric assay. Briefly, two solution A (2.5 g/L ammonium metavanadate NH_4VO_3, 13 wt.% HNO_3) and B (5 g/L ammonium heptamolybdate $(NH_4)_6Mo_7O_{24}$) are prepared. 1 mL of around 1 g/L NPs are incubated with 1 mL HNO_3 10 wt.% for 3 h at 105°C, then 0.4 mL HNO_3 65 wt.%, 2 mL solution A, 2 mL solution B and 3.6 mL water are added. After 15 min incubation at room temperature (RT), concentration was determined by reading absorbance at 405 nm. Standard curves were obtained from H_3PO_4 solutions with known concentrations.

Cell culture and cytotoxicity assay

To evaluate the cytotoxicity of the NPs, a resazurin Fluorometric Cell Viability Assay (#TOX-8 kit) was used on confluent Human Umbilical Vein Endothelial Cells (HUVECs). The cells were cultured in low glucose DMEM supplemented with 10 % v/v FBS and 1 % v/v antibiotic-antimycotic; the cells were kept in an incubator at 37°C in a humidified atmosphere of 5% CO_2. Cells were seeded into 96-well plates with 30'000 cells per well. Following 24 h of incubation, the medium was changed to Fuco-NPs resuspended in culture medium in a range of 100 mg/L to 1 g/L, and the cells were cultured for another 24 h. Cells cultured with equivalent PBS 1X medium dilution were set as control. Negative controls were culture medium only, and positive controls were 1 % (v/v) Triton X-100 in culture medium for 15 min. Then the medium was replaced with 100 µL 10 % (v/v) Resazurin solution in culture medium, and the plates were covered in foil and incubated for another 2 h. The Resazurin absorbance signals were monitored at 570 nm and 590 nm wavelengths with a Varioskan LUX multiplate reader (Thermo Fisher Scientific, Massachusetts, United States). The corrected absorbance values were blank corrected: $A' = A_{570nm} - A_{590nm}$, and the relative cell viability was expressed as $(A' - A'_{neg}) / (A'_{pos} - A'_{neg}) \times 100\%$, with the negative and positive control absorbances respectively averaged in the control wells as detailed above. To examine possible cell morphology changes after co-incubation with Fuco-NPs, HUVECs cells were seeded in 8-wells Lab-Tek II Chamber Slide (Thermo Fischer Scientific, Massachusetts, United States) with 10'000 cells per well. The medium was changed 24 h to Fuco-NPs resuspended in culture medium in a range of 100 mg/L to 1 g/L, and the cells were cultured for another 24 h. Cells cultured with equivalent PBS 1X medium dilution were set as control. Next, cells were fixed with 4% (v/v) paraformaldehyde for 30 min at 4°C. After rinsing with PBS, cells were permeabilized with Triton X-100 0.1 wt.% in PBS for 5 min at RT then washed twice with PBS before incubation for 60 min at RT with 1% (v/v) Phalloidin-Rhodamine in PBS. After two PBS washes, the slides are mounted with a Mounting Medium with DAPI. Visualization was performed with a confocal microscope (Zeiss LSM 780, Iena, Germany).

Hemolysis assay

To evaluate hemolysis, human whole blood was collected in EDTA tubes, then centrifugated at 500 G for 5 min. After plasma removal, add an equivalent volume of saline. Repeat centrifugation and saline addition. After a third centrifugation, add PBS instead of saline, then dilute the erythrocyte suspension to 1/50 in PBS. After visual verification (turbidity, sedimentation), mix 1 volume of samples to 19 volumes of diluted erythrocytes in V-bottom 96-well plates. For negative and positive controls, PBS and 20 % (v/v) Triton X-100 are respectively used. After 60 min incubation at 37°C with slow agitation, the plate is centrifuged for 5 min at 500 G, then the supernatants are collected, and the absorbance is read at 541 nm.

Blood margination

An *in vitro* blood flow assay was performed to evaluate the margination of NPs within blood flow. Micro-channels of Vena8 Fluoro+ chambers (width: 0.04 cm, height: 0.01 cm, and length: 2.8 cm; Cellix Ltd, Dublin, Ireland) were rinsed with NaCl 0.9 wt.% before use. Human whole blood was collected in sodium citrate tubes and labeled with 5 µM DIOC6, then NPs were added to a concentration of 1 mg/mL. The blood was then perfused at venous shear stress (here, 7 µL/min) for 2 min and fluorescence images were acquired with a microscope (Axio Observer, Carl Zeiss Microscopy, Oberkochen, Germany). Fluorescence was measured across 5 cross-sections per channel and averaged over 2 min for each sample.

In flow platelet aggregates targeting assay

An *in vitro* flow adhesion assay was performed to evaluate the targeting of NPs to activated platelets. Micro-channels of Vena8 Fluoro+ chambers (width: 0.04 cm, height: 0.01 cm, and length: 2.8 cm; Cellix Ltd, Dublin, Ireland) were coated overnight with fibrillar type I collagen (50 µg/ml) overnight at 4°C and rinsed with NaCl 0.9 wt.% before use. Human whole blood, collected in the PPACK tubes and labeled with 5 µM DIOC6, was perfused at arterial shear stress (here, 60 µL/min) for 5 min to induce platelet activation and aggregation. Platelet aggregation through contact with collagen was visualized in real-time with a microscope (Axio Observer, Carl Zeiss Microscopy, Oberkochen, Germany). After rinsing with NaCl 0.9 wt.%, fluorescent Dex-NPs or Fuco-NPs (unloaded or loaded with rtPA) resuspended in 0.9 wt.% NaCl at 1 mg/mL, were injected into the channels for 5 min. Their accumulation onto activated aggregates was monitored in real time. Channels were then washed for 5 min with NaCl 0.9 wt.%. Finally, quantification of bound NPs to aggregated platelets were performed with ImageJ by measuring total fluorescence intensity and colocalization with the Pearson's coefficient (with a PSF size of 6x6 pixels) on mosaic images composed of 10 aligned microscope images (corresponding to a whole channel).

Drug loading

rtPA was loaded onto the NPs by adsorption. Typically, 50 µL of NPs (5 mg/mL) were mixed with 50 µL rtPA (1 mg/mL) in ultrapure water then incubated for 15 min. Free unabsorbed rtPA was removed by ultracentrifugation (15 min, 15'000 g). The rtPA loaded NPs were resuspended in ultrapure water, and rtPA encapsulation was determined as described below by BCA and PefaFluor® tPA assays. DNase I was loaded onto the NPs by adsorption in acidic conditions. Typically, 50 µL of NPs (5 mg/mL) were mixed with 25 µL DNase I (1 mg/mL), 5 µL of HCl (2x10-2 M), 10 µL $CaCl_2$ (650 µM) and 10 µL ultrapure water then incubated for 15 min. Free

unabsorbed DNase I was removed by ultracentrifugation (15 min, 15'000 g). The DNase I loaded NPs were resuspended in 130 µM $CaCl_2$ and DNase I encapsulation was determined as described below by BCA and a fluorescent substrate DNAse detection kit assays.

Drug encapsulation efficiency and release rates

The amount of drug (rtPA or DNase I) loaded on the NPs was measured using the Pierce BCA protein assay kit (Life Technologies SAS, Courtaboeuf, France). Briefly, 200 µL of working reagent was added to 25 µL of each sample in 96 wells multiplate. The absorbance at 562 nm was read with a Varioskan LUX multiplate reader (Thermo Fisher Scientific, Massachusetts, United States) after 30 min incubation at 37°C. The concentration of the drug was extrapolated by a calibration curve prepared with different concentrations of rtPA or DNase I respectively. The encapsulation efficacy (EE) was calculated as EE (%) = 100% x $[Drug]_{loaded}/[Drug]_{initial}$ and the loading capacity (LC) was calculated as LC (%) = 100% x $[Drug]_{loaded}/[NP]$. The release of each drug was investigated after resuspending NPs in PBS 1X so that respective drug concentrations are 1 mg/kg rtPA and 5 mg/kg DNase I. During incubation at 37°C, supernatant samples are taken at regular intervals with respectively ultracentrifugation and ultrafiltration, then concentrations in supernatants is measured with respectively PefaFluor® and DNase detection kits.

Fibrin Agar Plate Assay (FAPA)

To assess the fibrinolytic activity of rtPA-loaded Fuco-NPs, a fibrinolysis experiment was performed. 5 mL of TBS Buffer (0.1 M Tris, 0.8 wt.% NaCl, 0.02 wt.% KCl, pH = 7.4) with 3 wt.% low melting agarose were heated above 65°C, while 5 mL of TBS buffer with 25 mg fibrinogen and 1 U plasminogen was slowly heated to 37°C. Once the agarose solution reached 65°C, it was cooled to 37°C, and 2 U of thrombin were added. Next, the two solutions were slowly mixed, then poured into a 9 cm Petri dish and incubated at 37°C for 2 h (gels can be kept a few days at 4°C). On the solidified agarose gel, round wells were formed using a 3 mm punch as sample reservoirs. 5 µL of each sample (diluted 1:10) was dropped into the wells and incubated at 37°C in a humid environment. Pictures were taken every hour for a commercial smartphone (64 MP F1.8 OIS camera) for 8 h. The degree of fibrin lysis was quantified with ImageJ by comparing the rate of expansion for fibrinolysis rings between samples and free rtPA standards as per the method described in Wang *et al*., 2012 [37].

NET degradation assay

To assess the NETolytic activity of DNase I-loaded NPs, a semi-quantitative assay was performed. Human whole blood was collected in EDTA tubes. Following the supplier's protocol for Polymorphprep, neutrophils were isolated and resuspended in 0.05 wt.% BSA in DMEM. Purity and cell count were determined with a hematology analyzer (ABX Pentra 60, Horiba, Vénissieux, France). Neutrophils were seeded at 1.0 x 10^5 cells/cm^2 on 8-wells Lab-Tek II Chamber Slide (Thermo Fischer Scientific, Massachusetts, United States) and incubated at a humidified atmosphere of 5% CO_2 for 60 min. PMA was then added to a final concentration of 50 nM, and the neutrophils were left to incubate for 4 h. Medium was then changed to incubate the formed NETs with DNase I-loaded Fuco-NPs resuspended in 0.05 wt.% BSA-DMEM to a concentration equivalent to 0.5 mg/mL or 0.1 mg/mL DNase I. After a 60 min incubation, the

samples were fixed with 4% (v/v) paraformaldehyde for 30 min at RT. After rinsing three times with PBS, the samples were blocked with 1% BSA in 0.1% (v/v) Tween 20 PBS (PBS-T) for 30 min at RT, then washed with PBS three times. Then, the samples were incubated with 100 nM SytoxGreen and 1 µg/mL DAPI in 1 wt.% BSA PBS-T for 10 min at RT, then washed with PBS twice before slide mounting and imaging with a microscope (Axio Observer, Carl Zeiss Microscopy, Oberkochen, Germany).

***In vitro* static thrombolysis**

For static thrombolysis assays, two types of blood clots were prepared *in vitro*: "young" and "old" clots. Human whole blood was collected in sodium citrate tubes, and 200 µL blood were added to glass tubes containing 10 µL water with 200 mM $CaCl_2$ and 2 U/mL thrombin. The tubes were closed and incubated at 37°C for 1 h for "young" clots. For "old" clots, 0.2 U/mL thrombin and 24 h incubation were used. The resulting clots were washed four times in PBS, weighted, then washed again three times. The clots were then incubated at 37°C with the different conditions (resuspended in PBS, with 0.25 U plasminogen added per clot) for 1 h with slow agitation. The clots were weighted again, and the supernatants were frozen at -20°C for 24 h. Quantification of released hemoglobin (Hb) was performed by thawing the supernatants then mixing ten volumes of Drabkin's reagent (200 mg/L potassium ferricyanide, 50 mg/L potassium cyanide, 140 mg/L potassium dihydrogen phosphate, 1% (v/v) Tween 20, pH = 7-7.4) with one volume supernatant. After 10 min incubation in the dark at RT, absorbance is read at 540 nm with a Varioskan LUX multiplate reader (Thermo Fisher Scientific, Massachusetts, United States). rtPA and DNase I concentrations used were 1 µg/mL and 50 µg/mL respectively. For NET content quantification, untreated "young" and "old" clots were retrieved after the first four PBS washes, then fixed with 4% (v/v) paraformaldehyde for 24 h at 4°C. After washing three times with PBS, then clots were incubated at RT for 30 min with 100 nM SytoxGreen and 1 µg/mL DAPI in PBS, then washed three times before imaging with a Leica Z16 APO macroscope (Leica, Nanterre, France) equipped with an Orca Flash 4.0 LT camera (Hamamatsu, Hamamatsu City, Japan).

***In vivo* FeCl3 mesenteric vein thrombosis model**

Animal studies were performed on 6–8 weeks old C57BL6J mice (Janvier Labs, Le Genest-Saint-Isle, France), with equipartition of males (24.9±2.3 g weight) and females (19.9±2.4 g weight) in each group. All experiment were adapted according to French (Decree 87/848) and European (2010/63/EU) ethical guidelines. The local ethic committee (C2EA-121 Paris Nord, France) and the French Ministère de l'Enseignement Supérieur et de la Recherche approved the fulfilling of the experiments with the reference number APAFIS#49260. After an acclimatation period of one week in an enriched environment, mice received analgesia (subcutaneous injection of buprenorphine 0.05 mg/kg), then were anesthetized for the whole procedure (4% isoflurane inhalation for initiation then continuous 2% isoflurane inhalation). A midline abdominal incision was performed to expose the mesentery, which was gently laid out over a transparent Petri dish and placed under an intravital macroscope: Leica Z16 APO macroscope (Leica, Nanterre, France) equipped with an Orca Flash 4.0 LT camera (Hamamatsu, Hamamatsu City, Japan). A retro-orbital injection of 30 µL DIOC6 50 µM was performed to label leukocytes and platelets. A 1 mm large

Whatmann chromatography paper band, previously soaked in 10 wt.% FeCl3 was deposed on a mesentery vein for one minute before removal. The thrombus formation was observed in real time for 10 to 20 min by fluorescence macroscopy. Once the thrombus was formed, images were acquired at 20 s intervals for 30 min. Between the second and third frames, samples were administered with a retro-orbital injection (150 µL injections, in saline suspension). When NPs were used, they were fluorescently labeled with TRITC, and the maximum final concentration of Fuco-NPs in the mice blood was 962±26 µg/mL (obtained for Fuco-NP-rtPA 5 mg/kg and empty Fuco-NPs). At the end of the image acquisition, the animals were sacrificed. Image analysis of thrombi with ImageJ included a SIFT-based alignment with rigid transformation. The thrombus area was measured over time in the DIOC6 channel to create thrombi binary masks by thresholding and the rate of thrombus degradation was analyzed after the thrombus reached its maximum size in the first 20 frames (7 minutes). For targeting measurements, the mean fluorescence intensity (MFI) was measured in the thrombus for both DIOC6 and TRITC over time, and in particular after 30 min as a ratio of MFI_{TRITC}/MFI_{DIOC6}.

Biodistribution in mice

For a limited number of animals (n=4) and for the saline and Fuco-NP conditions, organs (liver, spleen, kidney, lung) were harvested after the *in vivo* thrombosis model described above. They were fixed with 4% (v/v) paraformaldehyde for 24 h at 4°C, then transferred in 70% EtOH for storage. The organs were later embedded in paraffin. For each organ, representative slices were stained by hematoxylin-eosin and natural saffron (HES) and Alcian Blue (AB). Furthermore, for one animal for each condition, immunohistochemistry (IHC) was performed. Briefly, after deparaffinization, rehydration, and antigen retrieval (citric acid buffer, pH=6), slides were incubated with a primary anti-CD68 antibody (dilution 1:100) and then the supplier's protocol was followed for the IHC detection kit with horse radish peroxidase (HRP), with an acid Mayer's hemalum counterstaining. Digital slides with tissue slices were acquired using a Nanozoomer (Hamamatsu, Hamamatsu City, Japan).

Image analysis and statistical analysis

Images were analyzed with ImageJ (Fiji), and the macros that were used are made available in Supplementary Materials. When images are shown, the same contrast values are applied to each channel displayed. Quantitative data were analyzed with the statistical analysis software GraphPad PRISM 9.5.0., with a significance level α taken at 0.05. All presented data consisted of n=3 or more replicates per condition (when not shown on the graphs, replicate number is indicated in the legend). Whenever applicable, presented replicates consist of biological replicates, or, when appropriate, different NP batches. Unless explicitly mentioned, results are presented as mean ± standard deviation. Depending on the design of the experiments, data significance was evaluated with unpaired t-test (two groups, assumed equal variance), unpaired t-test with Welch's correction (two groups, variance not equal), paired t-test (two groups of paired values, with assumed equal variance), one-way ANOVA (one factor explored, with more than two groups, variances assumed equal) with Tukey's multiple comparison test, one-way Welch's ANOVA (one factor explored, with more than two groups, variances not equal) with Dunnett's T3 multiple

comparison test, repeated measures one-way ANOVA (one factor explored, with more than two groups of repeated measures compared to the initial group, variances assumed equal) with Dunnett's multiple comparison test, two-way ANOVA (two factors explored). Unless explicitly specified in the legend, unpaired t-tests and ANOVA with Tukey's test are performed. Every p-value below α threshold was represented as follows: * $p < 0.05$; ** $p < 0.01$; *** $p < 0.001$, **** $p < 0.0001$ (ns was indicated for "not significant" if no significant differences are present in the data presented).

Supporting Information

The following files are available free of charge.

Supplementary Figures: additional figures to provide context for presented results (PDF)

Supplementary Movies 1-5: flow targeting representative assays in microfluidic channels (TIFF)

Supplementary Movies 6-14: in vivo thrombolysis representative experiments (TIFF)

ImageJ Macros: ImageJ Macros used for image analysis (TXT)

Author Contributions

Thibault DE LA TAILLE: Conceptualization, Methodology, Investigation, Experimental work, Data Curation, Writing - Original Draft, Visualization; Pierre SARFATI: Methodology, Investigation; Rachida AID: Methodology, Investigation; Louise FOURNIER: Methodology; Graciela PAVON-DJAVID: Methodology, Investigation; Frédéric CHAUBET: Conceptualization, Resources, Writing - Review and Editing, Supervision, Project administration, Funding acquisition; Cédric CHAUVIERRE: Conceptualization, Resources, Writing - Review and Editing, Supervision, Project administration, Funding acquisition. All the authors approved the final revised version of the manuscript.

Acknowledgment

The Authors thank INSERM, Université Sorbonne Paris Nord, Université Paris Cité with the STRATEX "Reprobulles" RM27J22IDX87 and the ANR "FightClot" ANR-20-CE18-0005-01 for the financial support. They also express their gratitude to Algues & Mer for the supply of fucoidan. The authors would like to acknowledge Thomas BONNARD, Alina ZENYCH and Laura FORERO-RAMIREZ for the initial design of submicronic particles, Stéphane LOYAU for his help and expertise on experiments involving human blood, Deborah FRANCOIS for her help with the animal experimentation, Yoann LALATONNE for his help with the TXRF data acquisition, Yang ZHANG for procuring the HUVECs for cytotoxicity assays. We acknowledge the ImagoSeine core facility of the Institut Jacques Monod, member of the France BioImaging infrastructure (ANR-10-INBS-04) and GIS-IBiSA, for the TEM imaging. We acknowledge Olivier THIBAUDEAU from the Morphology Platform at INSERM UMR 1152-Bichat Hospital for his help with immunohistochemistry. The illustrations were designed with BioRender online

software (biorender.com). The graphical abstract was designed with BioRender and Blender 4.2, with an initial blood vessel design by Ryo Mizuta Graphics.

Abbreviations

CVD, cardiovascular disease; IHD, ischemic heart disease; AIS, acute ischemic stroke; DALYs, disability-adjusted life years; MI, myocardial infarction; VWF, Von Willebrand Factor; NET, neutrophil extracellular trap; rtPA, recombinant tissue plasminogen activator; EVT, endovascular therapy; NP, nanoparticle; HLD, hydrophilic lipophilic difference; EACN, effective alkane carbon number; Cc, characteristic curvature; PDI, polydispersity; LC, loading capacity; EE, encapsulation efficacy; Hb, hemoglobin; IHC, immunohistochemistry; HES, hematoxylin-eosin and natural saffron; AB, Alcian Blue; MPS, mononuclear phagocyte system; TEM, transmission electron microscopy.

References

(1) Ferrari, A. J.; Santomauro, D. F.; Aali, A.; Abate, Y. H.; Abbafati, C.; Abbastabar, H.; ElHafeez, S. A.; Abdelmasseh, M.; Abd-Elsalam, S.; Abdollahi, A.; Abdullahi, A.; Abegaz, K. H.; Zuñiga, R. A. A.; Aboagye, R. G.; Abolhassani, H.; Abreu, L. G.; Abualruz, H.; Abu-Gharbieh, E.; Abu-Rmeileh, N. M.; Ackerman, I. N.; et al. Global Incidence, Prevalence, Years Lived with Disability (YLDs), Disability-Adjusted Life-Years (DALYs), and Healthy Life Expectancy (HALE) for 371 Diseases and Injuries in 204 Countries and Territories and 811 Subnational Locations, 1990–2021: A Systematic Analysis for the Global Burden of Disease Study 2021. *The Lancet* **2024**, *403* (10440), 2133–2161. https://doi.org/10.1016/S0140-6736(24)00757-8.

(2) Alkarithi, G.; Duval, C.; Shi, Y.; Macrae, F. L.; Ariëns, R. A. S. Thrombus Structural Composition in Cardiovascular Disease. *Arterioscler. Thromb. Vasc. Biol.* **2021**, *41* (9), 2370–2383. https://doi.org/10.1161/ATVBAHA.120.315754.

(3) Di Meglio, L.; Desilles, J.-P.; Ollivier, V.; Nomenjanahary, M. S.; Di Meglio, S.; Deschildre, C.; Loyau, S.; Olivot, J.-M.; Blanc, R.; Piotin, M.; Bouton, M.-C.; Michel, J.-B.; Jandrot-Perrus, M.; Ho-Tin-Noé, B.; Mazighi, M. Acute Ischemic Stroke Thrombi Have an Outer Shell That Impairs Fibrinolysis. *Neurology* **2019**, *93* (18), e1686–e1698. https://doi.org/10.1212/WNL.0000000000008395.

(4) National Institute of Neurological Disorders and Stroke rt-PA Stroke Study Group. Tissue Plasminogen Activator for Acute Ischemic Stroke. *N. Engl. J. Med.* **1995**, *333* (24), 1581–1587. https://doi.org/10.1056/NEJM199512143332401.

(5) Bhatia, R.; Hill, M. D.; Shobha, N.; Menon, B.; Bal, S.; Kochar, P.; Watson, T.; Goyal, M.; Demchuk, A. M. Low Rates of Acute Recanalization With Intravenous Recombinant Tissue Plasminogen Activator in Ischemic Stroke. *Stroke* **2010**, *41* (10), 2254–2258. https://doi.org/10.1161/STROKEAHA.110.592535.

(6) de Havenon, A.; Sheth, K.; Johnston, K. C.; Delic, A.; Stulberg, E.; Majersik, J.; Anadani, M.; Yaghi, S.; Tirschwell, D.; Ney, J. Acute Ischemic Stroke Interventions in the United States

and Racial, Socioeconomic, and Geographic Disparities. *Neurology* **2021**, *97* (23), e2292–e2303. https://doi.org/10.1212/WNL.0000000000012943.

(7) Lapergue, B.; Blanc, R.; Costalat, V.; Desal, H.; Saleme, S.; Spelle, L.; Marnat, G.; Shotar, E.; Eugene, F.; Mazighi, M.; Houdart, E.; Consoli, A.; Rodesch, G.; Bourcier, R.; Bracard, S.; Duhamel, A.; Ben Maacha, M.; Lopez, D.; Renaud, N.; Labreuche, J.; et al. Effect of Thrombectomy With Combined Contact Aspiration and Stent Retriever vs Stent Retriever Alone on Revascularization in Patients With Acute Ischemic Stroke and Large Vessel Occlusion: The ASTER2 Randomized Clinical Trial. *JAMA* **2021**, *326* (12), 1158–1169. https://doi.org/10.1001/jama.2021.13827.

(8) Rai, A. T.; Link, P. S.; Domico, J. R. Updated Estimates of Large and Medium Vessel Strokes, Mechanical Thrombectomy Trends, and Future Projections Indicate a Relative Flattening of the Growth Curve but Highlight Opportunities for Expanding Endovascular Stroke Care. *J. NeuroInterventional Surg.* **2023**, *15* (e3), e349–e355. https://doi.org/10.1136/jnis-2022-019777.

(9) Ducroux, C.; Di Meglio, L.; Loyau, S.; Delbosc, S.; Boisseau, W.; Deschildre, C.; Ben Maacha, M.; Blanc, R.; Redjem, H.; Ciccio, G.; Smajda, S.; Fahed, R.; Michel, J.-B.; Piotin, M.; Salomon, L.; Mazighi, M.; Ho-Tin-Noe, B.; Desilles, J.-P. Thrombus Neutrophil Extracellular Traps Content Impair tPA-Induced Thrombolysis in Acute Ischemic Stroke. *Stroke* **2018**, *49* (3), 754–757. https://doi.org/10.1161/STROKEAHA.117.019896.

(10) Colasuonno, M.; Palange, A. L.; Aid, R.; Ferreira, M.; Mollica, H.; Palomba, R.; Emdin, M.; Del Sette, M.; Chauvierre, C.; Letourneur, D.; Decuzzi, P. Erythrocyte-Inspired Discoidal Polymeric Nanoconstructs Carrying Tissue Plasminogen Activator for the Enhanced Lysis of Blood Clots. *ACS Nano* **2018**, *12* (12), 12224–12237. https://doi.org/10.1021/acsnano.8b06021.

(11) Sarfati, P.; Taille, T. D. L.; Portioli, C.; Spanò, R.; Lalatonne, Y.; Decuzzi, P.; Chauvierre, C. REVIEW: "ISCHEMIC STROKE: From Fibrinolysis to Functional Recovery" Nanomedicine: Emerging Approaches to Treat Ischemic Stroke. *Neuroscience* **2024**, *550*, 102–113. https://doi.org/10.1016/j.neuroscience.2023.11.035.

(12) Lee, T.-R.; Choi, M.; Kopacz, A. M.; Yun, S.-H.; Liu, W. K.; Decuzzi, P. On the Near-Wall Accumulation of Injectable Particles in the Microcirculation: Smaller Is Not Better. *Sci. Rep.* **2013**, *3* (1), 2079. https://doi.org/10.1038/srep02079.

(13) Müller, K.; Fedosov, D. A.; Gompper, G. Margination of Micro- and Nano-Particles in Blood Flow and Its Effect on Drug Delivery. *Sci. Rep.* **2014**, *4* (1), 4871. https://doi.org/10.1038/srep04871.

(14) D'Apolito, R.; Tomaiuolo, G.; Taraballi, F.; Minardi, S.; Kirui, D.; Liu, X.; Cevenini, A.; Palomba, R.; Ferrari, M.; Salvatore, F.; Tasciotti, E.; Guido, S. Red Blood Cells Affect the Margination of Microparticles in Synthetic Microcapillaries and Intravital Microcirculation as a Function of Their Size and Shape. *J. Control. Release Off. J. Control. Release Soc.* **2015**, *217*, 263–272. https://doi.org/10.1016/j.jconrel.2015.09.013.

(15) Duan, X.; Li, Y. Physicochemical Characteristics of Nanoparticles Affect Circulation, Biodistribution, Cellular Internalization, and Trafficking. *Small* **2013**, *9* (9–10), 1521–1532. https://doi.org/10.1002/smll.201201390.

(16) Inggrid Setyawati, M.; Yong Tay, C.; Docter, D.; H. Stauber, R.; Tai Leong, D. Understanding and Exploiting Nanoparticles' Intimacy with the Blood Vessel and Blood. *Chem. Soc. Rev.* **2015**, *44* (22), 8174–8199. https://doi.org/10.1039/C5CS00499C.

(17) Pawlowski, C. L.; Li, W.; Sun, M.; Ravichandran, K.; Hickman, D.; Kos, C.; Kaur, G.; Sen Gupta, A. Platelet Microparticle-Inspired Clot-Responsive Nanomedicine for Targeted Fibrinolysis. *Biomaterials* **2017**, *128*, 94–108. https://doi.org/10.1016/j.biomaterials.2017.03.012.

(18) Zhang, N.; Ru, B.; Hu, J.; Xu, L.; Wan, Q.; Liu, W.; Cai, W.; Zhu, T.; Ji, Z.; Guo, R.; Zhang, L.; Li, S.; Tong, X. Recent Advances of CREKA Peptide-Based Nanoplatforms in Biomedical Applications. *J. Nanobiotechnology* **2023**, *21*, 77. https://doi.org/10.1186/s12951-023-01827-0.

(19) Xu, J.; Zhang, Y.; Xu, J.; Liu, G.; Di, C.; Zhao, X.; Li, X.; Li, Y.; Pang, N.; Yang, C.; Li, Y.; Li, B.; Lu, Z.; Wang, M.; Dai, K.; Yan, R.; Li, S.; Nie, G. Engineered Nanoplatelets for Targeted Delivery of Plasminogen Activators to Reverse Thrombus in Multiple Mouse Thrombosis Models. *Adv. Mater.* **2020**, *32* (4), 1905145. https://doi.org/10.1002/adma.201905145.

(20) Xu, J.; Wang, X.; Yin, H.; Cao, X.; Hu, Q.; Lv, W.; Xu, Q.; Gu, Z.; Xin, H. Sequentially Site-Specific Delivery of Thrombolytics and Neuroprotectant for Enhanced Treatment of Ischemic Stroke. *ACS Nano* **2019**, *13* (8), 8577–8588. https://doi.org/10.1021/acsnano.9b01798.

(21) Niu, Y.; Tan, H.; Li, X.; Zhao, L.; Xie, Z.; Zhang, Y.; Zhou, S.; Qu, X. Protein–Carbon Dot Nanohybrid-Based Early Blood–Brain Barrier Damage Theranostics. *ACS Appl. Mater. Interfaces* **2020**, *12* (3), 3445–3452. https://doi.org/10.1021/acsami.9b19378.

(22) Guan, L.; Wang, C.; Yan, X.; Liu, L.; Li, Y.; Mu, Y. Author Correction: A Thrombolytic Therapy Using Diagnostic Ultrasound Combined with RGDS-Targeted Microbubbles and Urokinase in a Rabbit Model. *Sci. Rep.* **2020**, *10* (1), 15767. https://doi.org/10.1038/s41598-020-72445-1.

(23) Akbarzadeh, A.; Rezaei-Sadabady, R.; Davaran, S.; Joo, S. W.; Zarghami, N.; Hanifehpour, Y.; Samiei, M.; Kouhi, M.; Nejati-Koshki, K. Liposome: Classification, Preparation, and Applications. *Nanoscale Res. Lett.* **2013**, *8* (1), 102. https://doi.org/10.1186/1556-276X-8-102.

(24) Perkins, L. A.; Anderson, C. J.; Novelli, E. M. Targeting P-Selectin Adhesion Molecule in Molecular Imaging: P-Selectin Expression as a Valuable Imaging Biomarker of Inflammation in Cardiovascular Disease. *J. Nucl. Med.* **2019**, *60* (12), 1691–1697. https://doi.org/10.2967/jnumed.118.225169.

(25) Chauvierre, C.; Aid-Launais, R.; Aerts, J.; Chaubet, F.; Maire, M.; Chollet, L.; Rolland, L.; Bonafé, R.; Rossi, S.; Bussi, S.; Cabella, C.; Dézsi, L.; Fülöp, T.; Szebeni, J.; Chahid, Y.; Zheng, K. H.; Stroes, E. S. G.; Le Guludec, D.; Rouzet, F.; Letourneur, D. Pharmaceutical Development and Safety Evaluation of a GMP-Grade Fucoidan for Molecular Diagnosis of Cardiovascular Diseases. *Mar. Drugs* **2019**, *17* (12), 699. https://doi.org/10.3390/md17120699.

(26) Zheng, K. H.; Kaiser, Y.; Poel, E.; Verberne, H.; Aerts, J.; Rouzet, F.; Stroes, E.; Letourneur, D.; Chauvierre, C. 99Mtc-Fucoidan As Diagnostic Agent For P-Selectin Imaging:

First-In-Human Evaluation (Phase I). *Atherosclerosis* **2019**, *287*, e143. https://doi.org/10.1016/j.atherosclerosis.2019.06.425.

(27) Bonnard, T.; Yang, G.; Petiet, A.; Ollivier, V.; Haddad, O.; Arnaud, D.; Louedec, L.; Bachelet-Violette, L.; Derkaoui, S. M.; Letourneur, D.; Chauvierre, C.; Visage, C. L. Abdominal Aortic Aneurysms Targeted by Functionalized Polysaccharide Microparticles: A New Tool for SPECT Imaging. *Theranostics* **2014**, *4* (6), 592–603. https://doi.org/10.7150/thno.7757.

(28) Zenych, A.; Jacqmarcq, C.; Aid, R.; Fournier, L.; Forero Ramirez, L. M.; Chaubet, F.; Bonnard, T.; Vivien, D.; Letourneur, D.; Chauvierre, C. Fucoidan-Functionalized Polysaccharide Submicroparticles Loaded with Alteplase for Efficient Targeted Thrombolytic Therapy. *Biomaterials* **2021**, *277*, 121102. https://doi.org/10.1016/j.biomaterials.2021.121102.

(29) Forero Ramirez, L. M.; Gobin, E.; Aid-Launais, R.; Journe, C.; Moraes, F.; Picton, L.; Le Cerf, D.; Letourneur, D.; Chauvierre, C.; Chaubet, F. Gd(DOTA)-Grafted Submicronic Polysaccharide-Based Particles Functionalized with Fucoidan as Potential MR Contrast Agent Able to Target Human Activated Platelets. *Carbohydr. Polym.* **2020**, *245*, 116457. https://doi.org/10.1016/j.carbpol.2020.116457.

(30) Abbott, S. J. *Surfactant Science: Principles & Practice*; DEStech Publications, Incorporated, 2017.

(31) Lovell, P. A.; Schork, F. J. Fundamentals of Emulsion Polymerization. *Biomacromolecules* **2020**, *21* (11), 4396–4441. https://doi.org/10.1021/acs.biomac.0c00769.

(32) Hong, C.; Alser, O.; Gebran, A.; He, Y.; Joo, W.; Kokoroskos, N.; Velmahos, G.; Olsen, B. D.; Hammond, P. T. Modulating Nanoparticle Size to Understand Factors Affecting Hemostatic Efficacy and Maximize Survival in a Lethal Inferior Vena Cava Injury Model. *ACS Nano* **2022**, *16* (2), 2494–2510. https://doi.org/10.1021/acsnano.1c09108.

(33) Gruber, S.; Nickel, A. Toxic or Not Toxic? The Specifications of the Standard ISO 10993-5 Are Not Explicit Enough to Yield Comparable Results in the Cytotoxicity Assessment of an Identical Medical Device. *Front. Med. Technol.* **2023**, *5*, 1195529. https://doi.org/10.3389/fmedt.2023.1195529.

(34) Guo, S.; Shi, Y.; Liang, Y.; Liu, L.; Sun, K.; Li, Y. Relationship and Improvement Strategies between Drug Nanocarrier Characteristics and Hemocompatibility: What Can We Learn from the Literature. *Asian J. Pharm. Sci.* **2021**, *16* (5), 551–576. https://doi.org/10.1016/j.ajps.2020.12.002.

(35) Fournier, L.; Abioui-Mourgues, M.; Chabouh, G.; Aid, R.; Taille, T. D. L.; Couture, O.; Vivien, D.; Orset, C.; Chauvierre, C. rtPA-Loaded Fucoidan Polymer Microbubbles for the Targeted Treatment of Stroke. *Biomaterials* **2023**, *303*, 122385. https://doi.org/10.1016/j.biomaterials.2023.122385.

(36) Orset, C.; Macrez, R.; Young, A. R.; Panthou, D.; Angles-Cano, E.; Maubert, E.; Agin, V.; Vivien, D. Mouse Model of In Situ Thromboembolic Stroke and Reperfusion. *Stroke* **2007**, *38* (10), 2771–2778. https://doi.org/10.1161/STROKEAHA.107.487520.

(37) Wang, M.; Yang, W.; Wu, Q.; Gu, H. Modeling of the Fibrin Agarose Plate Assay and Its Application for Thrombolytic Analysis. *Chin. Sci. Bull.* **2012**, *57*. https://doi.org/10.1007/s11434-012-5297-6.

(38) Jiménez-Alcázar, M.; Napirei, M.; Panda, R.; Köhler, E. C.; Kremer Hovinga, J. A.; Mannherz, H. G.; Peine, S.; Renné, T.; Lämmle, B.; Fuchs, T. A. Impaired DNase1-mediated Degradation of Neutrophil Extracellular Traps Is Associated with Acute Thrombotic Microangiopathies. *J. Thromb. Haemost.* **2015**, *13* (5), 732–742. https://doi.org/10.1111/jth.12796.

(39) Fitzgerald, S. T.; Liu, Y.; Dai, D.; Mereuta, O. M.; Abbasi, M.; Larco, J. L. A.; Douglas, A. S.; Kallmes, D. F.; Savastano, L.; Doyle, K. M.; Brinjikji, W. Novel Human Acute Ischemic Stroke Blood Clot Analogs for In Vitro Thrombectomy Testing. *AJNR Am. J. Neuroradiol.* **2021**, *42* (7), 1250–1257. https://doi.org/10.3174/ajnr.A7102.

(40) Powers, W. J.; Rabinstein, A. A.; Ackerson, T.; Adeoye, O. M.; Bambakidis, N. C.; Becker, K.; Biller, J.; Brown, M.; Demaerschalk, B. M.; Hoh, B.; Jauch, E. C.; Kidwell, C. S.; Leslie-Mazwi, T. M.; Ovbiagele, B.; Scott, P. A.; Sheth, K. N.; Southerland, A. M.; Summers, D. V.; Tirschwell, D. L. Guidelines for the Early Management of Patients With Acute Ischemic Stroke: 2019 Update to the 2018 Guidelines for the Early Management of Acute Ischemic Stroke: A Guideline for Healthcare Professionals From the American Heart Association/American Stroke Association. *Stroke* **2019**, *50* (12), e344–e418. https://doi.org/10.1161/STR.0000000000000211.

(41) Liu, L.; Chen, W.; Zhou, H.; Duan, W.; Li, S.; Huo, X.; Xu, W.; Huang, L.; Zheng, H.; Liu, J.; Liu, H.; Wei, Y.; Xu, J.; Wang, Y. Chinese Stroke Association Guidelines for Clinical Management of Cerebrovascular Disorders: Executive Summary and 2019 Update of Clinical Management of Ischaemic Cerebrovascular Diseases. *Stroke Vasc. Neurol.* **2020**, *5* (2), 159–176. https://doi.org/10.1136/svn-2020-000378.

(42) Gurewich, V. Therapeutic Fibrinolysis: How Efficacy and Safety Can Be Improved. *J. Am. Coll. Cardiol.* **2016**, *68* (19), 2099–2106. https://doi.org/10.1016/j.jacc.2016.07.780.

(43) Bannish, B. E.; Chernysh, I. N.; Keener, J. P.; Fogelson, A. L.; Weisel, J. W. Molecular and Physical Mechanisms of Fibrinolysis and Thrombolysis from Mathematical Modeling and Experiments. *Sci. Rep.* **2017**, *7* (1), 6914. https://doi.org/10.1038/s41598-017-06383-w.

(44) Kraal, G.; Mebius, R. New Insights into the Cell Biology of the Marginal Zone of the Spleen. *Int. Rev. Cytol.* **2006**, *250*, 175–215. https://doi.org/10.1016/S0074-7696(06)50005-1.

(45) Gustafson, H. H.; Holt-Casper, D.; Grainger, D. W.; Ghandehari, H. Nanoparticle Uptake: The Phagocyte Problem. *Nano Today* **2015**, *10* (4), 487–510. https://doi.org/10.1016/j.nantod.2015.06.006.

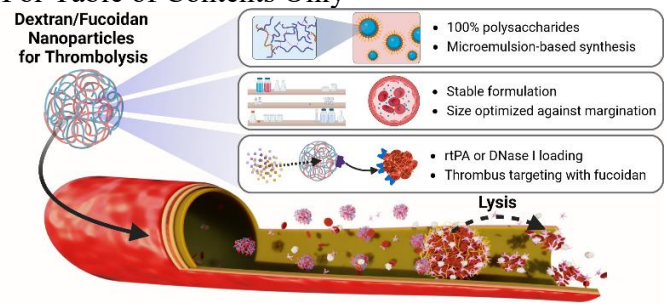
(46) Khalikova, E.; Susi, P.; Korpela, T. Microbial Dextran-Hydrolyzing Enzymes: Fundamentals and Applications. *Microbiol. Mol. Biol. Rev.* **2005**, *69* (2), 306–325. https://doi.org/10.1128/MMBR.69.2.306-325.2005.

(47) Maia, J.; Evangelista, M.; Gil, H.; Ferreira, L. Dextran-Based Materials for Biomedical Applications; 2014; pp 31–53.

(48) Wang, R.; Dijkstra, P. J.; Karperien, M. Dextran. In *Biomaterials from Nature for Advanced Devices and Therapies*; John Wiley & Sons, Ltd, 2016; pp 307–319. https://doi.org/10.1002/9781119126218.ch18.

(49) Lee, J. M.; Shin, Z.-U.; Mavlonov, G.; Abdurakhmonov, I.; Yi, T. Solid-Phase Colorimetric Method for the Quantification of Fucoidan. *Appl. Biochem. Biotechnol.* **2012**, *168*. https://doi.org/10.1007/s12010-012-9837-y.

For Table of Contents Only



ANNEX 7

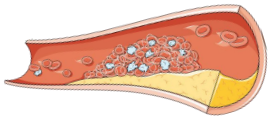
Development of functionalized polysaccharide nanoparticles for a targeted combo treatment of ischemic strokes

Thibault de La Taille [1], *Louise Fournier* [1], *Rachida Aid* [1, 2], *Frédéric Chaubet* [1], *Cedric Chauvierre* [1]

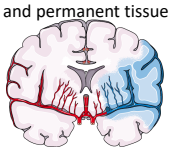
[1] INSERM U1148 - LVTS, UPC, USPN, Paris, France, [2] UMS34 FRIM, UPC, Paris, France

1/ Context

Cardiovascular diseases are held responsible for a **third of all deaths worldwide**, among which **85%** are due to **heart attacks and strokes**. These result from a **thrombotic event**, where a blood clot restricts the blood flow, which causes tissue ischemia and permanent tissue damage. [1]



Atherosclerotic blood clot formation

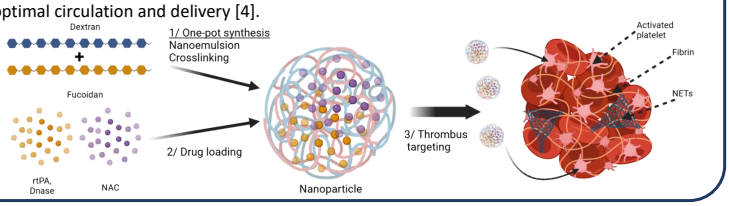


Brain ischemia due to a blood clot-induced stroke

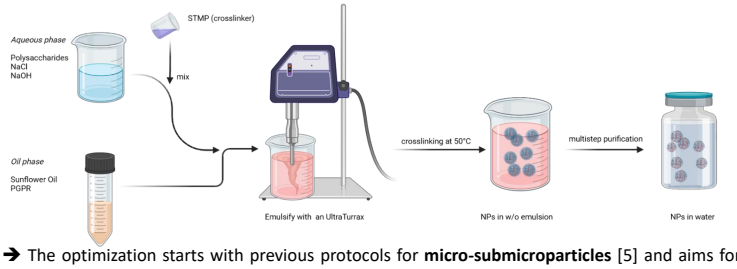
The blood clots are composed of **activated platelets**, red blood cells and immune cells, and binding elements such as **fibrin** network or **NETs** (DNA network released by neutrophils). Thus, treatments for strokes consist of **thrombolytic** drugs such as rtPA (fibrinolytic), which causes the degradation of the fibrin network to ensure the blood clot lysis. This is however limited by a low drug half-life, systemic adverse effects and low recanalization efficiency. **Targeted multi-drug delivery nanoparticles** can overcome these challenges [2].

2/ Nanoparticle design

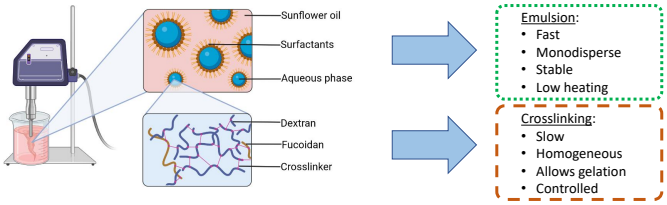
Nanoparticles (NPs) are synthesized through a **water-in-oil nanoemulsion**, where **crosslinking** of **polysaccharides** occurs in the aqueous phase. Drug loading will be performed by adsorption or chemical functionalization in this nanogel. The **fucoidan** allows specific **targeting** of P-selectin, a marker of activated platelets [3]. Selected drugs include **rtPA**, **DNase** (for NETs) and neuroprotectants: **N-acetylcysteine** (NAC), known for ROS scavenging and Von Willebrand Factor-dependent thrombolysis. Notably, NPs of a **few hundred nm** can be preferred for optimal circulation and delivery [4].



3/ Synthesis and size optimization



➔ The optimization starts with previous protocols for **micro-submicroparticles** [5] and aims for NPs in the range of a **few hundred nm** for better circulation, deeper clot access and surface ratio.
➔ **One-pot process**: simpler, faster, more robust.
➔ **Crosslinking** and **emulsion**: these two main steps must be controlled.



➔ Multiple optimization paths explored

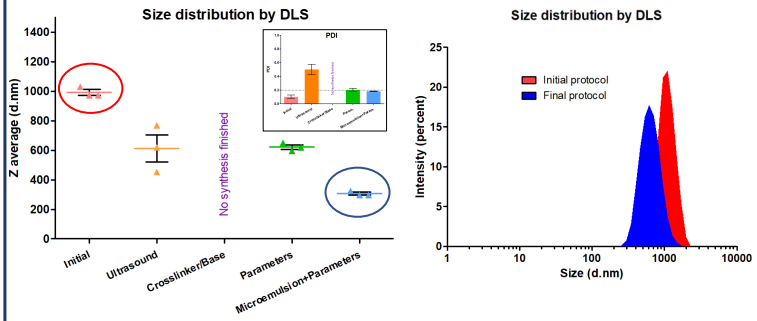
Ultrasound (US) ✗
Step added after Ultraturrax for **further size control** of droplets by increased shearing forces
➔ Rejected because of the heating induced

Crosslinker/Base ✗
Use **oil-soluble crosslinker** ($POCl_3$) or **base** (TBA) instead of STMP and NaOH
➔ Gels can be obtained but the emulsion is impaired

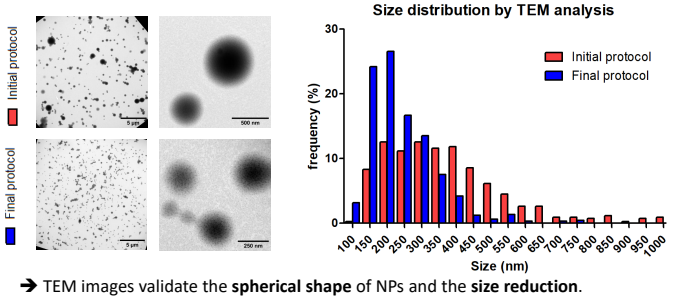
Microemulsion (HLD) ✓
Implement a semi-empiric model based on **thermodynamic** stability to choose the **surfactants** [6]
➔ Surfactants: PGPR/Tween 80 60:40 for size reduction

Parametric optimization ✓
The process is modified for slowing the crosslinking and minimizing emulsion time
➔ NP size reduced

4/ Size reduction

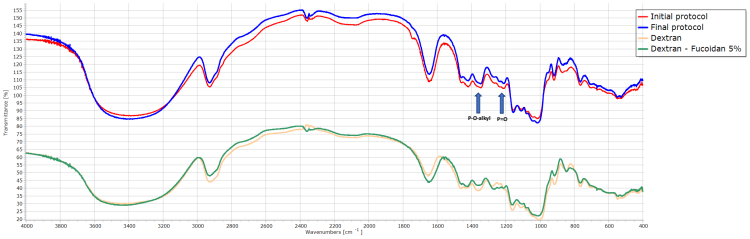


➔ The final **process optimization** coupled with the **microemulsion** based design allows a controlled synthesis of **330 nm NPs** with satisfactory dispersion (PDI below 0.2).
➔ Stability in water can be explained by a **low Zeta potential** (- 30 mV) for all formulations.

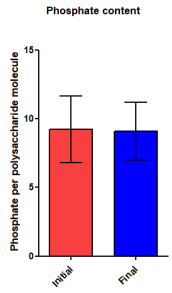


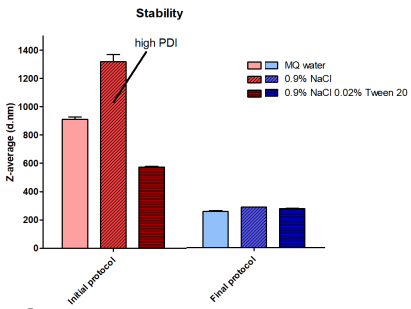
➔ TEM images validate the **spherical shape** of NPs and the **size reduction**.

5/ Characterization



➔ FTIR spectra of NPs batches show similar **chemical composition** with dextran.
➔ Crosslinking is suggested by relevant **phosphate peaks**.
➔ **Fucoidan** presence cannot be determined by FTIR, as shown by the physical blend.





➔ **Crosslinking** can be evidenced by phosphate determination with a spectrophotometric method.
➔ Final protocol allows **stability** in **saline suspension**.
➔ Removes the **need for stabilization**.

6/ Conclusion and *perspectives*

➔ **Spherical polysaccharide NPs** were synthesized according to an optimized protocol which incorporates parametric stepwise changes and a design by a **microemulsion** rationale. The resulting NPs were **stable** in **saline** suspension **without stabilizer**, with a size of **330 nm** (>1/3 reduction).
➔ ***Fucoidan*** *content will be quantified and NPs' ability to* ***target activated platelet*** *verified.*
➔ ***Drug loading and release kinetics*** *will be assessed.*
➔ *In vitro activity of these drugs (rtPA, Dnase, NAC) will be verified with appropriate assays and their* ***thrombolytic*** *activity measured.*
➔ ***Cytotoxicity*** *measurements will be performed.*
➔ ***Toxicity, biodistribution*** *and efficacy to* ***target*** *and* ***lyse*** *blood clots will be assessed in vivo with rodent models for ischemic strokes, to verify the* ***combo effect and neuroprotection.***

References: [1] Cardiovascular diseases (CVDs). https://www.who.int/news-room/fact-sheets/detail/cardiovascular-diseases-(cvds) (2022) [2] Thiebaut AM, *et al.* The Lancet Neurology 17(12): 1121-1132 (2018) [3] Chauvierre C, *et al.* Marine Drugs. 17(12):699 (2019) [4] Setyawati M, *et al.* Chem. Soc. Rev, 44, 8174-8199 (2015) [5] Zenych A, *et al.* Biomaterials 277: 121102 (2021) [6] Abbott SJ. Surfactant Science: Principles & Practice (2017).

Acknowledgements: This Ph.D. project is performed under the supervision of Dr. Frédéric Chaubet and Dr. Cédric Chauvierre. Financial support was provided by the joint fundings of Ecole Doctorale Galilée, Université Sorbonne Paris Nord, and the ANR project "FightClot" ANR-20-CE18-0005-01. We acknowledge the LVTS as hosting institution and the ImagoSeine core facility of the Institut Jacques Monod, member of the France BioImaging infrastructure (ANR-10-INBS-04). The website from Pr. Steven Abbott on HLD was used for HLD screening visualization. All schemes were created using Biorender.com.

Contact information:
Thibault.de-la-taille@inserm.fr

SFNano
FRENCH SOCIETY FOR NANOMEDICINE

ANNEX 8

Université Paris Cité

Institut des Sciences Cardiovasculaires

EUR Université Paris Cité

Cardiovascular Sciences
GRADUATE SCHOOL

Certificate of Best Poster Presentation

Is presented to

biotechne

Thibault de la Taille

For their outstanding presentation in the Early Career Research Congress

Awarded on Dec 9, 2022

9-12- 2022

Date

Prof. Jean Sebastian

Signature

ANNEX 9

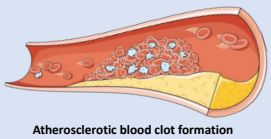
Development of functionalized polysaccharide nanoparticles for a targeted treatment of ischemic stroke

Thibault de La Taille [1], *Rachida Aid* [1,2], *Frédéric Chaubet* [1], *Cédric Chauvierre* [1]

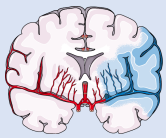
[1] *INSERM U1148 - LVTS, UPC, USPN, Paris, France,* [2] *UMS34 FRIM, UPC, Paris, France*

Unmet medical need

Cardiovascular diseases are held responsible for a **third of all deaths worldwide**, among which **85%** are due to **heart attacks and strokes**. These result from a **thrombotic event**, where a blood clot (thrombus) restricts the blood flow, which causes tissue ischemia and permanent tissue damage [1].



Atherosclerotic blood clot formation

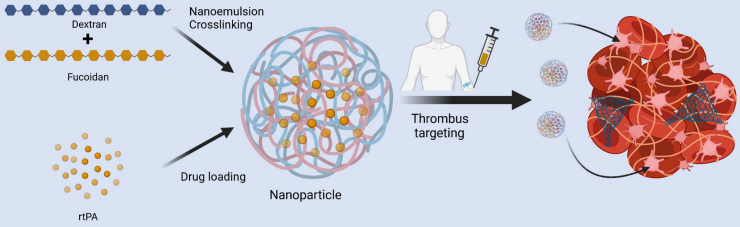


Brain ischemia due to a blood clot-induced stroke

The thrombi are composed of **activated platelets**, red blood cells and immune cells, and binding elements such as **fibrin** network or **NETs** (DNA network released by neutrophils) [2]. Thus, treatments for strokes consist of **thrombolytic** drugs such as **rtPA** (fibrinolytic), which causes the degradation of the fibrin network [3]. This is however limited by a low drug half-life, systemic adverse effects and low recanalization efficiency, as well as poor patient eligibility.
Targeted delivery nanoparticles can overcome these challenges by addressing the complex thrombus nature and limiting the side effects [4] .

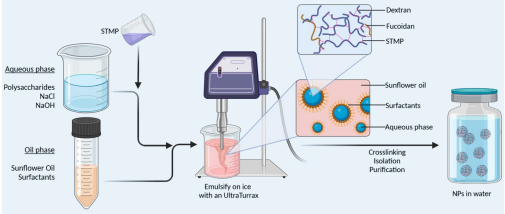
Nanoparticle design

Nanoparticles (NPs) are synthesized through a **water-in-oil nanoemulsion**, where **crosslinking** of **polysaccharides** occurs in the aqueous phase. Drug loading is performed by adsorption in this nanogel. The **fucoidan** allows specific **targeting** of P-selectin, a marker of activated platelets [5]. The main investigated drug consists of **rtPA** as the fibrinolytic and main thrombolytic drug. Notably, NPs of a **150 – 400 nm** size window can be desired for optimal circulation and delivery [6]. The NPs can then be injected in the blood, target the thrombus and then release the drugs to ensure thrombolysis and ischemic tissue recovery, while mitigating side effects with lower drug dose and specific targeting.

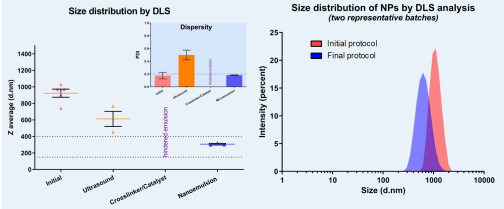


Synthesis

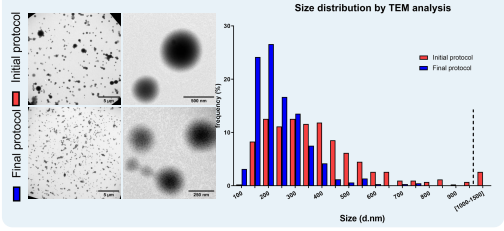
A **one-pot process** was designed to provide a simple, fast and robust synthesis with **green chemistry** reagents only, where an **emulsion** is performed to control the size and shape of STMP-crosslinked nanoparticles in the aqueous phase. Based on a previous protocol for **micro-submicroparticles** [7], a new method for NPs synthesis was searched with the following criteria:
- **Emulsion:** small droplet size, monodisperse, stable, fast, low heating
- **Crosslinking**: homogeneous, slow, sufficient for hydrogel gelation



Multiple optimization paths were explored, including ultrasonication, oil-soluble crosslinker/basic catalyst, and **nanoemulsion** (NE). NEs are nanoscale emulsions with very low surface tension and can provide suitable nanoreactors for NP synthesis. After careful determination of an adequate nanoemulsion domain for our different phases, this **nanoemulsion process was chosen as final synthesis** method:

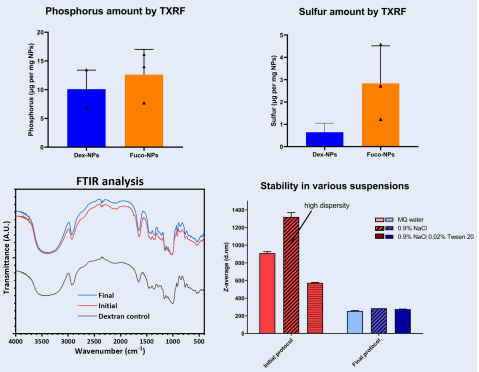


Size distribution were assessed by DLS (*above*) and TEM (*below*) to confirm **monodisperse 312 ± 12 nm NPs**. Zêta potential was also evaluated at **– 27 mV**, ensuring electrostatic stability in suspension, including **saline and PBS** suspensions. Sphericity was also established. Finally, **storage** was possible over 2 months at 4°C, and successful resuspension after **freeze-drying** was validated, which is critical for clinic applications and long-term storage.

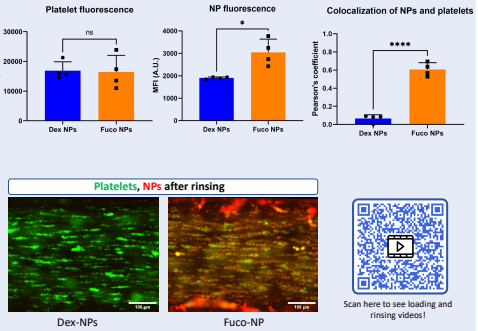


Characterization

Physico-chemical analysis confirmed the obtention of **polysaccharide Dex-NPs** made up of dextran (and incorporating fucoidan for targeting NPs: **Fuco-NPs**) by FTIR. Total reflection X-ray fluorescence spectrometry (TXRF) confirmed the **crosslinking** by phosphate bonds, as well as the **incorporation of fucoidan** in Fuco-NPs. This was also evidenced by converging chemical titrations methods. Finally, stability of NPs in saline and PBS suspensions was demonstrated, in contrary to previous protocols.

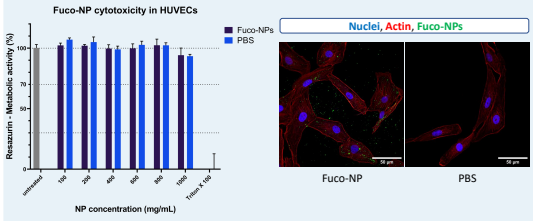


Moreover, the capacity of **fucoidan to target activated platelets** was investigated with Fuco-NPs. Platelet aggregates were formed in collagen-coated Vena8 Fluoro+ **microfluidic chips** from human whole blood under arterial flow conditions. Dex-NPs and Fuco-NPs were then added for 5 min, then rinsed to observe unspecific and specific binding of NPs to activated platelets. As shown (*below*), **Fuco-NPs readily accumulated on the aggregates**, and were retained even after rinsing contrary to Dex-NPs. This demonstrates the ability of **Fuco-NPs to successfully bind activated platelets** through the P-selectin receptor, which can be used for targeting the thrombus in strokes.

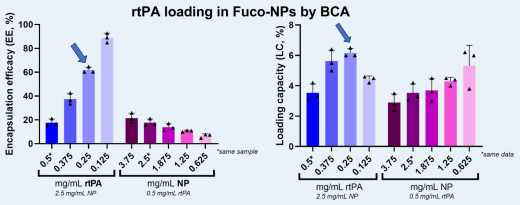


In vitro preclinical study

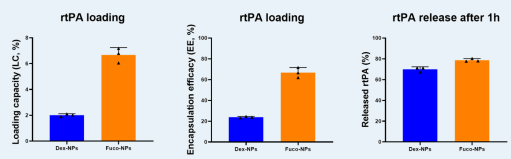
Preliminary cytotoxicity results of Fuco-NPs show **no toxicity on endothelial cells** (HUVECs) over 24 h by measuring metabolic activity *(below, left)*. No **morphological** changes (*below, right*) could be observed when HUVECs were cultured with Fuco-NPs, and no obvious **internalization** was seen.



The loading of **rtPA**, which has a **fibrinolytic** activity and thus degrades the fibrin network of thrombi, was investigated by total protein quantification (BCA assay). As shown below with the arrows, optimal conditions for loading in Fuco-NPs could be determined, while minimizing drug loss during encapsulation.



Notably, when comparing Dex-NPs to Fuco-NPs for rtPA loading, it was shown that in similar conditions much more **rtPA was loaded in fucoidan-functionalized NPs**. This was already evidenced in microbubbles [8] decorated with this polysaccharide and demonstrates an undescribed interaction between these two molecules that favors rtPA loading. Finally, **release in PBS** under relevant conditions reached more than 80 % under 60 min for Fuco-NPs.



Validation of rtPA activity with the quantitative PefaFluor fluorescent assay indicates a **retained enzymatic activity**, while fibrinolytic assays with fibrin agar gels are underway.

Conclusion and perspectives

- **Polysaccharide nanoparticles** made of dextran and fucoidan were successfully synthesized with a **green chemistry** and robust protocol to obtain **monodisperse 312 ± 12 nm** NPs. These could be fully characterized, including fucoidan's ability to **target activated platelets** and thus stroke thrombi. These NPs do not show cytotoxicity and can be loaded with notably rtPA, the activity of which is being assessed for thrombolysis. This could adequately provide a solution for **efficient stroke treatment** while also reducing the toxic side effects of rtPA.
- The quantification and loading of investigated drug is still ongoing, which will be followed by the assessment of release kinetics in physiological conditions.
- After that, the activity of rtPA is measured with both a quantitative test and a stroke-relevant assay.
- Then, the loaded NPs will be checked by targeting assay to validate if the targeting capacity of fucoidan is retained.
- Thrombolytic activity of the NPs will be measured *in vitro*.
- Safety assessment and biodistribution will be measured *in vivo*.
- Activity of the loaded Fuco-NPs will be assessed with *in vivo* rodent stroke models (thrombin injection in the middle cerebral artery, or inserted monofilament to the middle cerebral artery [9]).
- Recanalization, ischemic tissue recovery and neurological improvement will be assessed.

References: [1] Cardiovascular diseases (CVDs). https://www.who.int/news-room/fact-sheets/detail/cardiovascular-diseases-(cvds) (2022) [2] Novotny J, *et al.* Neurology 94(22): 2346-2360 (2020) [3] Tsivgoulis G, *et al.* The Lancet Neurology 22(5): 418-429 (2023) [4] Thiebaut AM, *et al.* The Lancet Neurology 17(12): 1121-1132 (2018) [5] Chauvierre C, *et al.* Marine Drugs. 17(12):699 (2019) [6] Setyawati M, *et al.* Chem. Soc. Rev, 44, 8174-8199 (2015) [7] Zenych A, *et al.* Biomaterials 277: 121102 (2021) [8] Fournier L, *et* al. SFNano Annual Meeting, 2021 [9] Desilles J-P, *et al.* Stroke 46(11): 3241-8 (2015)

Acknowledgements: This Ph.D. project is performed under the supervision of Pr. Frédéric Chaubet and Dr. Cédric Chauvierre. Financial support was provided by the joint fundings of Ecole Doctorale Galilée, Université Sorbonne Paris Nord, and the ANR project "FightClot" ANR-20-CE18-0005-01. We acknowledge the LVTS as hosting institution and the ImagoSeine core facility of the Institut Jacques Monod, member of the France BioImaging infrastructure (ANR-10-INBS-04). All schemes were created using Biorender.com, and graphs and statistical analysis were performed on GraphPad Prism 9.

Contact information:
Thibault.de-la-taille@inserm.fr

ANNEX 10

Functionalized polysaccharide nanoparticles for a targeted treatment of ischemic strokes

T. de La Taille[1], P. Sarfati[1], R. Aid[1,2], F. Chaubet[1] and C. Chauvierre[1]
[1] INSERM U1148 - LVTS, UPC, USPN, Paris, France
[2] UMS34 FRIM, UPC, Paris, France
Contact: thibault.de-la-taille@inserm.fr

Cardiovascular diseases are held responsible for a third of all deaths worldwide, leading with heart attacks and strokes, among which the latter is responsible for over **12.2 million cases** each year [1]. Notably, 80 % of **strokes** are of ischemic nature, and the recommended care for this pathological blood clot (thrombus) is the quick systemic injection of a **fibrinolytic drug**, rtPA, which suffers from severe side effects, offers a short therapeutic window, and does not guarantee recanalization [2]. It was also shown that the more complex nature of thrombi impedes their lysis [3]. Our approach is therefore to design a biocompatible nanosystem targeting the thrombus, to deliver drugs for improved blood clot bursting and improved recovery.

The technology consists in a **nanoparticle** made from a **polysaccharide hydrogel**, crosslinked after formation of a water-in-oil **nanoemulsion**. The resulting nanogels contain a sulfated polysaccharide, fucoidan, which was demonstrated to have high affinity to P-selectin, a marker of activated platelets and endothelial cells and can thus be used for **thrombus targeting**. Then they are loaded with drugs (such as rtPA) by controlled adsorption to provoke the thrombolysis through localized fibrinolysis at the clot site without exerting systemic side effects.

Currently, the particles' **one-pot synthesis** has been optimized with critical downsizing from micro- to **300 nm** nanoparticles, by concurring improvements to the nanoemulsion and crosslinking process. These objects were fully characterized, and the **loading** of chosen therapeutic agents was assessed. The loaded nanoparticles are tested *in vitro* for thrombus targeting, drug release, efficacy, and cytotoxicity; then they will be assayed *in vivo* for thrombolytic efficacy, safety profile and biodistribution.

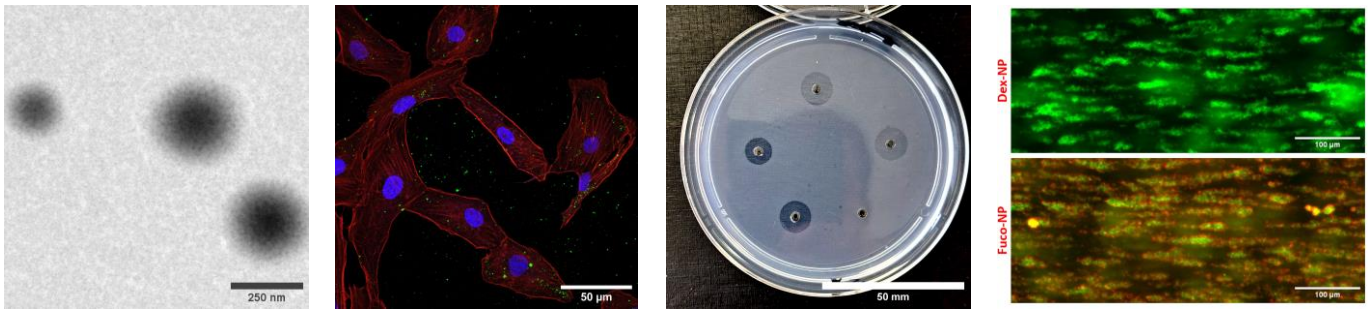


***Figure**: (left to right) TEM image of nanoparticles. Morphology of HUVECs incubated with nanoparticles. Fibrin agar plate assay for rtPA activity. In flow targeting assay.*

References

[1] Lindsay, M. P. *et al.* World Stroke Organization (WSO): Global stroke fact sheet 2019. Int. J. Stroke 14, 806–817 (2019).
[2] Campbell, B. C. V. *et al.* Ischaemic stroke. Nat. Rev. Dis. Primers 5, 70 (2019).
[3] Desilles, J.-P. *et al.* Composition and Organization of Acute Ischemic Stroke Thrombus: A Wealth of Information for Future Thrombolytic Strategies. Front. In N. 13, 870331 (2022).

ANNEX 11

Journées BIOMAT & MatSAN 2024
14-19 Janvier 2024
Super-Besse, France

FUNCTIONALIZED POLYSACCHARIDE NANOPARTICLES FOR A TARGETED TREATMENT OF ISCHEMIC STROKES

Thibault de La Taille[1], Pierre Sarfati[1], Rachida Aid[1,2], Frédéric Chaubet[1] and Cédric Chauvierre[1]
[1] INSERM U1148 - LVTS, UPC, USPN, Paris, France, [2] UMS34 FRIM, UPC, Paris, France

Keywords : Nanosystem; thrombolysis; hydrogel

ABSTRACT

Cardiovascular diseases are held responsible for a third of all deaths worldwide, leading with heart attacks and strokes, among which the latter is responsible for over **12.2 million cases** each year [1]. Notably, 80 % of **strokes** are of ischemic nature, and the recommended care for this pathological blood clot (thrombus) is the quick systemic injection of a **fibrinolytic drug**, rtPA, which suffers from severe side effects, offers a short therapeutic window, and does not guarantee recanalization [2]. It was also shown that the more complex nature of thrombi impedes their lysis [3]. Our approach is therefore to design a biocompatible nanosystem targeting the thrombus, to deliver drugs for improved blood clot bursting and improved recovery.

The technology consists in a **nanoparticle** made from a **polysaccharide hydrogel**, crosslinked after formation of a water-in-oil **nanoemulsion**. The resulting nanogels contain a sulfated polysaccharide, fucoidan, which was demonstrated to have high affinity to P-selectin, a marker of activated platelets and endothelial cells and can thus be used for **thrombus targeting**. Then they are loaded with drugs (such as rtPA) by controlled adsorption to provoke the thrombolysis through localized fibrinolysis at the clot site without exerting systemic side effects.

Currently, the particles' **one-pot synthesis** has been optimized with critical downsizing from micro- to **300 nm** nanoparticles, by concurring improvements to the nanoemulsion and crosslinking process. These objects were fully characterized, and the **loading** of chosen therapeutic agents was assessed. The loaded nanoparticles are tested *in vitro* for thrombus targeting, drug release, efficacy, and cytotoxicity; then they will be assayed *in vivo* for thrombolytic efficacy, safety profile and biodistribution.

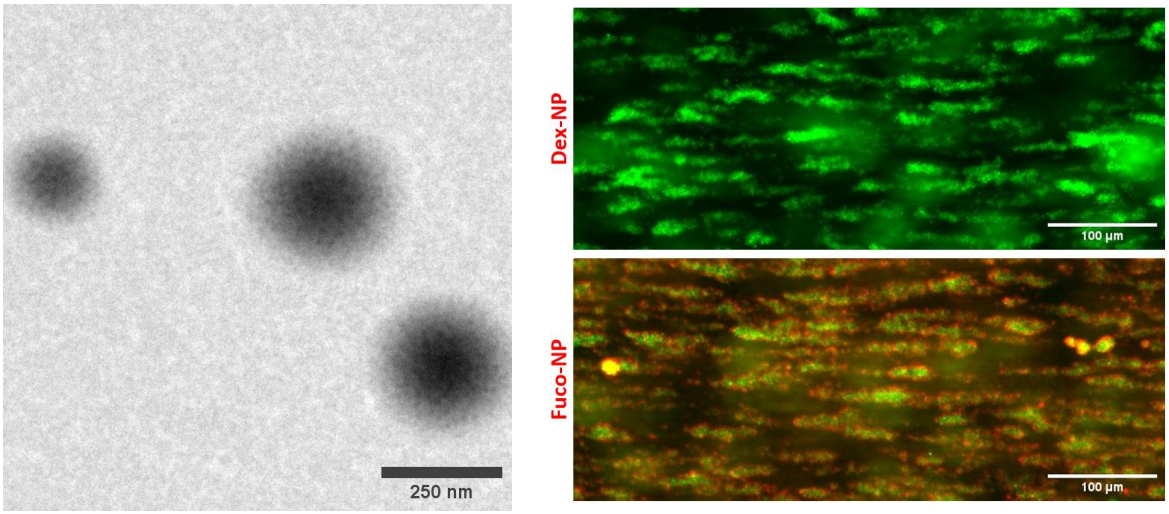


***Figure**: (left to right) TEM image of nanoparticles. In flow targeting assay showing only the targeted NPs (**red**) adhering to activated platelet aggregates (**green**).*

[1] Lindsay, M. P. et al. World Stroke Organization (WSO): Global stroke fact sheet 2019. Int. J. Stroke 14, 806–817 (2019).
[2] Campbell, B. C. V. et al. Ischaemic stroke. Nat. Rev. Dis. Primers 5, 70 (2019).
[3] Desilles, J.-P. et al. Composition and Organization of Acute Ischemic Stroke Thrombus: A Wealth of Information for Future Thrombolytic Strategies. Front. In N. 13, 870331 (2022).

ANNEX 12

Functionalized polysaccharide nanoparticles for a targeted treatment of ischemic strokes

T. de La Taille[1], P. Sarfati[1], R. Aid[1,2], G. Pavon-Djavid[1], F. Chaubet[1], C. Chauvierre[1]
[1] INSERM U1148 - LVTS, UPC, USPN, Paris, France
[2] UMS34 FRIM, UPC, Paris, France
Contact: thibault.de-la-taille@inserm.fr

Cardiovascular diseases are held responsible for a third of all deaths worldwide, leading with heart attacks and strokes, among which the latter is responsible for over **12.2 million cases** alone each year. Notably, 80 % of **strokes** are of ischemic nature, and the recommended care for this pathological blood clot (thrombus) is the systemic injection of a **fibrinolytic drug**, rtPA, which suffers from severe side effects, a short therapeutic window, and does not guarantee recanalization. It was also shown that the more complex nature of thrombi impedes their lysis, including DNA networks released from neutrophils (NETs). Our approach is therefore to design a biocompatible nanosystem targeting the thrombus, to deliver a combo of drugs for improved blood clot bursting and improved recovery.

The technology consists in **nanoparticles** made from a **polysaccharide hydrogel**, synthesized through a novel process through a water-in-oil **nanoemulsion**. The resulting nanogels contain a sulfated polysaccharide, fucoidan, which was demonstrated to have high affinity to P-selectin, a marker of activated platelets and endothelial cells and that can be used for **thrombus targeting**. They are loaded with drugs (rtPA and DNase I) by controlled adsorption and were studied for their improve thrombolysis.

These **300 nm** nanoparticles were fully characterized, including composition, stability, biocompatibility, in-flow behavior, targeting to thrombi, drug loading and release, and their retained activity. Notably, they demonstrated remarkable **stability** in various solvents and robust batch-to-batch synthesis. Finally, their **thrombolytic efficacy** was demonstrated with *in vitro* models and with an *in vivo* thrombosis model in mice. Overall, these nanoparticles open new perspectives for improving therapeutical care for thrombotic diseases.

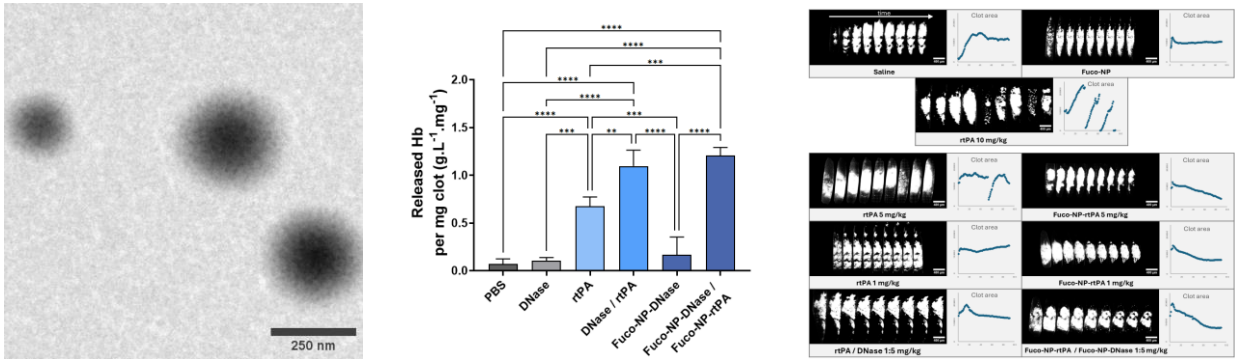


***Figure**: (left to right) TEM images of NPs. Static thrombolysis assay. Thrombi degradation from* in vivo *thrombolysis in mice.*

ANNEX 13

JCB

JOURNÉE DES JEUNES CHERCHEURS
DE BICHAT-BEAUJON

CERTIFICATE

Of the Best Oral Presentation

This document is proudly awarded to

Thibault De La Taille

The Young Researchers Bichat-Beaujon Association is proud to grant you this document, awarded on *Oct, 8th 2024*

Amélie VAUGRENTE

Head of the association

ANNEX 14

List of macros used in ImageJ:

Alcian_Overlay_mask.ijm
Alcian_treatment.ijm
Alcian_treatment_whole-organ.ijm
CD68_treatment.ijm
CD68_treatment_wholeorgan.ijm
Clot_areas.ijm
Flatten_images.ijm
Flatten_organ_images_andMake_Inserts.ijm
Format_JPEG_wholeorgans.ijm
Illustrate-montage_clots.ijm
MAsks_Analayse particles_organs.ijm
Merge_image_Alignclots.ijm
Multi_Alcian_treatment.ijm
Multi_Alcian_treatment_whole-organ.ijm
Multi_Alcian_treatment_whole-organ_REUSE-MASKS.ijm
Multi_Scale_make_bar_fornanozoomer.ijm
NETs_in_static-clot_analysis.ijm
Pearson_coloc.ijm
PlotprofileStack.ijm
Scale_make_bar_2X.ijm
Scale_make_bar_2X_forclots.ijm
Scale_make_bar_fornanozoomer.ijm
Single_Merge_image.ijm
Stack_measurements_Total intensity.ijm

_____Macros_____

Alcian_Overlay_mask.ijm

```
//This macro allows the display of positive blue staining over the original RGB image as yellow highlighted outlines

// VÃ©rifier s'il y a au moins deux images ouvertes
if (nImages() < 2) {
   showMessage("Erreur", "Vous devez avoir deux images ouvertes : une image RGB et un masque.");
   exit();
}

// Obtenir les deux images ouvertes

waitForUser("select the RGB image");
rgbinit = getTitle();

waitForUser("select the mask image");
maskinit = getTitle();
run("Duplicate...", "title=mask");
mask = getTitle();

selectImage(rgbinit);
run("Duplicate...", "title=rgb");
rgb = getTitle();

selectImage(mask);
run("Open");
run("Dilate");
run("Duplicate...", "title=outline");
run("Outline");
run("Dilate");
outline=getTitle();

selectImage(rgb);
run("Split Channels");

selectWindow(rgb + " (red)");
red = getTitle();
selectWindow(rgb + " (green)");
green = getTitle();
selectWindow(rgb + " (blue)");
blue = getTitle();

imageCalculator("Add create", red,outline);
imageCalculator("Add create", green,outline);

run("Merge Channels...", "c1=[Result of rgb (red)] c2=[Result of rgb (green)] c3=[rgb (blue)] create");
run("Stack to RGB");
rename(maskinit+"_overlay");
close(rgb);
close(mask);
//close(outline);
close("Composite");
close(rgb + " (green)");
close(rgb + " (red)");
```

_____

Alcian_treatment.ijm

```
//This macro is designed to create a mask of blue stained areas in Alcian Blue coloration images.

name = getTitle();
l=lengthOf(name);
name1=substring(name, 0, 10);
name2=substring(name, l-6, l-4);
print(name1+name2);
namef=name1+name2;
run("Duplicate...", "title="+namef);

run("Split Channels");
//selectImage(namef+" (blue)");
//selectImage(namef+" (green)");
//selectImage(namef+" (red)");

imageCalculator("Subtract create 32-bit", namef+" (red)",namef+" (blue)");
selectImage(namef+" (blue)");
close();
selectImage(namef+" (green)");
```

```
close();
selectImage(namef+" (red)");
close();

selectImage("Result of "+namef+" (red)");
getStatistics(areared, meanred, minred, maxred,
stdDevred);
print(stdDevred);
aux=0-stdDevred;
setThreshold(aux,
1000000000000000000000000000000, "raw");
run("Threshold...");
run("Convert to Mask", "background=Dark black
create");
run("Invert");
run("Measure");
```

Alcian_treatment_whole-organ.ijm

```
//This macro is designed to create a mask of blue
stained areas in Alcian Blue coloration images. It
is optimized to work with
//whole organ images as provided from
NDPViewer.

name = getTitle();
        l=lengthOf(name);
        name0=substring(name, 8, 10);
        name1=substring(name, 0, 10);
        namef=name1+"_whole_";
        print(namef);


                getDimensions(width, height,
channels, slices, frames);
                run("Duplicate...",
"title="+namef);
                //close(name);
                selectImage(namef);
                waitForUser("Select organ
region");

                getSelectionCoordinates(x, y);
                newImage("Mask_"+namef, "8-
bit black", width, height, 1);
                makeSelection("polygon", x, y);
                setColor(255);
                run("Fill", "slice");


                selectImage(namef);
                makeSelection("polygon", x, y);
                run("Clear Outside", "slice");
                run("Select None");
                run("Split Channels");
                imageCalculator("Subtract
create 32-bit", namef+" (red)",namef+" (blue)");
                selectImage("Result of
"+namef+" (red)");
                getStatistics(areared, meanred,
minred, maxred, stdDevred);
                print(stdDevred);
                aux=0-stdDevred;
                //aux=0;
                setThreshold(aux,
1000000000000000000000000000000, "raw");
                run("Threshold...");
                run("Convert to Mask",
"background=Dark black create");
                run("Invert");
                makeSelection("polygon", x, y);
                run("Measure");
                rename(namef + "_treated");
```

CD68_treatment.ijm

```
//This macro is designed to create a mask of
CD68 stained areas in CD68 coloration images.

pathOutput = getDirectory("Choose a folder for
saving treated CD68 images");

name = getTitle();
l=lengthOf(name);
//name1=substring(name, 0, 10);
name2=substring(name, 0, l-4);
//print(name1+name2);
namef=name2;
run("Select None");
run("Duplicate...", "title=test");

run("Split Channels");
//selectImage(namef+" (blue)");
//selectImage(namef+" (green)");
//selectImage(namef+" (red)");

imageCalculator("Add create 32-bit", "test
(blue)","test (red)");
rename("work1");
imageCalculator("Add create 32-bit", "test
(green)","work1");
rename("work2");
imageCalculator("Subtract create 32-bit", "test
(red)","test (blue)");
rename("work3");
setThreshold(-10,
1000000000000000000000000000000, "raw");
run("Threshold...");
run("Convert to Mask", "background=Dark black
create");
run("Invert");


selectImage("work2");
run("8-bit");
```

```
setThreshold(110,
1000000000000000000000000000000, "raw");
run("Threshold...");
run("Convert to Mask", "background=Dark black
create");
run("Invert");

selectImage("test (blue)");
close();
selectImage("test (green)");
close();
selectImage("test (red)");
close();
selectImage("work1");
close();
imageCalculator("Subtract create",
"work2","work3");
rename(namef+"work");
selectImage("work2");
close();
selectImage("work3");
close();
run("Analyze Particles...", "size=16-Infinity pixel
show=Masks summarize");
selectImage(namef+"work");
close();

selectImage("Mask of "+namef+"work");
rename("CD68_"+namef);

savePath = pathOutput + "CD68_"+namef;
saveAs("Tiff", savePath);

imageCalculator("Substract create",
name,"CD68_"+name);
rename("QCcheck1_CD68_"+namef);

savePath = pathOutput +
"QCcheck_CD68_"+namef;
saveAs("Tiff", savePath);

selectImage("CD68_"+name);
run("Invert");

imageCalculator("Substract create",
name,"CD68_"+name);
rename("QCcheck2_CD68_"+namef);

savePath = pathOutput +
"QCcheck2_CD68_"+namef;
saveAs("Tiff", savePath);
```

CD68_treatment_wholeorgan.ijm

//This macro is designed to create a mask of CD68 stained areas in CD68 coloration images, where the whole organ is displayed.

```
pathOutput = getDirectory("Choose a folder for
saving treated CD68 images");

name = getTitle();
l=lengthOf(name);
//name1=substring(name, 0, 10);
name2=substring(name, 0, l-4);
//print(name1+name2);
namef=name2;
run("Select None");
run("Duplicate...", "title=test");
waitForUser("Select the organ");
roiManager("add");
run("Clear Outside", "slice");


run("Split Channels");
//selectImage(namef+" (blue)");
//selectImage(namef+" (green)");
//selectImage(namef+" (red)");

imageCalculator("Add create 32-bit", "test
(blue)","test (red)");
rename("work1");
imageCalculator("Add create 32-bit", "test
(green)","work1");
rename("work2");
imageCalculator("Subtract create 32-bit", "test
(red)","test (blue)");
rename("work3");
setThreshold(-10,
1000000000000000000000000000000, "raw");
run("Threshold...");
run("Convert to Mask", "background=Dark black
create");
run("Invert");

selectImage("work2");
run("8-bit");
setThreshold(110,
1000000000000000000000000000000, "raw");
run("Threshold...");
run("Convert to Mask", "background=Dark black
create");
run("Invert");

selectImage("test (blue)");
close();
selectImage("test (green)");
close();
selectImage("test (red)");
close();
selectImage("work1");
close();
imageCalculator("Subtract create",
"work2","work3");
rename(namef+"work");
selectImage("work2");
close();
selectImage("work3");
```

```
close();
run("Analyze Particles...", "size=16-Infinity pixel show=Masks summarize");
selectImage(namef+"work");
close();

selectImage("Mask of "+namef+"work");
rename("CD68_"+namef);
roiManager("Select", 0);
savePath = pathOutput + "CD68_"+namef;
saveAs("Tiff", savePath);
roiManager("reset");
//imageCalculator("Substract create", name,"CD68_"+name);
//rename("QCcheck1_CD68_"+namef);

//savePath = pathOutput + "QCcheck_CD68_"+namef;
//saveAs("Tiff", savePath);

//selectImage("CD68_"+name);
//run("Invert");

//imageCalculator("Substract create", name,"CD68_"+name);
//rename("QCcheck2_CD68_"+namef);

//savePath = pathOutput + "QCcheck2_CD68_"+namef;
//saveAs("Tiff", savePath);
```

Clot_areas.ijm

```
//This macro is designed to analyze the clot area for previously aligned clots obtained from in vivo thrombolysis

run("Select None");
name = getTitle();
l=lengthOf(name);
namef=substring(name, 0, l-4);
print(namef);
run("Duplicate...", "title=test duplicate");
//run("Make Substack...", "channels=2");
run("Set Scale...", "distance=0 known=0 pixel=1 unit=pixel");
run("Scale Bar...", "width=100 height=100 horizontal bold overlay");
run("Split Channels");
selectImage("C1-test");
close();
selectImage("C2-test");
//close("\\Others");
setThreshold(0, 155, "raw");
run("Threshold...");
waitForUser("Select the thresholding parameters (do NOT apply, must work for all slices) \n Please note the values");
run("Convert to Mask", "background=Dark black create");
waitForUser("Make an ROI for the clot (working for all slices)");
run("Crop");
run("Invert", "stack");
run("Make Inverse");
run("Clear", "stack");
run("Select None");
Stack.getDimensions(width, height, channels, slices, frames);
for (j=1; j<=channels; j++){
        Stack.setChannel(j);

   for (i=1; i<=slices; i++){
                Stack.setSlice(i);
                run("Create Selection");
                run("Measure");
        }
};
rename("Clot-area_"+namef);
run("Select None");
selectImage("C2-test");
close();
selectImage("Clot-area_"+namef);
```

Flatten_images.ijm

```
//This macro is designed to flatten

path = getDirectory("Choose a folder for tiff image extraction");
filelist = getFileList(path);
for (i = 0; i < lengthOf(filelist); i++) {
   if (endsWith(filelist[i], ".tif")) {
      open(path + File.separator + filelist[i]);
      name = getTitle();
                l=lengthOf(name);
                name2=substring(name, 0, l-4);
                print(name2);
                Overlay.flatten;
                selectImage(name2+"-1.tif");
                saveAs("Tiff", path+"\\Flattened\\Flat_"+name2);
                close("*");
   }
}
```

Flatten_organ_images_andMake_Inserts.ijm

```
//This macro is used to make zoomed binary masks for presentation of previously obtained binary masks of alcian blue or CD68 colorations
//of whole organs, saved with their respective selection as used in the analysis process.
```

```
path = getDirectory("Choose a folder for tiff BA image extraction");
filelist = getFileList(path);
for (i = 0; i < lengthOf(filelist); i++) {
   if (endsWith(filelist[i], ".tiff")) {
      open(path + File.separator + filelist[i]);
      name = getTitle();
                  l=lengthOf(name);
                  name2=substring(name, 0, l-4);
                  print(name2);

                  roiManager("add");

                  //run("Measure");
                  run("Select None");

                  run("Duplicate...", "title=test");


                  selectImage("test");

                  //depending if the mask was saved black on white or reverse
                  run("Invert");

                  roiManager("Select", 0);
                  run("Make Inverse");

                  setForegroundColor(140, 140, 140);

                  run("Fill", "slice");

                  run("Set Scale...", "distance=220 known=50 unit=um");
                  run("Scale Bar...", "width=1000 height=50 thickness=200 font=500 color=Black bold overlay");

                  roiManager("reset");


                  selectImage("test");

                  makeRectangle(1500, 1500, 5500, 4500);
                  waitForUser("Position the selection");
                  run("Duplicate...", "title=test2");

                  run("Set Scale...", "distance=220 known=50 unit=um");

                  // for 10X images (saved at 40X resolution)
                  run("Scale Bar...", "width=200 height=100 thickness=50 font=100 background=[Dark Gray] bold overlay");

                  // for whole organs ((saved at 40X resolution)
                  //run("Scale Bar...", "width=1000 height=50 thickness=100 font=400 color=Black bold overlay");
                  Overlay.flatten;
                  selectImage("test2-1");
                  saveAs("Tiff", path+"\\Flattened\\Flat_"+name2);
                  close("*");
   }
}
```

Format_JPEG_wholeorgans.ijm

```
//This macro is designed to create JPEG images for whole organ binary masks obtained from analysed whole organ blue alcian or CD68 colorations.

name = getTitle();
l=lengthOf(name);
pathOutput = getDirectory("Choose a folder to save the resulting JPEG");
name2=substring(name, 0, l-4);
namef="JPG_"+name2;


roiManager("add");

run("Measure");
run("Select None");

run("Duplicate...", "title=test");
close(name);

selectImage("test");

//depending if saved black on white or reverse
run("Invert");

roiManager("Select", 0);
run("Make Inverse");

setForegroundColor(140, 140, 140);

run("Fill", "slice");

run("Set Scale...", "distance=220 known=50 unit=um");
run("Scale Bar...", "width=1000 height=50 thickness=200 font=500 color=Black bold overlay");

roiManager("reset");

run("Flatten");
rename(namef);
```

```
close("test");
selectImage(namef);
//run("Set Scale...", "distance=300 known=1 unit=inch");
savePath = pathOutput + namef;
saveAs("JPEG", savePath);
close();
```

Illustrate-montage_clots.ijm

```
//This macro is designed to work with binary masks of clot from in vivo thrombolysis, in order to make montage of
//clot evolution through time.

name = getTitle();
run("Make Montage...", "columns=9 rows=1 scale=0.25 increment=10");
run("Scale Bar...", "width=200 height=200 horizontal bold overlay");
rename("Montage_"+name);

name = getTitle();
//run("Flatten");
//rename("Flat-"+name);
//run("Save");
newImage("black", "8-bit black", 873, 348, 1);
selectImage(name);
run("Copy");
selectImage("black");
run("Paste");
run("Set Scale...", "distance=1849 known=10000 unit=um");
run("Scale Bar...", "width=400 height=200 thickness=10 font=20 bold overlay");
rename("scaled "+name);
run("Save");
run("Flatten");
rename("Flat_scaled_"+name);
run("Save");
```

MAsks_Analayse particles_organs.ijm

```
path = getDirectory("Choose a folder for tiff masks to be analyzed");
filelist = getFileList(path);
for (i = 0; i < lengthOf(filelist); i++) {
   if (endsWith(filelist[i], ".tiff")) {
      open(path + File.separator + filelist[i]);
      name = getTitle();
                  l=lengthOf(name);

                  run("Set Scale...", "distance=220 known=50 unit=um");
                  //run("Scale Bar...", "width=200 height=50 thickness=30 font=80 color=Black bold overlay");

                  run("Scale Bar...", "width=1000 height=50 thickness=200 font=500 color=White bold overlay");

                  run("Analyze Particles...", "size=5-Infinity pixel display clear summarize");
                  waitForUser;
                  close();
   };
};
```

Merge_image_Alignclots.ijm

```
//This macro is used to format, align and prepare TIFF images from videos acquired with intravital macroscopy of in vivo thrombolysis

//To be used when importing images as separate and not as stacks

//run("Images to Stack", "name=red title=channel001 use");
//run("Images to Stack", "name=green title=channel000 use");
//run("Merge Channels...", "c1=red c2=green create");

//new processing
path = getDirectory("Choose a folder for image extraction");
list = getFileList(path);
l=lengthOf(path);
date=substring(path, l-15, l-7);
print(date);
for (i = 0; i < list.length; i++) {
   //File.openSequence(path+list[i]+"Default/");
   open(path+list[i]+"Default/");
   print(list[i]);

      //waitForUser("Verify that you have a total of 182 slices; else, change variables");
      rename("Default");
      run("Make Substack...", "slices=1-91");
      selectImage("Default");
      run("Make Substack...", "slices=92-182");
      run("Merge Channels...", "c1=[Substack (92-182)] c2=[Substack (1-91)] create");
      run("Show All");
      selectImage("Default");
      close();

      rename(date+"_S"+(i+1)+".tiff");
```

```
	Stack.setChannel(1);
	run("Enhance Contrast", "saturated=0.35");
	Stack.setChannel(2);
	run("Enhance Contrast", "saturated=0.35");
};
waitForUser("Before saving, check that 1st channel, is red, and is NPs. Else, arrange.");
waitForUser("Do you want to align all images? WARNING, it takes some time");
titleList=getList("image.titles");
count = lengthOf(titleList);
for (s = 0; s < count; s++) {
	print(titleList[s]);
	selectImage(titleList[s]);
	run("Linear Stack Alignment with SIFT MultiChannel", "registration_channel=2 initial_gaussian_blur=1.60 steps_per_scale_octave=3 minimum_image_size=64 maximum_image_size=1024 feature_descriptor_size=4 feature_descriptor_orientation_bins=8 closest/next_closest_ratio=0.92 maximal_alignment_error=25 inlier_ratio=0.05 expected_transformation=Rigid interpolate");
}
```

Multi_Alcian_treatment.ijm

```
// This macro is used to automate the treatment of blue alcian images in order to analyze blue staining and provide quality Control images.

path = getDirectory("Choose a folder for tiff BA image extraction");
list = getFileList(path);

pathOutput = getDirectory("Choose a folder to save the resulting masks");

for (i = 0; i < list.length; i++) {
   open(path+list[i]);
   name = getTitle();
	l=lengthOf(name);
	name0=substring(name, 8, 10);
	name1=substring(name, 0, 10);
	name2=substring(name, l-6, l-4);
	namef=name1+name2;
	print(namef);
	if (name0 == "BA") {
		print(list[i]);
		run("Duplicate...", "title="+namef);

		run("Split Channels");

		imageCalculator("Subtract create 32-bit", namef+" (red)",namef+" (blue)");

		selectImage(namef+" (blue)");
		//close();
		selectImage(namef+" (green)");
		//close();
		selectImage(namef+" (red)");
		//close();

		selectImage("Result of "+namef+" (red)");
		getStatistics(areared, meanred, minred, maxred, stdDevred);
		print(stdDevred);
		//aux=0-stdDevred;
		aux=0;
		setThreshold(aux, 10000000000000000000000000000000, "raw");
		run("Threshold...");
		run("Convert to Mask", "background=Dark black create");
		run("Invert");
		run("Measure");
		savePath = pathOutput + namef + "_treated.tiff";
		saveAs("Tiff", savePath);
		//mask overlayed mask for rgb images
		//waitForUser("select the RGB image");
		rgbinit = name;

		//waitForUser("select the mask image");
		maskinit = getTitle();
		run("Duplicate...", "title=mask");
		mask = namef + "_treated.tiff";

		selectImage(rgbinit);
		run("Duplicate...", "title=rgb");
		rgb = getTitle();

		selectImage(mask);
		run("Open");
		run("Dilate");
		run("Duplicate...", "title=outline");
		run("Outline");
		run("Dilate");
		outline=getTitle();

		selectImage(rgb);
		run("Split Channels");

		selectWindow(rgb + " (red)");
		red = getTitle();
		selectWindow(rgb + " (green)");
		green = getTitle();
		selectWindow(rgb + " (blue)");
```

```
                blue = getTitle();

                imageCalculator("Add create",
red,outline);
                imageCalculator("Add create",
green,outline);

                run("Merge Channels...",
"c1=[Result of rgb (red)] c2=[Result of rgb
(green)] c3=[rgb (blue)] create");
                run("Stack to RGB");
                rename(maskinit+"_overlay");
                savePath = pathOutput + namef
+ "_overlay.tiff";
                saveAs("Tiff", savePath);

        };
        close("*");
};
```

Multi_Alcian_treatment_whole-organ.ijm

```
//This macro is used to automate the treatment
of Blue Alcian tiff images of whole organs in
order to analyze blue staining and save the
resulting binary mask.

path = getDirectory("Choose a folder for tiff BA
image extraction");
list = getFileList(path);

pathOutput = getDirectory("Choose a folder to
save the resulting masks");

for (i = 0; i < list.length; i++) {
   open(path+list[i]);
   name = getTitle();
        l=lengthOf(name);
        name0=substring(name, 8, 10);
        name1=substring(name, 0, 10);
        namef=name1+"_whole_";
        print(namef);

                print(list[i]);
                getDimensions(width, height,
channels, slices, frames);
                run("Duplicate...",
"title="+namef);
                close(name);
                selectImage(namef);
                waitForUser("Select organ
region");

                getSelectionCoordinates(x, y);
                newImage("Mask_"+namef, "8-
bit black", width, height, 1);
                makeSelection("polygon", x, y);
                setColor(255);
                run("Fill", "slice");
                saveAs("Tiff", pathOutput
+"Mask_"+ namef);
                close();

                selectImage(namef);
                makeSelection("polygon", x, y);
                run("Clear Outside", "slice");
                run("Select None");
                run("Split Channels");
                imageCalculator("Subtract
create 32-bit", namef+" (red)",namef+" (blue)");

                selectImage("Result of
"+namef+" (red)");
                getStatistics(areared, meanred,
minred, maxred, stdDevred);
                print(stdDevred);
                aux=0-stdDevred;
                //aux=0;
                setThreshold(aux,
10000000000000000000000000000000, "raw");
                run("Threshold...");
                run("Convert to Mask",
"background=Dark black create");
                run("Invert");
                makeSelection("polygon", x, y);
                run("Measure");
                savePath = pathOutput + namef
+ "_treated.tiff";
                saveAs("Tiff", savePath);
                //mask overlayed mask for rgb
images
                //waitForUser("select the RGB
image");

                //rgbinit = name;

                //waitForUser("select the mask
image");
                //maskinit = getTitle();
                //run("Duplicate...",
"title=mask");
                //mask = namef + "_treated.tiff";

                //selectImage(rgbinit);
                //run("Duplicate...", "title=rgb");
                //rgb = getTitle();

                //selectImage(mask);
                //run("Open");
                //run("Dilate");
                //run("Duplicate...",
"title=outline");
                //run("Outline");
                //run("Dilate");
                //outline=getTitle();

                //selectImage(rgb);
                //run("Split Channels");
```

```
                //selectWindow(rgb + " (red)");
                //red = getTitle();
                //selectWindow(rgb + " (green)");
                //green = getTitle();
                //selectWindow(rgb + " (blue)");
                //blue = getTitle();

                //imageCalculator("Add create", red,outline);
                //imageCalculator("Add create", green,outline);

                //run("Merge Channels...", "c1=[Result of rgb (red)] c2=[Result of rgb (green)] c3=[rgb (blue)] create");
                //run("Stack to RGB");
                //rename(maskinit+"_overlay");
                //savePath = pathOutput + namef + "_overlay.tiff";
                //saveAs("Tiff", savePath);

        close("*");
};
```

Multi_Alcian_treatment_whole-organ_REUSE-MASKS.ijm

```
//This macro is used to automate the treatment of Blue Alcian tiff images of whole organs in order to analyze blue staining and save the resulting binary mask.
//This specific implementation can be used with previously provided selections for whole organs.

path = getDirectory("Choose a folder for tiff BA image extraction");
list = getFileList(path);

pathOutput = getDirectory("Choose a folder to find the organ selection masks and save the resulting binary masks");
roiManager("reset");

for (i = 0; i < list.length; i++) {
   open(path+list[i]);
   name = getTitle();
        l=lengthOf(name);
        name0=substring(name, 8, 10);
        name1=substring(name, 0, 10);
        namef=name1+"_whole_stdev2_";
        print(namef);

                getDimensions(width, height, channels, slices, frames);
                run("Duplicate...", "title="+namef);
                close(name);
                selectImage(namef);

                open(pathOutput+"Mask_"+ name1+"_whole_.tif");
                setThreshold(1, 255, "raw");
                run("Create Selection");
                roiManager("add");

                selectImage(namef);
                roiManager("Select", 0);

                run("Clear Outside", "slice");
                run("Select None");


                selectImage(namef);
                run("Split Channels");
                close(namef+" (green)");
                imageCalculator("Subtract create 32-bit", namef+" (red)",namef+" (blue)");

                selectImage("Result of "+namef+" (red)");
                getStatistics(areared, meanred, minred, maxred, stdDevred);
                print(stdDevred);
                aux=0-stdDevred*0.5;
                //aux=-1;
                setThreshold(aux, 1000000000000000000000000000000, "raw");
                run("Threshold...");
                run("Convert to Mask", "background=Dark black create");
                run("Invert");

                roiManager("Select", 0);

                run("Measure");


                savePath = pathOutput + namef + "_treated.tiff";
                saveAs("Tiff", savePath);
                //mask overlayed mask for rgb images
                //waitForUser("select the RGB image");

                //rgbinit = name;

                //waitForUser("select the mask image");
                //maskinit = getTitle();
                //run("Duplicate...", "title=mask");
                //mask = namef + "_treated.tiff";

                //selectImage(rgbinit);
                //run("Duplicate...", "title=rgb");
```

```
                //rgb = getTitle();

                //selectImage(mask);
                //run("Open");
                //run("Dilate");
                //run("Duplicate...",
"title=outline");
                //run("Outline");
                //run("Dilate");
                //outline=getTitle();

                //selectImage(rgb);
                //run("Split Channels");

                //selectWindow(rgb + " (red)");
                //red = getTitle();
                //selectWindow(rgb + "
(green)");
                //green = getTitle();
                //selectWindow(rgb + " (blue)");
                //blue = getTitle();

                //imageCalculator("Add create",
red,outline);
                //imageCalculator("Add create",
green,outline);

                //run("Merge Channels...",
"c1=[Result of rgb (red)] c2=[Result of rgb
(green)] c3=[rgb (blue)] create");
                //run("Stack to RGB");
                //rename(maskinit+"_overlay");
                //savePath = pathOutput +
namef + "_overlay.tiff";
                //saveAs("Tiff", savePath);

        roiManager("reset");
        close("*");
};
```

Multi_Scale_make_bar_fornanozoomer.ijm

//This macro can be used for adding scale bars to nanozoomer obtained images (40X magnification).

```
path = getDirectory("Choose a folder for tiff BA
image extraction");
list = getFileList(path);

for (i = 0; i < list.length; i++) {
   open(path+list[i]);
   name = getTitle();
        l=lengthOf(name);
        run("Set Scale...", "distance=220
known=50 unit=um");
        // for 10X images (saved at 40X
resolution)
        run("Scale Bar...", "width=200 height=50
thickness=30 font=80 color=Black bold
overlay");

        // for whole organs ((saved at 40X
resolution)
        //run("Scale Bar...", "width=1000
height=50 thickness=100 font=400 color=Black
bold overlay");
        run("Save");
        close();
};
```

NETs_in_static-clot_analysis.ijm

//This macro is used to measure the total fluorescence of clots for NET content quantification.

```
path = getDirectory("Choose a folder for tiff NEt
clot image extraction");
list = getFileList(path);

for (i = 0; i < 13; i++) {

                open(path+list[i]);
                run("Enhance Contrast",
"saturated=0.35");
                waitForUser("Make a selection
detouring the clot");
                roiManager("add");
                run("Measure");
                close("*");


                open(path+list[i+13]);
                run("Enhance Contrast",
"saturated=0.35");
                roiManager("Select", 0);
                waitForUser;
                run("Measure");
                close("*");


};
```

Pearson_coloc.ijm

//This macro is designed to measure colocalization in in flow targeting experiments, based on 10x1 mosaic images (whole channels).

```
//PSF size: 6,6
Stack.setDisplayMode("composite");
Stack.setActiveChannels("011");
```

```
run("Duplicate...", "title=TEST duplicate channels=2-3");
run("Split Channels");
selectWindow("C1-TEST");
run("Measure");
selectWindow("C2-TEST");
run("Measure");
run("Colocalize...", "image1=C1-TEST image2=C2-TEST psfsizestring=6,6 icq=false ktau=false pearsons=true mtkt=false");
```

PlotprofileStack.ijm

//This macro is used to measure the distribution profile of particles across a microfluidic channel in flow.

```
run("Duplicate...", "title=test duplicate channels=1");
makeLine(208, 69, 208, 387);
waitForUser("Position the line to a new cross-section of the channel");


    if (!(selectionType()==0 || selectionType==5 || selectionType==6))
        exit("Line or Rectangle Selection Required");
    setBatchMode(true);

    run("Plot Profile");
    Plot.getValues(x, y);
    run("Clear Results");
    for (i=0; i<x.length; i++)
        setResult("x", i, x[i]);
    close();

    n = nSlices;
    for (slice=1; slice<=n; slice++) {
        showProgress(slice, n);
        setSlice(slice);
        profile = getProfile();
        sliceLabel = toString(slice);
        sliceData = split(getMetadata("Label"),"\n");
        if (sliceData.length>0) {
            line0 = sliceData[0];
            if (lengthOf(sliceLabel) > 0)
                sliceLabel = sliceLabel+ " ("+ line0 + ")";
        }
        for (i=0; i<profile.length; i++)
            setResult(sliceLabel, i, profile[i]);
    }
    setBatchMode(false);
    updateResults;
```

Scale_make_bar_2X.ijm

//This macro is used to make the scale bar for images acquired on the intravital macroscope at 2X magnification.

```
//2X zoom on -1 macroscope: 1813 pixels for 2.451 mm

run("Set Scale...", "distance=1813 known=2451 unit=um");
run("Scale Bar...", "width=500 height=200 thickness=30 font=50 bold overlay");
//run("Save");
//close();
```

Scale_make_bar_2X_forclots.ijm

```
//2X zoom on -1 macroscope: 1813 pixels for 2.451 mm

run("Set Scale...", "distance=1813 known=2451 unit=um");
run("Scale Bar...", "width=200 height=200 thickness=10 font=30 bold overlay");
run("Save");
close();
```

Scale_make_bar_fornanozoomer.ijm

//This macro is used to make the scale bar for nanozoomer acquired images (40X magnification).

```
run("Set Scale...", "distance=220 known=50 unit=um");

run("Scale Bar...", "width=200 height=50 thickness=30 font=80 color=Black bold overlay");


//run("Scale Bar...", "width=1000 height=50 thickness=200 font=500 color=White bold overlay");
run("Save");
//close();
```

Single_Merge_image.ijm

//To be used when importing images as separate and not as stacks instead of the Merge_image_Alignclots.ijm.

```
//run("Images to Stack", "name=red title=channel001 use");
//run("Images to Stack", "name=green title=channel000 use");
//run("Merge Channels...", "c1=red c2=green create");

//new processing
waitForUser("Verify that you have a total of 182 slices; else, change variables");
run("Make Substack...", "slices=1-91");
selectImage("Default");
run("Make Substack...", "slices=92-182");
run("Merge Channels...", "c1=[Substack (92-182)] c2=[Substack (1-91)] create");
run("Show All");
selectImage("Default");
close();
waitForUser("Before saving, check that 1st channel, is red, and is NPs. Else, arrange.");
```

Stack_measurements_Total intensity.ijm

```
//This macro can be used to make total fluorescence measurements on all frames of a fluorescence videos with multiple channels.
        //For instance, it is used on in vivo thrombolysis images to measures targeting of NPs on clots.

waitForUser("Make an ROI for the clot (working for all slices), or similar object to be analyzed");
Stack.getDimensions(width, height, channels, slices, frames);
print(channels);
for (  i=1; i<=channels; i++){

   for (j=1; j<=slices; j++){
        Stack.setChannel(i);
                Stack.setSlice(j);
         run("Measure");
        }
};
```
